The Development Of A Top-Surface Mounted Technique For the Measurement Of Moisture Profiles In Drying Concrete Slabs

J.W. Lovell-Smith

A Thesis submitted in fulfilment of the requirement for the Degree of Doctor of Philosophy in Chemical and Process Engineering to the University of Canterbury

University of Canterbury

February, 1997

for Jennie

ACKNOWLEDGMENTS

I could not have done this work without the support of my family. I especially thank my wife, Jennie, and my older children, Rita and Eden. They shouldered loads I should have otherwise carried and enabled me to disappear off for long periods to attend to various demands of the project and the writing of this thesis.

Many people were involved in this project, to all of whom I wish to express my gratitude.

Thanks go first to my Supervisor, Professor Roger Keey, of the Department of Chemical and Process Engineering, who guided me and oversaw most of the experimental work and enabled me access to large amounts of work space (then in short supply).

I have had the benefit also of four Associate Supervisors. To Dr. Basil Kerdemelidis of the Department of Electrical and Electronic Engineering, my thanks for many encouraging, interesting and fruitful talks. I thank also, my two supervisors in the Department of Physics and Astronomy, Dr. Colin Hooker and Dr. Bob Bennett who provided much advice and direction and kept a steady train of useful references and ideas headed in my direction. Malcolm Cunningham, of BRANZ was at all times a source of guidance and advice, keeping the project on track during his frequent trips from Wellington and also providing a steady stream of relevant material.

Technicians from four university departments have added their considerable expertise. The computerised version of the resistivity meter was built by Roger Govind, Ross Ritchie and Geoff Graham, technical staff from the Department of Physics and Astronomy. Dermott Sallis of the Department of Electrical and Electronic Engineering gave me much useful advice in the building of the manual version of the meter. George Clarke of Civil Engineering was instrumental in the construction and pouring of the early slabs and cylinders. Much of the technical work was carried out by Warwick Earl and Ron Boyce of the Department of Chemical and Process Engineering. I am particularly indebted to Ron Boyce with whom I was able to refine my technical vision, and who created out of custom wood, brass, stainless steel and plastic, what had hitherto been merely ideas.

For providing most of the concrete used, I thank Finn MacKenzie and Paul Jones of Firth Industries Ltd.

Finally, I must thank the Building Research Association of New Zealand who inspired and funded this project.

CONTENTS

ABSTRACT

Failure of surface coatings on concrete slabs can occur if there is excess moisture in the slab. There is a need for reliable standard measurement procedures to determine whether a concrete slab is dry enough to have a surface coating applied. Accordingly the Building Research Association of New Zealand commissioned this project to develop a top-surface mounted resistive technique for measuring moisture profiles in concrete flooring slabs.

Geophysical vertical electric sounding (VES) techniques have been adapted to determine resistivity profiles in concrete slabs through mathematical inversion of apparent resistivity readings made at the surface. Relative-humidity profiles may then be extracted when the relationship between relative-humidity and resistivity has been determined.

The project has involved the development and testing of:

- 'wet' electrodes (ie. wooden electrodes wetted with a conducting solution) which are able to reduce and stabilise the otherwise high, variable and non-reproducible electrode-concrete interface resistance,
- a VES instrument comprising an array of electrodes multiplexed to a computer controlled resistivity meter and operated through a graphical user interface and software able to 'invert' the apparent resistivity curves determined,
- embedded electrode systems for independent measurement of resistivity profiles for use in evaluating the VES instrument and technique and determining the relationship between relative humidity and resistivity.

Resistivity ρ and relative-humidity ψ profiles have been measured using a range of concrete samples and the relationship between them, away from the dry surface region, has been found to be described by the equation $\psi = -a\ln(\rho) + b$ where a and b are coefficients that are functions of depth and the age of the concrete.

The ability of the VES instrument to determine resistivity profiles from non-reinforced slabs is demonstrated in this report. However reinforcing at shallow depths (30 mm below the surface) does not allow profile recovery and makes commercialisation of the instrument unlikely. It is suggested that the embedded electrode systems developed here, provide a convenient and inexpensive method of directly measuring resistivity profiles from which relative-humidity profiles may be extracted with a high degree of precision.

1. Introduction

Surface coatings are commonly used on flooring slabs. Failure of the coating can occur if there is excess moisture in the slab. Several methods are presently used to estimate the internal moisture condition of a slab, but "the coating and flooring industry has not yet agreed on a measurement instrument or settled on measurement procedures that give repeatable and universally acceptable results"(Harriman 1995). Neither are there clear guidelines as to what constitutes a sufficiently dry slab, since moisture may be held in concrete with varying energy depending on the pore structure. The pore structure (characterised by the porosity - a measure of the volume fraction of pore space - and the pore-size-distribution) can vary widely with

1) variation in water-to-cement ratios,
2) variation in cement-to-sand-to-aggregate ratios,
3) variation in the density of the poured mix and
4) variation in curing conditions.

Excess moisture in concrete can arise through two main causes. The wicking action of porous concrete resting on bare soil or exposed to rain or other sources of moisture, can lead to unacceptable moisture levels elsewhere, for example on the top surface of a slab or the inside surface of a wall. Prevention or cure of this type of problem involves interposing a moisture-impermeable barrier between the bare soil and the concrete, or painting an impervious coating on exposed walls. The second source is water remaining after pouring and curing of concrete, which can be considered as a sometimes necessary by-product, since sufficient water is required for mixing and placing of the wet concrete. This water is in excess of the requirements for hydration, although even more water may be sprayed on the surface to ensure adequate hydration of surfaces most exposed to the elements. Over the course of time, exposure to the air will remove substantial quantities of moisture through drying. Nevertheless, steps must be taken to ensure that before exposed surfaces are covered, the free water remaining is at acceptable levels.

Floor surfacing materials are especially in danger of failure, since, for slabs resting on a moisture-impermeable barrier, drying may take place from the top surface only. Under excess moisture conditions "parquetry swell and buckles, and the usual adhesives for P.V.C., linoleum and rubber flooring lose their bond to the concrete so that the surfacing

materials curl and blister. Where sufficiently moisture resistant adhesives are used to prevent detachment, P.V.C. flooring may be swollen and softened above minor imperfections in the adhesive layer" (Waters,1974).

While an old flooring industry rule of thumb is to allow one month for every inch of concrete thickness for concrete to dry before laying a floor coating, this rule is crude and does not take into account local drying conditions. Harriman (1995) discusses common techniques presently used to determine when the concrete has reached the desired level of dryness (see Table 1-1). One type of technique involves the sealing of an area of the surface and allowing moisture from the slab to enter the sealed space. The amount of moisture entering the space reflects the moisture condition of the concrete. The moisture may be visually detected as condensation or may be measured as the relative-humidity in the air space. Placement of a highly hygroscopic material such as calcium chloride in the space enables measurement of the desorption rate of water from the floor.

Other techniques utilise the effect of moisture in the slab on an adhesive or a primer placed on the floor for 24 hours. A good bond and state of the adhesive or sealant is taken to indicate acceptable moisture levels.

Electrical resistance methods measure the electrical resistance between two electrodes placed on the surface or set into holes drilled in the concrete. Alternately electrical impedance or capacitance may be measured using an electromagnetic field set up by an instrument placed on the surface. To interpret readings, generic data to correlate measured resistance or impedance to acceptable moisture conditions must be provided for the range of concretes under test. (Attenuation of microwave signals has been used as a guide to the moisture content of walls, but, as it relies on transmission of the signal, has not been used on flooring slabs).

Finally, there are destructive methods. These require the removal of a sample of concrete which is treated to measure its moisture content (eg. to be weighed and dried), or else holes are drilled into the concrete into which relative-humidity probes or resistance meter electrodes are inserted.

The definition of an acceptable moisture level depends on the coating or covering to be applied and the method of measurement. Most specifications allow no more than 5% and sometimes no more than 3% free water in the concrete. The Rubber Manufacturers Association (RMA) specify a moisture desorption rate of 3 lb water / 24 hr / 1000 ft^2

(equivalent to 1.44 kg water / 24 hr / 100 m^2) of exposed concrete or less as indicating safe moisture levels for application of most flooring adhesives.

'For most mixtures of concrete, at a 5% moisture content at ...21°C...the material will neither absorb nor desorb moisture if the air above the surface is 75% RH. This is the basis of the standards for measuring moisture in the United Kingdom" (Harriman, 1995). Concrete supporting a relative-humidity of less than 75% in the sealed space is assumed to have a moisture content of less than 5% in the surface region.

These methods focus on the immediate surface regions of the slab. The shallow regions will vary rapidly under extreme atmospheric conditions and do not necessarily reflect the deeper moisture condition of the slab. Furthermore the methods offer varied assurance that subsequent floor coating or covering will not fail There is trade between accuracy and safety, less accurate methods requiring greater safety margins. More research is needed to refine the specifications required by coating and covering manufacturers and to identify the moisture content profiles defined by the existing specifications. Ideally, a complete picture of the moisture and its mobility within the slab is required to enable surface coating as soon as possible after pouring.

The goal of this project was to design and develop a top-surface-mounted instrument able to measure complete moisture-content profiles in concrete floor slabs and to assess its practicality for field use. Following a literature survey a geophysical technique known as vertical electric sounding (VES) was chosen as the measuring method, wherein a resistivity profile would be obtained. Relative humidity was chosen as the main measure of moisture-content. The VES technique was to be adapted to the particular requirements and limitations of concrete floor slabs, and concurrently, calibration procedures were to be established so that resistivity-relative-humidity relationships could be empirically determined for a wide range of concrete mixes and curing conditions.

An overview of the physical, chemical and electrical properties of concrete is given in the next two chapters of this report. The bulk of this report covers the development and testing of the VES technique and instumentation (Chapters 5, 6 and 7). Calibration of the relative-humidity-resistivity reationship (Chapter 10) required techniques for independent measurement of resistivity and relative-humidity (Chapters 8 and 9 respectively). An outline of the experimental part of the project is presented in Chapter 4.

Table 1-1: Methods of concrete moisture measurement in current use

	Sealed space methods	Measurement technique	Quality
1)	Plastic sheet Harriman (1995)	Visual inspection of condensation, darkening of concrete surface	Simple, lowest cost, non-destructive, subjective measurement, minimum time 16 hours, affected by temperature swings, 'worst-case indicator'
2)	Rubber Manufacturers Association (RMA Test method) Harriman (1995)	Mass change in quantity of hygroscopic salt sealed in the space, used to determine rate of desorption	Low cost, nondestructive, minimum 72 hours + transit time to laboratary, reliable
3)	Relative Humidity (RH) method Harriman (1995)	Measurement of relative-humidity using RH probe in sealed space	Low cost, non-destructive, measurement, minimum time 16 hours, affected by temperature swings and surface curing agents
	Other methods	**Measurement technique**	**Quality**
4)	Carbide method Harriman (1995)	Pressure of acetylene gas produced by grinding concrete samples with calcium carbide in a sealed container	Fast, repeatable, acccurate, destructive, accepted by standards authorities in many countries
5)	Resistance method Harriman (1995)	Determination of resistivity between two electrodes at or below surface.	Fast, repeatable. Requires accurate calibration for particular concrete mix.
6)	Capacitance method Harriman (1995)	Measurement of capacitance using instrument placed on surface	Fast, repeatable, reasonable cost. Requires accurate calibration for particular concrete mix
7)	Primer or Adhesive strip test	Visual inspection of bond after 24 hours	Simple, low cost, low reliability

2. Background I: Physical and chemical properties

2.1 Introduction

Concrete is a composite material, consisting, macroscopically, of aggregate, (ie. particles of gravel, crushed rock, sand, slag, or other similar material), locked into a matrix of hardened, highly porous, binding medium (cement paste). The physical, chemical and electrical properties of concrete will be of interest in this study. The microstructure of the fully hardened cement paste, is very much determined by the particular mix of materials before water is added, and of the conditions under which hydration is allowed to proceed. The compressive strength of concrete which depends on the connectivity of the porous cement paste, or gel, reflects both the micro-structure and the macro-structure. The electrical properties depend largely on the connectivity of the pore-space and more particularly on the connectivity of pore solution within the pore space as well as on the distribution of aggregate. The chemical and physical nature of concrete is discussed in Section 2.2. In Section 2.3 we look at the location and movement of moisture in concrete.

2.2 Chemistry and structure of hydrating cement paste

2.2.1 Definition of concrete

The chemistry of concrete has been described by many authors (eg., Neville, 1981, Czernin, 1980, Mindess and Young. 1981, and Double, 1983). "Concrete is made by adding water to a mixture of cement, sand (fine aggregate) and coarse aggregate. Hydration takes place between the water and cement, producing a matrix of compounds, which is known as cement paste. This matrix locks together the coarse and fine aggregate particles to form a material with considerable compressive strength. The coarse and fine aggregates are cheap, high-strength fillers and are not normally regarded as active

constituents, these being limited to cement and water" (Whittington and Wilson 1986, p265). A mix without coarse aggregate is known as mortar.

A concrete mix is normally defined by the mass ratios of constituents:

(a) water cement ratio [w/c]

(b) cement/sand/aggregate ratio

(c) cement/total-aggregate ratio [c/a or a/c]

The main constituents of unhydrated cement are tricalcium silicate and dicalcium silicate, tricalcium aluminate and tricalcium aluminoferrite . "It is customary in cement chemistry to indicate the individual ...[cement] minerals by the following abbreviated notation:

$CaO = C$

$SiO_2 = S$

$Al_2O_3 = A$

$Fe_2O_3 = F$

Thus the compound $3CaO.SiO_2$ [tricalcium silicate] is referred to as C_3S and $2CaO.SiO_3$ [dicalcium silicate] as C_2S etc." (Czernin 1980, p26). Similarly tricalcium aluminate and tricalcium aluminoferrite are abbreviated to C_3A and C_4AF respectively.

The chemical composition of a typical ordinary Portland cement (OPC) is given in Table 2-1 .

Table 2-1: Composition of a typical Portland cement (Neville 1978, p11)

Compound composition	(%)
C_3A	10.8
C_3S	54.1
C_2S	16.6
C_4AF	9.1
Minor compounds	-

2.2.2 Hydration

When water is added to cement a complex series of chemical reactions take place. When tricalcium silicate passes into solution, the aqueous solution is unstable and soon decomposes into calcium hydroxide and hydrated calcium silicate which being insoluble is precipitated from the solution. Dicalcium silicate reacts in a similar fashion, but more slowly.

The calcium silicate hydrates, which are precipitated in gel form on the surface of cement grains, are considered to conform to the following overall formula:

$3Cao.2SiO_2.3H_20$

which is abbreviated to C-S-H by cement chemists (Czernin 1980).

A summarised scheme of the hydration process taken from Double(1983) is shown in Figure 2.2-1.

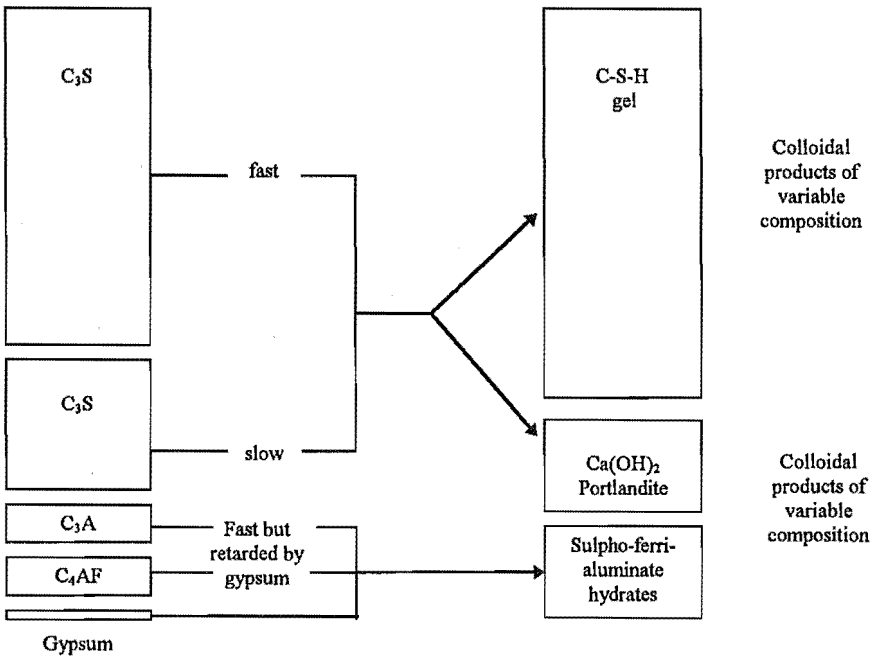

Figure 2.2-1:Summarised scheme of the hydration process. Schematic representation of the anhydrous constituents in Portland cement clinker and the products formed during hydration. The areas of the 'boxes' give approximate volume proportions of the phases (from Double 1983, p.54).

Calcium silicate hydrate is a "colloidal precipitate, which is mainly amorphous and has a rather variable composition. This occupies 60% (by volume) of the hydration products and is therefore the main binding agent in hardened cement. Calcium hydroxide is a by-product of the hydration of the calcium silicates and contributes a further 20% (by volume) approximately. The rest comprises various calcium sulphoaluminate and aluminoferrite hydrates , which are products of the hydration of the aluminate phases and gypsum. Gypsum (ca. 2%) is deliberately added to Portland cement to control the rapid hydration of C_3A, which otherwise tends to produce premature 'flash setting' of the cement. Apart from calcium hydroxide, crystalline products of hydration detectable by X-

ray diffraction include ettringite [$3CaO.Al_2O_3.3CaSO_4.32H_2O$]...and calcium monosulphoaluminate [$3CaO.Al_2O_3.$-$CaSO_4$]" (Double, 1983 p53).

When water is added, calcium silicate hydrate [C-S-H] is rapidly precipitated on the surface of individual cement grains, forming a spiny protective coating which inhibits the access of water and retards hydration for a time known as the induction period. Osmotic pressure effects, due to the selectively permeable character of the colloidal gel, may be responsible for the rupture of the coating. This leads to accelerated hydration and secondary growth of gel (see Figure 2.2-2). "The acceleration period is followed by a gradually decreasing rate of reaction and this is attributed to later infilling and accretion by hydration products. Effectively, as the layers of hydration products thicken by growth around the cement grains and as free water in the microstructure is consumed, longer range diffusional processes dominate and progressively slow down hydration." (ibid, p59).

Schematic representations of the sequence of hydration of cement are shown in Figure 2.2-2

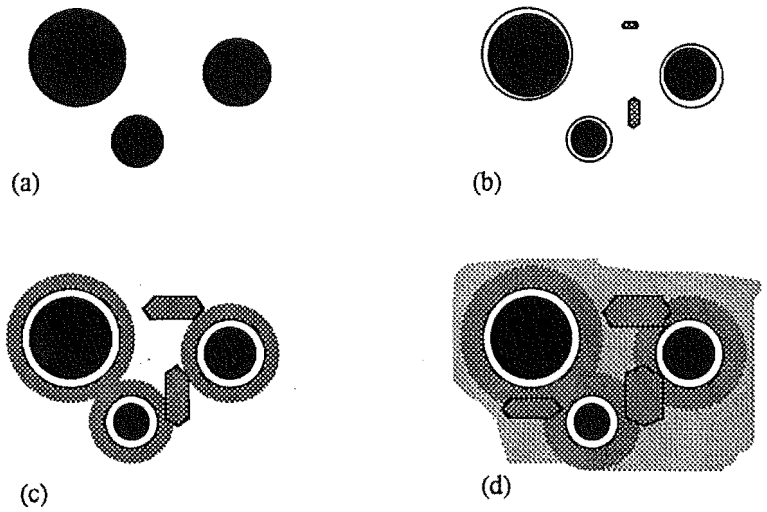

Figure 2.2-2 Schematic representation of the sequence of hydration of cement.(a) cement grains in water.(b) Formation of protective colloidal coatings of C-S-0H gel around cement grains. (c) Rupture of the protective coatings followed by secondary growth of C-S-H gel. (d) Later infilling of the microstructure by fine grained C-S-H gel and by growth of crystalline calcium hydroxide.

Most secondary gel forms at the base of the spines. As this secondary hydration layer grows, each cement grain effectively increases in size and the spines of calcium silicate hydrate begin to intermesh, beginning the formation of a solid bond between two cement grains and hence the formation of the solid matrix.

Thus the "structure of cement gel consists of irregular fibres of silicate growing from the surface of the cement grains and bridging the spaces between them....In fully aged cement there is considerable in-filling of the structure by fine-grained silicon-hydrate gel and by growth of crystalline hydration products. [Fine-grained and compact textured structures] are also formed on the inside of the grain coating "(Whittington and Wilson, 1986 p266).

"Because of its variable composition, C-S-H is not a well-crystallised material; in fact it is very nearly amorphous...As a consequence of [the] very finely divided state of C-S-H, hydrated cement pastes have very high surface areas...most C-S-H preparations...[having] surface areas in the range 250 to 450 m^2/g" (Mindess and Young, 1981 pp. 87-88). By contrast unhydrated cement has a specific surface of 0.2 to 0.5 m^2/g (Neville 1981).

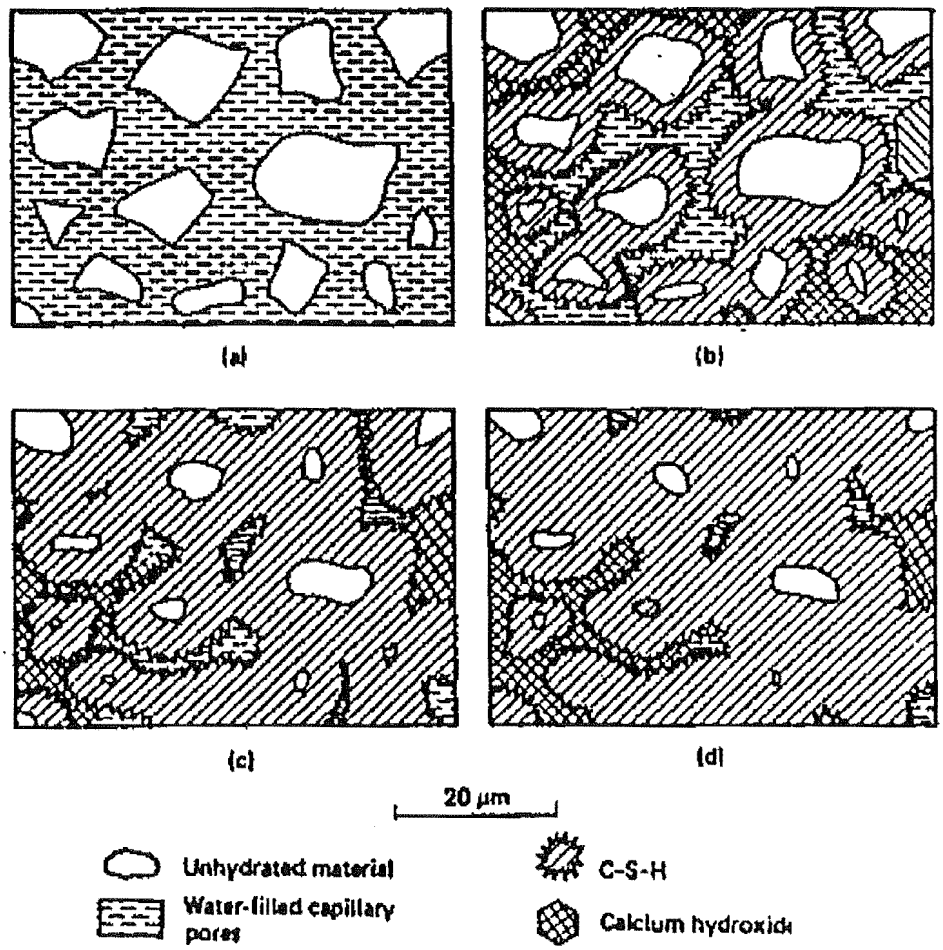

Figure 2.2-3 Schematic outline of microstructural of microstructural development in Portland cement pastes. (Calcium Sulphoaluminates are included as part of C-S-H for convenience, although they will crystallise as separate phases). (a) initial mix. (b) 7 days. (c) 28 days. (d) 90 days. (From Double 1983, p.59).

Calcium silicate hydrate gel is considered to have a degenerate clay structure in which the layers are crumpled and randomly arranged, so that the spaces between the layers are irregular and vary considerably in size.

A further discussion: 'When cement grains react with water, a cement gel is formed around each cement grain. The cement gel is composed of a system of very thin needle-like, sheet-like and crumbled crystals formed by the reaction between the cement and the mixing water. In addition a considerable number of coarser hexagonal crystals of calcium hydroxide are formed and are intermingled with the cement gel particles. The pore space located between the individual cement gel particles is called the gel porosity. The diameter of the gel pores is about some nm if they are considered cylindrical, see Fagerlund (1982). The gel pores are filled with water during normal conditions, called gel water, that is physically adsorbed on the surfaces of the gel particles.

'For w_o/c ratios larger than about 0.4 the cement gel volume is not large enough to fill all the space between the cement grains. Therefore larger, so-called capillary pores are formed in such cement pastes. The total volume of the capillary pores is called the capillary porosity. The diameters of the capillary pores are in the range 5 to 1000 nm", (Hedenblad 1993, p114).

2.2.3 Pore structure formation and the pore size distribution

There are several classification schemes for pores. Spaces having diameters less than 5 nm are called 'gel' pores and are considered to be part of the calcium silicate hydrate structure. In OPC, gel pores account for roughly 28% of the total volume of gel. Those pores in which capillary effects can occur (ie., a meniscus can form), are called 'capillary' pores. Generally speaking these are the remnants of water-filled space that exists between the partially hydrated cement grains. They have diameters in the range from 5 nm to 200 nm (McGlone 1990). Table 2-1, from Mindess and Young (1981), shows a slightly different classification scheme.

Capillary porosity is the ratio of capillary pore volume to the total volume of paste or concrete. As it depends on the original spacing of the individual unhydrated grains of cement, it is largely a function of the initial w/c ratio and may range from 0% to about 40%.

Table 2-1: Classification of pore sizes in hydrated cement paste (based on Mindess and Young 1982)

Designation	Diameter	Description	Role of water
Capillary pores	10μm-50nm	Large capillaries	Behaves as bulk water
	50 -10 nm	Medium capillaries	Moderate surface tension forces generated
Gel pores	10-2.5 nm	Small (gel) capillaries	Strong surface tension forces generated
	2.5~0.5 nm	Micropores	Strongly adsorbed water; no menisci form
	<~0.5 nm	Micropores "interlayer"	Structural water involved in bonding

As hydration continues, capillary pore volume is replaced by gel and the pore-size-distribution shifts toward smaller diameters. Consequently, the "randomly oriented, inter-connected pore network ...[developed after the cement paste first sets]... is in a constant state of change as filamentary pores which were continuous through the paste sample, become restricted or even blocked by gel growth. As access to pores becomes blocked, the continuous paths through the hardened cement paste...become more circuitous, hence as hydration continues, the pore tortuosity increases" (McCarter and Garvin, 1989 p1773).

2.3 Moisture in concrete

2.3.1 Where water is held

There are four main ways in which water is held in cement paste. Firstly, chemically combined water forms part of the hydrated compounds. Secondly, interlayer water is held between the clay-like layers of the gel by surface forces. Thirdly, as cement paste consists of particles connected over only a small fraction of their total surface, part of the water is within the field of force of the solid phase although external to it, ie., it is adsorbed. This water may be up to four molecules thick (McCarter and Garvin, 1989). Finally, there is the pore water contained within gel and capillary pores which is beyond the range of the surface forces. 'Strictly speaking, the pore water is an aqueous solution, often saturated with respect to lime and containing a wide variety of ions" (Parrott, 1990).

2.3.2 Definitions and measurement of moisture content

The definition of the moisture state of concrete will depend on the property of concrete being considered. The evaporable moisture-content (ewc) is that water which can be driven off at a certain relative humidity (for example by oven drying at 105°C for 24 hours as in Berg, et al. 1992, or until the weight has become constant as in Woelfl and Lauer, 1979). The division between evaporable and non-evaporable water is somewhat arbitrary, since there is a continuum of binding energies between water and a porous material with a continuous range of pore-sizes. Non-evaporable water, however, can be thought of as containing all chemically combined water and some not held by chemical bonds. "In well hydrated cement, non-evaporable water is about 18% of the mass of the original unhydrated cement...[rising] to about 23% in fully hydrated cement" (Whittington and Wilson, 1986).

The evaporable moisture-content may be expressed as a fraction of the dry weight of concrete (moisture-content by weight, eg. Nilsson 1977, Woelfl and Lauer 1979, Tashiro et al. 1987, Hashida et al, 1990), or as a fraction of the maximum water content. (eg. Berg et al. 1992, sometimes called capillary saturation: Hedenblad and Nilsson 1985). The two measures are not simply related since, if hydration is not complete, the pore-size-distribution will continue to change as hydration progresses. Concrete cured and stored under water will have constant capillary saturation (=1 or 100%) while the moisture-content by weight will decrease as the porosity decreases. Knowledge of the pore-size-distribution is important. A decrease in moisture-content by weight in a sample of concrete undergoing drying and hydration does not in itself say anything about the moisture state of individual pores. The degree of capillary saturation has a strong influence on the electrical properties, in particular the conductivity of concrete, since electrical conduction occurs mainly via continuous paths through the capillary and gel pore solution. A low moisture-content near the base of a slab may allow better conduction than the same moisture-content near the surface where an equivalent mass of water may be spread out over larger pores.

Measurement of capillary saturation or of evaporable moisture-content by gravimetric means, requires destructive techniques, and is impractical on concrete floor slabs, although excellent work has been done in measuring time dependent ewc profiles in walls using repeated drilling. (Parrott, 1990). The simplest and indeed the most common in-

situ moisture measurement is by using relative humidity (RH) probes (see for example Keey 1992 and Wiederhold 1987). Parrott (1990) and Hashida et al. (1990) describe their use with concrete samples. Relative-humidity probes may be inserted into pre-formed holes at various depths within a concrete slab, and readings taken without interfering with future measurement possibilities.

Relative humidity is a measure of the moisture state of the space within concrete not filled with pore solution. It is of interest because it is intimately related to the degree of saturation of the pore space, and to the size and shape of the pore space itself.

Humidity is generally " some measure of water vapour content of air. *Absolute humidity* is the ratio of water vapour present to the volume occupied by the mixture; that is, the density of the water vapour component.....*Relative humidity* is the ratio of the actual vapour pressure of the air, at any temperature, to the maximum of saturation vapour pressure at the same temperature. It expresses the vapour content as a fraction or percentage of the concentration necessary to render the vapour saturated at any given temperature...A rise of temperature without the addition of more vapour reduces the relative humidity (but not the absolute humidity) while a fall of temperature increases it and may bring about saturation (Considine 1983, p 1536).

The relative humidity immediately above a plane surface of water is 100%. If the surface is concave, water will condense at relative humidities less than 100%, the smaller the radius of curvature, the lower the relative humidity at which moisture will condense. Conversely, the lower the relative humidity, the smaller the maximum radius of curvature of cavity or pore which will still retain liquid water. Thus, the relative humidity measured within concrete will be a function of the capillary saturation and (since the degree of saturation will depend on the pore-size-distribution and hence the total moisture content), the moisture-content by weight. Further discussion of this will be with the drying concrete slab in focus.

2.3.3 Migration of moisture

After a concrete slab has been allowed to cure in conditions of high relative humidity the top surface is normally exposed to the local air of lower relative humidity and begins to dry – moisture moving down the relative humidity gradient. During the first stage, the concrete is more or less saturated, and the drying rate is determined by the rate of sur-

face evaporation, which itself is strongly influenced by air velocity and the condition of the surface. Once the surface dries out, "there is an abrupt interface between a shallow, dry surface layer and a wet internal region. The drying rate is faster near the interface as pores in this region give up their moisture, effectively into the dry surface layer, far easier than the pores deeper down where there are fewer sites for excess moisture to go" (McGlone, 1990, p4). As drying progresses, the interface, or 'evaporative front', moves deeper into the concrete and becomes less sharply defined.

At any point in the concrete, there will be a distribution of pore sizes. As drying takes place, the larger pores will 'empty' first. The degree of saturation or filling of pores is controlled by the relative humidity in the unfilled pore-space and by the pore-size. This dependency is expressed by the Kelvin equation

$$\ln p/p_0 = -\frac{2\gamma V}{rRT}\cos\varphi \qquad \textbf{Equation 2-1}$$

where r is the radius of curvature of the pore, p_0 is the saturated vapour pressure at the temperature T(K) of the concrete, γ and V are the surface tension and the molar volume of the pore solution, R is the gas constant per mole and φ is the angle contact between the liquid and the wall of the pore.

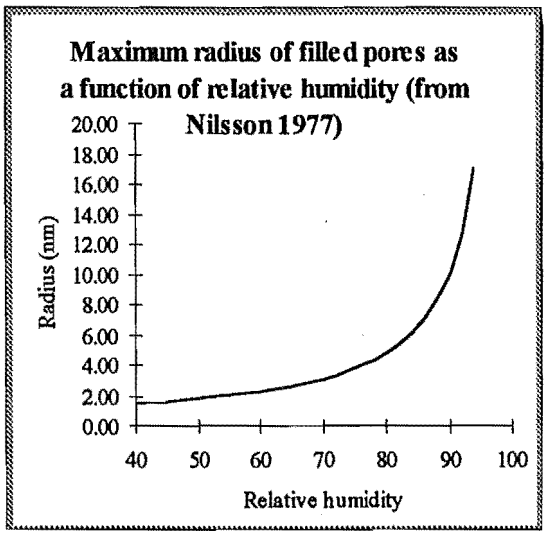

Figure 2.3-1: Maximum radius of filled pores as a function of relative humidity (from Nilsson 1977)

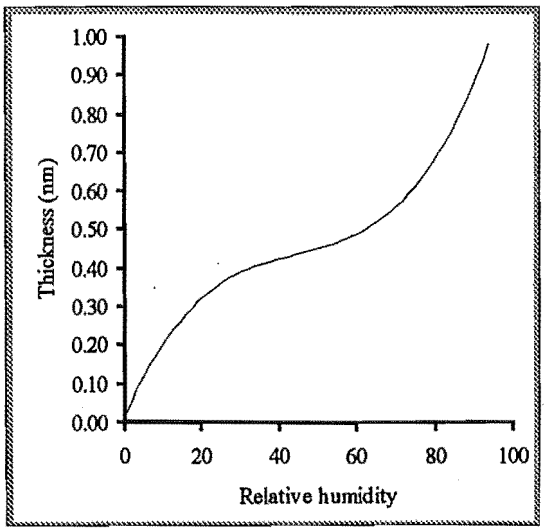

Figure 2.3-2. Thickness of adsorbate as a function of relative humidity (from Nilsson 1977)

The word 'empty' above is used advisedly. In fact the capillary water, or water that forms a meniscus, will evaporate, leaving water that is more tightly bound to the pore,

adsorbed onto the pore walls. This thin layer of adsorbed water covering the pore walls, has a thickness dependent on the relative humidity, The relationship is shown in Figure 2.3-2. The Kelvin radius represents the radius not of the pore itself but the of the 'inner pore', bounded by the adsorbed water layer.

As the concrete dries, moisture will evaporate from the larger pores first. Within pores, the pore water comprises the capillary-condensed liquid (of inner radius r_k),and the more tightly bound layer of water, of thickness t, adsorbed on to the pore surfaces. The process of desorption, when the relative-humidity falls from ψ_1 to ψ_2, may be considered to fall into two parts:

1. Evaporation of the capillary-condensed water takes place from the 'inner capillaries' having radii r_k lying between the values of r_1 (corresponding to ψ_1) and r_2 (corresponding to ψ_2) which are calculated using the Kelvin equation (see Equation 2-1).
2. The diminution from t_1 to t_2 in the average thickness of the adsorbed layer on the walls of all those pores which have previously lost their capillary condensed water; these pores will be those having a radius equal to or greater than $r_1 + t_1$ (Gregg and Sing 1969, p160). The thickness of the adsorbed layer in a nearly empty pore, is an order of magnitude smaller than the radius of pore itself (Figure 2.3-2). At high relative-humidities, the mass of water that the adsorbed layer represents is insignificant. Nevertheless, its presence and its diminution with decreasing relative-humidity is of consequence for the ability of the pore to conduct electricity. *(As the relative-humidity drops, the adsorbed layer makes up an increasing proportion of the total mass of moisture, since the ratio of* internal *surface area to the volume for pores still full, increases).*

Since the pores are not all of the same radius, there will be a wide range in degree of saturation locally and throughout the profile. Larger capillary pores will be 'empty' (of capillary water) at relative humidities barely less than 100%, and pores having a radius greater than 5 nm (ie. all capillary pores) will be empty at 80% relative humidity, apart from a layer of adsorbed water of approximately 0.6 nm thickness. Most gel pores remain full at much lower RH, reflecting their smaller diameters.

The relationship between the moisture-content by weight and relative humidity takes the form of a hysteresis loop (see Figure2.3-3).

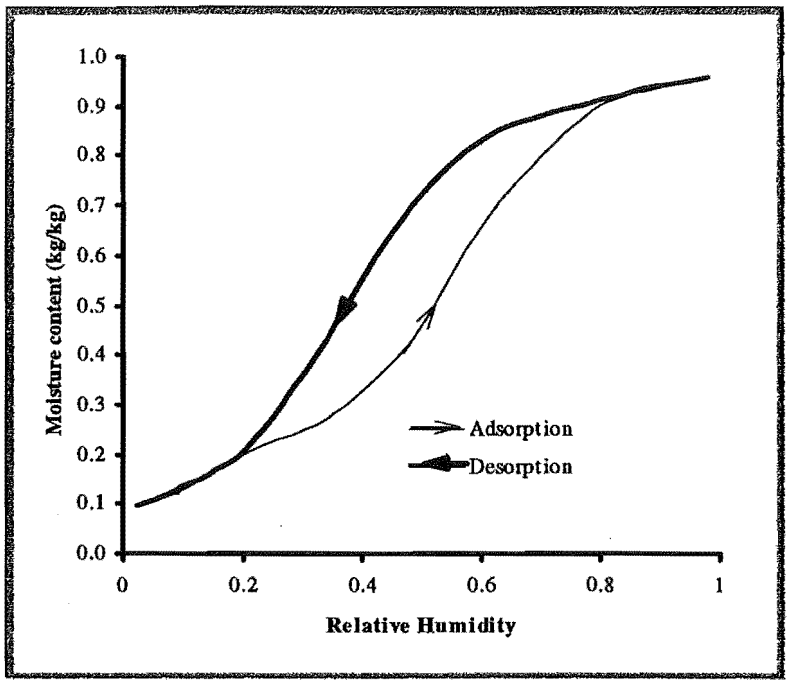

Figure 2.3-3: The relationship between the relative humidity and moisture-content for a micro-porous solid such as concrete exhibits a hysteresis loop. Over at least some of the range of relative humidity, the moisture-content at a given relative humidity depends on whether the relative humidity was approached by drying (desorption) or by adsorption.

"A very wet solid, on exposure to an atmosphere of fixed relative humidity, will lose moisture until the equilibrium amount in the solid is attained. Further moisture can be removed only by reducing the relative humidity, and a completely dry material can exist solely in a moisture free environment.

"The amount of moisture ultimately retained depends upon whether the equilibrium has been approached by wetting (adsorption) or by drying (desorption). There is a closed loop hysteresis and the desorption isotherm always shows the larger equilibrium moisture-content at a reduced vapour pressure" (Keey, 1972 p23).

The physical explanation for the hysteresis has not been settled and is still the subject of some debate. A variety of hypotheses have been put forward (Gregg and Sing, 1970). However it is generally believed that the emptying of pores via evaporation and capillary action can support quite different menisci from menisci formed as adsorbate condenses onto the pore walls, and that consequently the Kelvin equation does not apply or applies

differently in the two cases. It should be noted that pore geometry is complex and the Kelvin equation is, in the best of circumstances, an approximation.

In the following discussion a phenomenological description of the moisture content, pore-size-distribution and relative-humidity is given.

For concretes with low w/c ratios, which are well hydrated, the capillary porosity is very low. Earlier in the hydration process the range of pore sizes and density of pores of different sizes will be quite different. The particular porous state of the concrete is defined by the pore-size-distribution which may be measured in a number of ways. In the method of 'mercury penetration porosimetry', mercury is forced into the concrete or cement paste under pressure. The radius of the meniscus of mercury entering a pore space is a function of the applied pressure. The greater the pressure, the smaller the pore into which mercury may be forced; the smaller, in other words, the radius of the meniscus. Pore space is infinitely variable in size and shape, however the meniscus radius of mercury able to intrude a pore of a certain size range, may be equated to what may be termed the 'effective radius' of the pore. The incremental volume of mercury intruded at each increase in pressure, yields the total volume of pores having an effective radius within the corresponding size range. Some correction must be made to account for blocked off pores.

It is well established that the pore-size-distribution of cement paste shifts to smaller pores with increasing hydration (eg. Tashiro et al., 1987). A typical progression is shown in Figure 2.3-4. The total volume of pore space decreases, while the numbers of larger pores decrease and the numbers of the smallest pores increase. The volume of intermediate-size-pores increases and then decreases as the distribution shifts.

The moisture content of pores will depend largely on their effective radius. To the extent that the Kelvin equation holds, at a certain relative humidity, only pores having less than the corresponding effective radius, will be full (Equation 2-1). The volume of pore solution at a given relative-humidity will thus depend on the shape of the pore-size-distribution. The change in the pore-size-distribution is primarily an effect of increasing hydration. Using the mass of water absorbed by cement paste over the first six months after pouring, as an indication of the degree of hydration, it has been shown that when the ambient RH was 90%, the rate of hydration was only half that when

the relative-humidity was 100% (Neville, 1981). Hydration virtually ceases when the pore relative-humidity falls below 80% (Molina 1990, p. 13). As the concrete dries from the surface, once the relative-humidity falls below 80% at a certain depth, the pore-size-distribution above that depth will remain fixed, while continuing to change at deeper levels, at a rate depending on the relative-humidity. Very soon after the curing period, the pore-size-distribution within the slab will exhibit a depth effect, with the more shallow layers retaining more juvenile distributions than deeper layers which continue to mature.

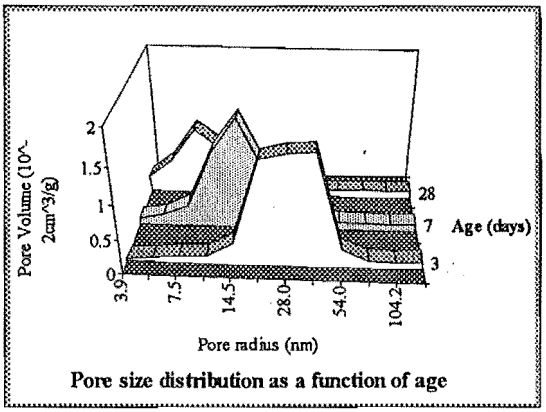

Figure 2.3-4: Possible pore size distribution as a function of age.

If there is a predominance of larger pores, as is typical of very young or poorly hydrated concrete, and of concrete with a high water-cement ratio, then a low relative-humidity will be associated with a low moisture-content compared to that of well hydrated concrete. On the other hand, it would have a larger moisture-content under conditions of high relative-humidity than more mature concrete.

Permeability, the ease with which liquids or gases can travel through a porous material is also important. Permeability is dependent on the water-cement (w/c) ratio, the aggregate-cement (a/c) ratio, and the degree of hydration insofar as all three factors affect the porosity and the pore size distribution. In general, concretes made with lower w/c ratios, or cured under conditions of higher RH, or cured for longer, have lower permeabilities because they have lower porosities. However, the same volume of pore space will result in a lower permeability if the pores are segmented and disconnected, or are on average smaller. " Although the porosity of... cement gel is 28%, its permeability is low ... because of the extremely fine texture of the gel and the very small size of the gel pores. The permeability of a hydrated paste as a whole is greater because of the presence of larger

capillary pores, and in fact, permeability is largely a function of capillary porosity" (from Neville and Brooks 1987, p263).

2.3.4 The effect of sealing the drying surface

Apart from capillary action in the wettest zone, the dominant driving force in the isothermal diffusion of moisture is the relative humidity gradient. This is seen quite dramatically when the drying surface of a partially dry slab is sealed. Hashida et al, (1990) report that although RH averages out in a drying concrete slab once it has been sealed, moisture does not redistribute significantly, remaining at higher levels deeper within the slab (see Figure 2.3-6 and Figure 2.3-7). This can be understood by inspection of the relevant hysteresis curve.

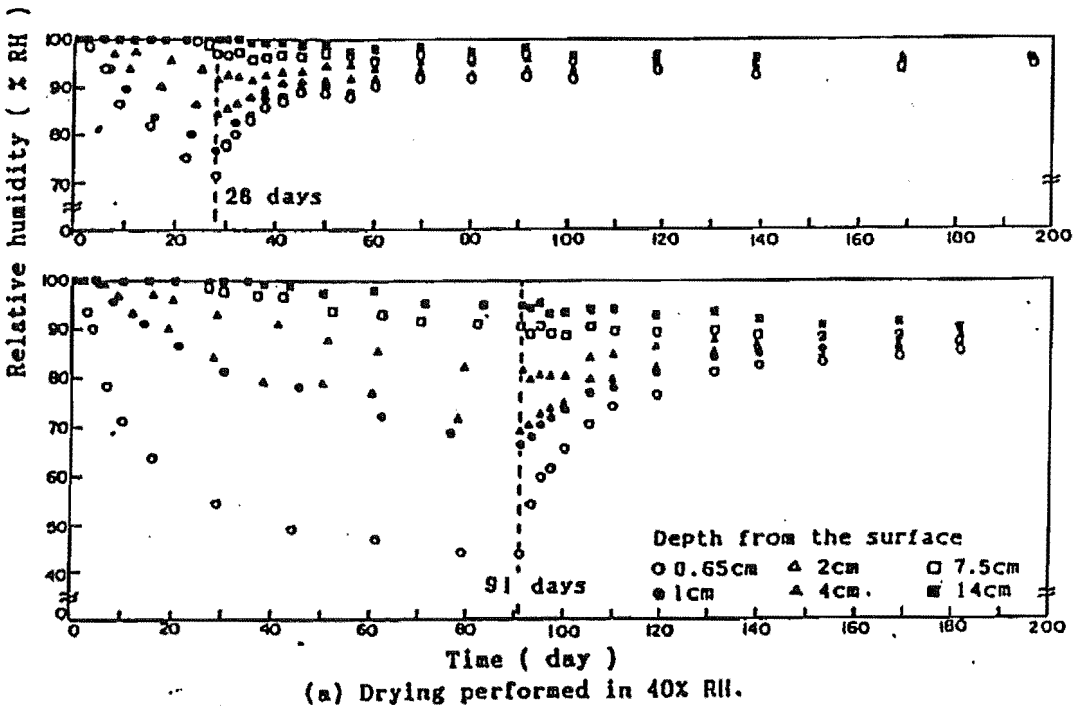

Figure 2.3-6: Changes in pore humidities in concrete before and after the drying surface is sealed (Hashida et al. 1990, p.306).

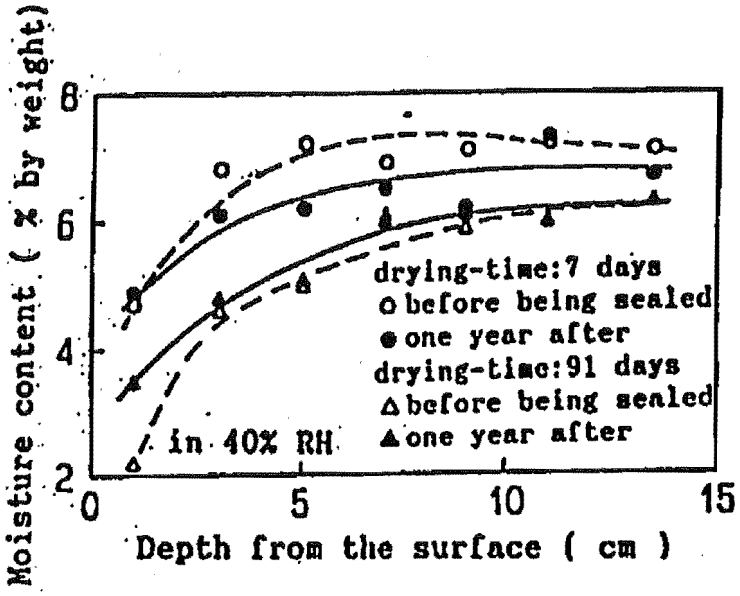

Figure 2.3-7: Changes in the evaporable moisture-content in concrete before and after the drying surface is sealed (Hashida et al. 1990, p.307).

On drying, the moisture state of the concrete can be represented on the desorption part of the hysteresis curve —the wetter deeper regions represented on the upper right and the drier more shallow regions to the lower left, of the desorption curve (see Figure 2.3-8). All parts of the concrete are becoming drier.

When the top surface is sealed, the relative humidity gradient will flatten off and become uniform throughout the slab at some intermediate level (Figure 2.3-9). To reach that equilibrium level, relative humidity will increase in regions above some depth corresponding to the equilibrium level, and decrease below this depth. The increase in relative humidity involves rewetting or adsorption, and the moisture state is said to 'scan' across the hysteresis loop towards the adsorption arm (the path CD in Figure 2.3-9 for example). At equilibrium, the concrete is left in a state represented by a vertical line (uniform relative humidity) cutting the hysteresis curve.. The spread in moisture-content remaining after the slab has achieved uniform relative humidity may be enhanced if porosity increases toward the surface. The accompanying shift to larger pores in the pore-size-distribution, will allow a lower moisture-content near the surface since a larger number of pores will be empty at that relative-humidity.

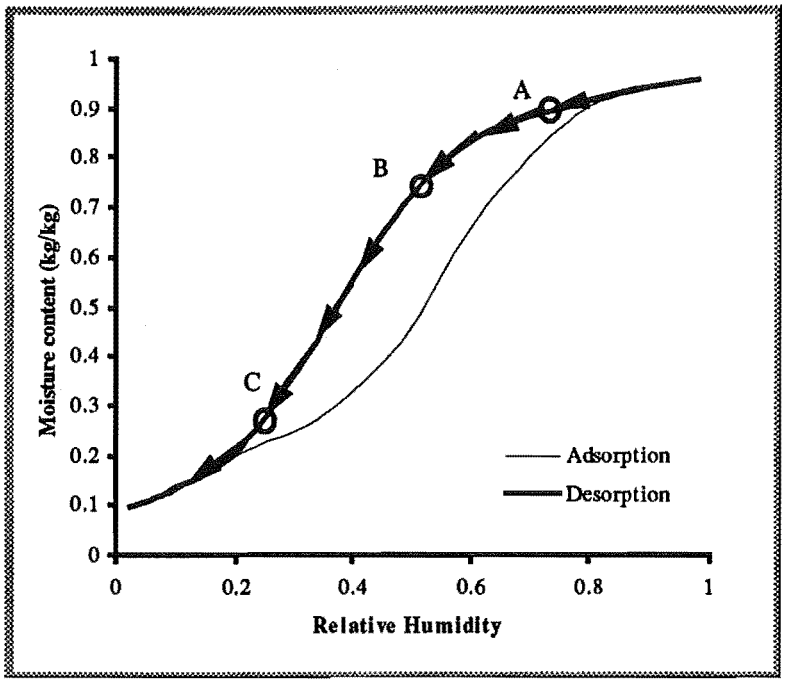

Figure 2.3-7: Concrete in a drying concrete slab represented on the hysteresis curve. 'A' is deeper and wetter than 'B', which in turn is deeper and wetter than 'C'.

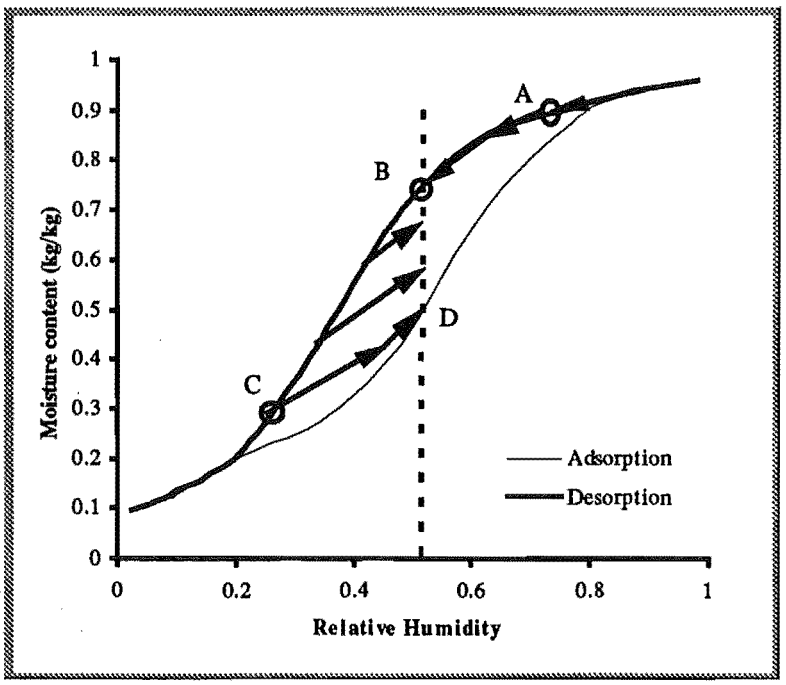

Figure 2.3-8: The effect of sealing of the surface of a concrete slab on the moisture state of the concrete. Concrete at state 'A' continues to dry where as that at state 'C' rewets. Eventually all concrete reaches a uniform relative humidity, but does so with differing moisture content. This equilibrium state is represented by the continuum between B and D on the dotted line.

Once a uniform RH is reached, transport by diffusion ceases and any further moisture transport must occur by capillary action. This may be slow because in a well-cured and well hydrated slab the capillaries will be small and segmented.

If relative-humidity is able to reach equilibrium at some level less than 100%, well before significant change takes place in the moisture-content profile, how is this level of relative-humidity able to cause difficulties for floor coatings or coverings? After all, condensation should not appear at relative-humidities less than 100% in large cavities. One possibility is that the very closeness of the floor coating to the concrete forms a layer of pores of a size such that condensation does occur. The presence of this water may then allow delamination. Under another scenario, a relative-humidity somewhat less than 100% may well be safe unless other influences such as changing temperature gradients upset the RH equilibrium. As Roper (1992) points out "the pore structures of most in situ concretes are such as to allow moisture diffusion under conditions of thermal gradients and differential pressures. Water vapour may accumulate and condense at the interface between the concrete and impervious coatings when differential temperature gradients, such that the surroundings are lower than the core, are present through the section" (p260). Under these conditions coating or covering failure may occur. Another possible mechanism to explain failure of coatings is osmotic pressure (Sasaki and Nakayama 1993, citing *Warlow, W.J. et al., 1978)*

On the other hand the coating may fail at an early stage while it is curing and susceptible to water damage. Resin based coatings may fail to cure properly in the presence of high relative-humidity but somewhat less than 100%..

2.4 Moisture-content data in the literature

Moisture profiles are reported in and Hedenblad and Nilsson (1985), Parrott (1990,1991) and Hashida et al. (1990, see Figure 2.3-6 and 2.3-7 above). From his data, Parrott (1990,1991) has derived empirical formulae relating RH at different depths (d in mm) from the surface of a slab in a constant ambient relative humidity (*RHa)*. His 1991 formula is

$$RH = RH_a + (100 - RH_a)e^{(-kT)}$$

where $k = 0.8 - 0.14T + 0.01T^2$

$$T = \frac{t}{t_{1/2}}$$

t = time in days

$t_{1/2} = 10d$, for d < 41.4 mm

$= 3d + 290$, for d ≥ 41.4 mm

Equation 2-2

Although this formula may not be very useful in predicting moisture profiles in the field, where ambient RH and temperatures vary widely, it may be used as an indication of expected profiles in controlled conditions. Profiles based on Parrott's formula are given in Figure 2.4-1.

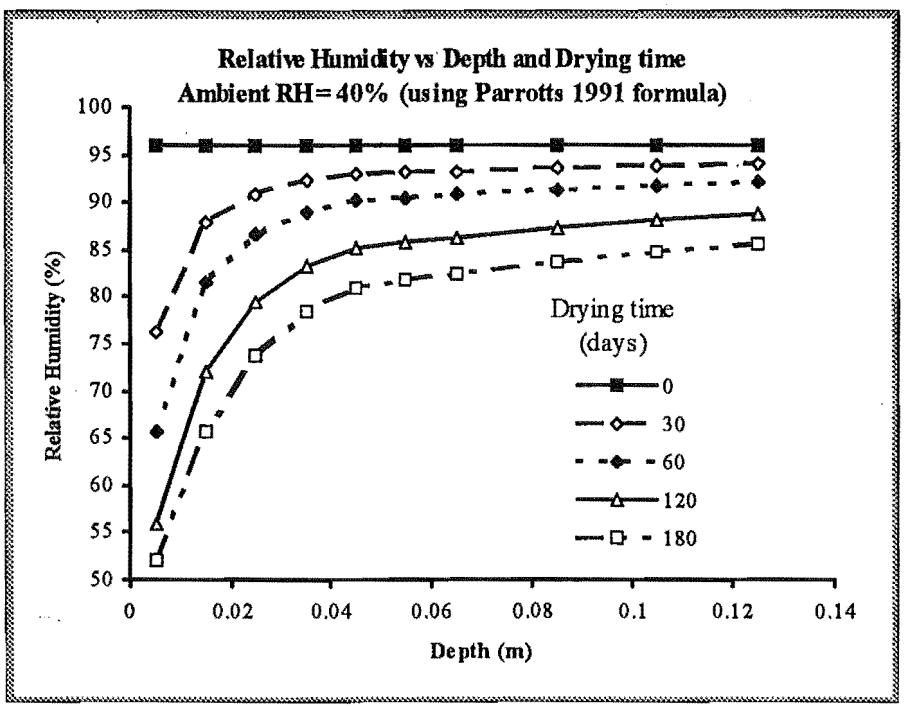

Figure 2.4-1: Relative humidity profiles based on Parrott's (1991) formula. Here the ambient relative-humidity has been set at 40%, and the relative-humidity of wet concrete set at 96%.

In the laboratory RH may be controlled using various saturated salts (see Chapter 9). It is a feature of Parrott's formula that RH does not depend on w/c content or porosity. Nilsson(1977) and Berg et al. (1992), on the other hand, show that greater porosity is associated with faster drying. In the latter paper for example, evaporation proceeds more than twice as fast from samples with w/c=0.78 than from samples with w/c=0.5. This

study used 80 mm cube samples of cement mortar whereas Parrot's samples were larger 100 mm cubes and of concrete.

There is in fact fairly large variation in profiles measured under different circumstances.

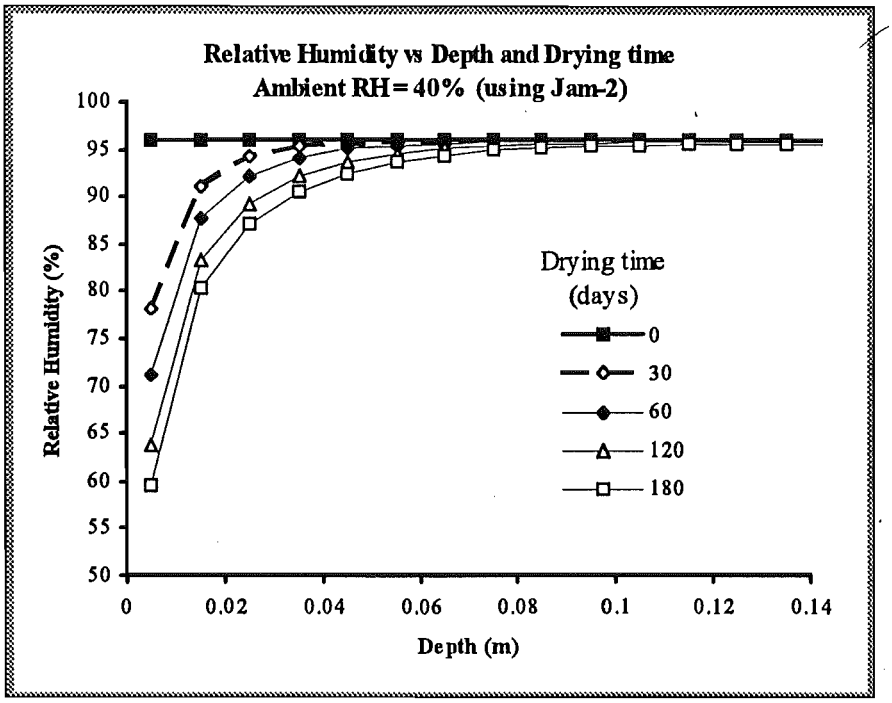

Figure 2.4-2: Relative humidity profiles calculated using Jam-2, a computer program based on a diffusion equation.

Relative-humidity profiles predicted using, a computer program (Jam-2, see Section 4.5-2) utilising numerical solution of a diffusion equation are shown in Figure 2.4-2. Experimentally determined desorption curves and diffusion coefficients must be provided. Profiles determined using Jam-2 differ significantly from those predicted by Parrott's equation (compare Figures 2.4-1 and 2.4-1). Most obviously, the relative-humidity drops throughout the profile much faster under Parrott's prediction than under Jam-2. The latter profiles retain the initial relative-humidity virtually unchanged in the deepest regions. Some of the variation can be accounted for in the implicit inclusion of the effect of ongoing hydration in Parrott's formula and explicit exclusion in Jam-2 (the material data being taken from fully cured samples). If this were the only effect, one would expect the two sets of profiles approximate each other more after sufficient time has passed to ensure hydration to be nearly complete. However there is no provision in Parrott's formula for

the drying rate in the deepest regions to slow down significantly and similarly no provision in Jam-2 for a corresponding increase in drying rate.

It is not possible at this stage, therefore, to predict relative-humidity profiles based on existing methods. Rather, in order to determine profiles in concrete slabs, relative-humidity sensors must be placed directly in the slab or in a smaller concrete sample of the same thickness and which has been allowed to cure and dry under similar conditions.

3. Background part II: Electrical properties of concrete

3.1 Electrical properties of concrete

3.1.1 Dielectric properties

When an electric field is applied to a material such as cement paste, some ions and electrons may be free to drift through the material, producing a conduction effect. Other charges, although not free to drift, will be displaced from an equilibrium position. This creates electric dipoles, the formation of which is referred to as polarization. Macroscopically, the combined effect of the individual dipole moments is represented by the electric polarization vector P, defined as the dipole moment per unit volume.

The polarizability of a material is reflected in its dielectric constant ε (also known as the relative permittivity). The permittivity is complex with the real part ε_r' associated with a change in phase of an alternating field. The imaginary part ε_r'', sometimes called the loss factor, is related to the attenuation of the field.

Under the action of an alternating electric field, the polarization will oscillate and energy may be transferred or 'lost' to the medium. "The ocurrence of dielectric loss can generally be understood as follows: at very low frequencies, the polarization easily follows the alternating field, thus its contribution to the dielectric constant is maximal, and no loss occurs. At very high frequencies the field alternates too fast for polarisation to arise and there is no contribution to the dielectric constant and no energy is lost in the medium. Somewhere between these two extremes, the polarization begins to lag behind the field and energy is dissipated. The loss factor has a maximum at a [critical] frequency" (van Beek, 1967, p72).

Some polarization mechanisms include

- the accumulation of ions at electrodes (electrode polarisation),
- the accumulation of ions at the blocked ends of pores,
- the accumulation of ions at the interfaces of cement particles and crystal boundaries,
- displacement of double layer charges, which are concentrations of ions of one sign adjacent to oppositely charged particle surfaces,
- the displacement of the ions from their zero field equilibrium positions (ion atmosphere distortion),

- rotation of dipoles and polar molecules (eg water)
- displacement of electron clouds relative to an atomic nucleus.

Different sources of polarization typically have different critical frequencies. Thus the time taken for ions to cross back and forth a blocked pore will depend on the length of the pores, and generally be much greater than that associated with ion atmosphere distortion. The effect of polarization is to increase the capacitance and the conductivity measured between the electrodes so that measurement of electrical properties at different frequencies points to different physical or chemical states of the concrete.

> "As portland cement hardens, the role of the water molecule changes from that of liquid water to water bound in various states of hydration or crystallization...profoundly affect[ing] the dielectric relaxation spectrum. The water molecule has a large dipole moment ... As it passes from one bonding state to another, its ability to orient in an applied electric field changes. Thus the bonding state is reflected in the dielectrc measurements. For example, in the liquid or gaseous state, the water molecule is able to orient easily in radio-frequency fields. Thus liquid water has a high dielectric constant. In the solid state, ie. ice, this rotation is hindered and the molecule can follow the field only at frequencies in the audio range and below...At 100 kHz the dielectric constant of water (at 0 C) in the liquid form is about 77, but in the solid form it is only 3.4. In states intermediate between ice and water, the dielectric properties will be different from either those of ice or liquid water" (Camp and Bilotta 1989, p6007).

Close study of the electrical behaviour of concrete or cement based materials over a range of frequencies has been undertaken by various researchers since the late 1980's. For example, McCarter (1987) measured the resistivity of cement paste at 28 spot frequencies over the range 100 Hz — 300 kHz, and found a strong frequency dependence. Alternating current impedance spectroscopy (ACIS) involves the measurement of complex impedance over a range of frequency. In early studies of cement pastes and mortar moist cured for 28 and 100 days, McCarter and Garvin (1989) obtained characteristic impedance plots over the 20 Hz-110 MHz frequency range. Other researchers (eg. Camp and Bilotta 1989, Scuderi et al. 1991 and Gu et al 1992) have developed the technique further. From such data, it has been possible to identify the

effects on impedance due to electrode polarisation, the degree of hydration and the moisture condition of the pores, although it is not necessarily possible to isolate one from the other entirely.

Thus McCarter (1987) sought to explain the frequency dependence of hydrating cement paste . At low frequencies ionic conduction predominates. As the cement paste cures, the rate of change of resistivity can be "regarded as the rate at which water and charges are removed from the acqueous phase (i.e., capillary water) and reflects a combination of grain segmentation and growth of the gel as it extends, constricts and blocks the continuous capillaries within the paste and the fractional volume of free evapourable water within these capillaries...[The] enhanced conductivity at higher frequencies is due to surface conduction effects on the adsorbed gel water ...The difference between the low and high frequency resistivity curves will thus represent the proportion of current flowing through the (adsorbed) gel water and will be a quantitative measure of the fractional volume of gel within the paste" (pages 59-61). In the present work, it is the evaporable water held in the larger capillary pores that is of interest, since, gel-pore water is relatively tightly held and will not be available at the relative-humidities capable of causing floor coating failure.

Camp and Bilotta (1989) carried out a series of admittance measurements on cement paste samples of various w/c ratios. Parameters measured were the equivalent parallel conductance and the equivalent parallel capacitance. The capacitance was generally highest at very low frequencies, and decreased with frequency and hydration and with decreasing moisture content. They suggested that the extremely high capacitance at low frequencies may be due to electrode polarization, a result of "very thin double dipole layers at the electrodes" or due to interfacial polarization, which could be a result of "very thin insulating layers between conducting paths in the bulk of the sample. Although the dielectric constant of the interfacial layer may be small, the capacitance can be large due to the very small thickness of the layer" Camp and Bilotta (1989, p6008).

Conductivity tended to fall with hydration and moisture content. After the first few days of hydration, if enough water was present to guarantee full or nearly full capillary pores, conductivity was almost independent of frequency between about 1 kHz and 1 Mhz. In this region ionic conduction is predominant. In general, the conductivity frequency-dependence was greatest at the early stages of hydration at low frequencies (electrode

polarisation effects) and at high frequencies as moisture content fell (interfacial or intergranular polarisation).

Camp and Bilotta, and other researchers (eg. McCarter 1987, Wilson and Whittington 1990, Scuderi et al. 1991 and Gu et al 1992) have attempted to model the complex impedance behaviour with simple resistance and capacitance networks. While details differ from model to model, the general form is shown in Figure 3.1-1. The leaky capacitor unit A., comprising R_1 and C_1 in parallel, represents the electrode and intergranular polarization, while unit B., is made up of a resistance R_3, representing the ionic conductance, in parallel with a frequency dependent element representing the high frequency dependence.

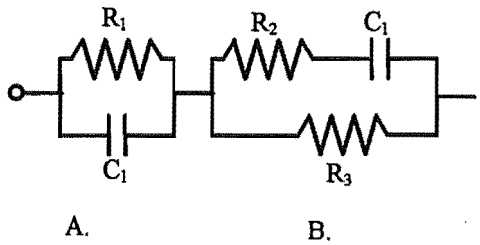

Figure 3.1-1. General electrical model of a cement paste, mortar or concrete sample based on impedance spectra. An explanation of the different elements is given in the text.

As Camp and Bilotta note, "all processes are dominated initially by ionic conduction and interfacial polarization. We can follow the loss of water most easily by following the conductance plateau. That is we must stay away from spectral regions [frequencies < 100Hz, and > 10 kHz] in which some process other than ionic conduction comes into play" (p. 6011).

Nevertheless, the use of microwave radiation to measure moisture content is well established (Krazewski 1991). Parrott (1990) notes that permittivity measurements at microwave frequencies have the advantage that free water has a high loss factor at microwave frequencies, whilst bound and adsorbed water are effectively seen as solid since they contribute little to permittivity above 8 GHz. Dissolved salts which contribute greatly to conductivity, and hence may be mistaken for a higher water content of lower concentration, have little effect on permittivity above a few GHz. At high frequencies, the trade-off between high resolution but low depth penetration, somewhat weakens these advantages for determination of moisture profiles. An early study by Bhargarva and

Lundberg (1972), using rectangular resonant cavities shows that the effective depth of penetration for 0.3 GHz microwaves is 150 mm. This reduced to 60 mm as the frequency increased to 0.8 GHz. Larger open ended coaxial probes may allow greater depth penetration at higher frequencies.

The determination of permittivity and conductivity using open ended waveguides is discussed in Gardiol (1984) and Marsland and Evans (1987). Similar nondestructive measurement has been described by Otto and Chew (1991) who used a large, open-ended, coaxial probe for the measurement of average complex permittivity of samples with large-grain inhomogeneities, such as rocks and concretes. The depth of penetration of the electromagnetic field decreases with frequency and increases with probe diameter.

3.1.2 Resistivity

Many studies have focussed on purely resistive properties of cement based materials rather than the broader dielectric properties. In general, as noted above, the resistivity of porous material decreases with increasing moisture content and increases with increasing cement hydration and decreasing w/c ratio (through their effects on capillary porosity and the volume of pore fluid).

When concrete is continuously moist cured, resistivity has been found to rise from around 4 ohm-m at initial set to about 40 ohm-m for w/c=0.6 or up to 80 ohm-m for w/c=0.4 (Hughes et al. 1985). Air-cured concrete samples attain much higher resistivities as the concrete dries out. The effect on porosity of curing in the relatively low RH of the open air is revealed by Woelfl and Lauer (1979), who show that the resistance of an air-cured sample re-immersed in water falls below that of a sample continuously moist-cured. This suggests that curing under conditions of low relative-humidity results in a more porous concrete. When rewetted the greater volume of water allows a greaer electrical conduction. (The effect of low relative-humidity on hydration and hence on capillary porosity has been discussed in Chapter 2).

Whittington et al. (1981) consider three possible conduction paths through concrete: through the aggregate and paste in series, through the aggregate particles in contact with one another and through the paste itself. As typical aggregate resistivities (at around 500-5000 ohm-m) are higher than cement paste by several orders of magnitude, the authors show that more than 90% of the current is conducted through the paste alone, the rest being conducted through the aggregate and paste in series. They conclude that

the paste is a controlling factor in the over-all resistivity of the concrete and that anything which affects the electrical conductivity of the paste will affect the overall conductivity of the concrete.

Furthermore, it is the moisture content that is responsible for most conduction of current through relatively moist concrete. As the resistivity of bone-dry cement paste can be up to 10^9 ohm-m (Neville 1981), significant conduction of electricity must take place only via the water content of cement paste. While electronic conduction may take place through cement compounds (ie. through the gel, gel-water and unreacted cement particles), it is accepted that at low frequencies, conduction through moist cement is primarily by means of ions in the evapourable water in the cement paste, the principal ions being Ca^{++}, Na^+, K^+, OH^-, and SO_4^- (Whittington et al. 1981). "As the gel pores in cement paste are of molecular dimensions it is unlikely that they will affect the conduction process significantly, as the ionic mobility is likely to be very low under these circumstances" Whittington and Wilson, 1986, p27). It follows that resistivity will be greater in pores small enough to significantly impede ionic travel, hence resistivity will be related to both permeability and the pore-size distribution. The actual moisture content of those pores will most likely be of prime interest

Whittington et al. (1981) state the virtual inseparability of the ionic and electronic conduction effects since the hydrating cement compounds control the concentration and type of ions in the evaporable water; and the water itself in cement paste is fluctuating between evaporable water, adsorbed water, interlayer water and chemically combined water.

The resistivity of the concrete will thus depend on:

1) the mix determined factors:
   - the resistivity, porosity and permeability of the aggregate,
   - the size and shape distributions of the aggregate,
   - the relative proportions of aggregate, cement and water in the initial mix,
2) and on the curing/drying history (ambient humidity, wind and temperature conditions) in its effects on
   - the porosity
   - the capillary and gel pore size distributions

- the connectivity of the pores or, more generally, the connectivity or percolation of the phases within the microstructure of the cement paste and
- the moisture condition of the pores.

A summary of the influences on resistivity are presented in Figure 3.1-2 on the following page.

Figure 3.1-2: Influences on the resistivity of concrete

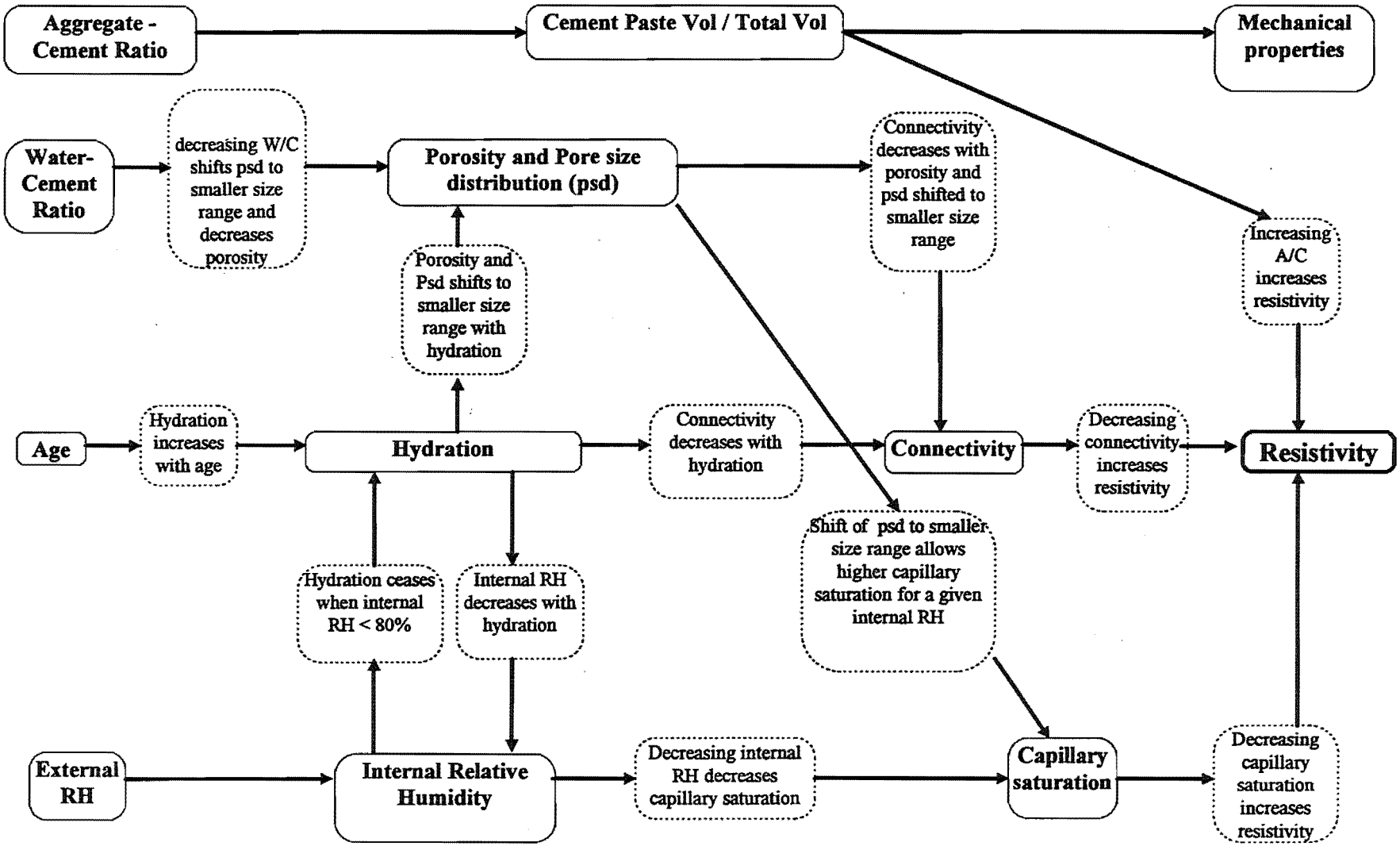

3.1.3 The relationship between resistivity and moisture content

Few studies directly relate moisture content and resistivity. Of those surveyed, only Woelfl and Lauer (1979) used relative-humidity ψ as the measure of moisture-content. They measured the electrical resistance R of moist cured concrete samples subsequently dried, weighed, and placed in relative humidity -controlled environments. Data taken from their graph (their Figure 1, p 65) are plotted in Figure 3.2-2. The data may be fitted quite well by the equation

$$\psi = -a \cdot \ln(R) + b \qquad \textbf{Equation 3.1-1}$$

where a and b are constants depending on (in this case) the w/c ratio.

- For w/c = 0.4, a = 21.8 ohm·%$^{-1}$ and b=216 ohm.
- For w/c = 0.4, a = 20.7 ohm·%$^{-1}$ and b=195 ohm.

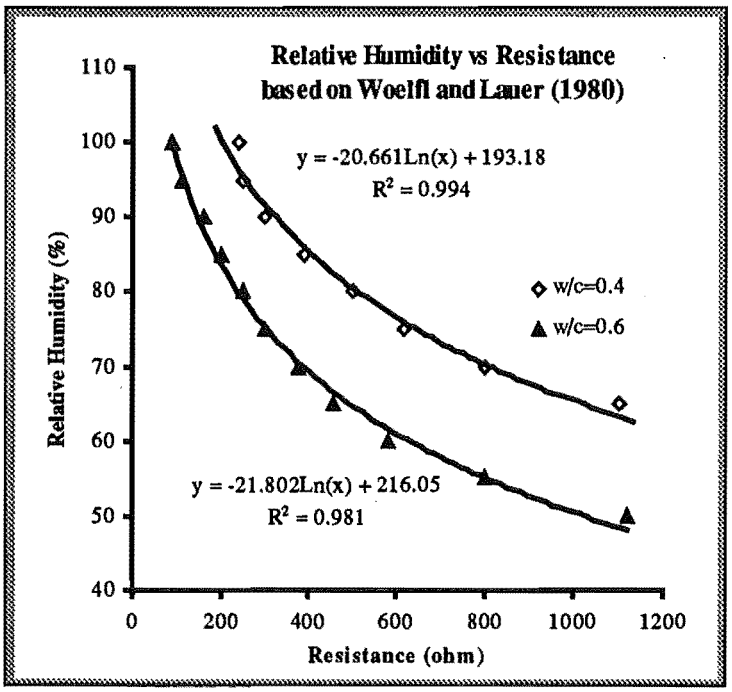

Figure 3.1-2: The relationship between resistance and relative-humidity for data based on Woelfl and Lauer (1980).

The samples were a standard size and shape so that the resistivity is directly proportional to the resistance and the resistivity- relative-humidity relationship will have the same form as the resistance- relative-humidity relationship. That is $\rho = kR$ where k is the calibration constant (see Section 3.3). Hence

$$\psi = -a \cdot \ln\left(\frac{\rho}{k}\right) + b$$
$$= -a \cdot \ln(\rho) + b' \qquad \textbf{Equation 3.1-2}$$

where $b' = a \cdot \ln(k) + b$.

The other studies surveyed (Tashiro et al. 1987, Berg, et al. 1992 and Takiguchi et al. 1992) used evaporable moisture content to characterise the moisture state. Before looking more closely at their work, we will consider the likely form of the resistivity-evaporable- moisture-content relationship.

When the resistivity of the aggregate exceeds that of the cement paste by several orders of magnitude, concrete or mortar may be treated as an agglomeration of nonconducting particles of various shapes (shape factor m) in a conducting matrix. In this case, Whittington et al. (1981) have shown that a modified form of Archie's law (Archie, 1942, quoted in Whittington et al) may be used to describe the resistivity ρ_c of concrete as a function of cement paste resistivity ρ_p and the fractional volume of cement paste φ_c.

$$\rho_c = \rho_p A \varphi_c^{-m} \qquad \textbf{Equation 3.1-3}$$

where A=1.04 and m=1.20 for their particular mix. The term $A\varphi^{-m}$ is known as the formation factor.

A similar relation could be expected to hold between the resistivity of the pore solution ρ_w and the cement paste,

$$\rho_p = \rho_w \varphi_p^{-m} \qquad \textbf{Equation 3.1-4}$$

where the paste porosity is

$$\varphi_p = \frac{V_{pores}}{V_{Paste}} \qquad \textbf{Equation 3.1-5}$$

For drier concrete, a term reflecting the degree of saturation could be factored in (Yaramanci, 1994),

$$\rho_p = \rho_w \varphi_p^{-m} s^{-n} \qquad \textbf{Equation 3.1-6}$$

where the capillary saturation s, is given by

$$s = \frac{V_{water}}{V_{pores}}$$ **Equation 3.1-7**

Combining the two equations,

$$\rho_c = A\rho_w \varphi_p^{-m} s^{-n} \varphi_c^{-q}$$ **Equation 3.1-8**

The equation above shows that in theory the resistivity of concrete could be expressed in terms of the water content. In this form it may not be very practical since it is impossible to determine accurately the resistivity of the evaporable water in the paste, nor to quantify the volume of water available for conduction at any one time. As Whittington et al (1981) note, the changes in electrical conductivity of the solid and solution phase of hydrating cement paste are closely linked with each other as the "composition and concentration of ions in the evaporable water depend upon the soluble compounds within the cement particles and residual water available; whilst the composition and structure of the solid phase depend upon the amount of water, both adsorbed and chemically combined, within the cement compounds during the hydration process" (p51). Furthermore, within pores, ionic concentration varies, increasing in so-called double-layers surrounding charged grains in cement paste. Chatterji and Kawasura (1992), for example, estimate that in low w/c pastes, most if not all positive ions are transported through these overlapping double layers (p774).

The second difficulty lies in the change in paste resistivity as hydration and drying continue. The resistivity of cement paste will increase as the pore structure changes (capillary pores becoming smaller and more segmented) and the pore saturation decreases (pores emptying). As the resistivity of the paste approaches that of the aggregate, the formation factor will change to take account of the current path through the aggregate. The approximation to insulating particles will become increasingly invalid.

After a period of time when most hydration has taken place (say after 28 days), φ_p, and ρ_w will be comparatively constant. The pore saturation, s, will be equal to the evaporable water content w if the pores were full at the beginning of the period. If in addition the paste resistivity is much less than that of the aggregate, an approximate form of Equation 3.1-8 may hold,

$$\rho_c = \rho_o w^{-n}$$ **Equation 3.1-9**

where ρ_o is the resistivity measured at the beginning of the period, when s = 1.

The pore saturation s is equivalent to a characteristic moisture content w^* expressed as

$$w^* = \frac{w - w_e}{w_o - w_e} \qquad \textbf{Equation 3.1-10}$$

where w_e is defined as the nonevaporable water or as that water remaining in equilibrium in the pores at some arbitrary dry state (heating in an oven at 105 C for 24 hours for example), and w_o is the total water content at saturation. w_o may be determined allowing the sample to take in water through free capillary suction (Hedenblad and Nilsson, 1985) or by immersing the sample in boiling water for two hours (Lopez and Gonzalez, 1993).

It is instructive to consider two attempts to express the resistivity in terms of the water content. Tashiro et al. (1987) measured the resistivity of hardened cement pastes as a function of curing time, evaporable moisture content w (measured by successive drying and weighing cycles) and cement type. They found that the resistivity could be expressed as

$$\rho = \rho_o e^{c/w} \qquad \textbf{Equation 3.1-11}$$

or

$$\ln(\rho) = \ln(\rho_o) + \frac{c}{w} \qquad \textbf{Equation 3.1-12}$$

or

$$w = c \cdot \left[\ln\left(\frac{\rho}{\rho_o}\right) \right]^{-1}$$

where c is an intrinsic quantity reflecting the microstructure of capillary pores in the paste. As hydration progresses and the pore size distribution changes, c increases so that the same evaporable moisture content yields higher resistivities, suggesting that conduction pathways are becoming restricted. After 28 days, c appears to approach a constant value, although only three data points are shown on the *c vs time* graph. The driest cement paste measured had a evaporable water content of about 0.06 kg(H_2O)/kg(paste).

Schulte et al (1978) measured the resistivity of samples of concrete of varying moisture content. For relative-humidities less than 40%, they expressed the resistivity moisture-content relationship in the form

$$\rho = \rho_o \exp\left(\frac{-\alpha \cdot \Delta w}{G}\right)$$ **Equation 3.1-13**

where α = 1.35 and G the mass of dry paste. Δw is the amount of water lost from the initial saturated state.

Berg, et al. (1992) report a detailed study of the dielectric properties of cement mortar as a function of water content. They define the relative water content (p in their paper) as the volume fraction of evaporable water in the sample divided by its initial volume fraction. This is a measure of the capillary saturation or characteristic moisture content w^* . They show that the conductance can be described as a power law of w^*, above a threshold value w_c. For water/cement ratios between 0.5 and 0.78, the conductivity G is proportional to $(w^*-w_c)^t$ with $w_c=0.05 \pm 0.003$ and $t=2.7 \pm 0.15$

In terms of the resistivity their equation may be written

$$\rho \propto \left(w^* - w_c\right)^{-t}$$ **Equation 3.1-14**

The samples were three months old at the time of measurement, when most hydration would have occurred. This is similar in form to Equation 3.1-9 above which may be written

$$\rho_p \propto w^{-n}$$ **Equation 3.1-15**

since the porosity φ is constant and the pore saturation s is proportional to the evaporable water content w.

The authors note that the conductance threshold is analogous to the percolation threshold which occurs in random networks, that is, the sharp decrease in conductivity occurs when continuous paths of water through the sample begin to break up. "The pore network is initially saturated with an ionic solution. As the water content decreases, it is mainly the water in the bulk of the pores that evaporates. Water closer to the pore surfaces is more strongly bound and remains to lower values of [w^*]....An estimate based on the measured internal surface area of cement paste shows that the conductance threshold occurs at roughly the value of [w^*] expected for monolayer coverage of the pore walls with evaporable water" (Berg et al, 1992, p5900-5902). The existence of the threshold may also indicate the increasing invalidity of the formation factor implicit in this equation.

The graph shown in the work by Berg et al., seems to indicate that the power law also applies in the region $w < w_c$ if a different value of $t > 2.7$ is used.

It is likely that even with full hydration and minimal capillary porosity, sufficient capillary porosity and permeability remain to allow relatively high levels of ionic conduction. Conduction paths blocked by gel are unlikely to be the cause of a percolation threshold. In one study, for example (Whittington et al. 1981), under conditions in which less than maximum segmentation of the capillary pores could be expected, concrete specimens increased their resistivity from about 25 ohm-m (24 hours after pouring) to about 38 ohm-m after continuous moist storage for 128 days. In this case the minimum w/c ratio was 0.6 , so that even at full hydration, the capillary porosity should be around 30%. At w/c ratios of 0.4, the capillary porosity should be at a minimum. Hughes et al (1985) report that after 25 days concrete with a w/c ratio of 0.4, had only increased its resistivity from 40 ohm-m at 24 hours to less than 70 ohm-m. It appears then, that great changes in resistivity are associated with the degree of capillary saturation, and thus that resistivity is a strong function of the evaporable moisture content of concrete.

Finally, concrete has a negative temperature coefficient of resistivity, an increase in temperature resulting in a decrease in resistivity. The resistivity of concrete at temperature T, can be related to its resistivity at a reference temperature θ, by the formula

$$\rho(T) = \frac{\rho(\theta)}{1 + \alpha(T - \theta)}$$

where $\rho(T)$ is the resistivity at T°C , $\rho(\theta)$ is the resistivity at θ°C and α is the temperature coefficient of the concrete (from Whittington et al. 1981, p.49).

An increase in resistivity could be attributed to any or all of the following:

- constriction of capillaries due to hydration (relatively small effect)
- increase in pore tortuosity (or decrease in pore connectivity, a similarly small effect)
- decrease in pore saturation due to drying (a major effect)
- decrease in ionic concentration (a strong effect but very difficult to measure or control)
- decrease in temperature (strong effect)

A porous concrete with nearly empty pores will be distinguishable from a relatively saturated but impermeable concrete, merely because high resistivity is associated with empty pores, low resistivity with full pores. It will be much easier therefore to determine the degree of saturation of pores, than to determine the pore structure itself. Fortunately we are interested in the former.

3.1.4 Profile recovery from measurements of electrical properties

When a slab is subject to some form of excitation (such as injection of current or electromagnetic radiation), the response will depend to a greater or lesser extent on the electrical properties throughout the slab. In particular, the resistivity or permittivity profile of a slab undergoing one-dimensional drying will affect the response be it the current distribution, the shape of the equipotential surfaces, or the attenuation of a reflected microwave beam. Altering the excitation in some way such as spreading the current electrodes, or altering the frequency or the direction of the microwave beam, will yield a different response. The process of profile recovery involves the determination of an excitation-response function which is sensitive to the profile. Then, which ever electrical property is measured, there are two types of profile recovery technique. Direct methods use some algorithm to generate a profile directly from the measured excitation-response function. Indirect methods compare the system excitation-response function to that calculated using a trial model profile. These methods are discussed more thoroughly in Chapters 6 and 7.

3.1.5 Resistivity as the electrical property of choice

Measurement of dielectric properties rather than pure resistivity, (in particular the use of microwaves to measure permittivity), is not without merit in its potential usefulness. However profile recovery using measurement of permittivity was considered and rejected early on in this study. It was decided that vertical electric sounding (VES), had most potential for the following reasons.

- Resistivity is thought to be fairly directly related to the evaporable moisture content in concrete.
- The measurement of resistivity using four-electrode arrays is a relatively inexpensive and straightforward technology.

- The accuracy of resistivity profiles recovered using VES techniques could be assessed by comparison with measurements of resistivity using electrodes embedded in concrete. Similar evaluation of recovered permittivity profiles would be more difficult.
- The theory of recovery of resistivity profiles using measurements of apparent resistivity made at the surface is well developed and used in geophysical situations.
- Measurement of resistivity profiles on concrete slabs therefore involved adaptation of existing technology, whereas the use of higher frequency measurements would require more relatively new and /or experimental technology.

3.2 The measurement of resistivity

Resistivity or specific resistance (in ohm-meter units), is defined as the resistance measured between opposite faces of a one m cube, so that, for any rectangular brick, the resistivity ρ, is given by

$$\rho = \frac{A}{l} R \qquad \textbf{Equation 3.2-1}$$

where the resistance, R, *is* measured between faces of area A, a distance l apart.

In practice, it is often not possible or desirable to use a cube or prism. In these cases measurement of resistivity involves measurement of the resistance (using two or four electrodes) of a material and then conversion to resistivity by means of a geometrical factor(or calibration constant) k so that $\rho = k \cdot R$

The geometrical factors depend on the size and shape of the sample and the position of the electrodes and have been calculated analytically for many electrode arrangements. Well known examples include the "Wenner" and the "Schlumberger" arrays (see Chapter 6), and the embedded "Wenner" array (McCarter and Barclay 1993). Other geometrical factors should be able to be calculated or determined from the measured resistance R_k using the same electrode arrangement on a sample having the same geometry and known resistivity ρ_k. The geometrical factor is then given by $k = \rho_k / R_k$.

3.2.1 Problems associated with the measurement of resistivity

Geometric factors such as those used for the Wenner and Schlumberger arrays, often assume point sources of current and voltage measurement at a point, whereas in practice electrodes of finite dimensions must be used. The validity of the geometrical factor must then depend on the degree to which the actual electrode (and indeed sample) dimensions approximate the ideal. The effects of finite electrode-concrete contact area in this study are discussed in Chapter 6. Where geometric factors are determined using the same electrode configuration on samples of known resistivity, this is obviously not a problem. Generally, geometrical factors are calculated assuming uniformity of resistivity throughout the sample. Resistivity is an intrinsic property of a material, and where the material has a nonuniform resistivity, or consists of a number of materials of differing resistivity, the measured resistivity is only an average value, that is, a weighted averaging of local resistivities (Koon and Knickerbocker, 1992).

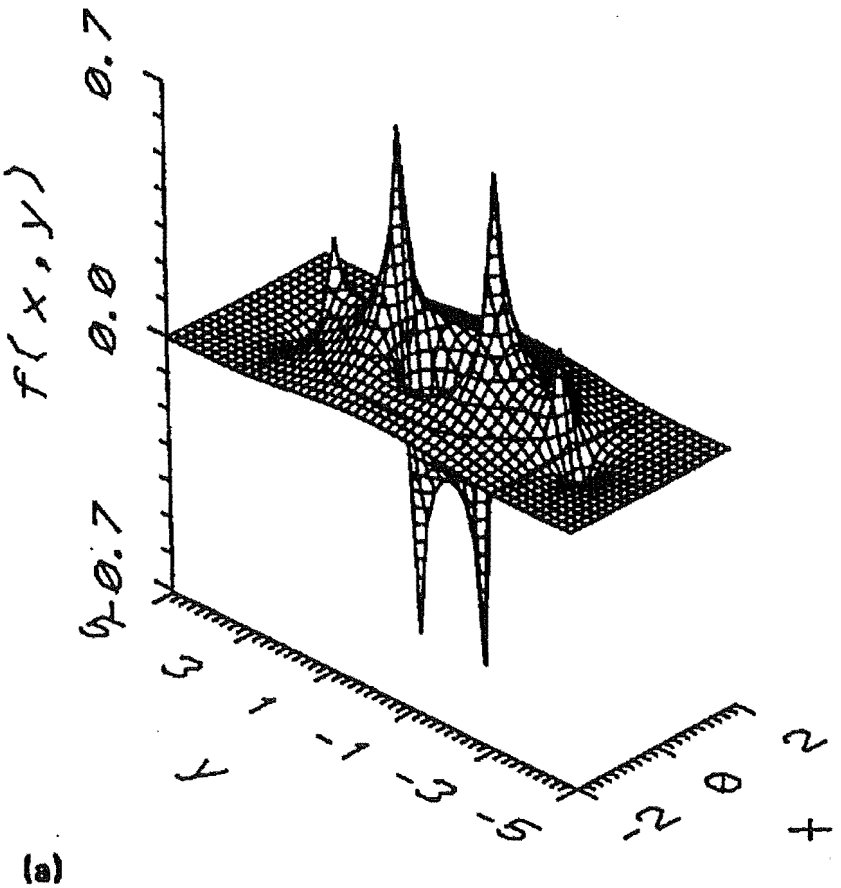

Figure 3.2-1: Weighting function for a single resistance measurement on a linear four point array (from Koon and Knickerbocker 1992)

Depending on the electrode arrangement and the nature of the nonuniformity, some regions will be weighted more strongly than others. Relatively, the effect of nonuniformity (and hence the detrimental effect on accuracy) will be greater when the sample and/or the electrode spacings are smaller, and when the resistivity contrasts within the material are greater. Koon and Knickerbocker calculated the weighting function for a number of four-electrode arrays on samples that varied horizontally. They show that the nonuniformity of a material being measured can result in negative weighting in some regions. A negative weighting means that if the local resistivity of the sample is higher than that assumed by the geometrical factor, the measured resistivity will be lower. The weighting function for a single resistance measurement on a linear four-point array, is shown in Figure 3.3-1. Note that in the region of the electrodes there is heavy negative and positive weighting. Since concrete is a very inhomogeneous material, having strong resistivity contrasts between the paste and aggregate, there are obvious hazards to measurement of resistivity, where the scale of the electrode spacings is of the same order of the scale of the nonuniformity. The effects of nonuniformity are discussed extensively in Chapters 5, 6 and 7 (dealing with vertical electric sounding) and in Chapter 8 (dealing with embedded electrodes).

Polarization at the electrodes is reponsible for much of the low-frequency-dependence of the electrical properties of concrete. Low frequency two electrode measurement is susceptible to overestimation of bulk resistivity due to the back-e.m.f. caused by polarization. That is electrode polarization will manifest as an extra resistance at the electrode-concrete interface. As concrete ages, any change in the relative size of the bulk resistance between the electrodes and the electrode contact resistance, will alter the measured resistivity. A reduction in polarization could lead to underestimate of bulk resistivity. Conversely an increase in contact resistance as the concrete dries, would lead to over-estimation.

The use of four-electrode resistivity measurement avoids much of electrode polarization problem, since the voltage (or measurement) electrodes do not draw significant current, and record the potential difference away from the current electrodes where polarization predominantly takes place.

3.3 Choice of relative-humidity and resistivity as measures of the moisture state

Although the hysteresis effect may allow relative-humidity and moisture-content to become decoupled once a slab is sealed or should the external relative-humidity swing markedly, in general, a drying concrete slab will consistently undergo desorption, moisture moving steadily toward the surface. The measurement of electrical resistivity may be correlated with measurements of relative-humidity since both are functions of moisture content.

If resistivity is the electrical property measured by the surface mounted device, calibration curves (or tables or equations) need be determined so that the moisture state of the slab may be readily calculated. It is only nearer the surface that this relationship maybe expected to breakdown, ie. near the surface calibration curves may become too easily influenced by otherwise minor environmental variations. Isothermal changes in external relative-humidity will not be accompanied by similar changes in resistivity as the sub-surface relative-humidity may scan from side to side of the hysteresis curve leaving relatively small changes in moisture-content. On the other hand, temperature fluctuations above the surface will affect both the relative-humidity and resistivity (rises in temperature causing falls in resistivity and relative-humidity).

However, for concrete deeper than some critical depth, the relative-humidity may be simply related to the moisture-content through the appropriate isothermal desorption curve. As the concrete ages, the mature pore-size-distribution will develop. If hydration has not progressed as far in the more shallow regions, which will dry faster, the pore-size-distribution will vary with depth. Correspondingly, the relative-humidity- moisture-content relationship will be likely to vary both with age and depth.

If the slab were continuously moist-cured for 28 days, then after this time the relative-humidity- resistivity calibration curves should stay relatively constant since the degree of hydration throughout the slab will be uniformly greater than 0.9 (say). In practice curing times are likely to be shorter than this. McGlone (1990) suggests that in New Zealand residential building sites, there might be up to 4 days water curing in the best circumstances. In such cases the calibration curves may be best applied to resistivity measurements below some depth that ensures appropriate hydration has taken place.

3.4 Summary

Hydrated cement paste mainly consists of insoluble calcium silicate hydrate (C-S-H) precipitated in gel form, and has a degenerate clay structure in which the layers of C-S-H crystal are crumpled and randomly arranged, so that the spaces between the layers are irregular and vary considerably in size. The complex microstructure has an inherent (gel) porosity of about 28%. Water in the gel pores is relatively tightly bound and is only released under conditions of very low relative-humidity. Under conditions of water-cement ratios greater than 0.4, or where hydration is incomplete, larger 'capillary' pores can form an interconnected network throughout the cement paste.

In concrete which is a composite of aggregate held in a matrix of hardened cement paste, most current is carried by the cement paste, at least while the concrete is young and/or wet, since the resistivity of aggregate exceeds that of the paste by several orders of magnitude. Within the cement paste, current is mainly carried by the evaporable water (which is an aqueous solution containing the ions Ca^{2+}, Na^{+}, K^{+}, OH^{-} and SO_4^{2-}) in the capillary pores. Most evaporable water is held in the capillary pores. Low resistivity basically indicates the presence of water. Conductivity is enhanced by dissolved salts and the presence of continuous pore pathways through the concrete. As hydration continues, capillary pores become smaller and continuous pore channels increasingly segmented as they become filled with the solid product of hydration (ie cement gel). Nevertheless the emptying of the capillary pores which corresponds to significant falls in relative-humidity, is associated with large rises in resistivity. Resistivity therefore is a convenient measure of moisture content.

Similarly relative-humidity is a convenient measure of moisture-content where cement paste is desorbing everywhere so that the decoupling of the resistivity-relative-humidity through hysteresis is not encountered. Relative-humidity is also appropriate because it is a measure of the energetic state of the moisture resident in the pore-structure and is the quantity likely to have physical effects on coatings and toppings.

A study of the literature suggests that the relationship between resistivity and evaporable moisture-content can be expressed as

$$\rho_p = aw^{-n} \qquad \textbf{Equation 3.4-1}$$

and that between resistivity and relative-humidity expressed as

$$\psi = -b \cdot \ln(\rho) + c \qquad \textbf{Equation 3.4-2}$$

with the various coefficients (a, b and c) showing dependence on the pore-size-distribution (determined in turn by the degree of hydration and the w/c ratio) and the aggregate-cement (a/c) ratio amongst others. The complex nature of the influences on resistivity means that the coefficients must be determined empirically, at this stage.

4. Experimental Design:

4.1 Introduction

The aim of this project is to develop a top surface mounted technique for measuring moisture profiles in drying concrete. Following a literature survey of the relevant physical and electrical properties of concrete (see Chapters 2 and 3), it was decided that we pursue the electric sounding approach. The theory of vertical electric sounding (VES) is outlined in Chapter 5. The practical component of project involved

1) the determination of resistivity profiles using VES, requiring
   - the development of an VES instrument (Chapter 6) and
   - the development of software for the recovery of resistivity profiles from the instument output (Chapter 7)
2) the development of a means for the independent evaluation of these resistivity profiles (Chapter 8)
3) the simultaneous measurement of relative-humidity and resistivity profiles and establishment of resistivity-relative-humidity calibration procedures for a wide range of concrete mixes and curing conditions (Chapters 9 and 10)
4) the generation of relative-humidity profiles from VES derived resistivity profiles using the calibration techniques and (Chapter 10)
5) the determination of the feasibility of the instrument and/or technique for use under field or laboratory conditions (Chapter 11).

The experimental plan followed four main lines. These were the development and testing of

1) the current generating and voltage measuring components of the resistivity meter,
2) the resistivity meter including array board and electrodes in its use as a vertical electric sounding (VES) instrument,
3) an alternative method for measuring resistivity profiles for use in evaluating the vertical electric sounding technique and the instrument's performance and
4) techniques for determining the relationship between relative humidity (RH) and resistivity to enable the generation of RH profiles from resistivity profiles.

The main details of the concrete models and concrete specimens are recorded here. A chart giving an overview of the work is presented in Figure 4.1-1.

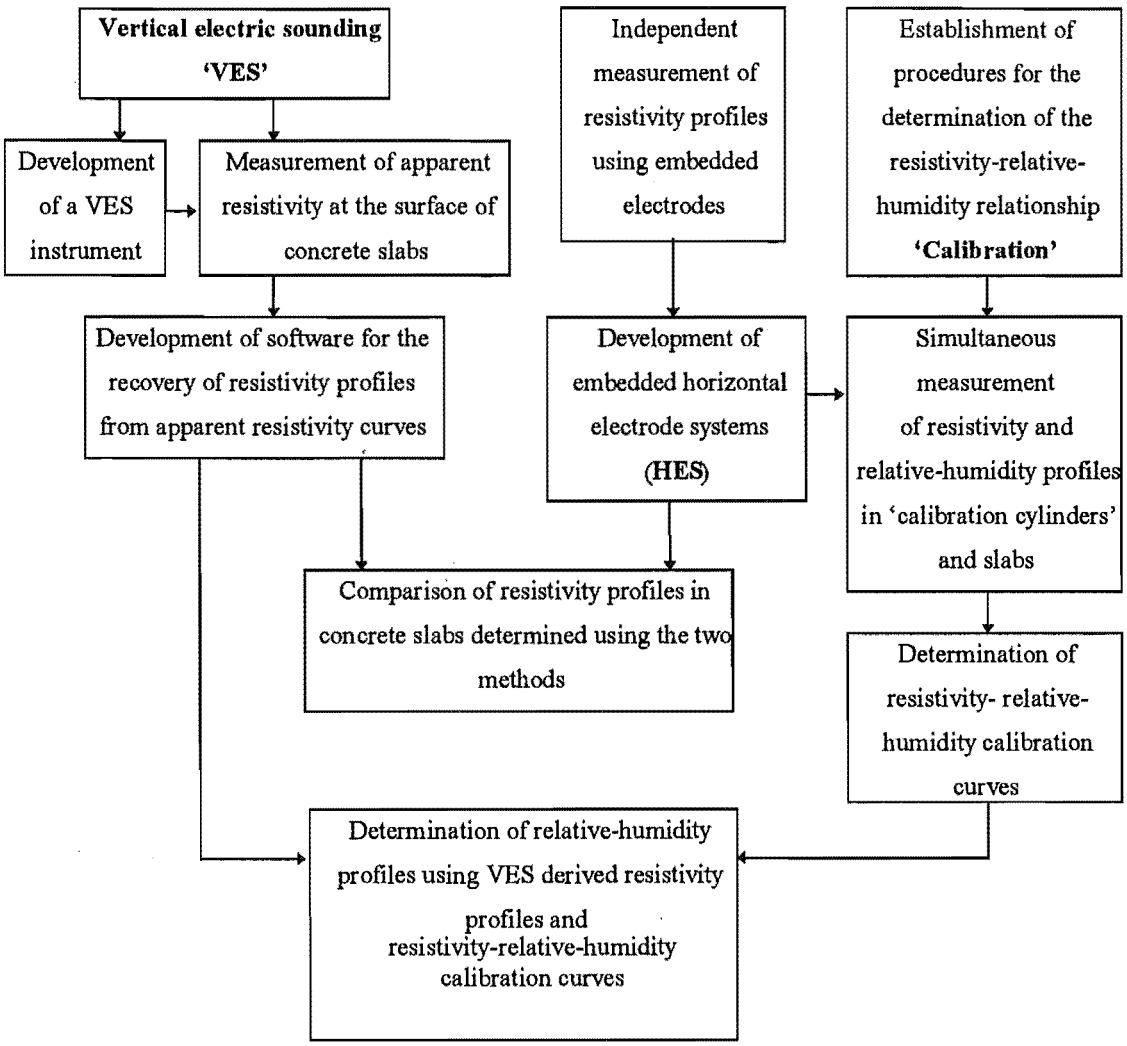

Figure 4.1-1: Project outline.

Associated with this work was a program of modelling studies (see Table 4.1-1).

Table 4.1-1: Summary of experimental and modelling work undertaken

Practical		**Modelling**	**Computer program**
Basic resistivity meter	x		
• circuit construction and optimization of components • automation of resistivity meter		• multi-resistance concrete models • circuit response models	Matlab[1]
VES instrument			
• trialling of electrodes and electrode placement methods • graphical user interface and control of computer controlled resistivity meter and data acquisition • determination of apparent resistivity curves (VES curves) • comparisons of VES curves obtained using different measurement probe spacings and different electrode configurations • 'inversion' of VES curve using a variety of starting models and constraints • special difficulties posed by the presence of rinforcing in Slab #5 • transformation from smooth recovered resistivity profile to relative-humidity profile •		• effect of wet electrodes on surface of concrete • effect of lateral nonconducting boundaries on apparent resistivity curves • effect of finite size of electrode contact area on VES • effect of finite measurement probe spacing on VES • generation of likely resistivity, relative-humidity and evaporable moisture-content profiles • generation of likely apparent resistivity curves and subsequent recovery of model profile • determination of the effect of recovery with different numbers of parameters and different constraints (such as the imposition of a fallling profile). • determination of optimal methods of generation of smooth, continuous resistivity profiles from the discrete layered recovered profile • determination of the nature and scope of uncertainty in the recovered profile owing to uncertainty in the apparent resistivity curve	Jam-2[2] Matlab Matlab (finite diff) Matlab (finite diff) Matlab Matlab Matlab (nverjn*.m) Matlab Matlab
Direct resistivity profile measurement			
• determination of optimum electrode spacing and size • trialling of PPES HES#1, HES#2 and HES#3[3] • determination of optimum calibration method (conducting solution and in situ) and the time of calibration • comparisons of two- and four-electrode measurement		• effect of embedded electrodes on the flow of moisture and the relative-humidity profile • ability of embedded electrodes to measure profiles as the resistivity gradient increases. • influence of electrode spacing on the reliability and accuracy of resistivity measurement • influence of nonconducting boundaries on resistivity measurement	JAM-2 Matlab (finite diff) Matlab (finite diff) Matlab (finite diff)
Measurement of relative-humidity			
• calibration of relative-humidity probes • analysis of relative-humidity raw and calibrated data		• determination of likely relative-humidity profiles	Parrott (1991)
Resistivity- relative-humidity calibration			
• interpolation of resistivity data to match relative-humidity data • fitting of curve to resistivity-relative-humidity data		• determination of likely resistivity- relative-humidity calibration curves	Matlabab and JAM-2

Notes 1:"Matlab ®for Windows" The MathWorks, 2: "Jam-2 version 1, Two-dimensional moisture flow model" copy given by the author Jesper Arfvidsson, 3: PPES: parallel plate electrode system, HES horizontal electrode system

4.2 'Specimens' used for the testing of the current generating and voltage measuring components of the resistivity meter

The development of the resistivity meter is described in some detail in Chapter 6. In order to test the current generating and voltage measuring characteristics of the meter, two simple, resistance-network models of a concrete slab were constructed. The components of the first, seven-resistor model comprised resistors to represent the four variable electrode-concrete interfaces (for the two current probes A and B, and two voltage measuring probes M and N) and resistors to represent the variable resistivity of the concrete between A and M, M and N, and N and B (Figure 4.2-1).

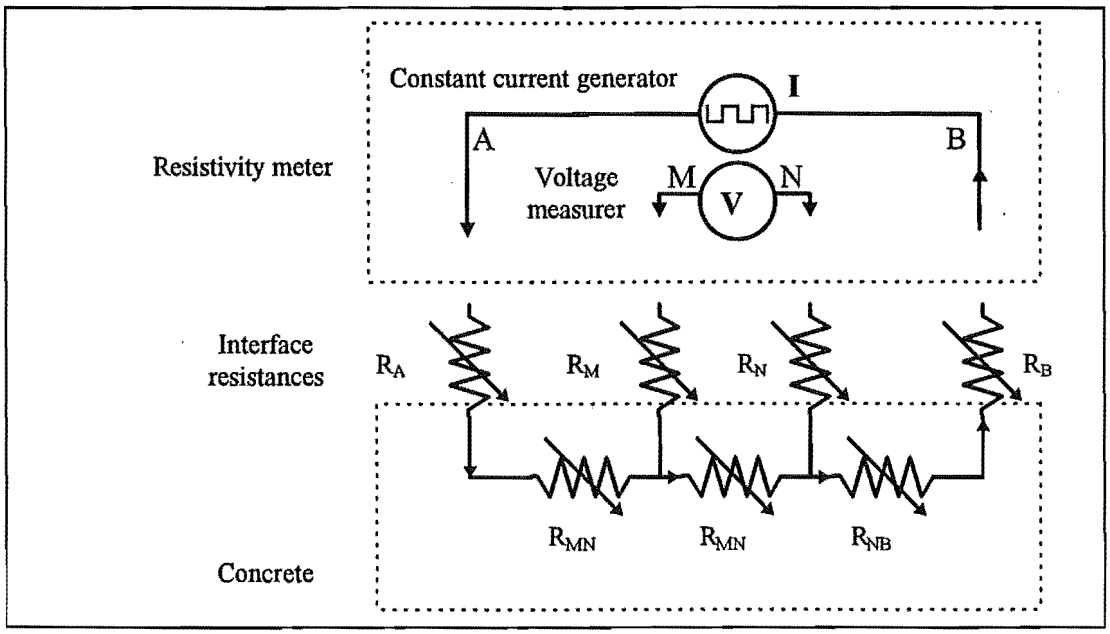

Figure 4.2-1: The seven resistor model of the concrete slab and interface with the - resistivity meter.

R_A, R_B, R_M, and R_N, could vary from zero to 20 M-ohms. R_{AM}, and R_{NB} varied from , zero to about one M-ohm and R_{MN} had two ranges from zero to 200 ohms and from zero to 10 K-ohm. Using this model a large range of conditions were able to be set up, including high and uneven interface resistances, low currents and low voltages between the measuring probes. This simple model was able to provide extreme test conditions.

4.3 'Specimens' used for the testing of the resistivity meter in its use as a VES instrument.

A series of concrete slabs were cast to investigate the sounding technique and electrode design. The VES instrument was designed to be placed on the top surface of a concrete flooring slab. In order to determine the instruments accuracy in measuring a resistivity profile, an independent method of measuring resistivity was sought. Consequently a series of slabs were cast incorporating horizontal electrode systems (HES) which are described in Chapter 8. Two sizes of slabs were poured. After the first trial slabs (#0, #1 and #2), the second, larger size was used to increase the surface area of the slab once it was realized that the VES 'wet' electrode systems slightly altered the local surface resistivity, and to weaken the effects of the non-conducting side boundaries. These slabs also had housings embedded to allow measurement of relative humidity.

The development of the VES instrument was ongoing and only towards the end of the project were particularly useful VES curves measured. Consequently the resistivity measurement record is broken in places and inaccurate in others. Nevertheless throughout the project the instrument, in whatever state it was currently in, was used to record VES curves. At the same time, embedded electrode systems and RH probes were used to measure resistivity and RH profiles.

Descriptions of the specimen slabs are given in the following sections. A summary of specimen slabs and and cylinders is presented in Table 4.4-2.

4.3.1 Slab #0

One slab (1m x 0.5 m x 0.15 m) was poured for initial investigation. In order to ensure drying from the top surface only, the slab mould was sealed with paint and internally lined with closed-cell foam. It was thought that the foam rubber would allow the slab to shrink away from the mould walls without losing the air and moisture seal. After pouring the slab was cured for seven days in a 'fog room', that is a room maintained at 100% relative-humidity. (This was located in the Department of Civil Engineering of the University of Canterbury).

The slab also had 10 mm x 18 mm horizontal holes cast into one side, into which, relative humidity (RH) probes could be introduced.The holes were sealed with rubber tubing when RH measurements were not being made and were positioned at various

depths from the surface. To ensure that each hole was unaffected by the others, no two holes were in the same vertical plane.

The Vaisala HM34 humidity and temperature meter was used with this slab. The meter has an extendable probe which houses at its tip Vaisala's Humicap© humidity sensor and a Pt 100 temperature sensor. RH and temperature values are displayed on a LCD disply panel on the main body of the meter. A remote control was constructed to allow the meter to be powered up and read without disturbing the sensor or the seal between the cavity and the relative-humidity probe. The sensitivity of the seal to probe movement and the 24 hour wait necessary between readings made the initial RH measurement process unsatisfactory, although the criticality of probe sealing was not appreciated fully at the time.

Table 4.3-1. Concrete mix specifications for Slab #0

Nominal strength	Coarse Aggregate		Concrete sand	Cement (c)	Water (w)	w/c ratio
	19 mm	12 mm				
25 (MPa)	660kg/m^3	400 kg/m^3	870 kg/m^3	260 kg/m^3	190 kg/m^3	0.73

4.3.2 Slabs #1 and #2

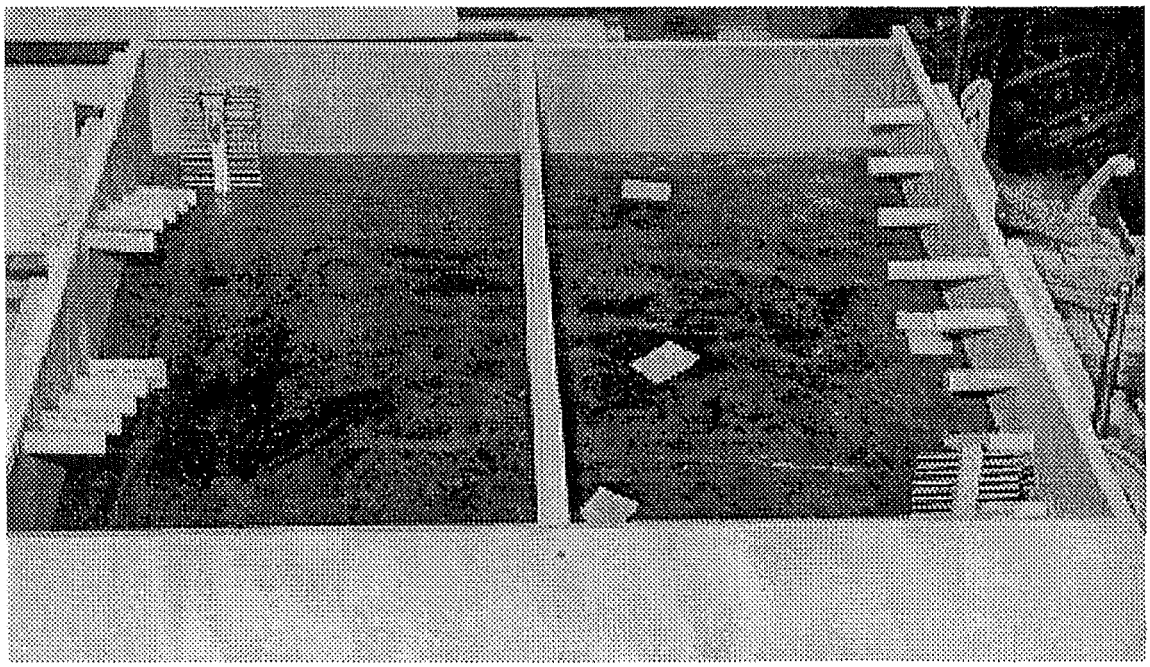

Figure 4.3-1: Molds for slabs #1 and #2 showing positioning of relative-humidity probe housings and positions of HES#1s.

The next two slabs (Figure 4.3-1) and Cylinders #1 and #2 (see Section 4.4) were poured at the same time as each other and from the same mix. This was the same as that for slab #0, except it had a lower w/c ratio (0.6). The slabs were the same size as Slab #0. However the slabs were fitted with different RH probe housings (see Chapter 9) and the, then new, horizontal electrode system (HES#1 see Chapter 8.). The HES#1 was cast in one corner 100 mm from the adjacent end and side. Along the same side 10 RH probe housings were cast. These housings and the HES were required for calibration and comparison (see the Introduction above) and were aligned along one side to ensure minimum interference with the VES process (Figure 4.3-2).

Like Slab #0, the slabs were demoulded after seven days moist curing in the fog-room. To ensure one dimensional drying the bottom, end and side surfaces were given several coats of with 'Sika Antisol A' curing compound to form a moisture impermeable membrane.

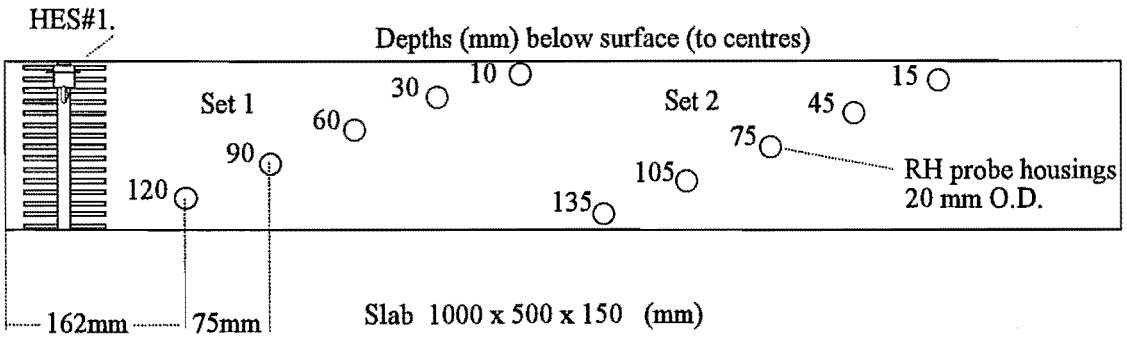

Figure 4.3-2. HES#1 and RH probe housing positions in slabs #1 and #2. The HES#1 was actually oriented parallel to the end and not to the side as shown here.

4.3.3 Slabs #3 - #8

By this time it was decided that larger slabs were necessary in order to minimise the boundary effects on the VES technique and enable adequate testing of the methods used for correction of these boundary effects. In conjunction with a corresponding set of calibration cylinders (see below), six more slabs (1.5 m x1.2 mx 0.15 m) were poured using concrete mixes common in the New Zealand commercial building industry.

Slabs #3, #4 and #5 had RH probe housings at the same depths and spacings as Slabs #1 and #1, and an additional five housings at 10, 20, 30, 40 and 50 mm depths to their

centres. These last five were added to enable better resolution of the shallow regions where RH changes the most. The housings were all located on the same (long) side of the slab.

In addition to the newer version of the HES#1, two new horizontal electrode systems (HES#2 and HES#3) were cast into the slabs. These were located facing each other at the other corner along the side with the RH housings. The relative locations of the three types of HES and the 15 RH probe housings are shown in photograph of Slab #5 in Figure 4.3-3.

Slab #5 was similar to Slab #4 in every respect except that a '665' reinforcing mesh was embedded in the slab at a depth of 30mm from the surface.

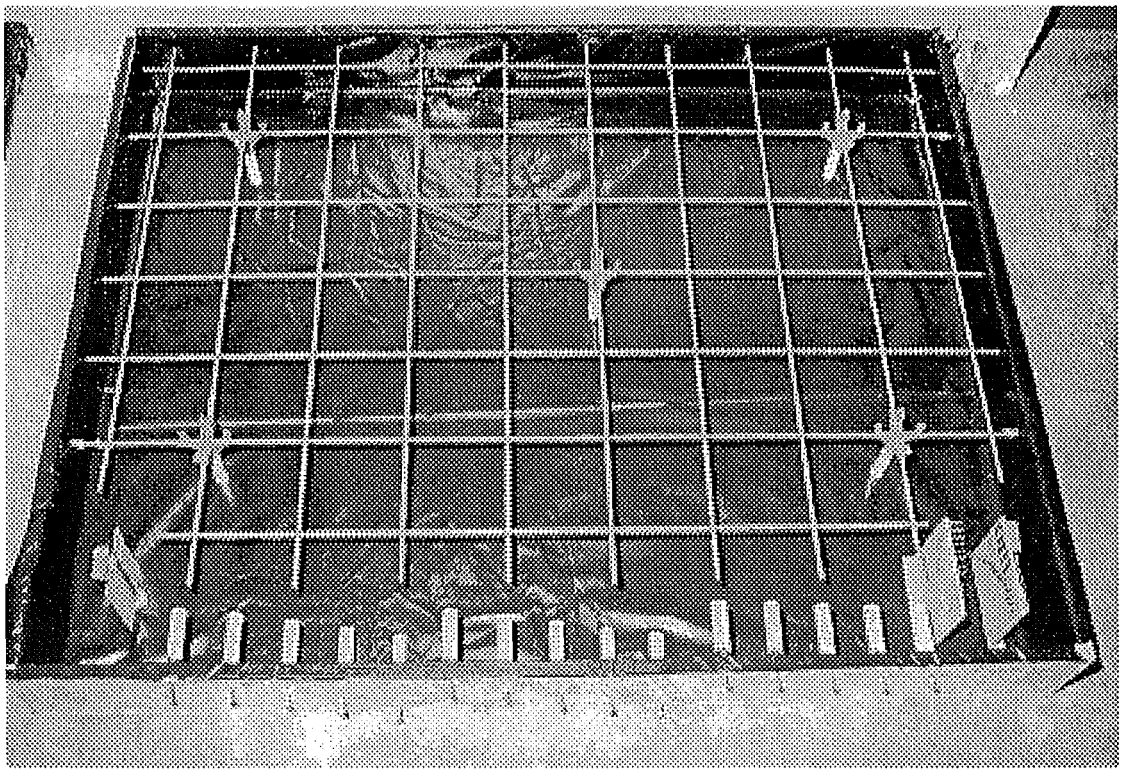

Figure 4.3-3: Slab #5 before pouring, showing the reinforcing mesh and the positions of the horizontal electrode systems (from left to right, HES#1, HES#3 and HES#2.

Slabs #6, #7 and #8 had a different arrangement of HES types and RH probes housings. In these slabs 10 housings were arranged at equal horizontal spacings on a downward parabolic curve so that the housings were more closely spaced vertically, the more shallow the depth.

Slab #6 had one HES#2 and two HES#1, one of which had an 'aerial' din plug that was held clear of the concrete surface so that resistivity measurements could be taken soon after pouring and before the concrete had set.

Slab #7 and #8 had just one HES#2 and one HES #1.

Because of their size, Slabs #3 to #8 were cast in situ and unable to be cured in a fog-room. Instead, for the first week after pouring, their top surfaces were covered with wet hessian over which plastic sheeting was laid. Peridically, the plastic sheet was lifted and the hessian rewetted.

4.4 Specimens used in the development and testing of techniques for determining the relationship between relative humidity (RH) and resistivity

The development and testing of alternative methods for measuring resistivity profiles involved the use of different embedded electrode systems. The positioning of HES types in slabs has been described above as has the positioning of RH probe housings.. In order to determine the relationship between RH and resistivity in drying profiles a direct correlation method was chosen. Thus the RH profile and the resistivity profile would be measured virtually simultaneously in the same specimen of concrete.

150 mm long sections of 400 mm outside diameter plastic stormwater pipe were attached to a base plate. From five (Cylinders #1 and #3) to ten (Cylinders #2 and #4) RH housings were set into the pipe at various depths (see Table 4.4-1). These housings were horizontally separated so that no RH probe housing would interfere with the drying of concrete in the vicinity of adjacent housings.

Table 4.4-1. Depth of RH housings in cylinders #1 to #13. Cylinders #1 and #3 had only Set 1, in conjunction with a parallel plate electrode system (PPES). The other cylinders used both sets in conjunction with an HES.

Set 1	Set 2
Depth (mm)	Depth (mm)
10	15
30	45
60	75
90	105
120	135

Cylinders #1 and #3 had a parallel plate system for measuring resistivity. In this method two sets of two parallel plate electrodes are suspended in the concrete at the same level

as one of the five RH housings so that RH and resistivity may be measured at the same depth. The parallel plate electrode system (PPES) is described in Chapter 8. Cylinders #2, #4, #5 -#9 and #11, had 10 relative humidity probe housings and a horizontal electrode system having 15 stainless steel rods. (Figure 4.4-1 and 4.4-2). Further details of the calibration cylinders are given in Table 4.4-2.

In order to calibrate the electrode systems used in Slabs #1 and #2 and in Cylinders #1-#4, a small parallel plate watertight conductivity measuring cell was constructed. For the rest of the concrete specimens, each time a fresh batch of concrete was poured, three 100 mm cubic calibration cells were filled with the same concrete. These underwent the same curing conditions as the concrete specimens. The electrode system calibration process itself is explained in detail in Chapter 8.

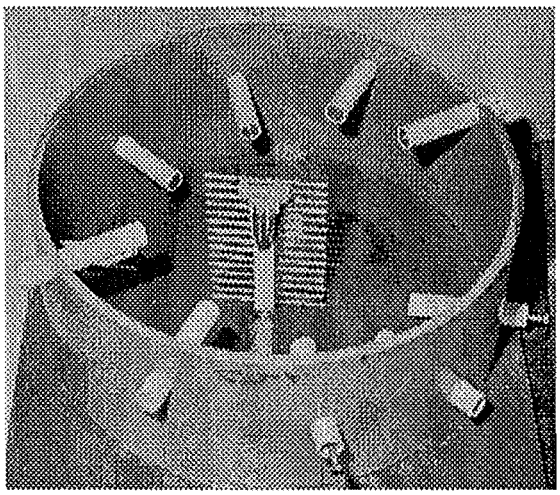

Figure 4.4-1: Cylinders #2, #4, #5 -#9 and #11, have 10 relative humidity probe housings and a horizontal electrode system having 15 stainless steel rods.

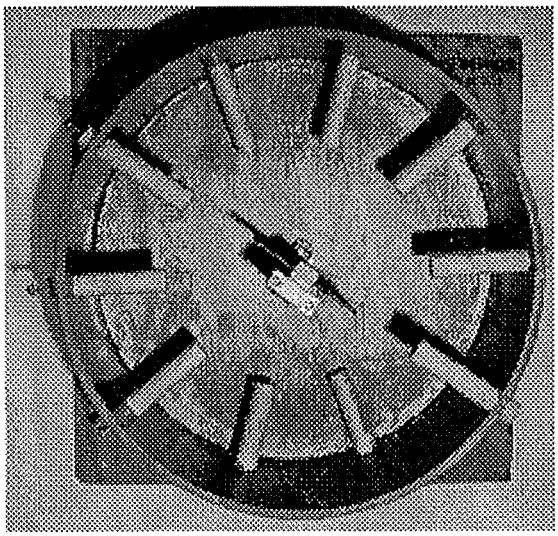

Figure 4.4-2:Top view of a cylinder showing the arrangements of ten rh probes and an HES #1.

Table 4.4-2 Summary of slab and cylinder characteristics

	Date Poured	w/c	Nominal strength	HES types	No. RH probes	Where stored	Special features
Cylinders							
#1	14/9/94	0.6	30 MPa	PPES#1	5	Fuels Lab	Warm/Dry
#2	14/9/94	0.6	30 MPa	HES#1	10	Fuels Lab	Warm/Dry
#3	13/10/94	0.6	30 MPa	PPES#2	5	Fuels Lab	Warm/Dry
#4	13/10/94	0.6	30 MPa	HES#1	10	Fuels Lab	Warm/Dry
#5 - #7	15/6/95	0.59	30 MPa	HES#1	10	Fuels Lab	Warm/Dry
#8 - #10	29/8/95	0.67	25 MPa	HES#1	10	Fuels Lab	Warm/Dry
#11	19/1/96	0.48	40 MPa	HES#2	10	MicroFilt Lb	Warm/Dry
#12	19/1/96	0.48	40 MPa	HES#1	10	MicroFilt Lb	Warm/Dry
#13	19/1/96	0.48	40 MPa	HES#2	10	MicroFilt Lb	Warm/Dry
Slabs							
#0		0.73	-	None	6	Fuels Lab	Warm/Dry
#1	13/10/94	0.6	30 MPa	HES#1	10	Fuels Lab	Warm/Dry
#2	13/10/94	0.6	30 MPa	HES#1	10	Fuels Lab	Warm/Dry
#3	27/6/95	0.59	30 MPa	HES#1,#2,#3	15	Packing Rm	Cool
#4	11/7/95	0.67	25 MPa	HES#1,#2,#3	15	Packing Rm	Cool
#5	11/7/95	0.67	25 MPa	HES#1,#2,#3	15	Packing Rm	Cool, reinforced
#6	29/8/95	0.67	25 MPa	HES#1,#2	10	MicroFilt Lb	Warm/Dry
#7	10/10/95	0.67	25 MPa	HES#1,#2	10	MicroFilt Lb	Warm/Dry
#8	19/1/96	0.48	40 MPa	HES#1,#2	10	MicroFilt Lb	Warm/Dry

4.5 Modelling

"Matlab®for Windows" by The MathWorks is referred to in this thesis as Matlab. As is evident in Table 4.1-1, a good deal of the modelling work was carried out using Matlab. In addition the inversion programs written to recover resistivity profiles from apparent resistivity curves were written in Matlab. Towards the end of the thesis work the virtues of Microsoft Excel version 5 were discovered. Excel proved excellent as means of data storage, manipulation, analysis and presentation. Although it was not used in the inversion process it was useful in determination of likely relative-humidity profiles and in determination of the relative-humidity-resistivity relationship.

4.5.1 Finite difference modelling

Some independent analysis of the measurement of resistivity was desirable since neither method (vertical electric sounding nor the use of embedded electrodes) was an established method of measuring resistivity profiles in concrete. Some work was undertaken using the commercial program Algor. However the program is large and unwieldy, and unsuitable for the need I had to generate a large number of models which

vary in one or two parameters only, such as age, resistivity gradient, electrode position and so on. Consequently a finite difference program was written in Matlab (although the non-Windows 386-Matlab version 5 was of most use here). A description of the finite difference program and its application to two-dimensional modelling of both the vertical electric sounding process and embedded electrode systems, will be found in the appendices.

4.5.2 Jam-2

A copy of "Jam-2 version 1" was donated by the author Jesper Arfvidsson. This program allows moisture flow to be determined in two-dimensional space for a great range of shape and complexity. The moisture state and flow conditions at different boundaries may be set inependently. Jam-2 was used to determine the influence of electrodes on local moisture flow and relative-humidity, the influence of 'wet' electrodes on the moisture state of the surface (both neglible) and to provide theoretical relative-humidity profiles. The difference in form between relative-humidity profiles and those generated using Parrotts (1990) equations and indeed those measured by the author, appear caused by the absence of the influence of hydration in Jam-2. The program was written to assess likely flows of moisture through buildings made of a cariety of materials in various moisture states, exposed to different conditions and it is assumed that the concrete (when used) is relatively well hydrated. It is not, as a consequence ideally suited to the experimental conditions used in this study, and the results of modelling studies using Jam-2 were taken to be indicative and not particularly accurate.

5. Vertical Electric Sounding I: Theory

5.1 Introduction

Techniques of vertical electric sounding (VES) have been extensively studied and practised in geophysics to obtain resistivity profiles beneath the surface to depths up to hundreds of kilometers (Zhdanov and Keller, 1994). The basic technique involves the introduction of current into the ground through point electrodes or line contacts and the measurement of potential at other electrodes in the vicinity of the current flow. It is then possible to obtain an effective or apparent resistivity of the subsurface. Increasing the separation of the two current electrodes forces the current to take a deeper path so that the apparent resistivity at the surface, as a function of current probe spacing, is a reflection of the resistivity profile of the subsurface. By mathematically 'inverting' the apparent resistivity curve (also known as the VES curve) the true resistivity profile may be recovered.

In this chapter some theoretical aspects of vertical electric sounding are presented. We consider the resistivity measured at the surface of a half-space with uniform resistivity before addressing the problem of the relationship between the apparent resistivity and the resistivity profile in a stratified half-space in Sections 5.3 and 5.4. The generation of apparent resistivity curves associated with some likely modelled profiles is discussed in Section 5.5. The theoretical analysis initially assumes that the electrodes are point sinks and sources and that, in the case of the Schlumberger array, the voltage measurement spacing is negligible. A two dimensional model is used to predict the effects on measurement of apparent resistivity when these ideal conditions are not fulfilled in Sections 5.6.

The recovery of resistivity profiles from apparent resistivity curves is presented in Section 5.7. Among the various methods of the recovery of profiles from apparent resistivity curves two so-called indirect methods have been particularly useful. The interpretation software that was developed based on these methods is described in Section 5.8. Surprisingly there is little difference between the VES curves predicted for model profiles with large numbers of layers and profiles that consist of just two or three layers. The ability of the inversion software to recover a range of model profiles is investigated.

For a full development of the theory of vertical sounding the reader is referred to Koefoed (1979), Parasnis (1982) or Zhdanov and Keller (1994) amongst others. In Chapter 6, the instrument developed for measurement and analysis of apparent resistivity curves will be described..

5.2 The apparent resistivity of a homogeneous earth

If current *I*, is injected into a homogeneous, semi-infinite slab, of resistivity ρ, a potential field *V(r)* will be set up.

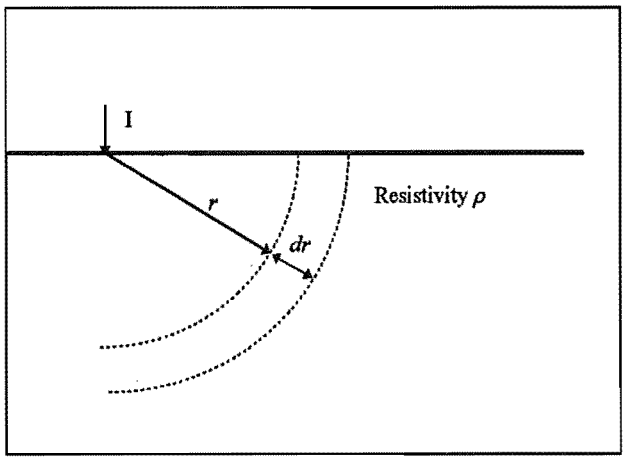

Figure 5.2-1. Point current on homogeneous earth of resistivity ρ

The resistance *dR* across a shell of thickness *dr* at a distance *r* (Figure 5.2-1) from the point source is given by

$$dR = \frac{\rho dr}{2\pi r^2}$$

The potential at *r* is given by

$$V(r) = -\int_{r=0}^{r} IdR = -\int_{r=0}^{r} \frac{I\rho dr}{2\pi r^2}$$

so that

$$V(r) = \frac{I\rho}{2\pi r} \qquad \text{Equation 5.2-1}$$

In practice current is injected at electrode A, and collected at another electrode B. The potential at any point *r* from A and *r'* from B is then

$$V(r) = \frac{I\rho}{2\pi}\left(\frac{1}{r} - \frac{1}{r'}\right)$$

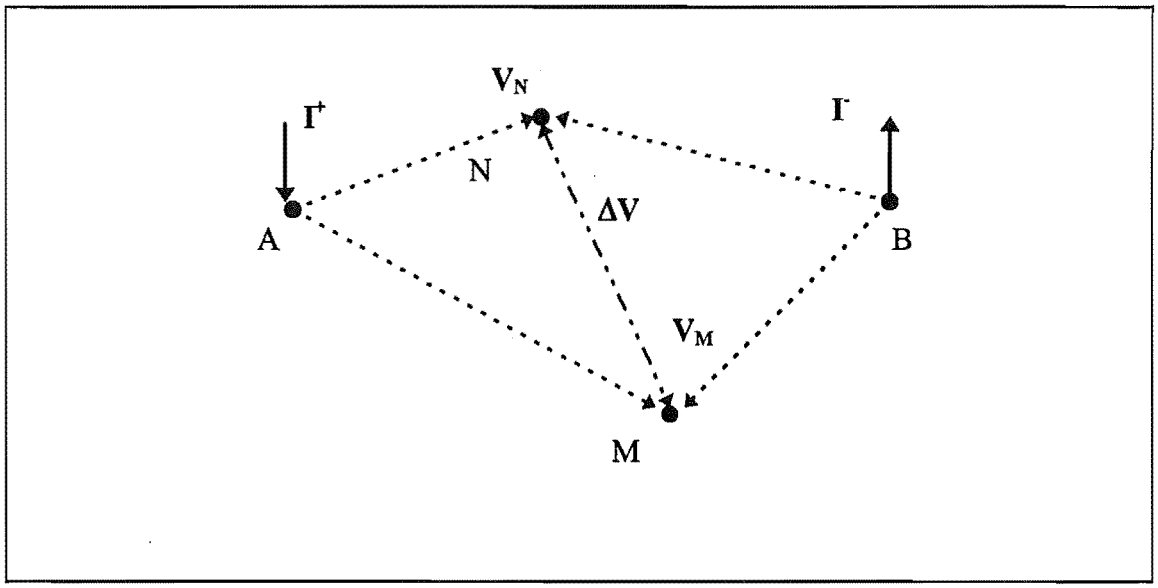

Figure 5.2-2. The injection of current into a homogeneous earth between two electrodes at A and B will result in a potential difference between two other points M and N which depends on the geometrical arrangement of the electrodes.

Resistivity determination is by measurement of the potential difference between two voltage measurement probes M and N (Figure 5.2-2).

At M,

$$V_m = \frac{I\rho}{2\pi}\left(\frac{1}{AM} - \frac{1}{BM}\right)$$

and at N,

$$V_n = \frac{I\rho}{2\pi}\left(\frac{1}{AN} - \frac{1}{BN}\right)$$

Putting

$$G = \left(\frac{1}{AM} - \frac{1}{BM} - \frac{1}{AN} + \frac{1}{BN}\right)$$

the potential difference between the measurement probes is

$$\Delta V = V_m - V_n = \frac{I\rho G}{2\pi}$$

and thus, the resistivity of a homogeneous slab is given by

$$\rho = \frac{2\pi}{G}\left|\frac{\Delta V}{I}\right|$$

G is a geometrical factor depending on the particular electrode configuration.

Two commonly used symmetrical electrodes configurations are the Wenner array and the Schlumberger array. In these arrays, the electrodes are in line and symmetrically spaced with the two current electrodes enclosing the measurement electrodes.

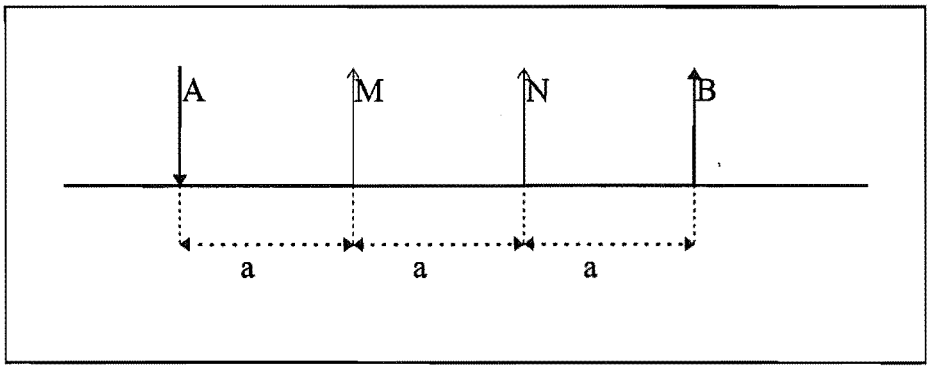

Figure 5.2-3. Probe configuration: Wenner array.

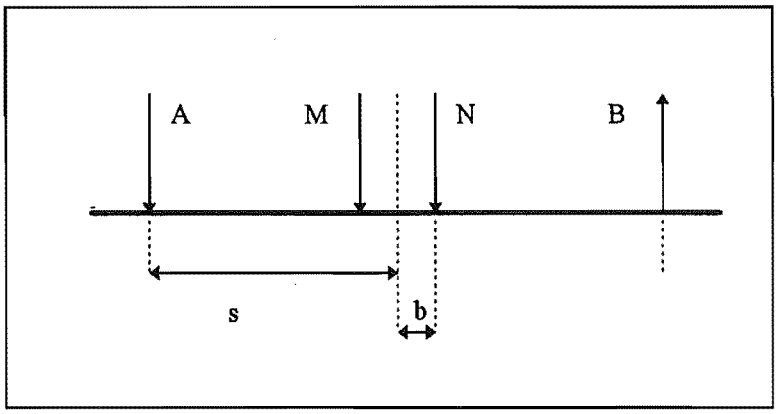

Figure 5.2-4. Probe configuration: Schlumberger array.

The Wenner array has electrodes equally spaced (Figure 5.2-3). Thus, when the current probe spacing is increased in the course of carrying out vertical electric sounding, the measurement probes must be moved proportionately.

Since AM=BN=a, and AN=BM=2a, G=1/a, the resistivity measured by the Wenner array is

$$\rho = 2\pi a \left| \frac{\Delta V}{I} \right|$$

For the Schlumberger array (Figure 5.2-4), the current electrode spacing AB (=2s) is generally taken to be more than five times the measurement electrode spacing MN (=2b). The main advantage of this array is that only the current probes need be spread wider. In

practice, however, when the potential difference drops below some critical level as the current probe separation increases, the measurement probe spacing is increased to AB/5. Since AM=BN=s-b, and AN=BM=s+b, the resistivity measured by the Schlumberger array is

$$\rho_s = \frac{\pi(s^2 - b^2)}{2b}\left|\frac{\Delta V}{I}\right| \qquad \text{Equation 5.2-2}$$

The ideal Schlumberger array has $b << s$ so that Equation 5.2-2 may be written as

$$\rho_s = \frac{2\pi s^2}{I}\left|\frac{\partial V}{\partial R}\right| \qquad \text{Equation 5.2-3}$$

where R is the distance between a current electrode and the center of the array and

$$\frac{\partial V}{\partial R} \approx \frac{\Delta V}{2b}$$

5.3 The apparent resistivity of a horizontally stratified slab

Apart from the local inhomogeneity caused by the small-scale concrete structure, a drying slab will exhibit a resistivity profile, that is, a variation of resistivity with depth. If the probes are moved about on the surface of the semi-infinite uniform slab, the resistivity measured using these equations will be the same as long as the appropriate configuration is maintained. On a horizontally stratified or otherwise non-uniform slab, the resistivity as determined by Equation 5.2-2 will vary as the spacings are changed. In this case the resistivity is termed the *apparent resistivity* ρ_a and represents a weighted average resistivity of the material beneath and between the current probes, reflecting the current distribution through the material.

To the extent that the resistivity profile can be assumed to consist of a number of discrete layers each of uniform resistivity, the apparent resistivity may be determined using the layer thicknesses h and resistivities ρ. An outline of the method follows. The method is based on Parasnis (1982). For full derivation the reader is referred to that work and also Koefoed (1979).

"Let *n-1* layers rest on an *n*th 'layer', the infinite substratum...Choosing a cylindrical coordinate system R, θ, z, with the electrode C as the origin and z positive downwards, Laplace's equation for the electric potential V in each layer can be written as

$$\frac{\partial^2 V}{\partial R^2}+\frac{1}{R}\frac{\partial V}{\partial R}+\frac{\partial^2 V}{\partial z^2}=0$$

since by symmetry V is independent of θ [Figure 5.3-1].

"Assuming $V(R,z)=F(R)G(z)$ where F is a function of R only and G of z only, the equation is separated into the two equations

$$\frac{\partial^2 G}{\partial z^2}-\lambda^2 G=0$$

$$\frac{\partial^2 F}{\partial R^2}+\frac{1}{R}\frac{\partial F}{\partial R}+\lambda^2 F=0$$

"...The most general solution for the potential in any layer j ($j\neq 1$ or n) is then

$$V_j=\int_0^\infty\left[A_j(\lambda)e^{-\lambda z}+B_j(\lambda)e^{\lambda z}\right]J_0(\lambda R)d\lambda \qquad \text{[Equation 5.3-4]}$$

" [where λ is a variable of integration and $J_0(\lambda R)$ is the zeroth order Bessel equation of the first kind]...For $j=n$ [the substratum]...

$$V_n=\int_0^\infty A_n(\lambda)e^{-\lambda z}J_0(\lambda R)d\lambda \qquad \text{[Equation 5.3-5]}$$

"...In the topmost layer ($j=1$),...

$$V_1=\frac{I\rho_1}{2\pi}\int_0^\infty e^{-\lambda z}J_0(\lambda R)d\lambda+\int_0^\infty A_1(\lambda)(e^{-\lambda z}+e^{\lambda z})J_0(\lambda R)d\lambda \qquad \text{[Equation 5.3-6]}$$

"...From the continuity of V_j and the current density normal to the layer interfaces we have, for depths $z=d_j$ ($j=1,2,...,n-1$),

$$V_{j-1}=V_j$$

$$\frac{1}{\rho_{j-1}}\frac{\partial V_{j-1}}{\partial z}=\frac{1}{\rho_j}\frac{\partial V_j}{\partial z} \qquad \text{[Equation 5.3-7]}$$

"...There are altogether $2n$-2 unknown functions $A(\lambda)$, $B(\lambda)$ to be determined...by solving the system of $2n$-2 linear equations obtained from the conditions [Equation 5.2-7]. The solution is tedious but straightforward" (Parasnis, 1972 p 372-373).

The result may be presented as

$$V(z,R) = \frac{1}{2\pi}\int_0^\infty T(\lambda)J_0(\lambda R)d\lambda \qquad \text{Equation 5.3-8}$$

where $T(\lambda)$ is known as the resistivity transform and must be be calculated from the layer parameters using recurrence formulae. The layer parameters are now expressed in terms of the layer resistivities ρ_j $(j=1,2,...n)$ and thicknesses h_j $(j=1,2,...n-1)$.

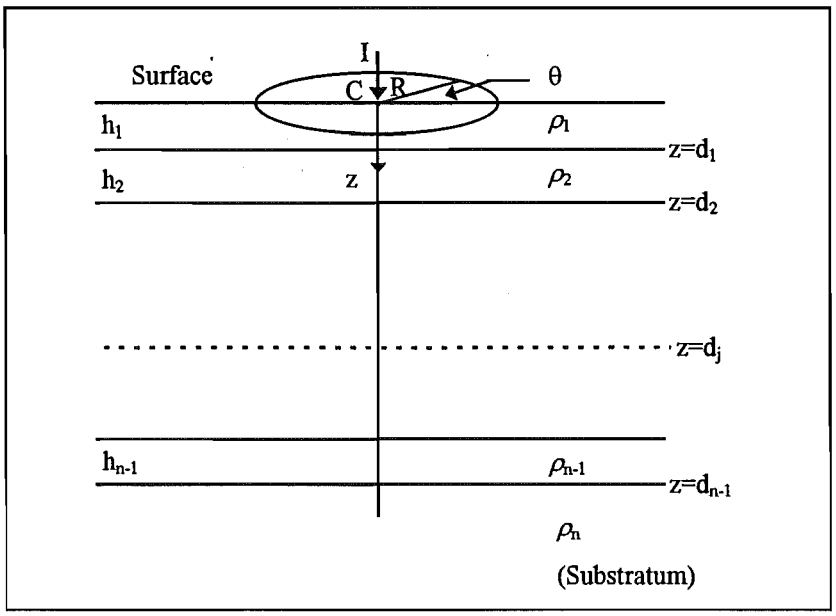

Figure 5.3-1: Point electrode on a stratified earth and a cylindrical coordinate system.

"For a layer (ρ_{n-1}, h_{n-1}) on top of a substratum (ρ_n)

$$T_{n-1}(\lambda) = \rho_{n-1}\frac{1-k_{n-1}u_{n-1}}{1+k_{n-1}u_{n-1}}$$

"where

$$u_{n-1} = \exp(-2h_{n-1}\lambda)$$

$$k_{n-1} = \frac{(\rho_{n-1}-\rho_n)}{(\rho_{n-1}+\rho_n)}$$

"For the transform T_j for a layer (ρ_j, hj) on top of the sequence ($\rho_{j+1},...,\rho_n$; $h_{j+1},...,h_n$) with the transform T_{j+1}, we have

$$T_j(\lambda) = \frac{W_j(\lambda)T_{j+1}(\lambda)}{1+W_j(\lambda)T_{j+1}/\rho_j^2};\ldots j = n-2, n-3,\ldots,2,1$$

"where

$$W_j(\lambda) = \rho_j \frac{1-u_j}{1+u_j}$$

"Starting from $T_{n-1}(\lambda)$ the transform $T_1(\lambda)=T(\lambda)$ of ...[Equation 5.3-8] can be obtained by recursive application of the expression for $T_j(\lambda)$" (ibid).

By differentiating V, and substituting into Equation 5.2-3, the Schlumberger apparent resistivity for a horizontally stratified earth can be expressed in terms of the resistivity transform

The reverse process of using recurrence relations to recover the profile from the transform is less straight forward. A brief description of this process is given in Section 5.7.1.

$$\rho_a(s) = s^2 \int_0^\infty T(\lambda) J_1(\lambda R)\lambda d\lambda \qquad \text{Equation 5.3-9}$$

where $J_1(\lambda R)$ is the first order Bessel equation of the first kind, and s is half the current probe spacing (that is s = AB/2).

Hankel's inversion (Arfken, 1985) may be applied to this equation to give an expression for the resistivity transform in terms of the apparent resistivity

$$T(\lambda) = \int_0^\infty \rho_a(s) J_1(\lambda s)/s\, ds \qquad \text{Equation 5.3-10}$$

Vertical electric sounding is based on the concept that if the resistivity in a semi-infinite slab varies with depth only, it can be determined uniquely from a complete knowledge of the surface potential produced by a pair of electrodes. Because of practical difficulties, our knowledge of the surface potential is limited, and there may be an infinite number of profiles that fit the VES data equally well (or equally poorly). Some of these difficulties are explored in later sections.

5.4 Interpretation of apparent resistivity data

We have shown that the resistivity transform may be calculated from the layer parameters (that is, the depths and resistivities of the horizontal layers). Given knowledge of the profile under investigation, it is possible, following from Equation 5.3.9, to determine the apparent resistivity expected from a VES session.

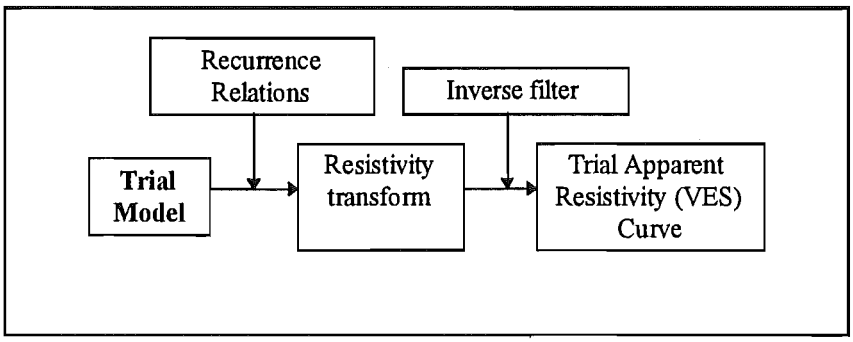

Figure 5.4-1: Determination of a VES curve from a trial model. The use of the inverse filter is described in Section 5.4-1.

In order to recover the layer parameters (ie. of the resistivity profile within the slab), it is necessary to reverse this process and calculate the layer parameters from the experimental apparent resistivity curve ρ_a, or, to strategically generate trial models and their associated VES curves and compare them with the experimental apparent resistivity curve. Either way, this requires the ability to generate either a trial ρ_a from $T(\lambda)$, or the transform $T(\lambda)$ from the experimental ρ_a or both (for example see Figure 5.4-1). However, ρ_a and $T(\lambda)$ are not readily evaluated from Equations 5.3.9 and 5.3-10 respectively. Instead, a linear digital filter is normally used.

5.4.1 Digital linear filters - Ghosh's filters.

"The word *filter* is derived from electrical engineering, where filters are used to transform electrical signals from one form to another, especially to eliminate (filter out) various frequencies in a signal. ..A digital filter is a linear combination of the input data... and possibly the output data..." (Hamming 1989, p 7,8) A linear digital filter is just a vector containing coefficients to be convolved with the values of the signal to be filtered. For example, a simple averaging filter may consist of the values {0.25 0.5 0.25} so that each output data point will be the weighted average of three input data points.

In the present case, values of apparent resistivity are determined at discrete spacings, by convolving the resistivity transform calculated at discrete values of λ, with an appropriate filter.

O'Neill and Merrick (1984) give a good overview of the design of filters suitable for determination of apparent resistivity from the transform. The following summary is based on this paper, which closely follows the original paper by Ghosh (1971) who first introduced the practical method to geophysics.

Defining λ and s in terms of new variables x and y

$$s = e^{x} \text{ and } \lambda = e^{-y}$$

the convolution integral

$$T(y) = \int_0^{\infty} \rho_a(x) J_1[e^{(x-y)}]dx \qquad \text{Equation 5.4-11}$$

is obtained, which in the frequency domain becomes

$$F(f) = G(f) \cdot H(f) \qquad \text{Equation 5.4-12}$$

where $T(y) \leftrightarrow F(f)$ and $\rho(a) \leftrightarrow G(f)$ are Fourier transform pairs, and $H(f)$ is the resistivity filter characteristic.

To determine $H(f)$, a partial apparent resistivity curve $\Delta\rho_a(x)$ is chosen whose exact resistivity transform $\Delta T(y)$ is known. Thus, from the transform pairs

$$\Delta\rho_a(x) \leftrightarrow \Delta G(f) \quad \text{and} \quad \Delta T(y) \leftrightarrow \Delta F(f)$$

the filter characteristic

$$H(f) = \frac{\Delta F(f)}{\Delta G(f)}$$

is obtained.

The filter characteristic is digitised by subjecting it to a sinc function input. The inverse Fourier transformation of the resulting sinc response spectrum gives the sinc response of the filter, sampled values of which constitute the required digital filter.

Hence, in the space domain, the discrete equivalent of - Equation 5.2-10 may be written

$$T_m = \sum_i a_i R_{m-i}$$

where a_i is called the ith forward filter coefficient and R_{m-i} is the m-i th sampled resistivity from the apparent resistivity curve.

To calculate the apparent resistivity from the resistivity transform we note from Equation 5.2-12 that

$$G(f) = \frac{F(f)}{H(f)}$$

The inverse filter sinc response is then obtained as in the forward case, replacing $H(f)$ by its inverse. The digital values of apparent resistivity are then given by

$$R_m = \sum_j b_j T_{m-j}$$

$m = 0,1,2...$

where b_j is the inverse filter coefficient

T_{m-j} is the sampled resistivity transform

5.4.2 Guptasarma's filters

The accuracy of Ghosh's filter is unacceptable for resistivity curves that have steep descending branches such as are likely to be found in drying concrete slabs exposed to low ambient relative humidities. His method, however, has been used and improved by many, including Koefoed (1972), Das and Ghosh (1974), Anderson (1975) and O'Neill (1975). Guptasarma (1982) published seven-, eleven-, and nineteen-point filters which are substantially more accurate than existing equivalent filters.

The filters are used in a slightly different way from Ghosh-type filters, compromising computational time for accuracy. With Ghosh-type filters, values of λ used to calculate $T(\lambda)$ from the layer parameters must be chosen to be logarithmically spaced at a rate of three data points per decade, although later Ghosh type filters generally use more. Once the resistivity transform is found at each value of λ, it is convolved with the digital filter to obtain the apparent resistivity ρ_a

Guptasarma's seven-point filter, for example, requires, at each chosen spacing, a reduced range of λ given by

$$\lambda_r = \frac{10^{a_r}}{s}$$

where a_r is the rth abscissa corresponding to the filter coefficient φ_r, r=1,2,..7

$T(\lambda_r)$ is then calculated for each value of λ_r. The apparent resistivity at the particular spacing is found by convolving the coefficients against the reduced $T(\lambda_r)$, thus:

$$\rho_a(s) = \sum_{r=1}^{7} \varphi_r T(\lambda_r, s)$$

The seven-point Guptasarma filter requires roughly seven times as much computational time as a Ghosh type filter, since the relatively lengthy recursive generation of $T(\lambda)$ from layer parameters must be carried out seven times for each spacing value, compared with only once per spacing using a Ghosh filter.

5.5 Modelling resistivity profiles and apparent resistivity curves

In this section we describe the modelling of the vertical electric sounding (VES) process by:-

- generating an apparent resistivity curve from a one dimensional profile (one in which resistivity varies in the vertical direction only) in a three-dimensional slab using the recurrence relations as discussed in Section 5.4,
- using finite difference techniques (see Chapter 4) to model a thin three dimensional slab undergoing excitation with line- rather than point-electrodes. Current injected on lines on the top edge of the model will result in a two-dimensional current distribution similar to that produced in a three-dimensional slab using line electrodes of infinite length. This is equivalent to modelling the slab in two dimensions rather than three.

5.5.1 Definition of resistivity profiles

A profile is defined by a number of horizontal layers each of uniform resistivity. The thickness or the depth of the bottom surface of each layer may be defined.

Table 5.5.1-1: Describing a resistivity profile.

Layer number	Depth to bottom of layer	Thickness of layer	Resistivity of layer
1	0.01	0.01	90
2	0.03	0.02	60
3	0.150	0.12	30
Sublayer	∞	∞	10^{100}

In matrix representation (as used in Matlab) the profile is written as a matrix containing two column vectors:

$$m = \begin{bmatrix} 0.01 & 90 \\ 0.02 & 60 \\ 0.15 & 30 \end{bmatrix}$$

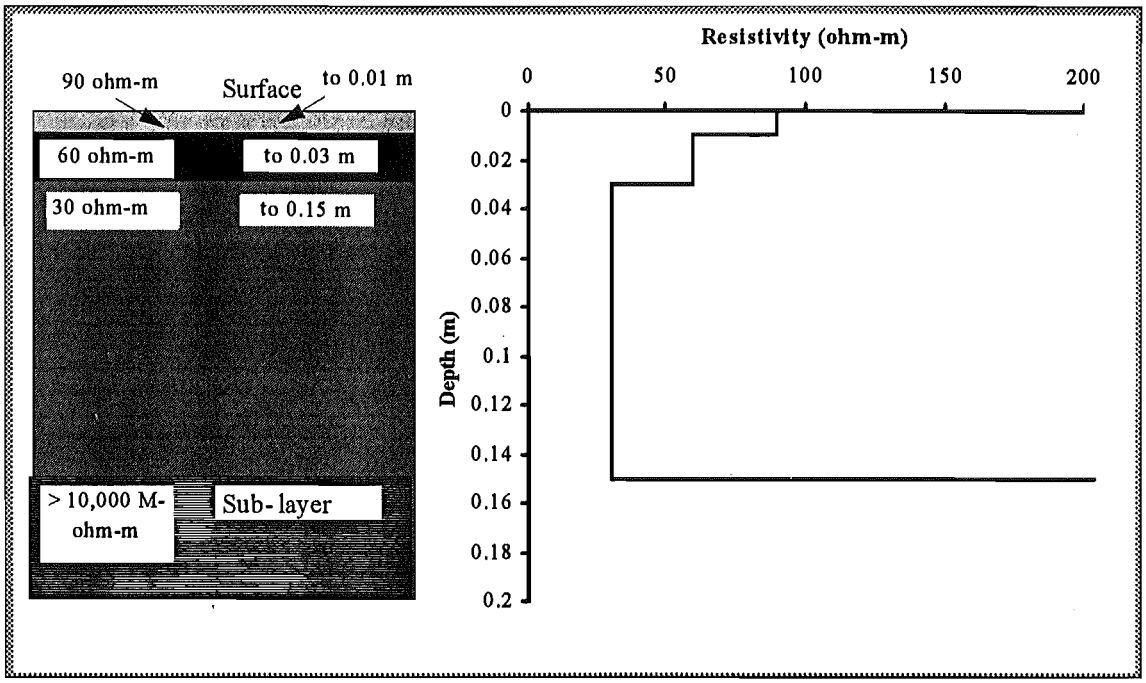

Figure 5.5.1-1: Two representations of a resistivity profile

We may present this in diagrammatic form: or as a graph where resistivity is on the horizontal axis and depth on the vertical axis (Figure 5.5.1-1) : I shall use the other commonly used presentation reserving the vertical axis for resistivity and the horizontal axis for depth (Figure 5.5.1-2).

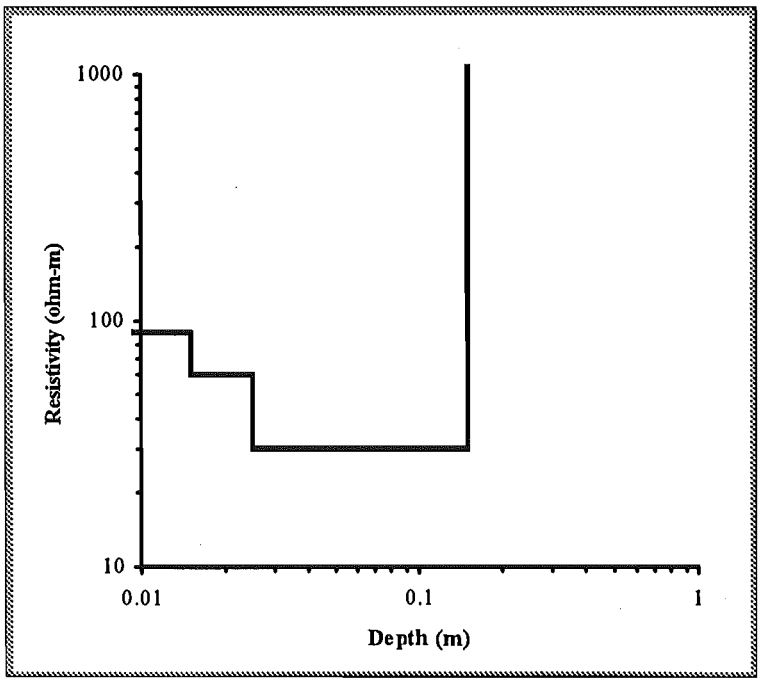

Figure 5.5.1-2: The standard method of presenting a resistivity profile in the present work.

5.5.2 Generation of model VES curves

Injection of current and measurement of apparent resistivity at the surface using the Schlumberger array has been described in Section 5.1. The apparent resistivity curve (or VES curve) theoretically obtainable may be generated using methods described in Section 5.4.

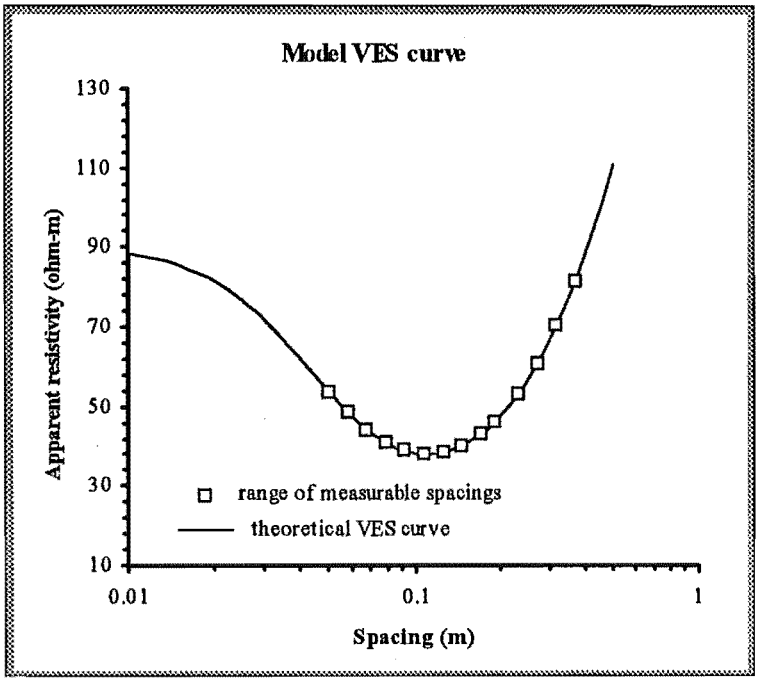

Figure 5.5.2-1: VES curve showing the range within which it is practical to measure apparent resistivity on concrete slabs

Software written in Matlab enables this to be easily achieved. For example the function "***roacmake***": {*roaf=roacmake(do,ro,s)*} has as input the depth and resistivity vectors *d* and *ro*, and the range of current probe spacings *s* for which theoretical apparent resistivity (*roaf*) data are required.

Roacmake carries out the following functions

- Convert depths (*d*) to thicknesses (*h*)
- Add the non-conducting sublayer. It is assumed that the sample in question is a slab of finite thickness and that the sublayer is of infinite depth and resistivity. However it is enough to add a layer that extends the same distance below the slab as the thickness of the slab with a resistivity of 10^100 ohm-m
- For each spacing (*s*) the function "***subgupt2***" is called. (For the ith spacing *s(i)*, *{roaf(i,1)=subgupt2(ro,h,s(i),phi,arr)}* where *phi* and *arr* are the Guptarsarma filter parameters see Section 5.4-2). ***Subgupt2*** determines the resistivity transform using

the recurrence relations and then applies the Guptasarma filter to obtain the VES curve.

For the resistivity profile shown in Figure 5.5.1-2 above the apparent resistivity curve is shown in Figure 5.5.2-1. Using this method apparent resistivity may be calculated at current probe spacings which are not practically possible to achieve. For a number of reasons, the minimum spacing for measuring apparent resistivity on concrete slabs is about 0.05 m (see Chapter 6). The actual range used lies in the region marked on the graph by open squares '□'.

We may plot the profile and the VES curve on the same graph (Figure 5.5.2-2). In this case, the horizontal axis represents depth (for the profile) and current probe spacing (for the VES curve). Note that by convention the current probe spacing s is defined to be half the distance between the current probes (ie, s=AB/2).

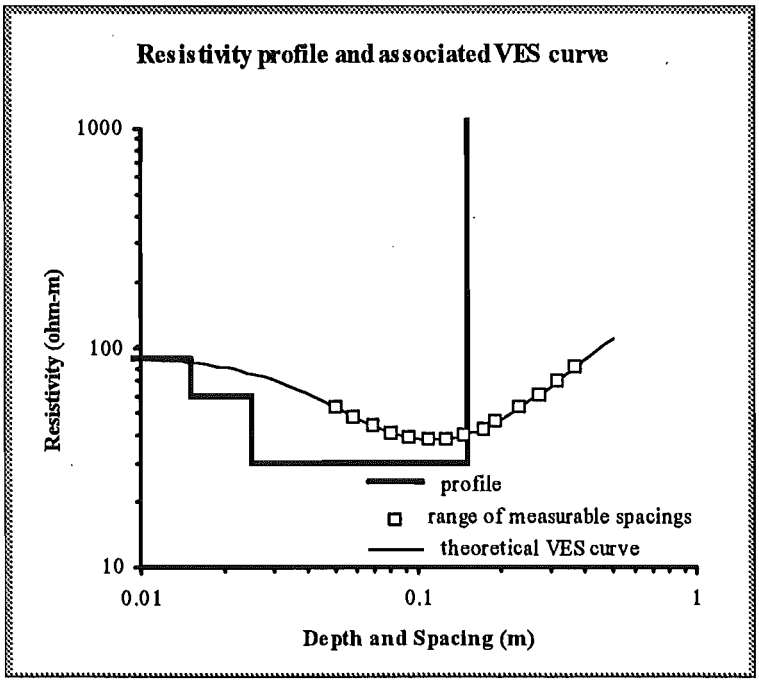

Figure 5.5.2-2: Resistivity profile and associated apparent resistivity curve plotted on the same graph.

5.5.3 Comparison of VES curves derived from different profiles

The effect of changing the profile parameters (increasing layer thickness or resistivity or increasing the number of layers) was investigated in order to determine the optimum slab size for the vertical electric sounding experiments.

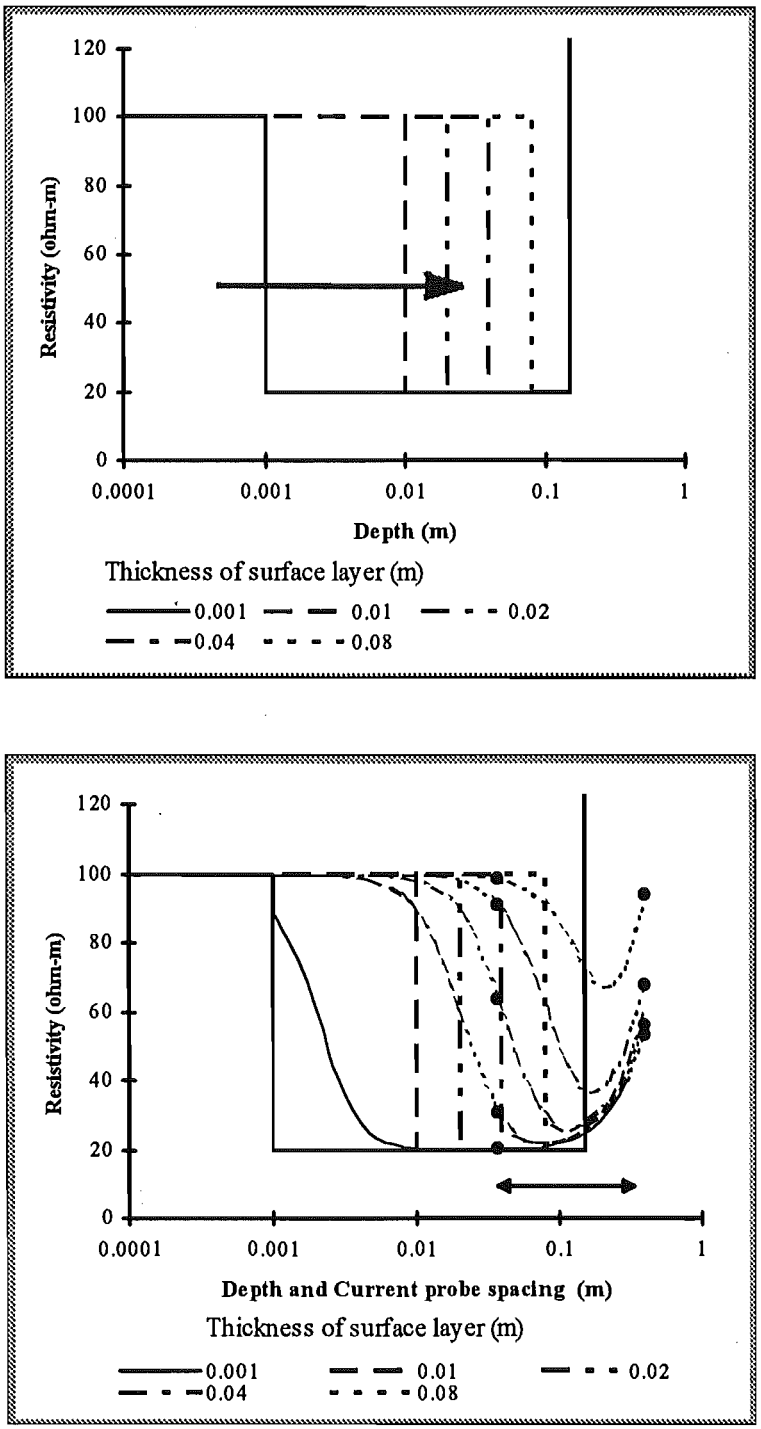

Figure 5.5.3-1. Increasing the thickness of the dry surface layer in a 2-layer model: (top graph) profiles only - the arrow indicates the increasing thickness of the dry surface layer, - (bottom graph) profiles with the corresponding VES curves. The range of practically measurable spacings is indicated by the double headed arrow and closed circles.

Consider a two layer model consisting of a dry surface layer and a wet deep region. The slab is 0.15m thick and there is a sublayer of 'infinite' resistivity to account for the non-conducting boundary. The top graph of Figure 5.5.3-1 shows a series of model profiles

in which the thickness of the surface layer increases. In the bottom graph the corresponding VES curves have been superimposed.

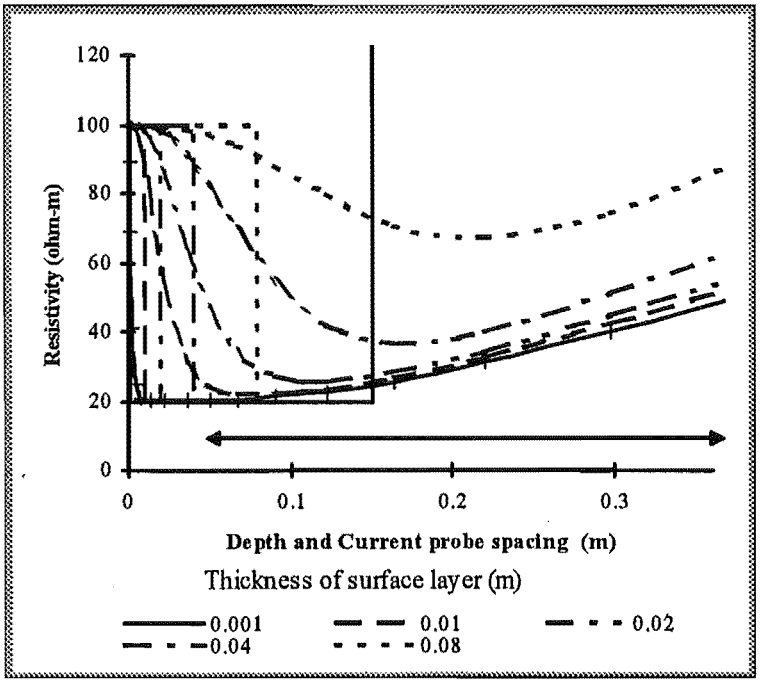

Figure 5.5.3-2: A linear representation of the graphs on the previous page. The range of measurable spacings is indicated by the double headed arrow. In addition some data points corresponding to actual spacings are marked by open circles (see Table 5.5.3-1).

Table 5.5.3-1: Theoretical apparent resistivity as a function of current probe spacing and the thickness of a dry surface layer (two layer model).

	Apparent resistivity (ohm-m)				
Spacing	Thickness of dry surface layer (m)				
(m)	0.001	0.01	0.02	0.04	0.08
0.050	20.2	24.5	47.4	82.5	97.3
0.067	20.5	22.3	34.4	69.5	94.0
0.091	21.2	22.1	27.3	54.4	88.3
0.122	22.7	23.4	25.7	41.9	79.8
0.164	25.7	26.6	28.2	36.7	70.9
0.221	31.2	32.5	34.3	40.1	67.2
0.297	40.3	42.2	44.6	50.8	74.2

Although the VES curves are all quite different, over the range of practical current probe spacings, it is difficult to distinguish the VES curves corresponding to dry surface layers of 0.001 m and 0.01 m (see Figure 5.5.3-2 in which the horizontal axis has a linear rather than logarithmic scale and Table 5.5.3-1). As the skin thickness increases from 1 mm to 10 mm, the apparent resistivity at the smallest spacing increases by just over 4 ohm-m. Much larger changes occur when the thickness increases a further 10 mm to 20 mm.

Figure 5.5.3-3 (a) shows a 10 mm thick surface layer undergoing an increasing resistivity. The apparent resistivity at very small spacings is very sensitive to the surface layer resistivity (Figure 5.5.3-3 (b)).

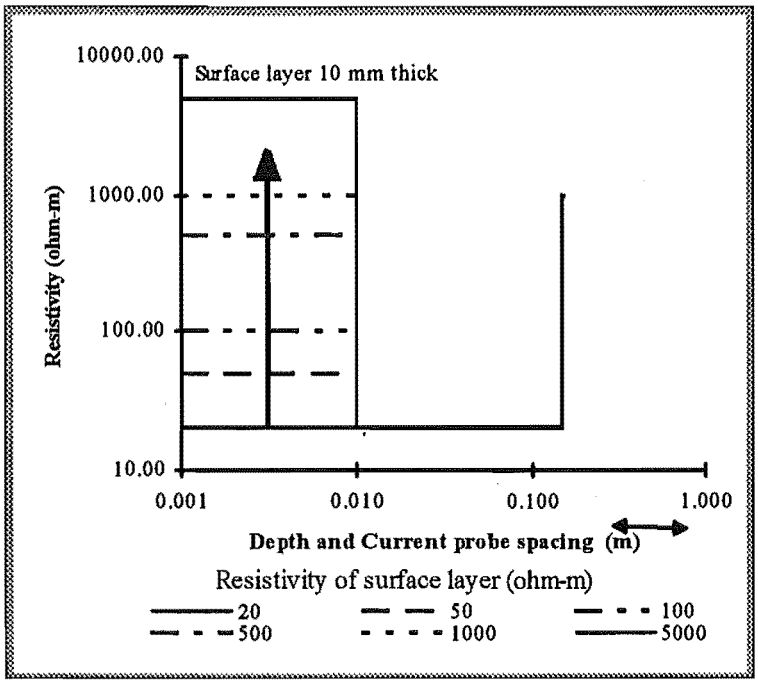

Figure 5.5.3-3: (a) A series of two-layer models of a concrete slab showing a progressive increase in the resistivity of a 10 mm thick, dry surface layer (grey arrow).

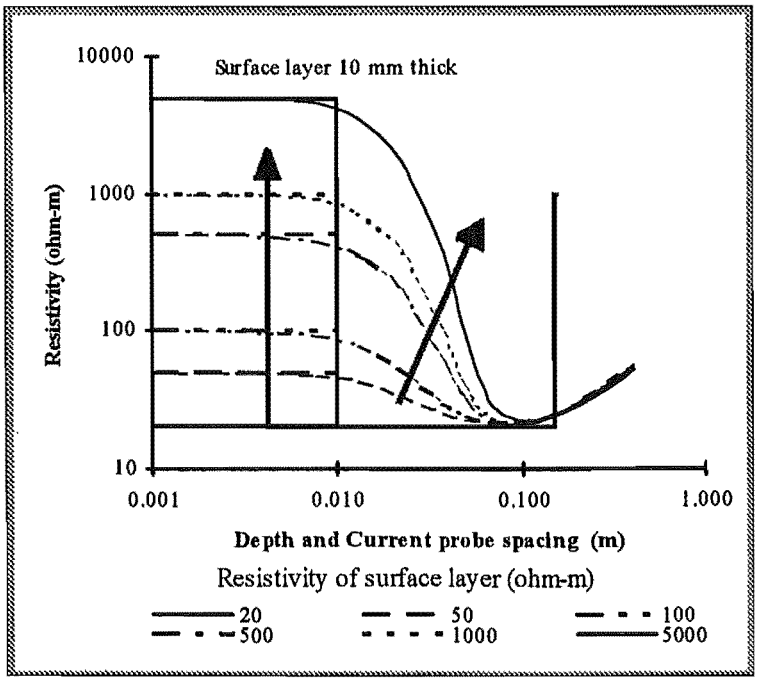

Figure 5.5.3-3: (b) A series of two-layer models of a concrete slab showing a progressive increase in the resistivity of a 10 mm thick, dry surface layer (grey arrow and the corresponding apparent resistivity curves have been superimposed. (see Table 5.5.3-2).

Whether or not the effect of varying the resistivity of the surface layer is measurable, will depend on the thickness of that layer. Model VES data for profiles in which the surface layer increases from 20 ohm-m to 5000 ohm-m is presented in Table 5.5.3-2 for three different surface layer thicknesses.

When the surface layer is only 1 mm thick, changing its resistivity has no measurable effect on the VES curve. When the thickness is increased to 10 mm, measurable effects extend to the first two current probe spacings. Changing the resistivity of yet thicker layers affects apparent resistivity measured at larger spacings.

Table 5.5.3-2 Apparent resistivity as a function of the resistivity of a 10 mm thick, surface layer (see Figure 5.5.3-3).

Spacing	Apparent resistivity (ohm-m) when surface layer is 1 mm thick. Resistivity of surface layer (ohm-m)					
(m)	20	50	100	500	1000	5000
0.050	20.2	20.2	20.2	20.2	20.2	20.1
0.067	20.5	20.5	20.5	20.5	20.5	20.6
0.091	21.2	21.2	21.2	21.2	21.2	21.4
0.122	22.6	22.6	22.7	22.7	22.7	23.0
0.164	25.6	25.6	25.7	25.7	25.7	26.0
0.221	31.1	31.2	31.2	31.2	31.3	31.5
0.297	40.1	40.2	40.3	40.3	40.3	40.5

Spacing	Apparent resistivity (ohm-m) when surface layer is 10 mm thick. Resistivity of surface layer (ohm-m)					
(m)	20	50	100	500	1000	5000
0.050	20.2	23.0	24.5	30.8	38.0	94.9
0.067	20.5	21.9	22.3	23.1	23.8	29.6
0.091	21.2	22.0	22.1	22.3	22.3	22.7
0.122	22.6	23.3	23.4	23.5	23.5	23.3
0.164	25.6	26.3	26.6	26.7	26.8	26.8
0.221	31.1	32.1	32.5	32.8	32.9	33.1
0.297	40.1	41.6	42.2	42.6	42.7	42.7

Spacing	Apparent resistivity (ohm-m) when surface layer is 20 mm thick. Resistivity of surface layer (ohm-m)					
(m)	20	50	100	500	1000	5000
0.050	20	32	47	156	289	1356
0.067	20	28	34	78	131	550
0.091	21	25	27	39	52	155
0.122	23	25	26	28	29	43
0.164	26	28	28	29	29	30
0.221	31	33	34	35	35	35
0.297	40	43	45	46	46	46

In general changes in the profile near the surface, affect the VES curve most in the region of smaller spacings (left-hand side of the curve). The right-hand side of the curve

is affected by deep profile changes. Profiles from drying concrete slabs will have very high, and most rapidly changing resistivity in the region near the surface. The deep regions will change slowly. The next graph and Table 5.5.3-3 shows the effect of varying the deep resistivity whilst leaving the 20 mm thick surface layer with a resistivity of 500 ohm-m. The change in the deep region is clearly reflected in the measurable part of the VES curve.

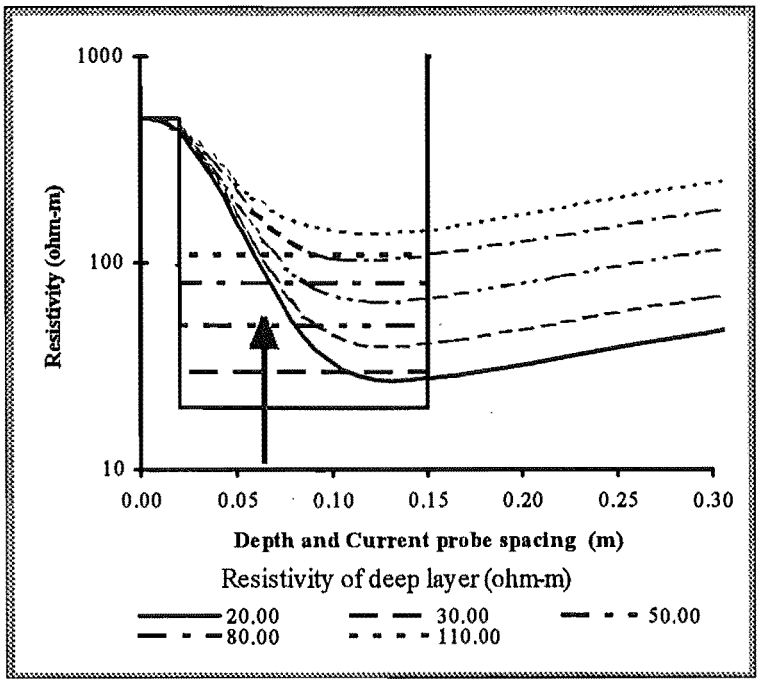

Figure 5.5.3-4. A series of two-layer models of a concrete slab showing the effect of increasing the resistivity of the deep wet layer.

Table 5.5.3-3: Apparent resistivity as a function of the resistivity of the deep layer below a 20 mm thick, surface layer

	Apparent resistivity (ohm-m)				
Spacing	Resistivity of deep layer (ohm-m)				
(m)	20.00	30.00	50.00	80.00	110.00
0.050	155.86	166.79	187.94	218.04	246.34
0.067	77.88	90.30	114.58	149.63	183.12
0.091	38.58	51.23	76.21	112.84	148.46
0.122	27.55	40.40	65.92	103.75	140.97
0.164	28.74	42.96	71.23	113.18	154.59
0.221	35.01	52.39	86.88	137.96	188.27
0.297	45.65	68.28	113.15	179.49	244.69

From these theoretical VES curves generated from simple model profiles, it was expected that the deeper regions of the profile would be able to be determined more accurately than the surface region[1].

5.5.4 Approximation to continuous profiles

We expect the resistivity profiles of a drying concrète slab to be continuous (and, as a rule, for the resistivity to decrease with depth). So the two or three layer models are not physically realistic. It is not possible to generate VES curves for truly continuous models using the theory of VES and profile recovery described here. Nor is it possible to recover a continuous model directly from a VES curve[2]. However, we may approximate a continuous model by increasing the number of layers (and decreasing their thickness. To illustrate, we shall take profiles based on the continuous function:

$$\rho = a\exp\left(\frac{b}{d+c}\right)$$

where d is the depth below the surface and a, b and c are parameters determining the shape of the curve (here, we have $a = 529$, b = 0.009 and $c = 0.005$). A series of such profiles with different numbers of layers is illustrated in Figure 5.5.4-1 below.

To construct a profile with n layers, the function is sampled at n values of d. This gives the resistivities of the n layers. The depth of the bottom surface of each layer is set at the midpoint between successive values of d (see Figure 5.5.4-2). This is a fairly arbitrary method of determining the layer parameters. The profiles generated in this way appear to be centred around the continuous function as long as the layer thicknesses decrease

---

[1] *The effect on VES curves of changes in the resistivity or thickness of very thin (less than 10 mm) surface layers has implications for the use of 'wet' probes (to be discussed in Chapter 6) which may act to reduce the effective resistivity of the highly resistive surface layer thickness or the effective thickness of that layer.*

[2] *As we shall see in Chapter 7, there are three reasons for this:*

- *There is a rapid increase in computation as the number of layers increases.*
- *The inversion process usually results in amalgamation of layers by giving them a common resistivity orin elimination of layers by making them vanishingly thin.*
- *A greater number of layers enables the noise to be fitted more exactly. This may yield a less realistic profile.*

towards the surface, otherwise small variations in layer thicknesses can result in an obviously poor fit.

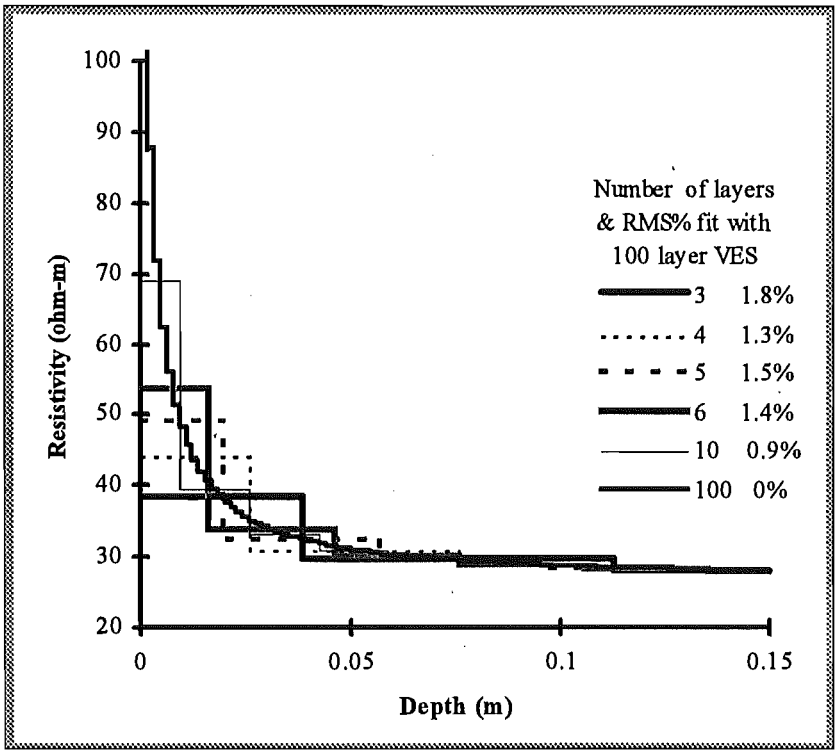

Figure 5.5.4-1: Resistivity profiles with different numbers of layers. The profiles all derive from the same continuous curve. The RMS % measure of fit indicates the degree of agreement of the VES curve generated from each profile with that generated from the nearly continuous (100 layer) profile. This is explained further in the text.

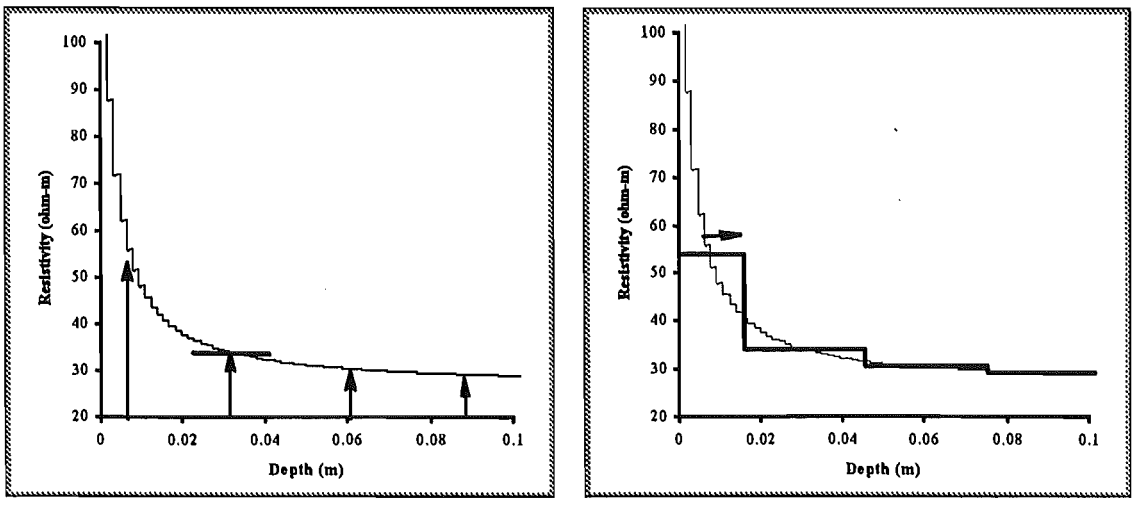

Figure 5.5.4-2: The construction of a layered or stepped profile based on a continuous function. The continuous function is sampled at *n* points (left) and then a stepped profile constructed about each data point (right).

To determine whether the different layered profiles are equivalent, we may generate from them, their associated VES curves and compare these using the RMS measure of goodness-of-fit (See Chapter 7). The VES curve associated with the most nearly continuous profile (n = 100) is chosen as the standard and the others are compared with it. As Figure 5.5.4-3 shows, very similar VES curves may be generated from profiles consisting of different numbers of layers. Generally, RMS values in Figure 5.5.4-1 and Figure 5.5.4-3 show increasing agreement as the number of layers increases.

As we shall see when we come to look at recovery of profiles from apparent resistivity curves, models with few layers have apparent resistivity curves that fit the original VES curves as well apparent resistivity curves from many layer models. For example, profiles recovered from the 100-layer model VES curve using trial models with from three to six layers, fit the 100 layer curve equally well, as well as matching the 10-layer model derived earlier.

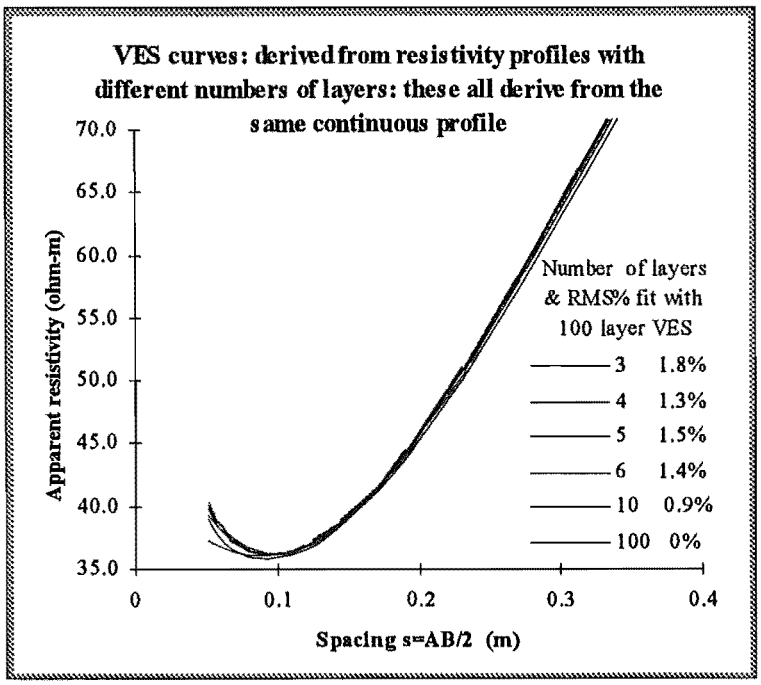

Figure 5.5.4-3: VES curves generated from resistivity profiles with different numbers of layers. The profiles are all based on the same continuous profile.

5.5.5 The effect of reinforcing

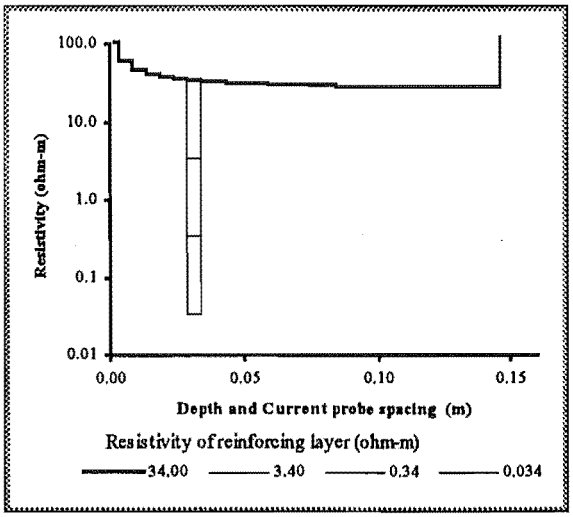

(a) Young concrete, profiles only

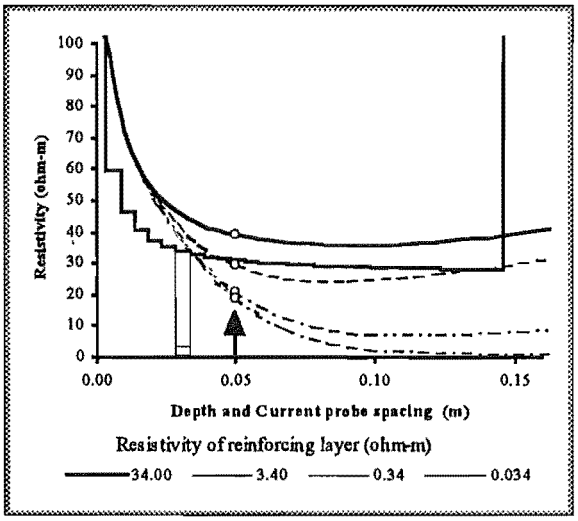

(b) Young concrete, profiles and VES curves

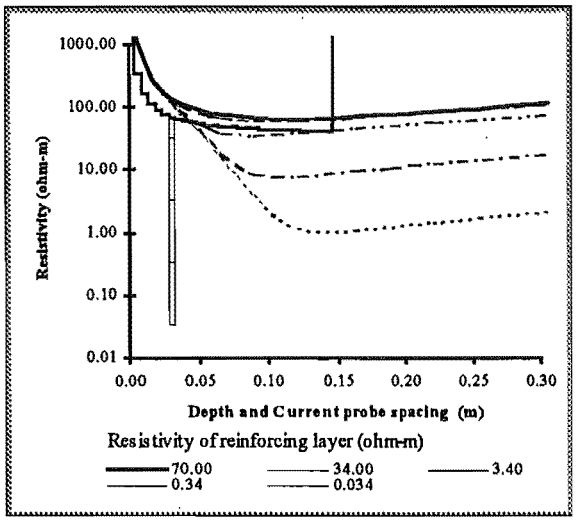

(c) Older profiles and VES curves

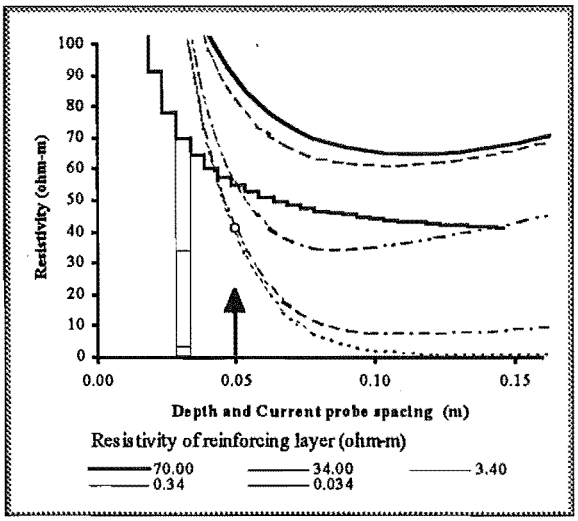

(d) Detail of the region of interest in (c).

Figure 5.5.5-1: Model profiles and associated VES curves for reinforced concrete slabs. The effective resistivity of the reinforcing layer varies giving different VES curves. Arrows indicate the smallest practical current probe spacing (Chapter 6).

The presence of steel reinforcing in a flooring slab may be modelled by setting a thin layer of low resistivity at an appropriate depth. Because the reinforcing is not actually a thin sheet but a mesh with relatively large dimensions (in our case we used '665' mesh which has a rod diameter of 5 mm and a 100 mm mesh square) the effective resistivity will be somewhat above that of steel but undetermined. Two 30-layer models were constructed to represent young and older concrete. The effective resistivity of the reinforcement layer was varied from 0.034 to 3.4 ohm-m. The models and VES curves generated are shown in Figure 5.5.5-1.

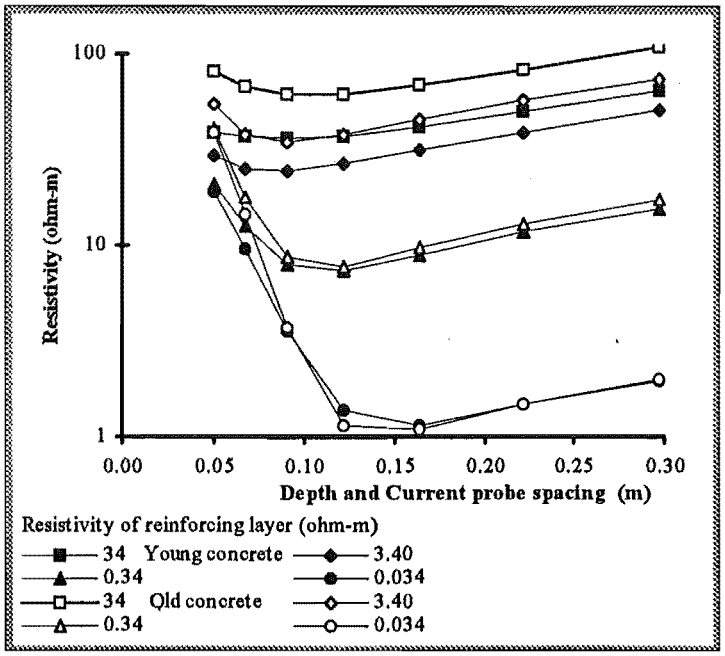

Figure 5.5.5-2: Comparison of VES curves for young and old reinforced slabs. The lower the effective resistivity of the reinforced layer, the less difference there is between the young and old slab VESs.

Table 5.5.5-1: The absolute difference between theoretical VES curves from young and old reinforced slabs.

	Absolute difference in apparent resistivity (ohm-m)			
Spacing	Effective resistivity of the reinforced layer (ohm-m)			
(m)	34.00	3.40	0.34	0.034
0.050	43	26	20	20
0.067	31	13	5	5
0.091	26	10	1	0
0.122	25	12	0	0
0.164	27	14	1	0
0.221	33	18	1	0
0.297	44	23	2	0

The reinforcing acts to lower the VES curve generally, but especially for current probe spacings above 0.05 m, that is, especially in the measurable region. However there appears to be little difference in the curves for concrete at different ages. In Table 5.5.5-1 and Figure 5.5.5-2, VES curves for young and old reinforced slabs are compared. If the effective resistivity of the reinforced layer is about, or below 0.34 ohm-m, the VES curves are nearly indistinguishable.

As we shall see in Chapter 7, the reinforcing may act to swamp out other, more subtle changes.

5.5.6 The effect of non-conducting boundaries

The testing of the vertical electric sounding technique was carried out on rectangular concrete slabs (see Chapter 4). The limited size of the slabs imposed boundaries not normally accounted for in the theory of vertical electric sounding although there is some treatment given to the case of a vertical discontinuities. Valdez (1954) presented a series of correction functions for use when measuring resistivity of thin slices of semiconductor using four surface probes in a Wenner array. Assuming the material is of uniform resistivity the functions enable determination of the resistivity when the array is near conducting or non-conducting boundaries.

Although the concrete slabs do not have uniform resistivity, it was felt worthwhile to derive similar correction functions for the Schlumberger array in the presence of the side and end faces of the slabs which will present non-conducting boundaries. At least they would provide some indication of the size of slab necessary to make the boundary influences negligible.

The Schlumberger apparent resistivity has been derived as

$$\rho = \frac{\pi \cdot \left(s^2 - b^2\right)}{2b} \left| \frac{\Delta V}{I} \right| \qquad \text{Equation 5.2-2}$$

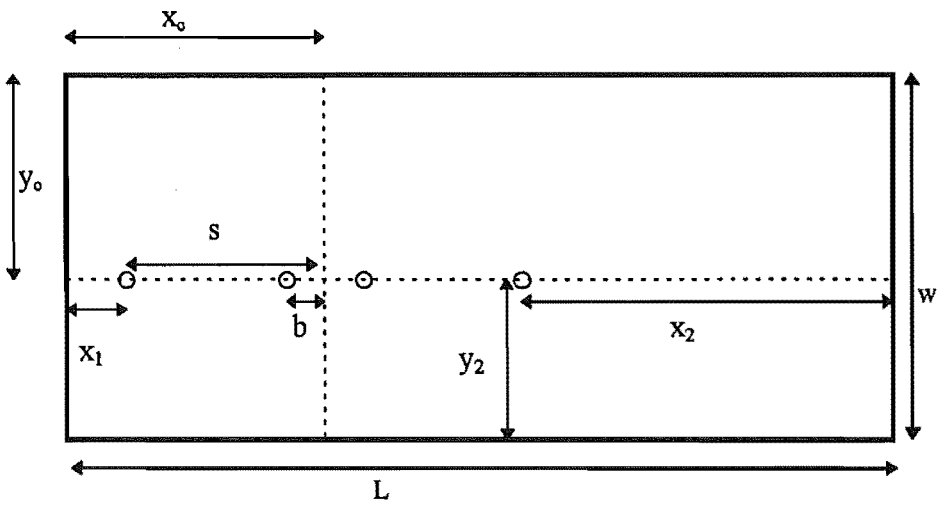

Figure 5.5.6-1: Parameters describing the position of the Schlumberger array on the top surface of a concrete slab.

We may describe the position of the array on the slab as in Figure 5.5.6-1. In this case, the line of the probes is perpendicular to the *end* boundary and parallel to the *side* boundary.

In the presence of non-conducting boundaries the expression for the unbounded Schlumberger apparent resistivity

$$\rho_o = \frac{\pi \cdot \left(s^2 - b^2\right)}{2b}\left|\frac{\Delta V}{I}\right|$$

must be multiplied by the correcting function

$$\frac{1}{G_{all}}$$

That is, the correct expression to use is

$$\rho = \frac{\pi \cdot \left(s^2 - b^2\right)}{2b}\left|\frac{\Delta V}{I}\right| \cdot \frac{1}{G_{all}} \qquad \text{Equation 5.5-1}$$

where

$$G_{all} = 1 + \left(\frac{s}{b} - \frac{b}{s}\right) \cdot \left[\frac{1}{4}\left(f_{end}(x_1) + f_{end}(x_2)\right) + \frac{1}{2}\left(f_{side}(y_1) + f_{side}(y_2)\right)\right] \qquad \text{Equation 5.5-2}$$

and

$$f_{end}(x) = \left(\frac{2x}{s} + 1 - \frac{b}{s}\right)^{-1} - \left(\frac{2x}{s} + 1 + \frac{b}{s}\right)^{-1} + \left(\frac{2x}{s} + 3 + \frac{b}{s}\right)^{-1} - \left(\frac{2x}{s} + 3 - \frac{b}{s}\right)^{-1} \qquad \text{Equation 5.5-1}$$

and

$$f_{side}(y) = \left\{\left(2\frac{y}{s}\right)^2 + \left(1 - \frac{b}{s}\right)^2\right\}^{-1/2} - \left\{\left(2\frac{y}{s}\right)^2 + \left(1 + \frac{b}{s}\right)^2\right\}^{-1/2} \qquad \text{Equation 5.5-2}$$

The derivations for these equations are presented in Appendix B.

The correction necessary for an end boundary is shown as a function of the ratio $\frac{x}{s}$, in Figure 5.5.6-2,

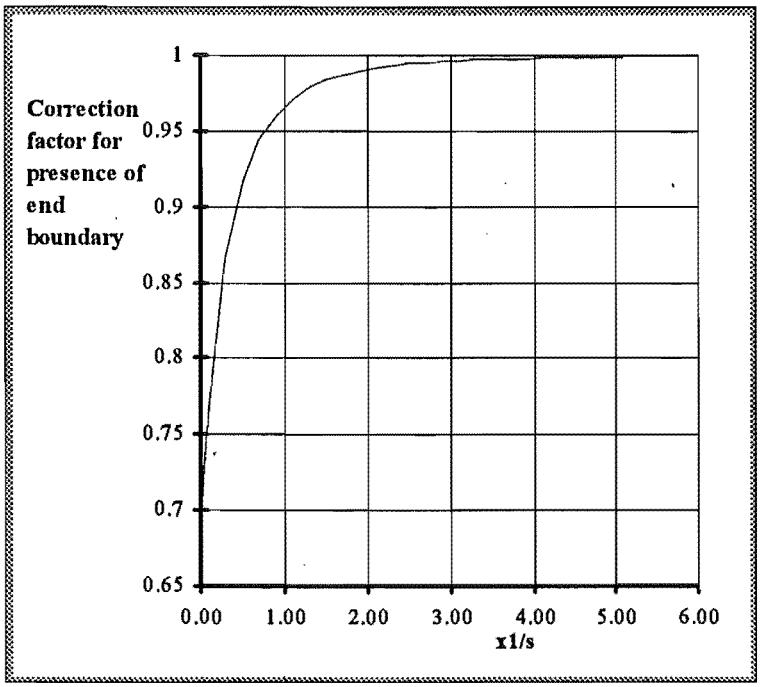

Figure 5.5.6-2: Correction factor G_{end} for the presence of an end (perpendicular) boundary.

To illustrate the varying effect of boundaries on apparent resistivity, theoretical uncorrected VES curves are shown in Figure 5.5.6-3 and Figure 5.5.6-4 for a simple two layer profile (90 ohm-m to 0.01 m, 30 ohm-m to 0.15 m). In these graphs a schematic diagram showing the position of the four probe array relative to the slab, has been included.

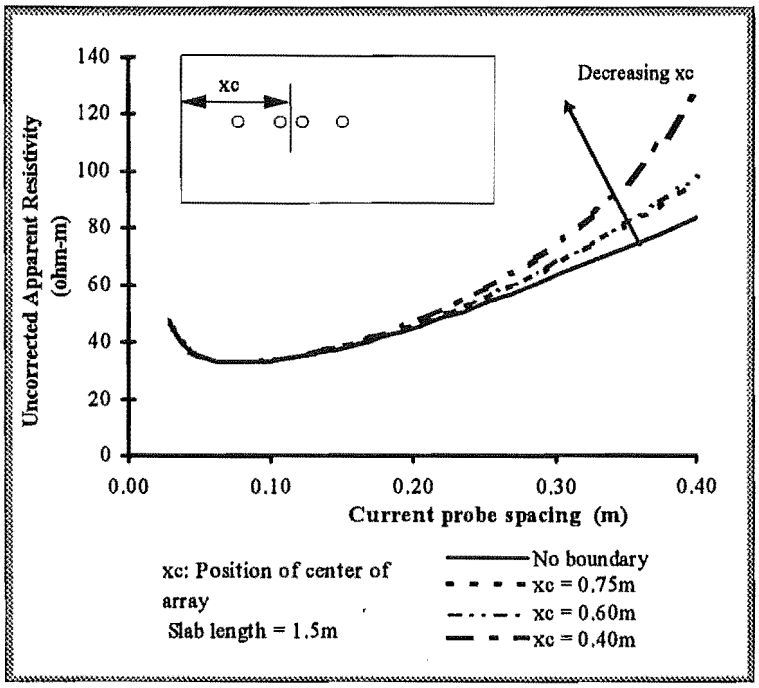

Figure 5.5.6-3: Uncorrected apparent resistivity curves showing the effect of proximity to a perpendicular non-conducting boundary compared to the unbounded condition. Measurement probe spacing *b* is 0.01m, but virtually identical curves result when *b* = 0.03m.

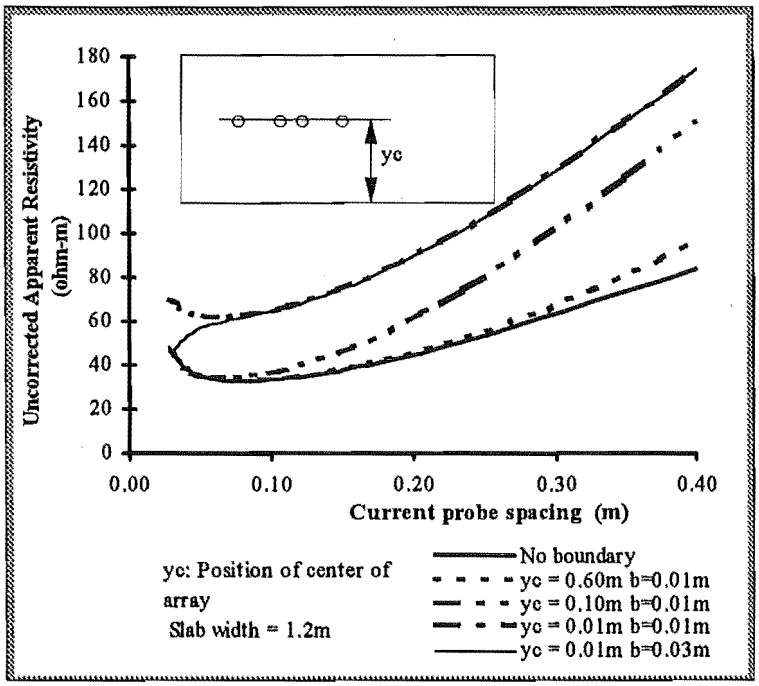

Figure 5.5.6-4: Uncorrected apparent resistivity curves showing the effect of proximity to a parallel non-conducting boundary compared to the unbounded condition. Measurement probe spacing *b* is 0.01m, but there is little change in the curves when *b* = 0.03m except when y_c is small.

5.6 Finite difference modelling

The finite difference model used in two-dimensional modelling of VES on concrete slabs has been described in Chapter 4. Of particular interest were the areas where the practical aspects of vertical electric sounding differed from the idealised situation. Thus the following areas were investigated:

1. the finite size of the electrodes (ideally these are point sources or sinks),
2. the finite measurement-electrode spacing 'b' (ideally b is vanishingly small),
3. the possible lowering of resistivity in the region of 'wet' electrodes (ideally the electrode does not influence the resistivity of the concrete) and
4. the effect of non-conducting boundaries (ideally the slab extends to infinity in all directions).

5.6.1 Finite electrode size

The size of the measurement electrode surface in contact with the concrete surface has little effect on the apparent resistivity. If anything a larger diameter electrode results in a underestimation of apparent resistivity, but the error was nowhere greater than 1% (Table 5.6.1-1).

Table 5.6.1-1: The effect of measurement electrode diameter on apparent resistivity.

	Apparent resistivity (ohm-m)			
Spacing	Measurement electrode diameter (m)			
(m)	0.001	0.002	0.004	0.008
0.050	199	199	199	199
0.066	185	185	184	184
0.086	183	183	183	183
0.114	196	196	195	195
0.150	225	225	224	224
0.197	274	274	273	272
0.259	345	344	343	342
0.340	440	439	437	435
	Percentage error			
Spacing	Measurement electrode diameter (m)			
(m)	0.001	0.002	0.004	0.008
0.050	0.0	0.0	0.1	0.1
0.066	0.0	0.1	0.2	0.3
0.086	0.0	0.1	0.2	0.5
0.114	0.0	0.1	0.3	0.6
0.150	0.0	0.2	0.4	0.7
0.197	0.0	0.2	0.5	0.8
0.259	0.0	0.3	0.6	0.9
0.340	0.0	0.3	0.6	1.0

Table 5.6.1-2. The effect of current electrode diameter on apparent resistivity.

Apparent resistivity)					
Spacing	current electrode diameter (m)				
(m)	0.001	0.002	0.004	0.008	0.016
0.050	200	199	199	200	202
0.066	185	185	185	185	186
0.086	184	184	183	183	184
0.114	197	196	196	196	196
0.150	226	226	225	225	225
0.197	275	275	274	274	274
0.259	347	346	345	345	345
0.340	443	441	440	439	440

Changing the current electrode diameter from 0.001 mm to 0.016m has very little effect on the apparent resistivity; an effect far less than 1% error in general (Table 5.6.1-2).

5.6.2 Finite measurement probe spacing.

Substantial error arises when the measurement probe spacing b is greater than about 30 mm (Table 5.6.2-3). The rule of thumb for the Schlumberger array is that the current probe spacing s should be no less than 5 times the measurement probe spacing b, that is $b/s < 0.2$. This rule is supported by the present modelling. The error (over-estimation) increases substantially when b/s > 0.2 whereas it is roughly constant for ratios below 0.2 (see Figure 5.6.2-1).

Table 5.6.2-3. The effect of current electrode diameter on apparent resistivity.

Apparent resistivity (ohm-m)					
Spacing	Measurement probe spacing (m)				
(m)	0.005	0.01	0.02	0.03	0.04
0.050	197	199	209	236	347
0.066	184	185	188	195	210
0.086	183	183	184	186	190
0.114	195	196	196	197	197
0.150	224	225	226	225	224
0.197	272	274	275	274	273
0.259	342	345	346	346	345
0.340	436	440	442	442	441
Percentage error					
Spacing	Measurement probe spacing (m)				
(m)	0.005	0.01	0.02	0.03	0.04
0.050	0.0	1.1	6.2	19.7	76.0
0.066	0.0	0.6	2.4	6.2	14.2
0.086	0.0	0.5	1.1	2.0	3.8
0.114	0.0	0.5	0.7	0.7	0.9
0.150	0.0	0.6	0.7	0.5	0.2
0.197	0.0	0.7	0.9	0.7	0.4
0.259	0.0	0.8	1.1	1.0	0.8
0.340	0.0	0.9	1.3	1.4	1.2

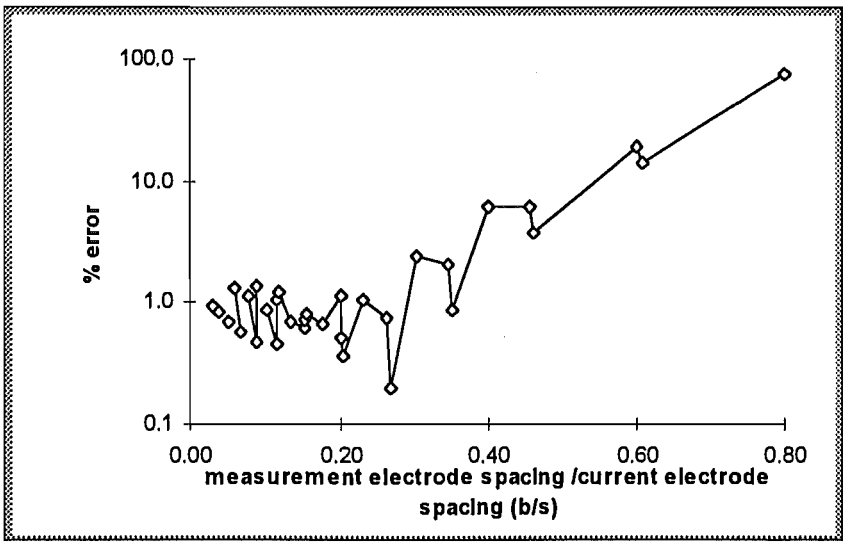

Figure 5.6.2-1: Error associated with finite measurement probe spacing. The error (over-estimation) increases substantially when b/s > 0.2 whereas it is roughly constant for ratios below 0.2.

5.6.3 The influence of 'wet' electrodes

The surface layer resistivity can become very high once the concrete slab has been allowed to dry. Placing wettened electrodes on the surface may extend a region of lowered resistivity through the surface layers, making contact with wetter more conductive regions in the slab. This will result in lower total resistance between the current probes and hence allow greater current flow and larger measured voltages. This extension of the electrode constitutes a further departure from the point current source at the surface, and the measurement of voltage at a point at the surface.

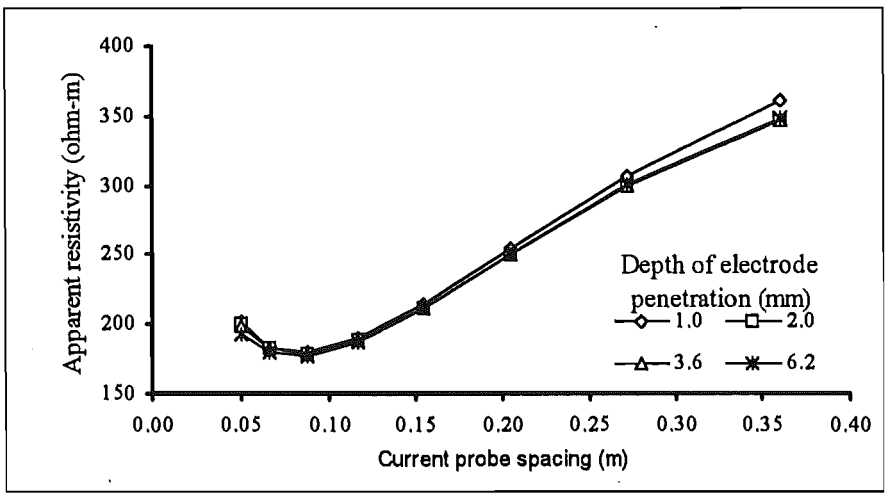

Figure 5.6.3-2: The effect of penetration of the electrode into the surface layers of the concrete. Note the slight lowering of the curve at small and large spacings.

To determine the effect of the weakening of the approximation, the low resistivity region associated with each electrode was allowed to extend progressively more deeply into the model slab. As Table 5.6.3-4 shows, while a nearly 10-fold reduction in resistance between the current probes results from a 6 mm penetration into the slab by the electrode, the apparent resistivity changes little (see also Figure 5.6.3-2).

Table 5.6.3-4: The effect of 'virtual probe' depth on apparent resistivity and resistance between the probes (b=0.01 m;bd=0.001 m)

(a) Apparent Resistivity (ohm-m)

Spacing	Depth of Virtual probes (mm)				
(m)	1.0	1.7	2.0	3.6	6.2
0.05	202	202	201	199	194
0.07	184	183	183	182	180
0.09	180	179	179	179	178
0.12	190	189	189	189	188
0.15	214	213	212	212	212
0.20	254	252	251	251	251
0.27	307	302	299	299	300
0.36	362	352	347	347	349

(b) Resistance between current probes (k-ohm)

Spacing	Depth of Virtual probes (mm)				
(m)	1.0	1.7	2.0	3.6	6.2
0.05	7.8	4.5	2.4	1.3	0.8
0.07	7.9	4.5	2.5	1.4	0.8
0.09	8.0	4.6	2.5	1.4	0.8
0.12	8.1	4.7	2.6	1.4	0.9
0.15	8.3	4.8	2.7	1.5	0.9
0.20	8.5	5.0	2.8	1.6	1.0
0.27	8.6	5.1	2.9	1.7	1.1
0.36	8.8	5.2	3.0	1.7	1.1

5.6.4 The influence of non-conductive boundaries

The effect of the non-conducting boundaries on the measurement of apparent resistivity on thin homogeneous slabs has been determined theoretically and experimentally by Valdez (1954) and extended to the Schlumberger array in the present work (Section 5.5.6). The relatively small size of the slabs (compared to the array-size) meant that both end boundaries and the two side boundaries would influence the apparent resistivity, and so the four correction factors were combined. The validity of the correction factors may be weakened if the slab is not homogeneous but contains a resistivity gradient. A series of two-dimensional modelling studies was carried out to determine the effect of

proximity of the array to the non-conducting boundary (analogous to the perpendicular, end boundary in three-dimensions), under a range of profiles.

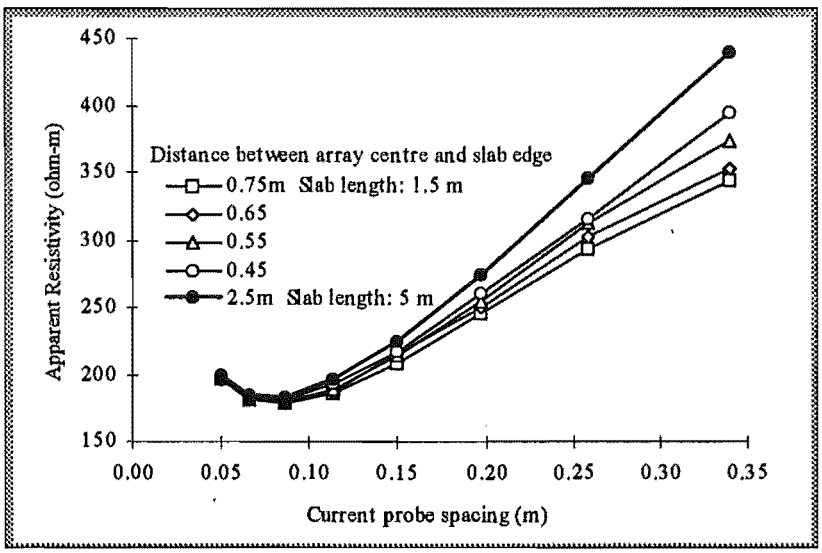

Figure 5.6.4-3: The effect of proximity of the array the nonconductive edge of the slab. The apparent resistivity for all current probe spacings rises as the array is brought closer to the boundary. Nevertheless, all the VES curves for the 1.5 m long slab are lower than the VES curve for the array in the centre of a larger slab (5 m long), where the boundary effects would be smaller.

Table 5.6.4-5: The effect of proximity of the array to non-conductive boundaries

	Apparent Resistivity (ohm-m)			
Spacing	Distance of array centre from boundary (m)			
(m)	0.75m	0.65	0.55	0.45
0.05	197	197	198	198
0.07	181	181	182	183
0.09	178	178	179	182
0.11	187	188	189	193
0.15	209	215	214	217
0.20	245	250	255	260
0.26	293	303	312	316
0.34	344	354	373	396

As Figure 5.6.4-3 and Table 5.6.4-5 indicate, as the array approaches the boundary (boundary influences becoming stronger), the VES curves tend to rise, especially at the larger spacings where once again boundary influences would be stronger. This behaviour is what is expected at a lateral discontinuity and reported by Valdez (1954), Parasnis (1982) , and Wilkins (1982) among others and agrees with theoretical uncorrected VES curves shown in Section 5.5.5.

On the other hand, this graph shows that the VES curve for the array in the centre of a 2.5 m slab, is of higher resistivity than those for the 1.5 m slab even though the boundary

influences would be expected to be less. This behaviour is confirmed in Table 5.6.4-6 and Figure 5.6.4-4 in where the array is placed in increasingly larger slabs, yielding a progression of steadily lifted VES curves. At this stage I am not able to explain this apparent contradiction.

Table 5.6.4-6: VES taken from increasingly longer slabs (progressively less influence of boundary).

	Apparent Resistivity (ohm-m)				
Spacing	Slab length (m, array centred)				
(m)	1.5	2	3.0	5.0	15
0.05	197	197	198	199	201
0.07	181	182	183	185	186
0.09	178	179	182	183	186
0.11	187	190	193	196	199
0.15	209	214	220	225	231
0.20	245	254	265	274	283
0.26	293	310	329	345	361
0.34	344	375	411	440	468

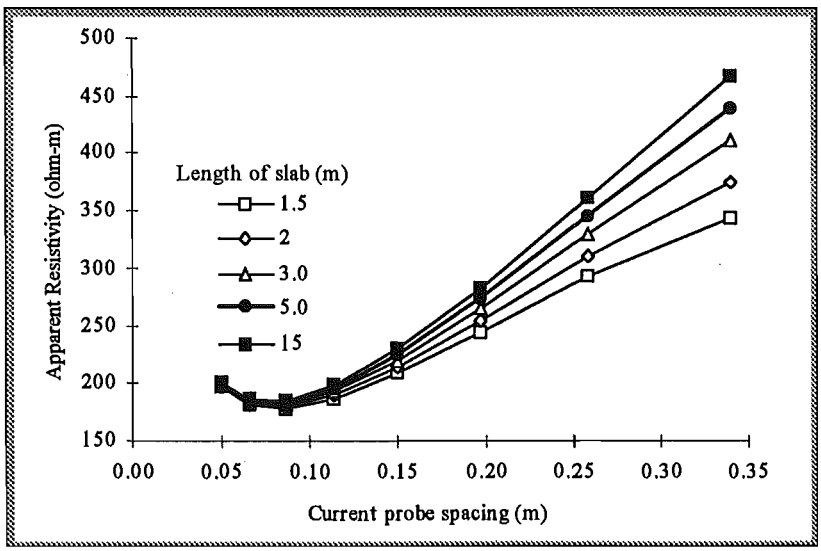

Figure 5.6.4-4. The effect of the slab length on the apparent resistivity curve. (Array centred on the slab).

5.7 Profile Recovery

Many ways of automatic recovery of resistivity profiles from VES curves have been developed. Two broad groups, direct and indirect methods are outlined in the next two sections (Figures 5.2-6 to 5.2-8). The difference between the two groups of methods has been well expressed by Zhdanov and Keller (1994).

> 'One may start with the field data and attempt to obtain an image of the earth by manipulation of that data. [direct methods]. One may use an arbitrarily conceived model of the earth, compute a synthetic set of field data for that model, and compare it with the field data, adjusting the model until a close correspondence is found between the synthetic data and the field data [indirect methods]" (p586).

5.7.1 Direct methods of profile recovery.

Direct methods are suggested and/or used by Ghosh (1971), Depperman (1973), Marsden (1973), Patella (1975), Koefoed (1972), Szaraniec (1980) and Basokur (1990). Slichter (1933) first pointed to the possibility of direct interpretation of VES data, by fitting the transform curve to families of two- and three-layer resistivity transform templates. Pekeris (1940) introduced a modified kernel function *G(s)*, the logarithm of which has the important property of being a linear function of λ . The slope of the function is controlled by the top layer thickness whereas its intercept with the ordinate axis *G* is controlled by the ratio of the resistivities of the top two layers.

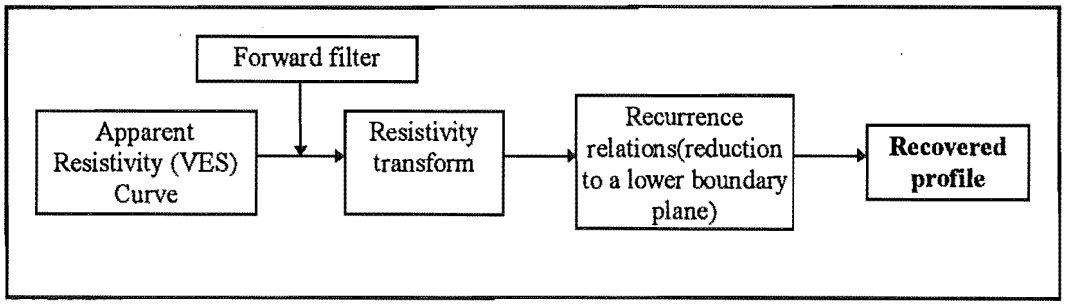

Figure 5.7.1-1: Direct interpretation of apparent resistivity curves.

Once the modified resistivity transform is calculated in some way (which was not easy before the introduction of the linear filter method) an alternation of two steps followed. In the first step, the first part of the transform curve (ie., for small *s*) is approximated by a straight line from which the resistivities of the first two layers and the thickness of the first layer can be derived. The second step is what is known as 'the reduction of the

transform function to a lower boundary plane" (eg. Koefoed 1976) in which the contribution to the transform curve made by the top layer is stripped away using a simple reduction formula. The effective boundary plane (ie. the earth-air interface) is now the top of the second layer. The two steps are iterated until a reduced transform curve is obtained that completely represents the linear function for the bottom two layers (Koefoed 1976, Parasnis 1982).

Basokur (1990) published a program for the direct interpretation of VES curves written in Basic, which was transcribed into Microsoft QuickBasic by the author. It required the user to determine the branch points from the resistivity transform curve, (ie. those points indicating existence of separate layers). It was not worthwhile proceeding in this direction. Direct interpretation methods suffer from error growth and propagation at each iteration. Error in determining layer parameters at the first iteration is carried into the next iteration which may, in addition, generate its own error. There is, in fact, guaranteed initial uncertainty in generation of the transform function, since forward filters require extrapolation of the VES curve. Finally, there is no obvious way to optimise the solution using direct methods; rather, as in Marsden (1973), a direct method may be used to generate the initial model for use in an indirect methods.

5.7.2 Indirect methods of profile recovery

Indirect methods require the initial input of a trial model. From this, the resistivity transform is calculated using recurrence relations. Then, an inverse linear filter is digitally convolved with the transform to obtain a trial apparent resistivity curve. This is compared with the actual VES curve. On the basis of this fit, layer parameters of the trial model may be adjusted or accepted. This process of optimisation may be automatic or user input may be requested. The new or modified trial model is used to generate a new trial apparent resistivity curve and the process continues until some pre-defined misfit or error criterion is reached (Figure 5.7.2-1).

One step per cycle is saved if comparisons are made in the resistivity transform domain (Figure 5.7.2-2). In this case a forward filter is used. However, as noted above, use of the forward filter requires extrapolation of the apparent resistivity curve at each end of the spacing range, thus using data that are not actually measured. It is also necessary to smooth the data. Both operations introduce sources of error. When comparing in the apparent resistivity domain, the unprocessed data are used for comparison purposes only

and the influence of the user's personal judgement is kept to a minimum (Johansen, 1975, Merrick, 1977). Working in the apparent resistivity domain thus allows the fullest interpretation of incomplete sounding curves since no information is lost or distorted through extrapolation.

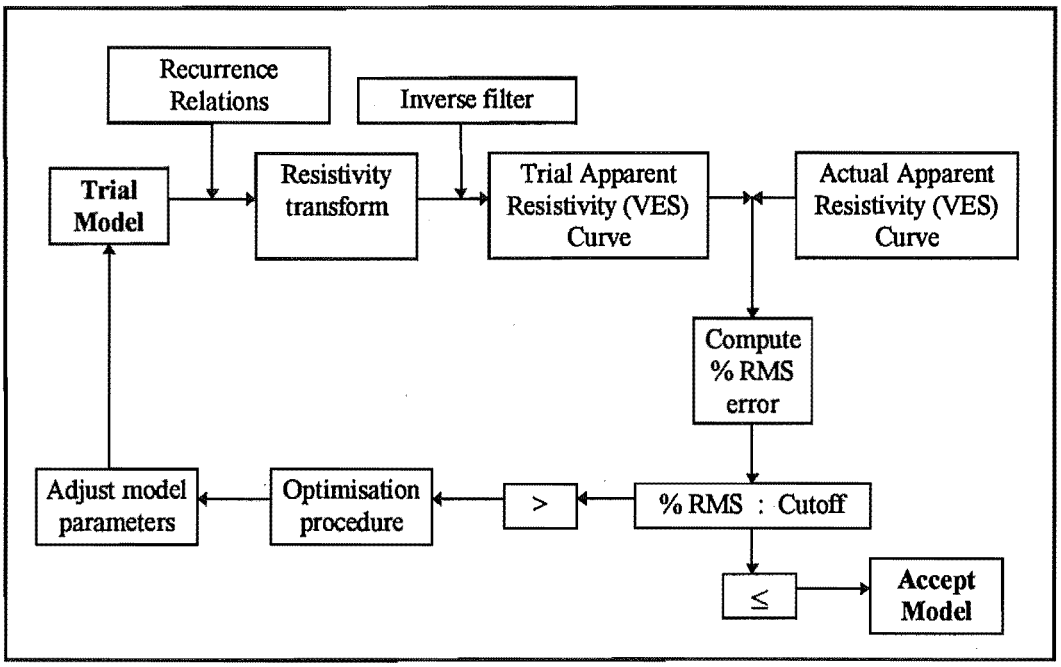

Figure 5.7.2-1: Indirect interpretation of apparent resistivity: comparison in the resistivity domain.

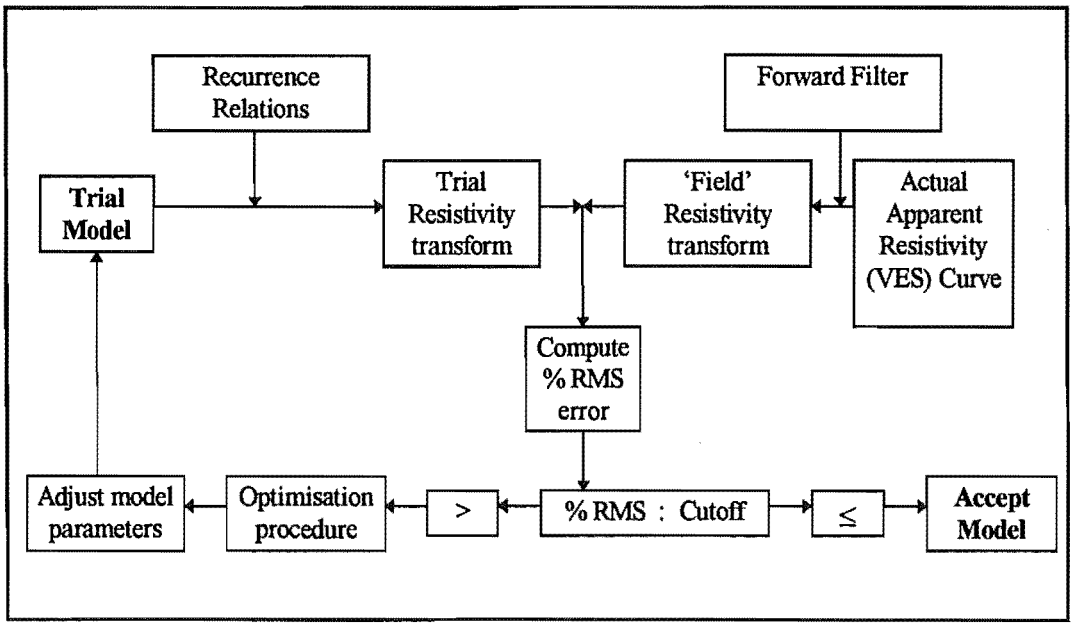

Figure 5.7.2-2: Indirect interpretation of apparent resistivity: comparison in the resistivity transform domain.

Once appropriately fast and accurate inverse filters are chosen, the key problem in indirect profile recovery is optimising the fit between the calculated and the actual apparent resistivity curves. Two papers utilising different indirect methods have been particularly useful. The first (Zohdy, 1989) relates each data point to a different layer, so that the misfit between each data point and the corresponding model VES data point, is used directly to adjust the resistivity of that layer. The second paper (Merrick, 1977) uses the Marquardt-Levenberg Least-Squares inversion scheme (Lines and Treitel, 1984) to obtain layer parameter corrections, from a matrix describing how the VES curve misfit changes with changes in the layer parameters.

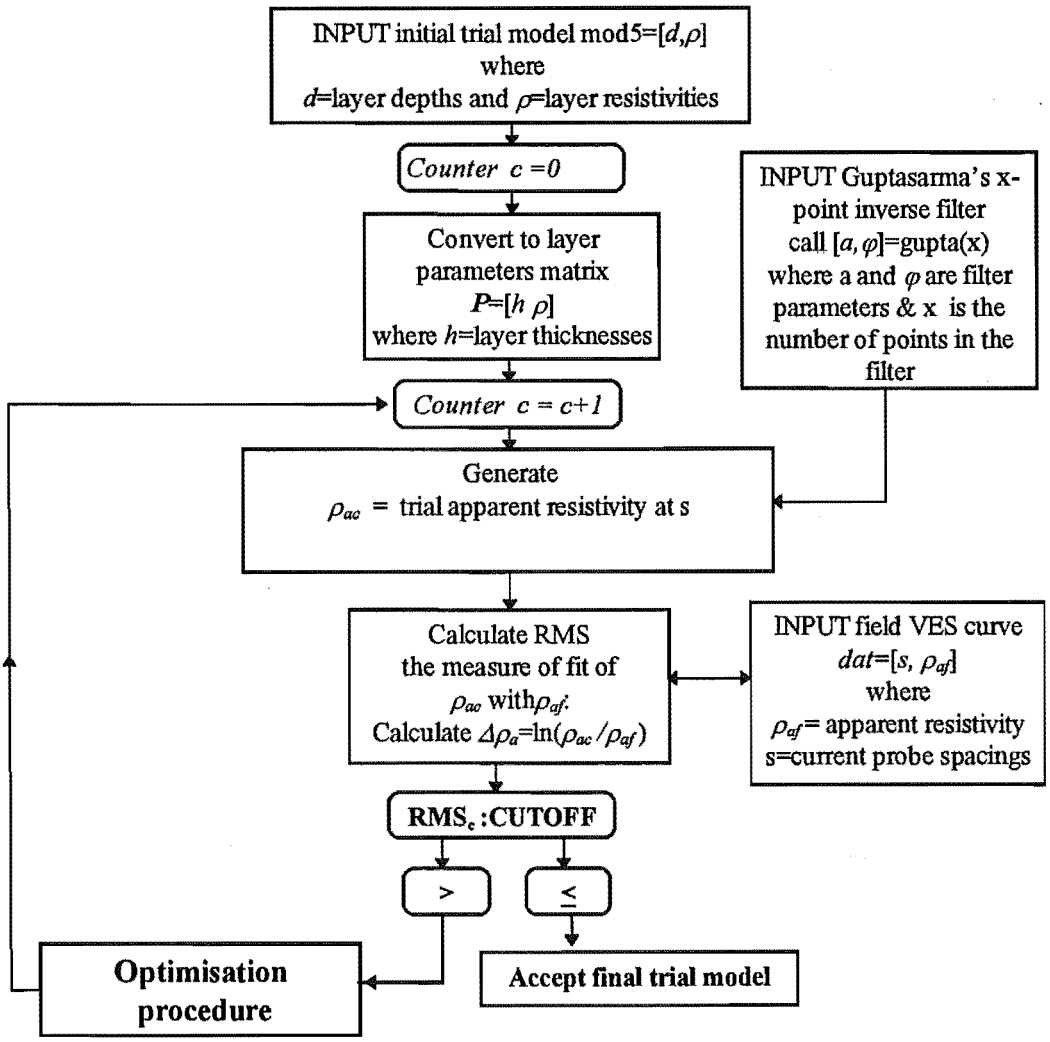

Figure 5.7.2-3: General outline of programs to 'invert' apparent resistivity curves to recover the resistivity profile.

I have written inversion programs in Matlab based on the two methods. They follow a scheme set out in Figure 5.7.2-3 and are described in the following sections. The main

differences between the two methods lie in the method of generation of the initial trial model and in the optimisation procedure.

5.8 Inversion programs developed in this study

5.8.1 Zohdy (1989)

Zohdy (1989) notes the following properties of Wenner and Schlumberger sounding curves:

(a) Computed apparent resistivities are always positive

(b) The form of a sounding curve follows the form of the true resistivity-depth curve.

(c) A sounding curve is always "out of phase" with the resistivity-depth curve and is always shifted to the right of the resistivity-depth curve.

(d) The amplitude of a sounding curve is always less than or equal to that of the true resistivity-depth curve, and,

(e) Changing the true resistivity of a thick layer changes the apparent resistivity along a corresponding segment of the sounding curve.

Assuming then, that the VES curve is related fairly directly in form to the resistivity profile, Zohdy notes that the problem becomes one of how to shift the VES curve more "in phase" with the actual layering, and how to scale the apparent resistivities to the actual resistivities.

5.8.2 The program inverjnz.m

An outline of the program is given in Figure 5.8.2-1. The method is also illustrated by the series of graphs (from Figure 5.8.2-2 on) showing the inversion of a VES curve generated from a 5-layer model profile. There are two optimisation procedures: The depth-shifting procedure which is entered first, uses the measured VES curve as the initial trial model, by setting model depths equal to the spacings and setting trial layer resistivities equal to the apparent resistivities (Figure 5.8.2-2 and Figure 5.8.2-3). The trial VES curve is compared with the actual VES curve and the RMS difference recorded. By multiplication by a shift factor (eg., 0.9) the trial depths are shifted to the left, and the cycle repeated. The RMS should normally be smaller (final shift-factors

appear to lie in the range 0.3 - 0.6 for Schlumberger readings in general). The cycle is repeated until the RMS reaches a minimum or other cutoff. In practice, with experience the optimal shift-factor is known. If this is the case the depth-shifting optimisation routine may be omitted and the known shift-factor used (in the example shown this was set at 0.3).

The program now uses resistivity scaling as the optimisation procedure (Figure 5.8.2-5). On the basis of point (e) above, each trial layer resistivity is scaled up or down by multiplying it by the measured apparent resistivity divided by the trial apparent resistivity. The cycle is repeated until again an RMS minimum or some other cutoff point is reached (Figure 5.8.2-6).

At each cycle, the profile is made to conform to the drying slab by preventing the resistivity from increasing with depth. Any layer resistivity higher than that of the layer immediately above, is lowered to conform (Figure 5.8.2-4). This is termed a "falling profile constraint" and generally enables faster recovery and more realistic profiles.

Although sharing the advantages of indirect methods generally, this method provides some ability to cope with noisy or anomalous data. As the best fitting trial apparent-resistivity-curve represents a smoothing of the actual VES curve, it may be used as the initial input to another round of interpretation, although, as Zohdy shows, this does not always work well.

As the VES curve is used as the initial model, when a Ghosh-type filter is used, the spacings must be logarithmically separated as noted above. If the data points were not measured at appropriate spacings, the VES curve must be interpolated at logarithmic intervals. This can represent a loss of information since the logarithmic end points may be some distance within the spacing range. Guptasarma's filter can thus be an advantage here as it does not require logarithmic spacing.

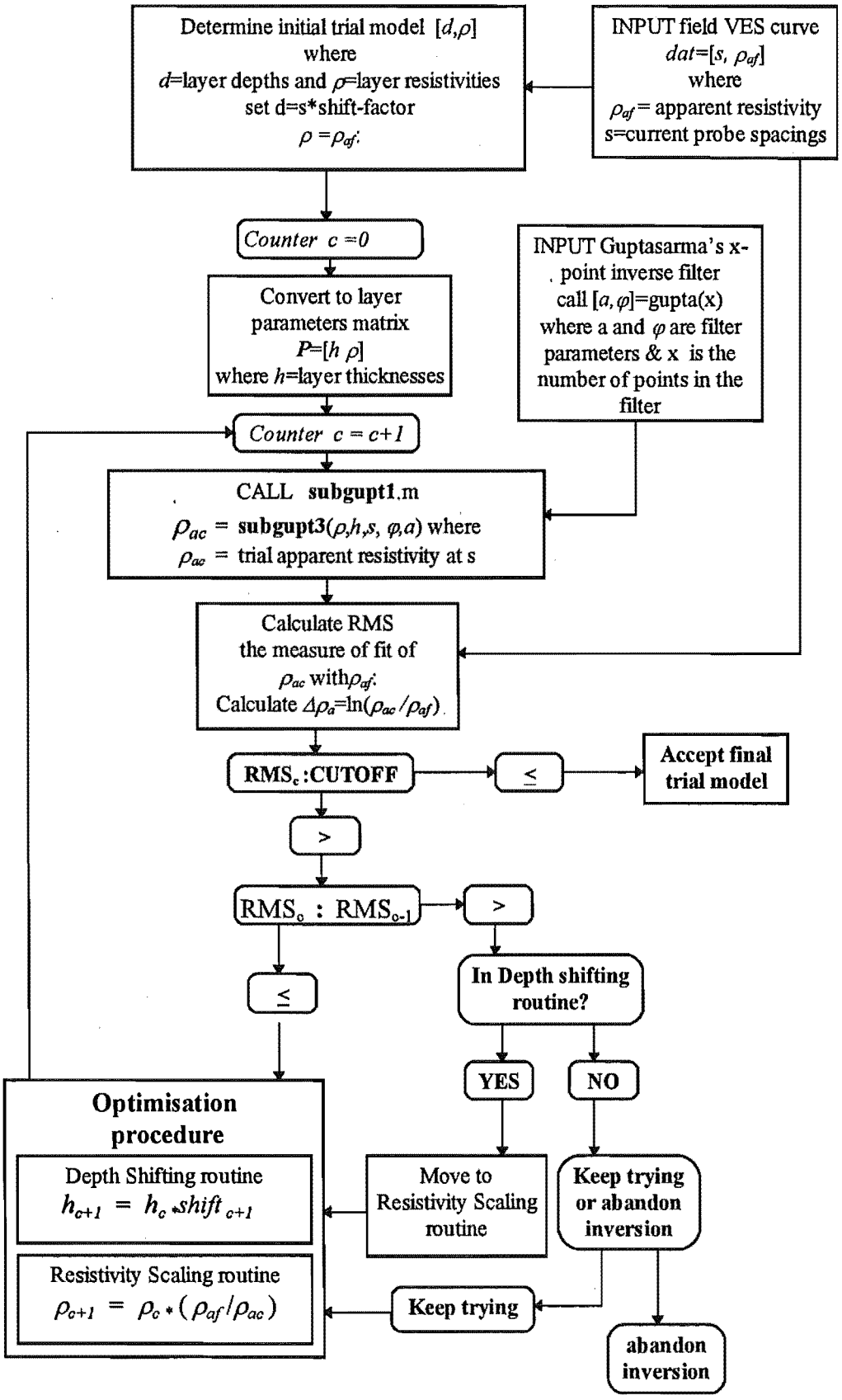

Figure 5.8.2-1: Flowchart showing profile recovery using the program inverjnz.m

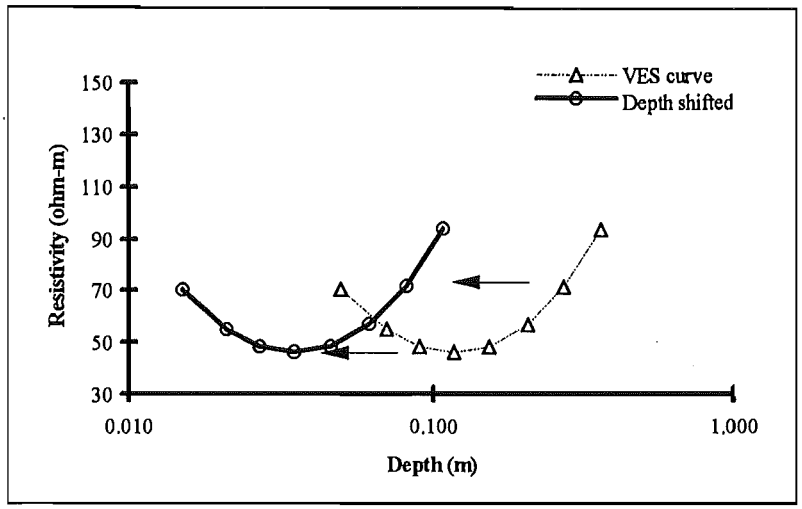

Figure 5.8.2-2: Stages in Zohdy's method: determining layer depths

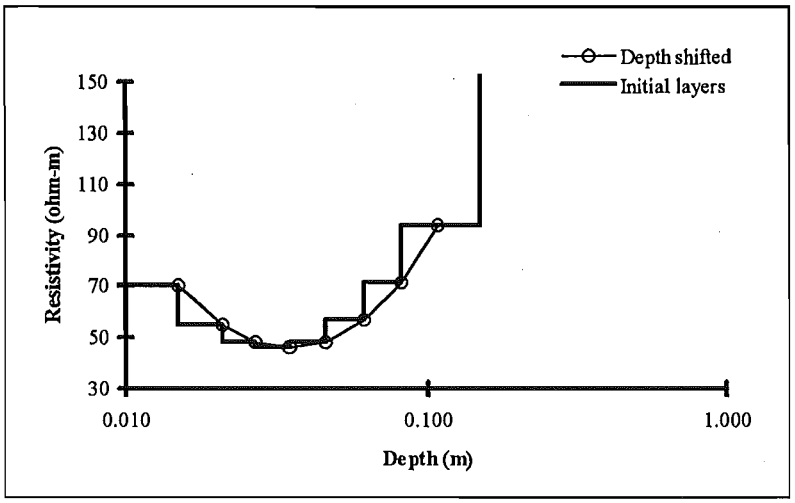

Figure 5.8.2-3: Stages in Zohdy's method: Step formation

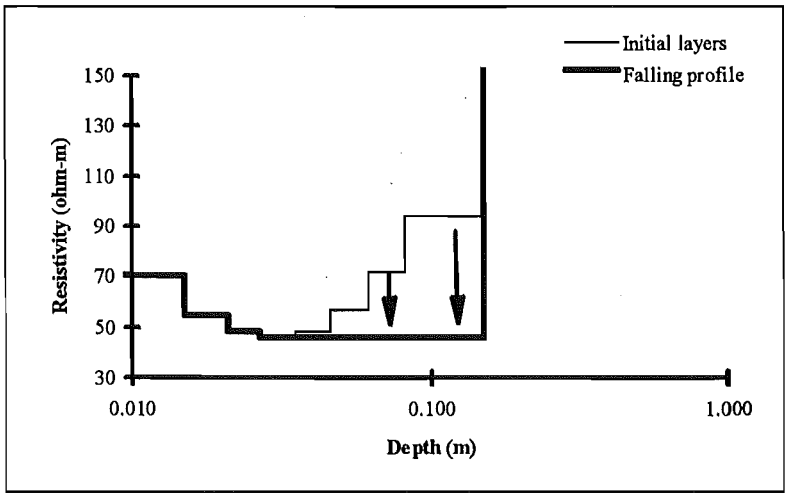

Figure 5.8.2-4: Stages in Zohdy's method: Impose falling profile constraint

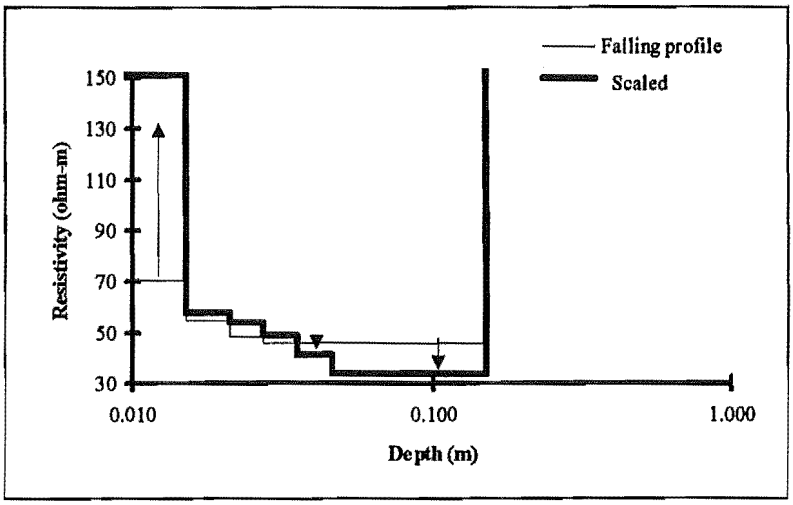

Figure 5.8.2-5: Stages in Zohdy's method: Scale resistivities.

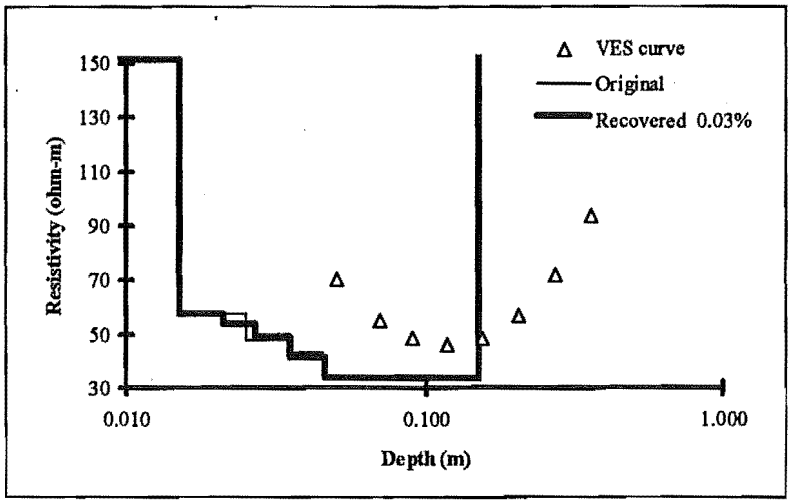

Figure 5.8.2-6: Stages in Zohdy's method: Final trial model

5.8.3 Merrick's method

This description is based on Merrick (1977).

We define an n-layer earth characterised by layer thicknesses

$$\underline{h}^* = (h_j^*); \quad j = 1,2,\ldots n-1$$

and resistivities

$$\underline{\rho}^* = (\rho_k^*); \quad k = 1,2,\ldots n$$

which are combined into a single vector

$$\underline{P}^* = (P_j^*) = (h_1^*, h_2^* \ldots h_{n-1}^*; \rho_n^*, \rho_{n+1}^* \ldots \rho_{2n-1}^*).$$

A set of m apparent resistivity data $\underline{\rho}_{a_i}^*$ is determined from vertical electric sounding on this earth

From a trial model $\underline{P}$, a resistivity transform curve $\underline{T_i}$ is generated using recurrence relations (see Section 5.3) and an inverse filter applied to give the trial apparent resistivity ρ_{a_i}.

Comparing data through their logarithms in order to reduce the bias toward high apparent resistivities, the sum of squares

$$S = \sum_{i=1}^{m} \{\log(\rho_{a_i}^*) - \log(\rho_{a_i})\}^2 = \sum_{i=1}^{m} \{R^* - R\}^2$$

is a suitable measure of the goodness of fit.

Writing $\Delta\underline{P} = \underline{P}^* - \underline{P}$ and $\Delta\underline{R} = \underline{R}^* - \underline{R}$ the problem of minimising S may be linearized by defining a matrix $\underline{\underline{A}}$ which maps the parameter correction vector $\Delta\underline{P}$ into the vector of data deviations $\Delta\underline{R}$. That is

$$\underline{\underline{A}}\,\Delta\underline{P} = \Delta\underline{R}$$

This process is equivalent to linearizing the apparent resistivity function by a Taylor series expansion about a trial model

$$R_i(\underline{P} + \Delta\underline{P}) = R_i(\underline{P}) + \sum_{j=1}^{2n-1} \left(\frac{\partial R_i}{\partial P_j}\right)\Delta\underline{P}_j$$

provided that the elements a_{ij} of the matrix $\underline{\underline{A}}$, are defined to be normalised apparent resistivity derivatives with respect to each model parameter

$$a_{ij} = \frac{\partial R_i}{\partial P_j} = \frac{1}{\rho_{a_i}} \frac{\partial \rho_{a_i}}{\partial P_j}$$

The derivatives are found by convolving a digital filter *{b(k)}* with transform derivatives

$$\frac{\partial \rho_{a_i}}{\partial P_j} = \sum_k b(k) \frac{\partial T_{i-k}}{\partial P_j}$$

defined recursively (Johansen 1975).

Because apparent resistivity is a non-linear function of the model parameters, there is no exact inverse $\underline{\underline{A}}^{-1}$ giving $\Delta\underline{P}$ when $\Delta\underline{R}$ is known. However, a generalised inverse $\underline{\underline{A}}^{+}$ may be found such that

$\Delta\underline{P} = \underline{\underline{A}}^{+}\Delta\underline{R}$ in a least squares sense.

A suitable form of $\underline{\underline{A}}^{+}$ may be found using the Marquardt-Levenberg method (see Appendix A and Section 5.8.4.3) and solved using singular value decomposition (Lines and Treitel, 1984).

I have used this method as the basis of a program inverjnm.m designed to automatically invert apparent resistivity curves output from the VES instrument. This program is described in the next section.

5.8.4 The program invrjnm.m

An outline of the program inverjnm.m is presented in flowchart form in Figure 5.8.4-1. Some of the main issues that needed to be addressed are discussed below.

5.8.4.1 Selection of initial trial model

The choice of the initial trial model is important as it sets the number of layers in the final model and influences the speed with which the final model is reached. Although it is possible to change the number of layers during the inversion process this really amounts to running through the program twice using the final model from the first run-through to generate an initial trial model (with more or fewer layers) for the second. The number of parameters that are allowed to vary must be no more than the number of data points. If some parameters are fixed more layers are possible. However because of layer suppression (see Chapter 7) the effective number of layers in the final model may be fewer than in the initial model. This leads to unnecessary processing time although speed is less of an issue with the rapidly increasing clock-speeds of contemporary computers.

The more realistic the initial model is, the faster a realistic final model will be achieved and the less likely convergence onto an incorrect solution or the possibility of non-convergence.

The initial model may be of the form {trialmod=[0.01 90; 0.02 60; 0.03 40; 0.15 30]} or, as in inverjnz.m, it can be based directly on the depth-shifted VES curve.

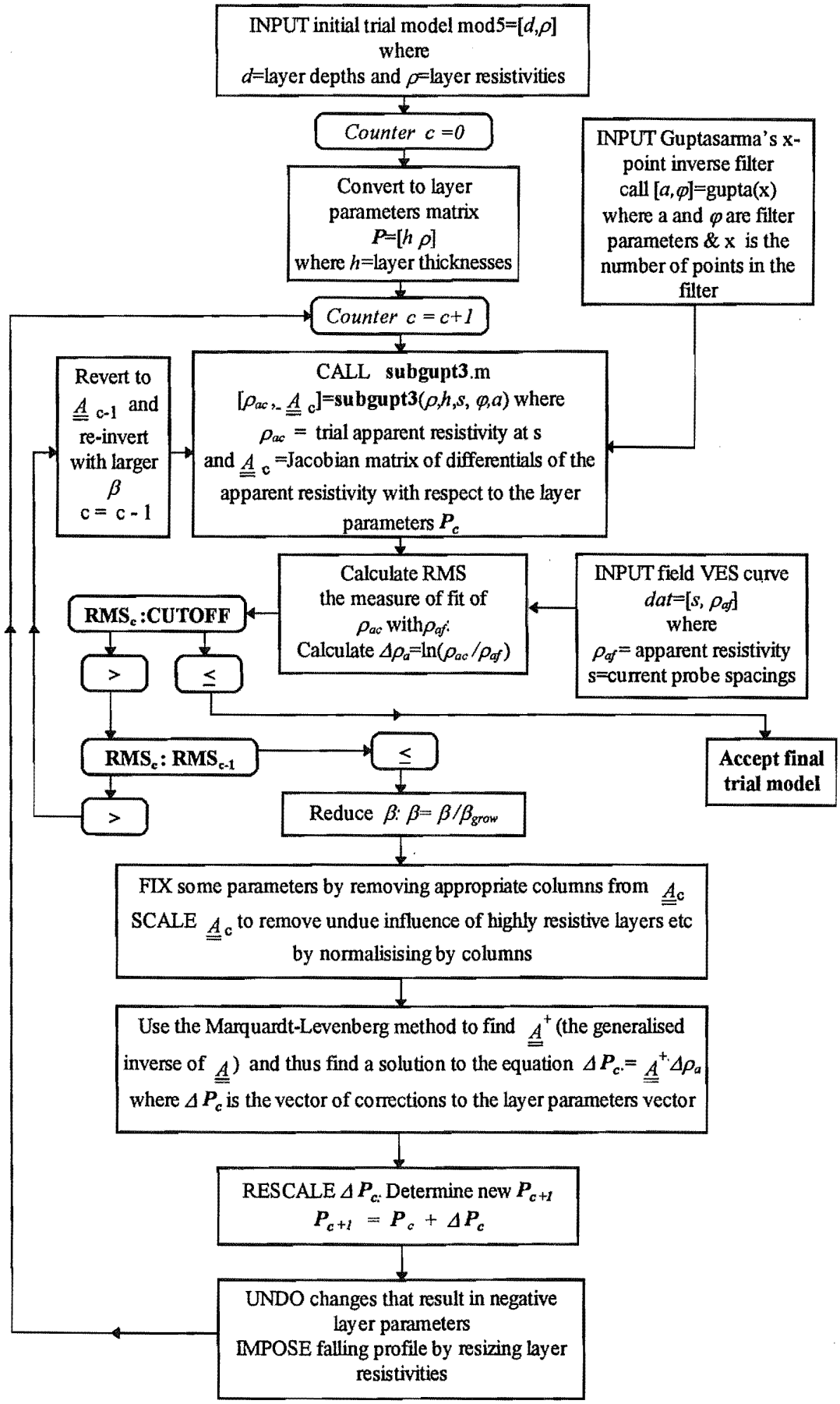

Figure 5.8.4-1: Flowchart showing profile recovery using the program inverjnm.m

5.8.4.2 Selection of layer parameters to fix or allow to vary

.As mentioned above, the number of parameters that are allowed to vary must be no more than the number of data points. The sublayer resistivity and depth must be included in the inversion process, however they may be preset (respectively at an arbitrary 10^{100} ohm - m and 0.5 m say).Generally the layer depths are kept fixed rather than resistivities. There are three reasons for this.

1. In this study it was the resistivity at particular depths that was of interest and our interest extended throughout the slab rather than in the places which may have a particular resistivity.
2. Perhaps more importantly, it is much easier to keep the thickness of the model slab at the known thickness (0.15 m in the study) if the depths are fixed. When depths are free to vary, the inversion process tends to fit the rising VES curve with a steadily rising resistivity profile rather than with a sharply defined one. This results in a lack of definition of the lower boundary of the recovered model slab. When depths are free to vary and the resulting model-slab is too thick or thin, an attempt can be made to find an equivalent model with thinner or thicker layers (see Section 5.8.4.4 below) however this has not proved particularly satisfactory.
3. Keeping depths fixed, allows the use of fewer data points. Thus with eight data points, eight layers are possible whereas the model must be restricted to four layers if depths are free.

It should be noted that, strictly speaking, it is the layer thicknesses that are free vary and are optimised by the inversion process. It is of little advantage then, to fix some and let others vary since the problem with overall slab thickness remains. It is easier to fix all depths and allow all resistivities to vary.

5.8.4.3 Marquardt-Levenvberg method

The Marquardt-Levenberg approach is to 'impose the constraining condition that the sum of the squares, or energy of the elements of the parameter change vector $[\Delta P]$ be bounded by a finite quantity, say δ_o^2 ... The effect of this constraint is to ...smooth the parameter change vector $[\Delta P]$...Thus we choose $[\Delta P]$ to minimise a cost function" (ibid p. 163)

$$S(\Delta P,\delta) = \Delta \underline{R}^T \Delta \underline{R} + \beta \left(\underline{\Delta P}^T \Delta P - \delta_o^2 \right)$$

with the solution

$$\underline{\Delta P} = \left(\underline{\underline{A}}^T \underline{\underline{A}} + \beta \underline{\underline{I}} \right)^{-1} \underline{\underline{A}}^T \underline{g}$$

This solution is 'hybrid because it combines the so-called 'method of steepest descent' [which is optimal when the cumulative squared error S is large] with the method of least squares [which becomes effective when S is small]...

A particular choice of β... allows either the linear least-squares method or the steepest descent method to dominate the parameter search. Setting $\beta = 0$ implies that the linear least squares method predominates, while allowing β to increase moves the technique towards the method of steepest descent. Initially β is set at a large positive value, so that the good initial convergence properties of the steepest descent method can come into play. Then, as this happens, β is reduced by multiplying it by a constant factor < 1 so that the linear least-squares method may take over in the region closer to a solution. If divergence occurs during an iteration, β is divided once more by this factor until the error drops and convergence resumes (at least one hopes it does) [sic]" (Lines and Treitel, 1984, pp. 164-166).

A fuller discussion of the method is presented in Appendix A.

5.8.4.4 Removal of non-physical layer parameters

Occasionally an ill-behaving problem may throw up such large changes in layer parameters that negative resistivities, or layer thicknesses result. A simple method of dealing with these is to replace any new parameter which is negative with a weighted average of the old and new layer parameters. If this replacement is negative also, the process is repeated until all new parameters are positive.

If layer thicknesses are allowed to vary, imposition of the 'falling profile" constraint (see below) and of an extremely high sublayer resistivity can result in the total thickness of non-sub-layers to exceed or be smaller than the physical slab thickness (0.15m in this study). When this is identified some adjustment to the thickness of the bottom layer may be made to bring the model slab thickness in line with the physical. Since this layer has a

smaller resistivity than that immediately below (the sub-layer), the "equivalence rules" (Koefoed, 1979) state that the parameters of this layer may be changed so that the ratio of its thickness over its resistivity (h/ρ – called the longitudinal conductance of the layer) remains constant. Where the excess or shortfall in model slab thickness slab is much less than h, this adjustment may be made. It is not wholly successful since, as Koefoed notes, the equivalence rules do have restricted validity. However normally the correction is not enough to give a worse measure of fit than the uncorrected and a better fit still may be achieved in the next iteration.

5.8.4.5 Imposition of the "falling profile constraint"

This has been mentioned in Section 5.8.2 (see also Figure 5.8.2-4). A slab drying from the top-surface only, will possess a resistivity profile which decreases from the surface to the base of the slab. The presence of the highly resistive sublayer results in the (now) familiar bowl-shaped apparent resistivity curve. Unconstrained inversion of such curves will not result in a similarly well defined profile. Rather a bowl shaped profile will be recovered. Enforcing the decrease in resistivity with depth over the layers representing the slab itself actually enables recovery of profiles with much better measures of fit (that is, with lower RMS) than when this "falling profile" is not imposed.

5.8.4.6 Decision-making

The measure of fit between the experimental and model VES curve is determined as

$$RMS = \left\{ \sqrt{\sum_{i=1}^{ns} \left\{ \frac{(roaf(i) - roac(i))}{roaf(i)} \right\}^2 \Big/ ns} \right\} \cdot 100\%$$

Let RMS(c) be that associated with the c^{th} iteration. At the time of decision this value is compared with the cutoff (often about 0.5%), and, if still larger than the cutoff, it is compared against the previous value RMS(c-1). If RMS(c) < RMS(c-1), the inversion parameter β will be decreased. If RMS(c) > RMS(c-1), β will be increased. If RMS(c) = RMS(c-1), β will remain constant.

Other conditions are tested. Thus if the RMS is decreasing but in asymptotic fashion, the ratio RMS(c)/RMS(c-1), will approach 1.0. A second cutoff of say 0.999 is used to test this ratio. The inversion process will be halted when RMS(c)/RMS(c-1) > 0.999.

While this may seem quite a small decrease, it may in some cases be too large. The RMS is a function of all the layer parameters and thus moves about on a multi-dimensional surface. A small decrease in RMS for 10 or more iterations can suddenly result in the discovery of an approach to a new minimum. The choice of each cutoff point, the choice of the factor by which β may grow or diminish, and the choice of how many iterations may take place without any improvement in RMS, will all have a bearing on how well the profile recovery process works.

Interestingly, I have not been able to use the other measure of fit, – that is, the sum of squares of errors between the model VES curve and the data – successfully as the basis for decision making.

Both the imposition of the "falling profile" constraint and the not wholly successful determination of an equivalent lower layer to ensure a physical slab thickness result in a new model not intended by the Marquardt-Levenberg inversion scheme. Normally the corrections are sufficiently 'real' for the RMS of the corrected model an improvement on that of the previous model, or for the corrected model to be in a better state from which a smaller RMS may be reached in future. Occasionally, the inversion induced changes which are corrected by the constraints, are repeated exactly and an cycle of change and counter-change is set up. When this happens the new RMS will be worse than the previous value and so the inversion parameter β will be increased. Normally the cycle will eventually be broken out of as the "steepest descent" method takes over. If not, at some arbitrary number of cycles (say 20), the inversion attempt will be abandoned and the model with the lowest RMS will be accepted as the final trial model.

5.8.5 Examples of profile recovery using inverjnm.m

If depths are fixed, models with up to 8 layers may be recovered from the sounding data. Different curves may be fitted best with different numbers of layers and it is not apparent before inversion what the optimum number is for a particular curve.

For example Figure 5.8.5-1 shows VES curves generated from to three different profiles: with three, five, and 100-layers. The three curves were then inverted using **inverjnm.m** using trial models with different numbers of layers. The results of the inversion are presented in Figures 5.8.5.2 to 5.8.5.4.

A number of points may be made on close scrutiny of these model results. We shall use the abbreviation VES3 for the VES curve generated from the original 3-layer model, VES5 for that generated from the 5-layer model and so on.

1. A range of dissimilar profiles can fit the same VES data equally well in the sense that they yield nearly the same RMS. Compare for example the 2- and 7- layer profiles recovered from VES3, and the 3- and 7- layer profiles recovered from VES100 in Table 5.8.5-1 (a) and (c) respectively (see also Figure 5.8.5-2 and Figure 5.8.5-3). The RMS may be a rather crude measure of how well the profile fits the data.
2. A recovered model may fit the original model better in one region than another. Compare the two 5-layer models in fitting VES3. The first (marked with a □) with RMS = 2.8%, fits the 3-layer profile almost exactly below 0.015 m whereas the second (marked ◆) with higher resistivity than the original profile in the region above 0.25 m has a lower RMS of 1.3%..
3. Adding more layers tends to result in a decrease in resistivity for the lowest layer.
4. Adding more layers does not necessarily enable the original profile to be fitted better (in the sense of having a lower RMS): the 7-layer recovered models do not generally have the smallest RMS.
5. Two layer models may be recovered from a VES curve with a fit as good as, if not better than models with higher numbers of layers (see that from VES3 and VES100)
6. Often the effective number of layers in the recovered profile is reduced as adjacent layers are given the same resistivity. The 5- layer model recovered from VES100 has the same number of effective layers and the same RMS as the three layer model for example.

7. As Point 6. indicates, whether the original model was layered (those generating VES3 and VES5) or virtually continuous (that generating VES100), is not reflected in the recovery process in any immediately obvious way.

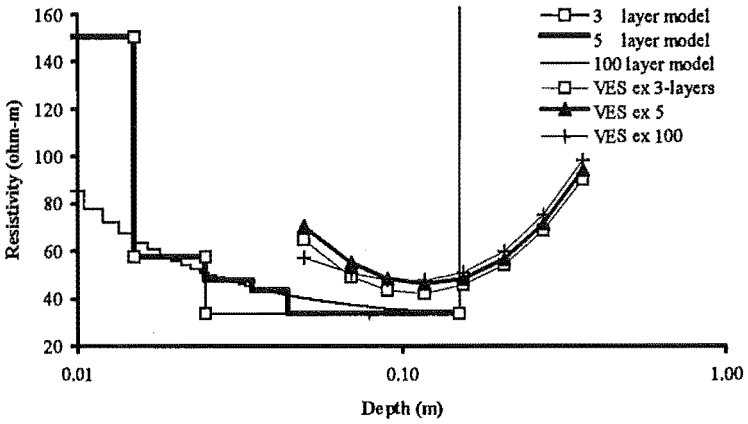

Figure 5.8.5-1: Three-, five-, and 100-layer profiles and the model VES curves generated *from* them (Note: these are not recovered profiles).

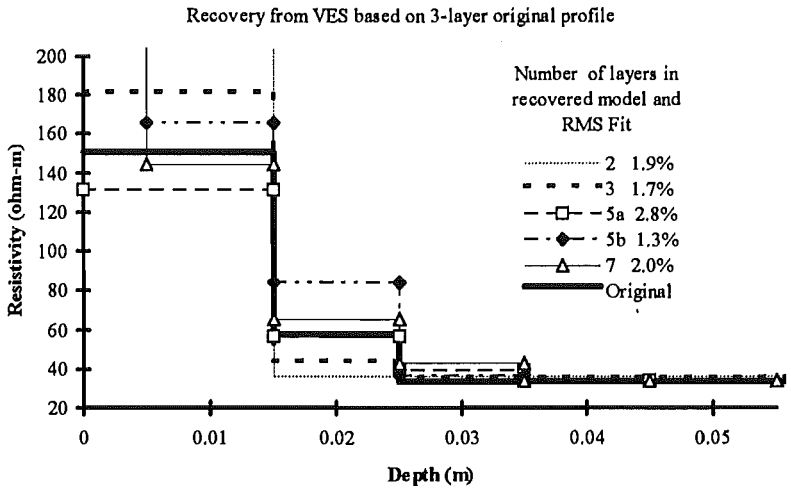

Figure 5.8.5-2: Profile recovery from a VES curve based on a 3-layer initial model.

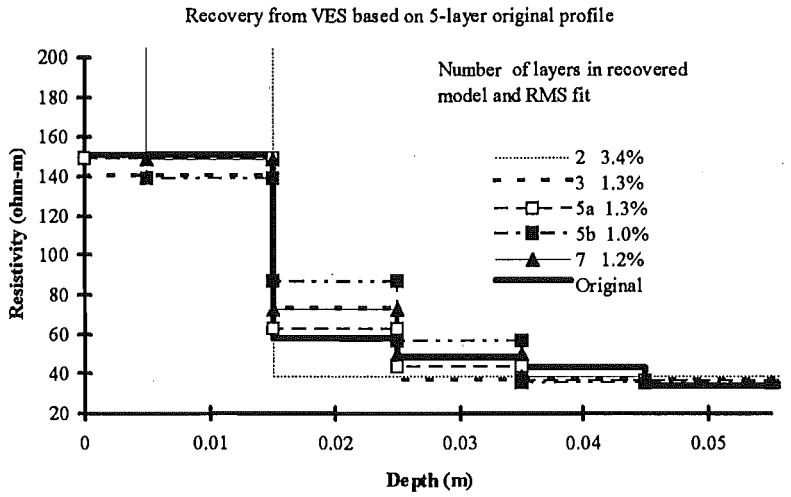

Figure 5.8.5-3: Profile recovery from a VES curve based on a 5-layer initial model.

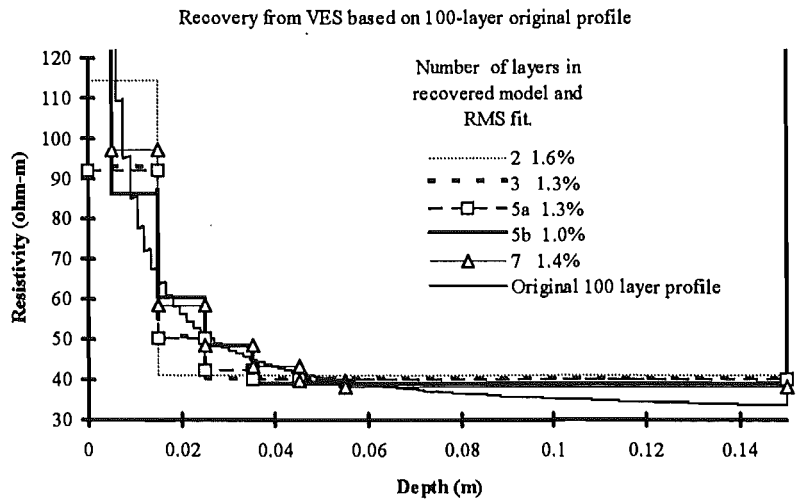

Figure 5.8.5-4: Profile recovery from a VES curve based on a 100-layer model.

Table 5.8.5-1: Profile recovery with different numbers of layers in the trial model. The VES curves inverted, derive from (a) a 3-layer original profile, (b) a 5-layer original profile and (c) a 100-layer original profile. Resistivity is measured in ohm-m. Note the difference in layer depths between the two 5-layer profiles.

(a) Profile recovery from VES based on 3-layer original profile

Depth	Number of layers in trial model				
(m)	2	3	5	5	7
0.005				2,421	361
0.015	208	182	132	166	144
0.025		44	57	84	65
0.035			39	37	43
0.045			34		34
0.055					34
0.150	36	36	34	35	34
RMS%	1.9	1.7	2.76	1.3	2.0

(b) Profile recovery from VES based on 5-layer original profile

Depth	Number of layers in trial model				
(m)	2	3	5	5	7
0.005				5,428	344
0.015	238	141	149	139	149
0.025		73	63	87	73
0.035			44	57	50
0.045			36		39
0.055					36
0.150	39	37	36	36	36
RMS%	3.4	1.3	1.3	1.0	1.2

(c) Profile recovery from VES based on 100-layer original profile

Depth	Number of layers in trial model				
(m)	2	3	5	5	7
0.005				4,324	3,076
0.015	114	93	92	86	97
0.025		51	50	61	59
0.035			42	48	48
0.045			40		43
0.055					40
0.150	41	40	40	39	38
RMS%	1.6	1.3	1.3	1.0	1.4

6. VERTICAL ELECTRIC SOUNDING II : INSTRUMENTATION

The determination of a moisture-content profile from a drying concrete slabs requires calculation of the resistivity profile from measurements of apparent resistivity at the surface and then conversion to a relative-humidity profile using predetermined calibration curves. In this chapter the development of the instrument used to measure apparent resistivity is described.

6.1 Background

Vertical electric sounding (VES) or resistivity profiling is the measurement of apparent resistivity at the surface and subsequent recovery of resistivity profiles by 'inverting' the apparent resistivity curve. The subject has been extensively studied and practised in geophysics (see for example Parasnis 1972, Koefoed 1979 or Zhdanov and Keller 1994). The theory of vertical electric sounding has been developed in Chapter 5 of the present work.

To measure apparent resistivity, current is introduced into the ground through point electrodes or line contacts, and potentials are measured at other electrodes in the vicinity of the current flow. It is then possible to obtain an effective or apparent resistivity of the subsurface. Increasing the separation of the two current electrodes forces the current to take a deeper path so that the apparent resistivity at the surface, as a function of current probe spacing, is a reflection of the resistivity profile of the subsurface. By mathematically 'inverting' the apparent resistivity curve (also known as the VES curve) the true resistivity profile may be recovered

Valdes (1954) described the laboratory use of four electrode arrays in measurement of the resistivity of germanium crystals or slices. Wilkins (1982) proposed the use of systematic measurements of apparent resistivity to give information on the resistivity distribution within the material, although he noted that simple measurements of the same type had been done previously.

Techniques and instruments designed to measure concrete resistivity have been described by several authors (for example Millard et al. 1989 and Ewins 1990) and a few instruments are commercially available (for example The C.N.S Electronics Ltd Resistivity Meter, described in 'Product information', p.35 of *New Zealand Concrete Construction* April 1990). Without exception, the measurement systems are based on the

Wenner array, generally with fixed current and voltage probe spacings (Figure 6.1-1 (a)) and are intended for the assessment of corrosion risk of reinforced concrete. Such assessment involves resistivity *mapping* rather than resistivity *profiling*. In resistivity mapping a two dimensional 'map' of average resistivity is constructed through the measurement of apparent resistivity at a number of points on the concrete surface. The electrode configuration and dimensions are fixed so that the effective depth of measurement is constant (by contrast the electrode configuration is expanded about a central point in resistivity profiling). For corrosion risk assessment, the region of interest is the 'cover' region of a concrete structure, that is, the relatively thin layer of concrete covering the outer layers of reinforcing. When the apparent resistivity is within a certain range the reinforcing is deemed more susceptible to corrosion. A low resistivity indicates conditions conducive to passage of electric current and ingress of water and air, all necessary for corrosion to take place.

Meters designed for resistivity mapping will share some of the resistivity- profiling design requirements and so are of interest in the present work.

Ewins (1985 and 1990) described a resistivity meter designed to overcome problems associated with the probe/concrete interface. In particular the use of square wave alternating current enables the meter to cope with very large differences between probes in interface resistance. The waveform frequency 'is fast enough for no polarization effects to occur during a half cycle, and slow enough for all the capacitive effects to have settled down for the large, central part of the waveform' (Ewins 1990, p122).

Millard et al (1989) described the development of a four probe resistivity meter-logger for use on concrete. This meter used sine wave alternating current. Millard goes on to discuss many of the advantages and drawbacks of using two and four electrode techniques in a later paper (1991a). He reports on theoretical and practical studies used to assess accuracy and reliability of different methods and outlines some of the issues relevant to resistivity mapping such as electrode diameter and electrode spacing.

McCarter and Barclay (1993) compared two four-electrode resistivity measurement techniques- one method using surface mounted and the other using electrodes embedded a short distance beneath the surface.

Millard (1991a, 1991b) and McCarter (1991) discuss the effect of surface layer resistivity. They note that the apparent resistivity is very sensitive to the resistivity of the

surface layer, especially when surface resistivity is low compared to that of the deeper regions, and when the spacing between the current probes is small. It is suggested that only by measuring at a range of spacings could a better picture of the resistivity profile be discovered. Subsequently there has been no further report of experimenters using the four probe technique to obtain profile information on concrete samples.

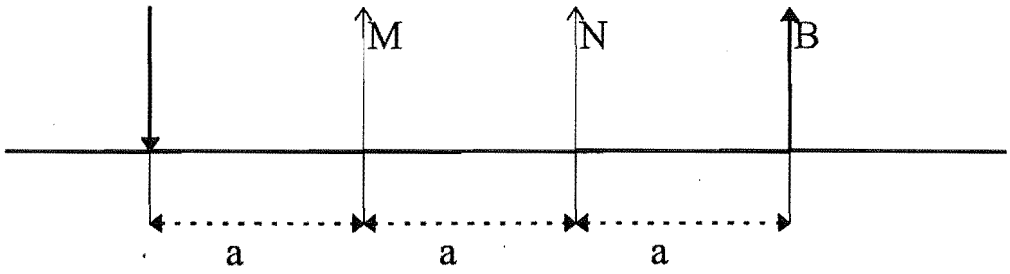

(a) The Wenner array

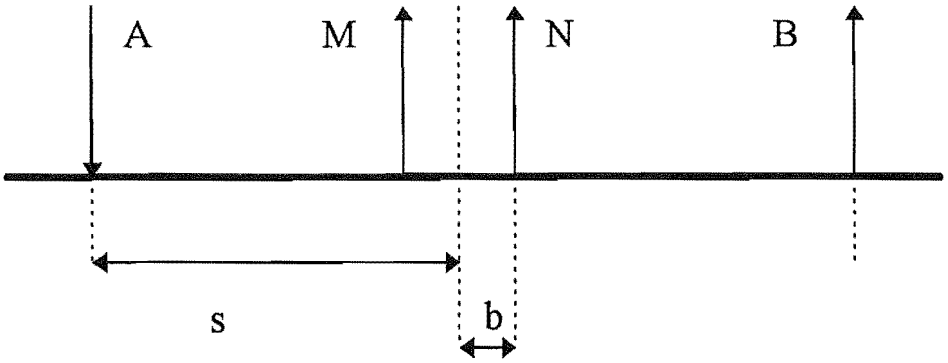

(b) The Schlumberger array.

Figure 6.1-1: Wenner and Schlumberger arrays. Current is injected into the concrete through probes A and B. The potential difference is measured between the 'voltage' or 'measurement probes M and N.

6.2 VES instrument development

The measurement of apparent resistivity involves the electrodes, the device used to position the electrodes and the current generation and voltage measuring device. In the present work, these were developed simultaneously although they evolved at different rates, as changes in one area called forth or allowed changes in other areas. Eventually, a

fourth constituent, automatic data acquisition and control of the meter, was added. This enabled investigation of the evolution of apparent resistivity curves over 24 hour periods and longer.

In the nondestructive surface mounted instrument, electrodes rest on the concrete surface. The electrode-concrete interface resistance can be very high and variable depending on the condition of the surface and the type of electrode. In addition, the resistivity of the surface or skin layers of concrete is very high since the relative-humidity (RH or ψ) will be in equilibrium with that of the surrounding air (the ambient RH), and thus be very dry relative to the deeper layers. This high resistance limits the current passing through the concrete and hence the potential difference between the measurement probes. To increase the signal-noise ratio one or both of the following must be done:

- the *current* through the concrete must be increased by decreasing the concrete-electrode interface resistance at the 'current probes',
- the *noise level* at the inputs to the instrumentation amplifier must be decreased by lowering the concrete- electrode interface resistance at the 'voltage probes' and the noise current through this resistance.

In attempting to lower the concrete- electrode interface resistance, a range of electrode types were trialed. including dry stainless steel and copper, conducting gel, conducting paint, conducting resin, conducting ink, copper-mercury amalgam. Apparent resistivity curves which were useful, (in the sense of being repeatable and having relatively low noise), were not attained until the introduction of 'wet' electrodes, that is wooden electrodes soaked in tap-water or in a conducting solution (Swarfega). The action of 'wet' electrodes is to reduce the electrode-concrete interface resistance, and to penetrate the highly resistive surface layer, by creating a small region of low resistivity in the immediate vicinity of the contact area (see Section 6.9).

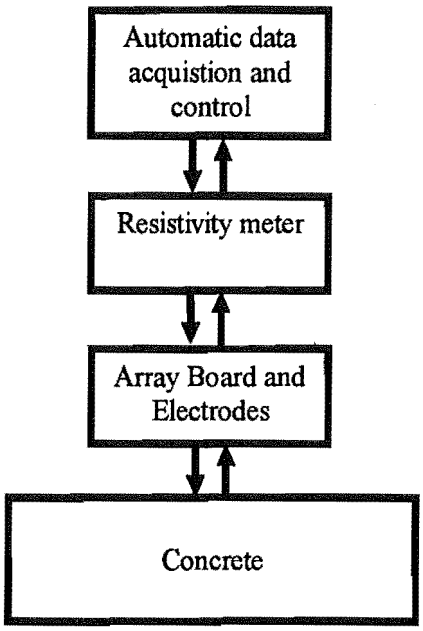

Figure 6.2-1: The main constituents of the vertical electric sounding instrument.

Originally, it had been the intention to use just two 'current' electrodes and two 'measurement' electrodes, moving them through the range of spacings during a sounding. However, 'wet' electrodes required a certain time for the reduction of electrode-concrete interface resistance to occur (presumably this is the time required for the moisture to diffuse into the surface layer). Thus, to be used efficiently, a whole set or array of electrodes, representing the complete range of spacings, needed to be placed on the concrete surface simultaneously. Part of the design problem then became how to position a large number of electrodes and select them during the sounding process.

The VES instrument comprises the electrode array, the resistivity meter and the associated 'inversion' software through which the resistivity profile is recovered (see Figure 6.2-1). The resistivity meter itself comprises the current generator, the voltage measurer, the electronic switching system enabling demultiplexing the current drive over the set of current electrodes and multiplexing the voltage measurer over the range of measurement electrodes, the data acquisition and control system and the computer control software. An outline of the final design of the VES instrument is given in following sections.

6.3 Electrodes and array board

The electrodes are short sections of wooden dowel, pressed into stainless steel housings. The combinination of housing and electrode is called a probe (see Figure 6.3-1).

Before use the probes are left to soak in a solution of a conducting solution made by diluting Swarfega (an industrial cleaning gel) with water in a ratio of 1:10. (It would be of interest to determine the relevant ionic nature of Swarfega solution and thence the optimal ionic content of the conducting solution but this problem was not addressed in the present work.) The wooden electrode swells on wetting, so that while the electrodes are held tight in the housing when wet, if they are subsequently allowed to dry out they shrink and are liable to fall out. Ideally they would be fastened to the housing more permanently.

6.3.1 Early positioning systems

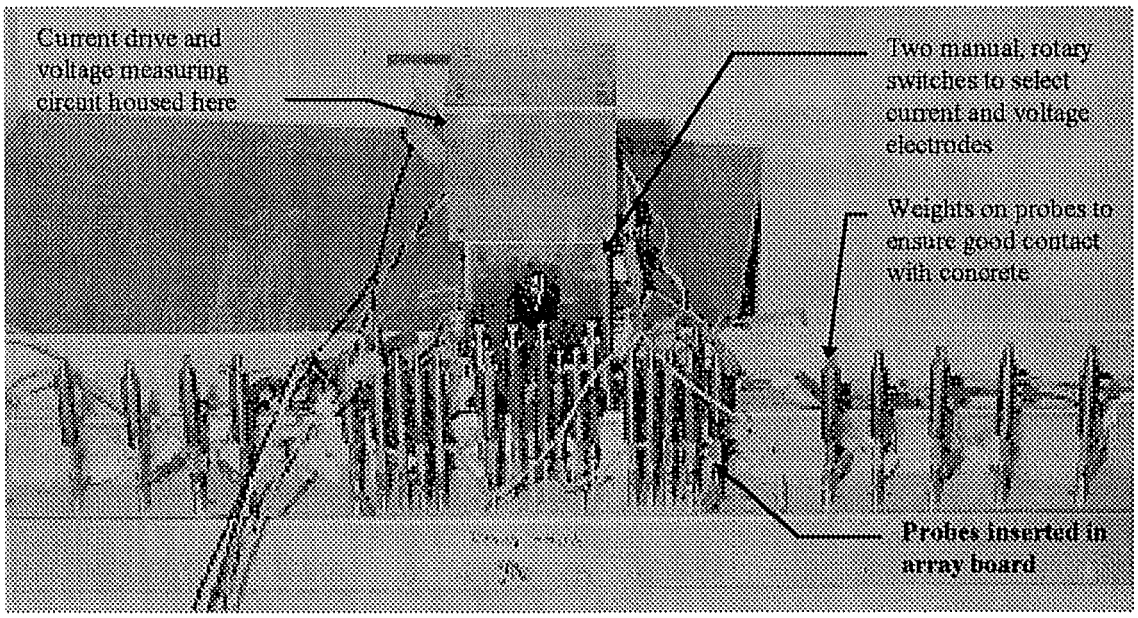

(a) The first fully functional array board and resistivity meter.

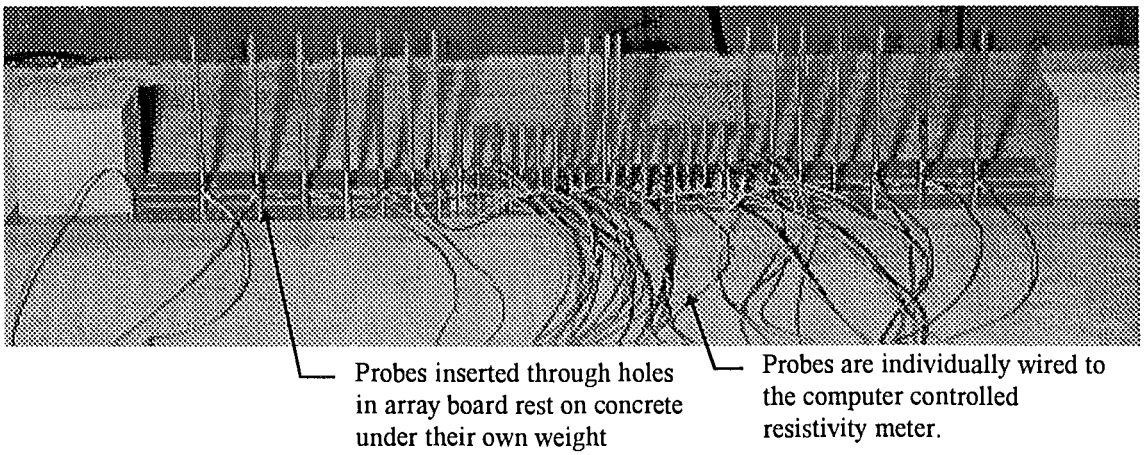

(b) An improved system: a simpler array board wired to the remote controlled resistivity meter.

Figure 6.3-1: Early versions of the array board and meter in operation.

Initially the wet probes were positioned in holes drilled in a wooden plank which became known as the array board.The first wet probes (using tap-water as the conducting solution) had individual weights to keep them in contact with the concrete surface and were quite pressure sensitive (see Figure 6.3-1 (a)). With the use of Swarfega solution the weights were no longer necessary as the contact resistance lost its pressure sensitivity (Figure 6.3-2 (b)).

6.3.2 The final design of the electrode positioning system

The final version of the array board is designed to

1. allow electrodes to be easily inserted and removed,
2. allow simultaneous recharging of all electrodes with conducting solution without the need to remove them from the array board,
3. allow the electrodes to be easily plugged into (and unplugged from) the resistivity meter and
4. be easily repositioned on the concrete slab (thus the electrodes are held in the array board when it is moved).

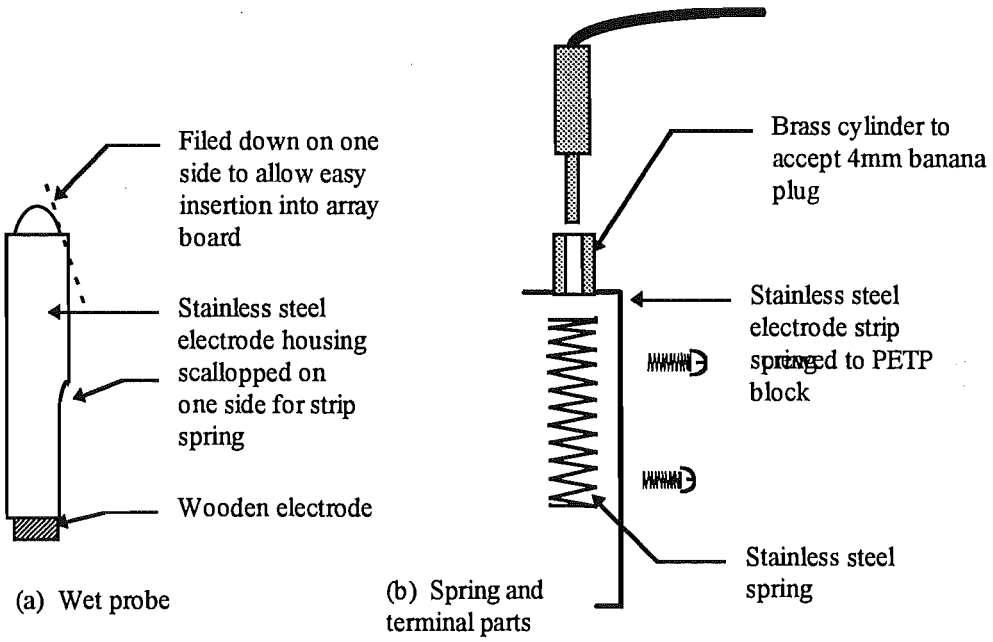

Figure 6.3-2: (a) Wet probe showing wooden electrode and the stainless steel housing. (b) Spring and terminal parts.

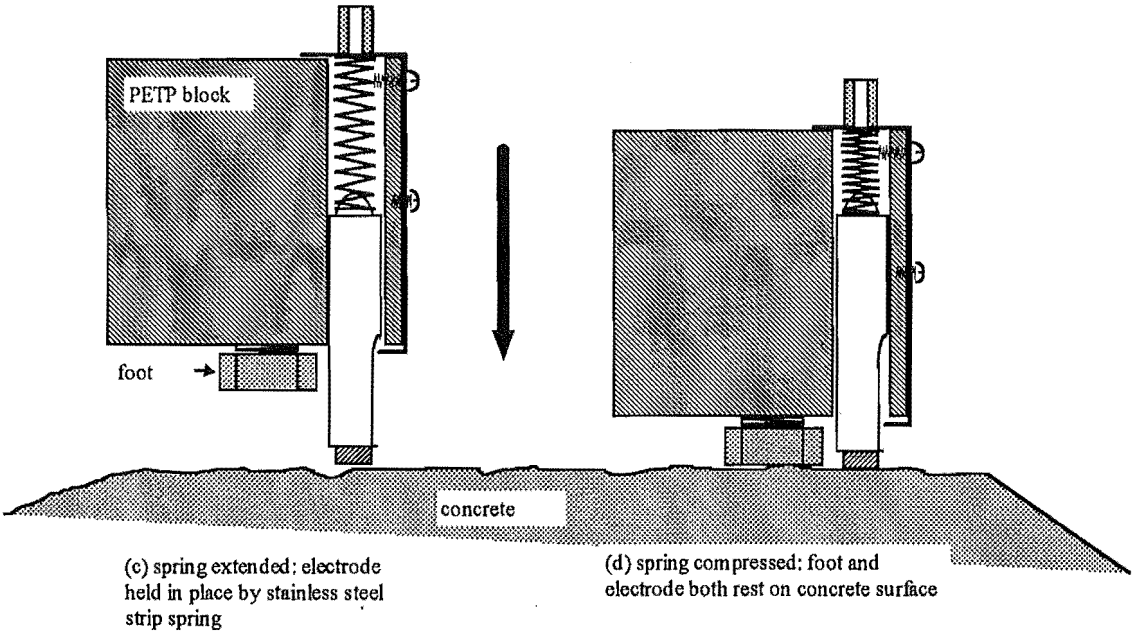

Figure 6.3-2 (continued):. The method of holding wet probe in position .The assembly of one wet probe and spring system in the array board is shown (c) before and (d) after placing on the concrete.

The final design is shown schematically in Figure 6.3-2 and in the photographs in Figures 6.3-3 and 6.3-4. The array board is a solid block of petp plastic chosen for its strength, low moisture absorption and electrically insulating properties. Petp is a thermoplastic polyester based on polyethylene terphthalate. Two rows of holes were drilled and when a hole is in use, a combined brass four mm banana-plug socket and stainless steel clip is attached by screw to cover one end of each hole. To provide flexibility in choice of spacings, more holes were drilled than needed for any particular sounding session.

The Schlumberger array (Figure 6.1-1 (b)) is the most useful configuration since it allows the voltage measurement probes to be left in position and requires only the current probes to be moved (or selected) through a range of positions. However, the range of electrodes positions was chosen so as to maintain the flexibility to select larger measurement probe spacings when the voltage signal is unacceptably low.

The possible current probe and measurement probe spacings are shown in Table 6.3-1. In practice only a small subset of the holes are used, since for useful VES curves, it was found necessary to set at 20 mm the minimum distance between adjacent probes.

At each end a permanent handle and a removable weight-bearing tray are attached.

While each probe position may be wired to the resistivity meter using the banana-plug socket, for even easier use, two to four 15-pin din plugs, each with leads to 15 current probes are attached to the top of the array board (Figure 6.3-4).

During the experiments reported here, the board was wired to allow eight current probe spacings per row, and two measurement probe spacings. These are relatively permanently wired in the optimal positions. Once the probes are in position in the board, they may be rewetted (described below) and the array board placed in position on the concrete (Figure 6.3-4).

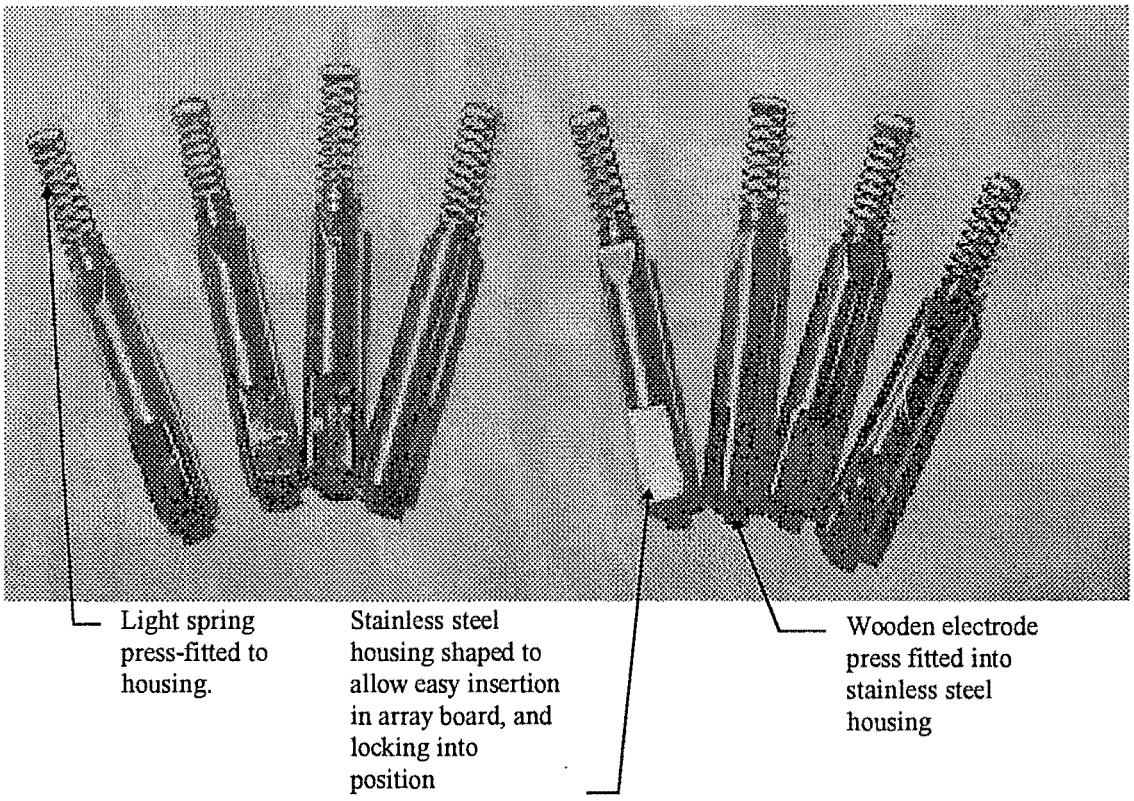

Figure 6.3-3: Electrodes

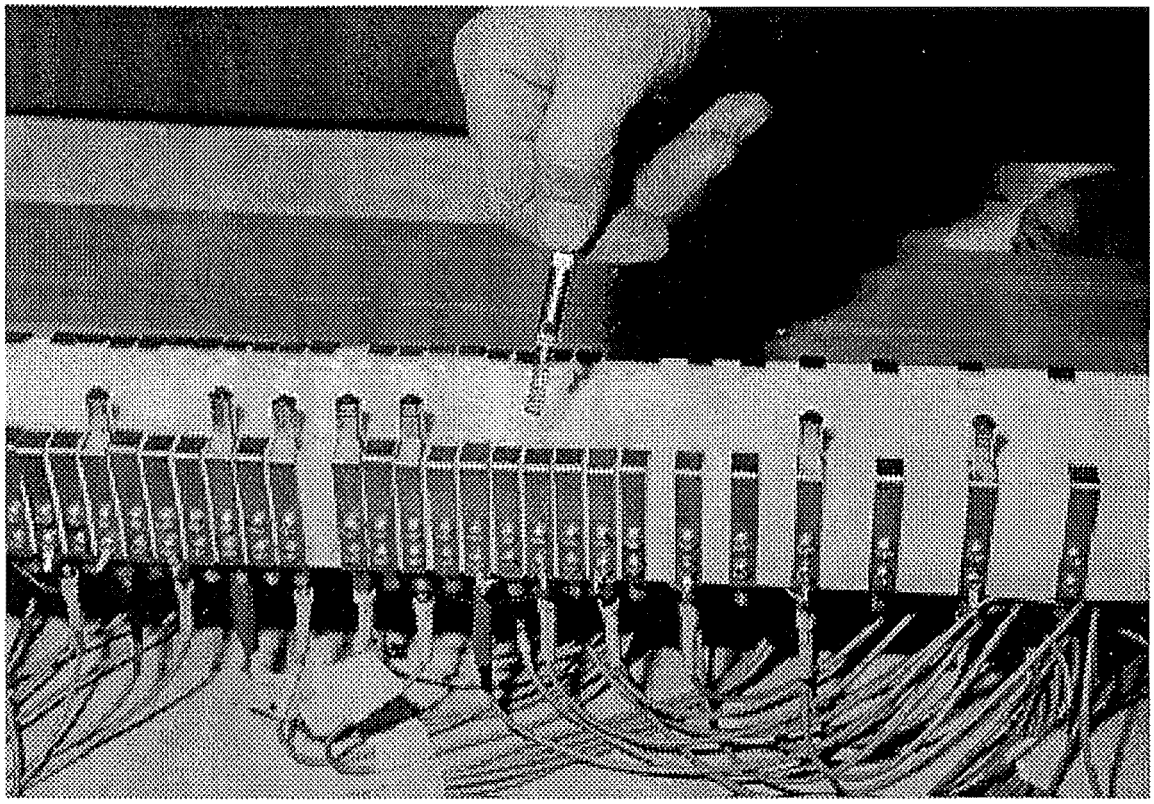

Figure 6.3-3 (continued): The final electrode design enables easy insertion into and removal from the array board. The array board is shown inverted (resting on the carry handles) so that the electrodes may be changed. In this photo the electrode positions are individually wired directly from the resistivity meter.The housing is shaped to enable easy insertion into and removal from the array board. The upper section of the housing is shaped to hold a press-fitted spring. The probe is held in the array board by a stainless steel spring clip.

Table 6.3-1: Possible probe positions in the array board. Commonly used positions are printed in bold.

Measurement probe positions (b)	Current probe positions (s) (mm from centre either side)		
5	**50**	117	**272**
10	60	134	313
15	**70**	**154**	**360**
20	80	178	415
30	**90**	**206**	
40	100	236	

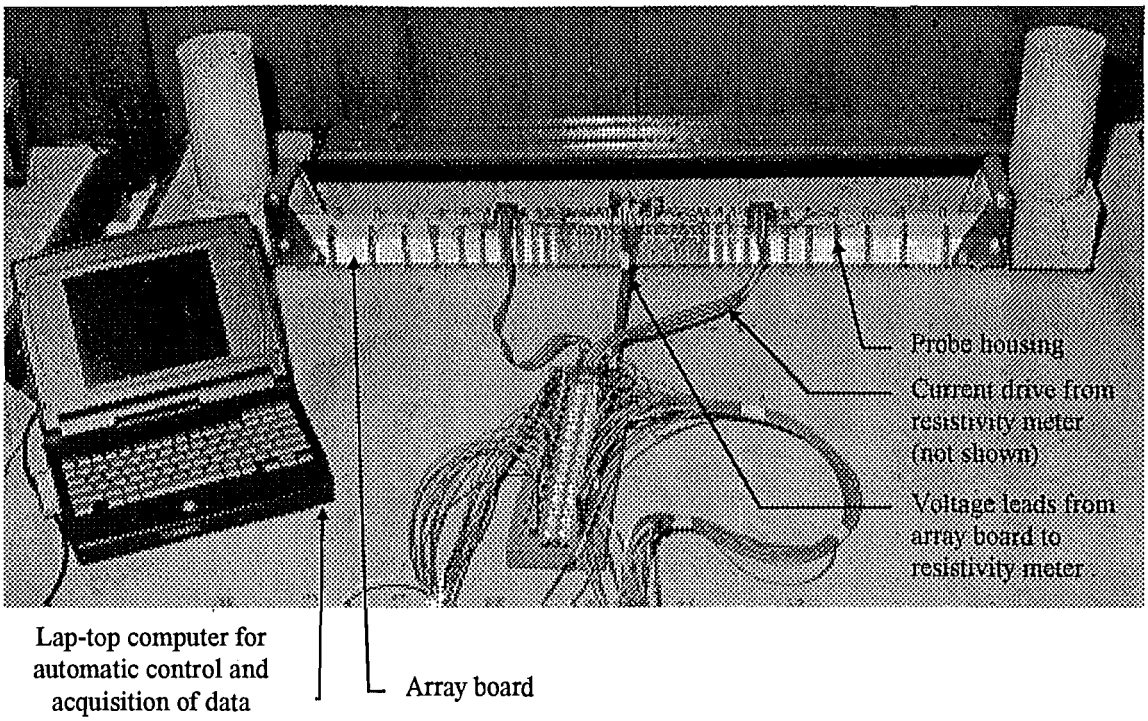

Figure 6.3-4: The array board and laptop computer set up for vertical electric sounding. The resistivity meter itself is out of the picture. In this setup, the device in the lower centre of the picture enables the the array board to be wired using 15-pin din plugs and unshielded ribbon cable whereas the meter itself has a total of 64 (32 current drive and 32 voltage measuring) leads running from it to the array board. Later versions of the meter will enable much simpler wiring. The conducting solution reservoir is shown behind the array board.

The array board under its own weight will rest on the probes but since there may be small differences in probe and spring-clip dimensions and variations in the height of the concrete surface, not all electrodes may be in contact with the surface. To ensure contact, weights are placed in the trays, until the array board rests on its four feet, the height of which having been adjusted to ensure each probe spring undergoes at least one mm (or so) compression. At present sufficient weight at each end is provided by one concrete 100 mm cubic calibration cell and one standard concrete test cylinder.

After each sounding session, the electrodes may be rewetted by lifting the array board and placing in a conducting solution reservoir. This is a fibre board plank with two narrow slots cut out in line with each row of electrodes (see Figure 6.3-2). When the electrodes are lifted from the solution a drop of liquid will be suspended from each one. Before re-positioning on the concrete, some of this drop must be removed. The amount of excess conducting solution is critical. Too much results in an unacceptable increase in effective electrode diameter (see Section 6.9), whereas too little can prevent the formation of a good low electrode-concrete interface (Figure 6.3-5). For fairly young

concrete, most of the solution can be wiped away. Older drier concrete will require more solution to ensure good electrical contact. As a rule of thumb, if electrodes are placed on the concrete and removed after 5 minutes, those with the optimal the amount of solution will leave a wet (dark) mark on the concrete of the same diameter as the electrode itself. Too much or too little solution will leave a correspondingly larger or smaller mark. The optimal amount can be left on the electrodes if, after it has been removed from the reservoir, the array is rested briefly on several layers of paper towel (fairly young concrete), or on a non-absorbent surface such as plastic sheet (older concrete).

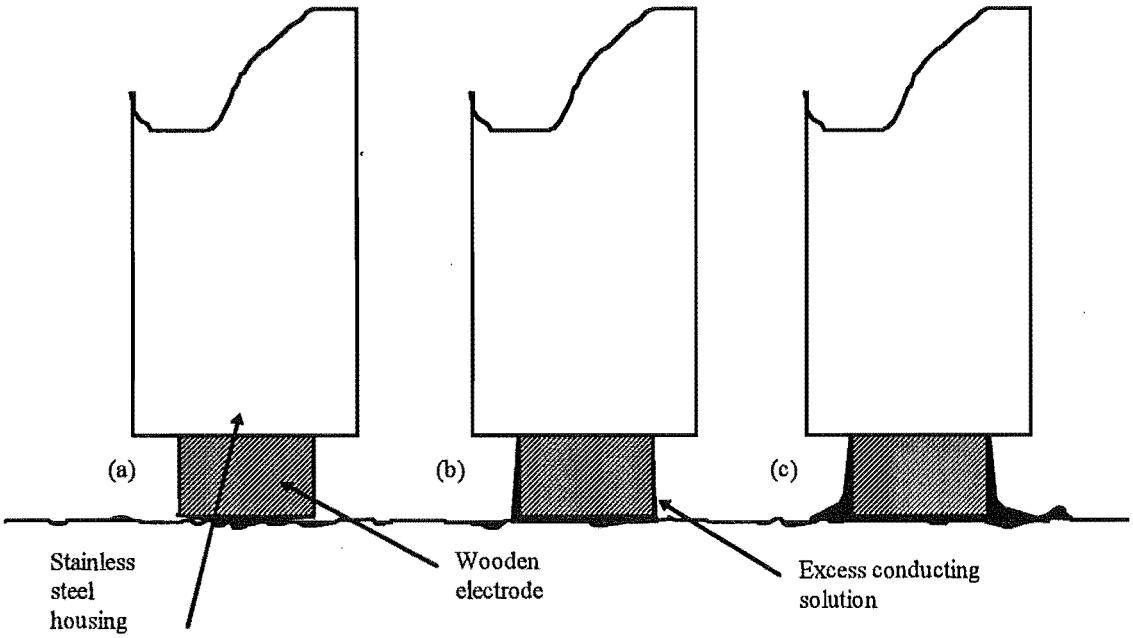

Figure 6.3-5: Schematic diagram of wet electrodes in contact with the concrete surface with (a) too little conducting solution (b) optimal solution and (c) too much solution.

6.4 The current generation stage

It is usual in vertical electric sounding to minimise electrode polarisation by using commutated direct current. A square wave current drive is generated by manually, mechanically or electronically reversing the direction of direct current. In the present design, a microprocessor controlled by a computer generates a square wave signal that is converted to a 'constant' square wave current. The frequency may be reset (through a range 1 - 45 Hz at 1 Hz intervals) at any time before and during the meter operation. Generally, 28 Hz has been used.

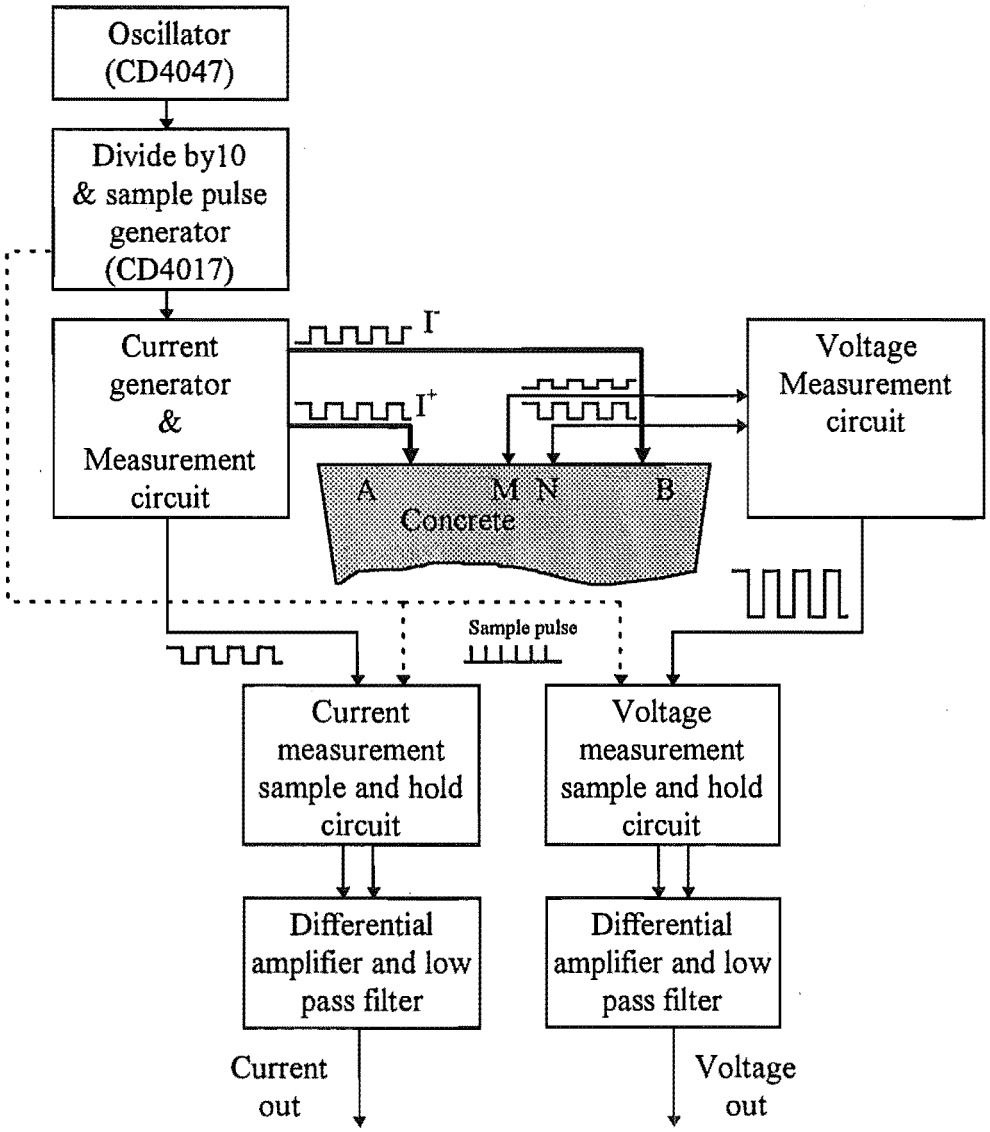

Figure 6.4-1. Outline of basic meter operation: before automation

The 'constant' current circuitry (Figure 6.4-2) owes much to the general design of the circuit described by Ewins (1985). The circuit has been adapted for the present purpose. Changes include the use of

1. operation amplifiers with higher common mode rejection ratios,
2. a different range of maximum current levels (1.25 μA, 12.5 μA and 125 μA),
3. several maximum voltage drives set by the Zener clamp (6V, 9V and 12V) and
4. programmable switching (using the DG309ACJ chip) to select the maximum current level and the maximum voltage drive.

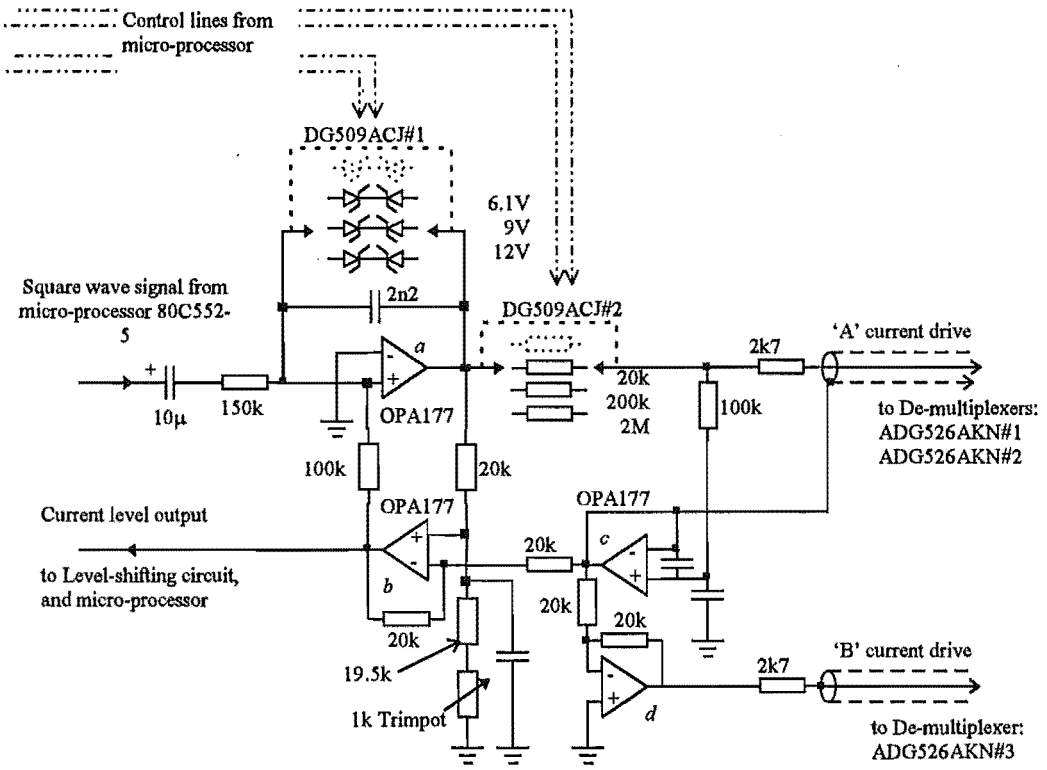

Figure 6.4-2: Outline of the constant current generation circuit.

The coaxial leads to the two output probes (the 'A' and 'B' current drives) have 'driven shielding', ie., the potential on the shield is kept at the same level as the signal which the lead is carrying.

The operation of this circuit is described by Ewins (1985). The four operational amplifiers are labelled from '*a*' to '*d*' and a range of functions. The output of operational amplifier *a* provides the voltage level for the current drives. This voltage swings to follow the input square wave signal. Its operation is described below. Because the current is 'constant' only when a certain critical load is not exceeded, the current must

be monitored. The output from operational amplifier '*b*' is a measure of the voltage drop across the 'current measuring' resistor R_4, as the current passes through it, and hence is a measure of the current. This output is called the current level signal.

Operational amplifier *c* acts as a unity gain buffer to ensure minimal current is drawn from the current path from R_4 to the load R_L by operational amplifier *b*. Operational amplifier *d* is a unity gain inverter providing the inverse current drive 'B'.

A schematic diagram of part of the circuit controlling the current is given in Figure 6.4-3. Much of the circuit has been omitted for simplicity. The load is actually R_L (equivalent to R_T in Section 6.5), with a load voltage of V_L ($=V_l^+ - V_l^-$), but the analysis applies with V_L^+ applied across $R_L/2$ referred to ground.

The output from operational amplifier *a* is clamped by the Zener diodes so that

$$V_{oa\max} = V_z$$

Where possible operational amplifier *a* attempts to swing V^- to V^+ (=0) so that

$$\frac{V_{in}}{R_1} = \frac{V_{ob}}{R_2}$$

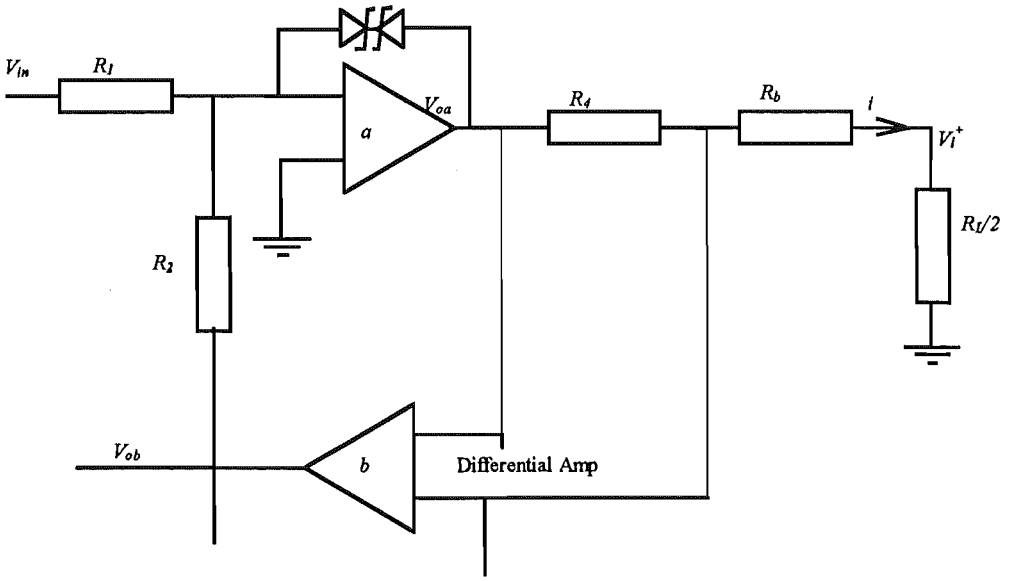

Figure 6.4-3: Schematic diagram of current generation circuit.

V_{ob} is the differential voltage measured across R_4:

$$V_{ob} = iR_4$$

thus the current is given by

$$i = \frac{R_2}{R_1 \cdot R_4} V_{in}$$ Equation 6.4-1

as long as operational amplifier *a* can swing far enough.

Generally

$$V_{oa} = i \times (R_4 + R_b + R_l / 2)$$

so that the current is always given by

$$i = \frac{2V_{oa}}{2R_4 + 2R_b + R_l}$$ Equation 6.4-2

The meter has three different operating conditions.

Condition 1: $R_L < R_{Lcrit}$ Constant Current regime

Here $V_{oa} < V_{oamax} (=V_z)$, so that Equation 6.4-1 applies. Thus

$$i_{const} = \frac{R_2}{R_1 \cdot R_4} V_{in}$$ Equation 6.4-3

In this case the value of V_{oa} is given by

$$V_{oa} = \frac{R_2 \cdot V_{in}}{R_1 \cdot R_4} \times (R_4 + R_b + R_l / 2)$$

Condition 2: $R_L = R_{Lcrit}$ Transition regime

Here $V_{oa} = V_{oamax} (=V_z)$, and so from Equation 6.4-2 the maximum value of resistive load allowing a constant current , is given by:

$$R_{Lcrit} = 2\left[\frac{V_z}{i_{const}} - R_4 - R_b\right]$$

Condition 3: $R_L > R_{Lcrit}$ Load-dependent current regime

Here current is given by Equation 6.4-3., ie.:

$$i = \frac{2V_z}{2R_4 + 2R_b + R_l}$$

and the voltage driving the current probes approaches a constant value of V_z as R_L continues to increase, since :

$$V_L^+ = V_{oa} - i(R_4 + R_b)$$
$$= V_z \cdot \left[1 - 1\Big/\left(1 + \frac{R_L}{2(R_4 + R_b)}\right)\right]$$

so that as $R_L \to \infty$, $V_L^+ \to V_Z$.

Thus the square wave current is 'constant' in the sense that up to some critical load, the amplitude of the current will equal the maximum current level. When the load exceeds the critical level, the current will be lower than the maximum, depending on the maximum voltage drive. The advantages of choosing a lower maximum current level include

- the critical load will be higher,
- the current measurement signal will be stronger.

De-multiplexing of the 'A' and 'B' current drives to the 32 electrodes available is accomplished using ADG526AKN chips (see Figure 6.4-4).

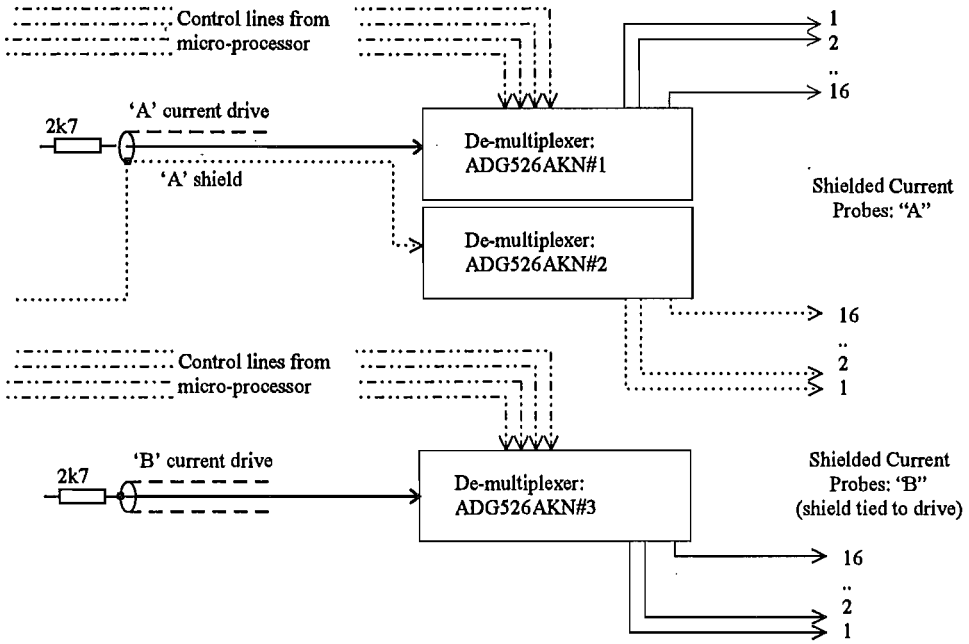

Figure 6.4-4: Schematic showing the de-multiplexing of the 'A' and 'B' current drives to up to 32 electrodes.

6.5 The voltage measurement stage

The measurement of the potential difference between the measurement electrodes (labelled M and N) is carried out using two programmable gain instrumentation amplifiers (Burr-Brown PGA205AP and PGA204AP) in series (Figure 6.5-2). At each of the inputs to the first instrumentation amplifiers a high input impedance (10^{14} ohm) unity gain buffer (Burr-Brown OPA2111) provides a low output impedance screen for the lead

from the measurement electrode. That is, the buffer output is used as a 'guard' voltage to reduce the effects of coaxial capacitance and leakage (see Figure 6.5-1).

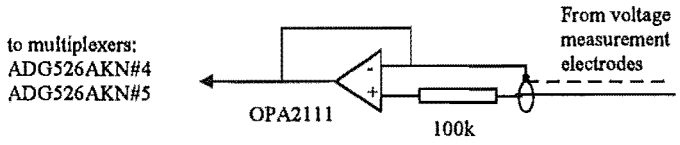

Figure 6.5-1: Schematic showing the unity gain buffer at each of the 32 measurement probe inputs immediately prior to multiplexing.

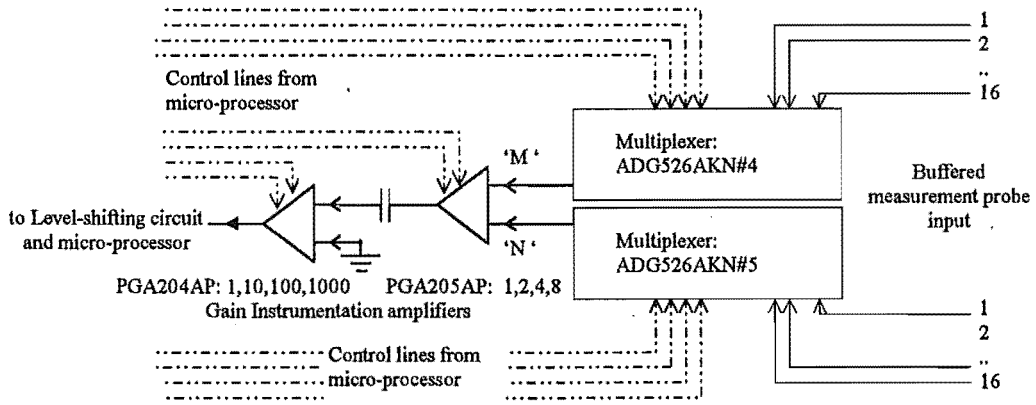

Figure 6.5-2: Schematic showing multiplexing and gain stages of voltage measurement circuitry.

The first instrumentation amplifier has programmable gain of 1, 2, 4 and 8, and the second instrumentation amplifier gain of 1,10,100 and 1000, thus providing 16 gain settings from 1 to 8000. The output from the second instrumentation amplifier is sampled at points toward the end of each direct-current portion of the square wave and converted to a digital signal for transmission to the computer.

The output from the voltage measurement stage and the current level signal from the current generation stage must be scaled and level-shifted to lie between 0 and 5V required by the analogue-to-digital-converter in the micro-processor. The analogue-to-digital-units (adu) received by the computer must be converted to voltage and current readings using suitable calibration factors determined by:-

- setting the zero current level when the current probes are open-circuited
- setting the zero voltage level when the measurement probes are shorted to each other and one open-circuited current probe

- using an oscilloscope to measure the voltage drive to current-probes across a known resistance

This last measurement enables determination of the true current and the corresponding calibration factors.

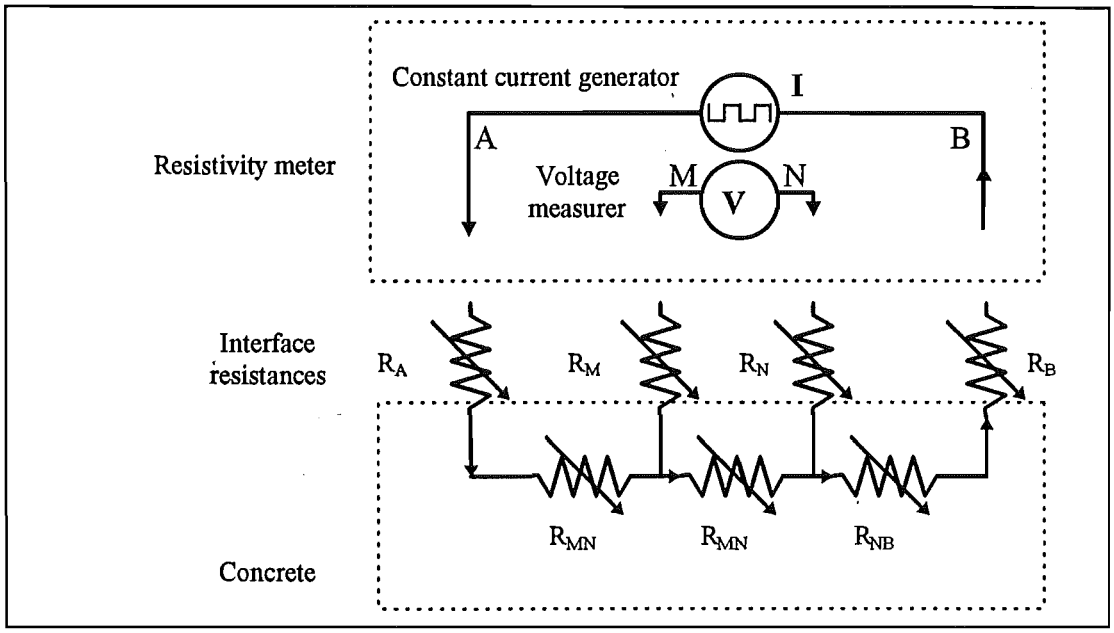

Figure 4.2-1 (see Chapter 4): The seven resistor model of the concrete slab and interface with the -resistivity meter.

It is worthwhile considering the process of voltage measurement and the attendant sources of error. For this purpose the seven resistance model of the concrete slab-electrode system presented in Chapter 4 (Figure 4.2-1) will be used.

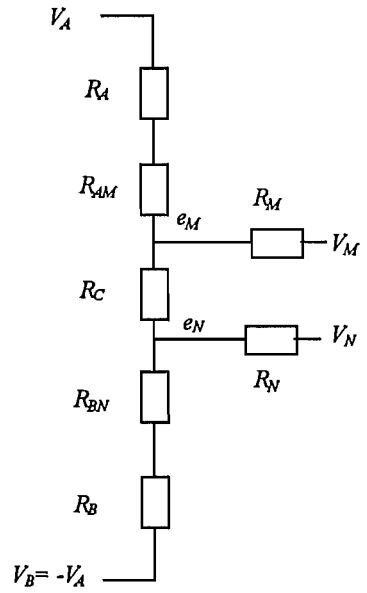

Figure 6.5-3: Seven resistance model of the concrete-electrode system.

Figure 4.2-1 is adapted in Figure 6.5-3 to show the voltages at the current electrodes (V_A and $V_B = -V_A$.), the voltages at the concrete (e_M and e_N) directly beneath the measurement electrodes and the voltages at the instrumentation inputs (V_M and V_N).

The applied square-wave voltage is symmetrical so that in the first half of the cycle V_A is positive and V_B is equal and opposite. In the second half, V_B is positive and so on.

The interface resistances R_A, R_M , R_N and R_B, will be large and variable depending on the moisture state of the wet-probe and on the condition of the concrete surface in the immediate vicinity. R_{AM} and R_{BN} represent the concrete between the adjacent current and measurement electrodes.

For the first half of a cycle, the potentials at the measurement electrodes may be found to be

$$e_M = \left[\frac{2(R_B + R_{BN} + R_C)}{R_T} - 1\right] \cdot V_A$$

$$e_N = \left[\frac{2(R_B + R_{BN})}{R_T} - 1\right] \cdot V_A$$

where

$$R_T = R_B + R_{BN} + R_C + R_{AM} + R_A .$$

These voltages will be of the opposite sign during the second half of a cycle.

The common-mode voltage will thus be

$$e_{CM} = \frac{e_M + e_N}{2}$$

$$= \pm\left[\frac{2(R_B + R_{BN})}{R_T} - 1\right] \cdot V_A \pm \frac{R_C}{R_T} \cdot V_A$$

that is

$$e_{CM} = \pm\frac{(R_B - R_A) + (R_{BN} - R_{AM})}{R_T} \cdot V_A .$$

The differential voltage between the two points will be

$$\Delta e = e_M - e_N = \pm\frac{2R_C}{R_T} V_A$$

Through the measurement electrode interface resistances R_M and R_N small currents i_{noise} may be induced through thermal noise and stray electromagnetic fields. These may result in substantial voltages $i_{noise}\ R_M$ and $i_{noise}\ R_N$ both of R_M and R_N Although the noise

current may well be different in each of R_M and R_N, the greater part will be due to stray fields and is likely to be the same in each resistance. Thus at the inputs to the instrumentation amplifier the differential voltage will be

$$\begin{aligned}\Delta V &= \Delta e + i_{noise}(R_M - R_N) \\ &= \pm\frac{2R_C}{R_T}V_A + i_{noise}(R_M - R_N)\end{aligned}$$

R_M and R_N act as source impedances to the first instrumentation amplifier. If these are unbalanced (that is, unequal), the common mode voltage e_{CM} is divided unequally upon the common-mode impedance Z_{CM} of the instrumentation amplifier, and a differential signal e_s is developed at the amplifier's input. This error signal is given by

$$e_s = \frac{e_{CM}\cdot Z_{CM}\cdot(R_M - R_N)}{(Z_{CM} + R_M)(Z_{CM} + R_N)}$$

Z_{CM} will be about 10^{10} ohm for the PGA205 instrumentation amplifier, whereas the maximum interface resistance reasonably expected would be about 100 to 1000 times smaller. In either case we can approximate the error signal as

$$e_s = \frac{e_{CM}\cdot(R_M - R_N)}{Z_{CM}}$$

The error signal and the differential voltage are subject to the full gain g of the instrumentation amplifier, whereas the common-mode voltage is amplified according to the common-mode-signal gain which is g divided by the common-mode-rejection-ratio (CMRR).

The output V_o of the first instrumentation amplifier will be given by

$$V_o = g\Delta e + g\cdot e_s + \frac{g}{CMRR}e_{CM}$$

that is

$$\begin{aligned}V_o = \pm\Bigg\{&2g\frac{R_C}{R_T} \\ &+ g\cdot\frac{(R_M - R_N)}{Z_{CM}}\cdot\left[\frac{(R_B - R_A)+(R_{BN} - R_{AM})}{R_T}\right]\cdot V_A \\ &+ \frac{g}{CMRR}\cdot\left[\frac{(R_B - R_A)+(R_{BN} - R_{AM})}{R_T}\right]\cdot V_A\Bigg\} \\ &+ i_{noise}(R_M - R_N)\end{aligned}$$

This expression may be simplified:

- Because they cannot readily be distinguished we shall combine R_{AM} and R_A and call the result R_A, and similarly combine R_{BN} and R_B and call the result R_B. The main point here is that they will be large and will vary as the moisture state of wet-electrodes (and the concrete in the immediate region) changes.
- The PGA205 has a typical CMRR of 94 when g = 1, increasing to 112 when g = 8 and so *g/CMMR* is between *1/14* and about *1/100*. As it is designed to do, the instrumentation amplifier thus rejects the common mode voltage quite well and the term containing this factor can be ignored.

The output voltage is now

$$V_o = \pm\frac{gV_A}{R_T}\left\{2R_C + \frac{\Delta R_{MN}\cdot\Delta R_{BA}}{Z_{CM}}\right\} + i_{noise}\Delta R_{MN}$$

where $\Delta R_{MN} = (R_M - R_N)$ and $\Delta R_{BA} = (R_B - R_A)$.

The effect of the varying interface resistances may now be seen clearly. If in the initial stages the total resistance R_T between the current electrodes decreases as R_A and R_B decrease, V_o will rise unless the current generator is in the constant current regime, in which case V_A. (the voltage drive to the current probes) will decrease with R_T. However, V_o may increase or decrease depending on the signs and sizes of ΔR_{MN} and ΔR_{BA}. It is most important therefore that the interface resistances be kept as similar and as small as possible. Similarly it is important that the concrete surface be as homogeneous as possible since exposed aggregate will greatly increase the interface resistance in that region.

The effect of the noise current will be greater if ΔR_{MN} is larger. However the effect is to change the common-mode level of the output square wave rather than to change the size of the square wave itself. This may be detrimental, nevertheless, since a lower level of gain will be required to prevent the instrumentation amplifier from saturating.

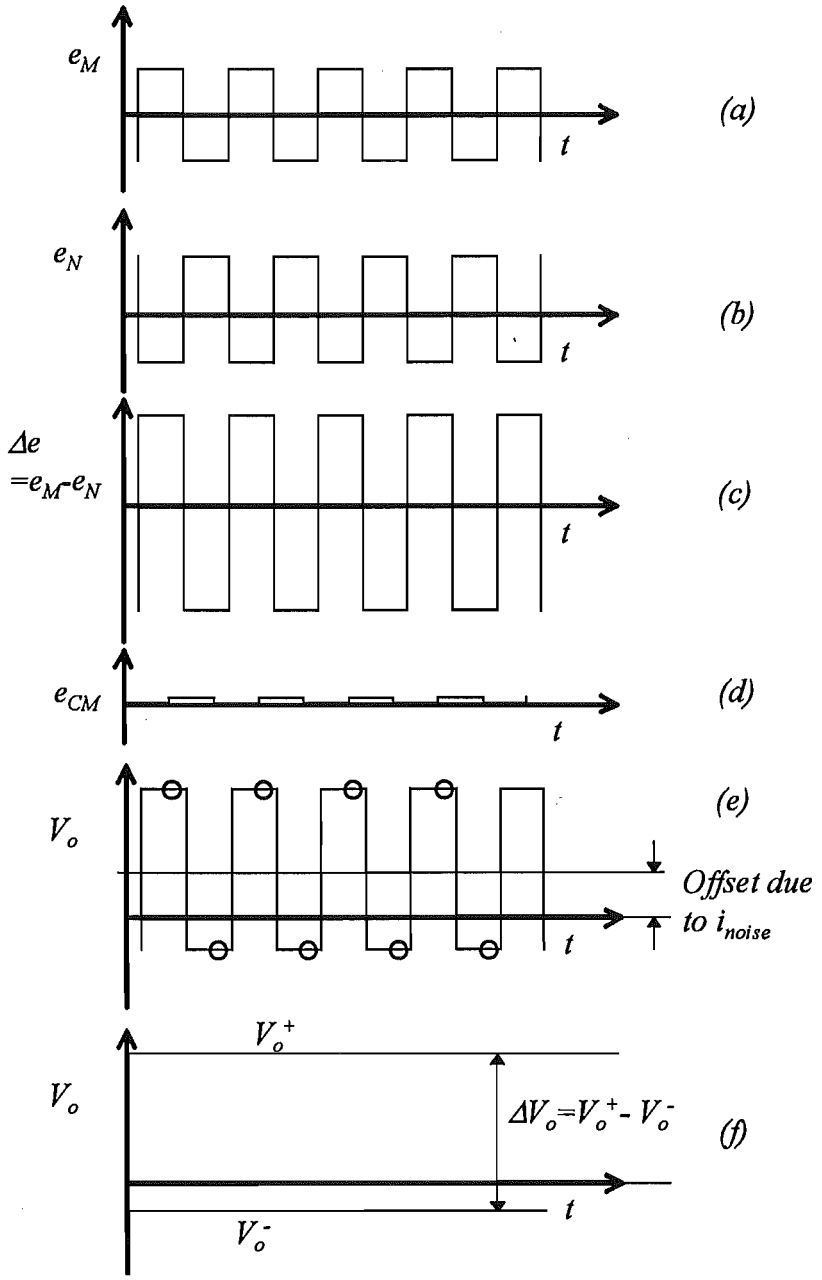

Figure 6.5-4: Idealised voltage signals of relevance to the discussion in this section.

(a) e_M beneath the measurement electrode 'M'
(b) e_N beneath the measurement electrode 'N'
(c) differential or 'normal' voltage $\Delta e = e_M - e_N$
(d) common-mode voltage $e_{CM} = (e_M + e_N)/2$
(e) output of instrumentation amplifier stage showing the amplified differential voltage offset by the amplified noise voltage (that is, by $i_{noise}\Delta R_{MN}$). The sample points along the direct current portions of the square wave are also shown.
(f) V_o^+ and V_o^- are sampled by the resistivity meter, scaled and sent to the computer in digital form. Determination of the differential voltage $\Delta V_o = V_o^+ - V_o$ and further analysis is carried out by the resistivity meter control software (see Section 6.10).
The output from the current measurement stage is similar to (e) and (f): $\Delta I_o = I_o^+ - I_o$.

6.6 Multiplexing

The current drive must be de-multiplexed to, (ie, distributed among) up to 16 pairs of probes(See Figure 6.4-3). While the Schlumberger array is symmetric and a change to a wider current probe spacing can be accomplished by changing the current drive from for example the 8^{th} to the 9^{nth} pair of current probes, for flexibility, the current probes can be independently selected. Thus the current drive A, could be sent to the 9^{nth} probe while B is sent to the 8^{th} probe and so on. This flexibility has proved useful when checking for broken leads and poor electrode-concrete contact, and for the use in measuring resistivity directly using the horizontal electrode systems (HES) described in Chapter 8, however it is likely that the extra control and multiplexing would be better used in providing for extra rows of electrodes.

The voltage measuring circuit is also multiplexed to 16 pairs of measurement probes, each pair member being individually selected (Figure 6.5-2). This design feature enables the use of Wenner arrays (where each change in current probe spacing is accompanied by a change in measurement probe spacing, see Figure 6.1-1), and the use of HES's. Since the Wenner array was not used, in practice only three pairs of measurement electrodes was required for vertical electric sounding.

The buffering of the measurement probe inputs to the meter, is done before the signals are multiplexed, each of the 32 inputs having its own buffer operational amplifier, and each having a driven shield (Figure 6.5-1).

To allow the shielding to extend to the electrodes, B.N.C. plugs and sockets for coaxial cable are used. The 32 current sockets are all used, however the design could be simplified using ribbon cable having a common driven shield for the A output and the inverted B output. At present the shields are demultiplexed with the signal, but this is an unnecessary complication. On the other hand, while fewer measurement probe inputs are necessary, they must all be separately shielded.

6.7 Data acquisition and control

The resistivity meter is controlled by a Phillips 80C552 microprocessor. The microprocessor is used to set the various switches and multiplexers, to generate square-wave and timing signals and to acquire current and voltage data as described in earlier sections (Figure 6.7-1).

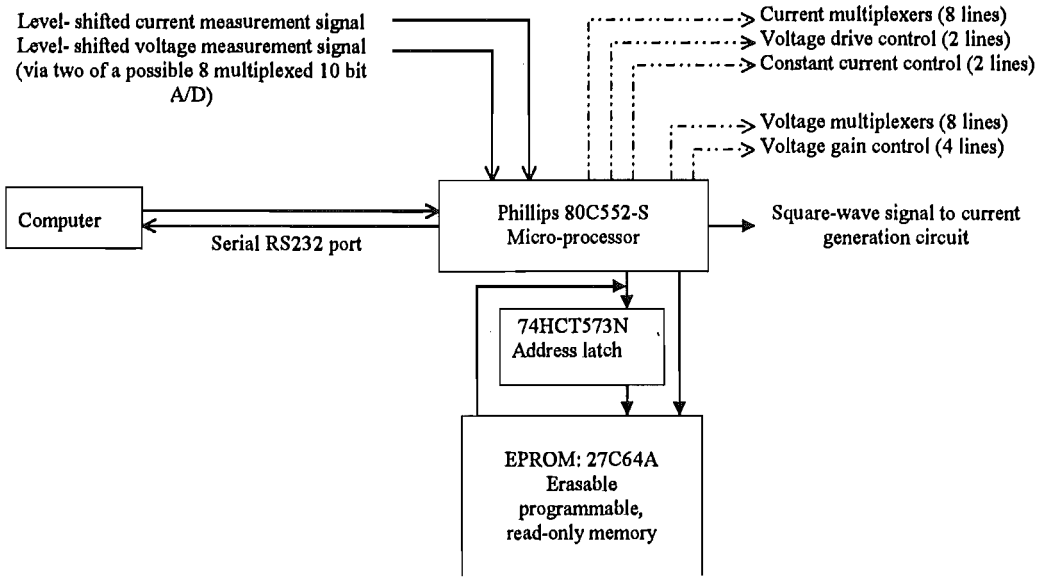

Figure 6.7-1: Schematic showing micro-processor control of the resistivity meter, and the flow of data and control to and from the computer.

The current level and voltage level signals are, ideally, square waves. Departures from the ideal behaviour occur due to polarisation effects within the concrete and at the concrete-electrode interfaces, and due to stray electromagnetic noise. While a certain amount of noise is eliminated when the one measurement probe signal is subtracted from the other by the instrumentation amplifier, the polarization effects occur mainly at the beginning of each half-cycle. Most, if not all, polarisation effects are able to be ignored by sampling the signals near the end of the direct current portion of each half-cycle (see Figure 6.5-4 (e)). Thus, during each cycle, the current and voltage level signals are each sampled twice, once in the positive and once in the negative portions of the cycle.

Originally the resistivity meter was manually controlled, and the current level and voltage level signals were passed into 'sample-and-hold' amplifiers, the outputs of which were passed to two differential amplifiers, one each for the current and voltage signals. The differenced outputs were measured with a voltmeter having first passed through low pass, or time averaging filters. The computer controlled resistivity meter uses a micro-processor to sample the current and voltage level signals, convert them from analog to digital and pass the four samples directly to the computer. It is left to the computer control software to subtract the two voltage and two current level samples, and carry out further pre-processing of the data.

6.8 Computer control software

The resistivity meter has a range of functions which are able to be controlled by the computer.

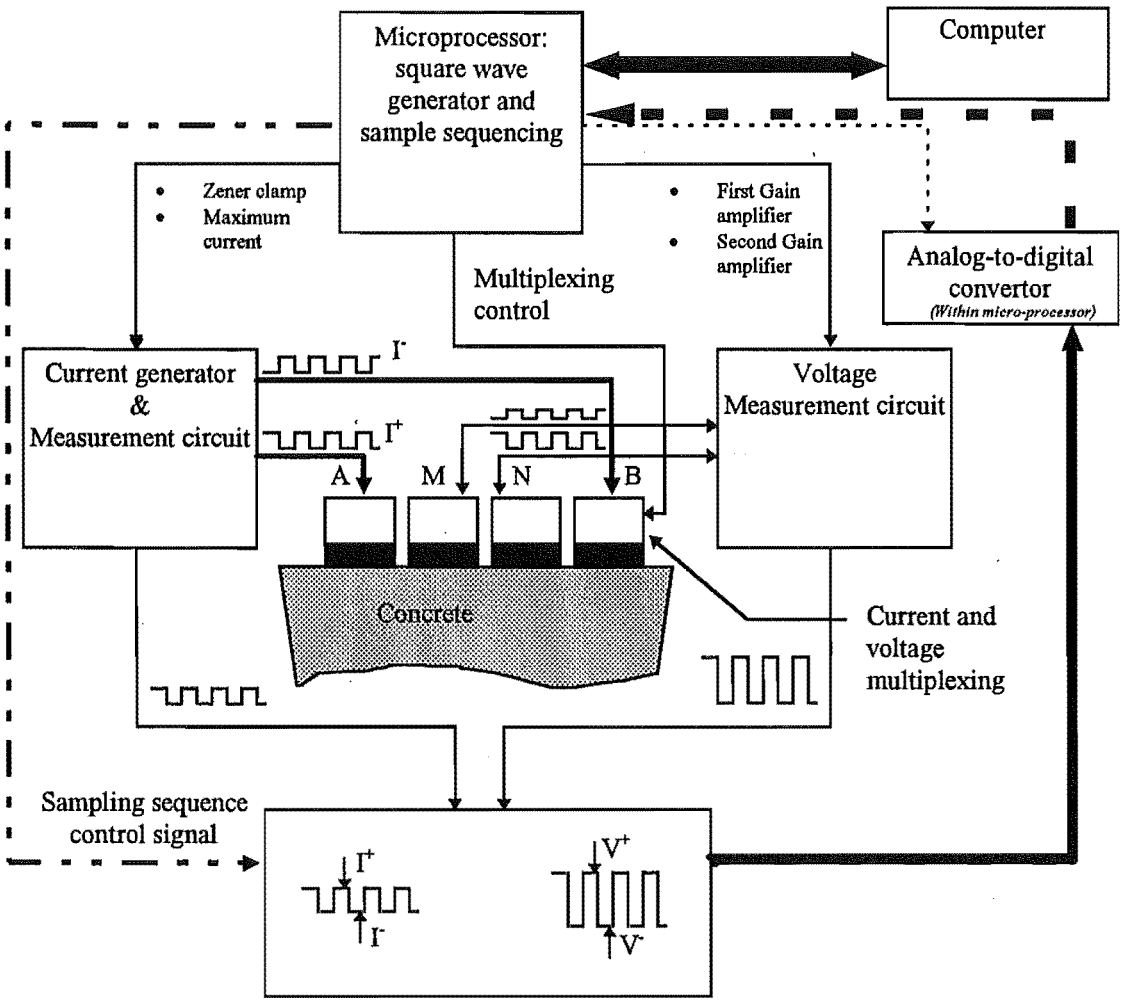

Figure 6.8-1: Outline of automated, computer-controlled resistivity meter

The computer may select

1. the frequency of the current drive square wave (from one Hz to 45 Hz in one Hz steps, default 28 Hz)
2. the maximum voltage drive to the current probes set by the Zener diodes (6V, 9V, and 12 V, default 6V),
3. the maximum ('constant') current level (1.25 μA, 12.5 μA and 125 μA, default 125 μA),
4. the particular probe (of 16 possible) to which the 'A' current drive is connected,
5. the particular probe (of 16 possible) to which the 'B' current drive is connected,

6. the particular probe (of 16 possible) to which the 'M' input to the voltage measurement instrumentation amplifier is connected,
7. the particular probe (of 16 possible) to which the 'N' input to the voltage measurement instrumentation amplifier is connected
8. the gain on the first (differential) instrumentation amplifier (default 1) and
9. the gain on the second instrumentation amplifier (default 1).

In addition the computer can send a signal to start or stop the current drive. When the current drive is running, on every cycle, the resistivity meter carries out the task of sampling the current and voltage signals and sending the digitised data to the computer.

The computer communicates with the resistivity meter via the serial (RS232) port.

The control software was written for M.S Windows 3.1, in M.S. Visual Basic 2, and has a graphical-user-interface (gui) that makes the computer more than a convenient remote resistivity meter control (Figure 6.8-2).

The gui includes features that enable

1. manual (push- or spin- button, or slider) control of the nine functions described above,
2. automatic control of functions 2 to 8, above,
3. manual and automatic control of the number of cycles that are read as data (default 100) and of the number of cycles that may be neglected while the transient response is dying down (default 100) and
4. starting, stopping and pausing the meter.

Additional features are required for the control, data analysis and storage functions necessary for automatic or semiautomatic vertical electric sounding sessions.

These gui design features are illustrated in the description of a typical vertical electric sounding session to be found in Appendix C:

The raw output from the resistivity meter is a series of current and voltage measurements taken with different current and measurement probe spacings. The expression for the Schlumberger apparent resistivity

$$\rho = \frac{\pi \cdot \left(s^2 - b^2\right)}{2b} \left| \frac{\Delta V}{I} \right| \cdot \frac{1}{G_{all}} \qquad \text{Equation 6.8-4}$$

has been derived in Chapter 5. It is a product of

- a geometric array factor $\frac{\pi \cdot \left(s^2 - b^2\right)}{2b}$,
- a correction factor $\frac{1}{G_{all}}$ to account for the presence of the non-conducting side and end boundaries of the rectangular slab and
- a 'resistance' factor $\left|\frac{\Delta V}{I}\right|$, which is the potential difference between M and N (the measurement probes) divided by the current passing between A and B (the current probes

Entering the array position and the slab size at the time of the sounding session enables the direct calculation and presentation of the VES curve as measurements are taken. The raw and treated data is stored in a text file suitable for further analysis and profile recovery using Matlab.

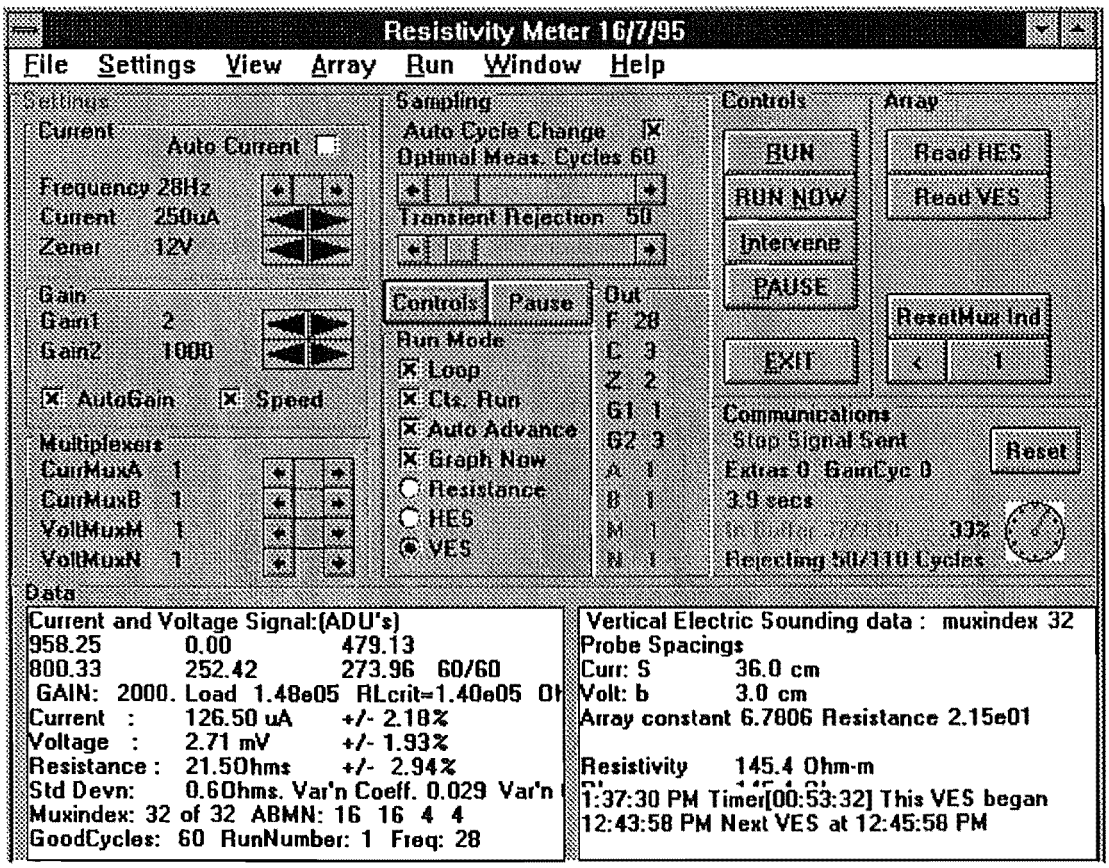

Figure 6.8-2. User interface showing "Data" window. For explanation of the graphical user interface see Appendix C.

6.9 Electrode investigation: results and discussion

It was originally the intention to use dry stainless steel probes. It seemed likely that many sets of readings needed to be taken to overcome problems of data scatter due to the finite size of highly resistive aggregate common to most concrete. However, it was found that the dry-probe-concrete interfacial- or contact-resistance became very high. Measurements of more than 500 M-ohms between the current probes were found. This resulted in very small currents (in the range 0.02 to 0.7 μA). Similarly large contact resistances at the voltage probes resulted in high noise levels at the inputs to the voltage measuring stage, as small noise currents surged through the large resistances. This noise would have been able to have been filtered out had it not been that the contact-resistances varied from probe to probe and with pressure on the interface (as a function of the weight resting on the probe to hold it in contact with the surface). Small inadvertent nudges when moving adjacent leads could render great changes in the interface resistance. Overall the measured apparent resistivities were very high and variable. 'Successful' VES readings required more suitable electrodes. Of the range of electrode types tried only the 'wet' electrodes charged with tap water (Section 6.9-1) or conducting solution (Section 6.9-2) enabled useful repeatable apparent resistivity curves to be made. It is not clear how 'wet' probes work and it is of interest to compare the use of tap water with that of a more highly conducting solution.

6.9.1 Wet probes: tap water

The initial 'wet probes' were charged with tap water and when placed on the concrete surface, they allowed a current to be passed immediately which was considerably larger than that attainable with dry probes. This indicated a drop in contact resistance compared to dry probes. If measurements are made over time however, current continues to increase for some time before, decreasing (Figure 6.9.1-1).

The potential difference between the measurement probes varied in a more complex fashion, especially at larger current probe spacings (Figure 6.9.1-2). The initial increase in current is not always reflected in an increasing voltage. However the voltage measurement is most stable around the time of maximum current, after about three hours. But whereas the current stays relatively constant for another hour before gradually dropping away, the measured voltage falls to a minimum three hours later

before rising steadily throughout the rest of the measurement period. Measured voltages using current injected at wider current probe spacings fluctuated apparently more randomly. The behaviour in all cases suggests a complex interaction between the changing interface resistances and the ability of the measurement system to cope with large differences in interface resistances between the two measurement probes.

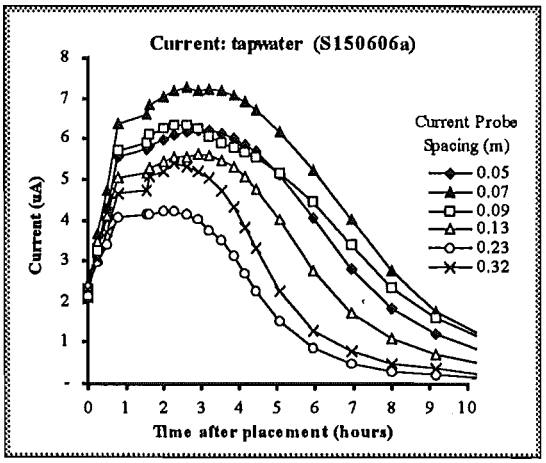

Figure 6.9.1-1. Evolution of current between 'wet' probes charged with tap water.

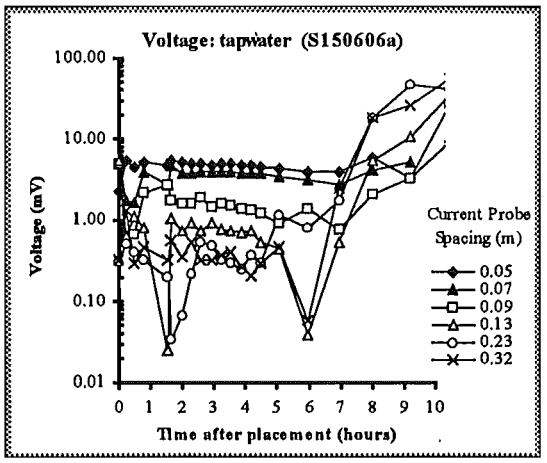

Figure 6.9.1-2. Evolution of potential difference between 'wet' measurement probes (MN) charged with tap water.

This behaviour agrees with that predicted in Section 6.5 above. The output from the instrumentation amplifier was shown there to be

$$V_o = \pm\frac{gV_A}{R_T}\left\{2R_C + \frac{\Delta R_{MN}\cdot\Delta R_{BA}}{Z_{CM}}\right\} + i_{noise}\Delta R_{MN}$$

where $\Delta R_{MN} = (R_M - R_N)$ and $\Delta R_{BA} = (R_B - R_A)$.

The fact that the measured voltage changes indicates that either ΔR_{MN} or ΔR_{BA} (see Section 6.5) or both are changing during the course of the measurement session. However, if the effect was primarily due to variation in ΔR_{MN}, the same variation in measured voltage should occur over all current probe spacings. Clearly, this is not the case (Figure 6.9.1-2).

This behaviour suggests that the probe moisture forms a 'virtual' or 'dynamic' electrode that reaches beneath the dry surface layers into the relatively moist layers beneath. It was thought likely that the moisture from the probe forms a continuous connection with deeper layers quite quickly and further increase in current arises from a deepening and widening of the 'virtual' probe. Moisture will continue to diffuse into the concrete and,

eventually, the 'virtual' probe will break down as the conductance pathways through pore solution shrink and become segmented until a critical percolation threshold is reached (see Chapter 3, Section 3.1-3). Occasionally isolated probes may break down much sooner than the others. Where this happens ΔR_{MN} or ΔR_{BA} will become very large positive or negative. However almost invariably, our results show an increase in voltage by the time all electrodes have had time to dry considerably. This appears to have more to do with the high total load (R_T in Section 6.5) and very small current resulting. The accuracy of the meter is lowest here and even a small error in voltage measurement will result in overestimation of the potential between M and N.

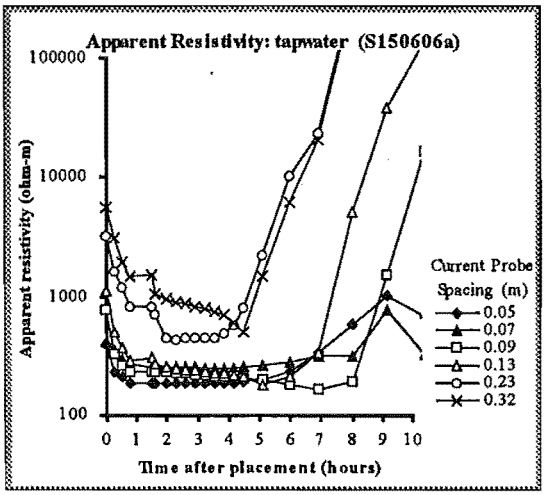

Figure 6.9.1-3. Apparent resistivity at some specific current probe spacings as a function of time after placement of 'wet' electrodes charged with tap water.

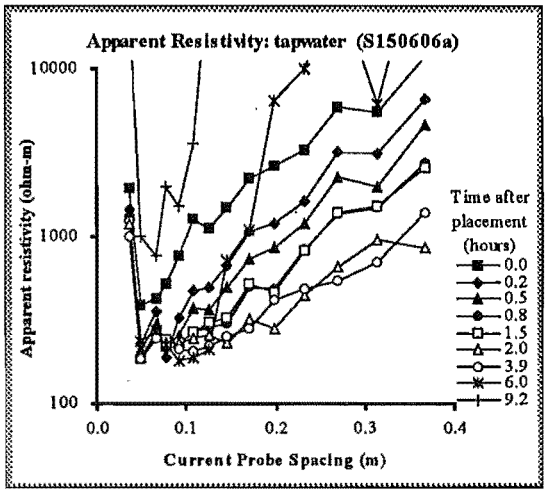

Figure 6.9.1-4. Evolution of apparent resistivity curves (VES curves) using 'wet' electrodes charged with tap water.

Because of the instability of the voltage measurement, the apparent resistivity changes in a fairly complex fashion in response to the moisture moving at all four electrodes (Figure 6.9 1-3. Note the relative stability of measured apparent resistivity between two and four hours after electrode placement.

Figure 6.9 1-4 illustrates the progress of sounding curves taken at various intervals after the wet probe array was lowered onto the concrete. Immediately, the broad structure is visible, however it is not until about two hours after placing that a semi-stable curve is achieved. Between two and three hours, the current and voltage are changing little (Figures 6.9.1-3 and 6.9-4). While the curves at this time are similar in form to those

predicted (see Chapter 5.), there is considerable scatter of data points about the ideal smooth curve.

After about four hours the current begins decreasing and apparent resistivity (beginning with that measured at the larger spacings) generally starts increasing.

While the use of wet probes reduces contact resistance, there is also general decrease in the apparent resistivity measured in the period following electrode placement. That is, the bowl shaped curve sinks with time over a certain period (for example Figure 6.9.1-4 during the first two hours). It is not clear at this stage exactly what this effect should be attributed to although comparison with the model profiles in Chapter 5 may be instructive.

Recalling the two graphs showing the effect of reducing either the resistivity or the thickness of a highly resistive surface layer, we note that reduction of the resistivity of the surface layer tends to lower the apparent resistivity at small rather than large spacings (see Figure 6.9.1-5 below). Reduction of thickness of this layer is associated with a lowering of apparent resistivity generally, although more markedly in the smaller current-probe spacing range.

Again, recall the finite difference model of a sounding session in which there is a lowering in resistivity in the zone of concrete immediately adjacent to each 'wet' electrode (Section 5.6.3). This showed a small but marked lowering of apparent resistivity at the smallest and largest of the spacings. Figure 6.9.1-4 shows much more change in apparent resistivity than the finite difference model determines, and seems more evocative of the combined effect of both decreasing the thickness (foremost) and the resistivity of the surface layer.

If the model holds we may suppose that the wet probe charged with tap water initially acts to reach into the resistive surface skin, effectively thinning it. As the wet probe dries the effective skin layer thickens again and the corresponding VES curve rises.

It appears, then, that the general lowering of the curve is more typical of a thick highly resistive top layer thinning out.

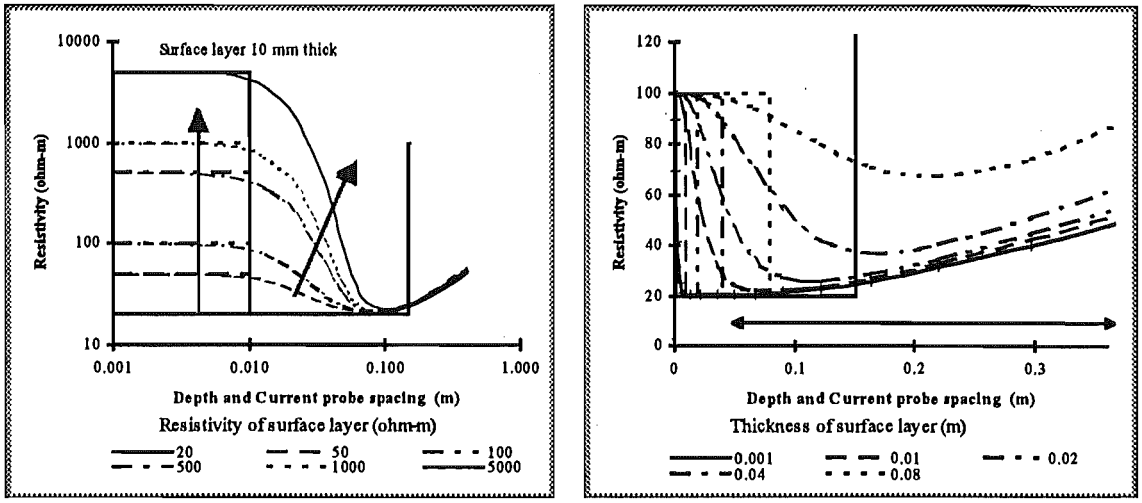

Figure 6.9.1-5: Two series of two-layer models of a concrete slab showing the effect on the resulting model apparent resistivity curves of increasing the resistivity (left-hand graph) and thickness (right-hand graph) of the dry surface layer (see Chapter 5).

6.9.2 Wet probes: conducting solution

The use of wet-electrodes charged with tap-water was ultimately unsatisfactory since considerable time was required between placement of the electrodes and the gathering of data. Furhermore at best the VES curves attained exhibit considerable scatter and are changing quite rapidly even at their most stable period (after about three hours). Fortunately, electrodes charged with conducting solution allow quite different current and voltage behaviour. Note in Figures 6.9.2-1 and 6.9.2-2, that although both the current and voltage vary for some time after placing the electrodes, the drift is relatively gradual and is shared (roughly) by measurements made at different spacings. It is likely that the differences in electrode-concrete interface resistances (ΔR_{MN} and ΔR_{BA}) are small compared to those noted in Section 6.9.1. Furthermore, the apparent resistivity appears stable from the start (Figures 6.9.2-3 and 6.9.2-4). Certainly there is some drift over time, at different spacings, however major changes do not occur (as a rule) until the electrodes begin to dry out. As can be seen, the VES curves are stable for at least three hours after placement of electrodes.

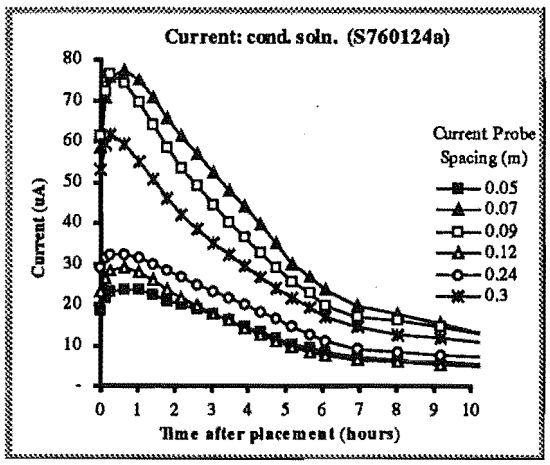

Figure 6.9.2-1. Evolution of current between 'wet' probes charged with conducting solution.(compare Figure 6.9.1-1).

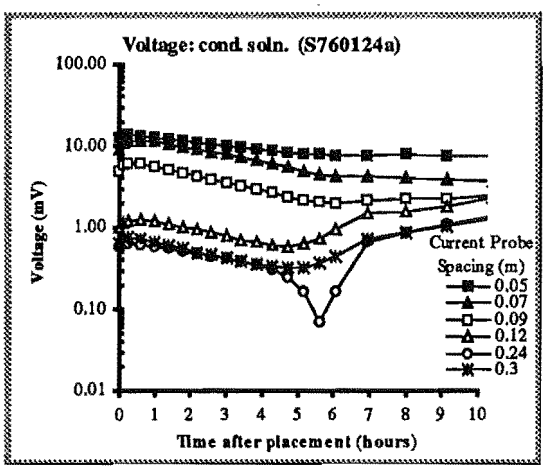

Figure 6.9.2-2. Evolution of potential difference between 'wet' measurement electrodes (MN) charged with conducting solution (compare Figure 6.9.1-2).

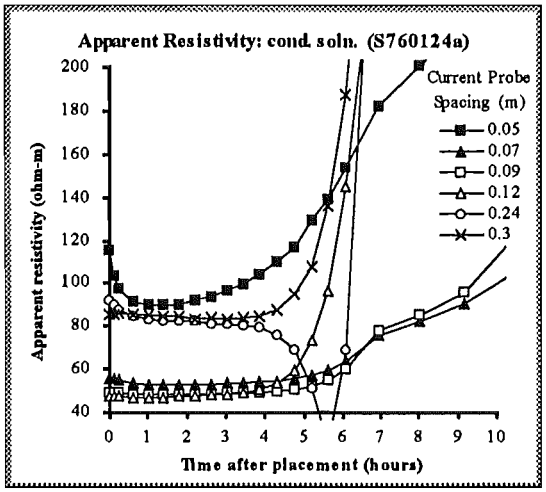

Figure 6.9.2-3. Apparent resistivity at some specific current probe spacings as a function of time after placement of 'wet' electrodes charged conducting solution (compare Figure 6.9.1-3).

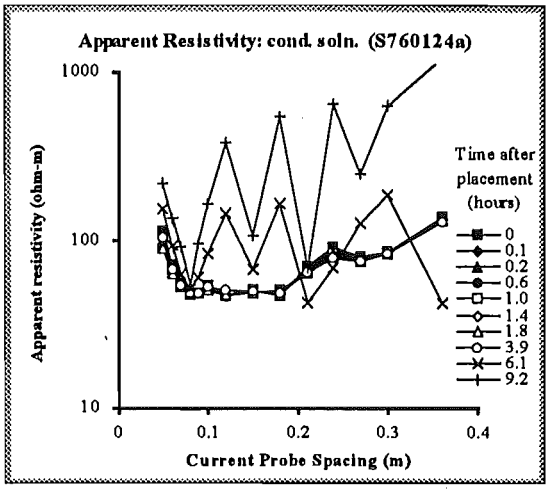

Figure 6.9.2-4. Evolution of apparent resistivity curves (VES curves) using 'wet' electrodes charged with conducting solution (compare Figure 6.9.1-4).

The advantage of wet probes charged with conducting solution is that the apparent resistivity curves may be recorded almost immediately and the probe array board then shifted to a new position. It is not clear what is responsible for this big advantage over tap water. However the three points below should be noted.

1. Since current is carried by ions in solution the ions contributed by the conducting solution enable a greater current to be passed.
2. Since the VES curves measured using conducting solution change little over the first hour or so it seems that the primary effect is to reduce the electrode-concrete contact resistance.
3. Tap water is relatively low in ionic charge so the slow increase in current must result from the moisture from the electrodes dissolving salts and other hydration by-products. The time taken to do this also may mean that severe imbalances in contact resistances between the four probes may remain for longer than with conducting solution. It would thus be the imbalance that leads to the relatively high error in the measured voltages compared to voltages measured using conducting solution. The penetration of the 'virtual' probes of the highly resistive concrete surface skin may be a minor effect. However this issue has not been resolved in the present work.

6.9.3 Spacing of electrodes

The Schlumberger array is a symmetrical pattern of spacings of two current probes, (A and B, each a distance '*s*' from the centre) in line with two voltage (or measurement) probes (M and N, each a distance '*b*' from the centre). Increasing the separation of the two current electrodes forces the current to take a deeper path so that the apparent resistivity at the surface, as a function of current probe spacing, is a reflection of the resistivity profile of the subsurface.

As a rough guide, the depth of investigation is about s/3, so that the maximum spacing between A and B necessary to recover a 150 mm profile should be about 900 mm. The spacing required in practice is less since at ages of between two and six months, the profile is roughly constant below about 60 mm.

On the other hand, the minimum depth able to be resolved depends on minimum measurement probe spacing *b* given that $s > 5b$. The minimum *b* is initially limited by the physical size of the probes. In practice, the electrode housing was set at 8 mm diameter. This allowed a maximum electrode diameter of 6 mm, and a minimum spacing between adjacent probes of 10 mm. The smallest *b*(=MN/2) is then 5 mm, and the corresponding minimum *s*(=AB/2) is 25 mm.

Ideally current probe spacings increase in size logarithmically. Since the resistivity profile changes more rapidly nearer the surface, the probes should be more densely packed at smaller spacings. Initially the measurements were made at up to 16 current probe spacings, with a minimum distance between adjacent probes of 10 mm. Fitting 16 spacings between s=50 mm and s= 500 mm logarithmically results in some the closest probes being closer than 10 mm. Some compromise arrays are shown in Table 6.9-1.

For example the array used to make most of the vertical electric soundings in Slabs #6, #7 and #8, is represented in the first and fourth column. This arrangement ensures that electrodes are spaced at least 20 mm centre-to-centre and allows two rows of 8 current probe spacings each. Normally the measurement probe spacings for this arrangement were at 10 mm and 30 mm.

It became apparent that at 10 mm centers, the presence of adjacent electrodes could influence the measured apparent resistivity. This effect is discussed below in Section 6.9-4. . Suffice it to say here, that to reduce the uncertainty in electrode position due to inter-probe interference, a minimum spacing between adjacent electrodes was set

at 20 mm centre-to-centre thus making a minimum measurement probe spacing *b* of 10 mm (=MN/2). The minimum current probe spacing is then *50* mm (five times minimum *b*), and the minimum depth of investigation about 16 mm. A more accurate estimate of the minimum depth resolvable was gained from modelling exercises.

Table 6.9-1: Arrays used in this study.

	Current Probe Spacing (m)		
Multiplexer index	1 row	1 row	2 rows
1	0.035	0.04	0.050
2	0.05	0.05	0.070
3	0.068	0.06	0.090
4	0.079	0.07	0.117
5	0.092	0.08	0.154
6	0.108	0.09	0.206
7	0.126	0.1	0.272
8	0.146	0.12	0.360
9	0.171	0.15	0.050
10	0.199	0.18	0.070
11	0.232	0.21	0.090
12	0.271	0.24	0.117
13	0.315	0.27	0.154
14	0.368	0.3	0.206
15	0.429		0.272
16			0.360
Measurement probe spacing (m)	(15mm) or (10mm & 20mm)	(15mm) or (10mm & 20mm)	(15mm) or (10mm & 30mm)
VES curves/run	1 or 2	1 or 2	2 or 4
Analysis file	ves1x15.m or ves2x15.m	ves1x15.m or ves2x15.m	ves2x15.m or ves8x2d

6.9.4 Uncertainty in electrode position

The 'wet' probes appear to act by reducing the concrete -electrode interface resistance through wetting of the very dry concrete surface. Ideally each current probe acts as a point source. The finite electrode contact area results in a patch of very low resistivity at the surface, and in uncertainty in the effective electrode position. The deviation from the ideal point current source or voltage measuring point, must introduce some variation from the ideal measured resistivity. However the finite-difference modelling studies (Chapter 5) indicated that variation in measurement electrode diameter from 0.001 m to 0.008 m resulted in less than 1% variation in measured apparent resistivity. The apparent resistivity is even less sensitive to current electrode diameter. The variation here was far

less than 1% for a 16 fold increase in diameter from 0.001 m to 0.016 m. This finding is in agreement with Millard (1991) who also noted a remarkable insensitivity to electrode diameter.

In the present experimental study however, there is a substantial variation in measured apparent resistivity when the array is lifted up and moved from one position to another. The electrodes are held firmly in the probe-housing and the probe housing is held firmly in the array board, so it is likely that the scatter in apparent resistivity reading at the same probe spacings but at different positions on the concrete is a result of the inhomogeneous nature of concrete itself. The inhomogeneity of concrete was not investigated in finite-difference studies, but some possible consequences can be proposed and discussed.

The surface of the concrete and the region below the surface may exhibit greater or lesser inhomogeneity depending on how the surface was worked in the first couple of days after pouring. Excess working can allow 'bleeding', where water containing a high proportion of soluble (and some insoluble) cement product rises to the surface and is washed away, or sets into a weak and dusty coating. Insufficient working may result in a very rough surface. In either case an electrode may not easily make good electrical contact with the bulk concrete and the degree of contact will vary considerably from electrode to electrode depending on the exact position of each on the concrete.

A smaller electrode diameter does not automatically result in less uncertainty overall. Larger diameter electrodes have the dual advantage of enabling a greater current flow by reducing the contact resistance and of 'averaging' surface inhomogeneity over a larger area. The averaging effect may be more important when the condition of the concrete surface is rough or is 'stony'. A well poured and finished concrete surface will have no aggregate showing through the surface. Rather, the surface skin will contain a higher proportion of cement paste. The skin acts to average the effect of the more inhomogeneous concrete below on the current pathways. In its absence, electrodes may rest partly on the highly resistive surfaces of aggregate, which will distort the initial current pathways. The larger the electrode diameter, the more the averaging effect will be restored.

The point at which the electrode does make electrical contact with the concrete may not be (almost certainly will not usually be) directly beneath the centre of the electrode. The path that the current takes may be diffused over a wide area or concentrated at a point of

exposed aggregate which happens to be exposed and raised directly beneath the electrode.

This deviation of the current distribution from a central (ie. beneath the centre of the electrode) position will vary with the electrode 'wetness' and with the nature of the concrete surface beneath the electrode. It cannot be predicted or quantified. The effect of this deviation may be explored briefly by letting it be represented by an uncertainty in 'effective' probe position and hence effective spacing. For example, the 'effective' measurement probe spacing b_{eff} is that value of b that will give the true apparent resistivity when used in the equation for the measured Schlumberger apparent resistivity,

$$\rho_{as}(s,b) = \frac{\pi s^2}{2b}\left|\frac{\Delta V}{I}\right|$$

Let the uncertainty in effective electrode position be Δx, so that $b_{eff} = b + \Delta x = b(1+\Delta x/b)$. The true value of apparent resistivity is then

$$\rho_{as}(s,b+\Delta x) = \frac{\pi s^2}{2b\left(1+\frac{\Delta x}{b}\right)}\left|\frac{\Delta V}{I}\right|$$

$$= \frac{\pi s^2}{2b}\left|\frac{\Delta V}{I}\right|\cdot\left(1-\frac{\Delta x}{b}+\left[\frac{\Delta x}{b}\right]^2-\left[\frac{\Delta x}{b}\right]^3+\cdots\right)$$

$$\approx \rho_{as}(s,b)\cdot\left(1-\frac{\Delta x}{b}\right)$$

It is evident that if the effective measurement probe spacing is smaller than assumed (say $\Delta x/b = -0.1$), the measured apparent resistivity for the whole curve will be high (in this case by a factor of 1.1, that is, high by 10%) If the uncertainty may mean b_{eff} that is sometimes higher and sometimes lower than the nominal value, several VES curves taken at different positions around the same time, may be shifted down or up relative to some mean, or 'true' value. Clearly, this error in the vertical position of the sounding curve, will be less for larger 'b', since $\Delta x/b$ will be smaller.

The uncertainty in probe position, means that there is uncertainty also in the current probe spacing 's' and the measurement probe spacing 'b', which will be more severe at smaller spacings. The effect will be less since $s \geq 5b$, $\Delta x/s \leq 0.2\ \Delta x/b$

The true apparent resistivity is

$$\rho_{as}(s+\Delta x,b)=\frac{\pi s^2\left(1+\frac{\Delta x}{s}\right)^2}{2b}\left|\frac{\Delta V}{I}\right|$$

$$=\frac{\pi s^2}{2b}\left|\frac{\Delta V}{I}\right|\cdot\left(1+\frac{2\Delta x}{s}+\left[\frac{\Delta x}{s}\right]^2\right)$$

$$\approx \rho_{as}(s,b)\cdot\left(1+\frac{2\Delta x}{s}\right)$$

If $\Delta x/b = -0.1$, at the smallest s, $\Delta x/s = -0.02$, so that the true apparent resistivity would be smaller than the measured value by a factor of 0.96. At the largest 's' some 10 times the smallest 's', the factor would be only 0.996. The uncertainty in current electrode spacing due to surface inhomogenity, presents much less of a problem than that of the measurement electrode spacing, if only because $s \geq 5b$.

However there is another source of current electrode uncertainty. If current electrodes are too close, the low-resistivity patch of concrete surface in the region of each electrode, may provide another pathway for current from probes at a wider spacing. The significance of the pathway will become more significant if the size of the patch increases, and/or if the proximity of adjacent current electrodes decreases. If some current from two electrodes is able to traverse along the surface to inner wet patches, before diving down into the bulk of the concrete, the effective current probe spacing will be reduced ($\Delta x/s < 0$) and the measured resistivity will be low. There is some evidence that something of this sort happened when adjacent current electrodes were spaced less than 10 mm apart (Figure 6.9.4-1).

To reduce the uncertainty in electrode position due to inter-probe interference, a minimum spacing between adjacent electrodes was set at 20 mm. To reduce the uncertainty due to finite electrode diameter, the measurement electrodes and the current electrodes at the three smallest spacings had a 3 mm diameter. The rest of the electrodes were of just over 4 mm in diameter.

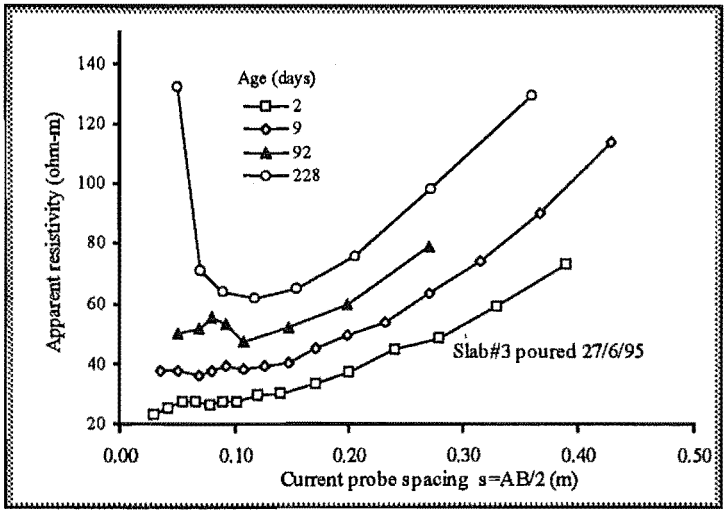

Figure 6.9.4-1: A series of sounding curves taken with different ranges of current probe spacings. The humping that can be seen in the region below $s = 10$ mm for the early curves may be a result of the low- resistivity wet patches from adjacent wet probes interfering and altering the effective s.

6.9.5 Finite Measurement Probe Spacing.

The use of the approximation $E = \Delta V_{MN} / 2b$, requires that the electric field be constant in the vicinity of the voltage measurement region. This will be more likely to be true the further apart the current probes are relative to the measurement probe spacing. A common rule of thumb is to ensure $s>5b$. This is supported by the (admittedly) two-dimensional finite-difference models reported in Chapter 5, where the error, while roughly constant for $s>5b$, increases logarithmically with b/s when $s<5b$. However as Bibby and Risk (1988) show, significant correction may be required even at $s>5b$ if the resistivity profile is sharply descending. Given the measured VES curve, correction factors were calculated based on these authors' work. However they were not able to be used in a practical way Ideally, apparent resistivity measurements taken with b=30mm, should be able to be corrected to coincide with those taken with smaller b at the same s. The correction factors tend to wildly overcorrect. This probably has to with attempting to take the second derivative of a splined curve that is only matched to two data points. Ie. the measured VES curve is unlikely to be accurate enough in the first place.

6.10 Apparent resistivity curves: results and discussion

Typically the apparent resistivity curves (or VES curves) show considerable scatter of data points. Sources of error in voltage and current measurements, in the array configuration parameters, the position on the concrete slab and the inhomogeneity of the concrete have been outlined and discussed in this and previous chapters. Nevertheless, we are left with the data scatter and must reduce it to manageable and useful proportions.

We can identify two types of noise affecting the measurement of apparent resistivity:

- **transient noise** results from the electromagnetic environment in which the soundings are made and is induced within the circuitry and especially at the voltage measurement stage. Transient noise is usually insignificant compared to
- **structural noise** which is associated with the inhomogeneity of concrete and will be reflected in the departures of actual VES curves from the smooth VES curves derived from model profiles and in differences between VES curves recorded at the same time in different positions on the concrete.

While the voltage measurement stage removes some transient noise, further noise reduction is done by the computer control software. The input to the computer is a series of sets of four signals: I_o^+, I_o, V_o^+ and V_o^- (see Section 6.5). Each set represents one cycle of square wave. The noise level detected and the gain, is used by the software to set the number of cycles to be measured at each probe position. The current and voltage curves above, are determined by calculating $\Delta I_o = I_o^+ - I_o$ and $\Delta V_o = V_o^+ - V_o$ for each cycle and averaged over all cycles. The "resistance" ($\Delta V/\Delta I$) is not obtained from the averaged current and voltage values. Rather it is calculated for each cycle and an average is calculated over all resistance values. This ensures that fluctuations in current and voltage which occur together do not affect the overall average.

The later VES sessions (from about the beginning of 1996), utilised the final design of array board using the array positions in the right hand column of Table 6.9-1. Thus, for each position of the array board on the slab, four VES curves were obtained, using each row of current probes with two measurement probe spacings.

Typical "resistance" curves are shown in (Figure 6.10-1) with the remaining transient noise marked in as error bars

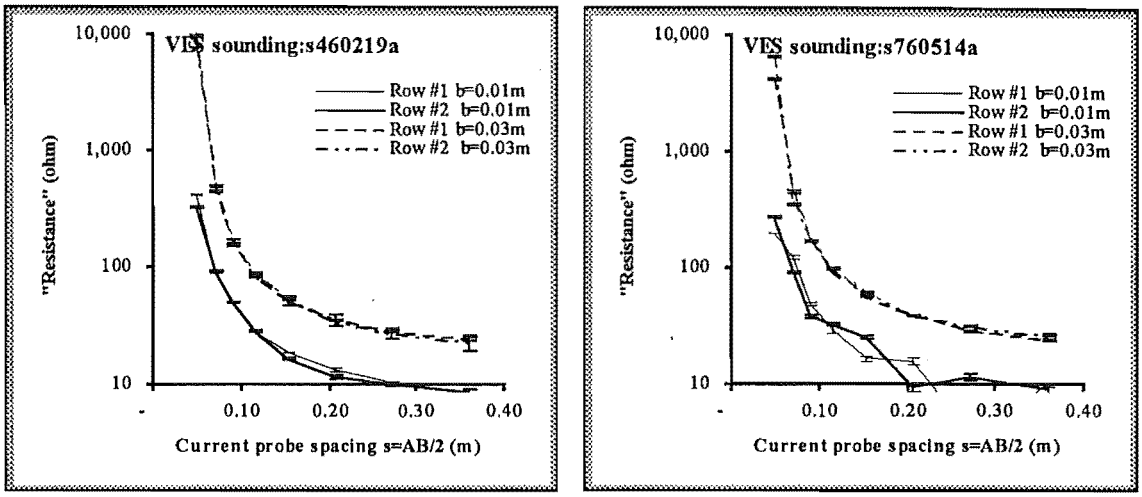

Figure 6.10-1:Typical "resistance" curves showing transient noise as error bars. The deviations from a smooth curve which are so apparent in each of the lower two curves in the right-hand graph, reflects 'structural' noise. This source of error is usually of greater significance than transient noise.

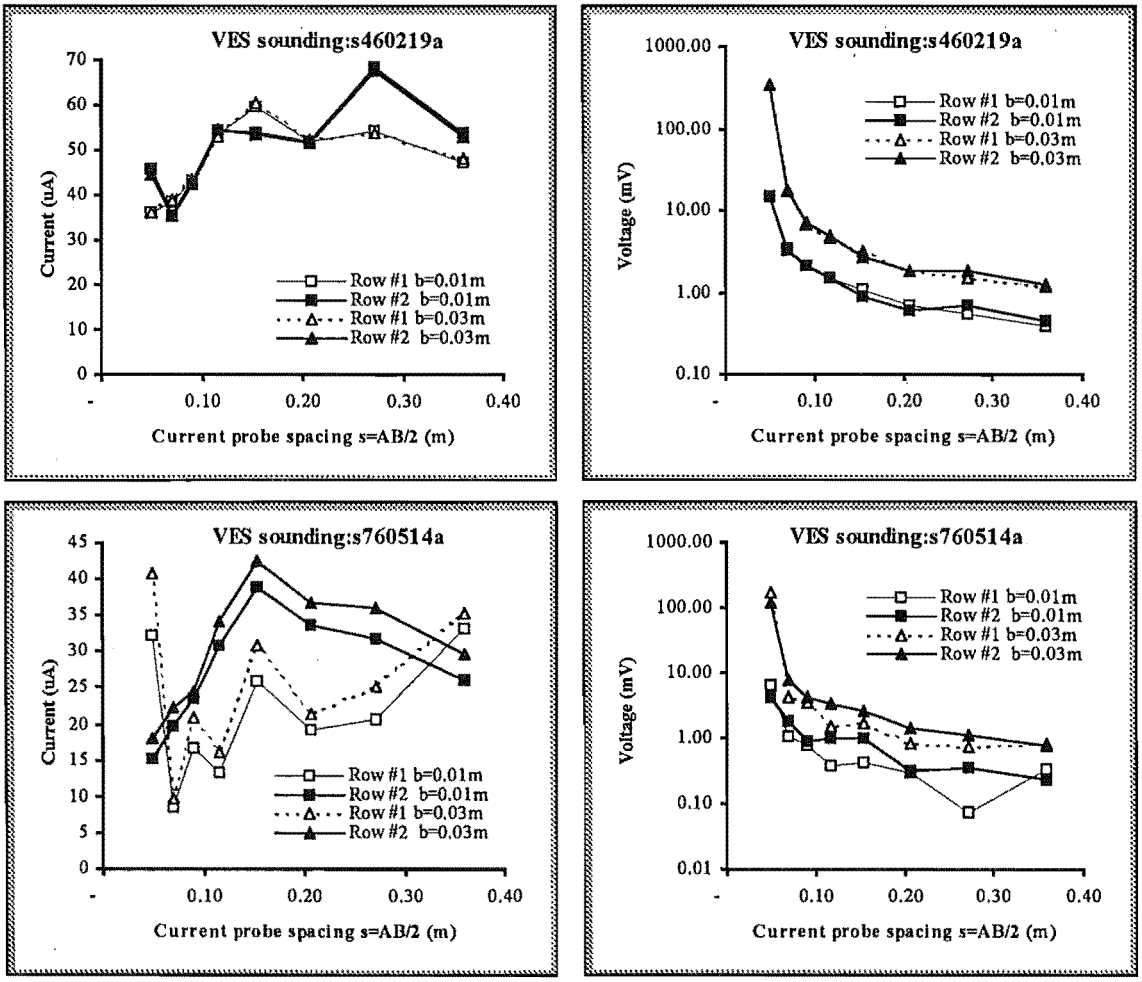

Figure 6.10-2: Typical current (left) and voltage (right) curves obtained during a sounding session.

Figure 6.10-2 shows the current and voltage measurements for the same sets of four curves as Figure 6.10-1. As expected, current measurements in a single row will change little when the measurement probe spacing *b* is changed (left-hand graphs). Any variation is likely to reflect the time lag between readings. On the other hand, there is considerable difference between the current curves measured in different rows. This is because they use different probes which will have different concrete-electrode interface resistance and different conditions in the concrete surface beneath the electrode. That is, these differences reflect structural noise.

In the top-right-hand graph, the voltage curves for different rows are approximately coincident. This will depend on the coincidence in current passing through at corresponding spacings. The large differences in current between rows seen in the bottom left-hand graph are reflected in the voltages in the bottom right-hand graph.

Note the large range in voltage measured - from about 0.5 mV to 400 mV. The range in voltage is greater for the reinforced slab (Slab #5, see Figure 6.10-3). The reinforcing lowers the resistivity within the slab markedly, whilst having little effect on the current since most of the load on the current drive is in the concrete-electrode interface resistance and in the highly resistive layer close to the surface. The maximum gain of 8000 in the voltage measurement stage of the resistivity meter was not enough to adequately resolve such low voltages although finer tuning and calibration would help.

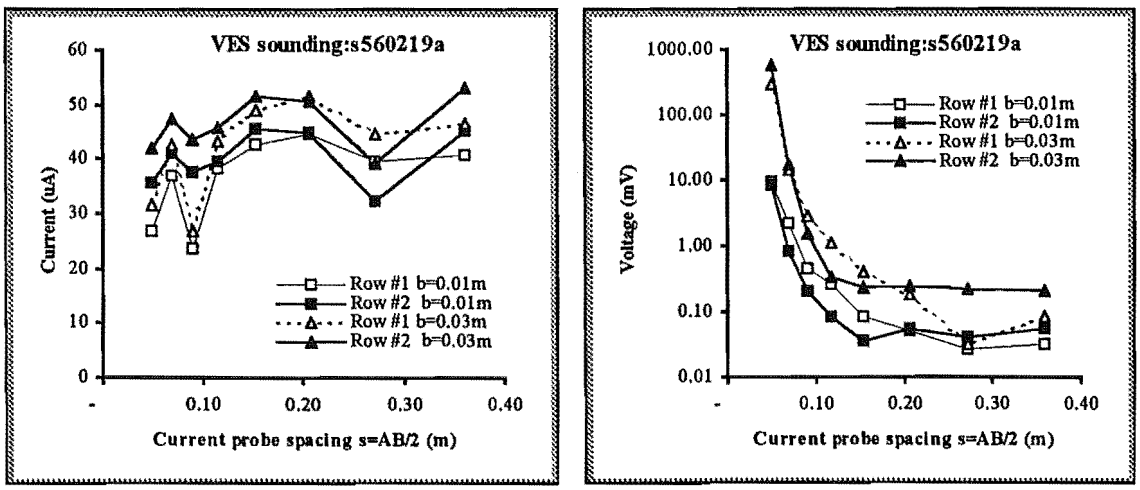

Figure 6.10-3: Current and voltage curves from the reinforced Slab #5. The order of sounding is as in the legend. The current curves for b=0.03 m are higher than those for b=0.01 m. This indicates that the 'wet' probe was still changing the interface resistance and the resistivity of the concrete in its vicinity at the time of sounding. Note the great range in voltage measured due to the low resistivity of the reinforced layer.

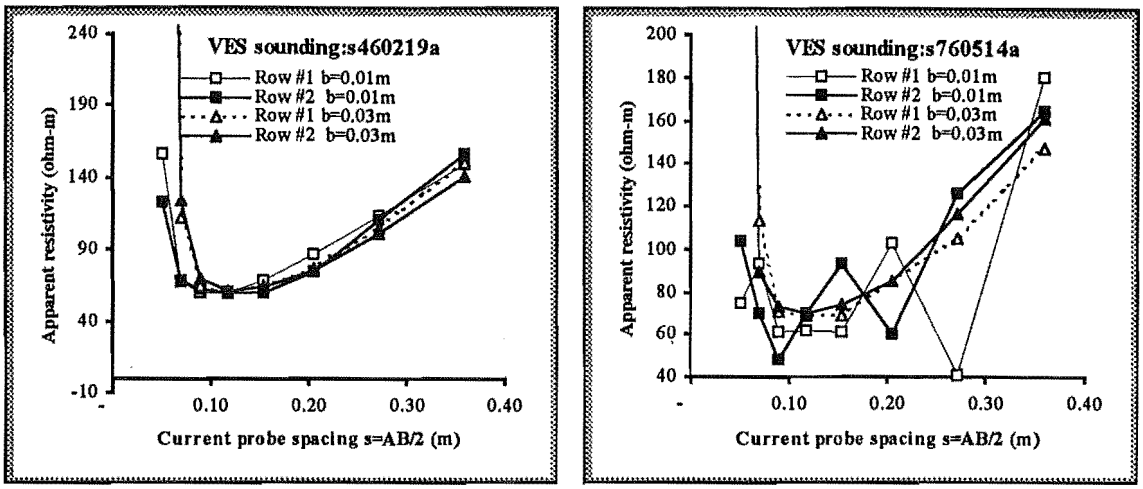

Figure 6.10-4: Apparent resistivity curves calculated using the "resistance" measurements in Figure 6.10-1.

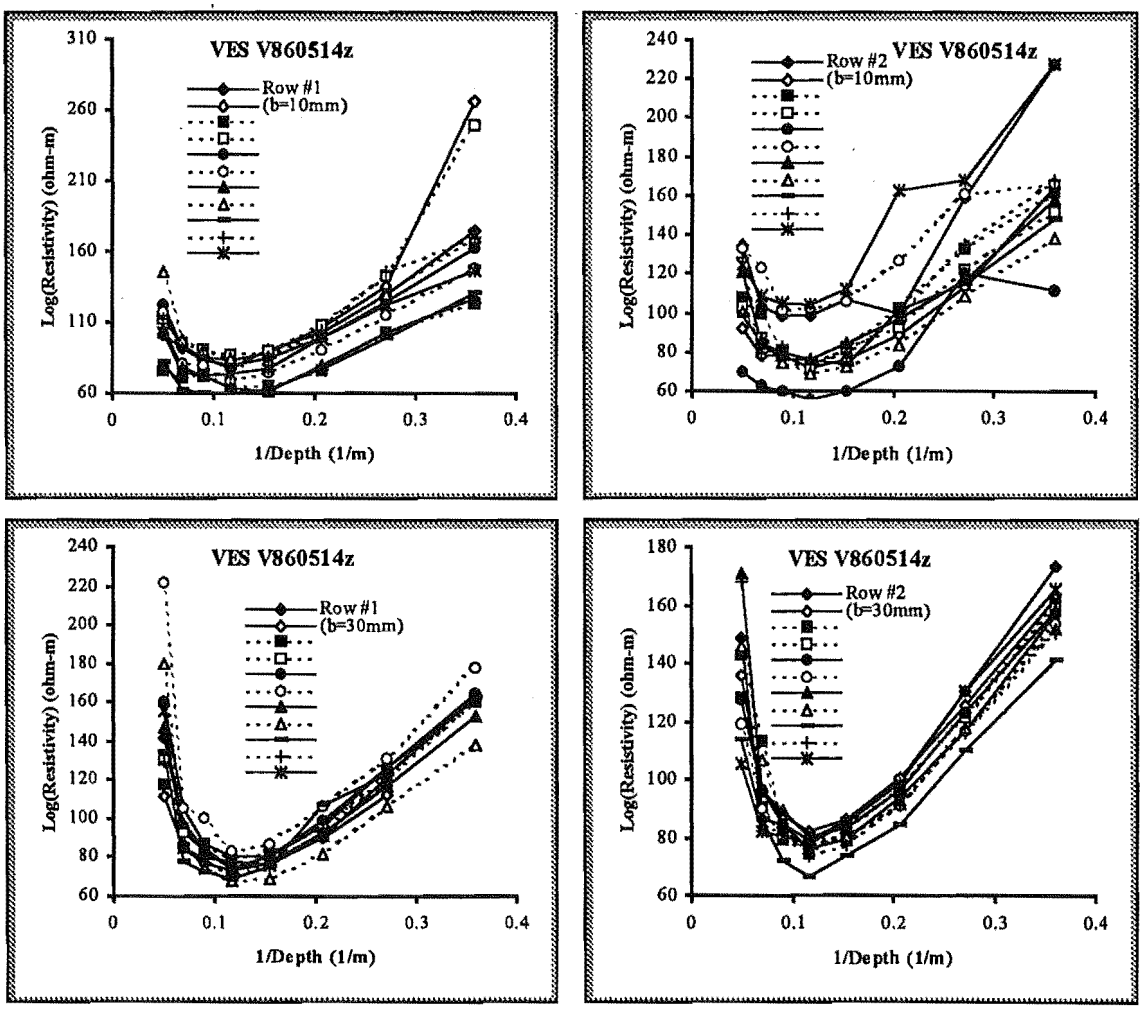

Figure 6.10-5: The results of a VES session in which the array board was moved 11 times (each time marked with a different symbol). Four VES curves are taken at each array board position.

The apparent resistivity curves (VES curves) associated with Figure 6.10-1 are shown in Figure 6.10-4. The data scatter shown in the right-hand graph is extreme, but not uncommon. Some form of treatment or elimination of extreme error is necessary.

Because the use of wet probes charged with conducting solution reduces but does not eliminate data scatter due to structural noise, further reduction is sought by averaging a number of VES curves. If the array board is moved to five positions (say) during a sounding session, 20 VES curves are available - ten curves based on a measurement probe spacing of 10 mm and ten based on 30 mm. Figure 6.10-5 shows the results of a VES session in which the array board was moved 11 times, making 44 curves in all. Note the different degree of scatter between the b = 10 mm and the b = 30 mm curves.

The curves for b = 10 mm are averaged separately from those for b = 30 mm. The means and standard deviations for each set are presented in Figure 6.10-6.

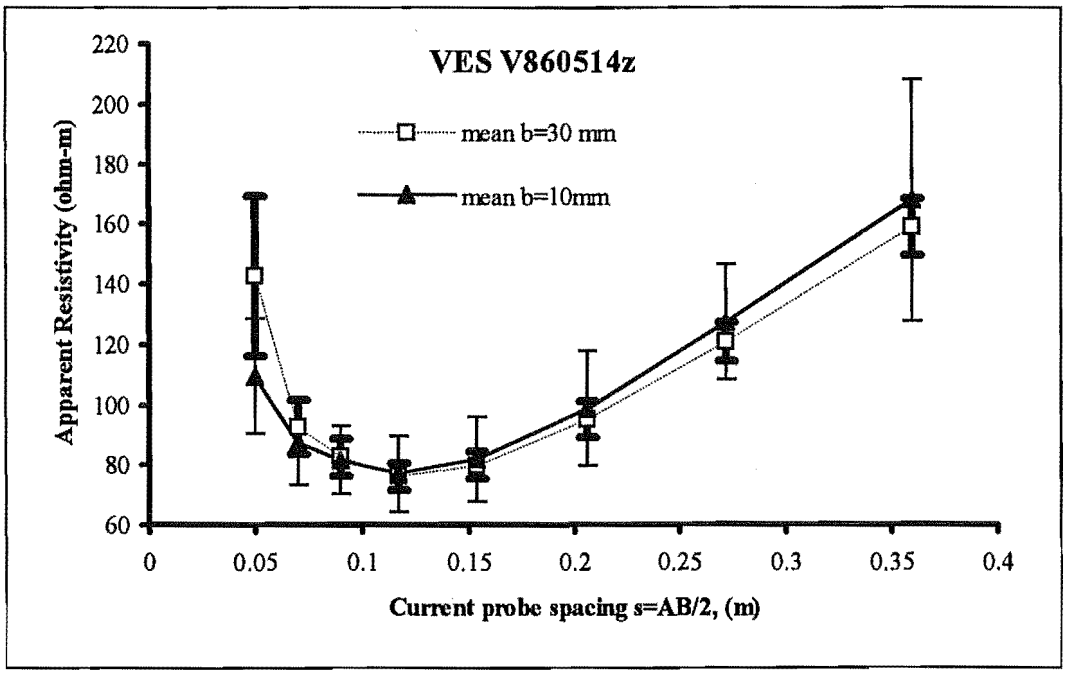

Figure 6.10-6: The sets of curves from the previous figure have been grouped and averaged. Standard-deviations at each *s* are shown as error bars.

In averaging and collating this data we may take into account the following points:

1. The use of smaller b results in a smaller measured voltage and hence a smaller signal-to-noise ratio. This would account for some of the variation in the form of VES curves from the model VES curve.
2. The use of smaller b may result in greater error because of the greater relative uncertainty in its actual value (Section 6.9.4). Such error would result in a raising or

lowering of the entire VES curve since the same b is used throughout the curve, but would not be responsible for significant change in form.

3. The larger b (= 30 mm) is likely to be less accurate at smaller current probe spacings s especially where $s < 5b$, and in any case
4. as the above graph shows (and probably due to the above points), there is more variation in the larger b curves at smaller current-probe spacings and in the smaller b curves at larger spacings.

At some current probe spacing, the balance will shift in favour of the larger b. The method of collating the data involves selection of an appropriate cut-off and matching the two curves there. This can be done in many ways. The method chosen uses the first four data points from the mean $b = 10$ mm curve and the last five from the $b = 30$ mm curve. It is assumed that because of Point 2. above, the shape of the $b = 10$ mm curve is likely to be more correct in the initial part of the curve but the level will be uncertain. On the other hand the level of the $b = 30$ mm curve at greater spacings will be relatively accurate. The strategy is to shift (where necessary) the $b = 10$ mm part of the curve to match the $b = 30$ mm curve at the fourth data point (where $s \approx 5b$, see Table 6.10-1 and Figure 6.10-7). Further examples of this process are shown in Figure 6.10-8.

Table 6.10-1. Averaging VES curves and combining data from VES curves determined using two different measurement probe spacing (b = 10 mm and b = 30 mm). Data not used is shown in italics.

Current-probe spacing	Apparent resistivity (ohm-m)			
	Measurement-probe spacing			
s (m)	b = 10 mm raw	b = 10 mm shifted	b = 30 mm	Collated data
0.050	109.3	→ **108.0**	*142.4*	**108.0**
0.070	87.5	→ **86.5**	*92.6*	**86.5**
0.090	81.5	→ **80.5**	*82.6*	**80.5**
0.117	76.9	→ **76.1**	**76.1**	**76.1**
0.154	*81.7*	*80.8*	**79.9**	**79.9**
0.206	*98.6*	*97.5*	**95.1**	**95.1**
0.272	*127.3*	*125.8*	**120.7**	**120.7**
0.360	*167.9*	*165.9*	**158.7**	**158.7**

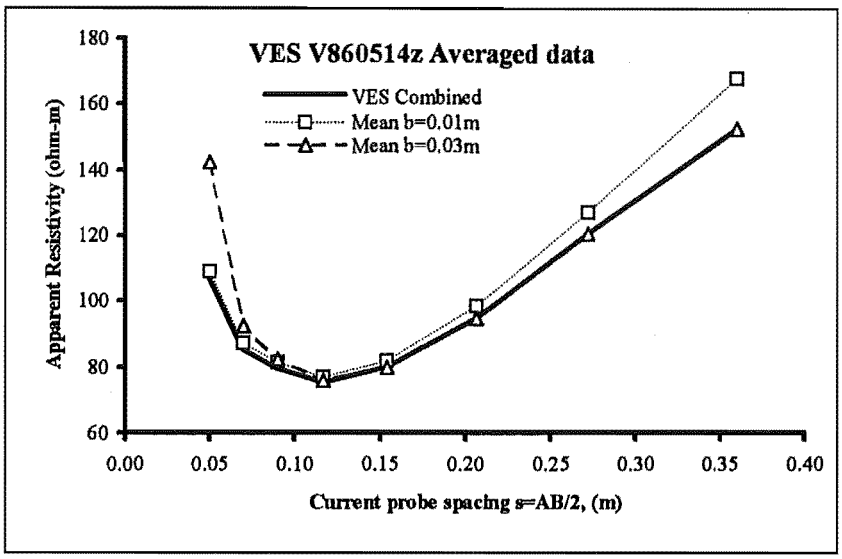

Figure 6.10-7: Collation of the two sets of data: the VES curve ready for inversion.

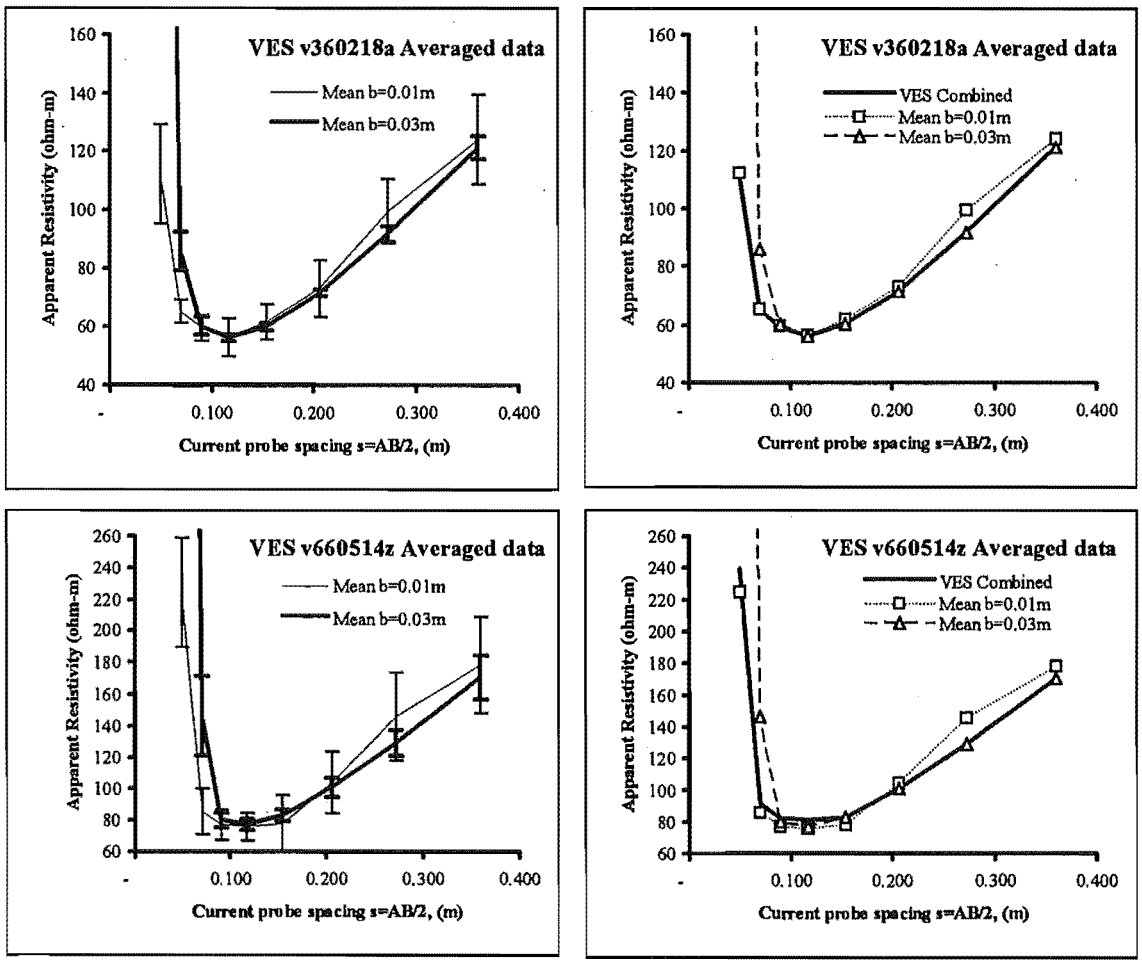

Figure 6.10-8: Some more examples of collation of VES curves to obtain final curves in which a lot of the structural noise has been averaged out.

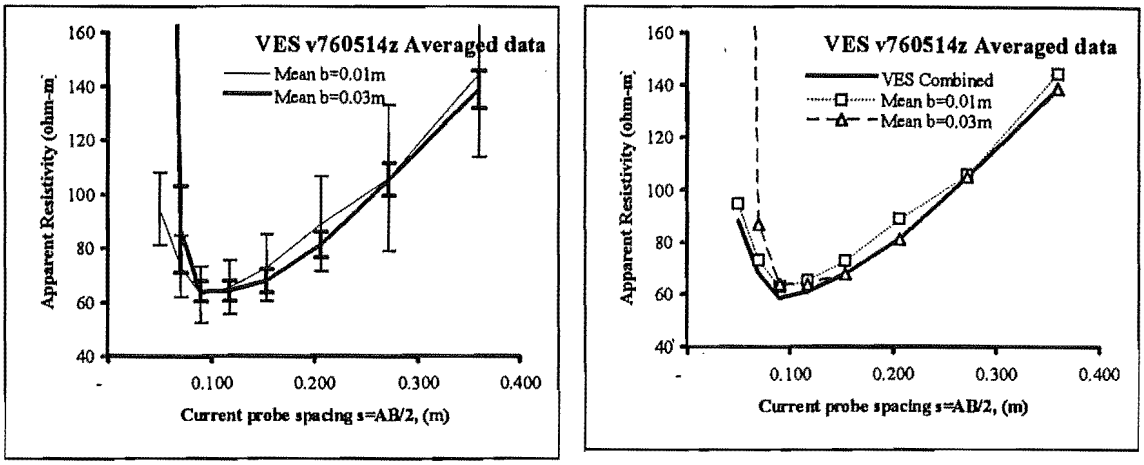

Figure 6.10-8: (continued) Some more examples of collation of VES curves to obtain final curves in which a lot of the structural noise has been averaged out.

6.11 Summary

In this chapter the design and development of the instrumentation and software required for the determination of apparent resistivity curves has been presented. Key features of this development include

1. **The development of 'wet' electrodes** which has enabled some of the problems associated with the dry and highly resistive surface of a drying concrete slab to be overcome. In particular, the electrode-concrete interface resistance is markedly reduced when a conducting solution (in our case a solution of Swarfega cleansing gel) is used to form an interface between the concrete and the electrode. The immediate decrease in contact resistance when wet-probes treated with conducting solution are placed on the concrete and the relative stability of the apparent resistivity curves measured almost immediately suggests that the any diffusion of moisture into the concrete does not significantly lessen the validity of the approximations to point- and surface-located electrodes that the vertical electric sounding theory assumes.
2. **Determination of an optimal array configuration**. Indications of possible horizontal spread of the moisture from the electrodes and consequent interference between measurements made using adjacent electrodes has led to the restriction of the minimum distance between adjacent electrodes to 20 mm centre-to centre. This restriction has further implications for the closest measurement- and current-

probe spacings (minimum b is 10 mm and minimum s is 50 mm) and for the range of current probe spacings (the next largest s must be at least 70 mm for example).

3. **A method of overcoming the data scatter inherent in measurement of apparent resistivity on a highly inhomogeneous material**. The restrictions on s and b act to limit the ability of the instrument to resolve the apparent resistivity at small spacings. However, as we have seen, the scale of the inhomogeneity of concrete with a maximum aggregate size of 19 mm imposes at least as a severe handicap, so that at the smallest s and b, the scatter or imprecision of measurements of potential difference and indeed of the effective measurement probe spacing, is only barely acceptable. A method of averaging and combining many apparent resistivity curves taken with two measurement probe spacings, and at different positions on the concrete has been described. This enables considerable data scatter to be removed, and enables the most accurate features of curves taken using different b to be used whist rejecting those most affected by inherent limitations of vertical electric sounding on concrete.

4. **Design of a method and device used to position 'wet' electrodes on the concrete**. An *array board* has been designed and constructed. This is a device that holds the wet electrodes in position on the concrete. The design allows for

   a) quick insertion and removal of the wet probes,

   b) easy repositioning of the electrode array at different locations on the concrete slab so that a series of vertical electric soundings may be taken during a single session,

   c) efficient recharging of the set of electrodes with conducting solution by placing the array board in a specially designed reservoir,

   d) choice of a variety of array configurations which may be selected by insertion of the wet probes into housings at different spacings (these must then be rewired which is slightly more time consuming: this option is unlikely to be used since the optimal configuration has been determined in this paper),

   e) simultaneous measurement of two sets of two apparent resistivity curves, each set comprising one curve taken with a measurement probe spacing b = 10 mm and one with b = 30 mm and

f) efficient wiring of the array board to the resistivity meter using multi-pin plugs.

5. The same basic design may be easily adapted to allow for measurement of a larger number of apparent resistivity curves simultaneously.

6. **Design and development of a computer controlled resistivity meter**. This integrated unit comprises

a) a variable frequency square-wave constant current generator (with a range of 'constant current' settings,

b) a sensitive multiple gain (16 ranges) voltage measuring circuit,

c) a data acquisition and control unit,

d) demultiplexing of the current drive to 16 pairs of current-probes,

e) multiplexing of the voltage measurement circuit from 16 pairs of measurement electrodes,

f) a graphical user interface used to control and acquire data from the resistivity meter allowing (automatic or manual) control over

i) the current drive frequency,

ii) the voltage at the current drive,

iii) the constant current level,

iv) the gain of the voltage measurement stage and

v) the multiplexer units associated with the current generating and voltage measuring stages.

g) In addition the graphical user interface allows the meter to be set up to take a full set of apparent resistivity curves from the present array position. In which case the meter will

i) automatically adjust the constant current level and the voltage measurement gain to maximise the signal-to-noise ratio whilst preventing saturation of the gain amplifiers,

ii) determine the optimal number of cycles sampled by the meter at each current probe spacing so as to maximise the precision of the measurement and minimise the time needed,

iii) take any number of sets of apparent resistivity curves at the present array board position should the interest be in the development of apparent resistivity curves over a period of time

iv) automatically calculate and display the apparent resistivity for the particular array configuration and save all current, voltage, resistance, apparent resistivity and time data at the end of each set of readings in a form suitable for further analysis.

7. The use of the meter to measure apparent resistivity curves has been described as has subsequent analysis and averaging of some curves to a point where they are ready for further processing.

Having brought the vertical electric sounding instrument to the present stage, I must emphasise that development is not complete. The meter is in fact over-designed in that it has a flexibility in the choice and number of electrodes that would not be needed by a commercial instrument, or at least not in the present form. Further consideration of the utility of the instrument and technique is offered in later chapters.

7. Vertical Electric Sounding III: Profile recovery

7.1 Introduction

In Chapter 5 the theory of vertical electric sounding (VES) was outlined and some theoretical profiles and associated apparent resistivity curves (VES curves) were generated. In Chapter 6, the instrument developed to measure VES curves at the surface of concrete slabs was described. Methods of obtaining relatively scatter-free data through averaging and combining several VES curves taken with different measurement probe spacings, were discussed toward the end of Chapter 6, which finished with a selection of VES curves obtained in this way.

Once apparent resistivity data has been determined, it may be 'inverted', that is, analysed to recover possible resistivity profiles that were responsible for the observed apparent resistivities. Two 'inversion' programs (computer software designed to recover resistivity profiles from VES curves) were described in Chapter 5. Although both inverjnm.m (based on Merrick's 1977 paper) and inverjnz.m (based on Zohdy's 1989 paper) were used at various stages of the project, the former was found to have the most useful qualities. Unless otherwise stated inverjnm.m was the recovery program used (examples of recovery using invrejnz.m may be found in Section 7.4.1.6).

The purpose of this chapter is three-fold:

- to report and discuss issues involved in the use of the inversion programs ,
- to discuss and assess the quality of the VES curves and the recovered profiles and
- to discuss further treatment of the recovered profiles to enable conversion to relative-humidity profiles.

7.2 Investigation of inversion schemes using experimentally derived VES curves

Principles of profile recovery through inversion of VES curves have been discussed in Chapter 5. The effects of varying the parameters of the inversion process on the recovery of profiles from noisy, experimentally derived, VES curves are illustrated in this section. In particular, this section will illustrate the effects of constraining the inversion process by imposing

1. a fixed, nonconductive sublayer,
2. a constant slab thickness of 150 mm,

3. a "falling" profile (that is resistivity never increasing with depth),
4. a fixed number of layers,
5. fixed layer thicknesses (that is, keeping the depths constant) and
6. different layer thicknesses.

The first condition is maintained by keeping the sublayer resistivity fixed at 10^{100} ohm-m . The second is maintained by keeping depths fixed (which is the fifth condition) or through increasing or decreasing the thickness of the bottom slab layer, maintaining the longitudinal conductance (see Chapter 5) of this layer by also changing its resistivity. This adjustment and that needed to maintain the third (falling profile) condition, are carried out (when necessary) after the new layer parameters have been determined by the inversion process at each iteration. The number of layers is imposed through choice of the initial trial model, although the effective number of layers in the final model may be smaller than this.

7.2.1 Different numbers of layers

The effect of recovering profiles from the theoretical VES curves using initial trial models with different numbers of layers has been illustrated in Chapter 5. This exercise was repeated using experimental VES data (see Figure 7.2-1 and Table 7.2-1)

Table 7.2-1. Inversion with fixed depths and the falling profile constraint using initial trial models with different numbers of layers (with the effective number of layers in the final model in brackets). In this series of inversions the sublayer resistivity was allowed to vary (Slab#8, 14/5/96, 116 days after pouring).

		Resistivity (Ohm-m)					
		Number of Layers (and effective number. in final model)					
	Depth (m)	2 (2)	3 (2)	4 (3)	5 (4)	6 (6)	7 (7)
Slab	0.01	1790	175	306	483	481	440
	0.02		175	112	102	108	112
	0.03			112	91	86	85
	0.04				91	82	79
	0.05					71	68
	0.06						60
	0.15	70	61	59	56	55	55
Sub-layer	*0.60*	*670*	*2735*	*4121*	*15159*	*145980*	*742550*
	RMS %	4.7	1.29	1.05	1.0	1.06	1.1

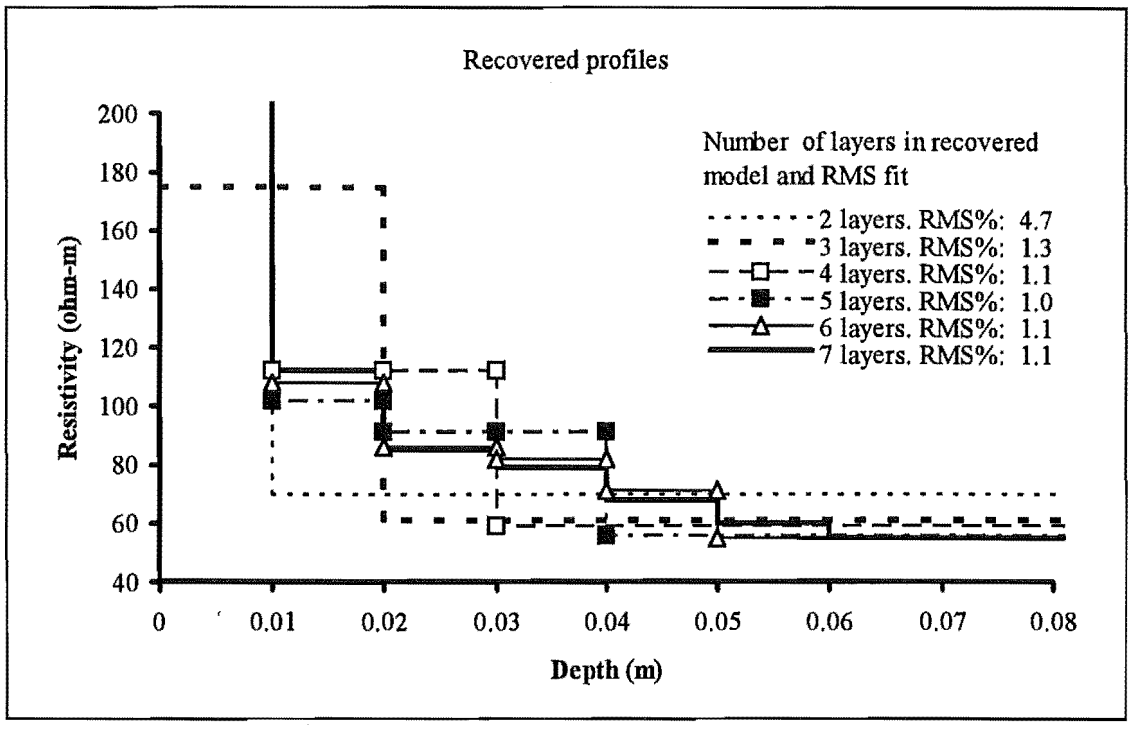

Figure 7.2-1: Inversion with fixed depths and the falling profile constraint using initial trial models with different numbers of layers. In this series of inversions the sublayer resistivity was allowed to vary (Slab#8, 14/5/96, 116 days after pouring).

It should be noted that the inversion process has different effects on different VES curves, so that while general rules for efficient inversion have been pursued, the multitude of factors affecting the inversion process will yield inconsistent results. Thus where in the present case, the two-layer inversion results in a markedly poorer RMS than inversion with larger numbers of layers, this is not invariably so. Over quite a large number of trials, however, inversion with a five-layer initial trial model has appeared optimal.

Note also, that in the present example, amalgamation of layers has taken place under 3-, 4- and 5-layer inversion, giving one fewer effective layer in the final recovered model, than in the initial model. Both the 2- and 3- layer inversions result in 2-layer final models. The 3-layer inversion has resulted in a better fit. This may be partly because of the added flexibility of more free parameters, although too many free parameters allows convergence on the wrong solution to occur more easily. The better fit may also be because the optimal thickness of the first effective layer happens to be 20 mm and not 10 mm as was imposed in the 2-layer initial trial model.

Finally, note that final models with effectively 3, 4, 6 and 7 layers fit the VES curve equally well (in this case!).

7.2.2 Depths free to vary

Inversion of VES curves of only 8 data points allows a maximum of 8 free parameters if the data is not splined. Although splining (and smoothing) of data was used early in this study, disadvantages in doing so outweighed the advantages (see Section 7.7.1: Discussion). Consequently, if depths and resistivities are allowed to vary, the maximum number of layers in the initial trial model is four.

However, as noted above, having too many free parameters can encourage convergence on the wrong, or an inappropriate solution. The possibility of this occurring is lessened if a better initial trial model is used. An efficient method is to use the solution found using a smaller number of layers as the initial trial model for further inversion. If an increase in the number of layers is desired, one of the layers is split in two – each sharing the same resistivity. This method has not been fully explored by the author but could prove fruitful in the future.

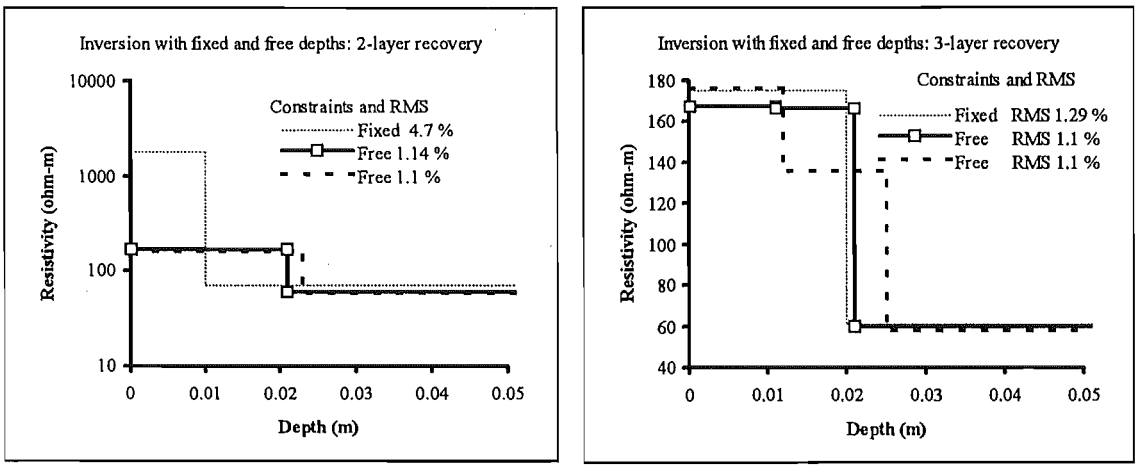

(a) (b)

Figure 7.2-2: Recovery using (a) two-layers and (b) three-layers by inversion with different constraints. Model #1 (dotted line and see the previous section) has fixed depths and was used as the initial trial model in (a) and (b) for a second inversion with free depths (–□–) to get Model #2 and Model #3. In Model #3 (- - -) the slab thickness is free to vary (see also Table 7.2-2) (Slab#8, 14/5/96, 116 days after pouring).

On the other hand, if the original model inverted with fixed depths has four or fewer layers, the final model for that inversion can be used for further inversion with depths

free to vary. If depths and resistivities are free to vary, the overall slab thickness may have to be constrained.

In Figure 7.2-2 and Table 7.2, the same data as in Figure 7.2-1 was inverted using two and three layer initial models with fixed depths. The recovered models were used as the trial model for inversion with free depths but fixed slab thickness (Model #2) and totally free depths (Model #3).

Table 7.2-2: Recovery using (a) two-layers and (b) three-layers by inversion with different constraints. Model #1 has fixed depths and was used as the initial trial model in (a) and (b) for a second inversion with free depths to get Model #2 and Model #3. In Model #3 the slab thickness is free to vary

(a): Two-layer recovery					Table 7.2-3
	Model #1		Model #2		Model #3
	Fixed depths		Free depths		Free depths
	Slab thickness fixed		Slab thickness fixed		Slab thickness free
Depth (m)	Resistivity (ohm-m)	Depth (m)	Resistivity (ohm-m)	Depth (m)	Resistivity (ohm-m)
0.01	1790	0.021	166	0.023	158
0.15	70	0.150	60	0.142	58
RMS %	4.7		1.14		1.10
(b): Three-layer recovery					
	Fixed depths		Free depths		Free depths
	Slab thickness fixed		Slab thickness fixed		Slab thickness free
Depth (m)	Resistivity (ohm-m)	Depth (m)	Resistivity (ohm-m)	Depth (m)	Resistivity (ohm-m)
0.01	175	0.011	167	0.012	176
0.02	175	0.021	166	0.025	136
0.15	61	0.150	60	0.144	58
RMS %	1.29		1.10		1.10

Recovery of a 4-layer model using fixed and free depths is illustrated in Figure 7.2-3 (see also Table 7.2-4). In this case the same initial trial model was used for inversion with fixed and free depths. As can be seen, allowing the depths freedom to vary with the restriction of fixed slab thickness, did not result in a better RMS measure of fit.

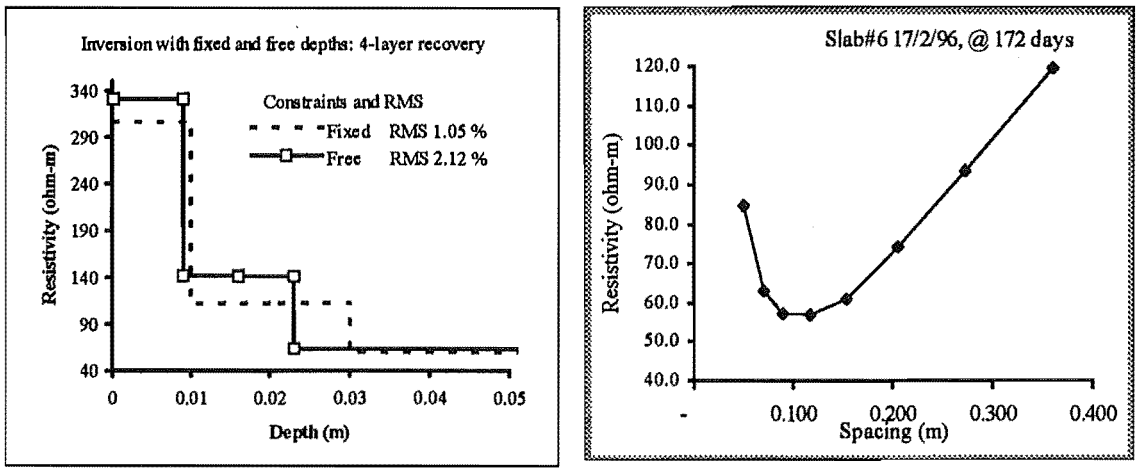

(a) (b)

Figure 7.2-3: (a) Recovery using four layers by inversion with different constraints. Models #1 (fixed depths) and #2 (free depths, fixed slab thickness) were inverted using the same initial trial model. (b) Original VES curve for the inversions discussed here.

Table 7.2-4: Recovery using four layers by inversion with different constraints. Models #1 and #2 were inverted using the same initial trial model.

(c): Four-layer recovery			
	Model #1		Model #2
	Fixed depths		Free depths
	Slab thickness fixed		Slab thickness fixed
Depth (m)	Resistivity (ohm-m)	Depth (m)	Resistivity (ohm-m)
0.01	306	0.009	331
0.02	112	0.016	142
0.03	112	0.023	141
0.15	59	0.150	63
RMS %	1.05		2.12

7.2.3 Inversion with different fixed-layer thicknesses.

The choice of the thicknesses of the layers of the initial trial model can have great effects on the final recovered model. In Table 7.2-5 and Figure 7.2-4, five 5-layer final models with different layer thicknesses are presented. The RMS measure of fit ranges from 1.1% to 6.0%. Except for #4, the models have depths that are logarithmically spaced between the lower surface of the top layer and the bottom of the lowest layer. By increasing the thickness of the top layer (from one mm to 15 mm), a range of layer thicknesses was obtained. In this example, Model#3 is optimal in the sense of giving the best fit to the measured VES curve. Note that only Model#2 retains five distinct layers in the final model.

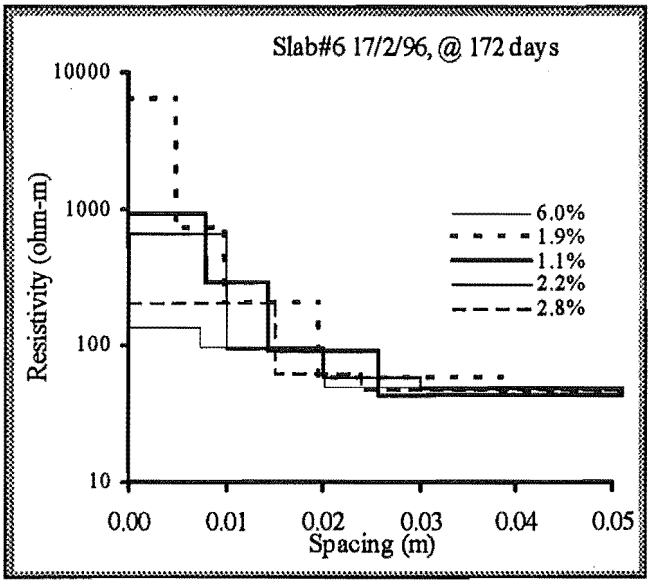

Figure 7.2-4: Profiles recovered using five-layer models with different layer thicknesses. Layer thicknesses were fixed throughout the inversion process.

Table 7.2-5: Recovery of profiles using five-layer fixed depth models with differing layer thicknesses.

Depth to bottom of layer (mm)					Resistivity (ohm-m)				
Model#1	Model#2	Model#3	Model#4	Model#5	Model#1	Model#2	Model#3	Model#4	Model#5
1	5	8	10	15	136	6480	930	659	208
2.7	9.9	14.4	20	23.8	136	729	292	95	63
7.4	19.5	25.8	30	37.7	136	209	91	59	48
20.2	38.5	46.4	40	59.7	99	59	44	48	48
150	150	150	150	150	50	46	44	48	48
				RMS%	6.0%	1.9%	1.1%	2.2%	2.8%

7.2.4 Imposition of the falling profile constraint

The falling profile constraint (FPC) was implemented to preserve the expected profile shape where resistivity falls with depth. Without this constraint, the recovered model tends to follow the shape of the VES curve, reaching a minimum at layer depths somewhere above the slab thickness of 0.15 m. Imposition of the falling profile constraint has the added advantage of reducing the model's sensitivity to noise, which otherwise may be fitted rather well (see Figure 7.2-5 and Figure 7.6-3)

The effect of imposition of the falling profile constraint may be observed by comparing its presence and absence when using the same initial trial model, as in Figure 7.2-5 and Table 7.2-6. Here, the optimal initial trial model from the previous section was used to recover profiles with and without the falling profile constraint. Notice the poorer RMS, the minimum resistivity at around 30 to 50 mm, and the secondary minimum around 10 mm, for the profile recovered without imposing the falling profile constraint.

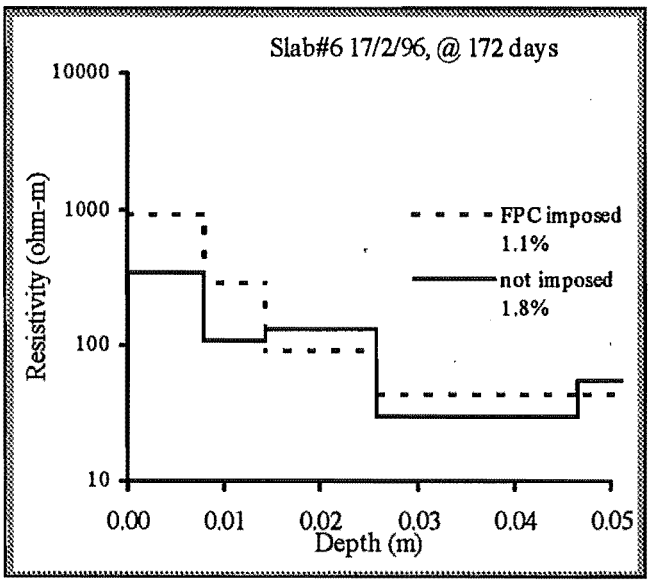

Figure 7.2-5: The effect of imposition of the falling profile constraint on the recovery process.

Table 7.2-6: The effect of imposition of the falling profile constraint on the recovery process.

Depth (mm)	Falling profile constraint	
	Yes	No
8	930.5	346
14	291.7	107
26	91.2	132
46	43.9	30
150	43.9	54
RMS	1.1%	1.8%

7.3 Profiles recovered using a standardised inversion scheme

Sequences of apparent resistivity curves were inverted using **inverjnm.m**. The inversion used a five layer trial model with fixed depths, and the falling profile constraint. The apparent resistivity curves and the recovered five-layer profiles are presented in this section in tabular and graphical form.

The VES curves measured on Slab #5, which had a '665' steel reinforcing mesh embedded at 30mm below the surface, presented particular difficulties for profile recovery. The VES curves and attempts at profile recovery from this slab are presented in Section 7.5.

7.3.1 VES curves and recovered profiles: Slab #3

Table 7.3-1. Vertical electric sounding curves and profiles recovered using five -layer initial trial model, fixed depths and falling profile: slab#3.

Slab #3, Vertical electric sounding curves

Current probe spacing s (m) and apparent resistivity ρ (ohm-m)									
Age (days)	2		9		18		92		228
s	ρ	s	ρ	s	ρ	s	ρ	s	ρ
0.054	27.4	0.050	33.0	0.050	40.4	0.050	50.1	0.050	132.3
0.066	27.3	0.068	33.9	0.068	38.5	0.068	51.9	0.070	71.2
0.078	26.2	0.079	34.8	0.079	38.3	0.079	55.5	0.090	64.0
0.090	27.7	0.092	36.8	0.092	35.8	0.092	53.2	0.117	62.1
0.102	27.7	0.108	36.8	0.108	37.6	0.108	47.6	0.154	65.0
0.120	29.5	0.126	39.3	0.126	37.8	0.146	52.1	0.206	75.8
0.140	30.0	0.146	42.0	0.146	40.2	0.199	59.9	0.272	98.5
0.170	33.3	0.171	45.8	0.171	44.7	0.271	79.2	0.360	129.6
0.200	37.3	0.199	50.5	0.199	51.2				
0.240	44.7	0.232	59.2	0.232	60.2				
0.280	48.5	0.271	68.0	0.271	66.7				
0.330	59.2	0.315	84.1	0.315	70.3				
0.390	73.4	0.368	96.0	0.368	102.6				
		0.429	113.7	0.429	107.1				

Recovered Profiles

Resistivity (ohm-m)					
Depth	Age (days)				
(m)	2	9	18	92	228
0.008	399	339	402	54	9760
0.014	51	38	62	54	691
0.026	24	33	34	54	74
0.046	24	33	33	54	74
0.150	24	33	33	38	44
RMS %	3.7%	7.9%	5.5%	4.6%	1.3%

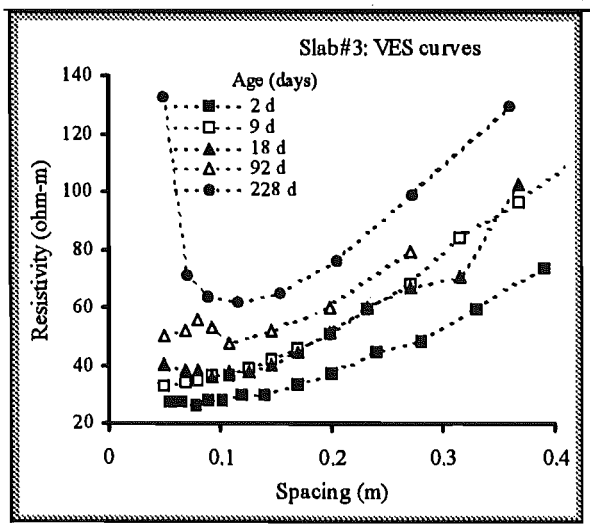

Figure 7.3.1-1.VES curves Slab#3.

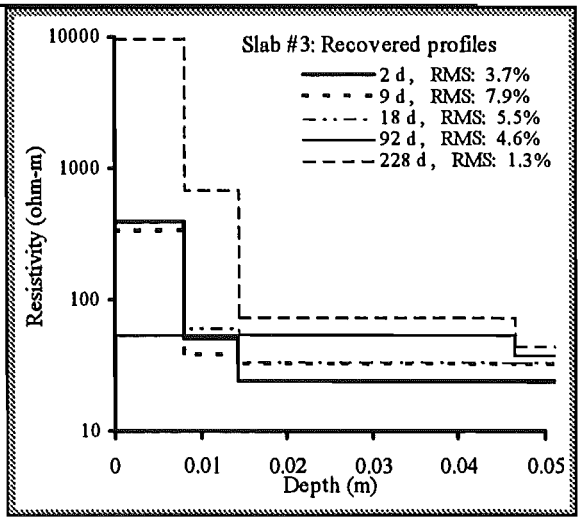

Figure 7.3.1-2. Profiles recovered using five -layer initial trial model, fixed depths and falling profile: slab#3.

7.3.2 VES curves and recovered profiles: Slab #6

Table 7.3-2. Vertical electric sounding curves and profiles recovered using five -layer initial trial model, fixed depths and falling profile: slab#6.

Slab #6, Vertical electric sounding curves, Apparent resistivity (ohm-m)					
Spacing (m)	Age(days): 163	172	189	229	258
0.050	90.6	84.2	99.0	102.9	239.6
0.070	61.6	63.1	75.0	70.1	91.5
0.090	53.7	57.3	72.3	64.3	82.3
0.117	53.5	57.0	67.7	65.9	81.2
0.154	58.1	60.9	85.2	69.1	83.2
0.206	70.1	75.0	114.5	91.2	101.3
0.272	90.0	96.7	146.6	115.5	129.3
0.360	119.4	129.1	145.2	159.4	170.6

Recovered profiles.					
Depth (m)	Resistivity (ohm-m)				
0.01	831	549	1029	1334	10017
0.02	116	100	91	106	89
0.03	61	61	64	62	84
0.04	45	47	63	55	84
0.15	43	46	63	55	62
RMS %	**0.9**	**1.7**	**9.1**	**3.9**	**2.1**

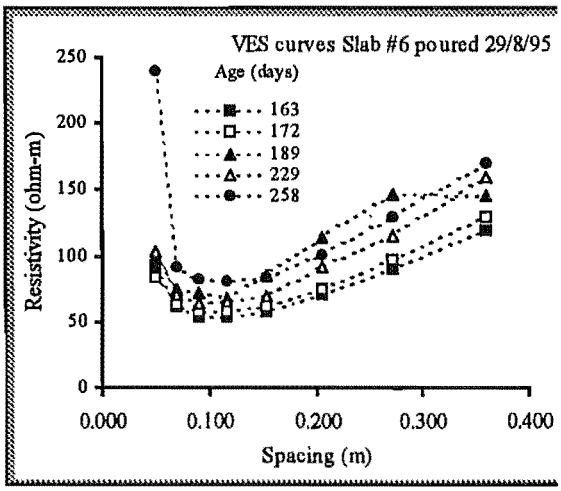

Figure 7.3.2-1.VES curves Slab#6.

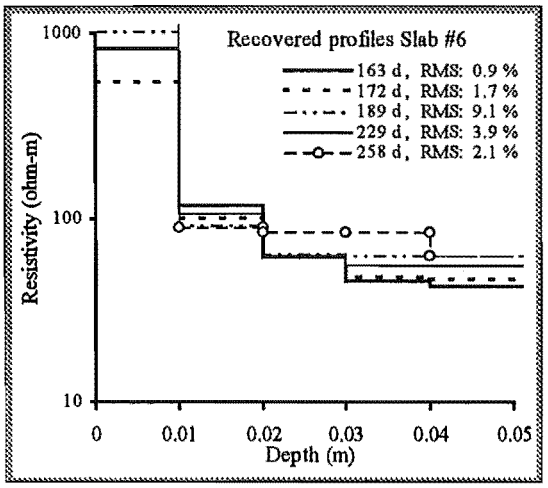

Figure 7.3.2-2. Profiles recovered using five -layer initial trial model, fixed depths and falling profile: slab#6.

7.3.3 VES curves and recovered profiles: Slab #7

Table 7.3-3.VES curves and profiles recovered using five -layer initial trial model, fixed depths and falling profile: slab#7 (Poured 10/10/95)

Slab #7, Vertical electric sounding curves, Apparent resistivity (ohm-m)					
Spacing (m)	Age(days): 121	130	147	187	217
0.050	53.2	54.4	56.7	63.4	88.3
0.070	45.5	46.9	51.4	54.2	68.4
0.090	42.5	43.5	46.9	51.4	58.5
0.117	41.6	42.3	45.7	50.3	61.1
0.154	42.9	45.0	48.7	52.8	67.9
0.206	51.5	53.6	60.4	63.8	81.4
0.272	67.2	73.0	71.5	82.1	105.4
0.360	92.3	89.4	101.1	108.4	138.7

Recovered profiles.					
Depth (m)	Resistivity (ohm-m)				
0.01	103	105	89	130	608
0.02	65	68	70	67	104
0.03	46	46	51	56	63
0.04	33	34	38	56	50
0.15	33	34	37	43	50
RMS %	**2.7**	**2.4**	**2.6**	**2.8**	**2.3**

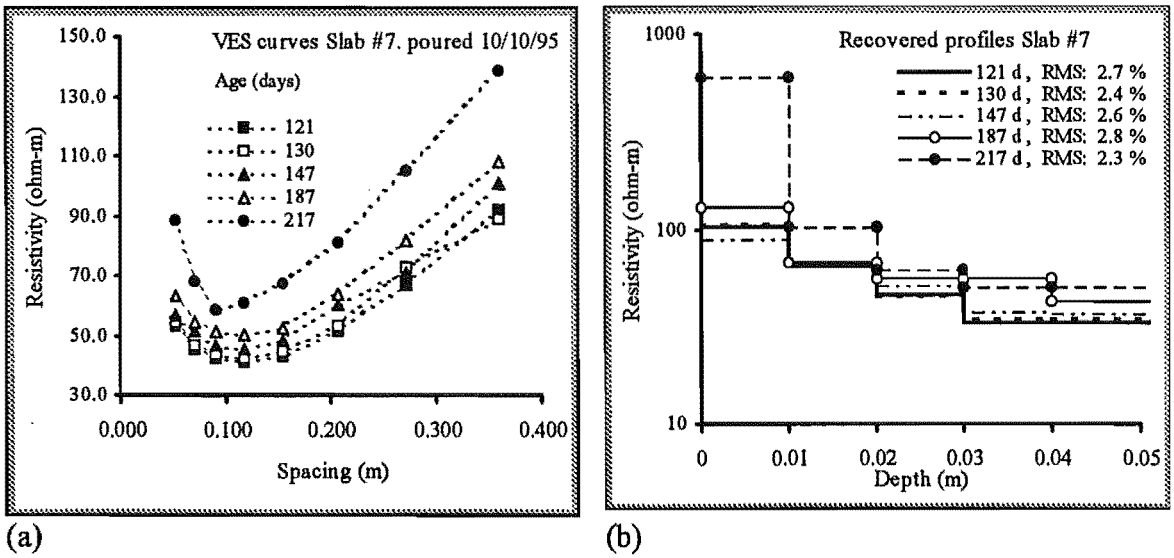

(a) (b)

Figure 7.3.3-1: (a) VES curves and (b) profiles recovered using five -layer initial trial model, fixed depths and falling profile: slab#7

7.3.4 VES curves and recovered profiles: Slab #8

Table 7.3-4: VES curves and profiles recovered using five -layer initial trial model, fixed depths and falling profile: slab#8

Slab #8, Vertical electric sounding curves

	Apparent resistivity (ohm-m)					
Spacing	Age (days)					
(m)	16	24	28	46	86	116
0.050	50.7	70.3	69.0	76.2	86.2	106.9
0.070	47.1	59.9	61.3	66.7	78.7	85.6
0.090	46.1	56.4	56.3	64.3	70.2	79.7
0.117	45.3	54.6	56.3	62.6	69.0	75.2
0.154	48.7	58.7	59.1	67.4	72.6	79.9
0.206	56.8	69.1	70.9	80.2	86.7	95.1
0.272	70.8	88.8	88.7	104.2	111.0	120.7
0.360	109.3	118.7	114.3	134.1	143.3	152.7

	Recovered profiles.					
Depth (m)	Resistivity (ohm-m)					
0.01	82	167	108	175	136	571
0.02	57	74	82	76	98	94
0.03	44	69	62	74	90	94
0.04	40	44	50	54	58	94
0.15	38	43	44	50	53	56
RMS %	**4.77**	**1.26**	**0.77**	**1.17**	**1.49**	**1.08**

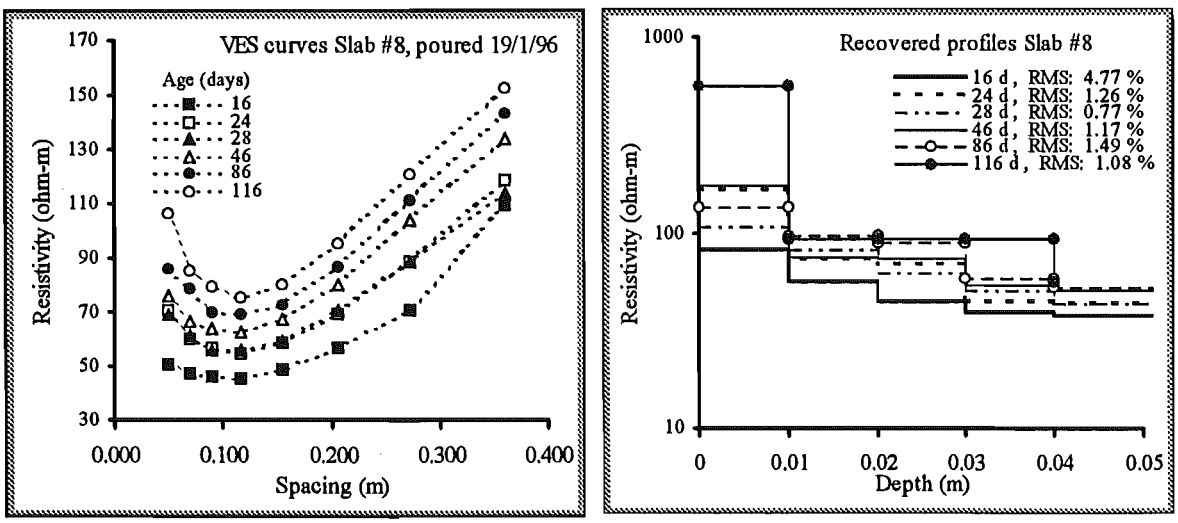

(a) (b)

Figure 7.3.4-1: (a) VES curves and (b) profiles recovered using five -layer initial trial model, fixed depths and falling profile: slab#8

7.4 Comparison of directly (HES) and indirectly (VES) recovered profiles

The method of directly measuring resistivity profiles using horizontal electrode systems (HES) is described in Chapters 4 and 8. In Chapter 8, the profiles measured in this way are presented and compared in an effort to evaluate the precision, if not the accuracy, of the method. That is, the uncertainty associated with use of the horizontal electrode systems is explored in the comparison of profiles determined from the same concrete samples, or from samples having identical mix and drying conditions.

The original purposes of horizontal electrode systems were two-fold, namely as means of

1. evaluating profiles recovered using vertical electric sounding and
2. determining the relationship between resistivity and relative-humidity (or calibration of the resistivity profiles).

The second purpose is addressed in Chapter 9, the first is addressed here.

In fact, it is not a particularly straightforward matter to compare the two methods of measuring resistivity profiles, although there are a number of ways in which it may be attempted.

1. The profiles may be graphically superimposed and compared visually.
2. The VES curves generated from the two profiles may be compared graphically and numerically by calculation of the RMS measure of fit.
3. The stepped (or layered) profiles recovered indirectly using the VES method can be converted to a continuous profile and compared graphically and numerically by calculation of the RMS measure of fit.

The first of these is presented in Section 7.4.1. The second two methods both involve continuous profiles. It is assumed that the data points of HES derived profiles lie on a continuous curve representing the true (locally averaged) resistivity profile. To generate a VES curve from it, the data must be transformed to represent the resistivity of a discrete number of layers of uniform resistivity. Methods for achieving this are discussed in Chapter 5 Section 5.5-4. Some comparisons are made for Slabs #6, #7 and #8 are presented in Section 7.4.1.6 using model VES curves derived from HES#2 profiles.

Conversion from a stepped to a continuous profile is more difficult where the number of layers in the stepped profile is comparatively small. Some conversion schemes are considered in Section 7.5.

7.4.1 Graphical superposition of directly and indirectly derived profiles

7.4.1.1 Slab #3

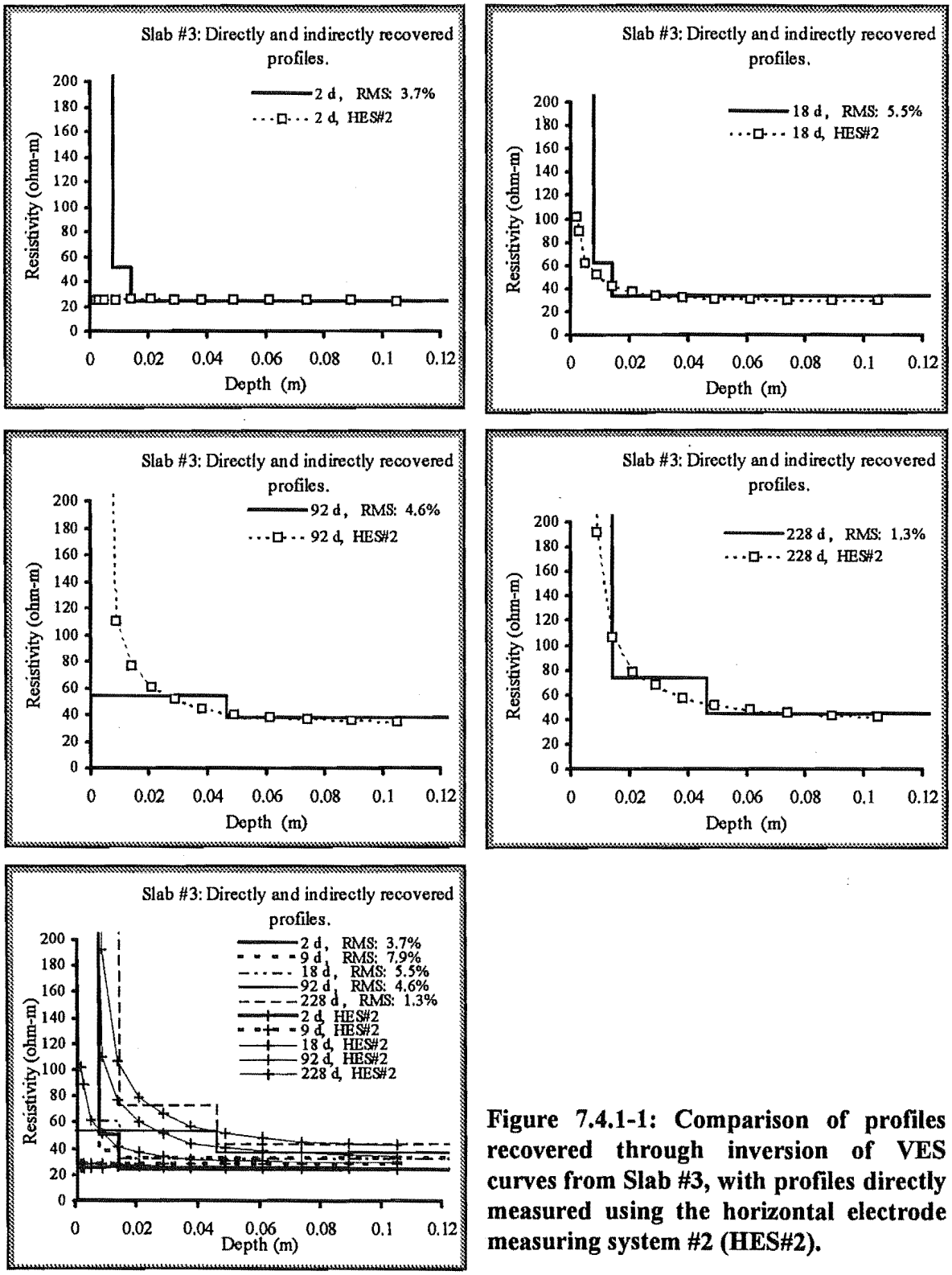

Figure 7.4.1-1: Comparison of profiles recovered through inversion of VES curves from Slab #3, with profiles directly measured using the horizontal electrode measuring system #2 (HES#2).

7.4.1.2 Slab #6

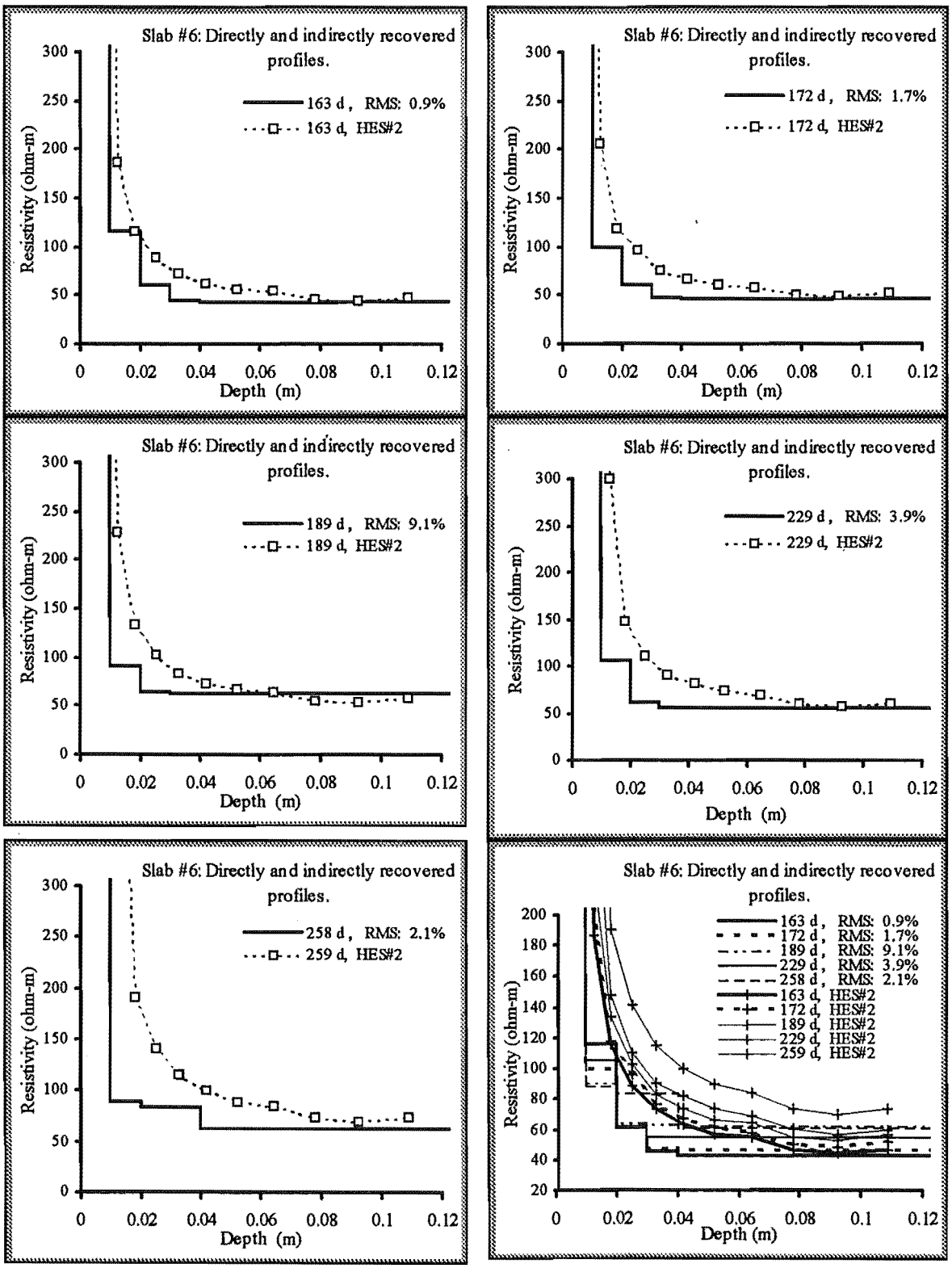

Figure 7.4.1-2: Comparison of profiles recovered through inversion of VES curves, with profiles directly measured using the horizontal electrode measuring system #2 (HES#2).

7.4.1.3 Slab #7

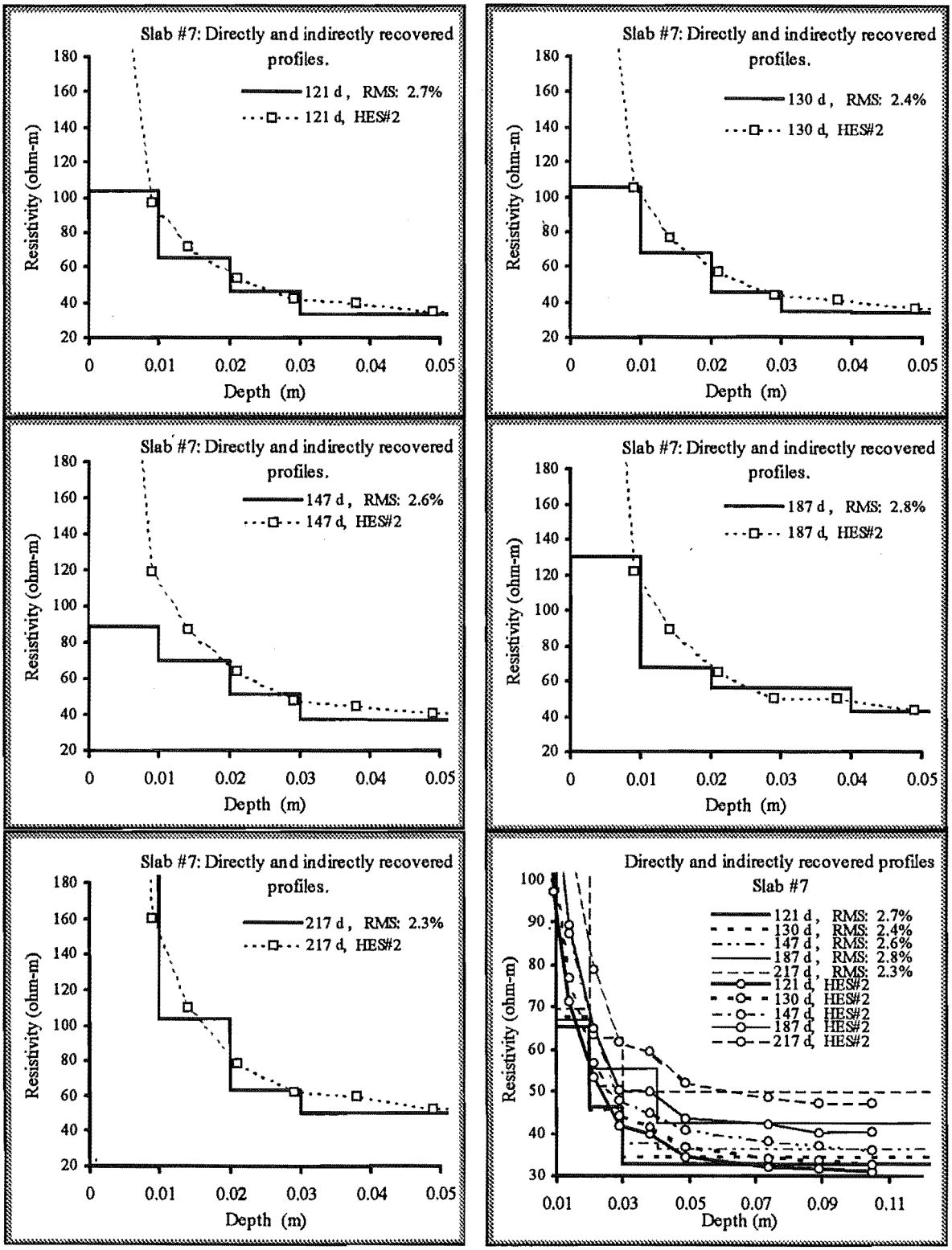

Figure 7.4.1-3: Comparison of profiles recovered through inversion of VES curves, with profiles directly measured using the horizontal electrode measuring system #2 (HES#2).

7.4.1.4 Slab #8

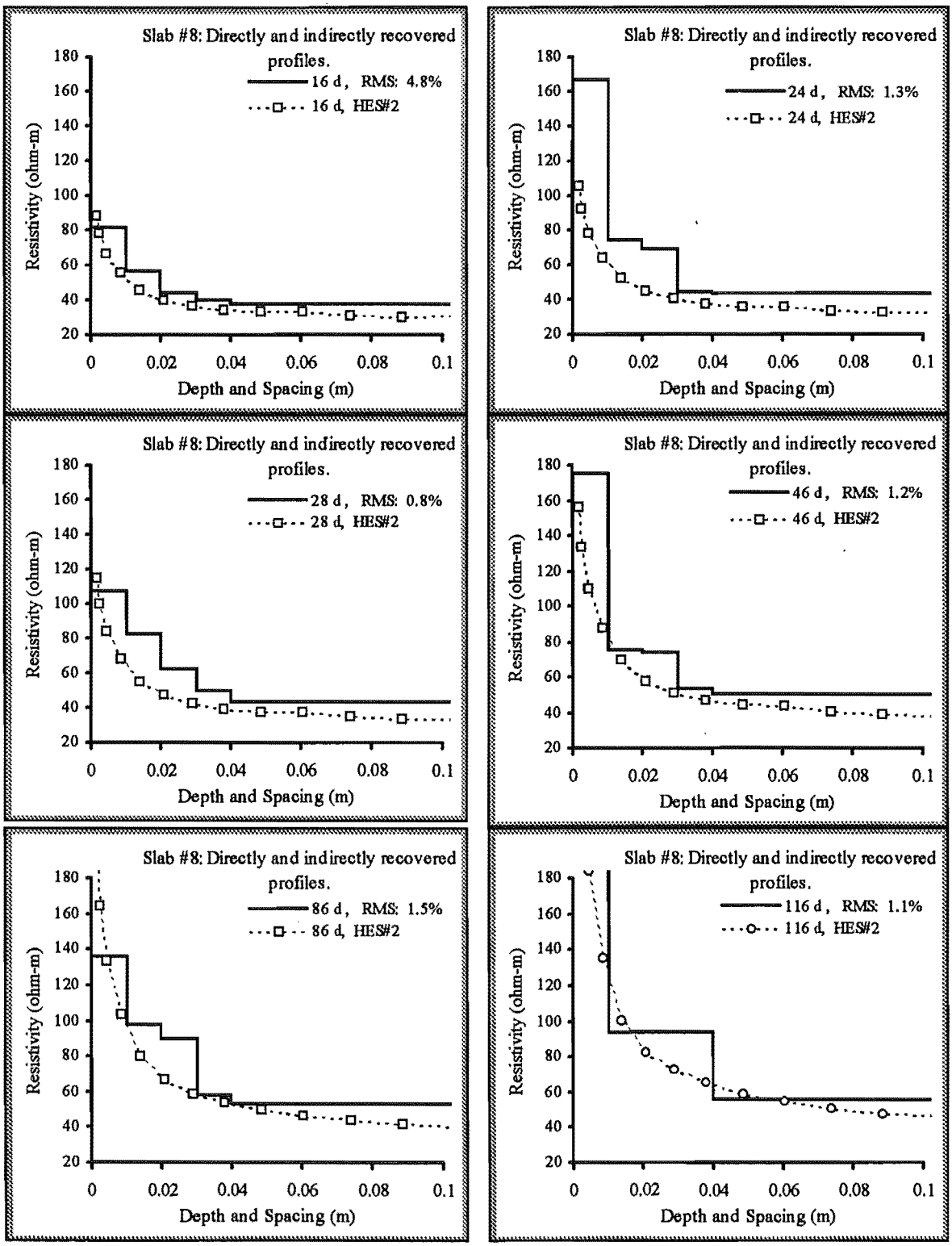

Figure 7.4.1-4: Comparison of profiles recovered through inversion of VES curves, with profiles directly measured using the horizontal electrode measuring system #2 (HES#2).

7.4.1.5 Slab #8, comparison of indirectly recovered (VES) profiles with corrected HES profiles

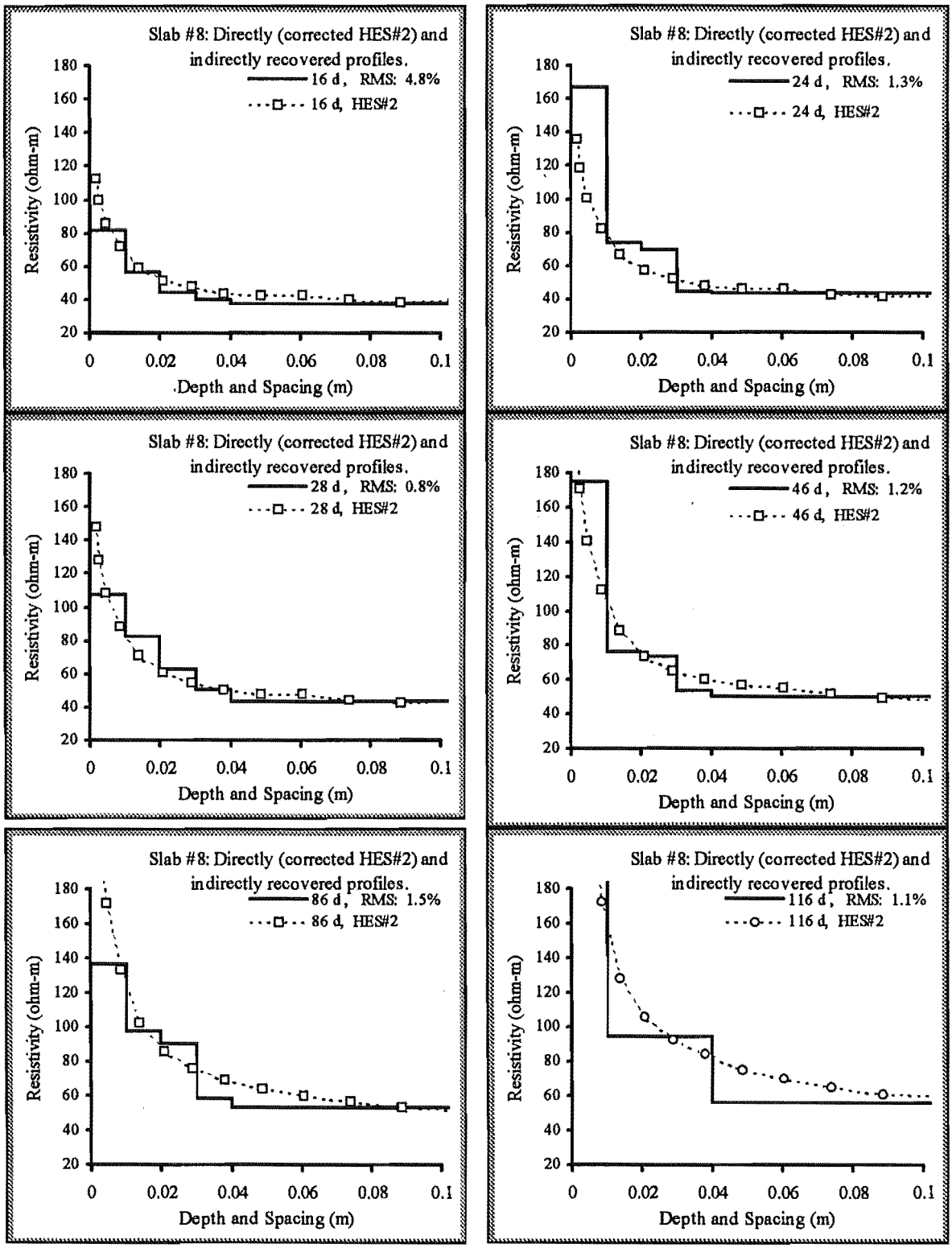

Figure 7.4.1-5: Comparison of profiles recovered through inversion of VES curves, with directly measured (HES#2) profiles scaled up by a factor of 1.3.

7.4.1.6 Slab #8, Zohdy's method: comparison of profiles recovered using inverjnz.m with those recovered using invernm.m and with corrected HES profiles

Generally the use of inverjnz.m, the recovery program based on Zohdy's (1989) method, did not seem to recover profiles as well as inverjnm.m (based on Merrick (1977), although when the VES curves recovered were well formed the profiles were recovered with a nearly as good a fit. To illustrate I include here some of the best Zohdy-type recovered profiles with those recovered using inverjnm.m and those recovered directly using the HES#2.

Notice the agreement in the resistivity of the lowest layer of the two indirectly recovered profiles.

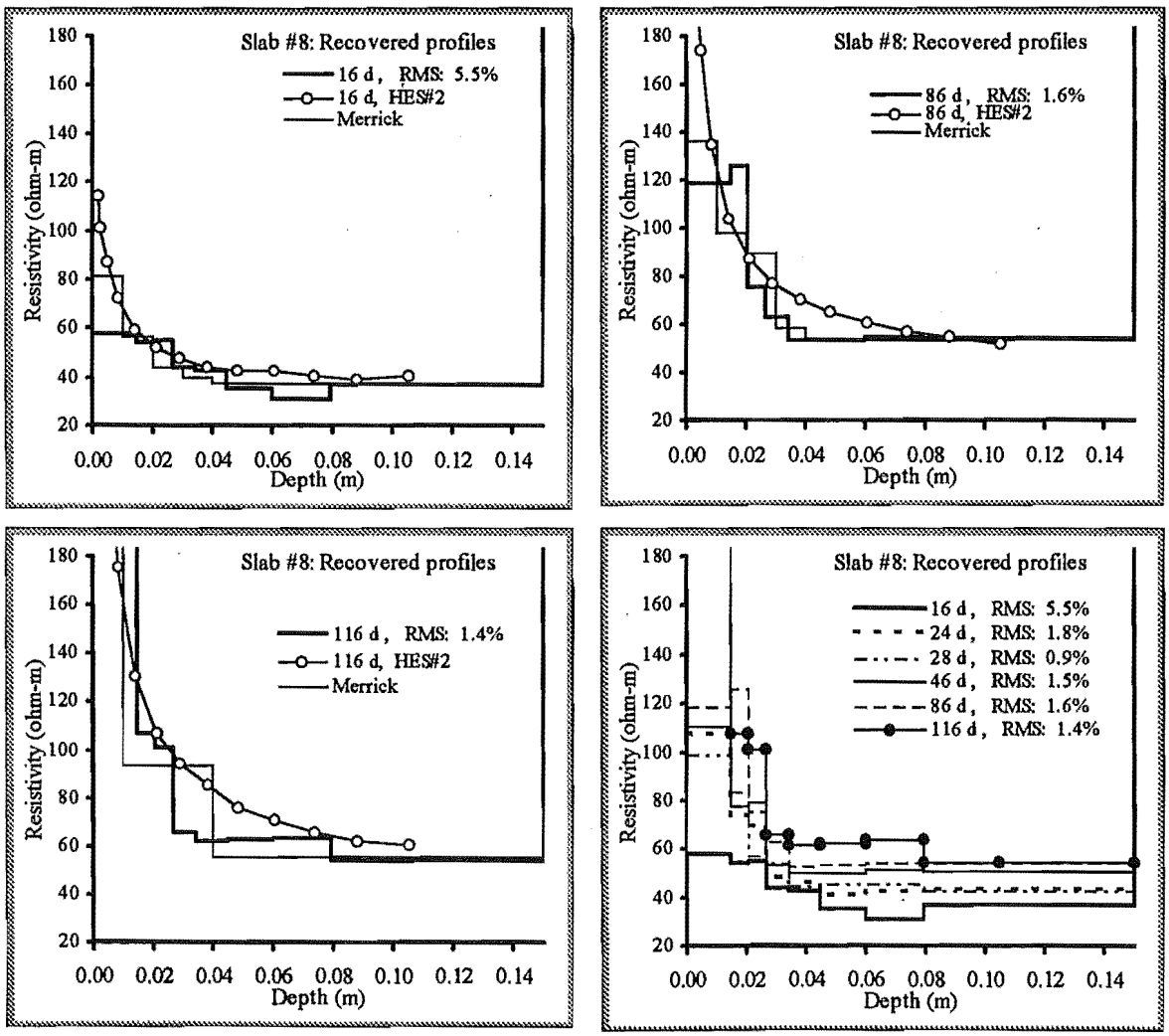

Figure 7.4.1-6: First three graphs: comparison of profiles recovered using Zohdy's (1989) method (*inverjnz.m: thick line in graph)* with those recovered using Merrick's (1977) method (*inverjnm.m: thin line*) and with directly measured (HES#2) profiles scaled up by a factor of 1.3 (open circles). The Merrick profiles have RMS values of 4.8%, 1.2% and 1.1% respectively. The bottom right graph presents the complete set of Zohdy-type recovered profiles from Slab #8.

7.4.2 Graphical superposition and numerical comparison of VES curves from directly and indirectly derived profiles

The RMS values in the Figure 7.4.2-2 reveal quite a large disparity between the apparent resistivity curves modelled from the directly measured profiles (VES exHES), and those determined by vertical electric sounding on the concrete slab (VES). However, if the VES data is divided by the VES exHES data, point for point, it becomes apparent that a large part of the disparity can be attributed to a constant scale factor. Such a constant scaling error is more likely to arise from error at the time of calibration of the HES (see Chapter 8), rather than from the VES technique. A calibration error would tend affect all subsequent measurements in the same direction whereas error associated with vertical electric sounding would be likely to be more evenly (if randomly) scattered around the mean.

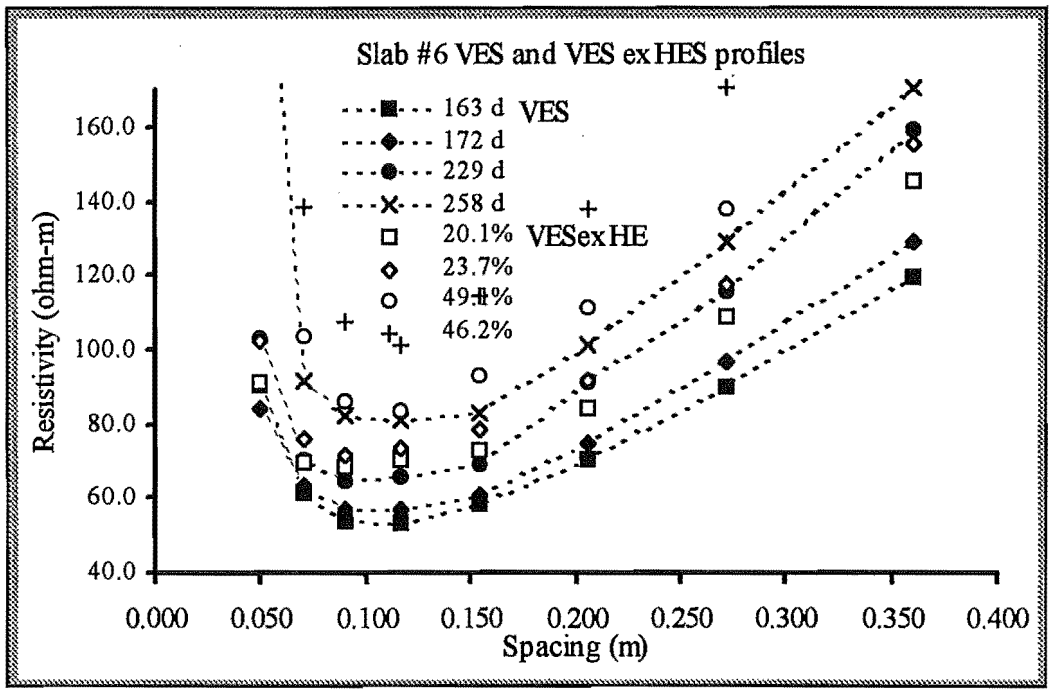

Figure 7.4.2-1: Comparisons for Slab #6: model VES curves generated from HES#2 profiles superimposed on VES curves (dotted lines) measured using the vertical electric sounding technique . The disparity (given as a RMS value) is quite large.

The VES data measured at the smallest current probe spacing accounts for another substantial part of the disparity. Reasons for greater data scatter at smaller spacings have been advanced in Chapter 6. If, the HES profiles are scaled, and the smallest current probe spacing data is eliminated from the comparisons, the VES curves show more agreement (see Figure 7.4.2-2 and Table 7.4-1 below).

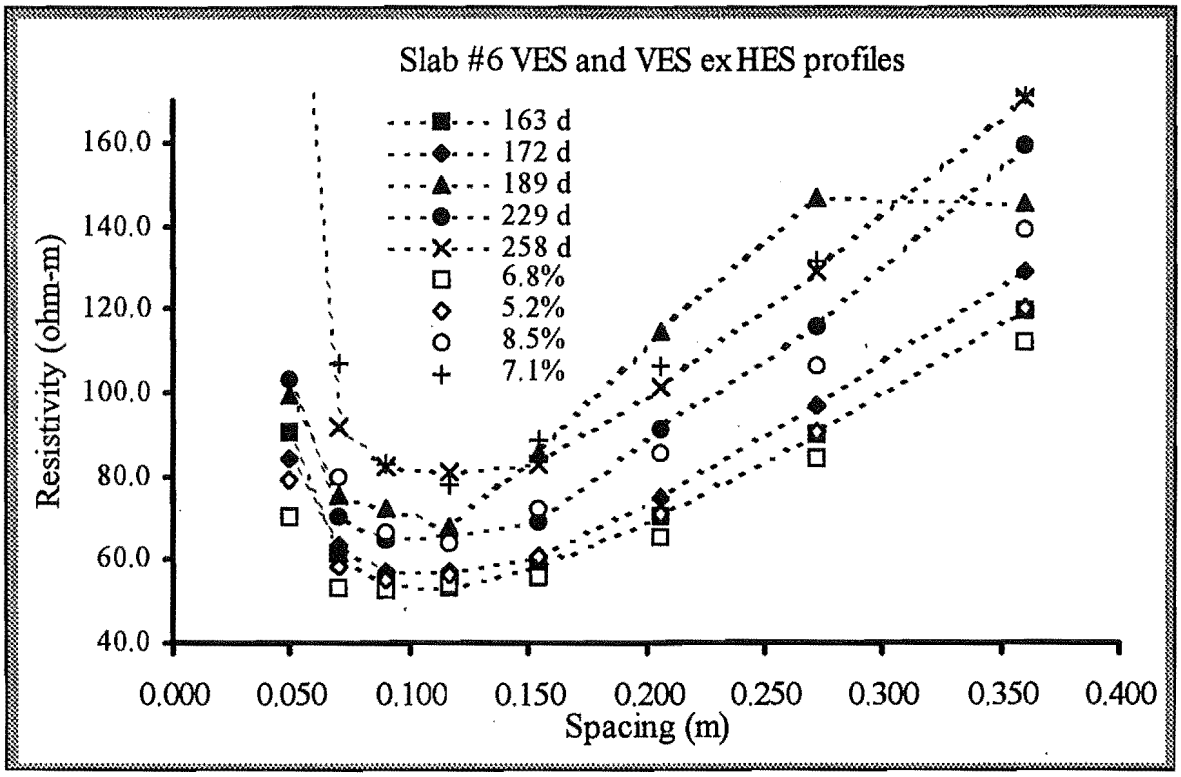

Figure 7.4.2-2: Slab #6 comparisons of measured VES (dotted) and model VES curves (VES exHES), which have been scaled down by a factor of 0.77. The RMS values are smaller because the curves are now aligned more closely and also because the data points for the smallest current-probe spacing have been eliminated.

Table 7.4-1: Evaluating VES curves from Slab #6 by comparing them with model VES curves derived from HES profiles. The RMS for the fit of the recovered profile to the VES is include for comparison.

RMS%	*Age of slab at the time of measurement (days).*			
	163	172	229	259
Recovered profile fit to VES	0.9%	1.7%	3.9%	2.1%
VES and VES exHES	20.1%	23.7%	49.1%	46.2%
VES and scaled VES exHES (scale factor 0.77)	10.2%	5.3%	45.7%	27.3%
VES and scaled VES exHES with the smallest spacing data point excluded	6.8%	5.2%	8.5%	7.1%

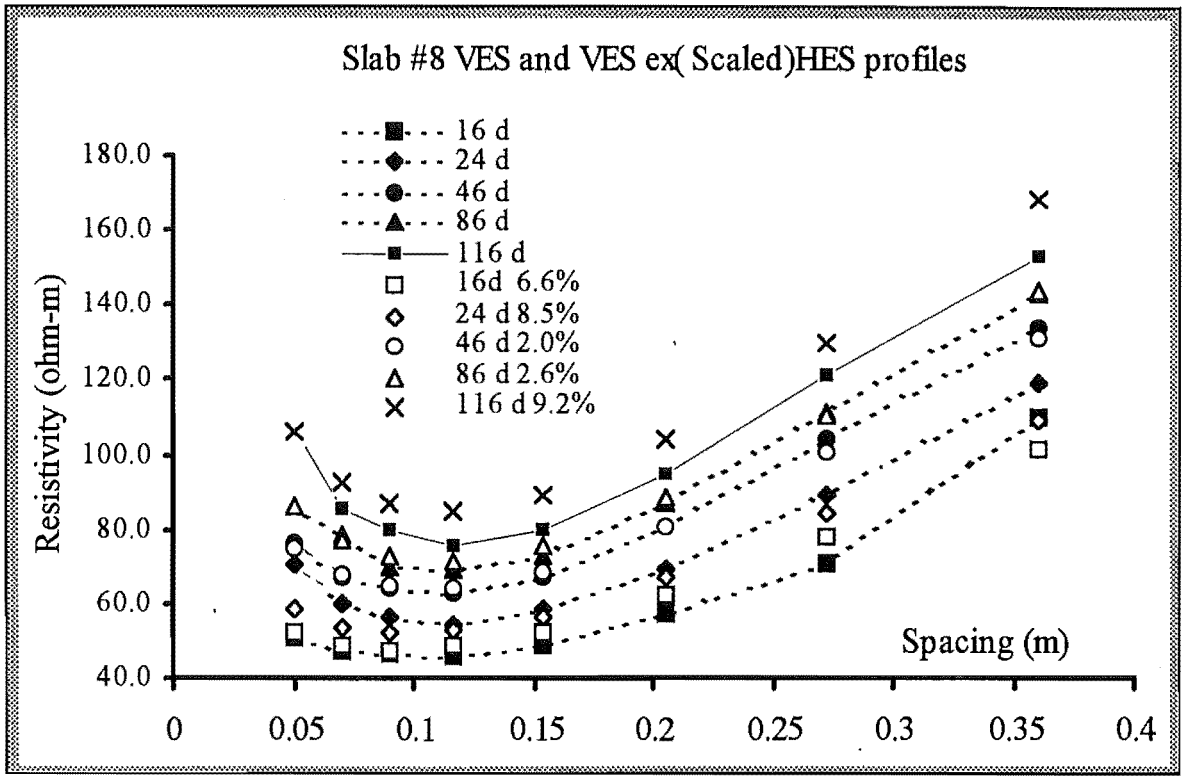

Figure 7.4.2-3: Slab #8 comparisons between actual VES curves (dotted) and those derived from scaled HES profiles. The RMS values include comparisons of the smallest spacing data points.

A similar analysis for the HES profiles and VES curves from Slab #8, suggests the need for a scaling *up* of the HES profiles, but comparatively little small-spacing data point error.

Table 7.4-2: Evaluating VES curves from Slab #8 by comparing them with model VES curves derived from HES profiles.

RMS%	*Age of slab at the time of measurement (days).*					
	16	24	28	46	86	116
Recovered profile fit to VES	4.8%	1.3%	0.8%	1.2%	1.5%	1.1%
VES and VES exHES	16.3%	25.3%	22.5%	19.3%	18.2%	12.8%
VES and scaled VES exHES (scalel factor 1.27)	6.6%	8.5%	5.2%	2.0%	2.6%	9.2%
VES and scaled VES exHES with the smallest spacing data point excluded	6.9%	6.5%	3.8%	2.1%	2.8%	9.9%

The HES profiles measured from Slab#7, require no scaling.

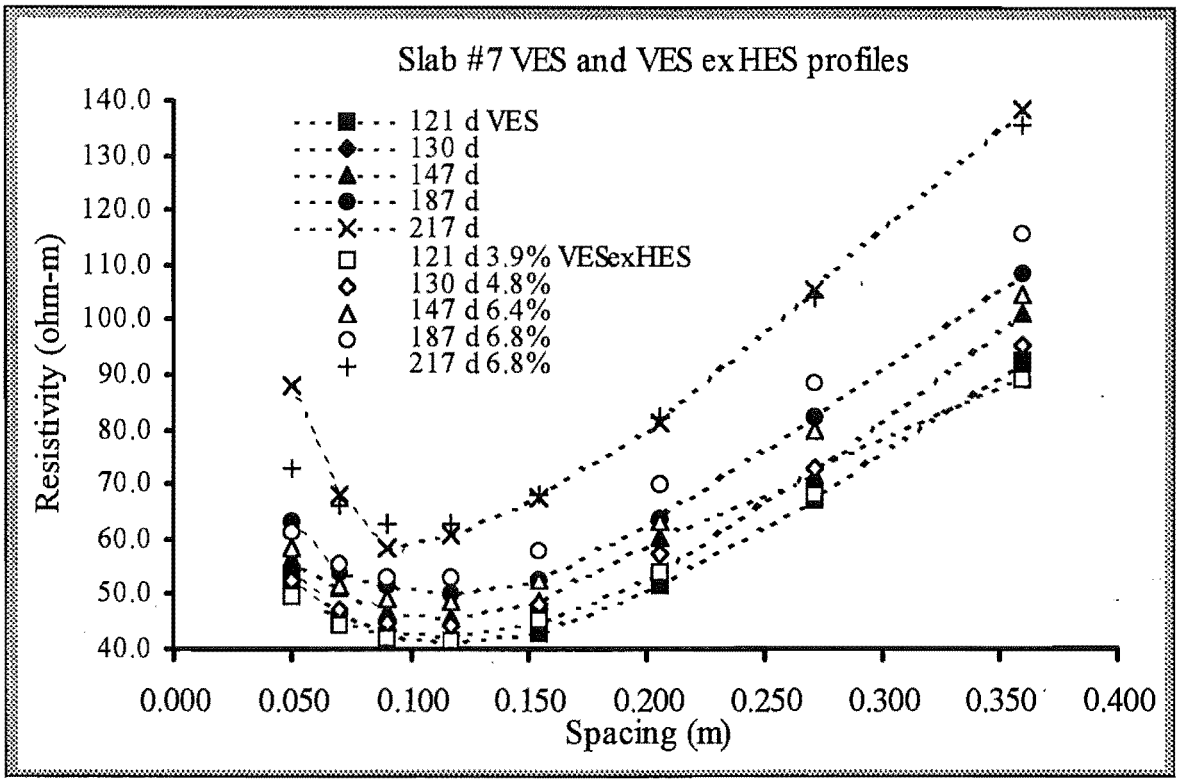

Figure 7.4.2-4: Slab #7 comparisons between actual VES curves and those derived from HES profiles. The RMS values include comparisons of the smallest spacing data points.

Table 7.4-3: Evaluating VES curves from Slab #7 by comparing them with model VES curves derived from HES profiles.

RMS%	*Age of slab at the time of measurement (days).*				
	121	130	147	187	217
Recovered profile fit to VES	2.7%	2.4%	2.6%	2.8%	2.3%
VES and VES exHES	3.9%	4.8%	6.4%	6.8%	6.8%
VES and VES exHES with the smallest spacing data point excluded	3.3%	5.0%	6.7%	7.2%	3.4%

7.5 The effect of reinforcement: VES curves and recovered profiles for Slab #5

7.5.1 VES curves

The vertical electric sounding curves measured from the reinforced Slab #5 are markedly different from those measured on non-reinforced slabs. Two views of typical VES curves are shown in Figure 7.5.1-1. The presence of reinforcing in Slab #5 has resulted in a drastic lowering of apparent resistivity compared to the non-reinforced but otherwise equivalent Slab #4. This is the behaviour predicted in Chapter 5. The right hand graph reveals the scatter in data points in what might from the left hand graph, seem fairly smooth curves. The apparent resistivity may be lower than that measured , because the resistivity meter was at the limits of its resolution. The individual VES curves are, of all VES curves measured, the least distinguishable from one another although there seems to be a slight progression or lifting of the curve with time.

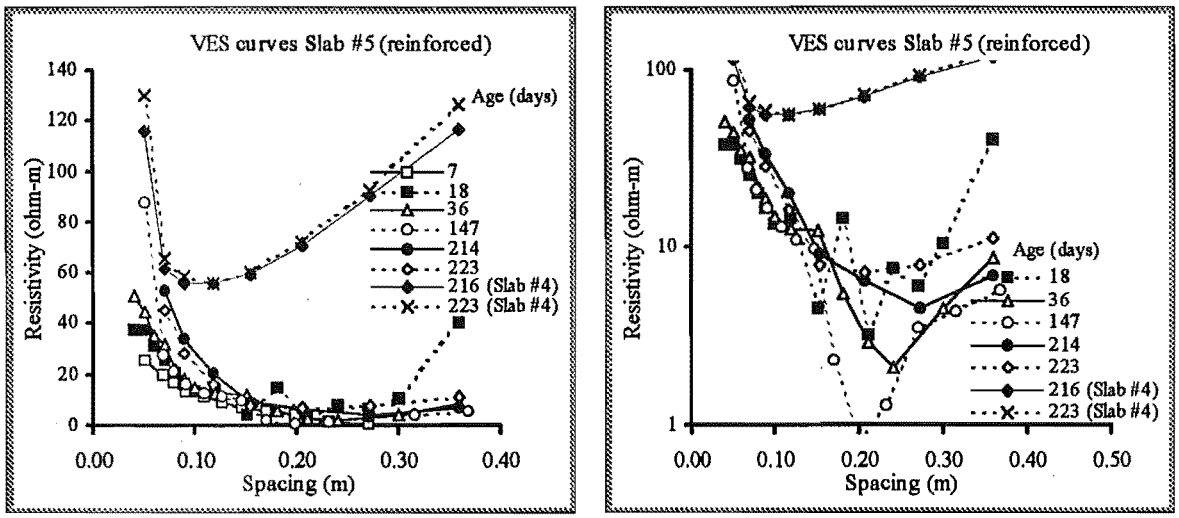

Figure 7.5.1-1: VES curves measured from Slab #4 and the reinforced Slab #5. Each of these curves is the result of averaging and combining at least 6 separate VES curves.

The 100 mm mesh means a weakening of the approximation to the horizontal uniformity of the layers assumed by the vertical electric sounding recovery program. The presence of a reinforcing bar directly beneath the electrode array should result in lower apparent resistivity than to one or the other side of the bar. The VES instrument was not sensitive enough to distinguish a horizontal positioning effect from the quite large scatter.

7.5.2 Profile recovery

Profiles from Slab #5 measured using the embedded horizontal electrode systems (see Chapter 8) do not differ significantly from the equivalent non-reinforced Slab #4 poured from the same mix at the same time. The embedded electrode system was placed in an non-reinforced area of the slab. It is assumed that the presence of reinforcing creates a horizontal layer which has a very low average resistivity of thickness equal to that of the reinforcing - about 5 to 10 mm. By providing highly conductive path for current to follow during vertical electric sounding, the layer acts to shield or screen the deeper areas of concrete from investigation. This effect is similar to the swamping effect of the highly resistive lower boundary of concrete at its base.

Imposition of the falling profile constraint (FPC), fixing of the total thickness of the slab and setting the sublayer resistivity at a very high value enabled good recovery of profiles in the region near the lower boundary.

The attempt to recover profiles from Slab #5 VES curves has involved several constraints and conditions.

1. Imposition of a highly conductive (0.1 1.0 ohm-m) fixed layer of about 1 mm at a depth of 30 mm below the surface.
2. Imposition of the falling profile constraint.
3. Smoothing of the VES curves.
4. Use of Zohdy's (1989) method (see Chapter 5).

Consider first, profile inversion with the first three conditions shown in the left hand graph of Figure 7.5.2-1. The imposed reinforced layer is indicated by an arrow and has a resistivity of one ohm-m. The profile falls to well below the directly measured HES#2 profile. When the falling profile constraint is removed (right hand graph), the resistivity first increases and then decreases as the depth increases. Beyond the reinforced layer the profile first decreases further and then rises to about 4 M-ohm-m. While this profile fits the data with a smaller RMS, both profiles are clearly not realistic, and do not match the directly measured profiles at all well. There is a clear advantage in using the falling profile constraint (see also the lower left graph of Figure 7.5.2-2).

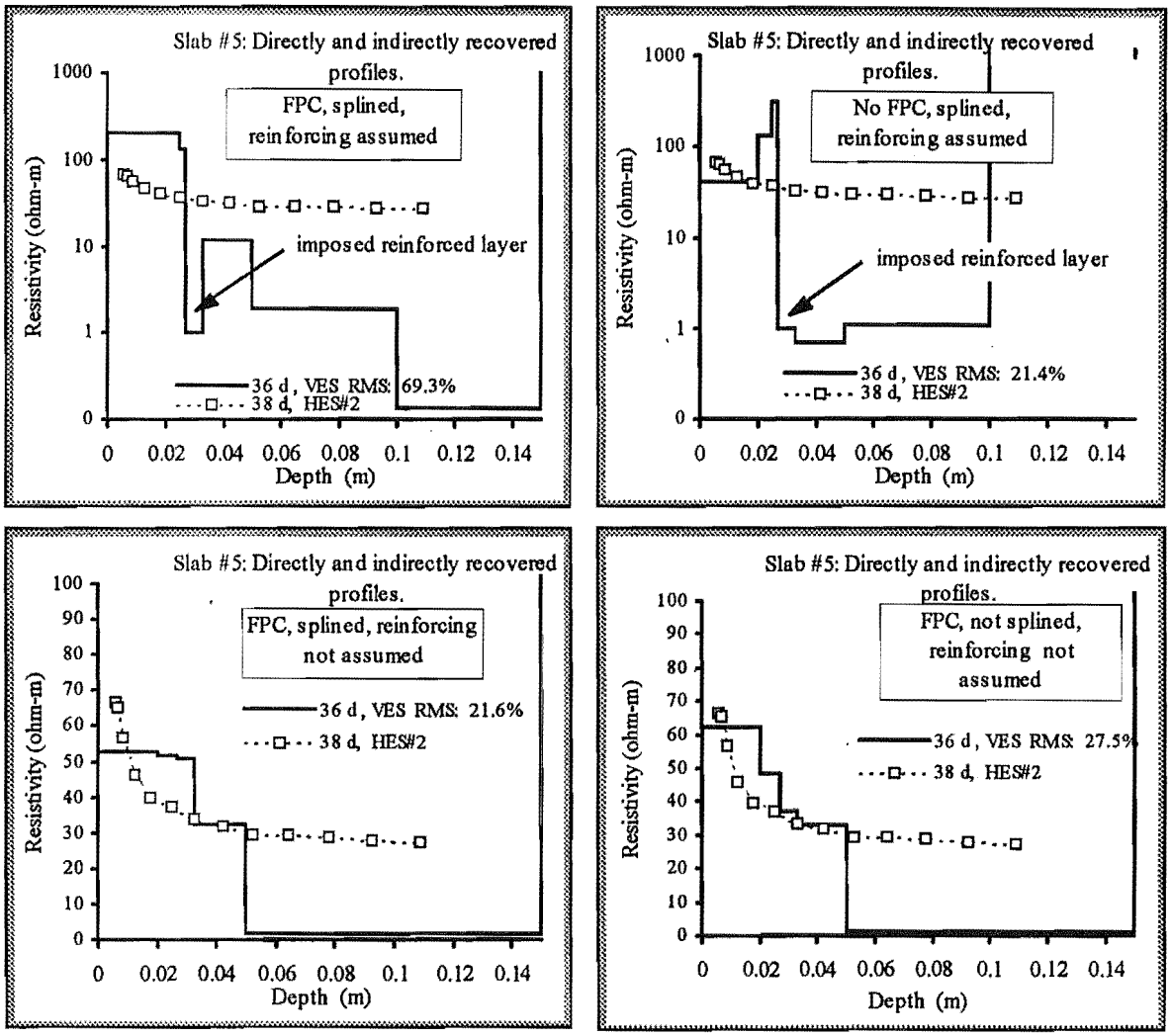

Figure 7.5.2-1: Recovery from Slab #5 at 36 days, with imposition of three conditions (falling profile constraint - except top right, smoothing of data - except lower right and highly conductive reinforced layer condition - except lower two graphs). The corresponding directly measured (HES#2) profile is shown in each graph for comparison.

Comparison of the two left-hand graphs of Figure 7.5.2-1, show that, removal of the reinforced layer constraint, allows a better fit to the VES curve. The resulting profile also shows more agreement with the HES#2 profile at depths less than 0.05 m. Below 0.05 m the resistivity is unrealistically low (about one ohm-m). Generally there is no advantage in imposition of the reinforced layer since the inversion program tends to interpret the VES curve as indicating low resistivity at a depth greater than the actual depth of reinforcing (see also the top two graphs in Figure 7.5.2-2).

The lower right-hand graph shows the effect of using raw rather than smoothed VES curves. Not surprisingly the RMS fit is poorer than the equivalent recovery of smoothed data (lower left-hand graph). However the profile is more realistic. As indicated earlier in

this chapter, there is very little advantage to be gained in smoothing the VES curves. Imposition of the falling profile constraint generally enables the inversion program to take best advantage of the recovered profile, effectively filtering the curve better than any smoothing function could. The apparently better fit (lower RMS) yielded by inversion of smoothed data is because the recovered model's VES curve may match the smoothed VES curve well without fitting the raw curve (see Figure 7.5.2-3).

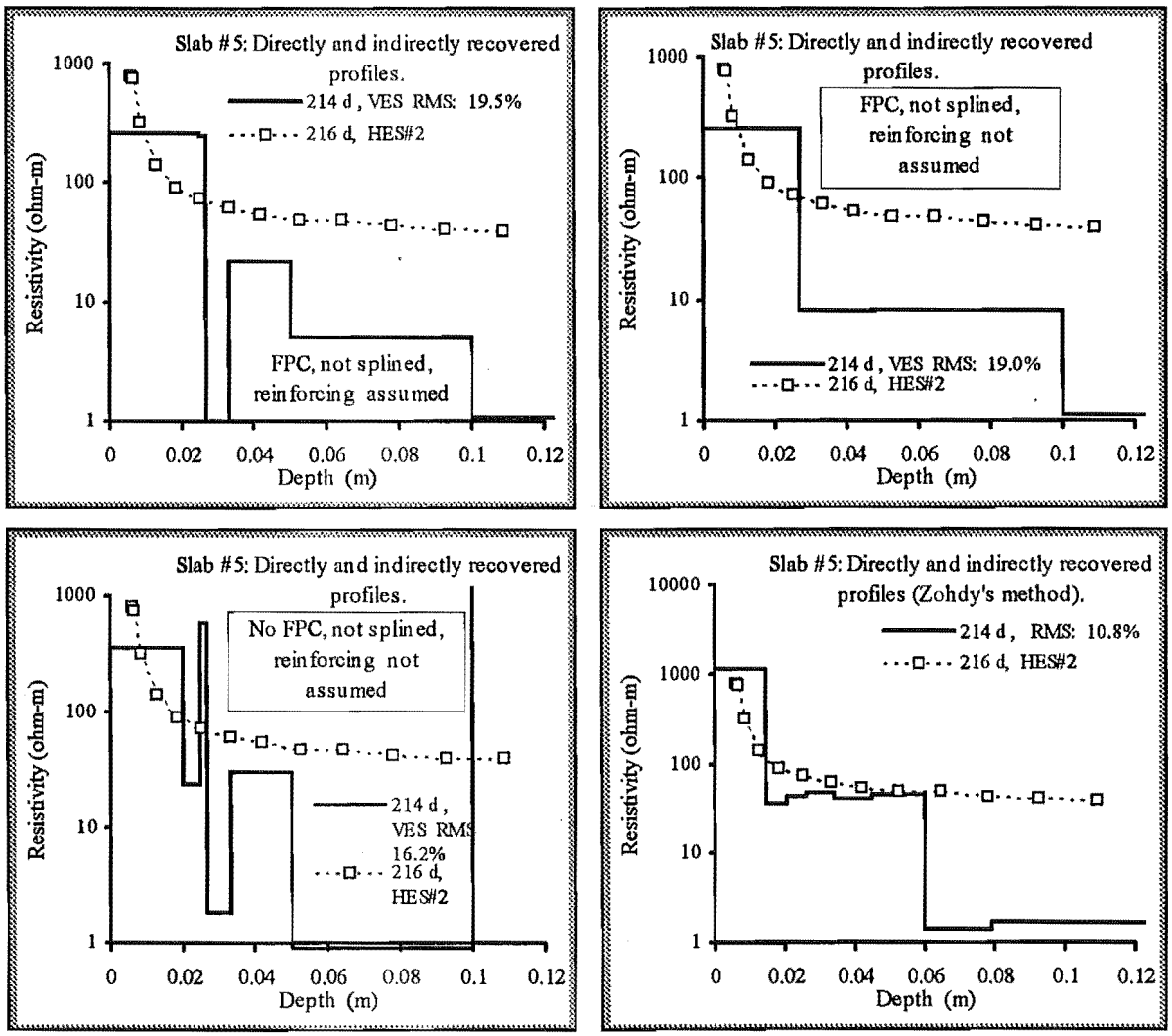

Figure 7.5.2-2: Recovery from Slab #5 at 214 days, with imposition of two conditions (falling profile constraint - except lower left and highly conductive reinforced layer condition - top left only). The corresponding directly measured (HES#2) profile is shown in each graph for comparison. The lower right graph shows the results of inversion using inverjnz.m, the program based on Zohdy's (1989) method. In this case inversion is of raw VES data using a loose imposition of the falling profile constraint.

The lower right graph of Figure 7.5.2-2 shows the results of inversion using inverjnz.m, the program based on Zohdy's (1989) method. This program strikes the same difficulties as the Merrick (1977) based program, inverjnm.m.

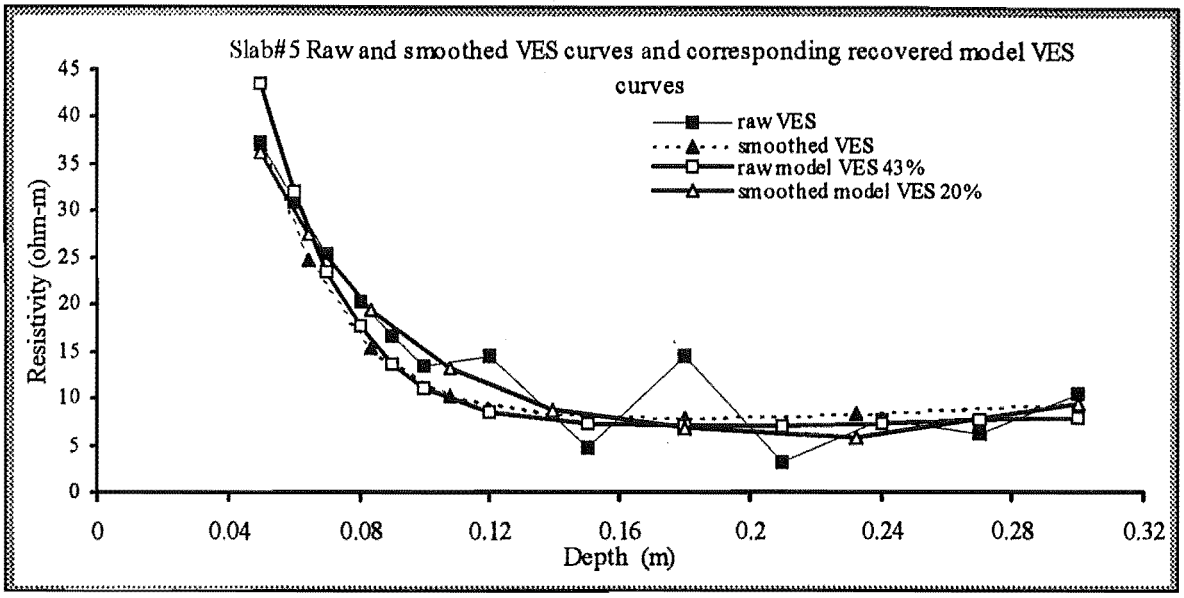

Figure 7.5.2-3: Raw and smoothed VES curves and their corresponding recovered model VES curves. The apparently better recovery using smoothed data is illusory. The RMS fit of the recovered model is to the smoothed VES curve. The model recovered using the raw VES data yields a poorer RMS because its VES is compared to the raw data. In fact there is little advantage in using smoothed data.

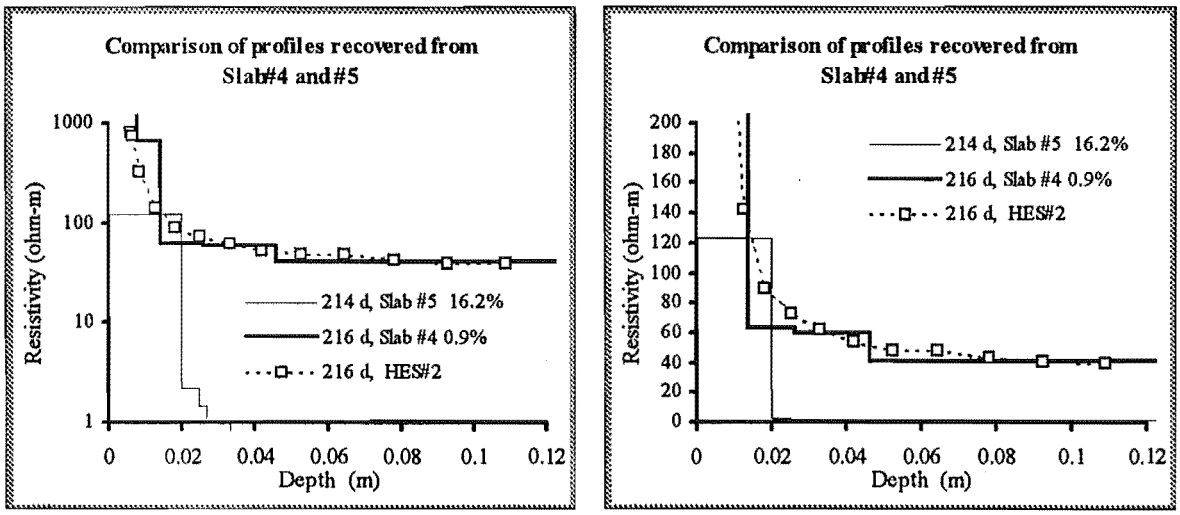

Figure 7.5.2-4: Comparison of profiles recovered from Slab #5 and the non-reinforced but otherwise equivalent Slab #4.

Comparison of the profiles recovered from Slabs #4 and #5 show just how far from determining the profile we are (Figure 7.5.2-4). The Slab #4 profile follows the HES#2 profile very closely. The Slab#5 profile merely touches the HES profile at some point but is otherwise well away from it.

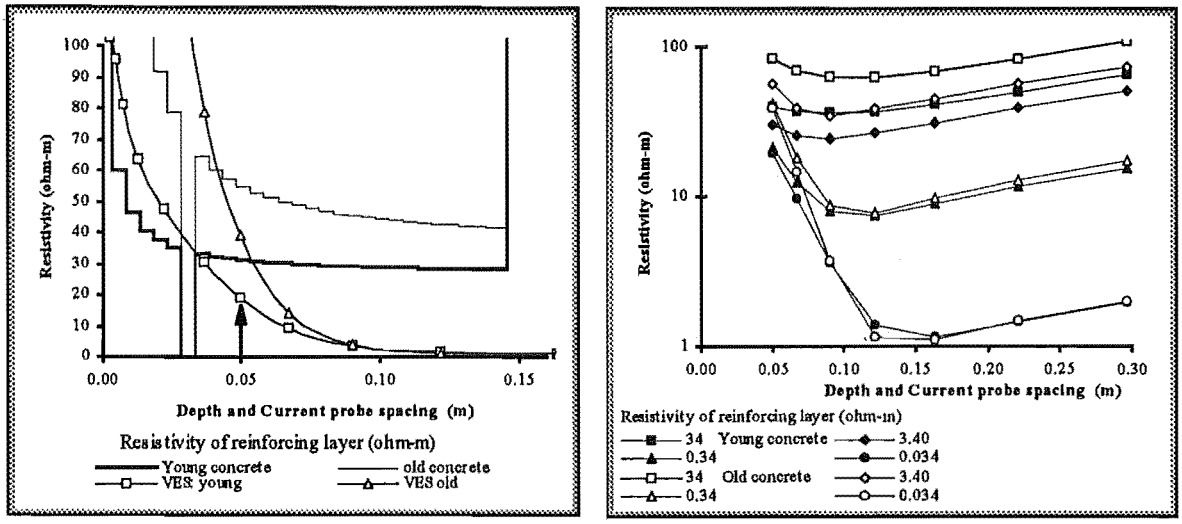

Figure 7.5.2-5: (Left) Model profiles and VES curves for a reinforced concrete slab. The smallest current probe spacing at which apparent resistivity is practically measurable is indicated by the arrow. (Right) Model VES curves for a range of reinforced layer resistivities and two ages of concrete.

The inability of the inversion programs to recover profiles from the reinforced slab is illuminated somewhat by a closer look at the model profiles and VES curves first presented in Chapter 5.

In the left-hand graph of Figure 7.5.2-5, two possible profiles of a reinforced slab are shown. The older profile has a higher resistivity than the younger, and although the difference is less at greater depths, it is still significant. The VES curves associated with the profiles are also shown. As long as the VES curves are separate, information distinguishing profiles of differing resistivity remains. As the current probe spacing increases, the difference between the two curves decreases and finally vanishes. Information about the resistivity of the slab below the reinforcing effectively vanishes at this point.

The extent to which information is 'lost' depends on the resistivity of the reinforcing layer. The right-hand graph of Figure 7.5.2-5 and Table 7.5-1 show how the VES curves are affected by the resistivity of the reinforced layer. Differences between the curves of 25 ohm-m or more when the reinforced layer resistivity is about the same as the surrounding concrete, shrink to one or two ohm-m when the reinforced layer resistivity is 0.34 ohm-m.

The curves are still quite separate at spacings around 0.05 m, but the data points are too few to extract much information. Furthermore, the measured apparent resistivity exhibits greater scatter in this range (see Chapter 6), so that the ability to recover profiles will be further degraded. Attempts to recover the original model profiles from these VES curves result in profiles very similar to those recovered from experimental data.

Table 7.5-1: Variation of apparent resistivity as a function of the resistivity of the reinforced layer: model VES curves.

	Apparent resistivity			
	Resistivity of reinforced layer (ohm-m)			
Spacing (m)	34.00	3.40	0.34	0.034
0.050	43	26	20	20
0.067	31	13	5	5
0.091	26	10	1	0
0.122	25	12	0	0
0.164	27	14	1	0
0.221	33	18	1	0
0.297	44	23	2	0

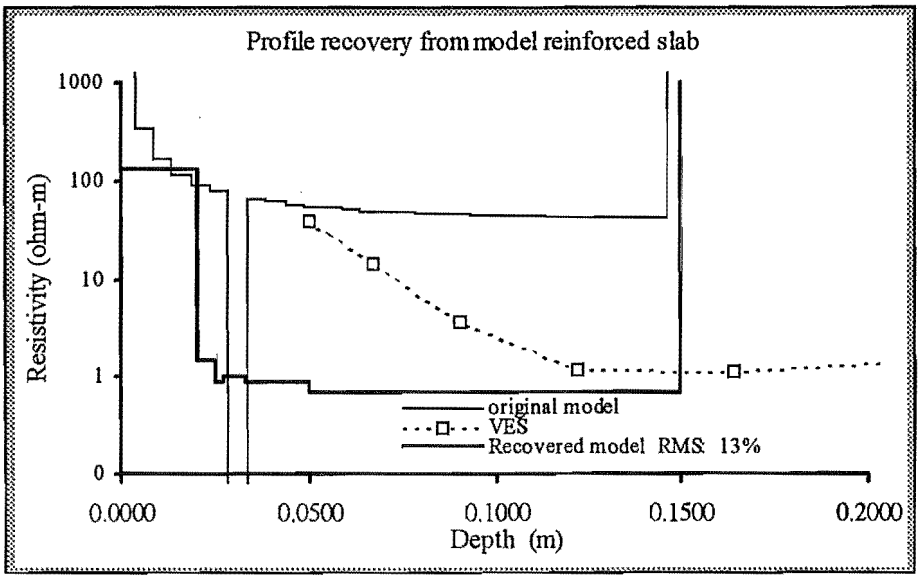

Figure 7.5.2-6: Profile recovery from a model reinforced slab. The original model and its associated VES curve have been generated from the reinforced slab model as described in Chapter 5. It is effectively noise-free. The recovered model shows the same characteristics as those recovered from the experimentally derived VES curves.

7.6 Conversion to a continuous profile

7.6.1 Introduction

A recovered profile typically consists of a small number of layers of uniform resistivity. It is represented on a graph by a stepped curve and has been referred to as a 'stepped' profile. The number of layers depends on the number in the initial trial model and on the degree to which layer suppression has taken place (see Section 7.2.2). A layer sandwiched between other layers of higher or lower resistivity may be amalgamated with one or the other as a consequence of imposition of the falling profile constraint, or just because the amalgamated profile happens to be equivalent to the earlier one in the sense that they fit the VES data equally well.

In any case, the final recovered model will not be the only possible model able to fit the data with the desired goodness of fit. The top layer may be thin and highly resistive or, as a result of amalgamation with the adjacent layer, relatively thick and of low resistivity (Figure 7.6.1-1). Furthermore, the actual locally averaged resistivity profile of the concrete (that is averaged to eliminate the effect of inhomogeneity caused by the presence of aggregate), is assumed to be continuous. The problem then arises of how, from the stepped profile, a realistic continuous profile is to be generated which fits the measured VES as well as or better than the stepped profile.

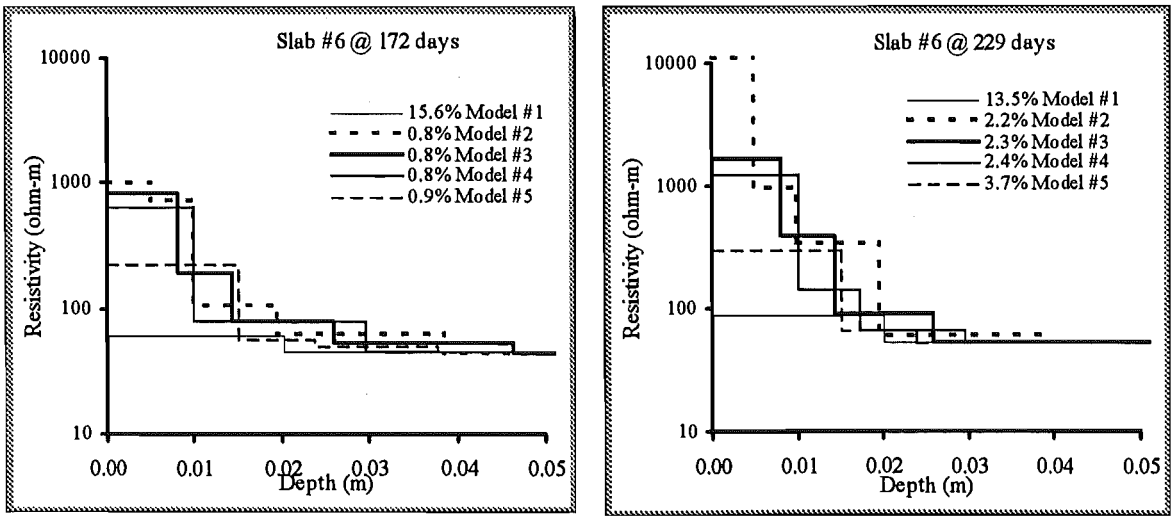

Figure 7.6.1-1: Typical stepped profiles recovered from a VES curve. (Left), three of these curves are 'equivalent; in the sense that their associated VES curves fit the VES data equally well as measured by the RMS %. (Right), the larger the RMS, the wider the range of profiles that may be said to be equivalent.

The simplest method is to find the midpoints of the vertical and horizontal portions of the stepped profile and draw a line through them (see Figure 7.6.1-2). That is, to convert a stepped to a continuous model, the first step is to assume that the curve passes through the midpoints of each step. This is equivalent to assuming that the given resistivity of each layer corresponds to the actual resistivity at the middle of the layer and that at the interface between adjacent layers, the resistivity is the average of those layers. Although the continuous profile will definitely be a continuous curve, in practice it easier to interpolate linearly the layer midpoints, so that the profile appears to be made up of a number of short sections of straight line.

The curve must also be extrapolated to the surface. The simplest way is to project the adjacent linear section of the profile. This may result in an artificially low surface resistivity, since the rate of change of resistivity increases towards the surface. The gradient near the surface can be increased arbitrarily. Modelling this change gives an idea of how important this section of the curve is. It also gives a good idea of how accurately profiles can be recovered for this section of the apparent resistivity curve is subject to considerable error.

Other methods can involve fitting a smoothing spline curve to the midpoints, and using that to project to the surface. Generally, fitting a curve to the sharply descending profiles as measured by the horizontal electrode system, results in a non-physical minimum as the slope of the resistivity profile changes from the steep gradient near the surface to the more gradual gradient deeper down. This may be removed by enforcing a falling profile constraint.

Another method involves determining likely forms of the resistivity profile from curve-fitting to the nearly continuous profiles as measured by HES#2. Then, the coefficients to this standard equation may be determined either by fitting it to the midpoints described above, or in a more sophisticated fashion, by comparing its associated VES curve with the measured one.

The result of fitting a continuous function to directly measured profiles, shows that the resistivity profile of the region below about 10 mm, can be expressed in the form $\rho = ae^{b/(depth-c)}$, where a is a parameter affecting the deep resistivity, b a parameter affecting the general steepness of the curve. This curve may be fitted with some success to recovered profiles, with the top 10 mm being extrapolated to a lower level.

The validity of all such curves will be reflected in the measure of fit between the VES that may be generated from them using the methods described in Chapter 5, and the measured, experimental VES curves.

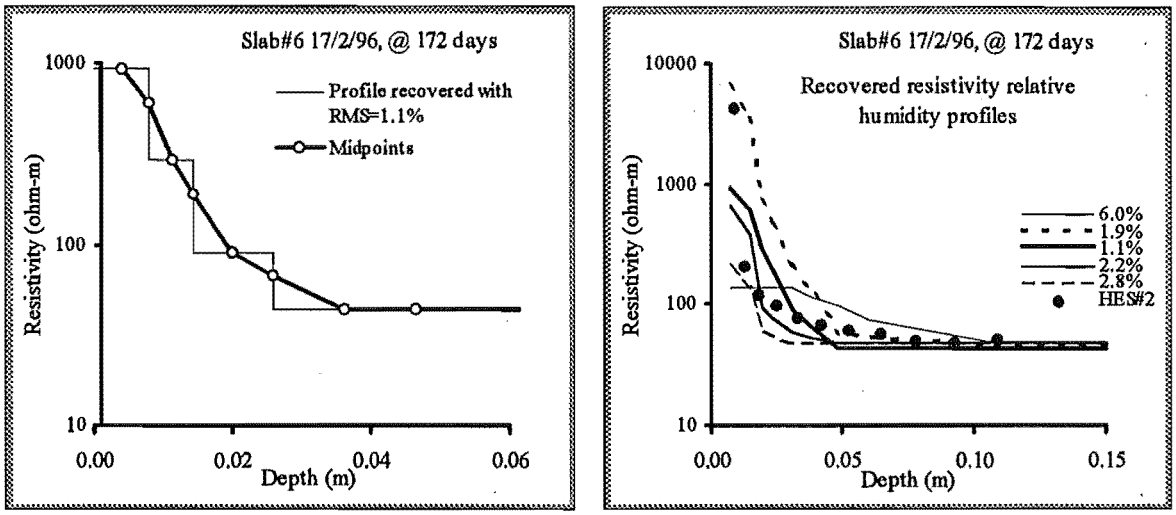

Figure 7.6.1-2: (Left) generation of a continuous profile by connecting mid points (right) examples of continuous profiles drawn through profiles shown in the right-hand graph of Figure 7.6.1-1.

7.6.2 Validity of continuous profiles

A continuous profile will have a corresponding apparent resistivity curve, and the validity of the continuous model will depend on the goodness of fit between the model VES and the actual data.. To calculate the continuous model VES, however, we must use a layered model. Thus the validity of a continuous model is limited to that of an apparently equivalent stepped model, consisting of a large number of thin layers. Methods of doing this are presented in Chapter 5.

7.7 Discussion

7.7.1 Inversion schemes

7.7.1.1 Smoothing of data

Substantial reduction in apparent data scatter has been achieved through judicious averaging and combination of many VES curves taken on the concrete sample during the same sounding session. Nevertheless, some scatter obviously remains and it is tempting to try to smooth curves where the data points appear to be 'out of line'.

Another reason why one might wish to smooth data is to enable, through interpolation, an artificial increase in the number of data points so that inversion can be carried out using more free parameters. In order to maximise the number of complete VES curves easily measured during a VES session, the optimal number of data points measured in a VES curve was set at 8 (see Chapter 6). The possible disadvantage of this trade-off is that a maximum of 8 layer parameters may vary during the inversion process. If all depths and resistivities are to be free, the trial model must have four or fewer layers.

Apart from visual inspection and manual smoothing of the noisy curve, one may use smoothing spline or some predefined function to fit the data points. However, all of these methods have dangers. The noise may have undue influence on the smoothed or splined curve. There is no guarantee that the shape of the splined or fitted curve owes more to data scatter than to the resistivity profile. It is significant that the most simple method of drawing a smooth curve through a noisy VES curve taken from a concrete slab, is to invert the curve using a two layer model, with the falling profile constraint and fixed depths. Furthermore, it is difficult to improve on the curve drawn in this way since the differences in VES curves when small changes in layer parameters are made can be very subtle.

However it would not make sense to use such a smooth curve as a basis for increasing the number of data points since it is fitted perfectly to a two-layer profile. It is best, therefore, to work with the existing data and to reduce the number of free parameters rather than to attempt to either artificially reduce data scatter or increase the number of data points.

7.7.1.2 Layer suppression

In a falling profile, a layer having a resistivity greater than the layer below and less than the layer above, may be suppressed by the inversion process, since removal of that layer (by

increasing the thickness of the adjacent layers), may give a nearly equivalent apparent resistivity curve.

This means that if, as in the present case, the profile shows a resistivity decreasing with depth, a model profile may generally be found having fewer layers, which fits the data just as well. In practice, a model having only two layers can often be found to fit the data as well, or even better than models with more layers. However the optimal number of layers appears to be about 4 or 5 .

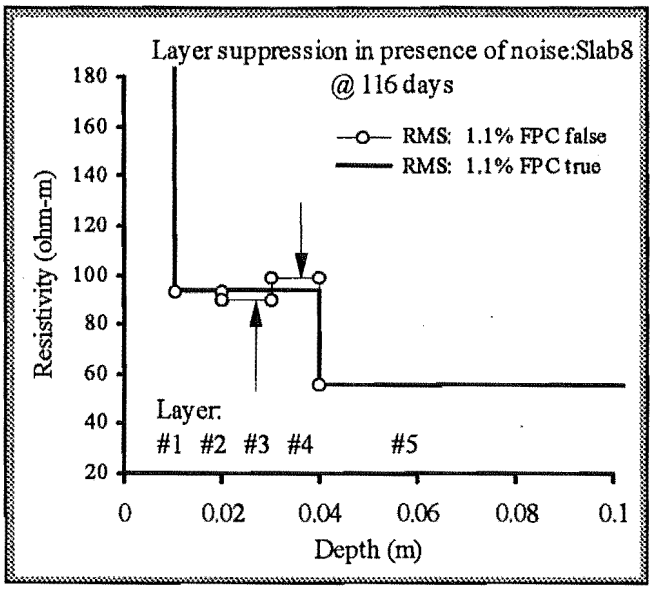

Figure 7.7.1-1: The effect of imposing the falling profile constraint (FPC) on profile recovery from noisy VES data. Without the FPC, the resistivity of layer 4 is a local maximum. When the FPC is imposed the program reduces the resistivity of layer 4 to that of layer 3. In later iterations the combined layer resistivity has climbed to that of layer 2.

When an initial model having a larger number of layers is used, the final model commonly has fewer layers, because of layer suppression. The suppression takes one of two forms.

1. Layer disappearance: if depths are free to vary, an intermediate layer may become vanishingly thin.
2. Layer amalgamation: if depths are fixed adjacent layers may come to share the same resistivity and thus together they effectively constitute one layer.

The second form of layer suppression occurs especially when the falling profile constraint is imposed (Figure 7.7.1-1). The unconstrained recovered profile may have local maxima and minima in response to noise or scatter of the data points. When the falling profile constraint is imposed, starting with the bottom slab layer, the program checks to see if the layer immediately above has a resistivity greater than or equal to the lower layer. If not, the upper

layer resistivity is set equal to the lower layer. If the noise is such that the inversion process tries to reduce the resistivity of the upper layers, the net result is to force the amalgamation of adjacent layers by giving them the same resistivity. In this way, a final trial model may have fewer layers (once adjacent layers with the same resistivity have been amalgamated) than the initial trial model.

7.7.1.3 Noise in data

Generally the goodness of fit between the model apparent resistivity curve and the raw data will tend to depend on the quality of the data rather than the choice of initial trial model. Occasionally however choosing a larger or smaller number of layers may result in a vastly poorer fit. The reason seems to be the convergence of the iterative process on a local minimum.

Nevertheless, a smaller misfit may not necessarily indicate a better model. A model with many layers may just fit the noise or scatter in the VES curve more closely.

7.7.1.4 Equivalent models

There are infinitely many models that may fit data with the same error of fit. This is because a practical data set represents only a small subset of the possible full, continuous VES curve, and because it contains considerable scatter. These models are therefore electrically 'equivalent' yet may be quite different, depending on how large the error of fit is. Obviously a greater range of models will fit the data badly, than well.

The actual misfit between the model and measured VES curves, will be different for different models. Some model VES curves may match better at higher and others at lower spacings. Or the misfit may be equally spread over the VES curve. It is important that the most important model parameters, or rather the most important region of the profile, be identified, so that the optimisation procedure may weight the corresponding range of current-probe spacings accordingly. VES data at small current probe spacings and at large spacings, exhibit greater scatter and for this and other reasons may be trusted less.[1] The

---

[1] This is because data at a small current probe spacing suffers from the high relative uncertainty in measurement probe position and spacing, which are correspondingly smaller. At large spacings the magnitude of the current is comparatively small, and so both the current and the voltage measurement signals have a higher noise-to- signal ratio. See Chapter 6 for a full discussion of this.

intermediate region may well be of most benefit since it corresponds to that part of the profile which is changing most rapidly and may give the best evidence for the location and slope of the receding evaporative plane.

When the data has substantial scatter, different models seem to attempt to fit the noise differently. Models with more layers may fit the noise more exactly, and be poorer models for that reason, than a model with a larger RMS.

7.7.1.5 Quantifying the uncertainty in the recovered model profile.

The uncertainty in the recovered model parameters will depend on the fit between the measured VES curve and the model VES curve. Sandberg (1990) has presented a method by which uncertainty in each recovered parameter is determined during the inversion process, depending on how well the model and field VES curves fit. Further work needs be done in the present study, however, before I can report on its usefulness here. Where it has been used (it was briefly written into inverjnm.m), it indicates a higher degree of certainty in the parameters than is necessarily the case. For example, two recovered models sharing the same RMS, often have resistivities that differ substantially more than the limits implied by Sandberg's method. This is not to disparage the method, rather, insufficient time has been spent in ensuring its correct operation here. Quantification of the uncertainty in recovered profiles is, nevertheless, an important issue and is worthy of further study. At present, judgement of the uncertainty is largely confined to observation of the range of profiles observed when the same VES curve is inverted using different constraints on the inversion process.

Some work has also been done in the investigation of parameter uncertainty, by perturbing parameters of the best final model and observing the resulting variation in RMS.

Once again it should be noted that a lower RMS does not necessarily indicate a better recovered profile. A good fit to poor field data may result in a poor model which fits the scatter in the VES curve well.

7.7.1.6 Recommended inversion scheme

Whilst, by exploring a large number of initial models and inversion schemes, a model may be found which fits the data much better than the rest, it is practical to use a standard, simplified inversion scheme. In the present case it was decided to use the 'Marquardt-Levenberg' inversion scheme as implemented in **inverjnm.m.** Inversion of a large number

of VES curves in the course of this study has shown that optimal results can be achieved using a five-layer initial model, with fixed depths, and using the falling profile constraint. However, failure to achieve a RMS less than 3% say, could prompt further inversion attempts using four or six layers. If the misfit is due to the scatter in the VES data, it is unlikely that further inversion will be of benefit.

7.7.2 Recovery of profiles from non-reinforced slabs

As the technique of vertical electric sounding on concrete slabs was developed along with the instrument to measure apparent resistivity, the form of the VES curves obtained came increasingly to resemble the form generated from model profiles, and from profiles measured directly using embedded electrode systems. The advances in form had mainly to do with a decrease in data scatter about the expected form. At this stage in the development of the technique and instrument, quite reasonable VES curves may be obtained if 10 or more curves taken in different positions and with different measurement probe spacings on the concrete are averaged and collated. The scatter in the data points is expected given the inhomogeneous nature of concrete, and the sensitivity of resistivity measurements to inhomogeneity near the electrodes (this was first discussed in Chapter 3).

Given the residual scatter in VES curves submitted for inversion, there is a limit to how well one should expect the recovered profile to fit the apparent resistivity curve. A very low RMS for a profile recovered from a VES curve with a large degree of scatter would suggest that the profile has been distorted to fit the noise. Use of the falling profile appears to limit this process somewhat at the expense of forcing amalgamation of layers.

In Table 7.7-1 the comparisons used for evaluating the VES curves and recovered profiles for Slabs #6, #7 and #8 have been collected. Overall, the RMS fit between the VES data and the VES curve generated by recovered model from non-reinforced slabs lies between 1% and 3%. On the other hand, when the VES data is compared with the VES curves generated from HES data, the agreement can give RMS values as high as 49%.

Table 7.7-1: Evaluating recovered profiles from Slabs #6, #7 and #8 (see text for details).

	Slab #6 Age (days)				
Basis of comparison	*163*	*172*	*229*	*259*	*Mean*
Inversion[1]	0.9%	1.7%	3.9%	2.1%	2.1%
VES and HES[2]	20.1%	23.7%	49.1%	46.2%	34.8%
VES and HES (scaled)[3]	10.2%	5.3%	45.7%	27.3%	22.1%
VES and HES (scaled/restr[4]**.)**	6.8%	5.2%	8.5%	7.1%	**6.9%**

	Slab#7 Age (days)					
	121	*130*	*147*	*187*	*217*	*Mean*
Inversion	2.7%	2.4%	2.6%	2.8%	2.3%	2.5%
VES and HES	3.9%	4.8%	6.4%	6.8%	6.8%	5.7%
VES and HES (restr.)	3.3%	5.0%	6.7%	7.2%	3.4%	**5.1%**

	Slab #8 Age (days)						
	16	*24*	*28*	*46*	*86*	*116*	*Mean*
Inversion	4.8%	1.3%	0.8%	1.2%	1.5%	1.1%	1.8%
VES and HES	16.3%	25.3%	22.5%	19.3%	18.2%	12.8%	19.1%
VES and HES (scaled)	6.6%	8.5%	5.2%	2.0%	2.6%	9.2%	5.7%
VES and HES (scaled/restr.)	6.9%	6.5%	3.8%	2.1%	2.8%	9.9%	**5.3%**

Notes: 1. Comparing VES data with that generated by the model profile.
2. Comparing VES data with that of the HES profile
3. Comparing VES data with that of the HES profile scaled to minimise the RMS
4. Comparisons made as for 2. or 3. but excluding the first data point (smallest current probe spacing).

A good deal of this lack of fit appears to be due to a scale factor. That is, if the HES data is multiplied by a constant (0.77 for Slab #6, 1.0 for Slab #7, and 1.3 for Slab #8), effectively shifting it up or down the resistivity axis, the agreement between the respective VES curves increases. This scale factor can be found by matching the recovered profile with the HES profile at the deepest level, where precision in each is greatest. Alternatively, the disagreement over the whole depth range can be minimised. Justification for this procedure could lie in inaccuracy in calibration of the horizontal electrode system, since an error here would be affect all subsequent readings on that slab in the same way. It is less likely that such a systematic error would be found in the vertical electric sounding data.

As is seen throughout this report, the variation in the values of both indirectly and directly measured resistivity and relative-humidity, is greatest near the surface. If we exclude the most shallow data point, or in the case of VES curves the data point with the smallest current probe spacing, the agreement between the HES and VES data is generally better,

but only in Slab #6 is the improvement significant. However, having made this restriction in the data compared, the agreement between the VES data and that deriving from the directly measured profiles roughly lies in the range from 5% to 7%.

Since VES curves generated from the directly measured profiles are compared with the *raw VES data* rather than the VES curve generated from the recovered profile, the disagreement between the recovered profile and the directly measured profile may be somewhat higher, depending on how well the recovered profile matches the raw VES[2].

7.7.3 Conversion to a continuous profile

Having recovered the layered profile, however well it fits the VES curve, it must be transformed to a continuous profile. This will engender more uncertainty, and it is important that efficient methods are developed. However whatever methods are developed, probably the best way to evaluate the continuous profile will be to compare its associated VES curve with the raw data.

7.7.4 Recovery of profiles in the presence of reinforcing

The presence of reinforcing imposes severe challenges to the recovery of resistivity profiles using vertical electric sounding. Reinforcing lowers the resistivity at a level within the slab and results in correspondingly low measured voltages at the surface. Since most of the resistive load between the vertical electric sounding instrument's current probes is due to the electrode-concrete interface resistance and the dry highly resistive region near the surface, the presence of reinforcing does not result in a significant increase in current. Hence the low apparent resistivity measured and the comparatively high degree of data scatter associated with a lower signal-to-noise ratio.

The high data scatter does not provide the most serious challenge. The inversion programs are unable to recover profiles even from noise-free VES curves generated from a nearly continuous model. The highly conductive reinforced layer results in a VES curve to which the nature of the concrete below that layer does not contribute significantly. Even in principle, recovery of profiles from reinforced slabs using vertical electric sounding does not seem possible.

---

[2] This comparison should be made, however, I ran out of time.

7.8 Conclusion

The application of the vertical electric sounding technique to the task of measuring resistivity profiles in concrete slabs has been shown to be reasonably successful. Profiles have been recovered from concrete slabs which range in age from about 9 days to over 250 days. The agreement of recovered profiles with those measured directly using embedded electrodes is variable. However, when corrections have been made for possible scaling errors (which affect the scale but not the form of the profile), and when excessive variation associated with shallow depths is removed, the agreement lies around 6% RMS.

The choice of inversion scheme is important to the quality of the recovered profile, although trial models with from 4 to 7 layers will result in final recovered profiles of roughly equal degree of fit to the VES data. Use of the falling profile constraint has proved critical in confining the solution to relatively well formed profiles, and consequently reducing the tendency of the recovered model to fit the scatter in the VES curve. In this sense the falling profile constraint acts as a data filter.

Both inversion programs, **inverjnm.m** and **inverjnz.m** performed well especially with the falling profile constraint imposed. The former generally resulted in smaller RMS values when tested on the same data, and was used to do the bulk of the inversion work reported here.

Recovery of profiles from the reinforced slab was poor. The reason for this initially appeared due to the inability of the resistivity meter to measure the very low voltages that were produced. Subsequent analysis and modelling now suggests that the reinforcing acts as a screen, removing information about the resistivity at lower levels, so that it is fundamentally impossible to recover full profiles. The possibility remains that the profile above the level of the reinforcing can be recovered. However, this is the very region in which most variation in measured values occur. On the one hand to make VES measurements corresponding to shallow depths, the probe spacings must be so small that they are of the order of the larger aggregate diameter, and data scatter becomes a large problem. Furthermore, the resistivity and gradient are high which is likely to lead to increased error in HES measurement (see Chapter 8). On the other hand, close to the surface there is more likely to be actual variation in resistivity and moisture state as this region is more sensitive to external conditions.

Given the poor performance of the vertical electric sounding technique on reinforced slabs, it will be one of the conclusions of this report that the vertical electric sounding technique cannot be recommended for development as a commercial instrument. Rather, the development of the horizontal electrode system (described in Chapter 8), as a cheap and simple alternative should be pursued. Nevertheless, the vertical electric sounding instrument should have use as a research tool, and may be adapted to the measurement of moisture profiles in other building materials such as timber in which the scale of inhomogeneity is considerably less than the size of the probe spacings needed to measure a useful range of depths.

8. Direct measurement of resistivity profiles

Resistivity profiles in drying concrete slabs may be determined in two main ways. In Chapters 5, 6 and 7, the technique of vertical electric sounding (VES) has been described. This involves the determination of resistivity profiles, indirectly, from apparent resistivity measurements made between electrodes at the surface. In the present chapter are described some methods for the direct measurement of resistivity profiles. These are methods which involve measuring the resistivity between two or more electrodes embedded in the concrete in or around the region of interest.

Direct methods are required in order to assess the validity and accuracy of resistivity profiles recovered using VES. Secondly, by simultaneously measuring resistivity and relative-humidity profiles directly in concrete samples, we may empirically determine resistivity- relative-humidity relationships for specific concrete mixes and curing histories. This procedure is described in Chapter 9.

The principle of direct measurement of resistivity profiles is simple. The resistance between pairs or quadruples of electrodes embedded in the region of interest is measured and multiplied by predetermined calibration factors to give the resistivity. In practice difficulties arise because of the highly inhomogeneous nature of concrete, which affects the validity of any calibration factors as the concrete dries.

In the following section, existing methods of measuring concrete resistivity are discussed. This is followed by the description of several embedded electrode systems that have been developed specifically for measuring resistivity profiles. Some implications for the design of embedded electrode systems from modelling studies are also presented here.

As noted above, calibration of electrode systems embedded in an inhomogeneous material presents special difficulties. Some of the issues and pragmatic solutions are described in Section 8.4. Assessment of the electrode systems relies on issues of repeatibility and precision of measurement. Without an independent standard method of measuring profiles, assessment of the validity of particular methods must lie in consistency of measurement between electrode systems of the same and of different type. A discussion of these issues follows a presentation of typical results in Section 8.6. Full

graphical records of directly determined resistivity profiles are to be found in Appendix E.

8.1 Previous studies

While several methods have been used to measure the resistance and resistivity of concrete, most studies have used samples of concrete which are assumed to be homogeneous in resistivity apart from the presence of highly resistive aggregate. These studies attempt to attain an average, or bulk resistance of the sample by using electrodes that are large relative to the aggregate.

The electrodes are usually cast into (that is, embedded in) the concrete (eg. Woelfl and Lauer, 1979, Tashiro et al., 1987, Brantervik and Niklasson, 1991, Berg et al.1992 and Takiguchi et al., 1992). Occasionally the electrodes may be painted on the sides of the sample (eg. Lopez and Gonzales, 1993) or may form two sides of a rectangular mould, or they may be clamped or cemented to the sides of the sample at the time of measurement. The results may be expressed in terms of resistance or resistivity (using calculated or empirically determined calibration factors.

It is not always made clear how moisture content is controlled or measured. Commonly, in order that the resistivity be uniform throughout the sample, the concrete, mortar or paste sample is of small enough dimensions, that any moisture content profiles set up within the sample, are not considered significant. Generally the moisture content (or RH), is equalised throughout the sample by placing it in an environment of known relative-humidity, or in an oven at a certain temperature (normally 105 °C) until no change in mass is observed.

For our purposes, determination of a relative-humidity -resistivity relationship using small samples allowed to reach a uniform relative-humidity, is inadequate. The isothermal moisture-content- relative-humidity relationship takes the form of a hysteresis loop (see Chapter 2). Thus the final moisture content of a sample stabilised at a known relative-humidity will depend on whether equilibrium has been achieved through drying (desorption) or rewetting (or adsorption). Within concrete, current is mainly carried by the evaporable water. Resistivity is a strong function of the evaporable moisture content (see Chapter 3), so the resistivity of a sample of concrete in equilibrium at a given relative-humidity, will likely depend on the how that moisture state was obtained. As we are interested in determining relative-humidity profiles from knowledge of resistivity

profiles, the resistivity- relative-humidity relationship should be determined from measurements of resistivity and relative-humidity in the profile itself.

Few have reported measurement of resistivity of a concrete sample in which a profile has been allowed to develop. Amongst them, Takiguchi et al. (1992) allowed a slender cylindrical specimen to dry from one end, and measured the resistance between pairs of electrodes, spaced along the developing profile. McCarter et al. (1995) used a multi-electrode system to monitor water and ionic movement in the top 50 mm of a previously dry concrete sample placed in a shallow bath of water.

8.2 Direct profile recovery methods developed in this study

The easiest way to measure resistivity of concrete in bulk, is to pour a rectangular block of length l in a mould having two plate electrodes of area A on opposite sides (known as a calibration cell). The resistance R measured between the plates can be converted to a resistivity of the concrete ρ_c, using the formula

$$\rho_c = \frac{RA}{l}$$

This method is used to determine bulk concrete resistivity when electrode systems are calibrated in situ (see Section 8.4.2).

If the dimensions of the block are sufficient the inhomogeneous nature of the concrete is relatively unimportant, as it exists on a scale much smaller than that of the calibration cell. For smaller samples of concrete the inhomogeneous nature becomes more important and the measured resistivity becomes a function of the exact proportions and arrangement of the aggregate within the cement paste matrix.

The determination of a resistivity profile set up in a slab or cylinder of concrete allowed to dry from the top surface only, requires measurement of resistivity of a horizontally restricted sample in which, in addition to the inhomogeneity caused by the aggregate, there is a resistivity gradient. Because this horizontal section is physically (and hence electrically) connected to the rest of the sample, the current distribution, resulting from a resistance measurement between any two electrodes, will fill the entire connected concrete space. The measured resistivity therefore is actually an average over the whole sample, weighted in a way that reflects the current distribution. The actual distribution will be unknown and will be expected to change as the resistivity gradient of the cement paste matrix changes. The closer together the electrodes are, the more heavily weighted

will be the region immediately between them, but, correspondingly, the sample will be less representative of the concrete as a whole.

Concrete is a highly inhomogeneous material. This makes determination of an average resistivity for a certain depth below the drying surface, particularly difficult. Electrodes far enough apart to render the inhomogeneity (due to aggregate) insignificant will be too far apart to allow good depth resolution. For maximum resolution, the ideal situation would be one where the current distribution between two well separated electrodes is confined to a thin horizontal layer. Allowing electrodes to extend horizontally through this layer will not adversely affect the vertical resolution but will give a better averaging of the material properties at that level. That is, increasing the length of horizontal electrodes will reduce scatter that is due to the inhomogeneous nature of concrete.

The requirements of direct profile measurement using embedded electrode systems thus include:

1. the need to minimise scatter by increasing the length or separation of the electrodes,
2. the need to increase vertical resolution by focussing the current distribution at the depth of interest and
3. the need to minimise interference with the moisture content profile.

Four designs were trialed for measuring resistivity profiles. The first used embedded parallel plates (parallel plate electrode system or PPES), while the other three used horizontal rods or screws (horizontal electrode system or HES). The electrode systems were originally designed to be used in calibration cylinders. A calibration cylinder is a cylindrical sample of concrete having both embedded electrode systems and embedded relative-humidity- probe housings so that resistivity and relative-humidity can be measured simultaneously. (A full description of calibrations cylinders used in this study may be found in Chapter 4). The cylinder is allowed to dry from the top surface only so that a moisture-content and resistivity develops.. Two such calibration cylinders are shown in Figure 8.2-1.

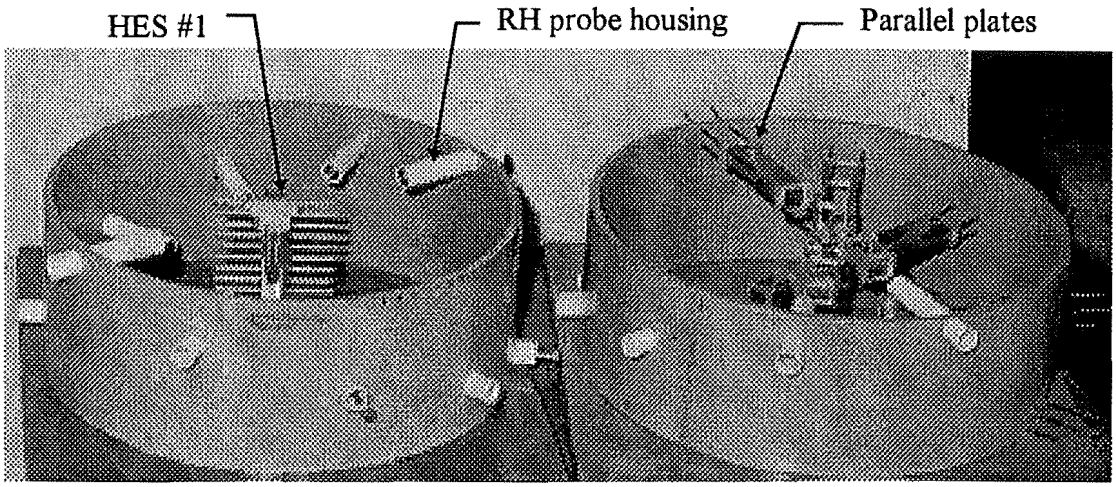

Figure 8.2-1: Cylinder #1 (right) has five relative humidity probe housings and five sets of parallel plate electrodes forming a parallel plate electrode system (PPES). Cylinder #2 (left), has 10 relative humidity probe housings and a horizontal electrode system (HES) having 15 stainless steel rods.

8.2.1 Parallel plate electrode system (PPES).

This parallel plate electrode system was implemented in the first and third calibration cylinders. The PPES used horizontally opposed parallel plates of stainless steel which were suspended by their leads at various depths below the surface. Two pairs of plates were assembled at each of five levels, in line with a relative-humidity housing (see Figure 8.2-1, Figure 8.2-2 and Figure 8.2-3).

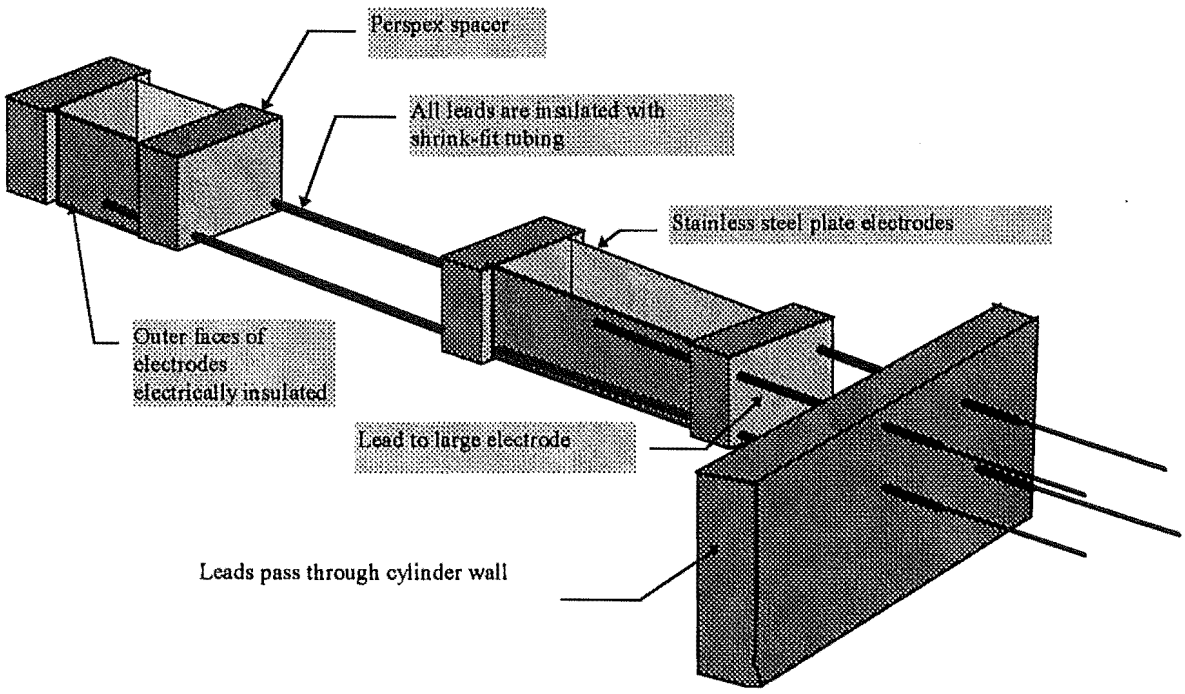

Figure 8.2-2: Schematic diagram of one level of the parallel electrode system.

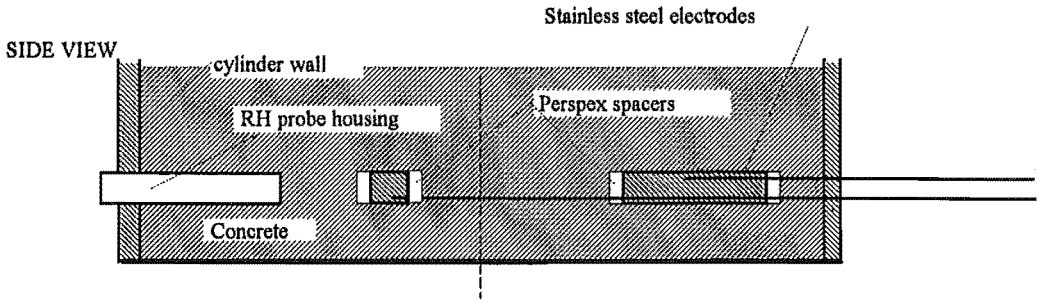

Figure 8.2-3:. Two pairs of parallel plate electrodes in line with a relative humidity probe housing are cast at each of five levels in calibration cylinders #1 and #3. The arrangement at one level is shown here. Levels above and below are offset by 36° so that all RH measurement windows and resistivity measuring regions enjoy unobstructed moisture flow through them.

The electrode system requirements included the need to:

1. **Minimise scatter**: At each level there is a long pair and a short pair of parallel plates. Measurements made with the long pair should exhibit less scatter.
2. **Maximise resolution**: To concentrate the current distribution between the plates, the edges and outer faces of the plates were electrically insulated. The current was further focussed by the perspex spacers holding the plates apart. However, the minimum plate separation is determined by the maximum size of aggregate (19 mm diameter) so that the smallest acceptable plate separation was 20 mm. Even at this spacing larger pieces of aggregate could be excluded. Should larger pieces be excluded, the cement-paste aggregate ratio would increase in that region.

   The effect of this, as is explained below, would become evident only later when the resistivity of the cement paste increased and approached that of the aggregate. The dimensions of the plates were 20 mm x 90 mm and 20 mm x 30 mm. In Cylinder #1, the spacing between electrode faces was 20 mm. In Cylinder #3, the longer plates were set 40 mm apart.
3. **Minimise obstruction to moisture flow**: The electrodes presented no barrier to moisture movement in the vertical direction the except along the bottom edge of the plate. Modelling of the system using Jam_2 suggested that the edges would not alter the RH between the plates significantly (see Chapter 6, Modelling). To ensure that the vertical moisture flow was not impeded by higher or lower sensors, the five

electrode pairs and corresponding RH probes were aligned along diagonals at progressively greater depths and which were offset by 36° from the preceding one.

Before concrete was poured, the resistance - resistivity calibration constants were determined for the entire electrode-system-cylinder using a solution of known resistivity (see Section 8.4).

8.2.2 Horizontal Electrode System #1 (HES #1)

To meet the need to measure a resistivity profile with a higher resolution than that attainable by the original parallel plate electrode system, stainless-steel rod electrodes. (100 mm long and four mm in diameter) were arranged as cross bars on a vertical stand (Figure 8.2-4). The horizontal electrodes were each displaced vertically (by 10 mm center-to-centre) from the one below . Threaded rod was used to increase the electrode surface area.

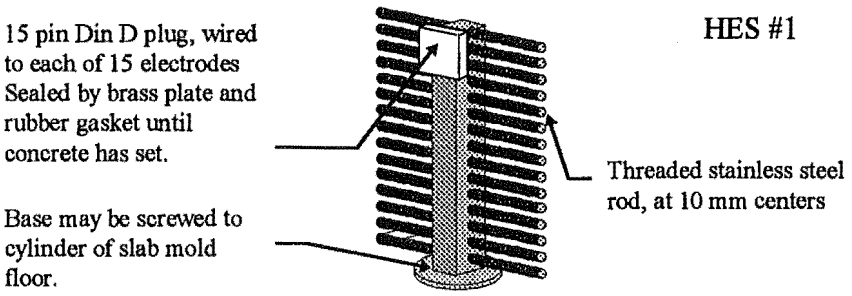

Figure 8.2-4: Horizontal electrode system #1 (HES #1) - concept.

This design enabled increased resolution by decreasing the distance between the electrodes. To counter the increase in scatter that decreasing electrode separation entails, a relatively long electrode was chosen (100 mm). Because the electrodes are too close to allow aggregate of all sizes to fit between them, minimisation of scatter relies on fringing. That is, we wish the current distribution between two electrodes to spread out through the horizontal layer between them, so that, the aggregate distribution is as typical as possible. The circular electrode cross section may encourage fringing but apart from that we cannot enhance it.

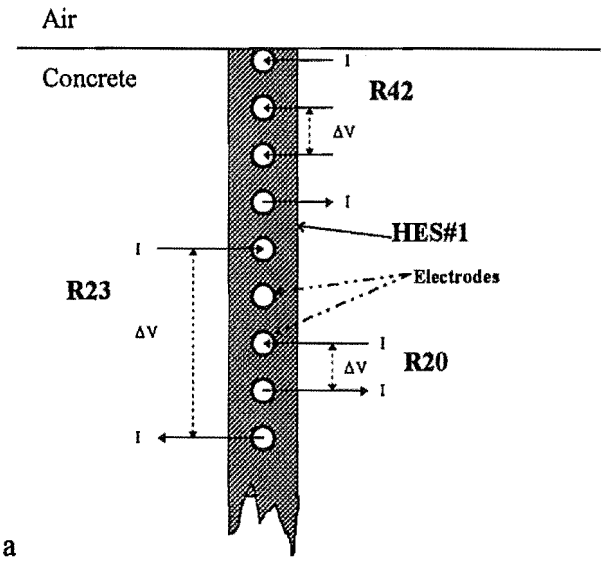

Figure 8.2-5: Schematic showing how different sets of electrodes can be chosen to measure resistivity at different levels. The R20 curve uses two adjacent electrodes. R21 uses two electrodes separated by one electrode, R22, separated by two electrodes and R23, separated by three electrodes. R42 refers to measurements made using four adjacent electrodes, the outer two being current electrodes and the inner two being measurement electrodes

Fortunately, the regularly spaced electrodes enable some investigation of the trade-off between scatter and resolution. Resistivity measurements can be made between any two electrodes (Figure 8.2-5). Letting the resistivity measured between pairs of adjacent electrodes be labelled 'R20', between electrodes 20 mm apart 'R21', between electrodes 30 mm apart 'R22' and between electrodes 40 mm apart 'R23', a series of profiles can be determined. R20 should have maximum resolution and maximum scatter. R23 should have minimum resolution and scatter. The effective depth is taken to be midway between the measuring electrodes.

Measurements of resistivity may also be made by injecting current through two electrodes and measuring the potential difference between two others. The measurement referred to here as 'R42', uses four adjacent electrodes, current being injected into the outer two electrodes, and voltage measured between the inner two. If the top electrode lies flush beneath the surface, the centers of the fifteen electrodes are at depths 2, 12, 22 mm and so forth. The depth of view is taken to be midway between the electrodes used. Thus the first R22 measurement uses the first and fourth electrode and a depth of view of (2+32)/2 = 17 mm. Electrodes chosen, and the corresponding depths of view (taken to be midway between the electrodes used), are listed in Table 8.2-1.

Table 8.2-1: Five methods of measuring resistivity profiles with HES#1. The four double columns show the electrodes selected for two-electrode resistivity measurement and the corresponding depths of view. The fifth double column shows the same for four-electrode measurements.

R20		R21		R22		R23		R42	
Electrodes (Number)	Depth (mm)	Electrodes (Number)	Depth (mm)	Electrodes (Number)	Depth (mm)	Electrodes (Number)	Depth (mm)	Electrodes (Number)	Depth (mm)
1 - 2	7	1 - 3	12	1 - 4	17	1 - 5	22	1-2-3-4	17
2 - 3	17	2 - 4	22	2 - 5	27	2 - 6	32	2-3-4-5	27
3 - 4	27	3 - 5	32	3 - 6	37	3 - 7	42	3-4-5-6	37
4 - 5	37	4 - 6	42	4 - 7	47	4 - 8	52	4-5-6-7	47
5 - 6	47	5 - 7	52	5 - 8	57	5 - 9	62	5-6-7-8	57
6 - 7	57	6 - 8	62	6 - 9	67	6 - 10	72	6-7-8-9	67
7 - 8	67	7 - 9	72	7 - 10	77	7 - 11	82	7-8-9-10	77
8 - 9	77	8 - 10	82	8 - 11	87	8 - 12	92	8-9-10-11	87
9 - 10	87	9 - 11	92	9 - 12	97	9 - 13	102	9-10-11-12	97
10 - 11	97	10 - 12	102	10 - 13	107	10 - 14	112	10-11-12-13	107
11 - 12	107	11 - 13	112	11 - 14	117	11 - 15	122	11-12-13-14	117
12 - 13	117	12 - 14	122	12 - 15	127			12-13-14-15	127
13 - 14	127	13 - 15	132						
14 - 15	137								

This system was known initially as a horizontal electrode system (HES), but came to be called HES #1 when two further horizontal electrode systems were designed.

In the initial design of HES#1, the rods forming the electrodes were set into a rectangular PVC electrical (Figure 8.2-7) but later versions used a cylindrical PVC rod machined to a rectangular cross-section with a wider circular base. The rods were individually wired, using ribbon cable, to a 15 pin D plug which was sealed with a glue (araldite) and silicone rubber sealant (RTV). Until the concrete had set the plug was covered by a rubber seal and a brass plate the top-surface of which at 150 mm high sat flush with the concrete surface. The horizontal electrode system had the advantage of being quite simply constructed, compact and portable, so that HES #1's were easily cast into calibration cylinders and slabs. The D plug enabled quick and efficient connection and measurement

Rear and front views of a HES#1 are shown on the left of Figure 8.2-7.

Moisture flow in the plane of the electrodes is obstructed by the electrodes, although on either side there is virtually no effect. Modelling of the system with the package JAM_2, shows that the RH of concrete directly between adjacent probes may be higher than unobstructed concrete, by no more than 1%, after 6 months drying in 50% relative humidity. As the electrode diameter is small, a moisture gradient is unable to support

large differences in RH between areas in the line of the electrodes and the surrounding area.

8.2.3 Horizontal Electrode Systems (HES) #2 and #3

In order to increase the resolution at shallow depths, two further electrode systems were developed. HES#2 and HES#3 had 14 or 15 short electrodes positioned on a parabolic arc reaching down in to the concrete (Figure 8.2-6 and Figure 8.2-7).

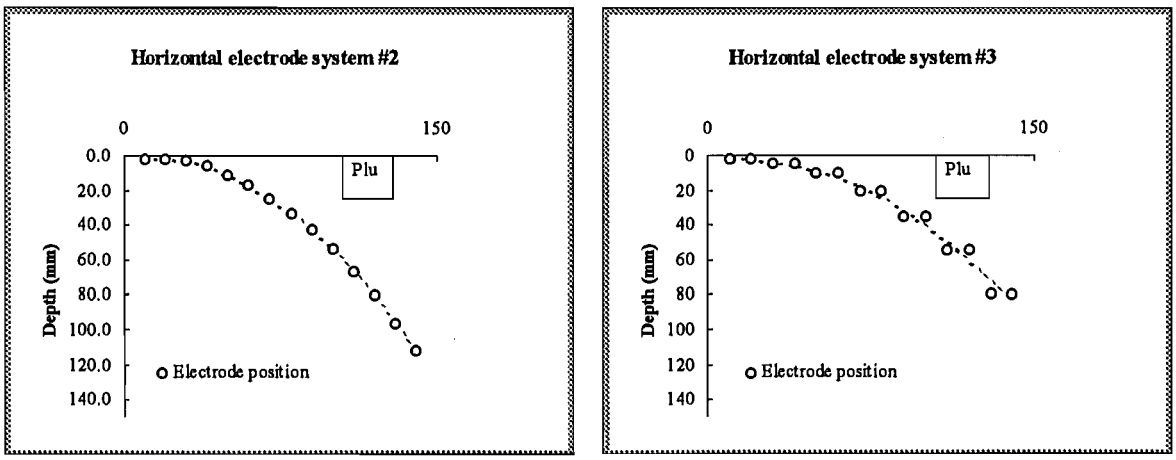

(a) HES#2 (b) HES#3

Figure 8.2-6: Schematic diagrams showing positions of electrodes and Din plug in HES #2 and HES #3. Only the 14 electrodes on the parabolic arcs, were connected to the plug.

Table 8.2-2: Depth of electrodes, and the electrodes selected for measurement and the corresponding depth of view : HES#2

Electrode details		Measurement details		
Number	Depth (mm)	Measurement number	Electrodes used	Depth of view (mm)
1	1.5	1	1 -2	2
2	2.0	2	2 -3	3
3	3.0	3	3 -4	5
4	6.0	4	4 -5	9
5	11.0	5	5 -6	14
6	17.0	6	6 -7	21
7	25.0	7	7 -8	29
8	33.0	8	8 -9	38
9	43.0	9	9 -10	49
10	54.0	10	10 -11	61
11	67.0	11	11 -12	74
12	81.0	12	12 -13	89
13	96.0	13	13 -14	104
14	112.0			

In HES#2, the electrodes were separated horizontally 10 mm and so the electrodes near the top have only horizontal separation, but deeper electrodes are offset vertically as well. HES#3 has 7 pairs of electrodes centred on the parabolic curve. The electrodes of each pair are 10 mm apart and have no vertical separation. The electrodes are formed from 25 or 30 mm stainless steel screws, wired to a 15 pin din plug.

Measurements with HES #2 were made between the 13 pairs of adjacent electrodes. The HES #3 measurements were made between the seven pairs of electrodes at the same levels (Table 8.2-2 and Table 8.2-3).

Table 8.2-3: Depth of electrodes, and the electrodes selected for measurement and the corresponding depth of view : HES#3

Electrode details		Measurement details		
Number	Depth (mm)	Measurement number	Electrodes used	Depth of view (mm)
1 and 2	1.5	1	1 -2	1.5
3 and 4	5	2	3 -4	5
5 and 6	10	3	5 -6	10
7 and 8	20	4	7 -8	20
9 and 10	35	5	9 -10	35
11 and 12	55	6	11 -12	55
13 and 14	80	7	13 -14	80

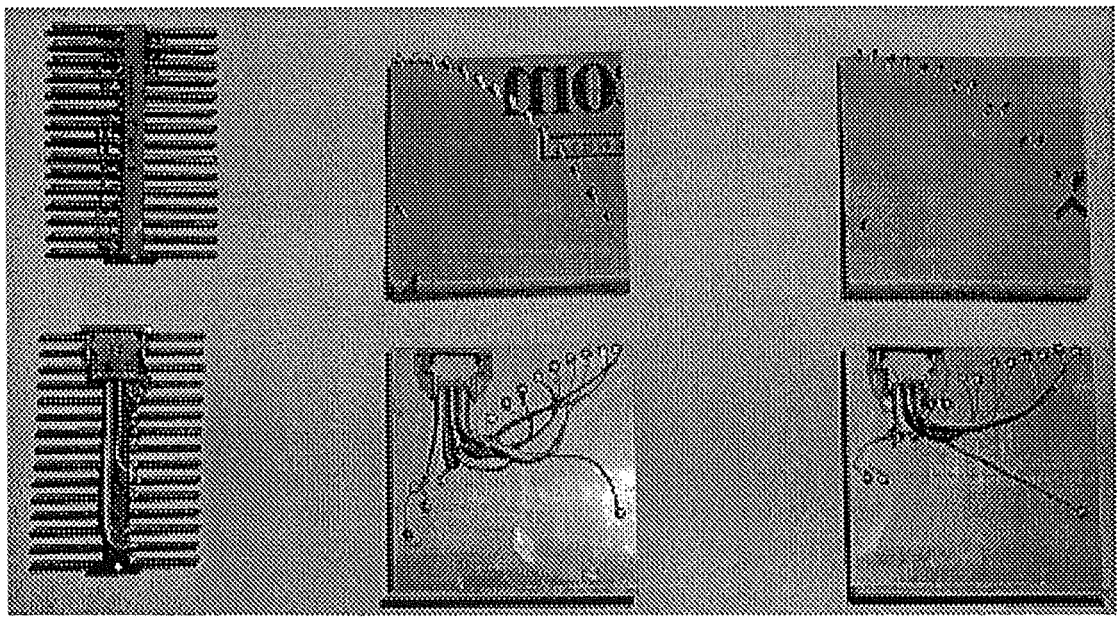

Figure 8.2-7: Front (top) and rear (bottom) views of HES #1, #2 and #3 respectively.

8.3 Method of measurement

As indicated in the introduction to this chapter, the measurement of resistivity profiles directly, using embedded electrode systems, was undertaken in order to

1. enable evaluation of the profiles measured using the vertical electric sounding technique and
2. allow empirical determination of the resistivity-relative-humidity relationship occurring in concrete samples drying from one face only.

Eight concrete slabs designed primarily to test the VES instrument (see Chapters 4, 5, 6 & 7) had embedded horizontal electrode systems. Additionally, 13 resistivity- relative-humidity calibration cylinders each had one of the electrode systems embedded. A summary of the concrete samples used and their embedded electrode systems is presented in Table 8.3-1.

Table 8.3-1: Concrete samples and their associated electrode systems

Calibration Cylinders	Electrode Systems			
#	PPES	HES #1	HES #2	HES #3
1	✓			
2		✓		
3	✓			
4		✓		
5		✓		
6		✓		
7		✓		
8		✓		
9		✓		
10		✓		
11			✓	
12		✓		
13			✓	
Concrete Slabs	**Electrode Systems**			
#	PPES	HES #1	HES #2	HES #3
1		✓		
2		✓		
3		✓	✓	✓
4		✓	✓	✓
5		✓	✓	✓
6		✓✓	✓	
7		✓	✓	
8		✓	✓	
Electrode System Totals	2	18	8	3

The resistance measurements made between various pairs or quadrupoles of electrodes were carried out with the same resistivity meter used in the vertical electric sounding instrument (see Chapter 5). Initially the current and voltage leads from the meter were attached to the appropriate electrodes manually, a rather tedious, time consuming business. A full HES#1 session (recording R20, R21, R22, R23 and R42) required 62 individual measurements. However, a manual switching method was developed which speeded the process considerably. Later, full automation was achieved using the automatic multiplexing abilities of the final resistivity meter prototype. This development allowed real-time display of the resistance profile as readings were taken, and with little further work, display of resistivity profiles in their formation is possible.

At certain times during the study, difficulties with the multi-lead system from the resistivity meter (where each electrode is independently wired to the meter) led to a reversion to a manual switching method.

The meter was designed for resistivity measurement. The low frequency square wave used is suitable for four-electrode measurement. A higher frequency should be used for two electrode measurements if electrode-polarization is to be minimised (see Section 8.4). Nevertheless the computer controlled version of the resistivity meter is suited for automatic measurement of resistance sequences and conversion to resistivity profiles.

Initially, the sequences labelled R20, R21, R22 and R23, as well as the four electrode sequence R42, were all measured during an HES #1 measurement session. In most of the calibration cylinders after cylinder #7 and most of the slabs, only the R20 sequence was measured.

The resistance measured was converted to resistivity using the predetermined calibration constants (see Section 8.4).

Early experience showed that the use of all measurement types was highly redundant. R20 appeared to characterise the profile sufficiently, giving good agreement with the other measurements, so no measurement of R21, R22 and R23 was undertaken for samples after cylinders #5 to #7. R42 measurements were made relatively rarely, which was unfortunate since four probe measurement enabled reduction of electrode polarisation effects (see Section 8.6, Discussion).

Measurements were taken at various times over the testing period. The actual measurement times were irregular as development of the resistivity meter was ongoing and meant, on occasions that it was unavailable.

The early version of the computer controlled resistivity meter was found to have a design fault which allowed the resistivity to be under-estimated under certain conditions. Nevertheless, the apparent error in measurement of profiles (indicated by the degree of agreement between measurements taken on similar samples) was no greater than that associated with the later version. That is the measurements were inaccurate but as precise as with the later instrument.

Besides the early measurements on Cylinders #1 to #4 and Slabs #1 and #2, more than 106 separate measurement sessions were undertaken on the HES's in cylinders #5 to #13, and 176 sessions on HES's in slabs #3 to #8. Generally the first measurements were made one or two days after each sample was poured. In Slab #6, the 15 pin Din plug was raised above the concrete so that measurements could be undertaken within one hour after pouring. The automatic functions of the computer controlled resistivity meter were utilised to record R20 and R42 profiles every 50 minutes or so over a period of two days.

8.4 Calibration of the embedded electrode systems

To determine the resistivity profile of the concrete sample, the resistance measured between two electrodes must be multiplied by a 'calibration constant' k predetermined specifically for the electrode pair. In this section the method of determining the calibration constants is discussed.

A resistivity measurement between any two electrodes will be a weighted average of the resistivity of the whole concrete sample. The weighting will be reflected in the current distribution which in turn is determined by

- the geometry and spacing of the two 'live' electrodes and of the other electrodes which are highly conductive regions (we can call this 'the electrode system geometric factor'),
- the geometry of the mould or form in which the concrete sample is cast ('the sample geometric factor') and
- the random distribution of the highly resistive aggregate ('the aggregate scatter factor').

The first two factors together make analytical determination of the calibration constants a difficult, although theoretically possible exercise. The aggregate scatter factor, which is unknown, makes exact determination impossible.

8.4.1 Calibration using conducting solutions

The standard method of calibrating an electrode system of complex geometry, is to make resistance measurements when the electrode system is placed in a known and homogeneous, conductive solution. For example, in this study, the PPES and some HES#1 were initially calibrated in the resistivity-relative humidity calibration cylinders by making resistance measurements when the cylinders were filled with a conductive solution (distilled water or a weak salt solution). In slabs #1, and #2, HES#1 were used near the corners to ensure least interference with the VES measurements. These electrode systems were calibrated using a smaller rectangular box filled to 150 mm with conducting solution.

The resistivity of the conductivity solution ρ_s was measured separately in small rectangular calibration cells. Dividing the solution resistivity by the resistance R_{si}

measured across the *i*th electrode pair yields the corresponding calibration constant k_i. Thus

$$k_i = \frac{\rho_s}{R_{si}}.$$

When the electrode system is embedded in the concrete sample, similar resistance measurements are made. The resistivity of the concrete is given by

$$\rho_i = k_i \cdot R_i.$$

The difficulty with this method is that the calibration constants are based on a uniform resistivity throughout the space. We cannot assume relative homogeneity of the concrete however. Because the dimensions of the embedded electrodes are of the order of the larger sized aggregate particles or smaller, the measured resistivity may still represent a weighted average resistivity of the whole space but will be particularly affected by the distribution of aggregate in the immediate region of the electrodes. The resulting resistivity may not be particularly meaningful[1].

---

[1] *As an example, consider the extreme case of two electrodes near the centre of a small cube of concrete with aggregate so arranged that the current is able to fill the half space above the electrodes which contains only paste, while below the electrodes there is a sheet of aggregate covering the rest of the cement paste (Figure 8.4.1-1).*

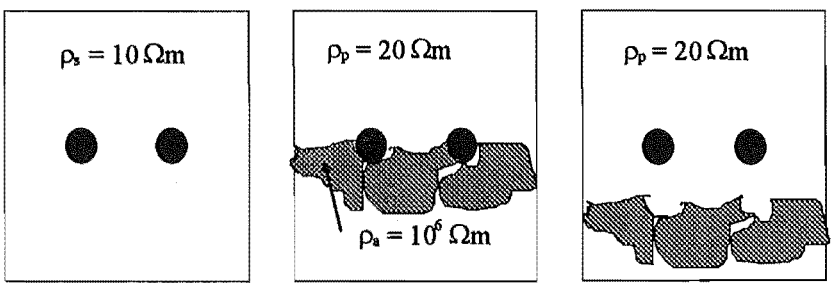

Figure 8.4.1-1. Three examples of a two electrode system to show the effect of aggregate arrangement on measured resistivity. (a). Calibration solution of uniform resistivity, (b). Concrete with 'sheet' of aggregate cutting space in half, (c). Same concrete mix as b., but with aggregate displaced.

Clearly, the measured resistivity will be very dependent on the aggregate arrangement even if extreme cases (as described in the footnote) do not appear. The validity of calibration constants so determined will depend very much on the size and spacing of the electrodes, relative to the aggregate dimensions. (Resistivity profiles generated using calibration constants determined according to this method are shown in the results section).

We assume the system has been calibrated using a conducting solution of resistivity $\rho_s = 10$ ohm-m. The resistance between the electrodes of $R_s = 50$ ohm, yielding a calibration constant $k = 0.2$ (ohm-m/ohm).

If the cement paste has a resistivity ρ_p of 20 ohm-m, and the aggregate a resistivity ρ_a of 10^6 ohm-m, we can roughly calculate the measured resistance and resistivity. If the cube was filled with cement paste rather than concrete, the measured resistance is

$$R_{meas} = \rho_p / k$$
$$= 20 / 0.2$$
$$= 100\ ohm$$

However, with the sheet of aggregate blocking the current from passing throughout the cell, the measured resistance will be approximately twice that of the paste alone, ie 200 ohm (since for the same applied voltage only half the current will flow). Applying the calibration constant, the measured resistivity will be

$$\rho_c = k \cdot R_{meas}$$
$$= 0.2 \times 200$$
$$= 40\ ohm - m.$$

If the aggregate entirely filled the bottom half of the cube the measured resistivity would be the same. An intermediate measurement would result if the sheet of aggregate was displaced downward somewhat from the electrodes.

8.4.2 In situ calibration

A second method of calibrating an electrode system is to take account of the aggregate distribution (or 'aggregate scatter factor') in the calibration process by calibrating the HES when embedded in the concrete. For in-situ calibration, measurements of resistance are made between each pair of electrodes before the sample has had time to develop a resistivity profile by drying.

At the same time as these measurements are taken, the resistivity of concrete in a calibration cell from the same batch and stored under the same conditions, must be determined as described in Section 8.2. The calibration cells used were 100 mm sided cubic moulds. The parallel electrodes were two stainless steel plates on to which a fine stainless steel mesh had been spot-welded. They made up two opposite sides. Calibration took place at some time between the setting of the concrete and the end of the curing period about seven days later (Figure 8.4.2-1).

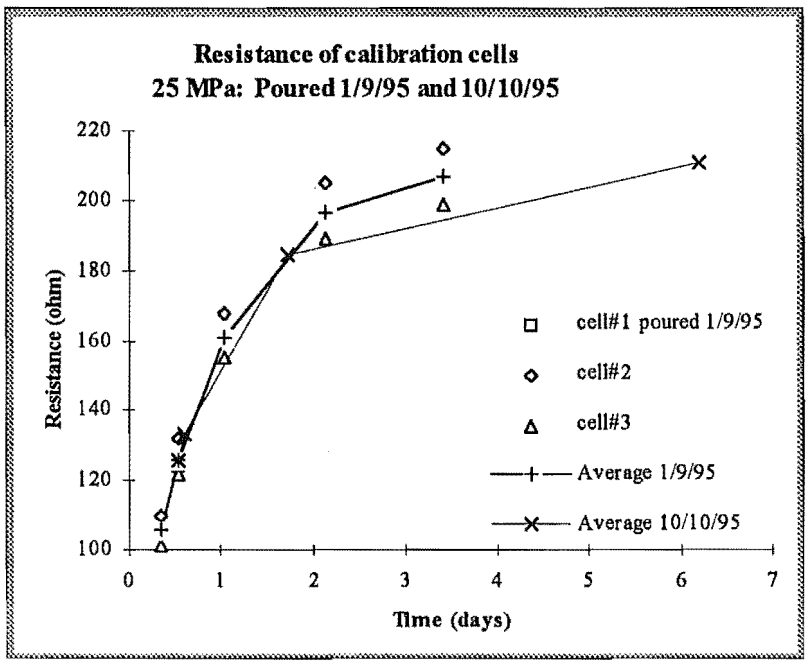

Figure 8.4.2-1: Examples of resistance measurements made from cubic calibration cells. The calibration factor k_{cell} to convert from resistance to resistivity is just the ratio of the area of one electrode (A= 0.01 m^2) divided by the distance between the electrodes (l = 0.1 m), that is k_{cell} = 0.1 (ohm-m/ohm).

Strictly speaking, the calibration factors determined using the in-situ method will remain valid only to the extent that the current distribution throughout the sample remains constant. In fact, their validity will weaken with time because:

- the resistivity of the cement paste will rise while that of a non-porous aggregate will change little and
- as a profile develops the current density will increase in the lower resistivity regions relative to the drier regions.

Differences in the cement-paste-aggregate distribution around two pairs of electrodes at the same level which are calibrated at the same time, will be reflected in their respective calibration factors. Consider the situation illustrated by Figure 8.4.2-2, in which pairs of electrodes are shown surrounded by different distributions of aggregate. Because the paste has a lower resistivity than aggregate, the resistance R_a measured between the electrodes in (a), will be greater than R_b measured between the electrodes in (b). Thus the calibration constant k_a for (a) will be less than k_b for (b).

As the cement paste dries, the actual average resistivity in the region around the electrodes in (b) increases faster than in (a) so that the resistivity measured in (b) will be greater than in (a).

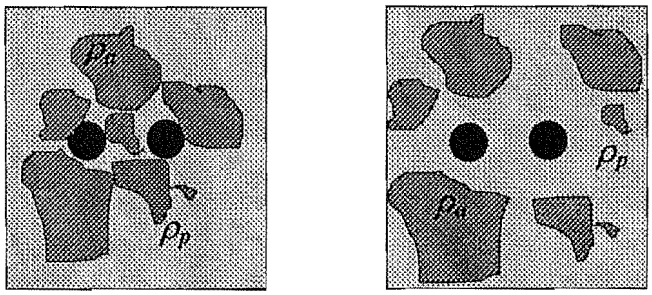

Figure 8.4.2-2. Schematic showing two random distributions of aggregate around two measurement electrodes. The left-hand electrodes have a higher cement-paste-aggregate ratio in the region immediately surrounding the electrodes and will result in a higher scale factor. On the other hand, as the paste dries and increases in resistivity, the change in resistance will be higher around the two electrodes in b), so that this pair will indicate a higher resistivity than the left-hand pair.

The deleterious effect of the development of a resistivity profile within the paste matrix, on the validity of the calibration constants may be reduced by keeping the electrodes close together so that the bulk of the current passes through as small a vertical range as possible.

The validity of calibration constants will depend also on the concrete having a uniform resistivity at the time of calibration. This must be carried out before a profile has time to develop.

8.5 Modelling of embedded electrode systems

Modelling of embedded electrode systems was undertaken to determine how the validity of the calibration constants is maintained as the resistivity gradient increases. The effects of increasing the electrode separation, of changing the depth of measurement, and of changing the electrode dipole orientation were also investigated.

The finite difference program used to model the behaviour of embedded electrode systems, was based on earlier work by the author using a resistance grid and a paper by Radstake et al. (1991). The program is described in Chapter 4.

The two dimensional model[2] assumed a pair electrodes of square cross-section, 4 mm wide. To determine the calibration constants the electrodes were set in an environment of uniform resistivity ρ_{cal}. At this time, a potential difference of 2 volts between them was applied and the resulting current calculated. Then the resistance R_{cal} between the electrodes was determined and the calibration constant k was calculated as in Section 8.4. That is

$$k = \frac{\rho_{cal}}{R_{cal}}.$$

The resistance R between the electrodes was then determined as the resistivity gradient was increased. The measured resistivity ρ_{meas}. was then calculated using

$$\rho_{meas} = k \cdot R_{meas}.$$

The error in measurement was calculated using

$$Error = \frac{\rho_{act} - \rho_{meas}}{\rho_{act.}} \cdot 100\%$$

where ρ_{act} is the actual resistivity midway between the electrodes.

The effect on the measurement error of increasing resistivity gradient is illustrated in Figure 8.4.2-3, for vertical and horizontal pairs of electrodes. The positive error indicates that the calibrated system under-estimates the resistivity between the electrodes. The

---

[2] Some work was done in attempting to transform from the two dimensional case or its equivalent of infinitely long line electrodes on a three dimensional half-space. In particular a line of argument outlined by Niwas and Israil ( ) was explored. However the resulting Matlab program was unable to adequately carry out the transformations. At the time of writing a satisfactory solution has not been found.

error is nearly twice as great for the vertically aligned pair. Nevertheless, the error is less than 1% and is virtually constant for resistivity gradients above 10^5 ohm-m/m.

This asymptotic behaviour of measurement error could be due to the finite thickness of the slab. As the gradient increases, When a gradient exists, the measured resistivity equals the resistivity at some point beneath the midpoint of the electrode pair. As the gradient increases, the matching resistivity occurs further below the electrode pair midpoint. However the base of the slab is nonconducting. The current distribution will increasingly concentrate near the base as the gradient increases, but eventually large increases in gradient will result in increasingly minor changes in current distribution and hence in measurement error.

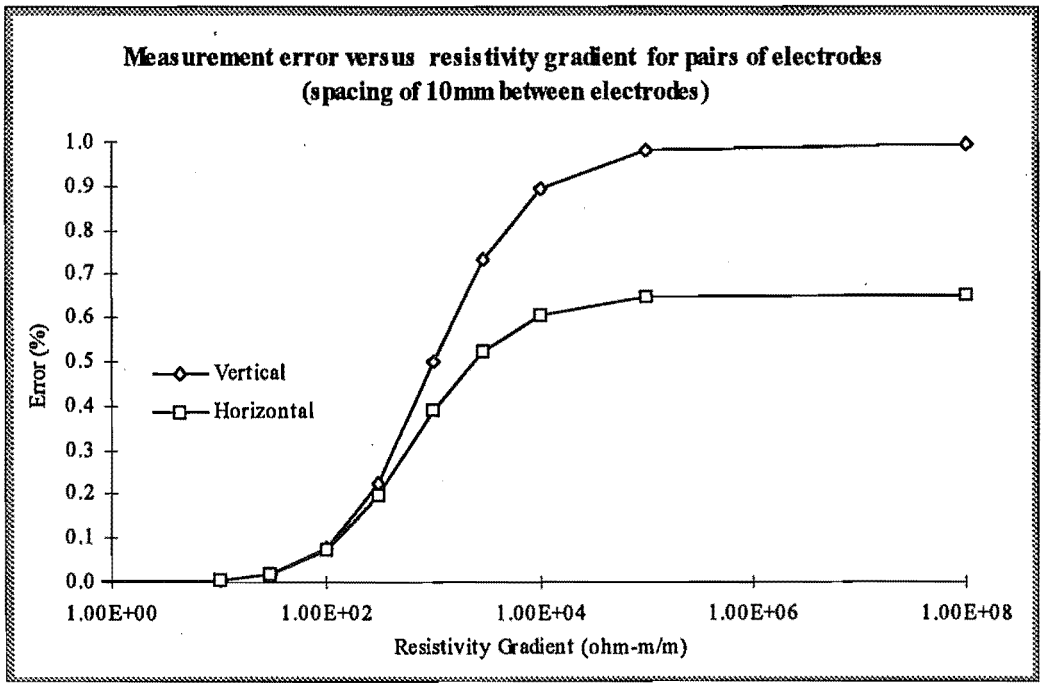

Figure 8.4.2-3: The error in measurement of the resistivity between electrodes in a resistivity gradient for vertically and horizontally aligned electrode pairs.

When the electrode spacing is increased, the measurement error increases (Figure 8.4.2-4). A similar behaviour is noted when the electrode depth is decreased (Figure 8.4.2-5).

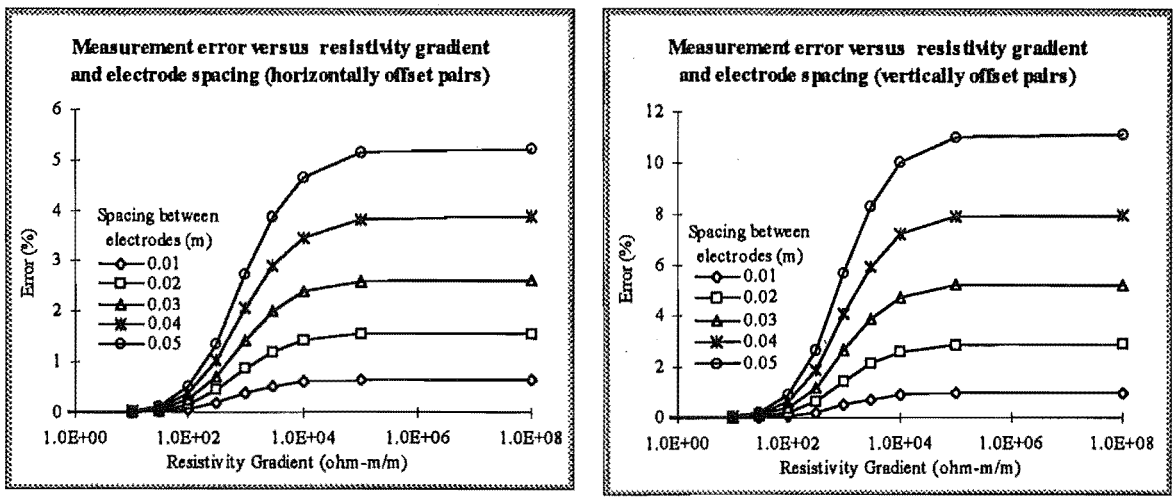

(a) (b)

Figure 8.4.2-4: Effect of resistivity gradient and electrode dipole spacing on measurement error using electrodes which are (a). horizontally aligned and (b). vertically aligned. Depth of measurement is 0.05 m.

Thus two dimensional modelling of embedded electrode pairs in a resistivity gradient suggests that measurement error due to the gradient:

1. increases with resistivity gradient, asymptotically approaching a maximum error (this last behaviour may reflect the finite thickness of the slab),
2. increases with decreasing distance between the electrodes and the surface,
3. increases with increasing spacing between the electrodes,
4. is always positive, that is, the calibrated system underestimates the resistivity between the electrodes and
5. is quite small when electrode spacing is 10 mm (a maximum of 1%).

Furthermore, the error associated with a vertically aligned pair of electrodes (as in HES #1) is nearly twice that associated with a horizontally aligned pair (as in HES #3 and the more shallow measurement pairs in HES #2).

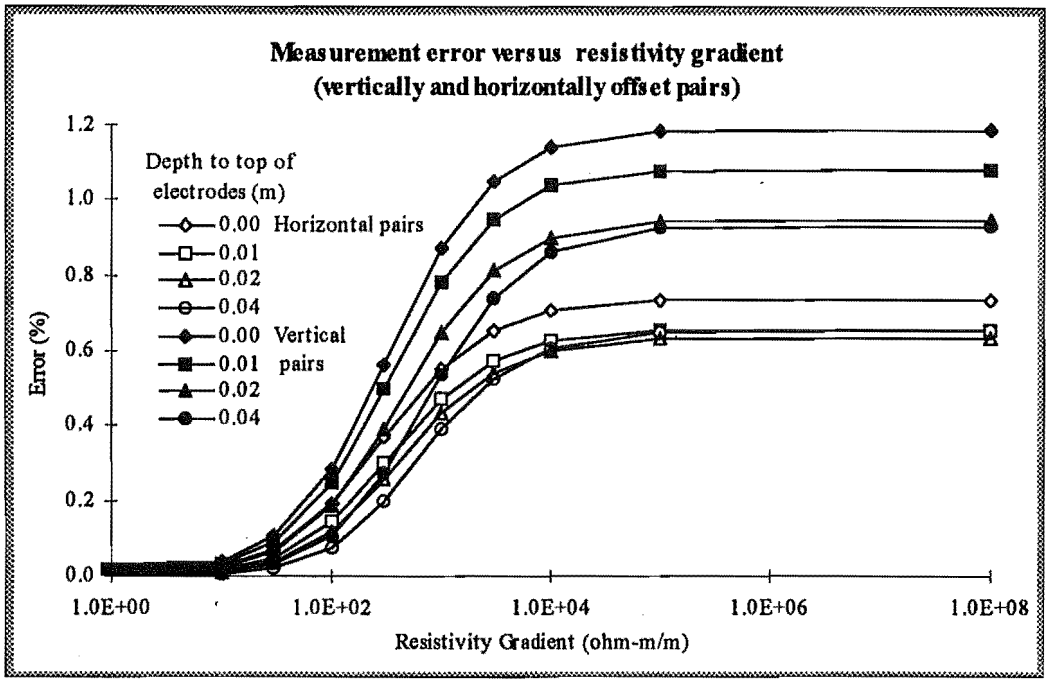

Figure 8.4.2-5 Effect of the resistivity gradient and the depth of measurement on measurement error. The electrode pair has a spacing of 10 mm centre-to-centre. The depth is measured to the top surface of the upper electrode (diameter 4 mm) so that 7 mm must be added to get the depth midway between the electrodes.

8.6 Results and Discussion: Part 1, Calibration and typical profiles

8.6.1 Parallel plate electrode system

The parallel plate electrode system allowed measurement of resistivity at five depths. Calibration of the electrode system was carried out using conducting solution (Section 8.4). Because these profiles did not have the form expected from a sample undergoing one-dimensional drying, the in-situ method (Section 8.4) of electrode system calibration was instituted. Profiles typical of each method are shown in Figure 8.6.1-1.

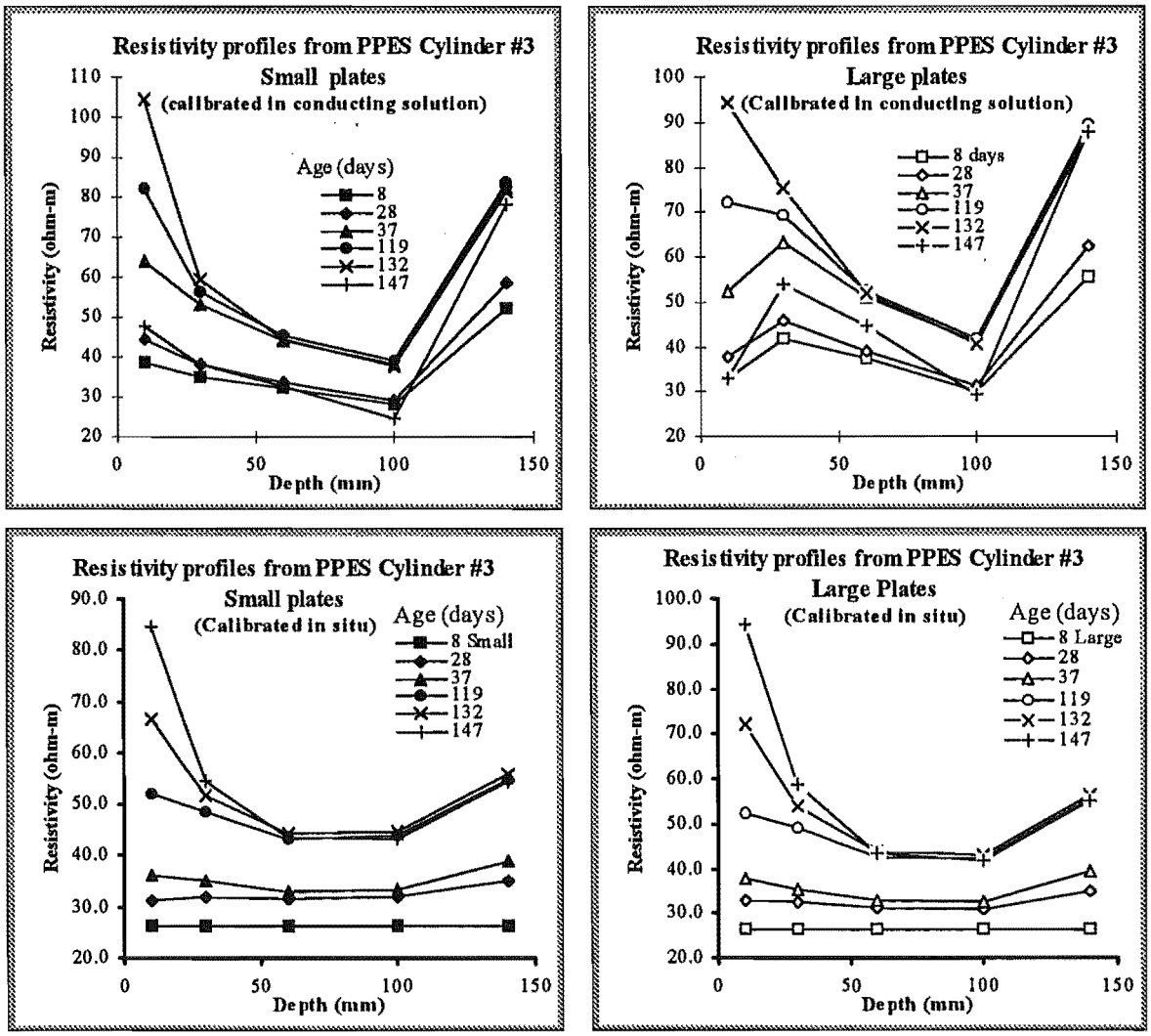

Figure 8.6.1-1: Resistivity profiles determined using the parallel plate electrode system (PPES) showing the effects of calibration constants determined using (top row) conducting solution and (bottom row) the in situ method.

The profiles from cylinders calibrated in situ are more in line with those expected, that is, falling from a high resistivity near the surface an having a gradient increasing most rapidly nearer the surface. However, the rise in resistivity near the sealed bottom surface

is surprising (Figure 8.6.1-1). This could indicate that the profiles were drying from the bottom surface as well. A similar rise was found in the profiles measured using horizontal electrode systems (HES) in Cylinders #2 and #4. The bases of cylinders #1 to #4 were plywood sealed with polyurethane. As polyurethane does not form a perfectly moisture impermeable layer, some drying could be expected from the bottom surfaces of the cylinders, and the slab coating may have failed. This may explain the profile form.

Later cylinder moulds were given several coats of a moisture impermeable membrane (Sika), and Slabs #3 to #8 each had a poly-vinyl-chloride membrane lining the base and sides. Profiles for these samples did not show a rise in resistivity as the bottom surface.

The calibration factors resulting from the two methods are shown in Figure 8.6.1-2 (a) for Cylinder #3. Interestingly, the factors determined for the smaller, closer pair of electrodes show more agreement between the two methods, than do those for the larger pair. I would have expected that there be greater averaging of non-uniformity for larger plates with greater spacing.

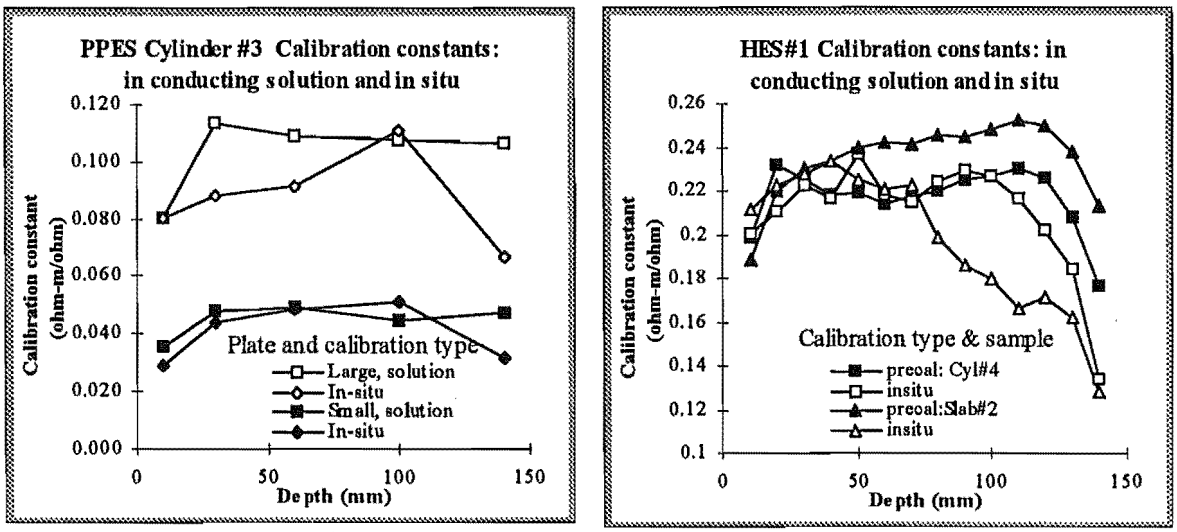

(a) (b)

Figure 8.6.1-2: Calibration constants determined using conducting solution and the in situ method. The graphs show those for (a) the PPES in Cylinder #3, and (b) the HES#1's in Cylinder #4 and Slab #2.

8.6.2 Horizontal electrode system #1: calibration

Horizontal electrode systems were used in all slabs and in all cylinders except #1 and #3. A comparison of HES#1 R20 calibration factors obtained using the two methods of calibration is given in Figure 8.6.1-2 (b) above. (An explanation of the terms R20, R21 etc is given in Section 8.2). If the two HES#1 used in the two samples (Cylinder #4 and

Slab #2) were identical, we would expect the conducting solution calibration factors to also be identical. Differences must be attributed to small differences in electrode alignment, variations in the solution conductivity or other unidentified causes. More work could have been done refining the conducting solution calibration method. However this method was abandoned in view of its inability to deal with the aggregate scatter factor and the relative ease and success of the in-situ method.

Considerable variation in calibration factors is associated with the use of in-situ calibration (Figure 8.6.2-1). This is largely due to the aggregate scatter factor, that is, to the non-uniformity of the concrete due to the presence of aggregate. Scatter may also be caused by differences in electrode-concrete interface resistance. Two-electrode measurements are very sensitive to interface resistance which may vary with the distribution of aggregate. The effective interface resistance may change also due to changes in polarisation at the electrodes.

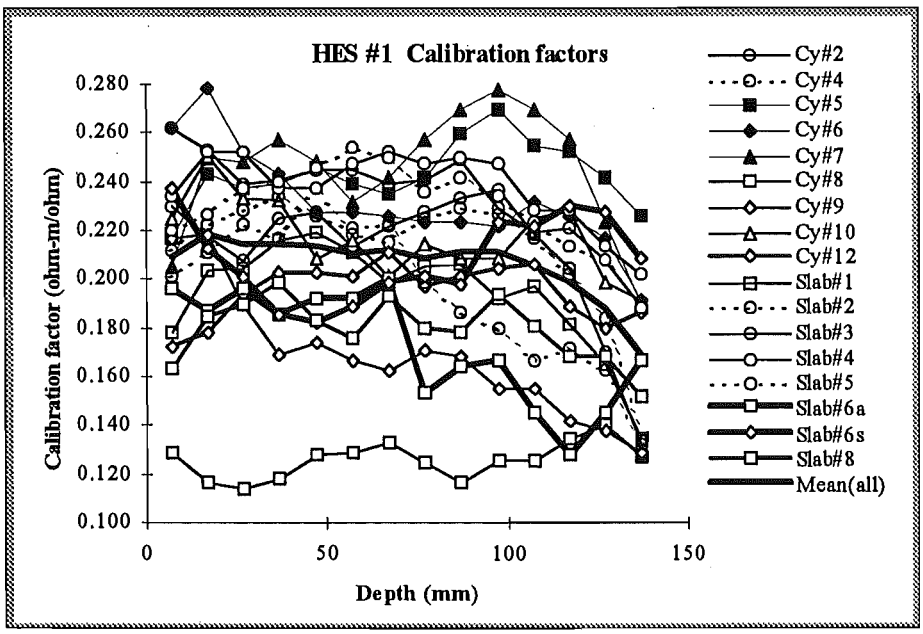

Figure 8.6.2-1: Calibration factors for all HES#1, determined using the in-situ calibration method. These factors are for R20 measurement, that is, for measurements between two adjacent electrodes in HES#1.

If variation in interface resistance and polarisation is a significant effect, we would expect more scatter in the two electrode measurements (R20, R21, R22 and R23) than the four electrode measurement (R42) since the measurement electrodes in a four electrode measurement draw very little current. However when calibration factors are collated for the samples using the five types of measurement (R20, R21, R22, R23 and R42), there is

marginally less variation in the two electrode measurements than in the four electrode measurement (Figure 8.6.2-2).

Furthermore, measurements made with larger spacing between electrodes exhibit slightly lower average variation than those from more closely spaced electrodes. This small effect is likely to be due to the more dispersed current distribution lowering the weighting given to the concrete immediately between the electrodes.

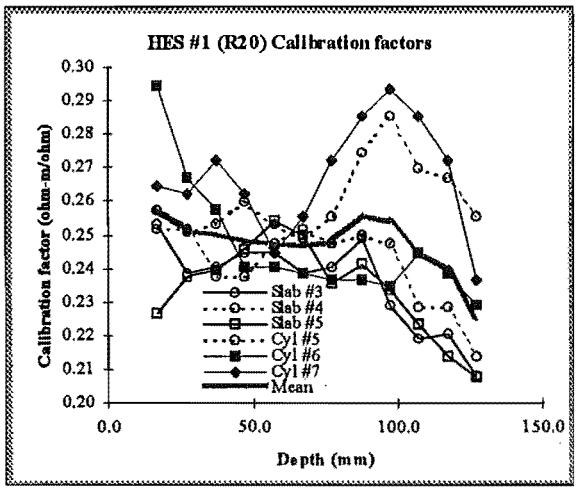

(a) R20

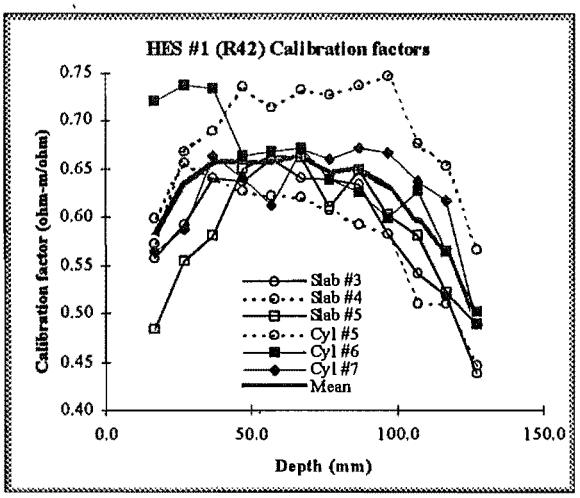

(b)

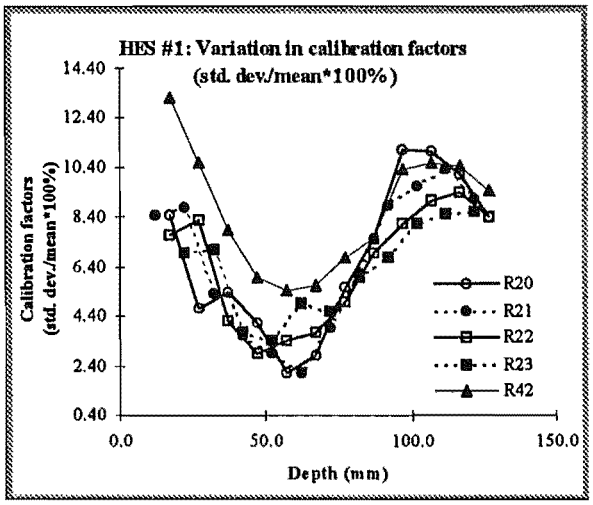

(c)

Figure 8.6.2-2: Calibration factors for (a) R20, (b) R42 measurements carried out using HES#1 in six concrete samples:. In (c) the relative variation in calibration factors for all five types are shown. For each measurement type and at each depth, the variance is calculated as the standard deviation over the six samples expressed as a percentage of the mean.

Scatter in calibration factors is due more to the variation in aggregate distribution in the vicinity of the electrodes than to variation in electrode-concrete interface resistance.

The other factor that appears to influence the calibration factors is the age of the concrete at the time of calibration (see Table 8.6.2-1).

Table 8.6.2-1: Curing conditions and age at calibration of concrete samples.

Sample	Age at calibration (days)	Curing conditions	Electrode system
Cylinder[1] #2	*29*	*Fog room*	*HES #1*
Cylinder #4	8	Fog room	HES #1
Slabs #1 & #2	8	Fog room	HES #1
Cylinders #5, #6 & #7	7	Fog room	HES #1
Cylinders #8, #9 & #10	3	Covered outside	HES #1
Cylinders #11, #12 & #13	2	Covered, warm	HES #2, HES #1 & HES #2 respectively
Slab #3	9	Covered, cool	HES #1, #2 & #3
Slab #4 & #5	7	Covered, cool	HES #1, #2 & #3
Slab #6	2	Covered, warm	HES #1 & #2
Slab #7	0.6	Covered, warm	HES #1(failed) & #2
Slav #8	2	Covered, warm	HES #1 & HES #2

Note 1.: Cylinders #1 and #2 are anomalous in that the curing time and age of calibration was 29 days after pouring. Later samples had much shorter curing times.

If the calibration factors are grouped by age at calibration, the influence of this factor becomes clear. Figure 8.6.2-3 shows that calibration factors determined within three days of pouring (left-hand graph) show more variation those determined a week or more after pouring (right-hand graph). The HES#1a in Slab #6 is so far below the general trend that it has been omitted from the calculation of the means and variances. Even without this data, the mean and variance of the two groups show marked differences between the two groups (see Figure 8.6.2-4 and Table 8.8.2-2).

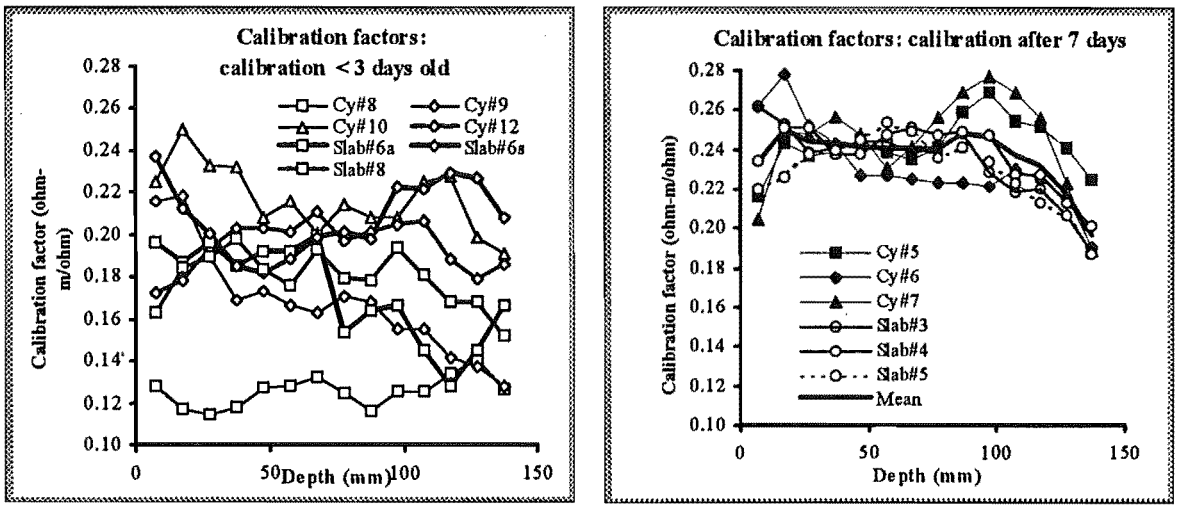

Figure 8.6.2-3: The influence of the age at calibration on variation in calibration factors.

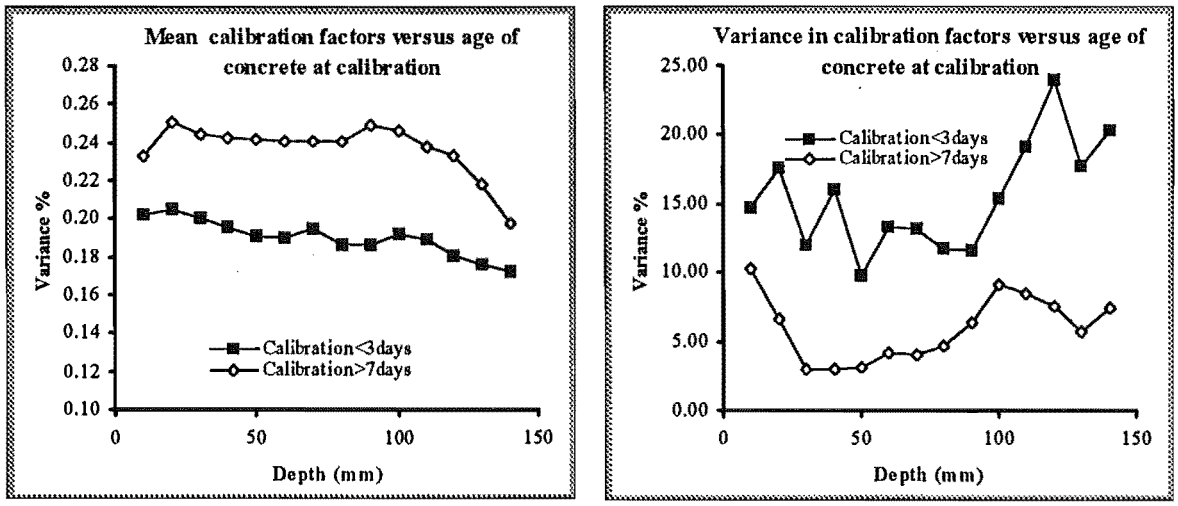

Figure 8.6.2-4: Comparison of mean and variance in calibration factors for different groups of concrete samples showing the influence of the age of concrete at calibration. (see Table 8.8.2-2).

Of the samples which were calibrated a week or more after pouring, there appear marked differences between the earliest cylinders and slabs and the later ones (Figure 8.6.2-5). The early samples show a more rapid fall-off in calibration factor near the base of the sample and exhibit greater extremes in the value of the calibration factors, than do the later samples .This may be a result of the imperfect sealing of the earlier samples. Should they have been allowed to dry from the bottom surface, the resistivity would increase rapidly toward the base although somewhat less rapidly than it would towards the top surface. The sample is assumed to have a uniform resistivity at the time of calibration so

that the calibration factors would decrease toward the base as shown. The calibration factors of the early group also show greater variance.

Table 8.6.2-2: Comparison of the mean and variance of calibration factors for groups of concrete samples cured under different conditions and calibrated early (< 3 days after pouring) or late (>7 days after pouring).

Mean and variance of calibration factors for HES #1

	Age<3days at calibration[1]		Age >7 days at calibration[2]	
Depth (m)	Mean	variance[3]	Mean	variance
0.01	0.202	15	0.233	10
0.02	0.205	18	0.250	7
0.03	0.201	12	0.244	3
0.04	0.196	16	0.243	3
0.05	0.190	10	0.241	3
0.06	0.190	13	0.241	4
0.07	0.194	13	0.240	4
0.08	0.186	12	0.241	5
0.09	0.186	12	0.249	6
0.1	0.192	15	0.247	9
0.11	0.189	19	0.238	8
0.12	0.181	24	0.233	8
0.13	0.176	18	0.218	6
0.14	0.172	20	0.198	7
Mean	0.190	15.4	0.237	6.0

Note: 1. Cylinders #9, #10 and #12, Slabs #6 (HES#1a in Slab #6 omitted) and Slab #8.
2. Cylinders #5, #6 and #7, Slabs #3, #4 and #5.
3. Variance defined as standard deviation/mean * 100%.

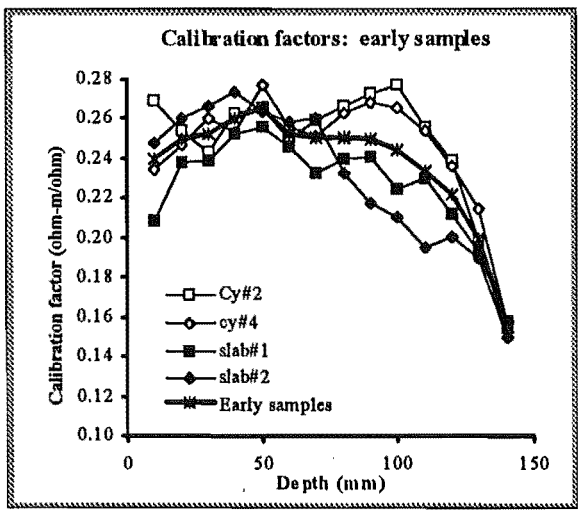

(a) Early concrete samples

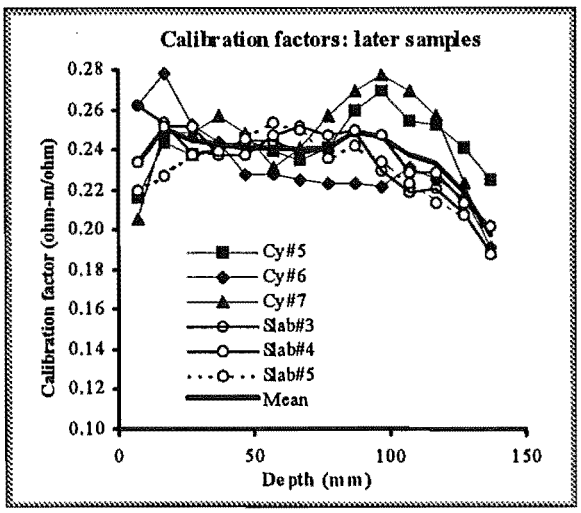

(b) later concrete samples

Figure 8.6.2-5: Calibration factors for HES#1 used in different groups of samples (continued on the next page).

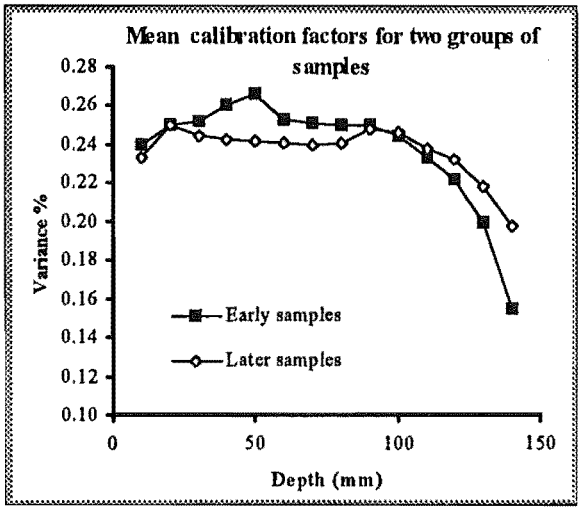

(c) Comparison of the means of the calibration factors from early and later samples

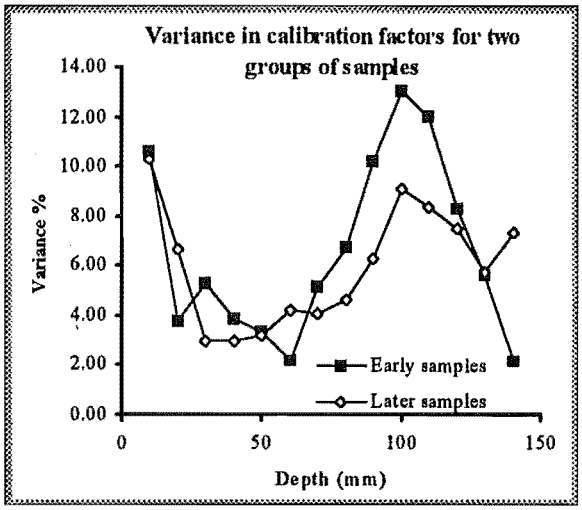

(d) Comparison of the variance in calibration factors.

Figure 8.6.2-5: (continued) Other influences on the calibration factors may be responsible for the differences between the two groups of calibration factors shown here. The most likely difference between the two groups is the possibility that the "early group" may have lost moisture through the base of the sample.

The anomalous HES#1a in Slab#6 was used to measure profiles from within the first hour of pouring (see Section 8.6.4). It is possible that polarisation of the electrodes took place at this stage that was irreversible. The higher resistance resulting would yield lower calibration factors. If so, doubt could be cast on the validity of profiles measured at such an early stage. However, as will be seen in Section 8.7, the profiles recorded by the HES#1's in Slab#6 show agreement as good as if not better than any other pairs of electrode system.

Perhaps here is the time to note that lack of agreement in the calibration factors is not necessarily a problem. That profiles may show good agreement when calibration factors differ markedly speaks for the robustness of the resistivity measurement system!

8.6.3 Horizontal electrode system #1:profiles

Profiles determined using HES#1 are shown in Figure 8.6.3-1. Over the 194 day measurement period, the differences between profiles measured using the different measurement types are small. The two-electrode-measurement profiles are very close, whereas the R42 profile is about two ohm-m below the others after 50 days.

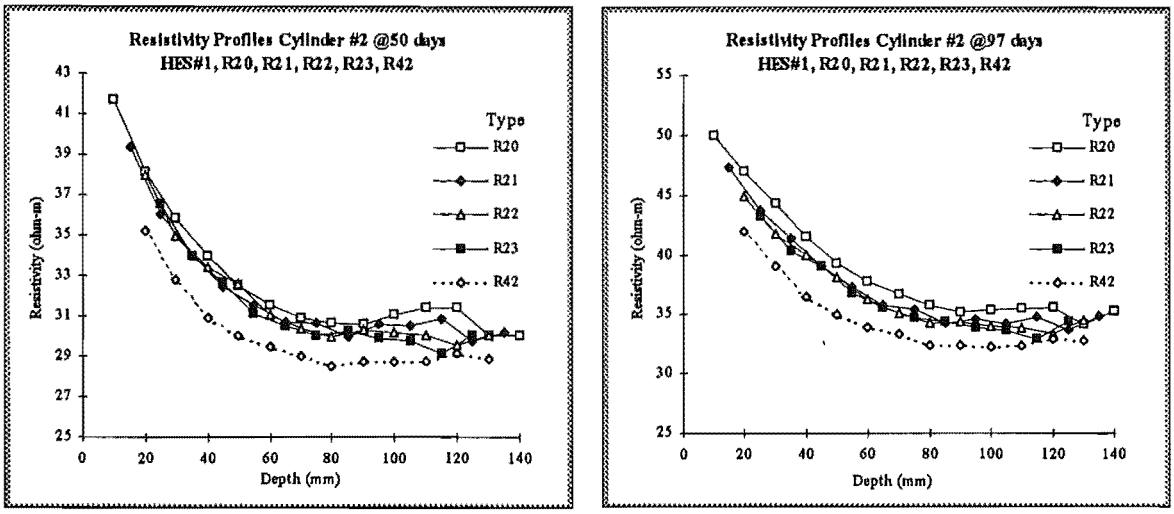

(a) (b)

Figure 8.6.3-1: Profiles measured in Cylinder #2 at (a) 50 days and (b) 194 days, using the five measurement types (R20,R21, R22, R23 and R42).

Further profiles are shown in Figure 8.6.3-2. These are taken from the HES#1 in Cylinder #5 and show a similar close agreement between the measurement types. Note that the resistivity profiles have greater gradient than those from Cylinder #2. After 194 days the greatest resistivity measured in Cylinder #2 is less than 105 ohm-m. After 75 days, the resistivity reaches above 1700 ohm-m in Cylinder #5. The difference is due to the short curing time (7 days) of Cylinder #5 compared to Cylinder #2 (28 days).

Hydration can only proceed if there is sufficient moisture available (see Chapters 2, 3 and 10). After fresh concrete has set , the surface should be kept wet to ensure maximum hydration of concrete near the surface. The curing period refers to that period where the concrete is kept moist by (for example) spraying with water, covering with wet hessian or being placed in a fog-room. Well cured concrete is characterised by high strength and low porosity. If the surface is allowed to dry before hydration is complete, hydration will slow or cease completely leaving the surface regions in a relatively immature, porous state. As the pores will tend to be large compared to well cured concrete, they will also contain less condensed water at a given relative-humidity and hence those regions will have a higher electrical resistivity.

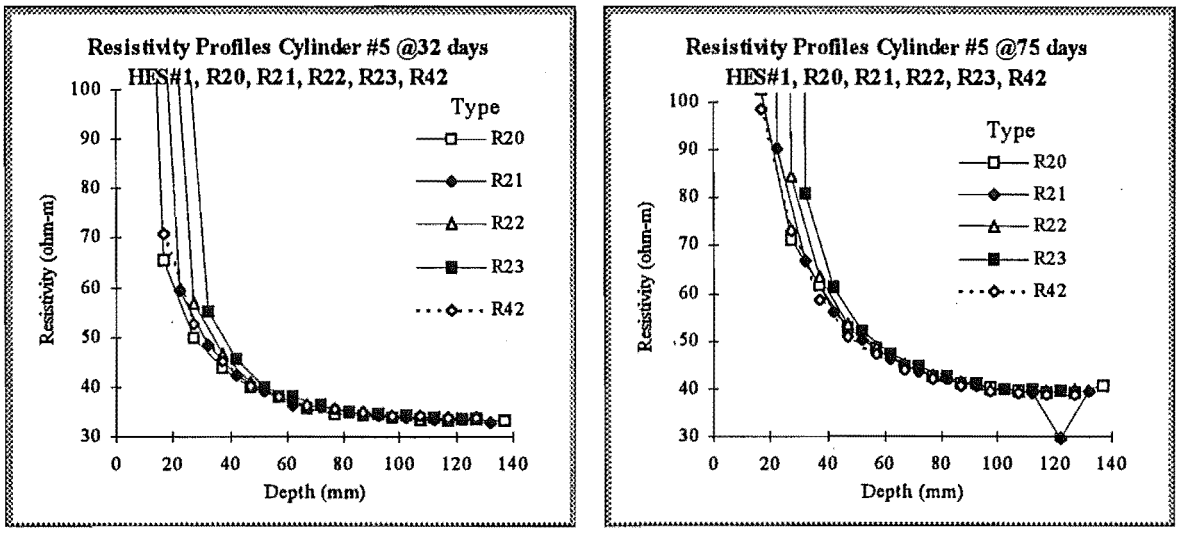

(a) (b)

Figure 8.6.3-2: Profiles measured in Cylinder #5 at (a) 32 days and (b) 75 days, using the five measurement types (R20,R21, R22, R23 and R42).

Cylinders #5 to #13 and Slabs #3 to #8, had curing times of about seven days and shared with Cylinder #4 the steep profiles shown in Figure 8.6.3-2. The earlier cylinders (#1 - #4) and slabs (#1 and #2) had longer curing times and had relatively gradual profiles.

Where samples have undergone short periods of curing, their resistivity profiles near the surface are more steeply rising with a more rapidly increasing gradient, compared to profiles from samples cured for longer.

Table 8.6.3-1: Typical measurement of resistivity at 17 mm beneath the surface.

Type	Electrodes used	Resistivity (ohm-m)
R20	2 and 3	103
R22	1 and 4	1008
R42	1,2,3 and 4	99

The most shallow measurement of each measurement type uses the top electrode. The air concrete boundary and the high resistivity near the surface results in a higher measured resistivity, if the top electrode is used rather than one lower down. Thus, to measure at 17 mm below the surface, R20 uses electrodes 2 and 3 (where the top electrode is labelled '1') and R22 uses electrodes 1 and 4 (see Table 8.6.3-1). The R22 measurement is ten times higher than the R20 measurement. The R42 measurement agrees with the R20 one.

The R42 resistivity measurements agree with the R20 measurements which are centred at the same depth. They share measurement electrodes at these measurement depths.

This suggests that it is the separation of the measurement electrodes that determines the resolution of R42 measurements.

It is likely that the top measurement is always higher than the true value. Electrode pairs of smaller separation will yield higher resolution. The 10 mm separation of electrode centers in R20 measurement does not result in significantly more scatter. *The close agreement of the measured profiles suggested that it was unnecessary to use all five measurement types. It was decided to use R20 as the main measurement type with the remaining concrete samples, although some R42 measurements were taken.*

8.6.4 Changes in resistivity at the time of calibration

The HES#1 embedded electrode system in Slab#6 was used to study the development of the resistivity profile from the time of pouring. This HES#1 had a 15 pin din plug raised above the surface of the concrete (hence the label HES#1a(erial)! The other HES#1 in Slab #6 was submerged as usual - hence HES#1s). This enabled the HES to be plugged in immediately rather than awaiting unsealing when the concrete had set and water relatively tightly bound.

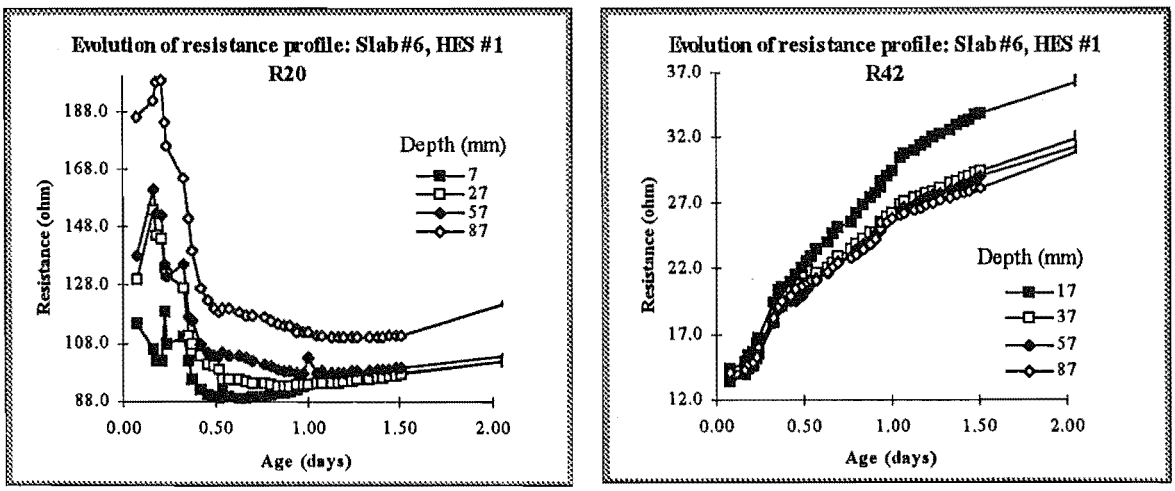

(a) (b)

Figure 8.6.4-1: The evolution of resistance between electrodes using (a) R20 and (b) R42 measurement.

R20 and R42 measurements were taken and the resistance profiles obtained are shown in Figure 8.6.4-1. The resistance measured at the time of calibration is equated to the resistivity measured in a cubic calibration cell. At this time the resistance curves illustrated in these graphs, should be moving together. If the resistance at one depth is

growing faster than at another, then the calibration constants will be highly dependent on the time of calibration.

Note the rapid decrease in R20 resistance in the first 12 hours after pouring. This contrasts markedly with the steady increase in R42 resistance. Note also the different rates of change of R20 resistance measured at different depths. The optimal time for calibration may be about 36 hours after pouring in this slab, but there is a certain arbitrariness about the time, for the relationships between the resistance measured at different depths is constantly changing.

The difference between the R20 and R42 measurements arises because the two electrode measurement is sensitive to changes in the electrode-concrete interface resistance. The fall in R20 resistance in the first 12 hours is coincident with the dissolving of the outer layers of cement grains and the resultant increase in ionic concentration. The major effect is probably to do with polarisation at the current electrodes rather than in the bulk concrete since the R42 resistance shows a steady rise during this period.

8.7 Results and discussion: Part 2, precision

The assessment of the horizontal electrode systems (HES's) includes judgement of accuracy and precision. The accuracy of a resistivity measurement requires it to be compared with some independent measure of resistivity of known accuracy. In practice, the independent measurements are just those of other HES's in the same concrete sample, or in concrete from the same batch, stored under the same conditions. That is, absolute accuracy cannot be determined. On the other hand, the variation in resistivity measured using different HES in the same or equivalent samples at the same depth enables determination of the precision with which resistivity profiles can be measured. In this section methods of comparison of measured profiles will be investigated. A summary of possible comparisons is given in Table 8.7.1-1.

Table 8.7.1-1: Comparisons that could be made between profiles measured with different HESs of the same or different type in the same or similar samples. Where different profiles measured with different HES types are to be compared, one or other profile must be interpolated to match depths.

Description of comparison	Reference
The same HES type in similar samples	**Section 8.71**
HES#1 in Cylinders #5, #6, and #7,	
HES#1 in Cylinders #8, #9, and #10,	
HES#1 in Slab #4 and #5	
HES#2 in Slab #4 and #5	
HES#3 in Slab #4 and #5	
Different HES types in the same sample	**Section 8.7.2**
HES#1, #2 and #3 in Slab #3 (interpolate)	
HES#1, #2 and #3 in Slab #4 (interpolate)	
HES#1, #2 and #3 in Slab #5 (interpolate)	
Two HES#1s and one HES#2 in Slab #6 (interpolate)	
HES#1 and HES#2 in Slab #8 (interpolate)	
Different HES types in similar samples	**Section 8.73**
HES#1 and HES#2 in Slab #8 and HES#1 in Cylinder 12 and HES#2s in Cylinders #11 and #3	

A measure of error commonly used in the decision making processes when recovering resistivity profiles from vertical electric sounding (VES) data, is the root-mean square (RMS). The RMS error is a measure of the goodness-of-fit between model data ρ_i (based on the trial or model profile) and the measured data ρ_i^*, {i = 1,2,3...m where m is the number of data points in the VES curve}. The RMS is defined as

$$RMS = \sqrt{\frac{\sum_{i=1}^{m}\left[\left(\rho_i - \rho_i^*\right)/\rho_i^*\right]^2}{m}}$$

and may be used as a measure of the overall agreement between two sets of data.

For three or more sets of data this method is not suitable. Instead the standard deviation provides a convenient measure. However, since, profiles may range between moist deep areas having resistivities of the order of 10 ohm-m and dry surface layers with resistivities around 100,000 ohm-m. We define a normalised variance as the standard deviation of a set of two or more points expressed as a percentage of the mean of the points. Each of the comparisons have been evaluated using this parameter.

The variance varies with both depth and age. Where appropriate an overall 'goodness-of agreement' can be assigned to two or more profiles by determining the mean of the variation over the depth range. This enables a similar normalising of the error as dividing by ρ_i^*, does in the *RMS* formula.

The comparisons generally show a strong rise in variance with decrease in depth through about 20 mm. To avoid the undue influence of this locally poor precision on judgement of the precision of measurement at greater depths, an average 'variation' may be determined for a subset of depths.

8.7.1 Comparisons of the same HES type in equivalent samples.

8.7.1.1 HES#1 in Cylinders #5, #6, and #7.

The 75- and 160-day profiles from resistivity- relative-humidity calibration cylinders #5, #6 and #7 are shown in Figure 8.7.1-1. The semilog scale in the right-hand graphs shows clearly how resistivity climbs sharply towards the surface. The left-hand graphs show profiles up to 200 ohm-m on a linear scale. This enables a visual appreciation of the agreement between the three independent measurements and its deterioration above 25 mm. The standard deviations (each three points) at all times and depths is presented in Table 8.7.1-1. The standard deviation for the top data point grows rapidly, reaching 13.9 k ohm-m after 160 days. This represents 54% of the mean measured resistivity at this depth (see Table 8.7.1-2). The variance (standard deviation as percentage of the mean) is shown in Figure 8.7.1-2. Generally, below about 25 mm, the variance is largely independent of depth but tends slowly, to rise with resistivity.

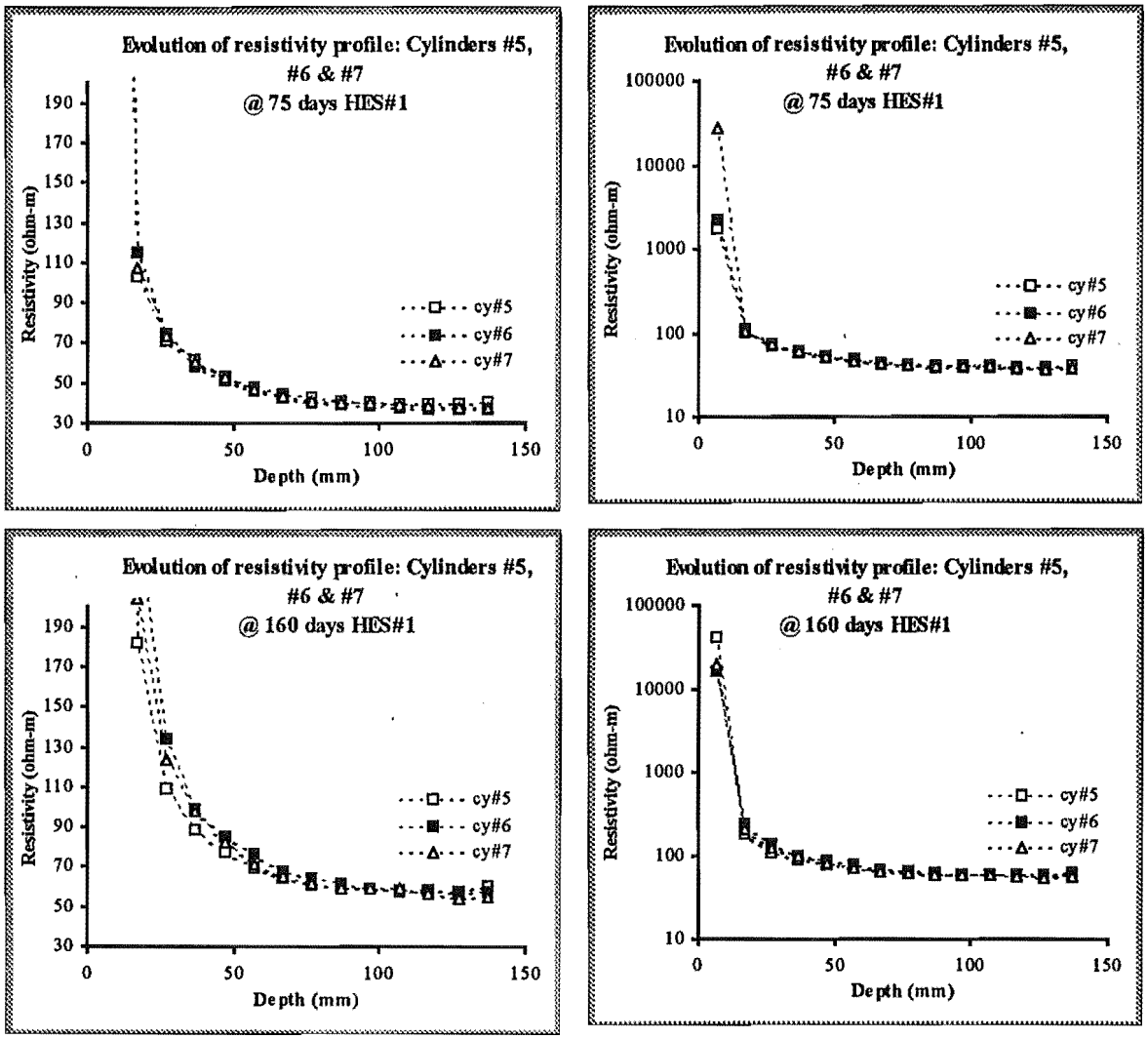

Figure 8.7.1-1: Resistivity profiles for three concrete samples of the same mix and poured at the same times.

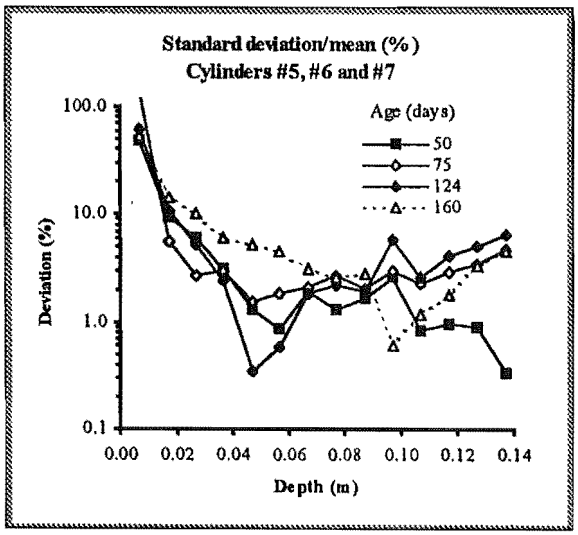

Figure 8.7.1-2: Variance or standard deviation of profiles from Cylinders #5, #6 and #7 expressed as a percentage of the mean.

Table 8.7.1-1: Standard deviation of profiles measured in Cylinders #5, #6 and #7.

Depth (m)	Standard deviation (ohm-m)					
0.007	7.9	63	553	14742	18341	13891
0.017	2.1	6.9	8.7	6.1	18.5	29.8
0.027	1.1	3.2	3.9	2.0	5.5	12.5
0.037	0.3	1.1	1.7	1.8	2.1	5.8
0.047	0.3	0.3	0.6	0.8	0.3	4.2
0.057	0.4	0.1	0.4	0.9	0.4	3.3
0.067	0.6	0.2	0.8	0.9	1.1	2.0
0.077	0.4	0.1	0.5	1.1	1.3	1.6
0.087	0.4	0.2	0.7	0.8	1.1	1.7
0.097	0.3	0.8	1.0	1.2	3.1	0.4
0.107	0.3	0.4	0.3	0.9	1.4	0.7
0.117	0.1	0.4	0.4	1.1	2.2	1.0
0.127	0.3	10.4	0.3	1.3	2.6	1.8
0.137	0.4	8.5	0.1	1.8	3.4	2.6
Age (days)	15	41	50	75	124	160

Table 8.7.1-2: Mean, standard deviation and variation of profiles from measurement of HES#1s in cylinders #5, #6 and #7, aged 160 days.

	Resistivity (ohm-m)		Variation
Depth (m)	Mean	Std.dev.	(std.dev/mean)*100%
0.007	25849	13891	54
0.017	209	29.8	14.3
0.027	122	12.5	10.2
0.037	95	5.8	6.1
0.047	81	4.2	5.2
0.057	72	3.3	4.5
0.067	66	2.0	3.1
0.077	62	1.6	2.6
0.087	60	1.7	2.8
0.097	59	0.4	0.6
0.107	58	0.7	1.2
0.117	57	1.0	1.8
0.127	56	1.8	3.3
0.137	58	2.6	4.5
Average variation for depth ≥ 0.027 m			4%

8.7.1.2 HES#1 in Cylinders #8, #9, and #10.

Compared to those of Cylinders #5 to #7, the profiles recorded in Cylinders #8, #9 and #10 show more variation generally (around 12%), but less variation near the surface (Figure 8.7.1-3). However most of the variation appears to be due to Cylinder #10's curve being lifted above the other two.

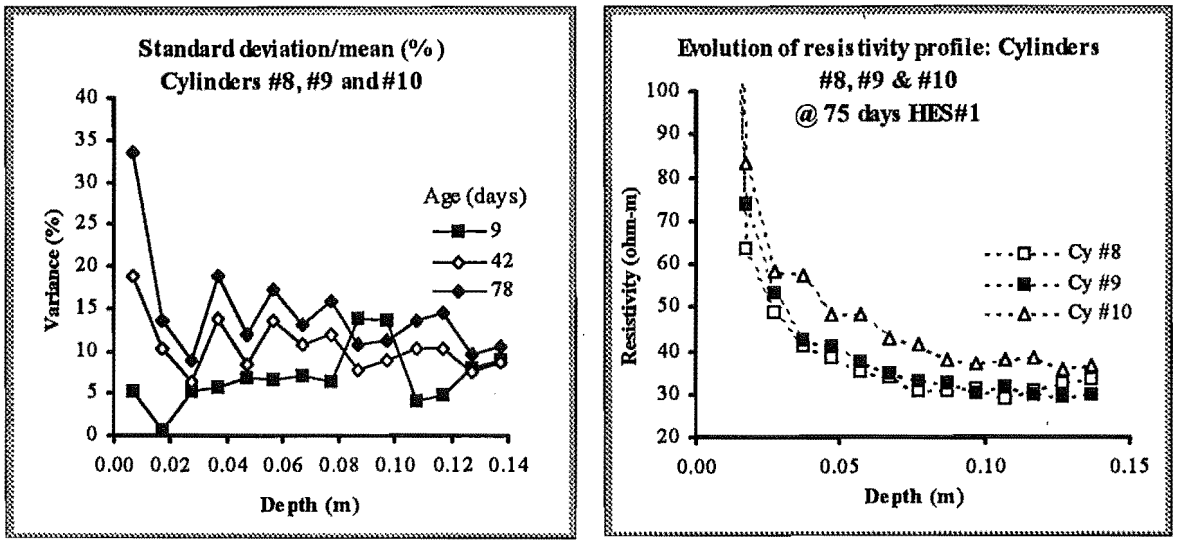

(a) (b)

Figure 8.7.1-3: (a) Variance of profiles from Cylinders #8, #9 and #10 during the first 78 days after pouring (b) Comparisons of the resistivity profiles at 78 days.

Table 8.7.1-3: Mean, standard deviation and variation of profiles from measurement of HES#1s in cylinders #8, #9 and #10, aged 78 days.

Depth (m)	Resistivity (ohm-m)		Variance
	Mean	Std.dev.	(std.dev/mean)*100%
0.007	307	103.1	34
0.017	74	10.0	14
0.027	53	4.8	9
0.037	47	8.8	19
0.047	43	5.1	12
0.057	40	6.9	17
0.067	37	4.9	13
0.077	35	5.6	16
0.087	34	3.6	11
0.097	33	3.8	11
0.107	33	4.5	14
0.117	33	4.7	14
0.127	33	3.1	10
0.137	33	3.5	11
Average variance for depths ≥0.027 m			13%

8.7.1.3 HES#1 in Slabs #4 and #5

Table 8.7.1-4: HES#1 in Slabs #4& #5 at 216days

Depth (m)	Resistivity (ohm-m)		Variance
	Mean	Std.dev.	(std.dev/mean)*100%
0.011	1813	1503.5	82.9
0.021	104	9.9	9.5
0.031	73	3.2	4.3
0.041	63	1.8	2.9
0.051	56	0.8	1.4
0.061	52	0.7	1.3
0.071	49	1.2	2.4
0.081	49	2.4	4.9
0.091	47	1.3	2.7
0.101	45	0.1	0.2
0.111	44	0.5	1.2
0.121	43	1.0	2.2
0.131	44	1.3	3.0
0.141	44	1.5	3.5
Average variation for depth ≥ 0.021 m			3%

8.7.1.4 HES#2 in Slabs #4 and #5

Table 8.7.1-5: HES#2 in Slabs #4 & #5 at 216 days

Depth (m)	Resistivity (ohm-m)		Variance
	Mean	Std.dev.	(std.dev/mean)*100%
0.006	545	359	66
0.007	562	282	50
0.009	363	58	16
0.013	153	14	9
0.018	102	17	17
0.025	79	9	11
0.033	65	4	6
0.042	58	5	9
0.053	52	6	11
0.065	51	3	7
0.078	45	3	7
0.093	43	5	10
0.109	43	5	12
Average variation for depth ≥ 0.025 m			10%

8.7.1.5 HES#3 in Slabs #4 & #5

Table 8.7.1-6: HES#3 in Slabs #4 & #5 at 216 days

Depth (m)	Resistivity (ohm-m)		Variance
	Mean	Std.dev.	(std.dev/mean)*100%
0.007	2496	416	17
0.009	2038	186	9
0.014	174	30	17
0.024	141	13	9
0.039	99	10	10
0.060	82	5	6
0.085	65	1	2
Average variation for depth ≥ 0.024 m			7%

According to these comparisons, we may say resistivity profiles measured with any of the HES types have good precision (variance $\leq 13\%$ for depths below about 0.025 m). Furthermore apart from the comparisons across Cylinders #8, #9 and #10, the HES #1 has the best precision with average variances of 5% or less for depths below about 20 mm.

- *This analysis shows that the HES system can be very reliable.*

8.7.2 Comparisons of different HES types in the same sample.

8.7.2.1 HES#1, #2 and #3 in Slab #3

Slabs #3, #4 and #5 had HES's of all three types embedded. Examples of profiles measured by the three types in slab #3 are shown in Figure 8.7.2-1 below.

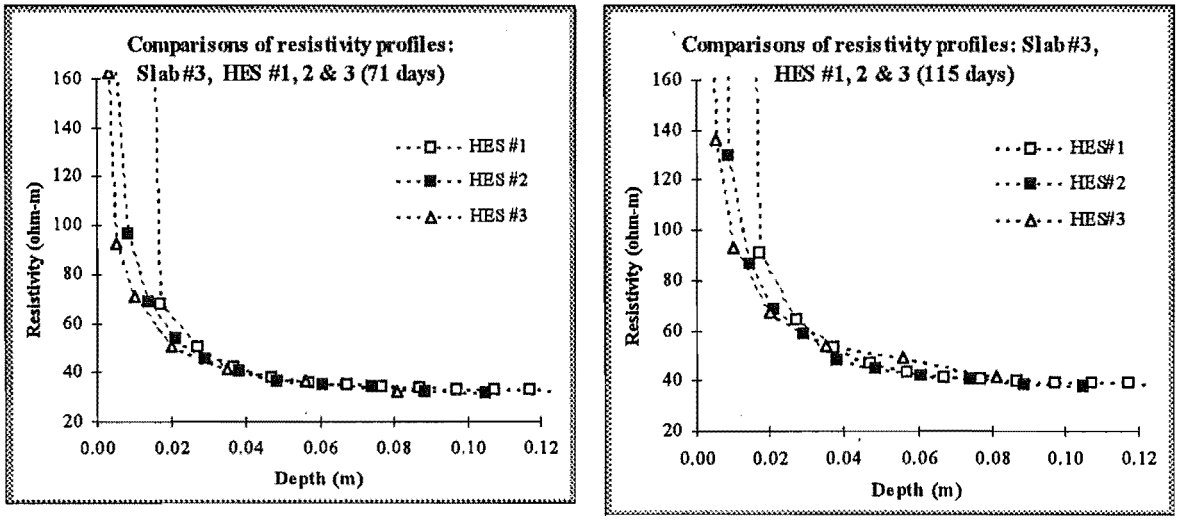

Figure 8.7.2-1: Resistivity profiles from Slab #3 determined using the three types of horizontal electrode system (a) 71 days and (b) 115 days after pouring.

HES#2 and #3 profiles are smoother without the abrupt change in slope at about 17mm typical of profiles from HES#1. At this early age they have better resolution of the profile near the surface. The different HES types measure resistivity at different depths. To compare them numerically, the respective profiles were interpolated at 10 mm intervals. The mean, standard deviation and coefficient of variance at each depth are also shown in Table 8.7.2-1. The large rise in variance near the surface is largely due to the presumably poor resolution of the HES#1 at shallow depths.

Table 8.7.2-1: Interpolated resistivity profiles from the three types of HES embedded in Slab #3. Data was taken on the 71st day after pouring.

Depth	Interpolated Resistivity (ohm-m)					
(m)	HES #1	HES #2	HES #3	Mean	Std Dev	Coeff Var.[1]
0.01	580	89	71	247	288.8	117.1
0.02	63	56	51	56	6.1	10.7
0.03	48	46	45	46	1.8	3.8
0.04	41	40	40	41	0.6	1.5
0.05	38	37	38	38	0.8	2.0
0.06	36	36	36	36	0.3	0.9
0.07	35	35	35	35	0.2	0.7
0.08	35	34	33	34	0.9	2.5
	Average coefficient of variance for depth ≥ 0.02 m					3%

Note 1.i.e Coefficient of Variance: Standard deviation as a percentage of the Mean

The complete set of profiles derived from Slab #3 is shown in Figure 8.7.2-2. These graphs illustrate the improved resolution of HES#2 and HES#3 over HES#1.

Table 8.7.2-2: Variation in resistivity measured using HES #1, #2 and #3 in Slab #3.

Variance: (stdev/mean)*100%				
Depth	Age(days			
(m)	55	71	115	230
0.01	90	117	160	157
0.02	13	11	11	25
0.03	6	4	3	35
0.04	3	1	5	43
0.05	2	2	6	52
0.06	2	1	6	52
0.07	3	1	5	41
0.08	4	3	2	25

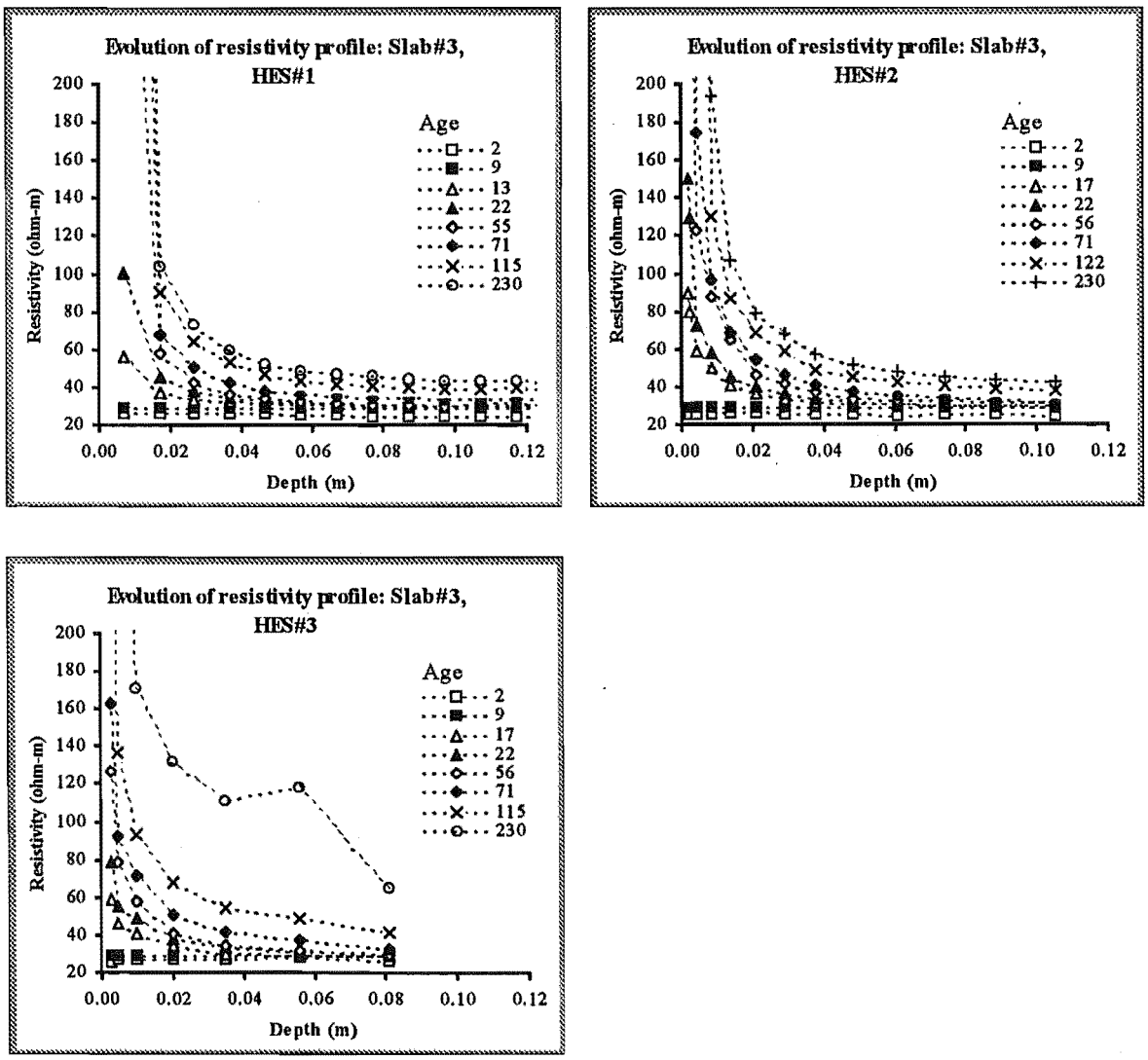

Figure 8.7.2-2: The complete set of profiles derived from Slab #3. The anomalous behaviour of HES#3 after 230 days was replicated in Slabs #4 and #5.

The anomalous behaviour of HES#3 after 230 days was replicated in Slabs #4 and #5. This is responsible for the loss in precision (high variance) at 230 days (Table 8.7.2-2). Apart from the data at that date, the agreement between the different HES types is quite good (variance 11% or less for depths of 20mm or greater and less than 7% for depths greater than 30mm).

8.7.2.2 Two HES#1s and one HES#2 in Slab #6

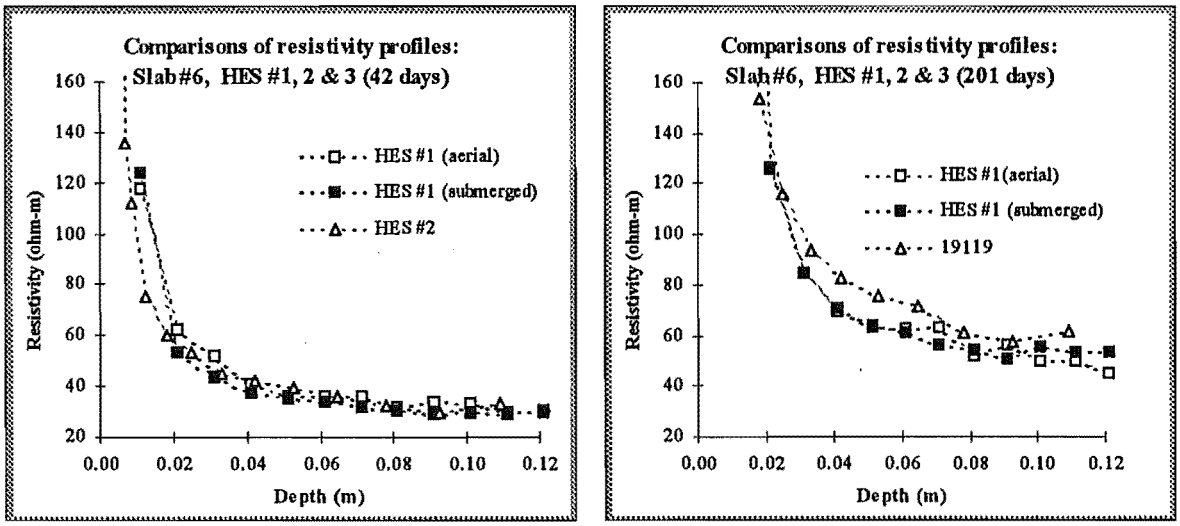

Figure 8.7.2-3: Resistivity profiles from Slab #6 determined using the three horizontal electrode systems (left) 42 days and (right) 201 days after pouring..

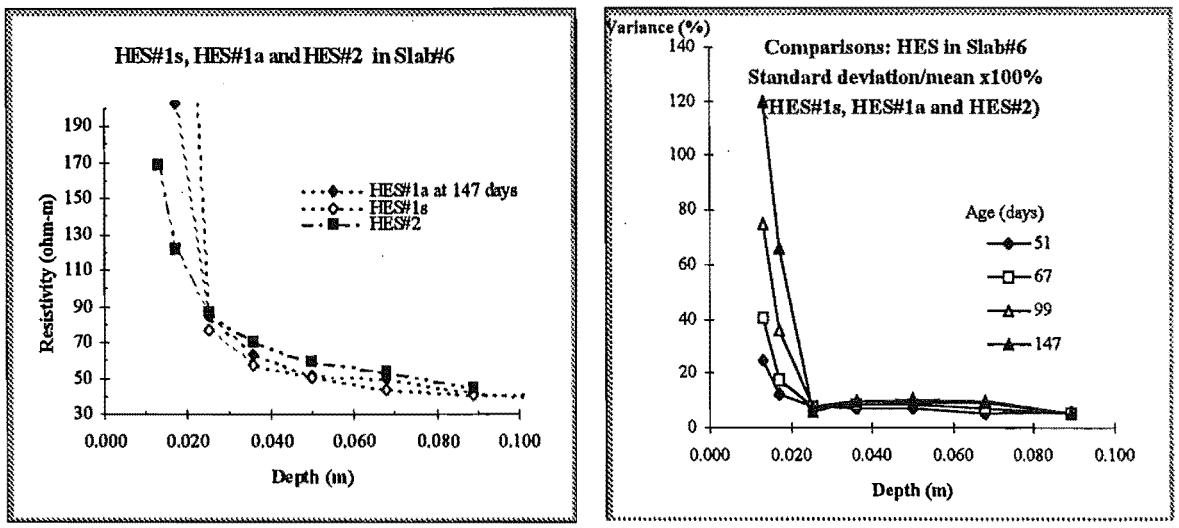

(a) (b)

Figure 8.7.2-4: Comparison of profiles measured in Slab #6 after 147 days. (a) Profiles and (b) Coefficient of Variance.

Further comparisons are shown in Figures 8.7.2-3 and 8.7.2-4 for the HES profiles from Slab #6. Here the HES#2 profile has increased faster than the two HES#1 profiles, which show good agreement even after 201 days (see also Table 8.7-2.3 below).

Table 8.7.2-3: Mean, standard deviation and coefficient of variance of profiles measured in Slab #6 with two HES#1s and an HES#2 after 147 days.

Depth (m)	Resistivity (ohm-m)		Coefficient of Variance
	Mean	Std.dev.	(std.dev/mean)*100%
0.013	959	1152	120
0.017	258	170	66
0.025	83	5	6
0.036	64	6	9
0.050	53	5	9
0.068	49	5	10
0.089	42	2	5
	Average variation for depth ≥ 0.025 m		8%

8.7.2.3 HES#1 and HES#2 in Slab #8 and HES#1 in Cylinder 12 and HES#2s in Cylinders #11 and #13

Cylinders #11, #12 and #13, and Slab #8 share mix and curing history. Comparisons of profiles derived from various HES's embedded in them are shown in Figure 8.7.2-5 and Table 8.7.2-4.

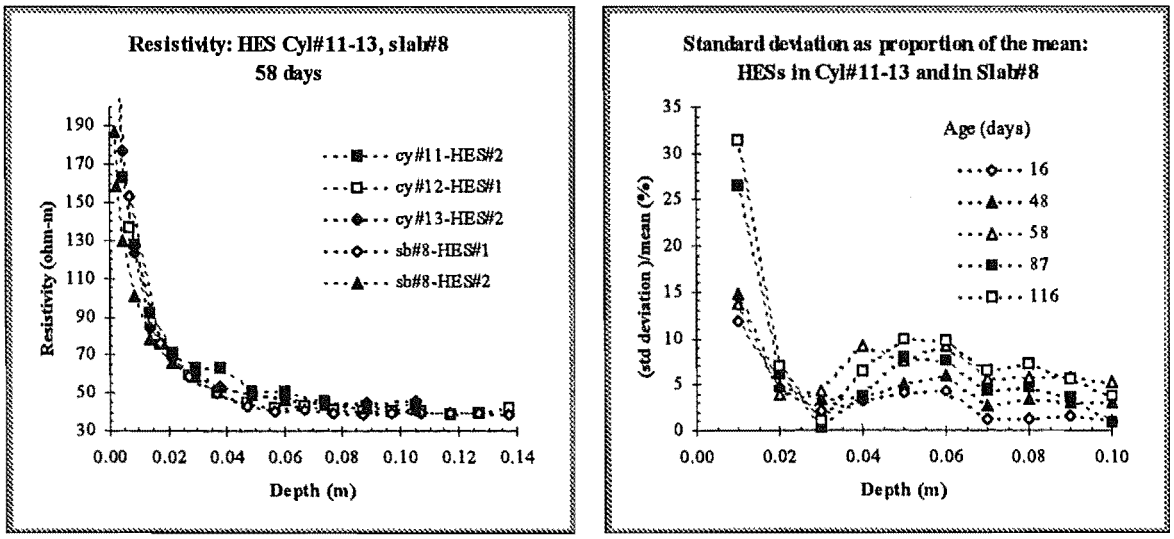

(a) (b)

Figure 8.7.2-5: Comparison of profiles measured in Slab #8 and Cylinders #11, #12 and #13 using HES#1s and HES#2s. (a) Profiles taken 58 days after pouring, (b) Coefficient of variance in measured resistivity.

Table 8.7.2-4: Mean resistivity measured in Slab #8 and Cylinders #11, #12 and #13 using HES#1s and HES#2s after 116 days. The standard deviation (5 data points) is shown in the third column and the coefficient of variance in the fourth column.

Depth (m)	Resistivity (ohm-m)		Coefficient of Variance
	Mean	Std.dev.	(std.dev/mean)*100%
0.01	119	16	12
0.02	72	3	4
0.03	59	3	4
0.04	53	5	9
0.05	47	4	8
0.06	46	4	9
0.07	44	3	6
0.08	43	2	6
0.09	42	2	6
0.10	42	2	5
	Average coefficient of variance for depth ≥ 0.02 m		7%

8.7.3 Discussion

The results of the comparisons made are presented in Table 8.7.3-5.

Table 8.7.3-5: Comparisons made between profiles measured with different HESs of the same or different type in the same or similar samples.

Description of comparison	Range where measure of comparison applies		Measure of Comparison
	Age (days)	Below depth (mm)	Coefficient of Variance (std.dev./mean) x100%
The same HES type in similar samples			
HES#1 in Cylinders #5, #6, and #7,	160	27	4%
HES#1 in Cylinders #8, #9, and #10,	78	27	13%
HES#1 in Slab #4 and #5	216	21	3%
HES#2 in Slab #4 and #5	216	25	10%
HES#3 in Slab #4 and #5	216	24	7%
Different HES types in the same sample			
HES#1, #2 and #3 in Slab #3 (interpolate)	71	20	3%
HES#1, #2 and #3 in Slab #4 (interpolate)			
HES#1, #2 and #3 in Slab #5 (interpolate)			
Two HES#1s and one HES#2 in Slab #6 (interpolate)	147	25	8%
HES#1 and HES#2 in Slab #8 (interpolate)			
Different HES types in similar samples			
HES#1 and HES#2 in Slab #8 and HES#1 in Cylinder 12 and HES#2s in Cylinders #11 and #3	116	20	7%

The variation between the profiles measured in different samples grows rapidly as the depth reduces below 20 mm. The large variation for shallow depths can be due to a number of factors.

1. There is a fall off in calibration constant validity as paste resistivity increases, which could account for errors up to 100% since the maximum overestimation of the resistivity can be shown to be 100%.
2. There is likely to be both an increase in electrode-concrete interface resistance and an increasing difference in the interface resistance between the two electrodes involved in a two-electrode resistance measurement. Both of these effects may result in substantial measurement error. This may account for over-estimation of resistivity by much more than 100%. The use of four-electrode measurements is able to substantially reduce this source of error.
3. Variation in measured resistivity may really reflect actual differences in concrete resistivity due to actual physical differences in the concrete near the surface. The concrete near the surface is most influenced by the relatively rapid changes in environmental conditions. It is in this region that the rate of hydration may vary most since in this region the moisture state of the concrete can be expected to vary most. One might expect that such external influences would not vary horizontally. This may be true. However the relationship between pore-size-distribution, relative-humidity, moisture-content affect and hydration is complex. Small variations in the rate of hydration may change the pore-size-distribution which may affect the rate at which moisture is adsorbed or released in response to changes in external relative-humidity or temperature. Thus the surface may develop a horizontal resistivity distribution adding to the not inconsiderable inhomogeneity already existing.

The first two factors will be exacerbated by the inhomogeneity of concrete which itself may increase. That is, the calibration factors will lose validity unevenly depending on the nature of the paste aggregate distribution that they ostensibly take into account.

There are a number of less serious sources of measurement error near the surface.

1. There is likely to be a fall off in calibration constant validity as the resistivity gradient increases. However the finite difference modelling study suggests that this probably results in a maximum resultant error of about 1% for electrodes 10 mm center-to-center and so is not a significant source of error.

2. Furthermore, as the resistivity gradient increases, any uncertainty in the vertical position of the electrodes would result in ever increasing difference between the actual resistivity at the nominal depth and that at the true depth of view of the electrodes. This should express itself as increasing variance between resistivity measurements made at the same nominal depth by different HES's. However as the variance does not always grow with age and therefore with resistivity gradient, it is unlikely that this is a significant source of error.

Having discussed some of the sources of variation in the measured values of resistivity near the surface it is perhaps surprising that there is not larger variation. In fact, the precision in measurement of resistivity away from the surface is reasonably good considering the highly inhomogeneous nature of the concrete. It is the in the transition zone between the deeper regions of the slab that act as a moisture reservoir and the volatile surface regions that our interest lies. The precision of measurement using the horizontal electrode systems developed here, yields about 10% variation. That is, if the resistivity of regions below about 20 to 25 mm is measured using several HES's, at each depth the corresponding data points should lie within about 10% of each other. Furthermore the HES#1 appears to allow even higher precision than 10 %, but not always. It is difficult to be more specific than that.

8.8 Conclusion

Embedded electrode systems may be used to measure resistivity profiles in concrete samples. Four electrode systems were designed and tested.

The process of calibration of the electrode systems was explored. The in situ method of calibration enables the considerable scatter introduced by the presence of aggregate to be taken into account.

Comparisons of measurements from systems of the same or different type within equivalent concrete samples showed that *in the worst cases*, the lack of precision of measurement yields uncertainties of up to 13% for the regions below about 25 mm from the surface, while uncertainty is even larger closer to the surface. While not all the variation in measurement has been explained, a number of causes for loss of precision have been discussed. The inhomogeneous nature of concrete is the one. Electrode polarisation at the time of measurement or calibration may account for some of the error. The uneven electrode-concrete interface impedance that may result from this inhomogeneity and from the steep resistivity gradient which develops near the surface, may account for further error.

The use of four-electrode resistance measurements and long horizontal electrodes, (that is, the HES#1) can substantially reduce some of these problems.

Most importantly, apart from the extreme error mentioned, all three HES types were able to be used to measure resistivity profiles in concrete slabs for 8 months or more with uncertainty of less than 10% for depths below 20 mm.

9. Measurement of relative-humidity profiles

9.1 Introduction

In this study we wish to determine the moisture state of concrete floor slabs using a top surface mounted instrument. Our motivation is to determine when the slab is dry enough for a surface coating to be applied without danger of later failure due to excess moisture. The nature of concrete, its moisture state and the movement of moisture through it, have been discussed in Chapter 2. It was shown that relative-humidity is a suitable measure of the moisture state of concrete since it indicates how tightly the moisture is bound and because it involves a relatively simple, nondestructive measurement system. This chapter concerns the measurement of relative-humidity — in the concrete slabs used for testing and development of the vertical electric sounding technique, and in the cylinders used for calibration of the resistivity -relative-humidity relationship.

9.2 Method

9.2.1 The relative-humidity housings and the measurement cavity

To measure relative-humidity in concrete at specific depths, relative-humidity sensors are inserted and sealed into cylindrical cavities cast (at a range of depths) in the concrete samples. Experience has shown that corrosion occurs on the electrodes of probes kept permanently in concrete so after a suitable period (usually 24 hours), the relative-humidity is read, the sensors withdrawn and the cavities resealed. The process is repeated at later times, allowing the evolution of relative-humidity profiles to be determined.

It is supposed that the relative-humidity measured in the cavity is in equilibrium with that in the exposed concrete. To ensure that the measured relative-humidity represents the moisture state typical at the measuring depth a number of factors must be taken into account.

1. The cavity must be small enough that significant loss of moisture into the cavity does not occur between measurement sessions. For this reason the cavity must also be well sealed at all times. Similarly the cavity during a measurement session should be small enough that equilibrium between the cavity air space and the concrete is quickly reached.

2. The concrete exposed to the cavity must be typical of concrete at that depth throughout the slab. The presence of the cavity or other cavities should not significantly alter the flow of moisture (or the drying path) in its vicinity. The vertical extent of the exposed concrete should be small enough to allow good resolution of the relative-humidity profile, especially in regions where the gradient is greatest. In other words, the cavity should not provide a significant 'short-cut' to the surface for moisture.

In both the slabs and the cylinders, from five to fifteen relative-humidity-probe housings were cast. A housing is a 100 mm section of polyvinylchloride (PVC) electrical conduit of 20 mm outside diameter. While the concrete is setting and between measurement sessions, a brass plug and 'o'-ring seals the otherwise exposed concrete at one end of the housing from the outside air. The housing has been internally machined to allow a good seal with the plug, and, when it is inserted, with the relative-humidity probe (Figure 9.2-1 and Figure 9.2-2). To allow a good seal between the plug or probe and the housing, when either is fully inserted, the internal diameter of the housing is slightly reduced at the concrete end. The seal here should ensure a minimal sized cavity.

In practice, a good plug seal meant that air trapped in the cavity could not escape. This air acted as a cushion preventing insertion of the plug right up to the exposed surface. However, the relative-humidity probes used had sufficiently dissimilar dimensions, that some were either too tight (and jammed or could not be inserted at all) or were loose and could not seal the cavity. Consequently, housings were machined to accept all probes, and plasticine was used to ensure the cavity was sealed during a measurement session. The brass plugs were machined to fit the slightly larger housing design.

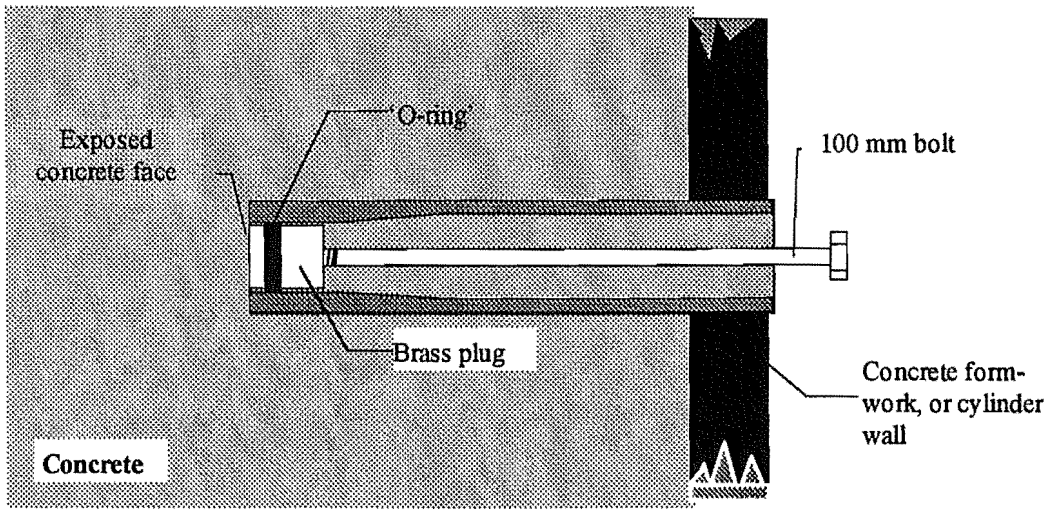

Figure 9.2-1: Brass plug inserted in relative-humidity probe housing. The bolt is used to insert or withdraw the plug.

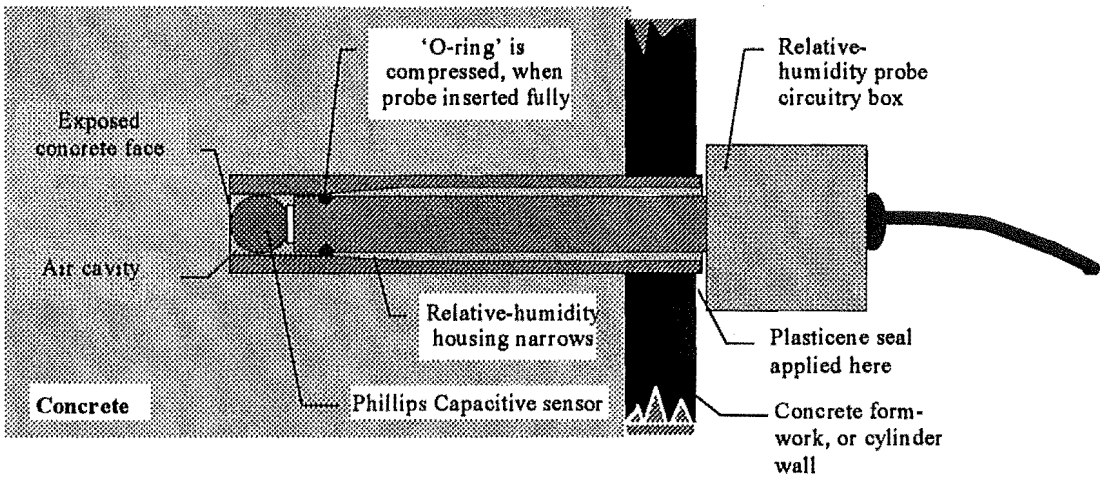

Figure 9.2-2: Side (or top) view of a relative-humidity probe inserted into a probe housing. Note that the volume of the cavity around the sensor is minimised by the 'o'-ring seal. Plasticine is used near the circuitry box to provide a backup seal.

9.2.2 Relative-humidity probes

Fifty Phillips capacitive humidity sensors and associated electronics assembled into probe units were supplied by the Building Research Association of New Zealand (BRANZ). Each sensor is mounted on a hollow PVC tube through which two leads feed into the box housing the circuitry (see Figure 9.2-2). Each probe requires a 0-5V supply and has an output voltage between 0 and 1V corresponding roughly to 0% -100% relative-humidity. The probes were used in batches of 10. Each batch was powered and read using a separate control unit to which each of the 10 probes was connected.

9.2.3 Calibration of relative-humidity probes

The probes were calibrated locally using saturated salt solutions, and periodically returned to BRANZ for calibration using a "Two-Pressure Relative Humidity Generator " to set several points from 50% to 95%. Initial checks using standard saturated salt solutions suggested that the sensors did not retain their calibration between BRANZ's Judgeford office and Canterbury University. Subsequently the probes were recalibrated locally (see below), and we relied less on BRANZ's calibration.

When a saturated salt solution is placed in a container of non-hygroscopic material, and the container and contents kept in thermal equilibrium, the relative-humidity measured in the sealed space above the solution can be determined to an accuracy of 2% (Young, 1967). Higher accuracy can be obtained under certain conditions (Molina 1990, Hedenblad 1993).

Ideally the solution surface area should be as large as possible relative to the air space above the surface.

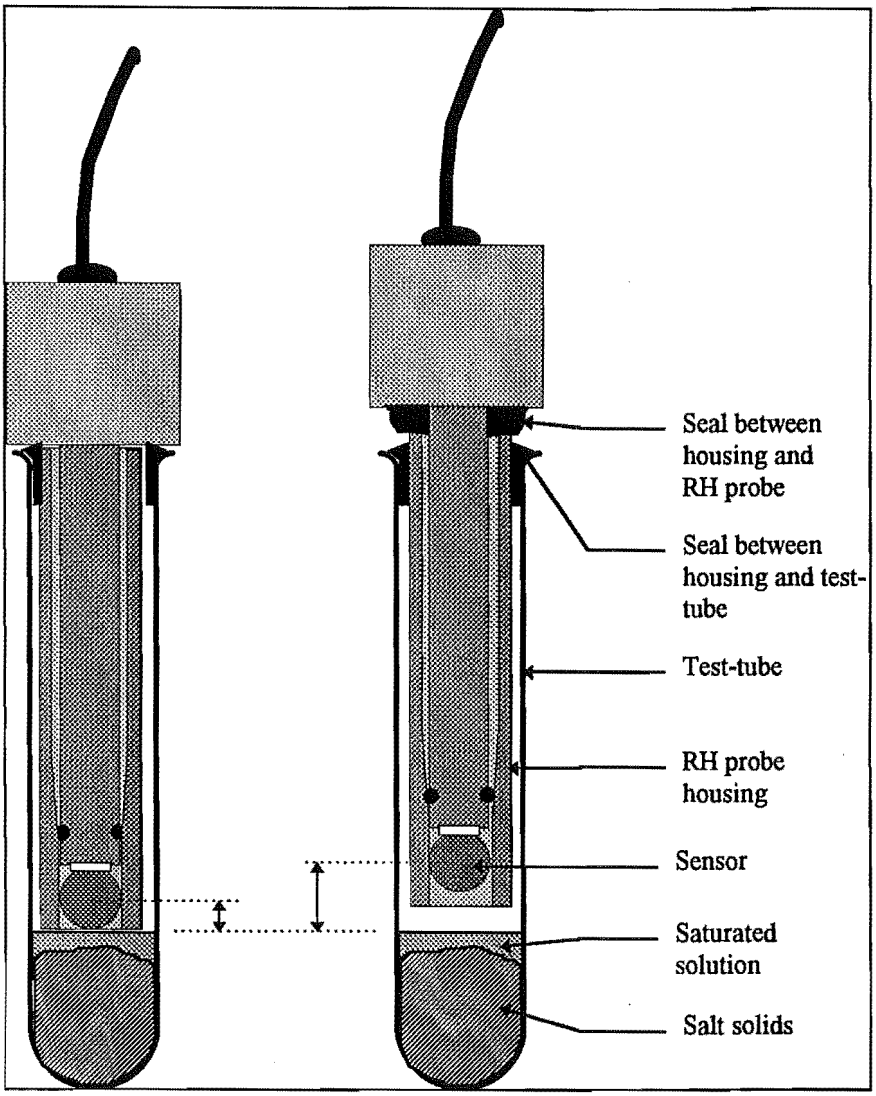

Figure 9.2-3: Calibration of relative-humidity probes using saturated salt solutions. The right-hand diagram shows the effect of using plasticine to ensure a good seal between the housing and the probe, on the separation between the sensor and the solution surface.

The local calibration used three set points: 64.4%, 75% and 100%. The relative-humidity set points were obtained using saturated salt solutions placed in test-tubes (of 25 mm diameter). Thirty test-tubes were divided among three test solutions. Ten held distilled water (100%), ten held NaCl (75%), and ten held NaNO2 (64.4%). Relative-humidity housings (as used in the concrete samples) were fixed into the test-tubes with plastic tape and sealed with plasticine (see Figure 9.2-3). For calibration, the relative-humidity probes were inserted fully into the housing so that the sensors were suspended just above the

solution. The output voltage was read after 24 hours. When not in use the housing was corked to prevent contamination of the solution.

The original calibration procedure was to set high and low test points alternately in an iterative manner until the probe output (in volts) converged on the nominal RH of each test-point solution. However, to save time, once the probes had been calibrated by BRANZ, local re-calibration involved merely noting the outputs at the set points and using this data to correct the RH measurements by interpolating between set points. Thus, for each probe three set points were obtained. Towards the end of the study the three point calibration was replaced by a six point calibration.

This reliance on a three-point calibration was unfortunate for three reasons.

1. The Phillips sensor is designed to operate between 10% and 90% relative-humidity. The use of a 100% set point was therefore inappropriate.
2. ***The 100% set point was checked by measuring the vapour pressure above distilled water. This is an unreliable procedure. Subsequent independent measurement suggested that relative-humidity above the distilled water lay between 95% and 97%.***

The majority of relative-humidity readings lay between 75% and 95%. Later six-point calibration which included set-points at 75%, 82%, 91% and 97% revealed a lack of linearity between 75% and 100%. Generally the three point calibration tended to over estimate the relative-humidity in this region.

If the true value of the relative-humidity at the 100% set point was actually 95%, then the agreement between the three-point and six-point calibration would be enhanced.

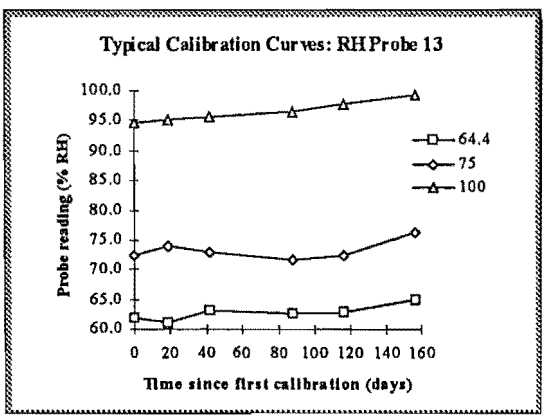

(a). Drift in calibration for probe 13.

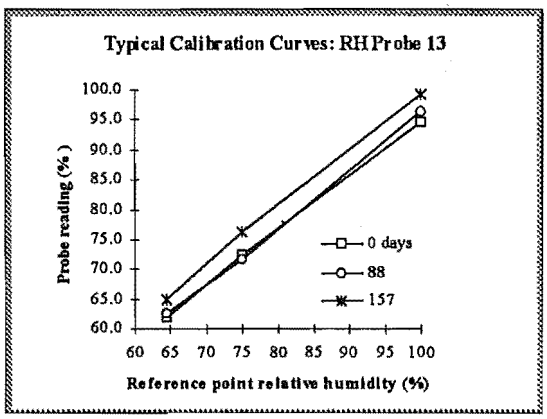

(b). Change in calibration curves over time, probe 13.

Figure 9.2-4: Relative-humidity calibration curves for a single probe. The vertical axis shows the nominal relative-humidity measurement of the probe which is just the probe output voltage multiplied by 100%.

Typical relative-humidity-probe calibration curves are shown in Figure 9.2-4. For Probe 13, the calibration curves show a slight drift. Other probes exhibited significantly more.

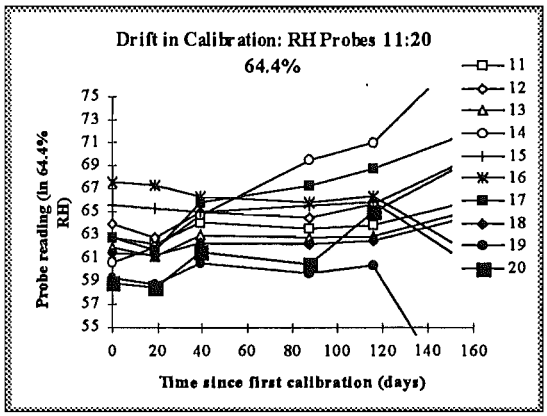

(a). Drift in calibration: probe output in RH of 64.4%

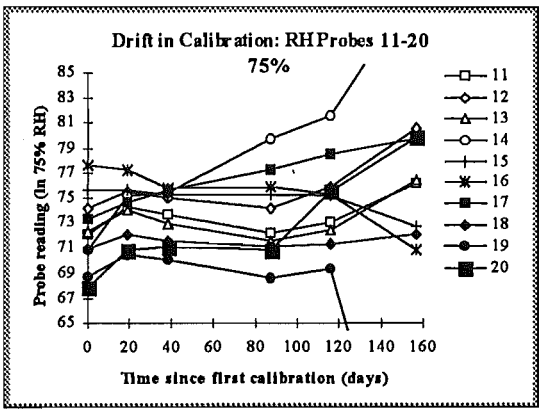

(b). Drift in calibration: probe output in RH of 75%

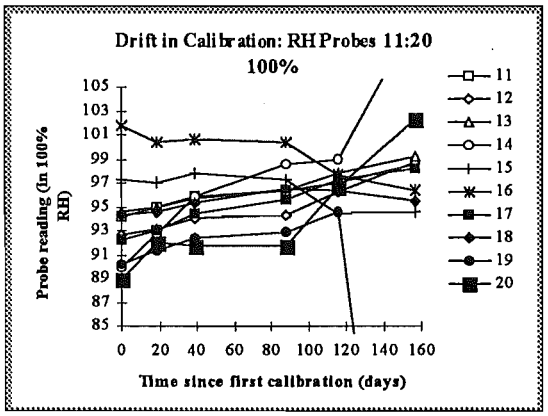

(c). Drift in calibration: probe output in RH of 100%

Figure 9.2-5: Typical calibration curves for probes 11-20.

The calibration curves for a set of ten probes are shown in Figure 9.2-5. Full sets of calibration curves are presented in Appendix G.

9.2.4 Measurement

To measure a profile, ten or fifteen relative-humidity probes were inserted in the housings in the slab or cylinder under test. After 24 hours the probe output was recorded. As a check on the measurement the probes were usually removed and inserted into different housings, and re-read 24 hours later. In this way each probe could be used to measure the humidity at a range of depths. The practice of rotating the set of probes through a subset of the possible

housings, was to ensure that failure of one or more probes did not jeopardise the measurement of relative-humidity at a particular depth.

9.2.5 Sources of error

There are a variety of sources of error in the measurement of relative-humidity. Some of these are described below.

- Random fluctuations in sensor response to constant RH. This error can not be determined since it cannot be distinguished from that associated with changes in the nominal RH.
- Fluctuations in the true relative-humidity due to variation in the temperature in the air-space during calibration. Molina (1990) gives an equation describing the temperature dependent correlation between the relative-humidity at 20°C and at other temperatures:

$$\psi(T) = \frac{\psi(20^\circ C)\cdot(T+273)}{76.27\cdot(1+0.02T)^4} \qquad \textbf{Equation 9-1}$$

A drop of temperature from 20°C to 18°C, may result in a rise in relative-humidity in a sealed space of up to 10%. This effect is compounded for the airspace above saturated salt solutions, since the vapour pressure maintained by the solutions is generally temperature dependent (see Table 9-1). However the temperature coefficients are small compared to the effect of temperature on the airspace itself (5%/°C at 20°C).

Table 9-1: Saturated salt solutions and their temperature coefficients (based on Young, 1967).

Salt	% Relative-humidity at 25°C,	Temperature range °C	d(ψ)/dT, % per °C
$NaNO_2$	64.4	20 – 40	-0.19
NaCl	75.1	5 – 60	-0.02
K_2SO_4	97	15 – 60	-0.05

The effect of variations in temperature on measurements of relative-humidity in concrete should be of less importance than during calibration of the probes, since the concrete provides a buffering effect on temperature and relative-humidity.

A fall in temperature will cause a temporary rise in the relative-humidity within pores. This will result in condensation, increasing slightly the menisci radii in the pores,

lowering slightly the absolute humidity and hence the relative humidity. The new equilibrium relative-humidity at the new temperature will be somewhere between the original relative-humidity and that given by the equation. A fall in temperature in the airspace between the sensor and the concrete will have a similar effect. In practice one would expect that the reservoir of water within the concrete is large enough that the change in relative-humidity resulting from a change in temperature will be negligible

- Relative-humidity gradients are formed above the surface of the calibration solution, so that it is important to keep the sensor as close to the liquid surface as possible. The design of the calibration system used allowed the distance between the centre of the sensor and the solution surface to vary from 8 to 18 mm (see Figure 9.2-3).
- There is an inherent drift in relative-humidity probe output over days and months. This behaviour has been well documented. After 200 days, for example, Visscher and Kornet (1994) found drift of up to 7.5%RH amongst the 18 sensors (from 10 manufacturers) tested. Nearly all capacitive types tested drifted to a higher output. The sensors were also tested on delivery from the manufacturers. The average difference between the manufacturers calibration and the experimenters was (+1.3 $\pm$ 3.0) % RH at 90% RH.

There are then three main sources of error. The first is associated with calibration of the relative-humidity probes. The second is associated with the drift in calibration with time and the third is associated with measurement in the concrete.

If drift is linear, simple interpolation of the calibration constants may be used to find calibration curves for measurements made between calibration dates. Where the drift in calibration appears anomalous (see the curves for probes 31-40 at 40 days in Appendix G, for example), the calibrations made on that day have been rejected and interpolation carried out using the remaining calibration constants. Generally the graphs provide a good guide to whether readings made with probes will be useful. Probes, whose calibration curves swing markedly generally yield relative-humidity measurements which go against the general trend of the bulk of measurements.

9.2.6 Analysis of raw relative-humidity data

The raw output from the humidity probes is converted to a relative-humidity using the calibration constants determined for that time. At each depth, there may have been up to five measurements taken with five different probes. Typical corrected relative-humidity readings are shown in Figure 9.2-6(a). The number alongside each data point refers to the

probe number responsible for the reading. At each depth the average of the relative-humidity data points is calculated.

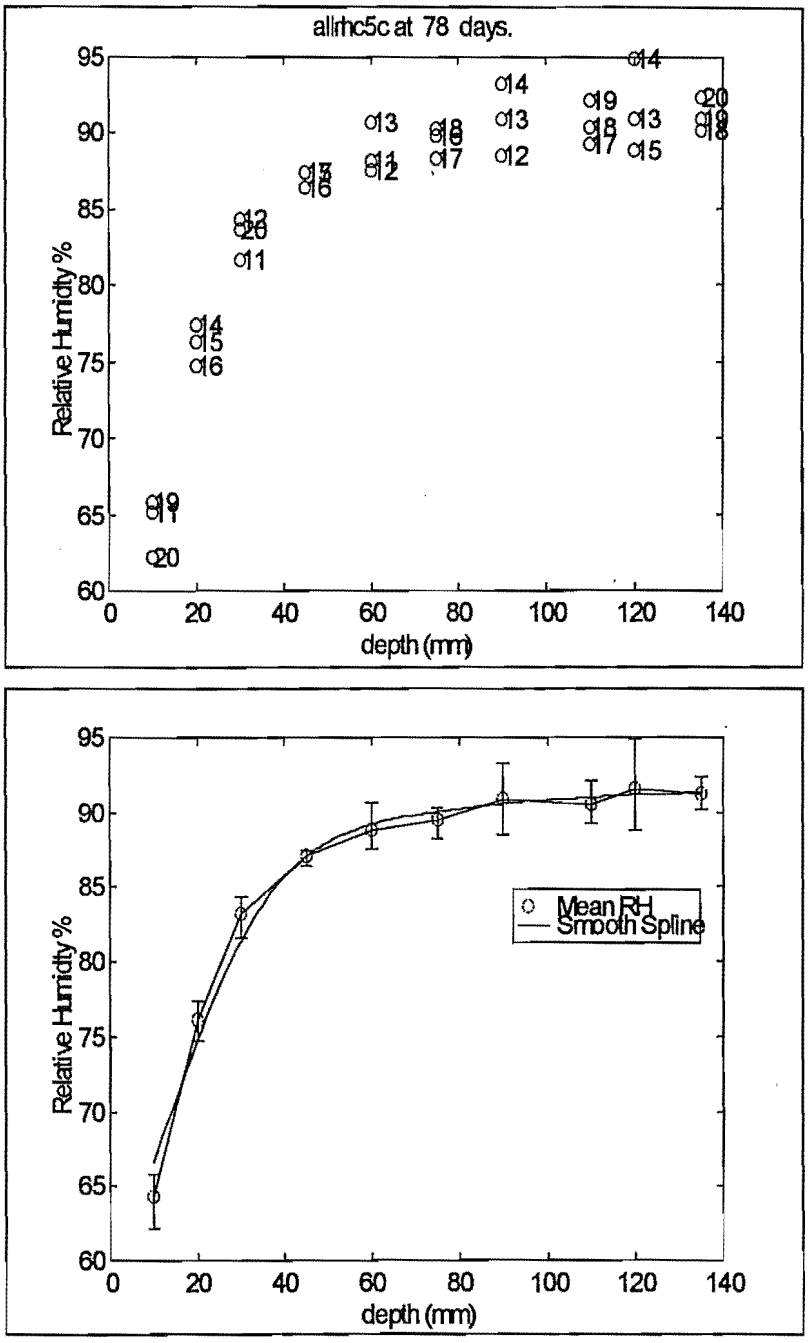

Figure 9.2-6: Calibrated relative-humidity measurements for Cylinder #5, 78 days after pouring. The relative-humidity probes have been rotated through three positions, so that there are three data points for each probe housing depth. In the upper graph the data points are labelled with the number of the measuring probe. In the lower graph mean humidities are plotted with the range of measured humidity shown as error bars. A smoothing spline curve through the averaged data points is also shown although the spline curve is not used in further analysis.

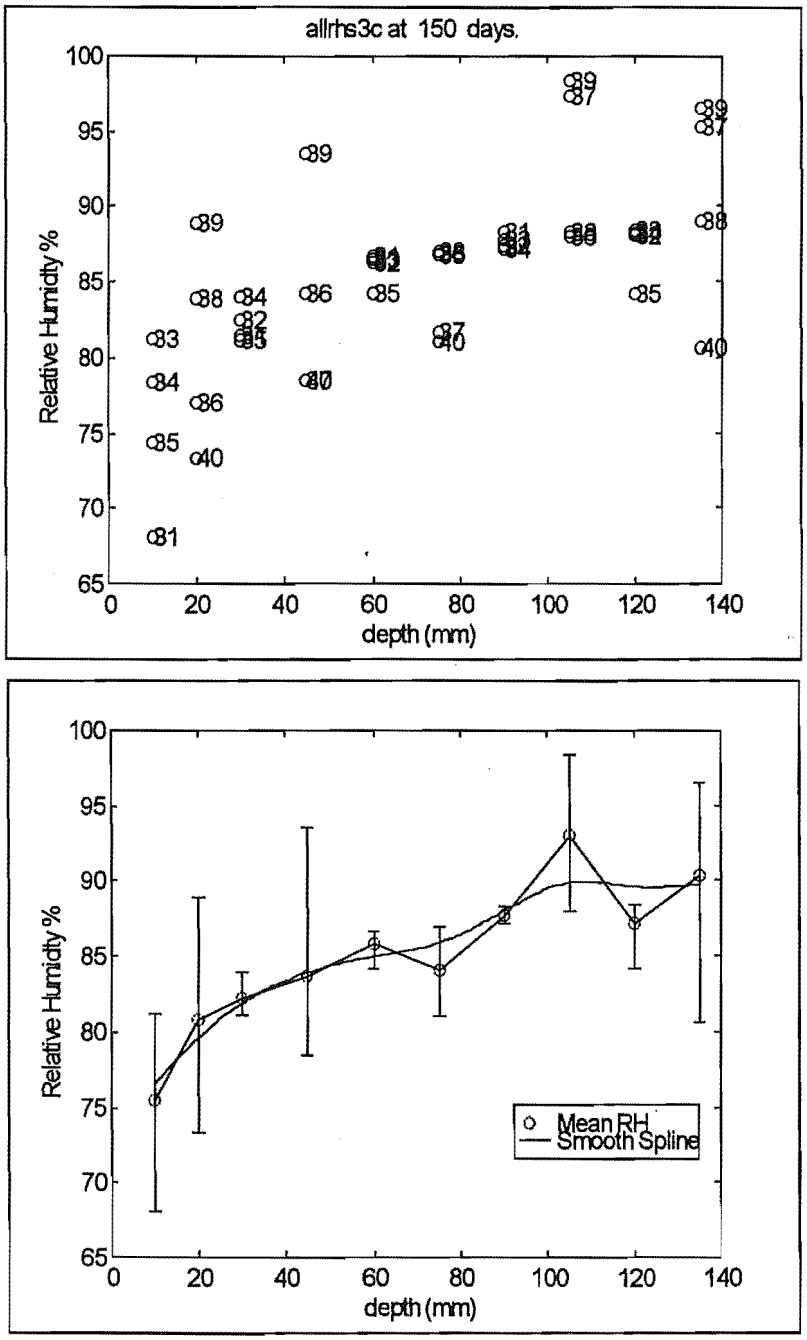

Figure 9.2-7: Calibrated data for Slab #3, 150 days after pouring. (a) all corrected data points, (b) averaged data points and spline,

Occasionally, and particularly with the two sets of probes 1-10 and 41-50, individual data points indicate unacceptable error. Whatever the cause, whether because of poor calibration, uncontrolled drift or poorly sealed probe cavity, if readings were definite outliers, the probes contributions to the data set were eliminated. In Figure 9.2-7 (a),

readings for probes 37, 39 and 40 seem well away from the general trend. The resulting profile Figure 9.2-7 (b) shows considerable uncertainty. The effect of removing the data from these probes, and from probe 35, is shown in Figure 9.2-8 (a) and (b).

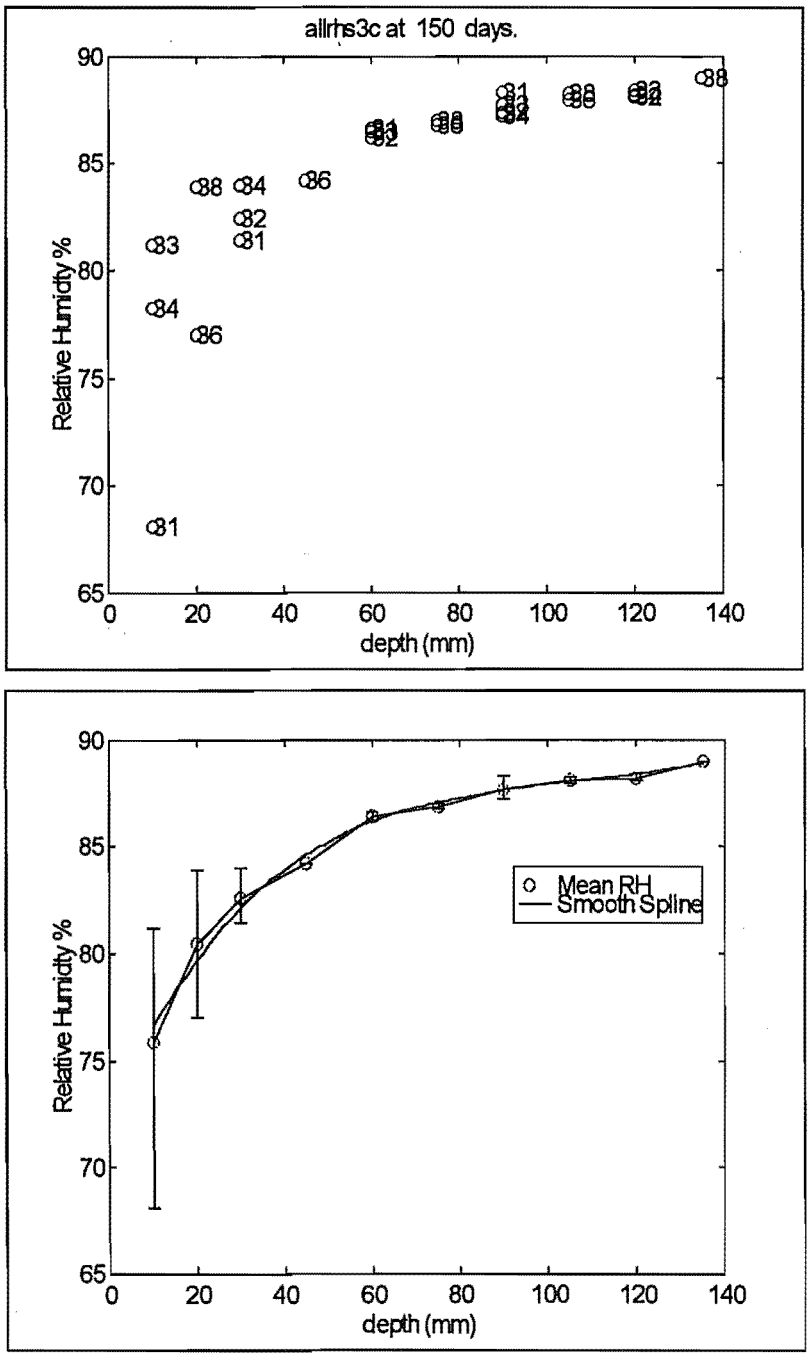

Figure 9.2-8: Calibrated data for Slab #3, 150 days after pouring (a with data from probes 35, 37, 39 and 40 removed and (b) resulting averaged data points and spline.

This process is not wholly satisfactory, since it relies on a subjective judgement of what 'looks right' as much as an objective assessment of the failure of one probe or another to provide accurate data. Nevertheless, inspection of the calibration curves for probes 31-40, reveals anomalous drift for probes 35, 37, 39 and 40, when measuring 64.4% and 75% relative-humidity (Figure 9.2-9).

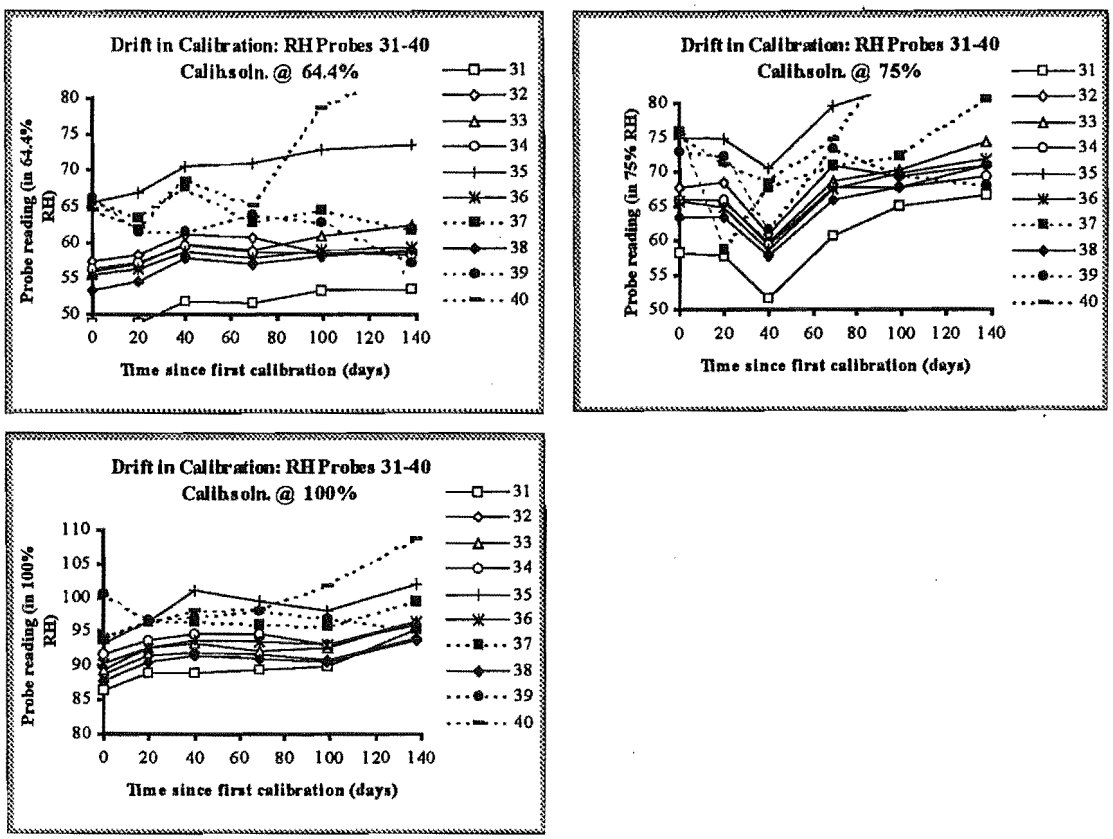

Figure 9.2-9: Drift in calibration (uncorrected probe output multiplied by 100%), for probes 31-40.

Clearly there have been problems in the measurement of relative-humidity in this study. Admitting this, we shall let the relative-humidity profiles as presented here, stand as representative but without claims made as to their accuracy.

9.3 Results: Relative-humidity profiles

Relative-humidity profiles have been measured and collected for seven cylinders and six slabs. Some representative examples are presented here. The full set is presented in Appendix F.

In the following figures, the left-hand graph shows the evolution of relative-humidity profiles over the measurement period. The right-hand graph shows the same data presented as the evolution of relative-humidity at particular measurement depths. Both presentations are useful in evaluating the measured profiles.

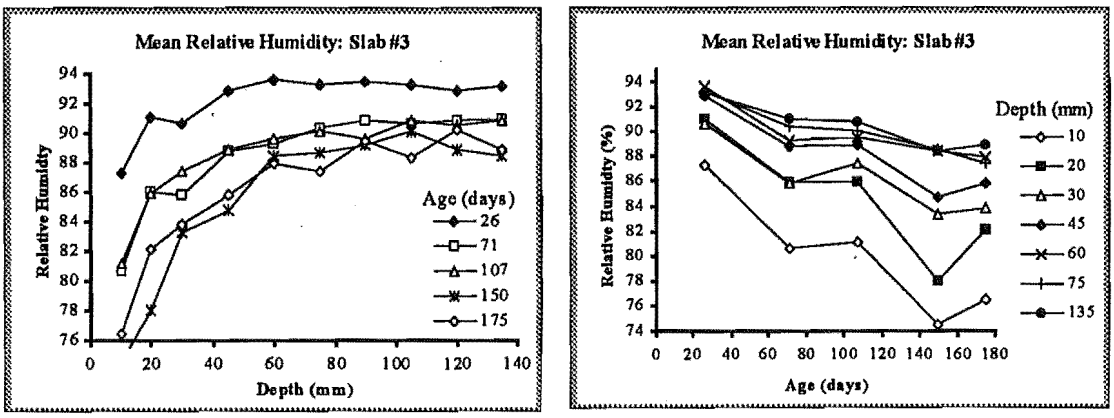

Figure 9.3-1: Evolution of relative humidity profiles in Slab #3

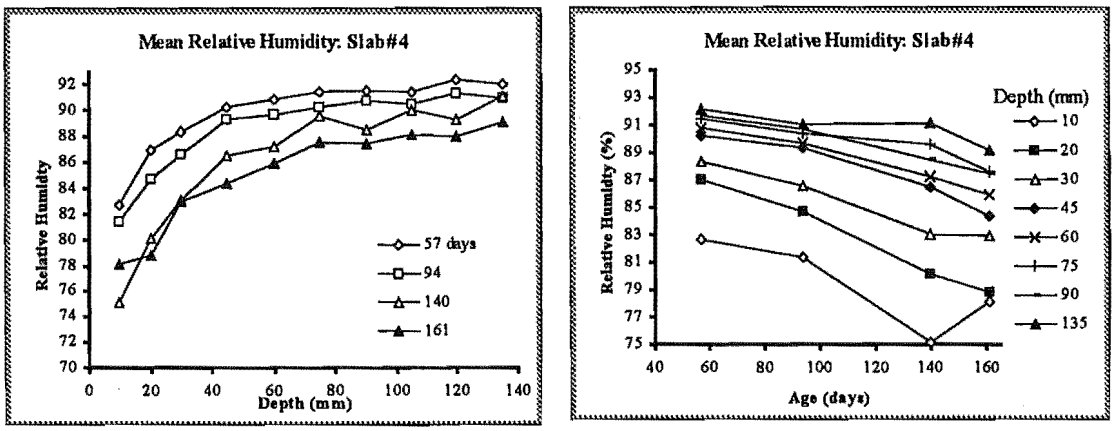

Figure 9.3-2: Evolution of relative humidity profiles in Slab #4

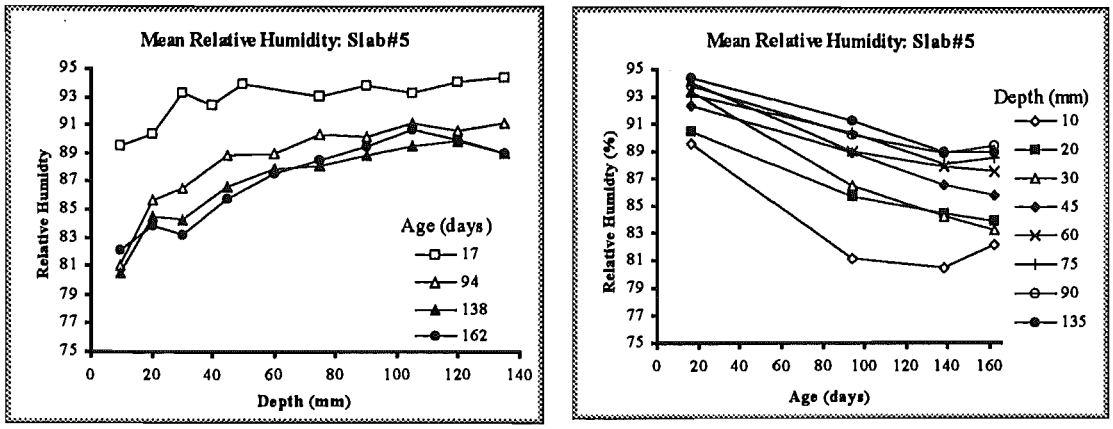

Figure 9.3-3: Evolution of relative humidity profiles in Slab #5

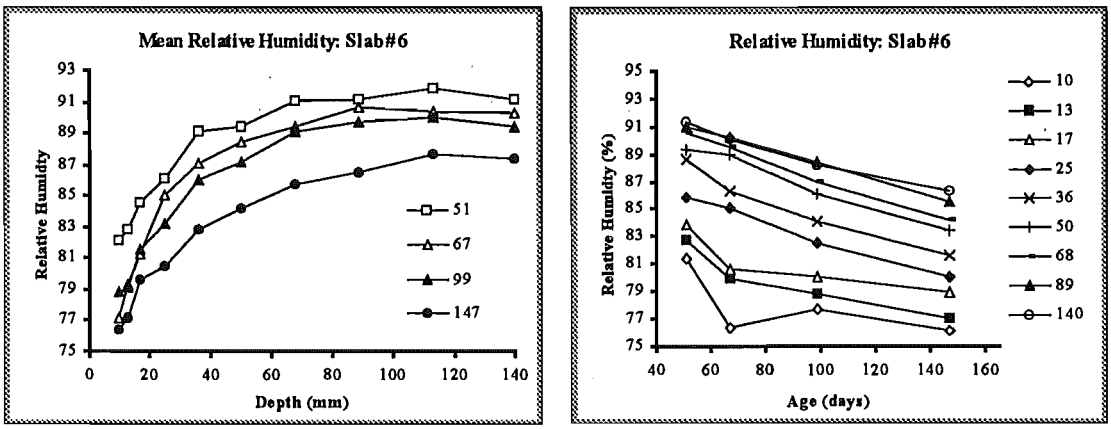

Figure 9.3-4: Evolution of relative humidity profiles in Slab #6

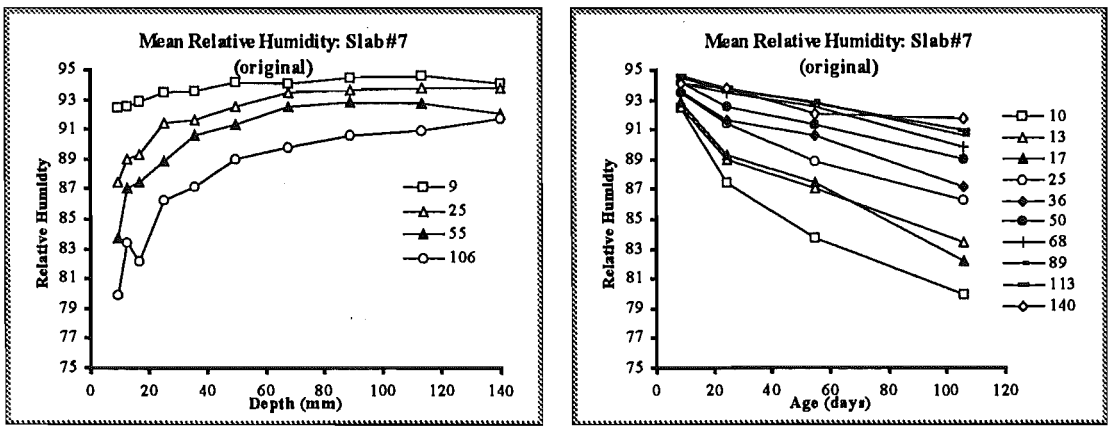

Figure 9.3-5: Evolution of relative humidity profiles in Slab #7

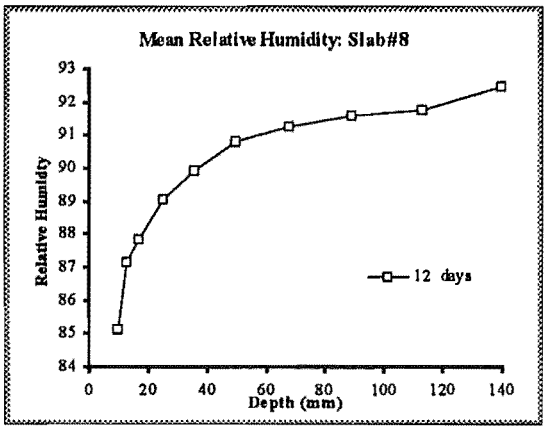

Figure 9.3-6: Relative-humidity profile in Slab #8

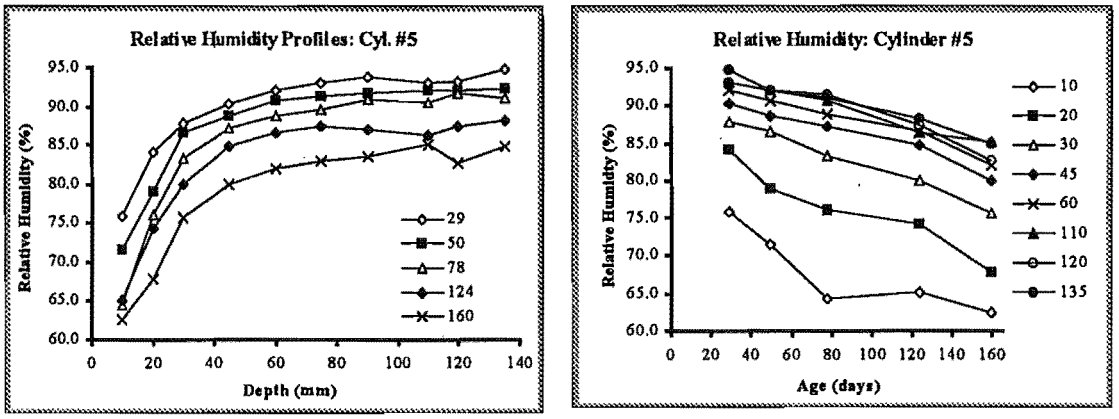

Figure 9.3-7: Evolution of relative humidity profiles in Cylinder #5.

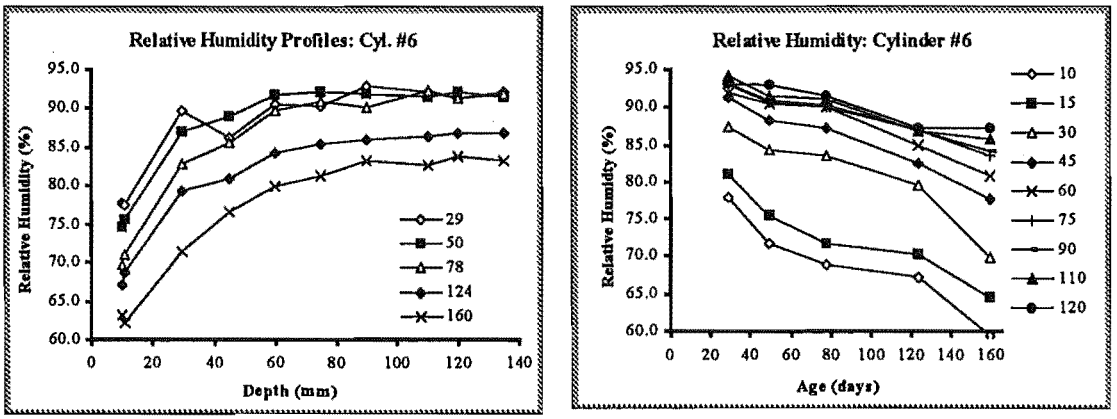

Figure 9.3-8: Evolution of relative humidity profiles in Cylinder #6

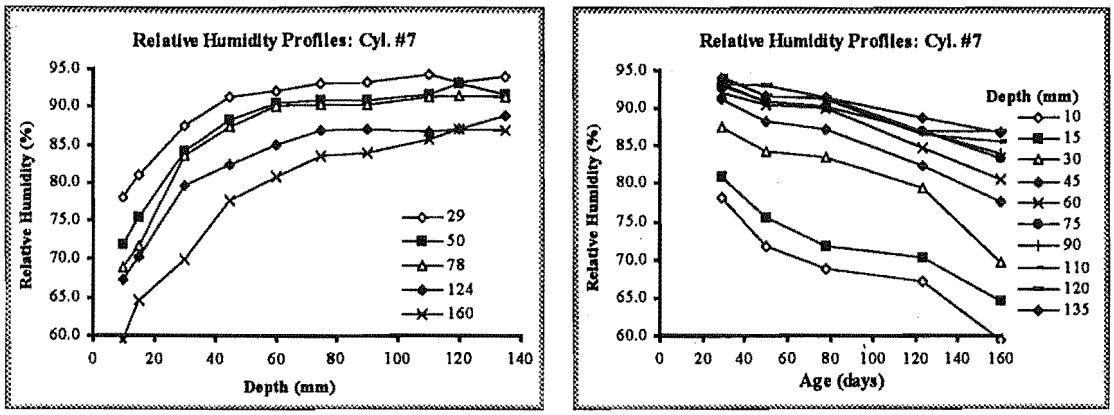

Figure 9.3-9: Evolution of relative humidity profiles in Cylinder #7

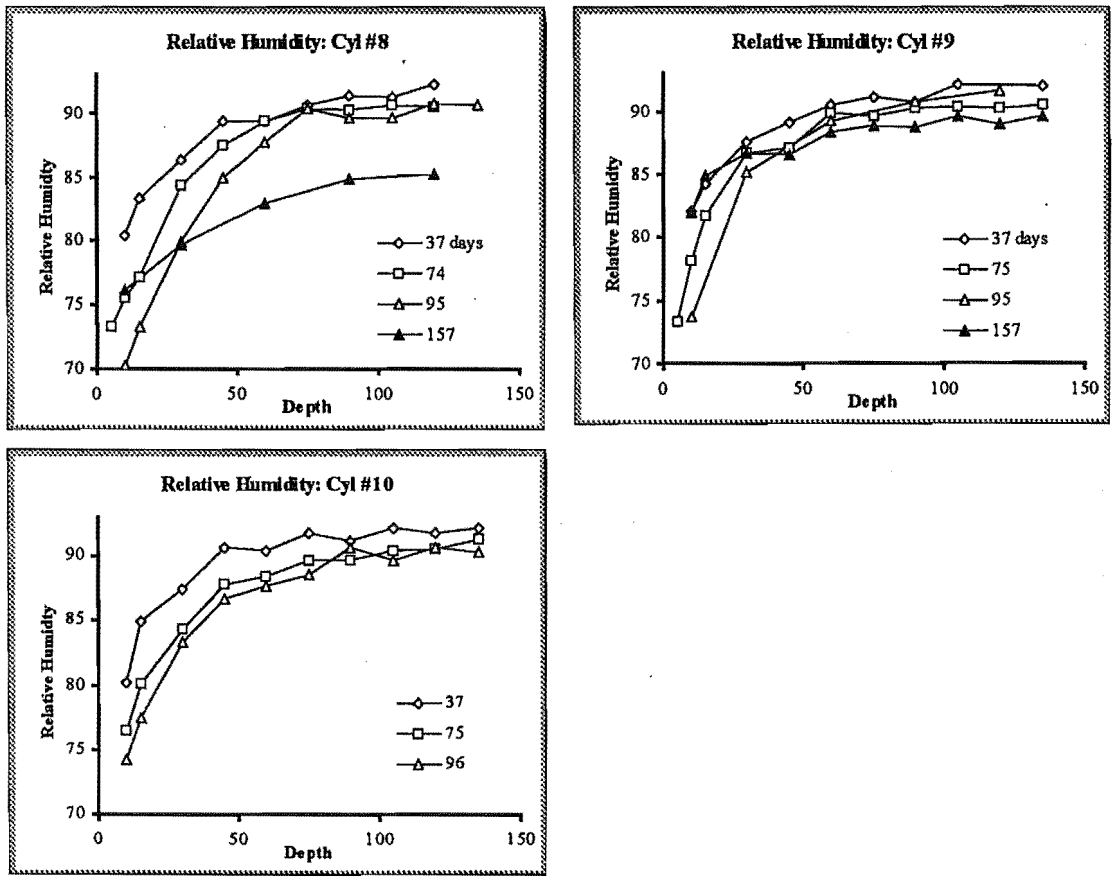

Figure 9.3-10: Evolution of relative humidity profiles in Cylinders #8, #9 and #10

9.4 Discussion

Generally, we expect the relative-humidity at every point in the slab is to decrease as the slab dries. Exceptions to this behaviour may arise in conditions where the surface has come

to equilibrium in dry low relative-humidity conditions and subsequently adsorbs moisture as the ambient relative-humidity increases. Under this scenario, the relative-humidity at points below the surface may follow the change in relative-humidity at the surface to an extent dependent on the relative-humidity gradients which are brought about locally. Evidence of this occurring may be shown in the relative-humidity profile for Slabs #3 to #5 where the relative-humidity at 10 mm depth shows an upswing in the last measurement.

However other similar swings in relative-humidity which occur deeper in the slab (or cylinder) unaccompanied by similar changes nearer the surface are unlikely to be accurate. Rather they reflect the lack of precision of the relative-humidity measurement attained in this study.

While relative-humidity profiles have been obtained from six slabs and seven cylinders the graphs showing the evolution of humidity over the measurement period, illustrate the uncertainty associated with the measurement. Causes of error have been discussed in Section 9.2.5 . It is difficult to estimate the error associated with calibration and with measurement. Given that the temperature was not controlled, nor (on the whole) measured, it is likely that the uncertainty in relative-humidity is at least $\pm$ 5% RH.

The ability to compare relative humidity profiles taken from equivalent samples provides us with one measure of the precision in measurement. Equivalent samples may be defined as those which are poured from the same mix, at the same time and kept under similar conditions: (thus Cylinders #5, #6 and #7, Cylinders #8, #9 and #10 and Slabs #4 and #5). In addition we may compare the profiles from Slab #6 and #7, which share concrete specifications (25 MPa) and were kept in the same room, but which were poured some six weeks apart. We expect some differences in curing conditions as a result of the time difference, but otherwise the two samples can be considered equivalent.

The standard deviation gives a measure of the agreement between equivalent profiles. This may be compared with the absolute value of the relative humidity to get the variance (= standard-deviation/mean). The mean profiles and variance are plotted in variance Figure 9.4-11. The variance is generally below 2% for depths below 20 mm. This shows fairly good agreement between the equivalent profiles. However, variance does not assess how well the profiles may be distinguished from one another. Plotting the standard deviation as error bars on the mean profile enables the fit to be assessed visually (Figure 9.4-11 lower

left). The agreement between the two 94 day profiles is very good. The agreement between the two 138 day profiles is relatively poor, as is that between the two 162 day profiles. The last two profiles (138 and 162 days) are not well resolved, yet both are well resolved from the 94 day profile. Profiles taken less than about a month apart, do not appear to be well resolved, although this well depend on the drying rate which in turn will be most obviously related to the age of the concrete. (Note, the 17 and 57 day profiles are each derived from just one of the slabs, so this analysis does not apply).

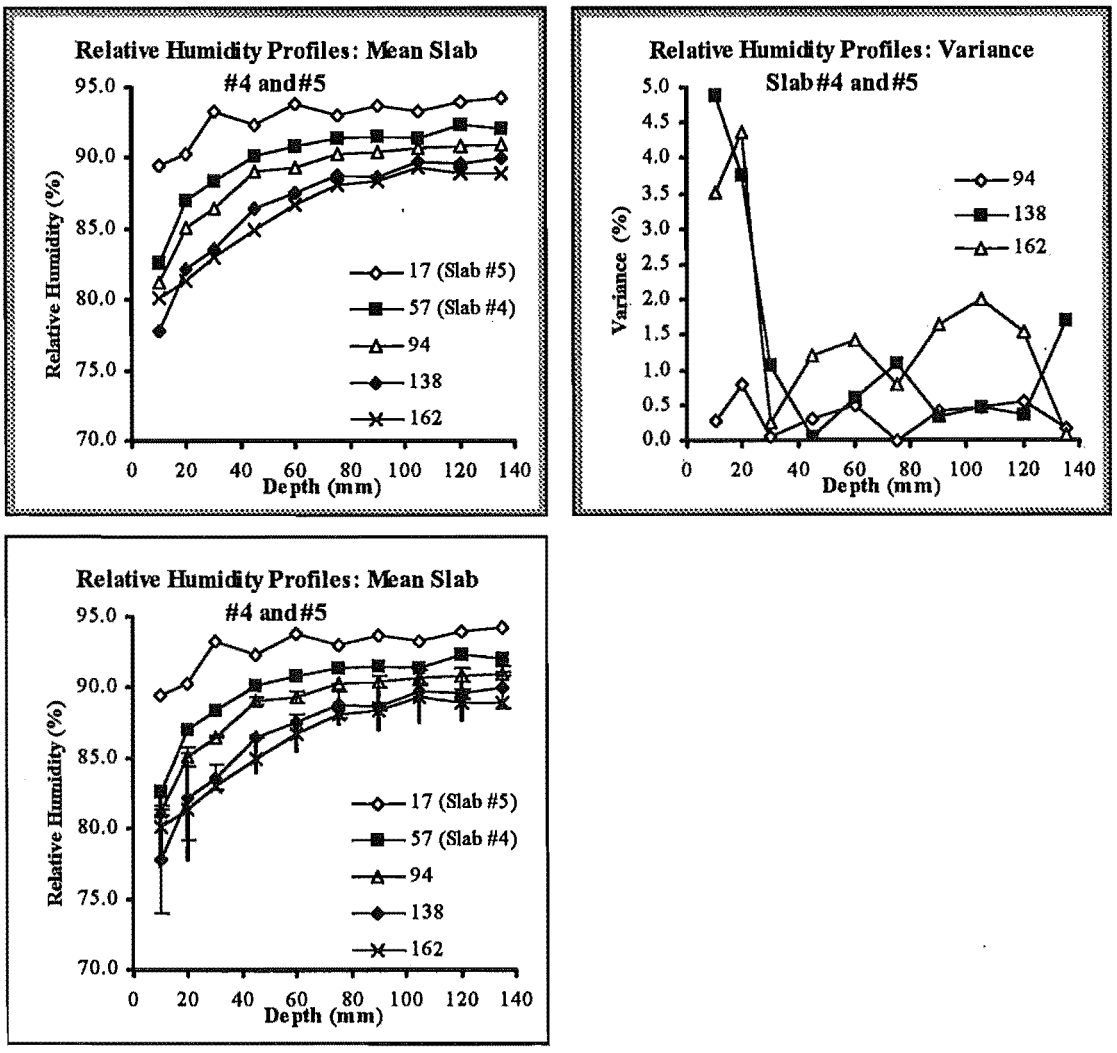

Figure 9.4-11: Evolution of relative humidity profiles: mean (left top) and variance (left right) of profiles from Slabs #4 and #5. Slab #5 was reinforced (see Chapter 4). These slabs were poured at the same time from the same mix and kept under identical conditions. Imposition of standard deviations of the differences between the two profiles as error bars on the mean profiles gives an indication of how well and where the profiles are resolved.

A similar analysis may be applied to the nearly equivalent Slabs #6 and #7. Here the ages at which measurements were taken are different so the Slab#6 profiles have been interpolated

at the Slab #7 ages (Figure 9.4-12). Once again the variance shows a remarkably good agreement between the two profiles and the standard-deviation-error-bars show that the mean profiles are well resolved from one another. Of interest is the fourth (lower right) graph of this set which expresses the standard deviation as a percentage of the difference between the two profiles. This way of assessing the resolution of the measurement must be interpreted with care. The profiles change more slowly at greater depth. The same standard deviation will result in a greater standard-deviation/difference deeper down than near the surface where the differences are greater.

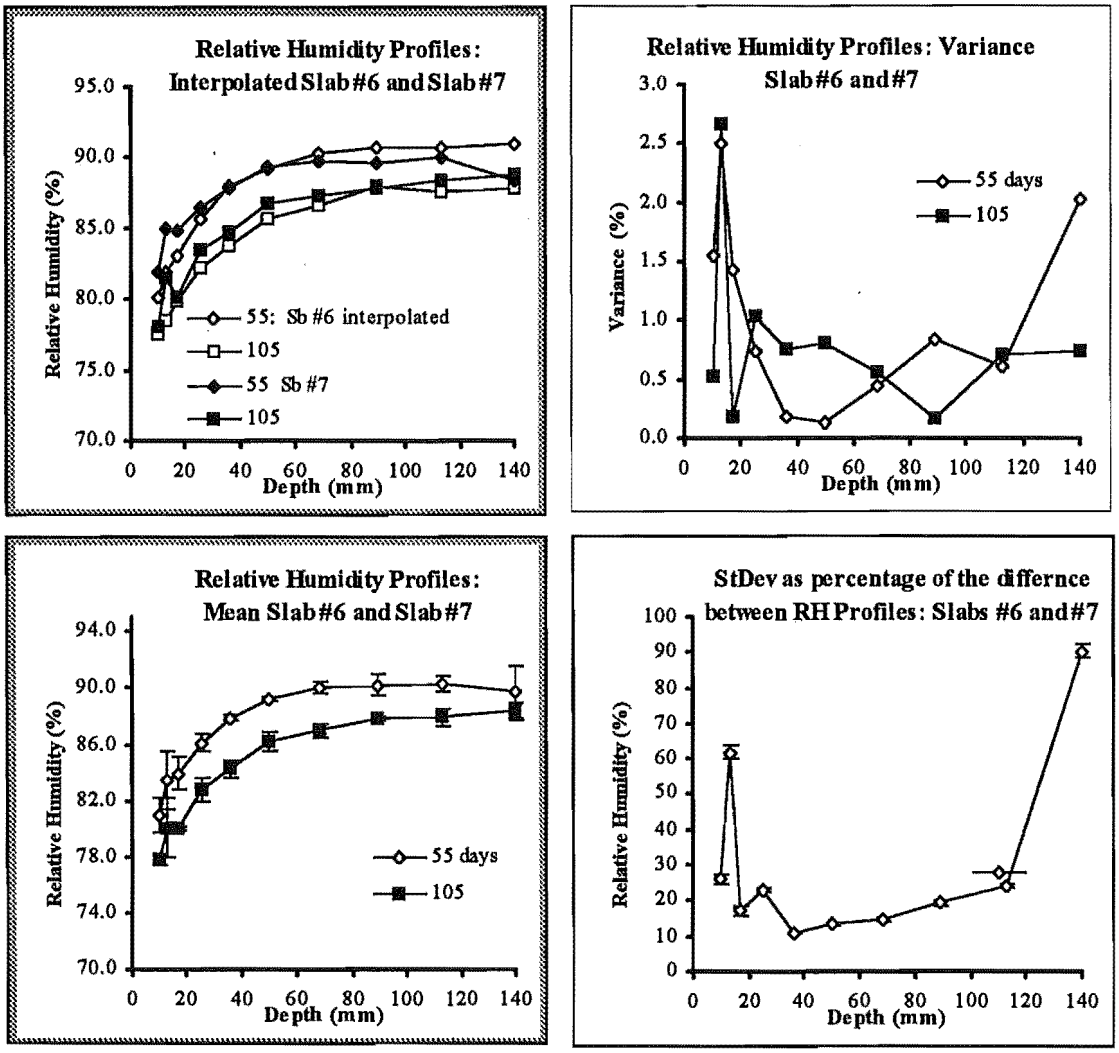

Figure 9.4-12: Evolution of relative humidity profiles: (left) comparing Slab #6 and #7 (right) mean and variance. These slabs were poured at the different times (29/8/1995 #6, 10/10/95 #7) but with the same specifications and kept under identical conditions.

Figure 9.4-13 shows the mean and standard-deviation and variance of the profiles from Cylinders #5, #6 and #7. Generally the agreement and resolution is good for depths below 20 mm.

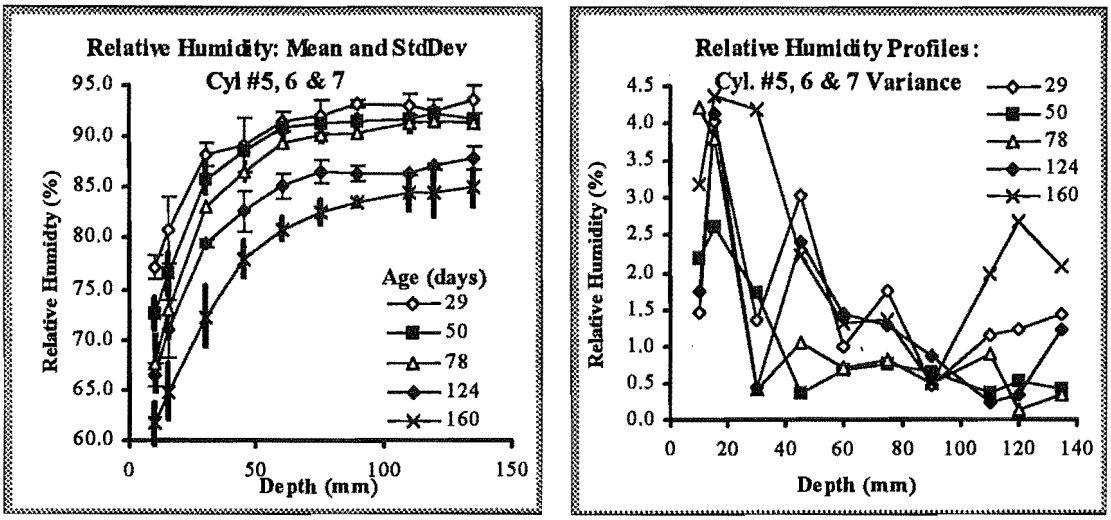

Figure 9.4-13: Evolution of relative humidity profiles: Mean and variance of Cylinders #5, #6 and #7. These cylinders were poured at the same time from the same mix and kept under identical conditions.

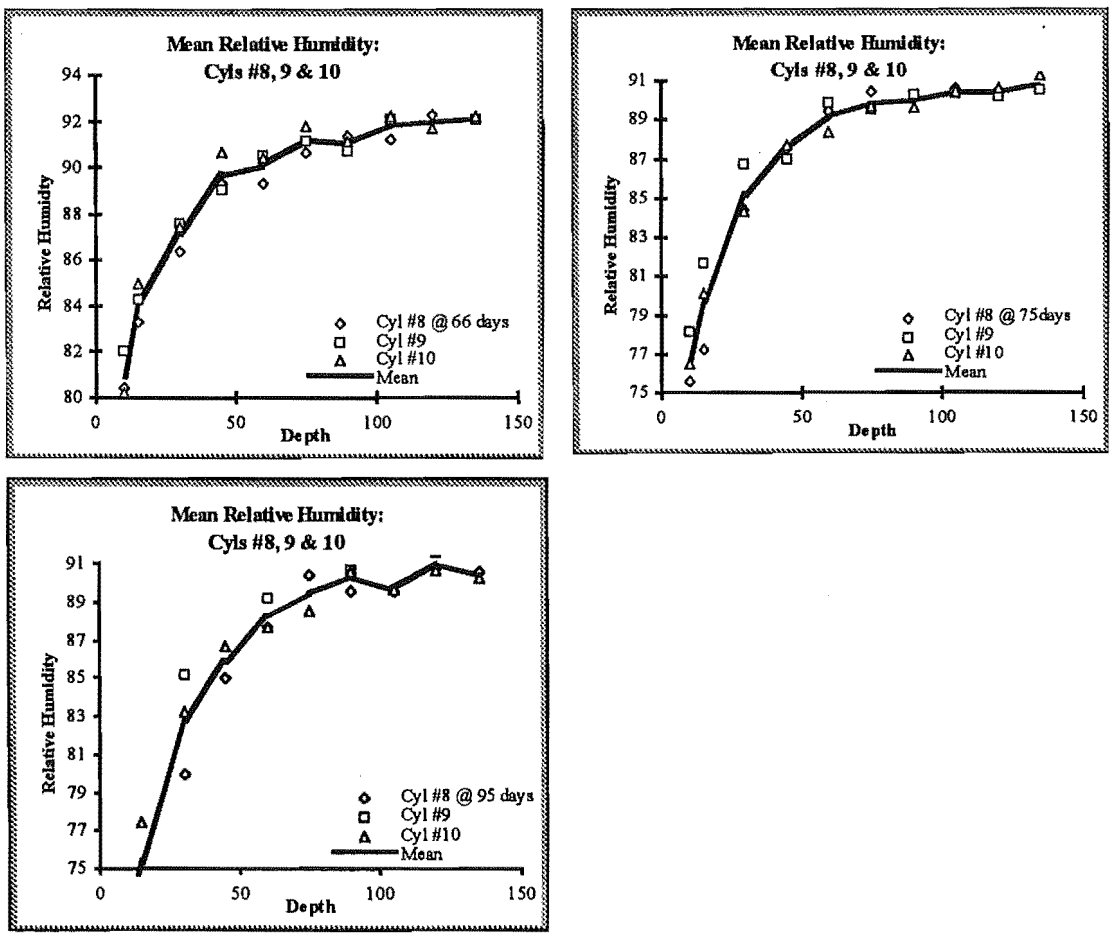

Figure 9.4-14: Mean and variance Cylinders #8, #9 and #10. These slabs were poured at the same time from the same mix and kept under identical conditions.

Figure 9.4-14 shows mean and variance of profiles from Cylinders #8, #9 and #10 at ages 37 days, 75 days and 95 days. The 75 and 96 day profiles are not well resolved. They are only about three weeks apart.

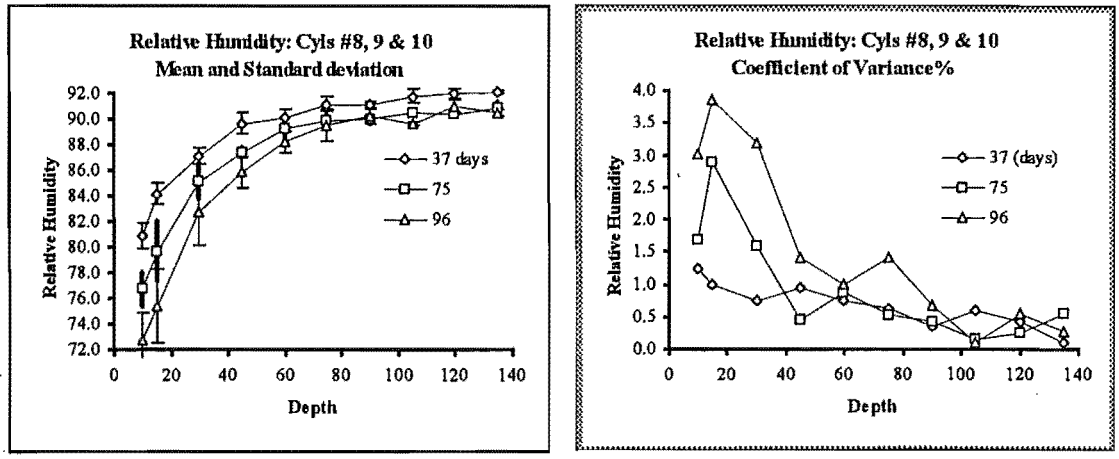

Figure 9.4-14 (continued): Mean and variance Cylinders #8, #9 and #10. These slabs were poured at the same time from the same mix and kept under identical conditions.

More accurate measurements are possible. This would involve more frequent calibration of the probes under more tightly controlled temperature conditions. It is important also that the calibration solutions be kept at the same temperature as the concrete samples under test. Nevertheless, admitting the uncertainty of the measurements made, certain of the relative-humidity profiles do appear to have the form predicted by Parrott's 1991 equation (see Figure 9.4-1). Others may be eliminated when they obviously depart sufficiently from the general trend of drying.

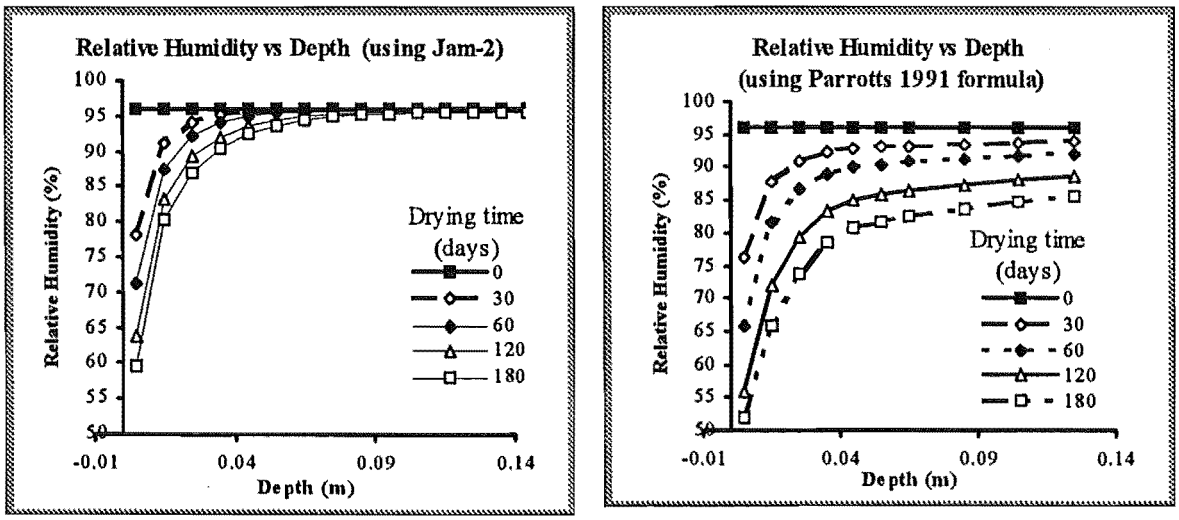

Figure 9.4-1 (a) (b)

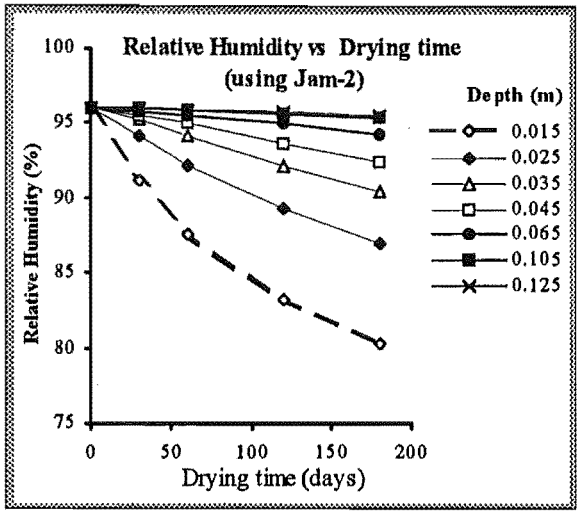

(c)

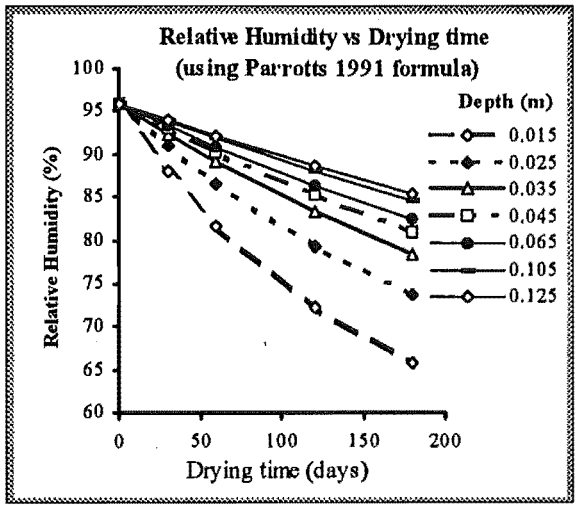

(d)

Figure 9.4-1 (continued): (a) and (b) the evolution of relative-humidity profiles over the measurement period (c) and (d) progress of relative-humidity at particular depths: theoretical data generated by the computer program Jam-2 {(a) and (c)} and Parrotts's 1991 equation {(b) and (d)} (see Chapter2).

9.5 Conclusion

In spite of the apparent simplicity, the measurement of relative-humidity in the concrete samples has been fraught with difficulty. The problems arose in particular with the calibration of the relative-humidity probes, and future work in this area requires a more carefully planned (and more faithfully carried out) calibration and measurement regime. Attention needs to be paid to the sealing of the relative-humidity probes both during calibration and when inserted in the concrete samples for measurement.

At each measurement session, lasting up to a week, up to five relative-humidity profiles were measured in each sample, by rotating the probes through the housing positions. Outlying data points were eliminated and the resulting data averaged.

While the error associated with the measurement seemed high, especially nearer the surface, the agreement between profiles measured simultaneously in equivalent samples was surprisingly good. As with the direct measurement of resistivity profiles (see Chapter 8), the variation in measured values is highest nearer the surface with good agreement (low variance) for depths greater than about 20 mm to 25 mm.

The relative-humidity profiles determined were then used to generate resistivity - relative-humidity calibration curves. This process and the results are described in Chapter 10.

10. Determination of the relative-humidity- resistivity relationship

10.1 Introduction

A system for calibration of the relationship between resistivity and relative-humidity in concrete samples drying from one surface only, has been devised and tested. The resultant calibration curves are required in order to transform into relative humidity profiles, the resistivity profiles recovered using the vertical electric sounding instrument (Chapters 5, 6 and 7) or the embedded-electrode-systems (Chapter 8).

In this project the focus is on naturally hydrating and drying floor slabs. Generally it is assumed that the drying takes place from the top surface only (although, for upper level floor slabs drying will occur from the bottom surface as well). Thus, unless there are extreme changes in environmental conditions which may affect moisture transport direction in the surface region, the concrete at all depths will be losing moisture and the relationship between the moisture content and RH will be expressed by a desorption isotherm (see Chapter 2). As the pore size distribution will change as hydration progresses, so we might expect the desorption isotherm may change. Thus the moisture-content-resistivity relationship should be determined using these naturally occurring profiles, rather than using small samples of concrete dried or wetted to a predetermined moisture content or RH where a different relationship will exist.

10.2 Determination of relative-humidity-resistivity calibration curves

The calibration process involves in the first place, the simultaneous measurement of RH and resistivity at different depths. This has been described in Chapters 4, 8 and 9. Next, the relative-humidity must be reckoned as a function of the resistivity using depth and time as common parameters. Issues involved in the determination of relative-humidity-resistivity calibration curves will be described in the following sections using particular concrete samples.

10.2.1 Interpolation of resistivity profiles

Resistivity was often measured at different times and different depths from, and more often than, the relative-humidity. Because they are generally smoother and exhibit less scatter than relative-humidity profiles, resistivity- rather than relative-humidity- profiles were interpolated to obtain resistivity profiles corresponding to the relative-humidity measurement times and depths.

There is a tendency for resistivity to increase exponentially with reducing depth, so the logarithm of the resistivity was linearly interpolated. Subsequent analysis has shown that over a useful depth range, the relationship between resistivity ρ and depth d may be expressed as

$$\ln(\rho) = -a\ln(d)$$

so that ideally, more accurate interpolation would require linear interpolation of $\ln(\rho)$ with respect to ln(depth). In view of the data scatter in both resistivity and relative-humidity measurement this extra accuracy would not be achievable in practice and was not carried out in the present study.

10.2.2 Fitting a curve to relative-humidity-resistivity data points

When relative-humidity is plotted against resistivity, the relationship between the two physical properties becomes evident (Figure 10.2-1). In this graph, a linear relationship between relative-humidity ψ and the logarithm of resistivity appears to hold loosely, for depth below 20 mm. If the data points corresponding to the most shallow depth are removed, a curve of the form

$$\psi = -a\ln(\rho) + b$$

(where a and b are coefficients that may be functions of depth and the age of the concrete) may be fitted reasonably well to calibration curves measured at different ages. This is the same equation that was found to fit the data presented in Woelfl and Lauer (1979, see Chapter 3, Section 3.1.3 of this thesis).

The least-squares fitting of calibration curves to the calibration data (using the "Insert trendline" function in MicroSoft Excel), is shown in Figure 10.2-2.

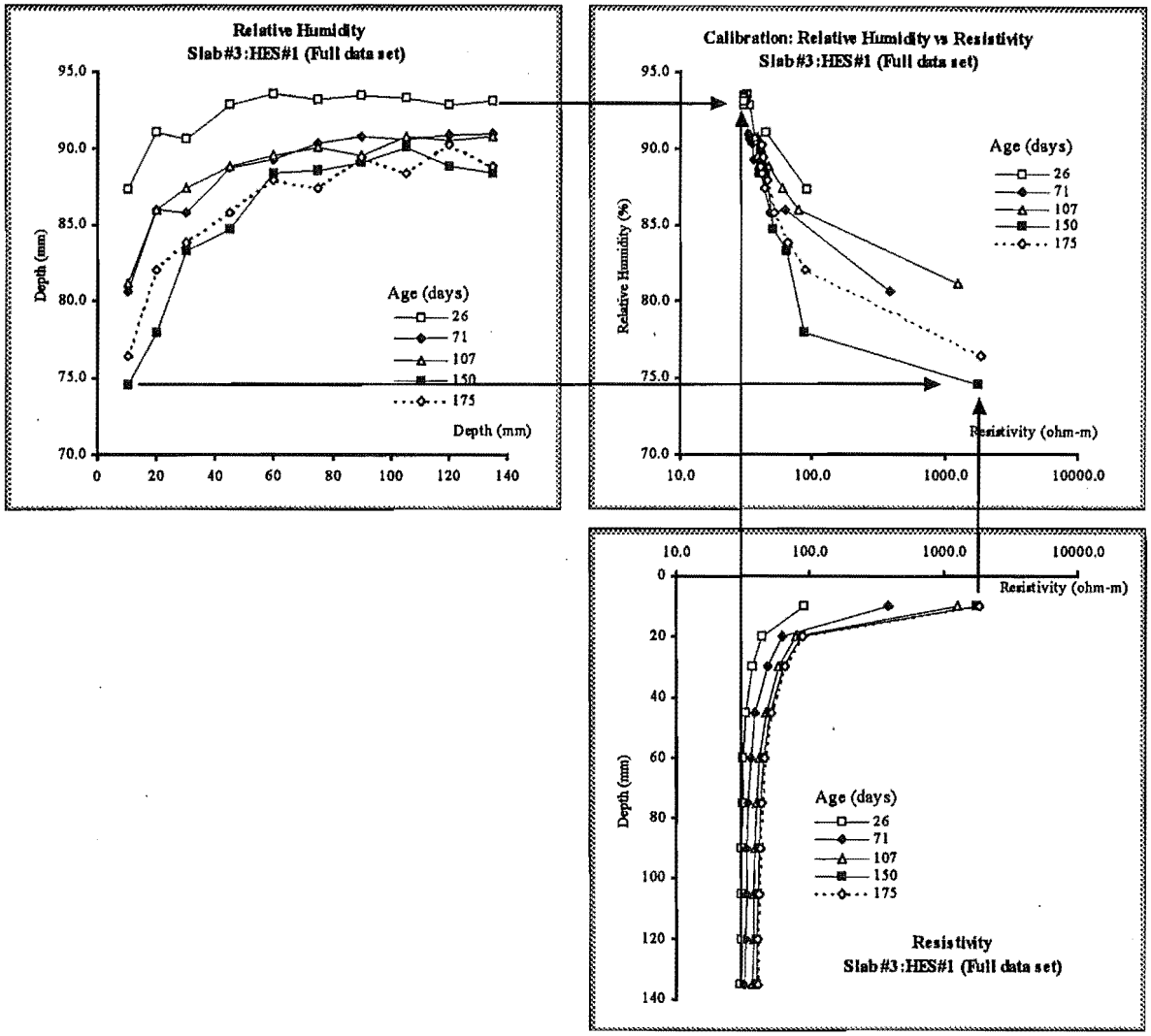

Figure 10.2-1: Generation of relative-humidity- resistivity calibration curves by plotting relative-humidity versus resistivity through their common parameters of depth and time. Notice the linear relationship between relative-humidity and the logarithm of resistivity that appears to hold below 20 mm. The departure from this relationship appears to derive from the very high resistivity (and a resultant break from the smooth curve) shown at the most shallow data point.

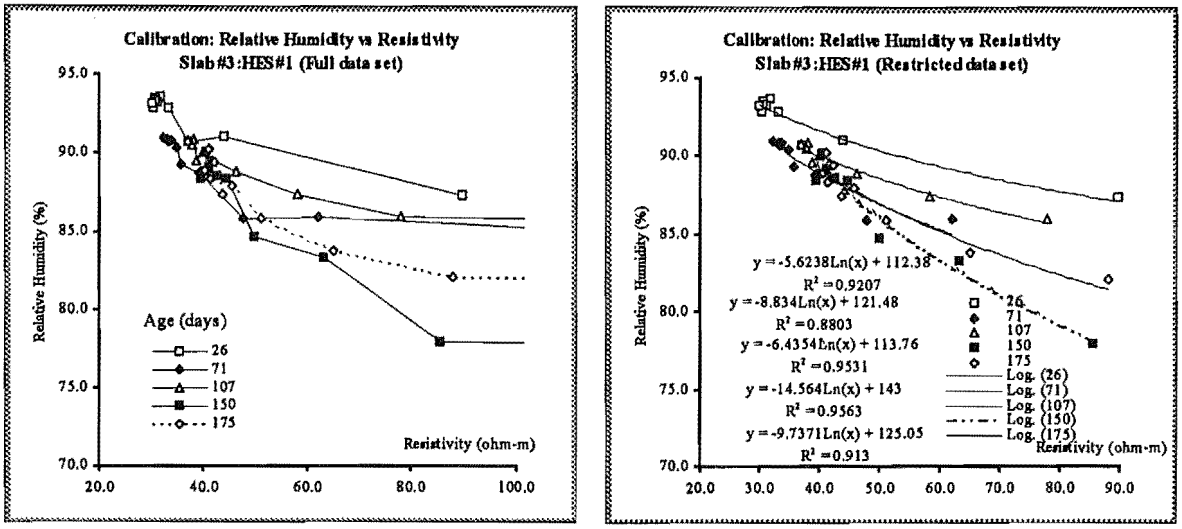

Figure 10.2-2: Calibration curves for Slab#3 using resistivity profiles measured with HES#1. The left hand graph contains or points towards the full set of data points. The right hand graph shows curves of the form $\psi = -a\ln(\rho) + b$ fitted to calibration curves in which the most shallow data point has been removed. The equations shown on the graph are in order of the age at which the measurements were taken.

10.2.3 The effect of profiles derived from HES#1 or HES#2

For this set of curves shown in Figure 10.2-2, there seems to be no clear progression in the calibration equation with age. Perhaps this is not surprising in view of the erratic nature of the relative-humidity profiles responsible. However, the calibration curves determined using the HES#2 resistivity profiles are a little more consistent. HES#2 profiles often show more continuity at shallow depths than HES#1 profiles. Accordingly, the interpolated profiles yield less-extreme data points in the corresponding relative-humidity-resistivity calibration curves (see Figure 10.2-3).

The coefficients for the fitted equations are presented in Table 10.2-1. Notice the agreement of the equations for the 26 day, 71 day and 175 day data sets. Once again it must be emphasised that the relative-humidity curves in particular are not reliable. It is likely that the calibration curves will show some development with age - as the pore-size-distribution develops and the chemistry of the pore solution changes. Furthermore it is likely that if equations of the form shown can be fitted to the data, then there will be a continuous development of the coefficients. However, on the basis of the curves from Slab #3 illustrated here, it is not possible to determine such a progression. Possibly the relative-humidity

profiles most similar to those predicted by Parrott's 1991 equation, were those measured in Slab #7. The determination of relative-humidity-resistivity calibration curves from Slab #7and subsequent analysis is discussed in the next section.

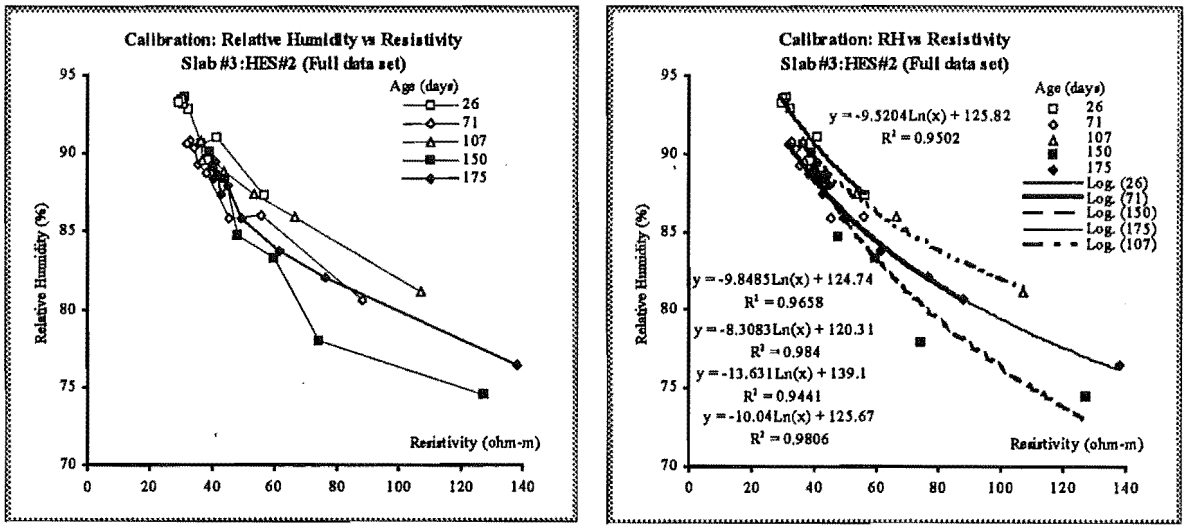

Figure 10.2-3: (Left) Calibration curves for Slab#3 using resistivity profiles measured with HES#2 . (Right) Curves of the form $\psi = -a\ln(\rho) + b$ fitted to the calibration curves. The equations shown on the graph are in order of the age at which the measurements were taken.

Table 10.2-1: Coefficients of the equation $\psi = -a\ln(\rho) + b$ for some selected fitted curves from Figure 10.2-3

Age (days)	a (%RH/(ohm-m))	b (%RH)
26	9.5	126
71	9.8	125
107	*8.3*	*120*
150	*13.6*	*139*
175	10.0	126

10.2.4 Relative-humidity-resistivity calibration curves grouped by age or by depth

The original relative-humidity profiles and the interpolated resistivity (HES#2) profiles from Slab #7 are presented in Figure 10.2-4. The resulting calibration curves are presented grouped by age as in the previous section. Calibration curves grouped by depth are also shown since it is of interest to investigate the resistivity-relative-humidity relationship occurring at each depth.

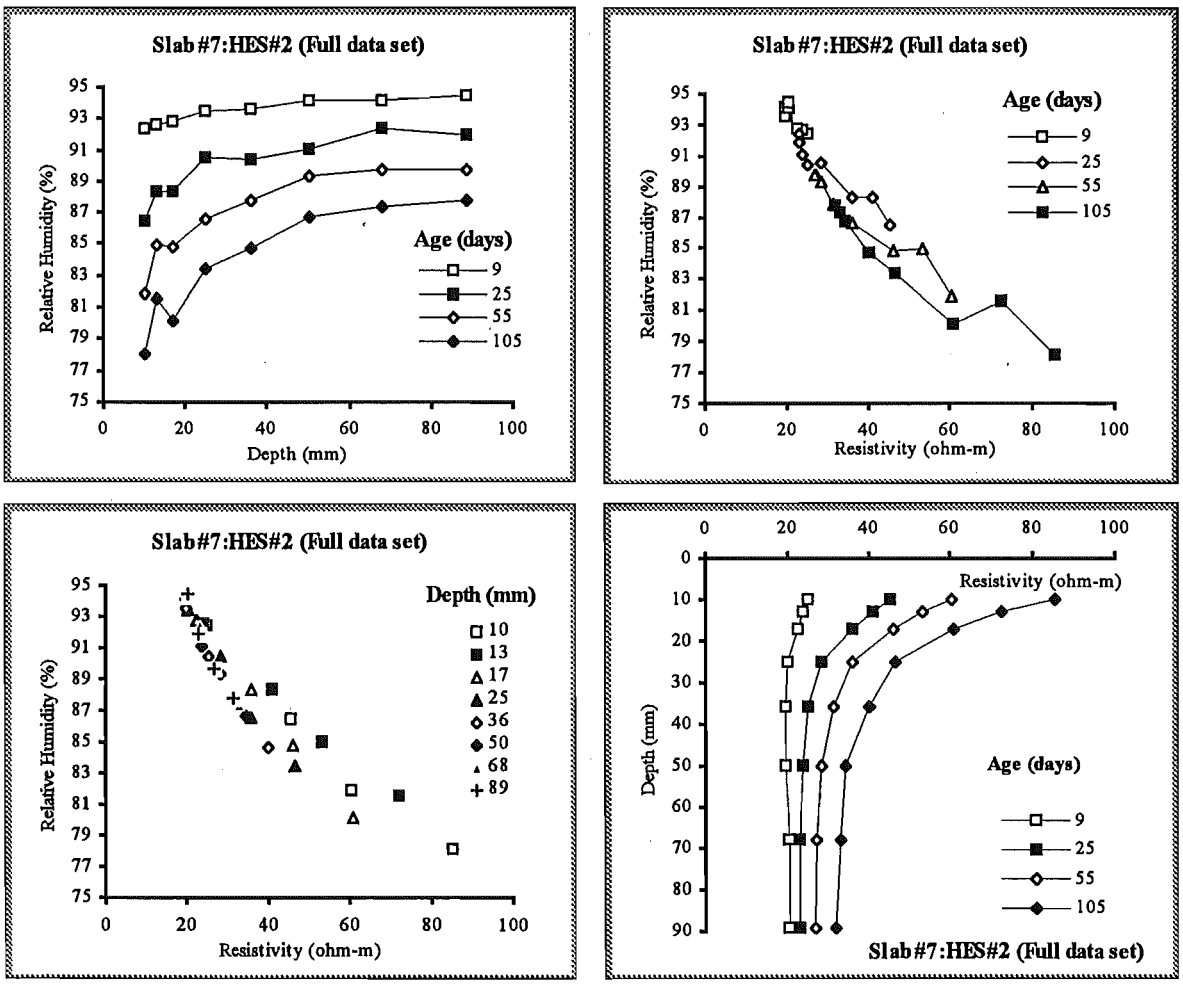

Figure 10.2-4: Generation of relative-humidity- resistivity calibration curves from measurements made on Slab #7. The relative-humidity profiles are shown in the graph at top-left. The resistivity data which was taken from an HES#2, is shown in the lower-right graph. Calibration curves are presented in two ways. The graph at top-right shows the curves grouped by age. The lower-left graph shows the curves grouped by depth.

Consider first the calibration curves grouped by age. Each curve is a summary of the relationship between the relative-humidity and resistivity as a function of depth, at a particular concrete age (that is, the time since pouring). The lower right data point of each curve originates from the most shallow depth. Back along the curve are data points originating from successively greater depths. The data points lie on a broad band extending from the upper-left (high relative-humidity, low resistivity) to the lower right (low relative-humidity, high resistivity). With time, the data points appear to slide down this broad band towards low relative-humidity and high resistivity as expected. If the relationship between relative-humidity and resistivity did not change with time, the data points would lie on a single curve (within the bounds of error). Inspection of Figure 10.2-4 suggests that the data points for the deeper regions of the slab do lie on a single curve whereas the shallower regions yield a range of relationships.

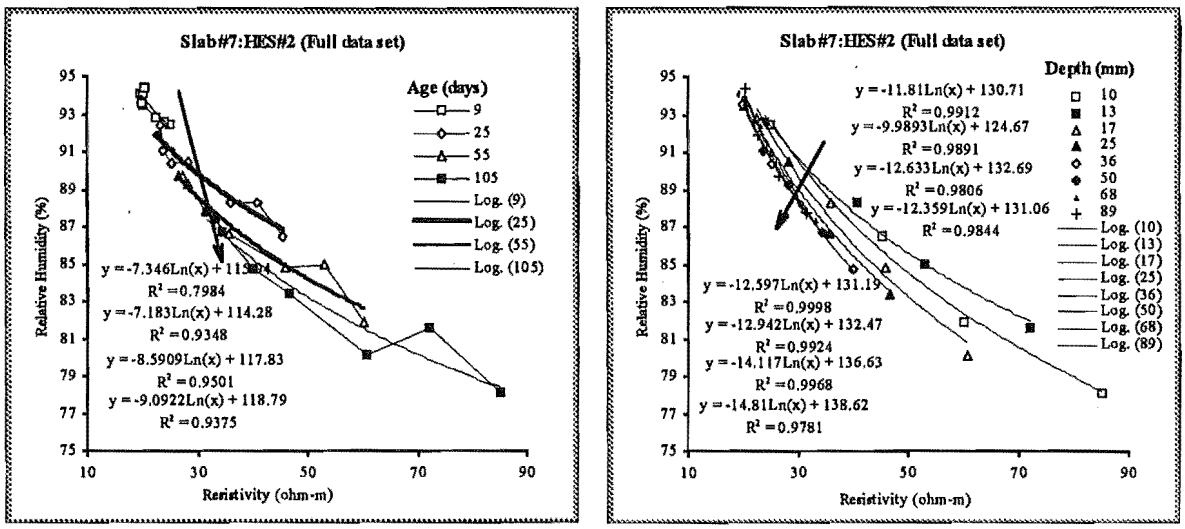

Figure 10.2-5: Fitting equations of the form $\psi = -a\ln(\rho) + b$ to the resistivity-relative-humidity calibration data grouped by age (left) and by depth (right). The arrows indicate curves fitting data of increasing age and depth respectively. In both of these graphs, there is a clear development of the calibration curves. The coefficients *a* and *b* taken from these graphs are presented in Table 10.3-1.

Table 10.2-2: Coefficients of the equation $\psi = -a\ln(\rho) + b$ fitted to the graphs in Figure 10.2-5.

Calibration data grouped by age				Calibration data grouped by depth			
Age (days)	a	b	R^2	Depth (mm)	a	b	R^2
9	7.3	116	0.8[1]	10	11.8	131	0.99
25	7.2	114	0.93	13	10.0	125	0.99
55	8.6	118	0.95	17	12.6	133	0.98
105	9.1	119	0.94	25	12.4	131	0.98
				36	12.6	131	1.00
				50	12.9	132	0.99
				68	14.1	137	1.00
				89	14.8	139	0.98

[1] R^2 is the R-squared measure of fit determined by M.S.Excel in calculating the least-squares fit through the data points using the equation y=a·ln(x)+b.

Note that the calibration curves grouped by age have a lower (negative) slope than those grouped by depth, and thus cut across the latter. The coefficients of the fitted calibration equations are shown in Table 10.2-1. There is a clear progression of the values of a and b with both age and depth. The fit of the equation to the curves for data grouped by depth is much better than for data grouped by age. Curves may be fitted to the coefficients as functions of depth and time (Figure 10.2-6).

The coefficients are fitted relatively poorly by the linear function shown in the graphs. Actually, one would expect that the coefficients would approach constant levels with increasing age and depth, however for the relatively small range of age and depth, and the small number of data points, a linear function is sufficient to illustrate the effect of age and depth on the calibration curves. Calibration curves generated using these derived age- and depth- dependent coefficients are shown in Figure 10.2-7.

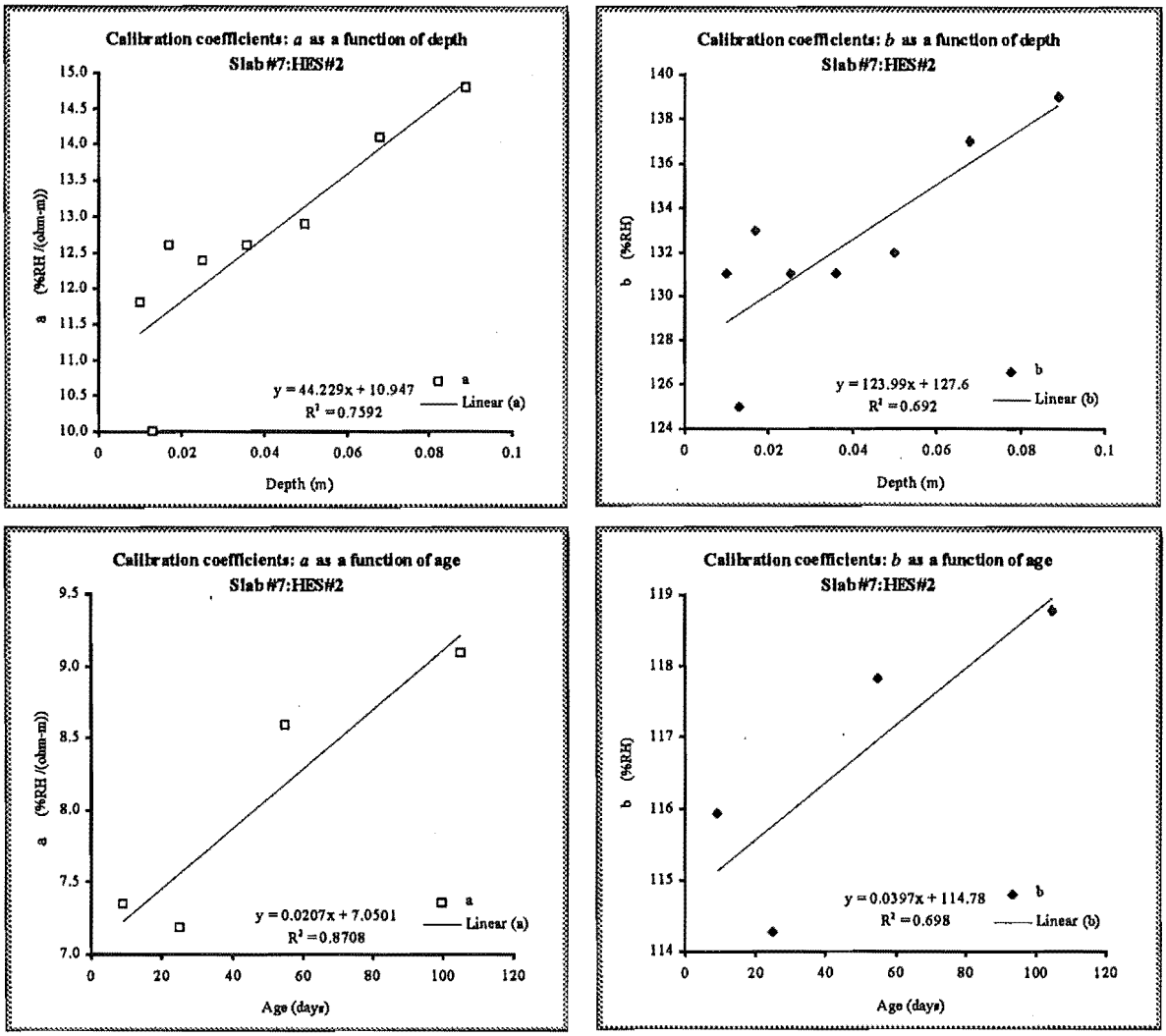

Figure 10.2-6: Determination of the depth dependence (top two graphs) and the age dependence (lower graphs) of the calibration curve coefficients. The fitted equation shown in the top left graph is to be read as $a \cong 44.d + 11$. The other equations are to be read correspondingly.

It is likely that the most useful form of the calibration curves will be as functions of depth. Then, resistivity measurements made at selected depths, may be transformed to relative-humidity using the appropriate depth dependent calibration curve.

Note the same relative-humidity (for example the cutoff point of 75% mentioned in Chapter1), is reached with decreasing resistivity as the concrete ages, and as the depth of measurement increases.

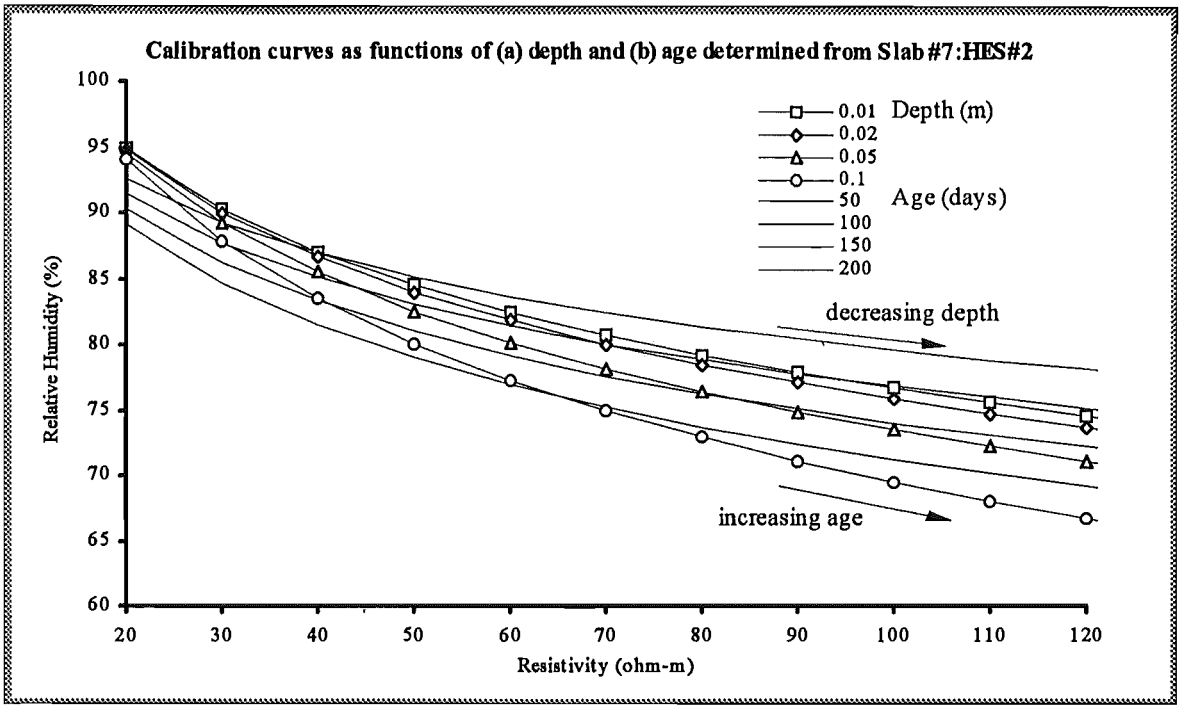

Figure 10.2-7:. Derived calibration curves determined through fitting equations to the 'raw' calibration curves. This graph shows the two ways of determining calibration curves (as functions of age or depth) and the relationship between them. The calibration curves identified by markers, vary with depth. The location along the curve will depend on the age of the concrete. The lower arrow indicates the increase in resistivity and decrease in relative-humidity of concrete at a certain depth, as it ages. The markerless calibration curves vary with age. The upper arrow indicates the variation with depth, in the resistivity and relative-humidity of concrete of a certain age.

10.2.5 Use of Parrott's (1990) equation to enhance determination calibration curves.

The relative-humidity profiles from slab#7 exhibit a certain amount of data scatter, that is variations from a smooth relative-humidity profile that are not likely to be physical. A number of smoothing and curve fitting routines were used in an effort to find realistic smooth curves through the data points. The smoothing spline routine was able to be used, however where the scatter was extreme, the profile would remain determinedly non-physical in appearance. Increasing the smoothing in these cases resulted in curves increasingly approximating a straight line, allowing information in the region of fastest change (associated with the 'wet-dry' interface) to be lost. In order to preserve the expected physical appearance, the raw data was fitted to profiles generated by Parrott's(1990)

equation (see Section 10.4). This equation uses one function of drying time and depth beneath the surface, and another of the ambient, and initial relative-humidities. The curves were fitted by allowing the ambient relative-humidity to vary (see Figure 10.2-8). The fit is not good at depths below 120 mm, and the 106 day curve is not as gradual as the measured profile, but overall the fit is surprisingly good, with differences between profile and fitted curve less than 2% (relative-humidity).

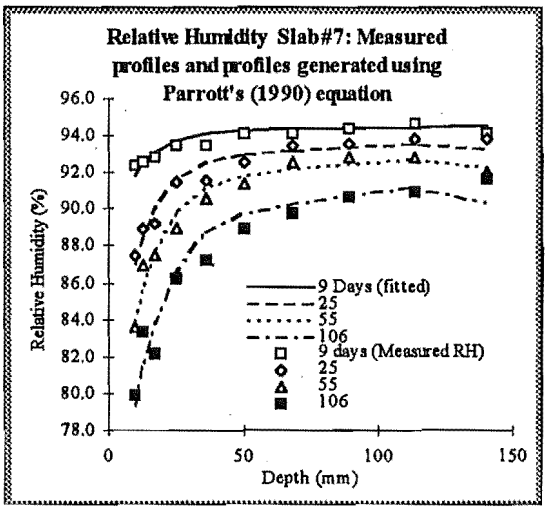

Figure 10.2-8. Relative-humidity profiles measured for slab #7and curves fitted using Parrott's (1990) equation.

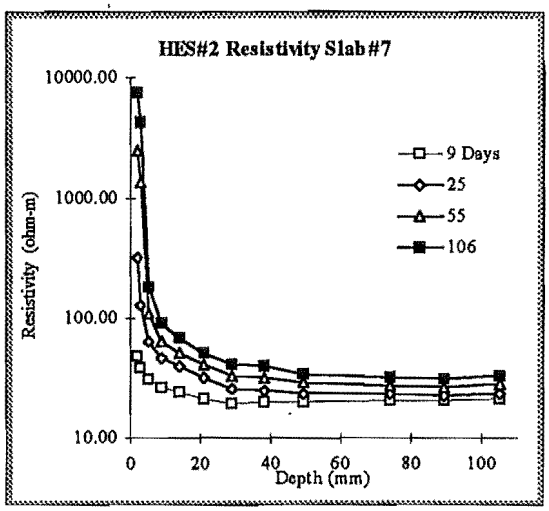

Figure 10.2-9. Resistivity profiles measured for slab #7 using a HES#2. The original profiles have been interpolated at times corresponding to the relative-humidity measurement times.

The fitting of Parrott's equation to the relative-humidity enables the relative-humidity curves to be interpolated at the resistivity depths which, for HES#2 profiles, are more frequent closer to the surface. This is interpolation, since the relative-humidity profile is assumed to be smooth and continuous to the surface which is fixed at the ambient relative-humidity.

In Figure 10.2-10 , the relationship between relative-humidity ψ, and resistivity ρ, is demonstrated.

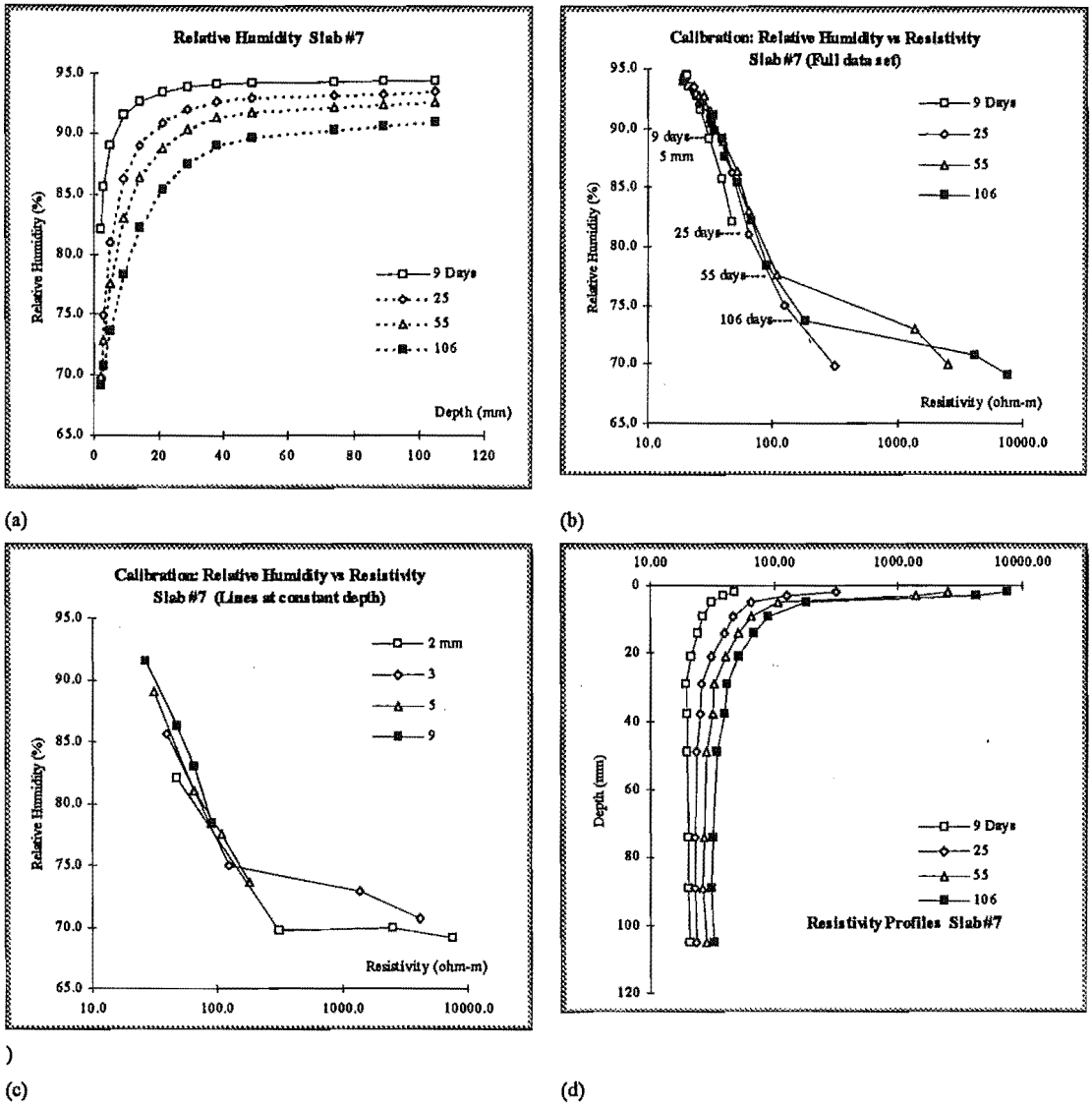

Figure 10.2-10. Determination of relative-humidity-resistivity calibration curves (b), by relating (a) relative-humidity and resistivity (d) through the shared parameter of depth. In (c), calibration curves are plotted for concrete at a few selected depths.

The calibration curves lie close to the curve defined by the calibration equation $\psi = -10.3 \cdot \ln(\rho) + 126$. This is very similar to the equation attained using a simpler method described in Section 10.3. It may be that the method described in this section, although interesting, does not provide much advantage.

10.3 Results

In the following sections, data taken from the slab and cylinders is treated in a number of ways.

1. The data may be grouped by age or by depth.
2. The data set may be restricted, that is, outlying points corresponding to the highly resistive surface regions may be eliminated.
3. The data may be pooled for all ages and depths, and a calibration curve generated by fitting an equation to the pooled data.
4. 2. and 3. may be combined.

10.3.1 Cylinders #5, #6 and #7 compared

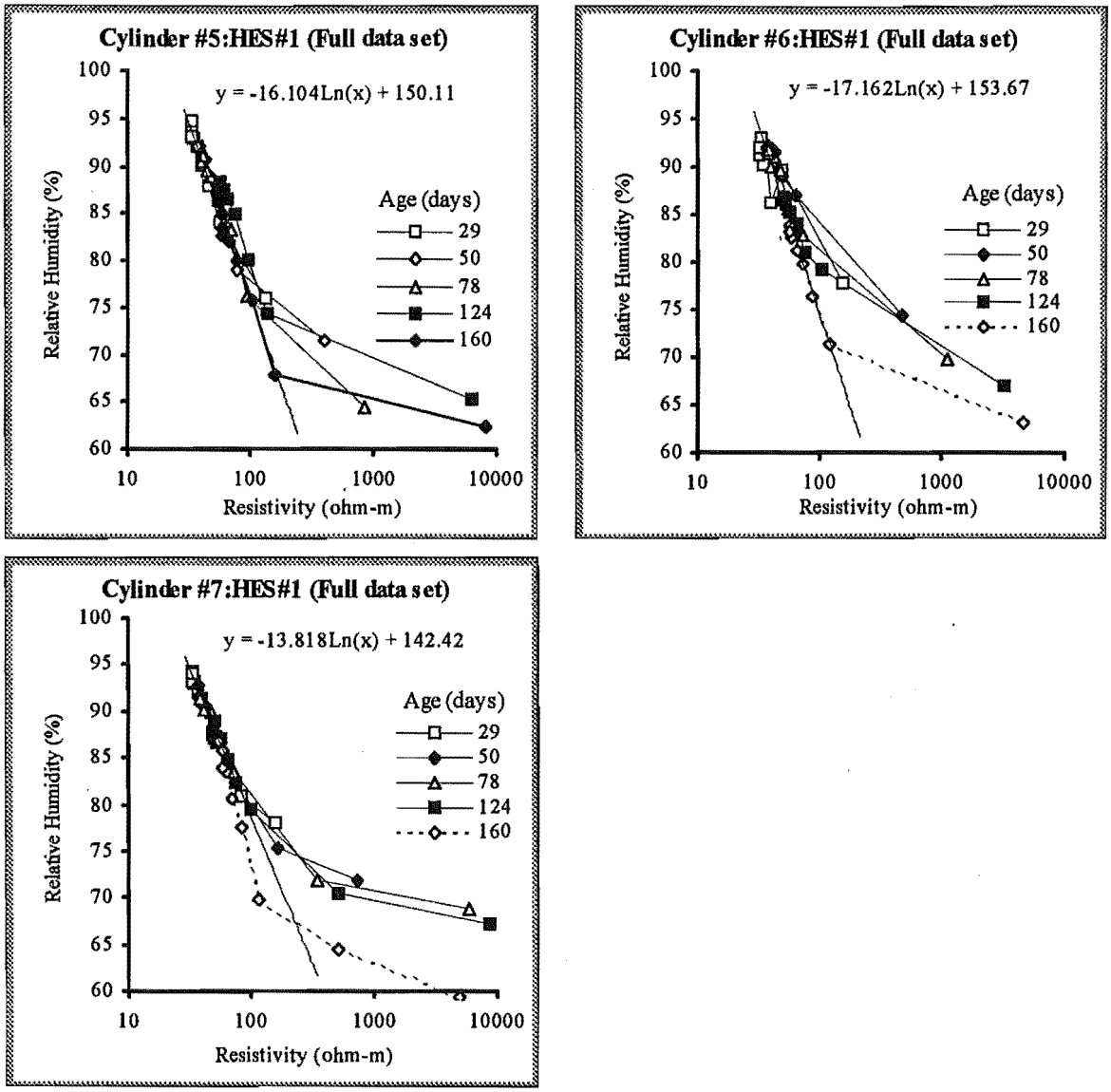

Figure 10.3-1: Calibration data for Cylinders #5, #6 and #7. In each graph, a line through the broad mass of data points has been drawn. The calibration equation corresponding to each line is also given for comparison. Calibration curves coefficients have also been determined for each cylinder

Cylinders #5, #6 and #7 contained an HES#1. The calibration data grouped by the five relative-humidity measurement times are presented in the following graphs and table. In the first set of linear-log graphs, the calibration equation $\psi = -a\ln(\rho) + b$ has been fitted by eye, to the broad mass of data points (that is, pooled data) that appear to lie in a straight line

on the linear-log graph. This is merely to give an indication of differences between the cylinders.

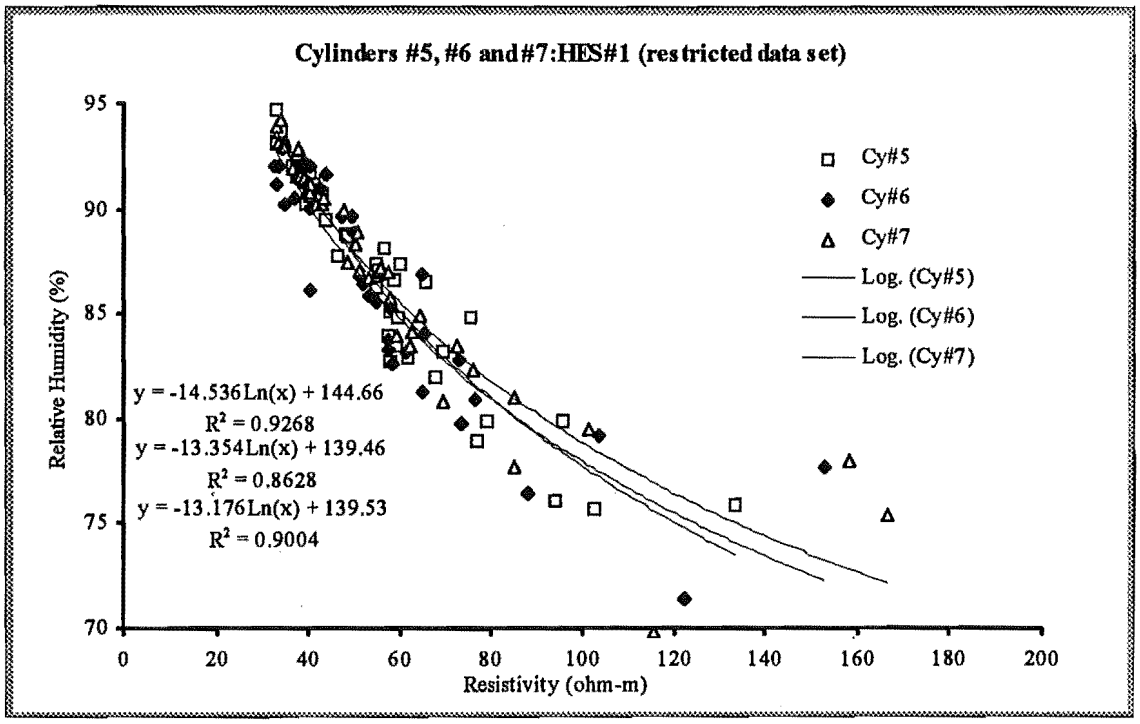

Figure 10.3-2: Comparison of calibration data from the equivalent samples Cylinders #5, #6 and #7.

In Figure 10.3-2 the data for each cylinder has been pooled and the data set restricted by removing all data points where the relative-humidity is less than 74%. Calibration equations fitted to each of the restricted data sets show quite good agreement. A mean calibration equation was calculated as $\psi = -13.9\ln(\rho) + 141$. In Figure 10.3-3 enveloping curves have been drawn to show the uncertainty in the calibration equation. From this analysis, the relative-humidity for a given measured resistivity would lie between $\psi = -14.3\ln(\rho) + 141$ and $\psi = -13.3\ln(\rho) + 141$. At the range of relative-humidity of interest, that is at about 75%, the uncertainty in relative-humidity for a given value of resistivity, is about $\pm$ 3% RH.

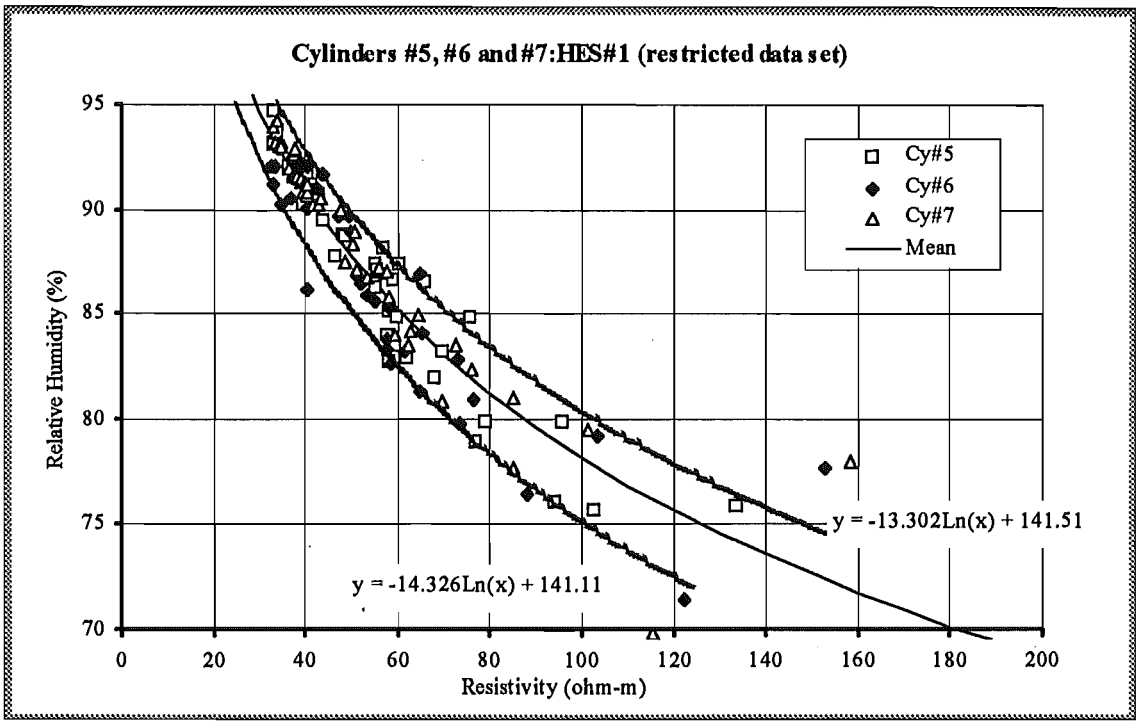

Figure 10.3-3: The mean calibration curve obtained from averaging the separate calibration curves for Cylinders #5, #6 and #7. The outer envelope lines contain most data points and indicate the precision of the measurement.

Table 10.3-1: Coefficients for the calibration equations fitted to the data grouped by age, for each cylinder. In the lower set of coefficients outlying data points (corresponding to very high resistivity at shallow depths, have been removed.

	Cylinder #5			Cylinder #6			Cylinder #7		
	Including 10 mm depth data point			Including 10 mm depth data point			Including 10 mm depth data point		
age (days)	a	b	r2	a	b	r2	a	b	r2
29	13.2	139	0.97	9	123	0.89	10.9	131	0.96
50	9	124	0.9	7	117	0.98	7.3	117	0.91
78	9	123	0.92	6.5	114	0.94	4.9	108	0.87
124	4.4	105	0.84	4.6	104	0.93	4.3	103	0.86
160	4.4	100	0.74	4.5	99	0.82	6.2	108	0.81
	Excluding 10 mm depth data points			Excluding 10 mm depth data points			Excluding 10 mm depth data points		
age	a	b	r2	a	b	r2	a	b	r2
29	17.7	156	0.99	8.7	122	0.35	13	142	0.99
50	17	154	0.96	9.2	126	0.9	11.3	133	0.98
78	16.9	154	0.98	14.4	144	0.95	12.4	137	0.98
124	14.4	146	0.95	11.2	131	0.97	12.6	137	0.96
160	16.1	150	0.98	16	148	0.99	22.4	176	0.99

Coefficients for the calibration equation fitted to the data grouped by age, have also been determined for each cylinder. These are presented for the three cylinders in Table 10.3-1.

Although it is more difficult to compare the calibration equations in this form, there appears to be much less agreement between the cylinders than when the data is pooled. Note that the R^2 measure of fit indicates that when the data sets are restricted (removing the 10 mm data points, the calibration equation is a very good expression of the relative-humidity-resistivity relationship.

10.3.2 Slab#6

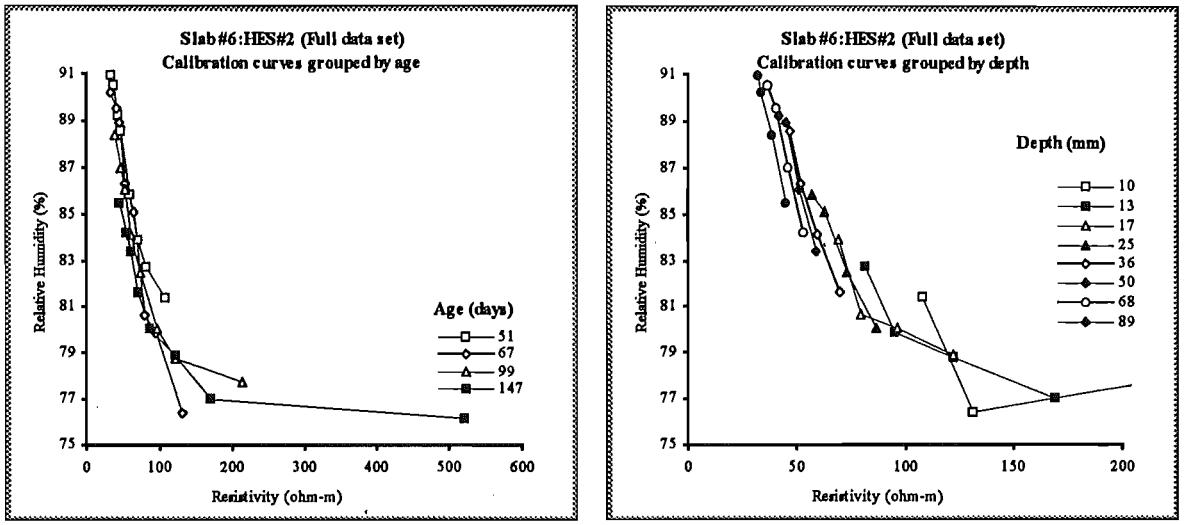

Figure 10.3-4: Calibration data for Slab #6 HES#2, grouped by age (left) and by depth (right).

Table 10.3-2: Coefficients of the equation $\psi = -a\ln(\rho) + b$ fitted to the graphs in Figure 10.3-4 :Slab #6, HES#2.

Calibration data grouped by age (for depths ≥ that in the 5th column)					Calibration data grouped by depth (including ages between 51 and 147 days)			
Age (days)	a	b	R^2	for d≥	Depth (mm)	a	b	R^2
51	8.7	122	0.98	10	10	2.2	89	0.39
67	11.0	130	0.98	10	13	7.2	113	0.91
99	8.7	120	0.99	13	17	7.9	116	0.82
147	6.4	109	0.97	13	25	14.4	144	0.99
				(mm)	36	17.2	155	0.99
					50	17.4	155	0.98
					68	17.2	153	0.98
					89	15.8	146	0.99

The data in this table should be compared with that in Table 10.2-2 for the (nearly) equivalent Slab #7, HES#2. There is quite a large disparity between the calibration coefficients. Slightly closer agreement between the coefficients (data grouped by depth) arises, if the 147 day data here is eliminated, in which case the age range of the data sets are more nearly equivalent.

10.3.3 Slabs #4 and #5

Calibration equations have also been fitted to the data (grouped by age only) from Slabs #4 and #5 (Table 10.3-3). Apart from the 94 day profiles, there is not much agreement between the calibration curves obtained from the two slabs, when analysed in this way. A different picture emerges when, as in the next section, the data is pooled.

Table 10.3-3: Calibration equation coefficients for relative-humidity-resistivity data measured in the equivalent Slabs #4 and #5.

Calibration data grouped by age							
Slab#4	including d=10mm			**Slab#5**			
age (days)	a	b	r^2				
57	6.8	116	0.98	(no data points for d=10mm)			
94	6	112	0.95				
140	7.7	116	0.91				
161	4.2	102	0.72				
Slab#4	excluding d=10mm			**Slab#5**	excluding d=10mm		
age (days)	a	b	r^2	age (days)	a	b	r^2
57	7.9	120	0.97	17	9.3	126	0.73
94	7.3	117	0.92	94	7.2	116	0.95
140	12.1	133	0.95	140	6.5	112	0.86
161	11.1	128	0.97	161	7.8	118	0.8

10.3.4 Slabs #3 to #7 compared.

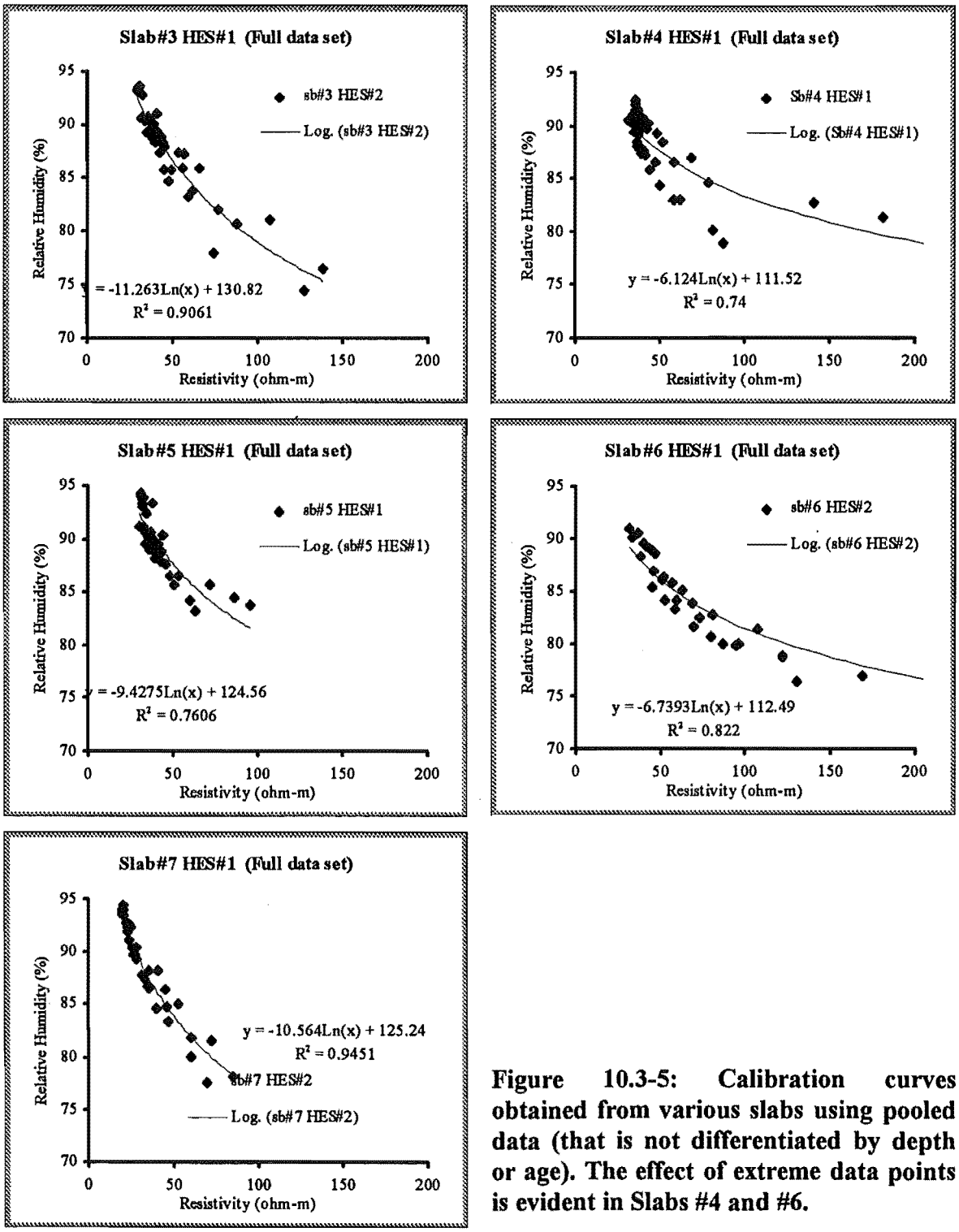

Figure 10.3-5: Calibration curves obtained from various slabs using pooled data (that is not differentiated by depth or age). The effect of extreme data points is evident in Slabs #4 and #6.

In Figure 10.3-5, for each slab, the calibration equation has been fitted to pooled unrestricted data. The effect of the shallow highly resistive data points is evident, pulling some curves apparently well away from the visually appropriate position. The resulting calibration equations do not exhibit good agreement between the slabs. When the weight of the extreme points is removed, by restricting data to resistivities less than 100 ohm-m, the calibration equations are less differentiated. Nevertheless, the variation in relative-humidity yielded by the individual equations from the nearly equivalent slabs(#4, #5, #6 and #7 all have a nominal strength of 25 MPa), is up around $\pm$ 5% RH. This lack of agreement could indicate that the curing conditions may have a significant effect on the relative-humidity-resistivity calibration curves. Indeed, the agreement between the equations for Slab #4 and #5 which were poured at the same time from the same mix and kept under the same conditions is much better. The differences in relative-humidity determined from their respective calibration equations is only around 1% RH. Slab #6 and #7 which were stored in the same room but poured at different times yield a variation of about 2%.

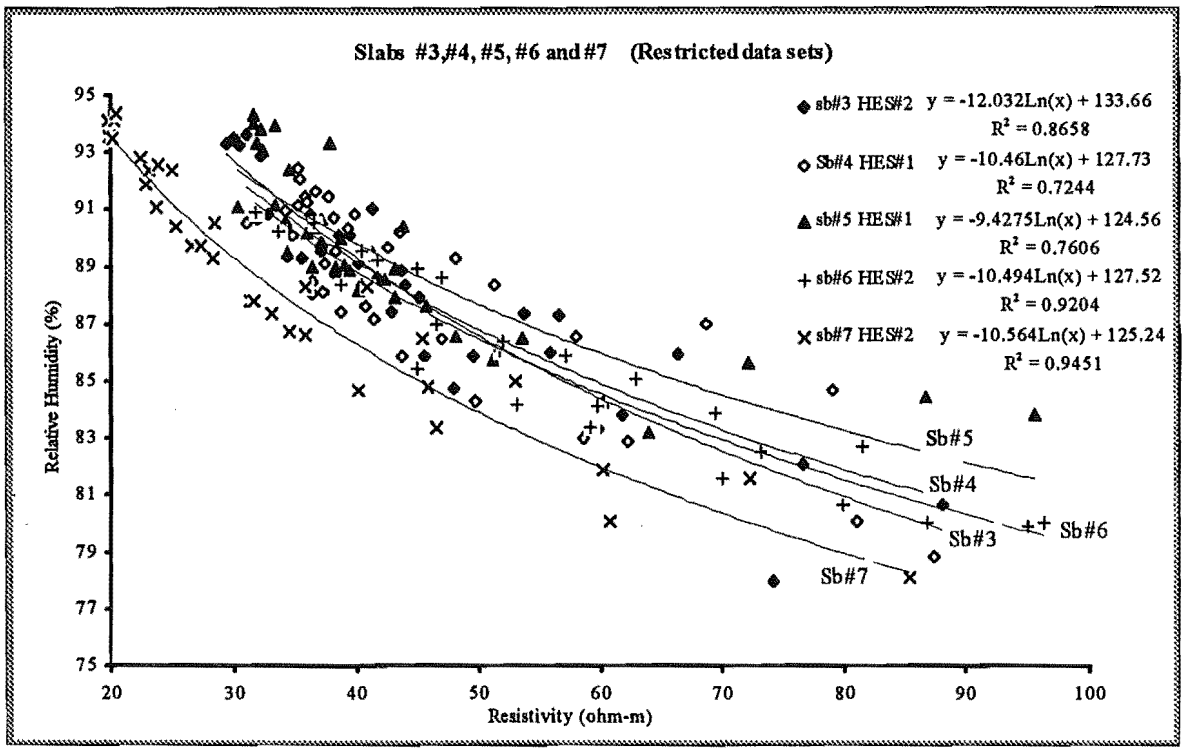

Figure 10.3-6: Comparison of calibration curves for Slabs #3 to #7. The curves are based on a restricted data set, that is, all data points with resistivity > 100 ohm-m are excluded. The agreement between the sets of data points is much higher than when the high resistivity (shallow depth) points are included.

10.4 Further analysis and discussion

10.4.1 The surface regions

The determination of relative-humidity near the surface of a slab will be more inaccurate and lacking in precision than at lower depths. Direct measurement of resistivity profiles (Chapter 8) and indirect method of vertical electric sounding (Chapters 5 - 7), are both least precise in the region near the surface. Similarly direct measurement of relative-humidity has been shown to be least precise near the surface of the concrete slab (Chapter 9). Thus the relative-humidity profiles derived by transforming the recovered resistivity profiles from vertical electric sounding to relative-humidity using the relative-humidity-resistivity calibration curves will be especially inaccurate in this region.

Reasons for the high variation in measurements made near the surface have been advanced in the respective chapters. The calibration process itself may be inherently inaccurate near the surface since, the susceptibility of the surface regions to fluctuations in ambient temperature and relative-humidity may result in the decoupling of the relationship between resistivity (which is largely dependent on the moisture content) and the relative-humidity.

As the air temperature above the slab varies, so will the ambient relative-humidity and, although in a markedly damped fashion, the temperature of the slab. The slab's thermal conductivity and the heat capacity will both increase with increasing moisture content (less airspace and more water). The low heat capacity near the surface will ensure maximum response to swings in ambient temperature. The low thermal conductivity near the surface will act to insulate (relatively) the deeper layers from the changes. In effect, the surface layers will experience the greatest temperature swings.

The various points along the profile of the slab will be in approximate equilibrium between the moisture content (or pore saturation) and the relative-humidity within the pore space, given that typical movements in relative-humidity are from around 0.125%/day to around 0.025% day for slabs drying in ambient relative-humidities of 40% and 80% respectively (see McGlone, 1990, Figure 15). When the temperature changes the absolute humidity within the pore space will lag behind the relative-humidity. For example a rise in temperature will cause the relative-humidity within the pore space to drop. The immediate effect will be

to set up micro-gradients between the bulk of the pore-space and the local relative-humidity close to the pore liquid which will increase the rate of evaporation into the pore space. Moreover the Kelvin equation (Chapter 2), suggests that either (or both) a drop in relative-humidity and a rise in temperature will reduce the effective pore radius, ie., that radius that will just empty of capillary water when the particular combination of relative-humidity and temperature is reached. An increase in temperature will be associated with an increase in the desorption rate. This may be expressed as an increased diffusivity which may nearly double between 15 and 25 °C (see McGlone, 1990, his Figure 11).

Will the relative-humidity near the surface become decoupled from moisture content and hence from resistivity? There are three considerations:

1. What is the rate at which the moisture content and bulk-pore relative-humidity may come into equilibrium? It will take a relatively small mass of water to change relative-humidity, so that menisci may shrink back into the pores only slightly, increasing the absolute pore humidity enough to raise the relative-humidity to a level in equilibrium with the pore radius.
2. The measurement of relative-humidity close to the surface may be inherently inaccurate, since at the surface where the concrete is drier, the desorption rate is very low, and it may require a considerable period for the cavity around relative-humidity probe to come into equilibrium with the concrete.
3. With fluctuations in temperature it would be likely that relative-humidity inversions would occur, that is, a cooling of the surface may cause the relative-humidity to increase to the local dew point, condensing water on pore surfaces. The relative-humidity deeper down may be unchanged but now lower than the surface relative-humidity, so that movement of moisture may occur away from the surface to deeper levels. The hysteresis effect common to all micro-porous materials will then ensure that relative-humidity and moisture content become decoupled.

10.4.2 Extrapolation of relative-humidity profiles to the surface.

Given that the recovered relative-humidity near the surface will be inaccurate, some consideration is given in this section to use of other methods to improve knowledge of the

surface region. As we saw in Chapter 2, Parrott (1991) has derived empirical formulae relating RH at different depths (d in mm) from the surface of a slab in a constant ambient relative humidity (*Rha)*. This formula expresses the relative-humidity potential, in terms of a function of the drying time and the depth from the surface. The relative-humidity potential is

$$\frac{RH - RHa}{100 - RHa} = f(d,t).$$

where

$$f(d,t) = e^{-kT}$$

$$k = 0.8 - 0.14T + 0.01T^2$$

$$T = \frac{t}{t_{1/2}}$$

t = time in days

and, for Ordinary Portland Cement,

$$t_{1/2} = 10d, \text{ for d} < 41.4$$

$$= 3d + 290, \text{ for d} \geq 41.4$$

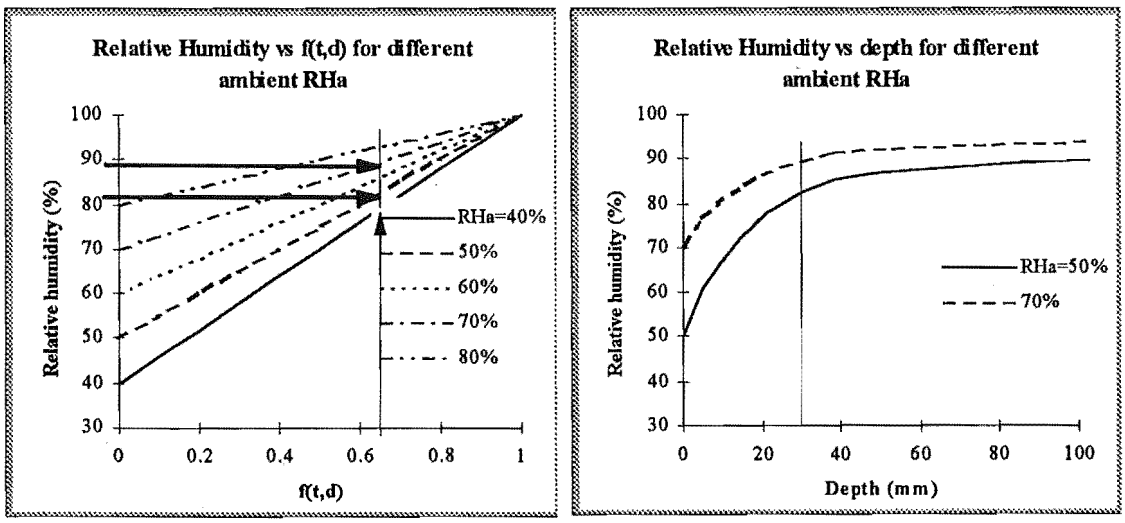

Figure 10.4-1 (Left) The arrow refers to the f(t,d) for t=180 days, and d=30mm, ie f(180 days, 30mm)=0.65. If the RH is determined to be 85+-3% say, then the RH at the surface (=RHa) could correspondingly lie between 50% and 70%. (Right) The boundaries of the range of possible relative-humidity profiles where at 180 days and 30 mm depth, the relative-humidity is determined to be 85% ± 3%. The 75% level is reached at depths of 4mm and 18mm when the ambient relative-humidities are 70% and 50% respectively

We may use Parrott's equation to investigate our ability to predict the shallow part of the profile given restricted information about the deeper part. Initially, consider the determination of the relative-humidity at 180 days and 30 mm depth in which case *f(180 days, 30 mm)=0.65*.

Using the VES instrument and the relative-humidity- resistivity calibration curves, the relative-humidity at 30 mm depth may have been determined to be 85% ± 3% say. If the relative-humidity potential is plotted against *f(d,t)*, it may be seen (left-hand graph of Figure 10.4-1) that relative-humidity curves passing through the range of relative-humidity (85% ± 3%) measured at *f(d=30 mm,t)* have surface relative-humidity between about 50% and 70%.

The ideal profiles corresponding to these are shown in the right hand graph of Figure 10.4-1. The same uncertainty associated with a point closer to the surface will more accurately define the range of profiles. A number of recovered data points could allow greater definition.

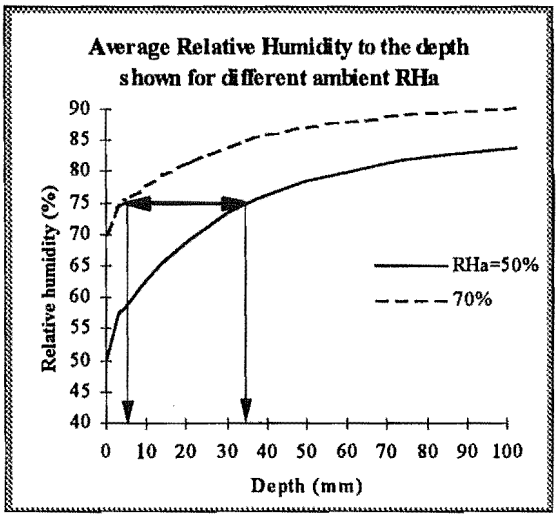

Figure 10.4-2: Mean relative-humidity as a function of the depth above which the humidity is averaged. This graph is explained in the text.

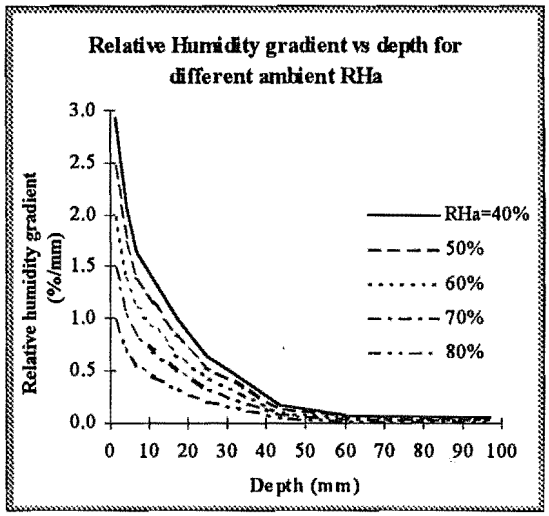

Figure 10.4-3: Relative-humidity gradient as a function of depth and ambient relative-humidity.

The two boundary profiles will represent substantially different total moisture contents, and in particular, different moisture contents near the surface. McGlone (1990) shows how one may integrate the profile to obtain an average relative-humidity for the entire slab. To

determine the total moisture content, reference must be made to the appropriate desorption curve.

The average relative-humidity to a depth D, is given by

$$RH_{ave} = \frac{1}{D}\int_0^D \psi\,(t,x)dx$$

where $\psi(t,x)$ is the relative-humidity at depth x after a drying time of t days. The average relative-humidity for the profiles above, are plotted in Figure 10.4-2.

The arrows indicate the depth at which an average of 75% relative-humidity is reached. At an ambient relative-humidity of 50%, this occurs at 35mm, whereas only the top 5 mm averages to 75% when the ambient relative-humidity is 70%.

Amongst the existing methods of determining whether a slab is dry enough for a surface coating to be applied, some require the measurement of the amount of moisture evaporated from the slab into a sealed space above the surface within a given time (see Chapter 2). They thus measure the rate at which water desorbs from the concrete although the moisture in the sealed space may be expressed in terms of the relative-humidity or of the desorption rate. These methods are not equivalent since the relative-humidity may quickly come to equilibrium within the cavity as long as the cavity is not too large. Where a hygroscopic material is used, the relative-humidity will remain low and the desorption rate will not change significantly over the time period. Other methods measure the resistivity or capacitance between two electrodes at or near the surface. The electrical measurement must be converted to a moisture content using predetermined calibration charts.

The accepted cutoff is generally 75% relative-humidity or 5% moisture content. (by weight of dry concrete) or a desorption rate of 0.13 kg water/ 24 hr/m^2. How do these criteria relate to relative-humidity profiles that may be obtained by the use of vertical electric sounding or embedded electrodes and resistivity- relative-humidity calibration curves? The sealed space methods depend on the desorption rate. This will be a function of the relative-humidity gradient within the slab (Figure 10.4-3) and across the slab-cavity interface, and the appropriate diffusion coefficients. Further work must be done in order to identify relative-humidity profiles which are acceptable for surface coatings of concrete slabs.

10.5 *Conclusion*

A method determination of relative-humidity-resistivity calibration curves has been described and illustrated in this chapter. The calibration curves may be determined using calibration data grouped by age or depth. Away from the surface regions (that is deeper than 10 to 15 mm) the calibration data appears to be fitted very well to equations of the form

$$\psi = -a\ln(\rho) + b$$

The coefficients a and b vary with age and depth. While there does seem to be systematic development of the coefficients as the concrete samples age, coefficients determined for data grouped by age and by depth, tend to be quite variable. Quite different coefficients seem to be associated with equivalent age or depths in other samples. While this may be because of the relatively large error associated with the measurement of relative-humidity profiles, such variation may be reduced by collating the data for different depths and ages and removing data points corresponding to shallow depths. Where this has been done, the agreement between calibration curves obtained from different samples shows marked improvement. So that if the resistivity at some point in the slab is known exactly and if the test concrete and the calibration cylinder have been cured under similar conditions, the expected uncertainty in derived relative-humidity could be as low as $\pm$2% RH.

It is unlikely that the test concrete slab will be cured under the same conditions as the concrete cylinders used to determine the calibration curves. In this scenario the uncertainty rises to $\pm$ 5% RH or more. In addition, in practice the resistivity measurement will have uncertainty associated with it so that the uncertainty in the relative-humidity at some point around 20 mm beneath the surface may be around 8% RH.

11. Conclusion: Results, feasibility and recommendations for future work

In this report the development of a top-surface mounted instrument to measure resistivity profiles in concrete has been described. The work has involved the concurrent development of an alternative and independent technique for measurement of resistivity profiles and a calibration method for the extraction of relative-humidity profiles from resistivity profiles. In this final chapter, I summarise the achievements of the project, review the feasibility of the techniques presented here in terms of the stated goals of the project and suggest directions for further research and development.

11.1 Results

11.1.1 Development of a top-surface-mounted instrument and technique for the measurement of relative-humidity profiles in concrete.

The instrument is designed to measure two-dimensional resistivity profiles which are subsequently transformed to relative-humidity profiles. The measure of the moisture state was chosen as the relative-humidity rather than moisture-content.

The technique borrows from established geophysical techniques *of vertical electric sounding* (VES), in which the apparent resistivity of the body under investigation is determined through the injection of current and measurement of voltage at the surface using a spreading four-probe array. The apparent resistivity data (visualised as a curve of apparent resistivity as a function of the current-probe spacing - the so-called VES curve) is then 'inverted' in the sense that a search is made using optimisation techniques for a two dimensional, layered, resistivity profile that under the same four-probe array, would yield a model VES curve that closely matches the measured VES curve. We also speak of the *recovery* of the profile from the VES curve.

The recovered layered- (or *stepped-*) model may then be converted to a continuous profile, that is, to a profile which changes continuously with depth as opposed to changing discontinuously at the boundaries of layers of uniform resistivity. The continuous profile ideally, is electrically *equivalent* to the layered model in the sense that it would yield a model VES curve that matches the measured VES curve as well as or better than that of the layered model. Techniques for doing this have not been developed fully at this stage.

Key features of the development of the instrumentation and software are reviewed here.

11.1.1.1 Development of 'wet' electrodes

This has enabled some of the problems associated with the dry and highly resistive surface of a drying concrete slab to be overcome. In particular, the electrode-concrete interface resistance is markedly reduced when a conducting solution (in our case a solution of Swarfega cleansing gel) is used to form an interface between the concrete and the electrode. The immediate decrease in contact resistance when wet-probes treated with conducting solution are placed on the concrete and the relative stability of the apparent resistivity curves measured almost immediately suggests that the any diffusion of moisture into the concrete does not significantly lessen the validity of the approximations to point- and surface-located electrodes that the vertical electric sounding theory assumes. This is supported by finite-difference modelling of wet-probes on concrete slabs.

11.1.1.2 Determination of an optimal array configuration.

Indications of possible horizontal spread of the moisture from the electrodes and consequent interference between measurements made using adjacent electrodes has led to the restriction of the minimum distance between adjacent electrodes to 20 mm centre-to centre. This restriction has further implications for the closest measurement-probe spacings b and current- probe spacings s (minimum b is 10 mm and minimum s is 50 mm) and for the range of current probe spacings (the next largest s must be at least 70 mm for example).
The use of 8 current probe spacings (yielding 8 data points in the VES curve) seems to be adequate, as does the present array configuration (see Chapter 6).

11.1.1.3 A method of overcoming the data scatter inherent in measurement of apparent resistivity on a highly inhomogeneous material.

The restrictions on s and b act to limit the ability of the instrument to resolve the apparent resistivity at small spacings. However, as we have seen, the scale of the inhomogeneity of concrete with a maximum aggregate size of 19 mm imposes at least as a severe handicap, so that at the smallest s and b, the scatter or imprecision of measurements of potential difference and indeed of the effective measurement probe spacing, is only barely acceptable.
A method of averaging and combining many apparent resistivity curves taken with two measurement probe spacings, and at different positions on the concrete has been described in Chapter 6. This enables considerable data scatter to be removed, and enables the most

accurate features of curves taken using different b to be used whilst rejecting those most affected by inherent limitations of vertical electric sounding on concrete.

11.1.1.4 Design of a method and device used to position 'wet' electrodes on the concrete.

An *array board* has been designed and constructed. This is a device that holds the wet electrodes in position on the concrete. The design allows for

1. quick insertion and removal of the wet probes,
2. easy repositioning of the electrode array at different locations on the concrete slab so that a series of vertical electric soundings may be taken during a single session,
3. efficient recharging of the set of electrodes with conducting solution by placing the array board in a specially designed reservoir,
4. choice of a variety of array configurations which may be selected by insertion of the wet probes into housings at different spacings (these must then be rewired which is slightly more time consuming: this option is unlikely to be used since the optimal configuration has been determined in this paper),
5. simultaneous measurement of two sets of two apparent resistivity curves, each set comprising one curve taken with a measurement probe spacing b = 10 mm and one with b = 30 mm and
6. efficient wiring of the array board to the resistivity meter using multi-pin plugs.

11.1.1.5 Design and development of a computer controlled resistivity meter.

This integrated unit comprises

1. a variable frequency square-wave constant current generator (with a range of 'constant current' settings,
2. a sensitive multiple gain (16 ranges) voltage measuring circuit. The sensitivity of the instrument may need to be improved further. At present, the resistivity of dry concrete is such that the current able to be injected at the wider current-probe spacings is insufficient to generate large enough voltages between the measurement electrodes to enable accurate voltage measurement.
3. a data acquisition and control unit,
4. demultiplexing of the current drive to 16 pairs of current-probes,

5. multiplexing of the voltage measurement circuit from 16 pairs of measurement electrodes, (*this flexibility was useful for research purposes but is not necessary in a commercial instrument*)
6. a graphical user interface used to control and acquire data from the resistivity meter allowing (automatic or manual) control over
   a) the current drive frequency,
   b) the voltage at the current drive,
   c) the constant current level,
   d) the gain of the voltage measurement stage and
   e) the multiplexer units associated with the current generating and voltage measuring stages.
7. In addition the graphical user interface allows the meter to be set up to take a full set of apparent resistivity curves from the present array position. In which case the meter will
   a) automatically adjust the constant current level and the voltage measurement gain to maximise the signal-to-noise ratio whilst preventing saturation of the gain amplifiers,
   b) determine the optimal number of cycles sampled by the meter at each current probe spacing so as to maximise the precision of the measurement and minimise the time needed,
   c) take any number of sets of apparent resistivity curves at the present array board position should the interest be in the development of apparent resistivity curves over a period of time
   d) automatically calculate and display the apparent resistivity for the particular array configuration and save all current, voltage, resistance, apparent resistivity and time data at the end of each set of readings in a form suitable for further analysis.

11.1.1.6 Inversion (profile recovery) software for use in vertical electric sounding on drying concrete slabs

The inversion software (described in Chapter 5) and its ability to recover resistivity profiles from the experimental VES curves has been illustrated and discussed in Chapter 7. The ability of the sounding software to recover useful profiles depends in the first place on the

amount of scatter and noise in the vertical electric sounding data. The final form of the instrument and the technique was remarkable in its ability to record apparent resistivity curves which were well formed and comparatively free of data scatter. Earlier models and techniques yielded VES curves suffering from data scatter to the extent that they were often unusable.

Consequently, only Slab #8 has a full set of good VES curves following its development from the time of pouring. The older slabs have these 'good' curves for later stages of their development only. These curves show good form in the sense that they resemble closely theoretical curves based on predicted and measured resistivity profiles. However, the recovered profiles from slabs #6, #7 and #8 generally show good agreement with profiles directly measured using the horizontal electrode systems (HES).

The technique and instrument have been proved inadequate to the task of measuring resistivity (and hence relative-humidity) profiles in reinforced slabs. Modelling studies suggest that while the measurement of VES curves for reinforced slabs takes the vertical electric sounding instrument to the limit of its resolution, even an accurate and noise-free VES curve may not contain sufficient information about the profile beneath the reinforcing layer for the profile to be recovered even in principle. This is because the reinforcing layer acts to screen the influence of the deeper regions on the apparent resistivity curve.

11.1.2 Development of methods for the direct measurement of resistivity profiles using embedded horizontal electrode systems.

A direct method of measurement of resistivity profiles was required because independently measured resistivity profiles were needed to:

1. assess the validity and accuracy of resistivity profiles recovered using vertical electric sounding and to
2. empirically determine resistivity- relative-humidity relationships for specific concrete mixes and curing histories.

Consequently several embedded horizontal electrode systems (HES) were designed and tested (Chapter 8). These systems were able to be used for measuring resistivity once they had been calibrated to convert from the resistance measured using two or four electrodes to an average resistivity associated with a certain depth of view. It has been found that calibration of the electrode system was best carried out in-situ, that is, with the electrode system embedded in the concrete as opposed to calibrating the system in a conducting

solution. This means that each electrode system is calibrated individually, the calibration taking account of the particular distribution of aggregate in the concrete sample. The calibration is carried out within a week of pouring and before a resistivity gradient has time to develop. There is less variation in the calibration constants between electrode systems of the same type and embedded in the same or similar samples, if at the time of calibration the concrete is older and has been cured under conditions of high relative-humidity for longer.

Several embedded electrode systems were trialed and three horizontal electrodes systems (HES) in particular, labelled HES#1, HES#2 and HES#3 (see Chapter 8), were used to obtain resistivity profiles with high precision, especially in the deeper regions of the concrete samples.

While the bulk of resistivity profiles obtained using the embedded electrode systems involved two-electrode resistance measurements using the same vertical electric sounding resistivity meter, it is likely that greater accuracy and precision would be obtained using four-probe resistance measurements with the resistivity meter set at a higher frequency (around 100 Hz). The two electrode measurements made using HES#2 and #3 do allow a high resolution near the surface nevertheless, which is more difficult to obtain using four electrode measurements.

Embedded electrode systems suffer from some of the same problems as the vertical electric sounding method – ie. problems associated with the highly inhomogeneous nature of concrete. However, these are more easily dealt with and overall, the use of embedded electrode systems (and of HES in particular) presents a relatively simple and efficient solution to the problem of measuring resistivity profiles.

11.1.3 Development of techniques for the determination (or calibration) of the relative-humidity-resistivity relationship

A technique for the determination of the relative-humidity-resistivity relationship has been developed. This involves the use of '*calibration*' cylinders, to determine efficiently, the relative-humidity-resistivity relationship for any particular concrete specification and curing regime.

1. Each calibration cylinder has ten housings, or sealed entry points into the concrete at specific depths below the exposed surface. Suitable relative-humidity probes may be inserted into these housings to measure the relative-humidity profile of the concrete.

2. Each calibration cylinder has an embedded *horizontal electrode system* (HES) with which resistivity profiles may be measured at the same time as the measurement of relative-humidity profiles.
3. The HES and the depths of relative-humidity housings may be selected so that data points are more closely spaced (relative to depth below the surface) nearer the surface where the resistivity and relative-humidity are changing faster.
4. Using depth as the common parameter relative-humidity-resistivity calibration curves may be determined for the concrete sample. These curves vary with time and depth as well as being a function of the concrete mix and curing regime.

11.1.4 Determination of the relative-humidity-resistivity relationship for specific concrete samples

Resistivity ρ and relative-humidity ψ profiles have been measured using a range of concrete samples and the relationship between them, away from the dry surface region, has been found to be described by the '*calibration equation*' $\psi = -a\ln(\rho) + b$ where a and b are coefficients that are functions of depth and the age of the concrete.

Problems associated with the measurement of relative-humidity meant that the accuracy of the relative-humidity profiles was compromised, resulting in an associated uncertainty in relative-humidity-resistivity calibration curves. Nevertheless there is enough agreement between the calibration curves determined from equivalent concrete samples (that is, samples poured from the same or similar mix and cured under similar conditions), to suggest that the calibration equation is a good description of the relationship between resistivity and relative-humidity both at certain depths over a period of time and at certain ages over a wide depth range.

It is noteworthy that the relative-humidity-resistivity calibration equation coefficients are functions of concrete-age and of depth within the concrete. It is suggested that this derives from the uneven development of pore structure. As hydration continues, pores become smaller and continuous paths within the cement paste become constricted and blocked. The size of pores, indeed the pore-size-distribution, is thus largely a function of the degree of hydration.

Conduction of current which is largely dependent on ionic transport through pore solution is strongly related to the moisture content of the pores. This will in turn depend on the pore-

size-distribution and the relative-humidity in a manner described by the Kelvin equation (see Chapter 2) in which the local relative-humidity at which condensation of moisture occurs in a pore, is a function of the effective pore radius.

Hydration largely ceases when the local relative-humidity falls below 80%. The pore-size-distribution will then no longer change. In a concrete slab drying from the top surface only, the surface regions will dry before those deeper down so that the pore-size-distribution nearer the surface will be fixed in a relatively immature state compared to the wetter deeper regions where hydration will continue for longer. Thus the porosity will be greater and the pore-size-distribution will favour larger pores at shallower depths allowed to dry out faster.

As a result a given relative-humidity will be associated with higher moisture saturation at deeper levels (where the pore-size-distribution favours smaller pores which are full at low relative-humidity), than at shallower levels (where the larger pores will tend to be empty of adsorbed moisture).

It follows from this that the resistivity at a given relative-humidity will be higher if the concrete is in a more immature state (that is, where the concrete is younger, or where hydration has ceased at an early age). The calibration equation describing the relationship between resistivity and relative-humidity will thus be largely a function of the maturity of the concrete as it is expressed in the pore-size-distribution. It is quite apparent in comparisons of resistivity profiles measured on concrete samples cured at different times that concrete that is cured under conditions of high relative-humidity and for longer, the gradient of resistivity near the surface is far less steep than that cured under drier conditions.

Because concrete of lower w/c ratio has a pore-size-distribution which also favours smaller pores, it was expected that the trend in the calibration coefficients as the w/c ratio reduces would be similar to the trends seen as concrete aged. There is some evidence for this but further support must await future research.

11.2 Feasibility

It was intended that the instrument and technique would be brought to a point where the feasibility of commercialisation could be considered. That point has not been reached in the sense that the instrument is not ready for commercialisation. It is likely, however, that the instrument will not be able to resolve resistivity profiles in the presence of reinforcing, so that it would find no application in commercial and practical situations (see Section 11.2.2

below) and may therefore be restricted to research applications. Nevertheless future prospects may be considered and to this end the characteristics of the instrument and technique and recommendations for further work are summarised here.

11.2.1 A top-surface-mounted instrument for the measurement of relative-humidity profiles in concrete

We have seen that vertical electric sounding techniques for measuring resistivity profiles in concrete slabs have been developed with reasonable success. Problems associated with the highly resistive surface layers and with potentially high and unequal electrode concrete interface resistance have been largely overcome through the use of so called wet probes, appropriate electrode spacings and through judicious averaging and collation of VES curves measured with at least two different measurement probe spacings. A vertical electric sounding instrument has been developed which has built in a high degree of flexibility of selection of current and measurement probes. The same basic design may be easily adapted to allow for measurement of a larger number of apparent resistivity curves simultaneously. In fact the present flexibility of the meter which allows (nearly) independent selection of 32 current-probes and 32 measurement probes, could easily be adapted to allow 8 sets of two apparent resistivity curves, once again each set comprising one curve taken with a measurement probe spacing $b = 10$ mm and one with $b = 30$ mm. This would allow 16 curves to be taken at one session but would require 160 separate electrodes. There will always be a trade off between the amount of data able to be taken automatically and the complexity of the instrument, however the ability to measure 16 VES curves in one location could remove the need to move the array to other locations and considerably increase the speed and ease with which soundings may be taken.

The use of an additional measurement probe spacing (say at $b = 50$ mm) would enhance the measurement of apparent resistivity at large current-probe spacings s. This would also enable a more precise fix on the vertical position of the VES curves on a apparent resistivity versus current probe spacing graph which is more uncertain for smaller b. This would allow a more accurate determination of the resistivity of deeper regions of the slab and allow better determination of a cutoff resistivity indicating whether or not, the slab is too wet for a surface coating to be applied.

At present the recovered resistivity profiles are in stepped form which is an approximation to the locally averaged continuous resistivity profile which is assumed to be associated with

one dimensional drying, and which is in fact measured using the embedded electrode systems. A scheme for transforming from a stepped to continuous profile has been discussed. Inversion techniques that recover continuous rather than layered profiles would be very useful.

The ability to obtain accurate relative-humidity profiles by transforming from (or calibrating) resistivity profiles will depend on the accuracy with which the continuous profiles are obtained, the accuracy with which the relative-humidity-resistivity calibration curves have been measured and the degree to which the calibration curves actually represent the relationship holding in the particular concrete under investigation.

11.2.2 Profile recovery in the presence of reinforcing.

The inherent difficulties presented to the problem of profile recovery, by the presence of reinforcing in the slab have been outlined. The screening effect of the reinforcement make it unlikely that the profile below the level of reinforcing can be recovered. At present the recovery of that part of the profile above the reinforcement has not been successful. Indeed the top 20 mm of the concrete has presented most difficulties in measurement of resistivity and relative-humidity. Certainly the precision is worst in this region.

Prospects for recovery of profiles in the presence of reinforcing using the vertical electric sounding method do not look good. This clearly puts a shadow over the likelihood that the technique and instrument will be commercially feasible given that most flooring slabs are reinforced in some way. The use of the instrument will then be confined to non-reinforced slabs and therefore to research purposes.

It is likely however, that the instrument and technique may find some application in the measurement of moisture-content profiles in timber slabs or other relatively homogeneous materials. The dimensions are smaller, the boundary effects may be greater and suitable electrodes capable of making good electrical content with the surface of the timber must be developed, but it should not be too difficult to adapt the technology developed so far. Many of the principles and lessons learned in the application of vertical electric sounding to concrete slabs will be useful in making a further transition to drying timber.

11.2.3 The use of embedded electrode systems

Embedded electrode systems were developed as an independent method of measuring resistivity profiles. They do not fit the specifications of the original intentions of this project

since they must be fixed into the concrete form work before the concrete is poured and. care must be taken when finishing the concrete around them since (at present) they must present a brass plate flush with the surface. However the failure of the vertical electric sounding technique to recover profiles in the presence of reinforcing and the precision of the horizontal electrode systems (HES) described in this report make them prime candidates for further development and eventual commercialisation. They may be built very cheaply and under mass production costs would reduce further. Given their low cost, several could be placed at strategic positions in a floor which may be subject to several different drying conditions depending on proximity to doors and windows and unfinished roofing for example. The low cost may easily make them a standard item to be used when pouring concrete floors so that the need for a removable top-surface mounted instrument will be removed.

Embedded electrode systems may find further use in walls and concrete cladding where the possibility of reinforcement corrosion may necessitate a resistivity survey at some time in the future.

The three designs of horizontal electrode systems described in this report may be improved upon. The ability to recover resistivity at depths less than 20 mm with greater precision is one area where a little further work could bring great improvement. It is likely that adaptation of the HES#1 or HES#2 to allow more use of four-electrode measurements will reduce the electrode polarization effects which have increased data scatter at shallow depths. The ability of HES#2 and HES#3 to resolve the near surface profile is likely to be of great importance since present methods of determining slab dryness are very much surface based and it may be useful to determine the characteristics of resistivity or relative-humidity profiles which correlate with the existing standards (see Chapter 1).

A resistivity meter of a little less complexity could be designed to read the embedded electrode system, although the use of a laptop or similar computer would seem mandatory in view of their flexibility and sharply decreasing cost.

11.2.4 The technique for calibration of the relationship between resistivity and relative-humidity

The relative-humidity-resistivity calibration technique developed here will be of as much use no matter which system (HES or VES) for measuring resistivity is chosen. The technique is straight forward and allows use of a range of horizontal electrode systems. The cylinders are

relatively cheap and portable and if necessary could be poured at the same time as the floor in larger jobs if there does happen to be doubt over whether established calibration data applies.

11.3 Suggestions for further research and development

11.3.1 The vertical electric sounding technique

Should the vertical electric sounding technique have application in the present field of concrete flooring slabs, in research or in other areas of the building industry, some thought should be given to the profile recovery software, which, although working well, can be improved vastly. Indeed serious consideration could be given to using a new scheme entirely which would fit coefficients of a continuous function rather than a layered profile to the VES curve. The determination of the form of such a function will depend, at least in part, on those features of the resistivity profile or relative-humidity curve deemed to be most important in deciding whether or not a slab is dry enough to have a surface coating applied. Fitting of the function may then tend to ignore non-salient features of the VES curve in the same way that enforcing the falling profile constraint on the inversion process forces the program to 'filter' at least some of the data scatter. Fitting such a function will also obviate the need to convert the stepped profile to a continuous profile which is governed by the same goals.

Alternatively existing schemes for inversion of continuous data could be adapted to the present use.

11.3.2 Embedded electrode systems

Further work could be done in determining ***optimal HES design*** and development of a dedicated resistivity meter to read the system. It is likely that the simplicity and resolution of two-electrode resistance measurements will prove the adequacy of the design of any one of HES#1, HES#2 or HES#3. However an understanding of just what features of a resistivity or relative-humidity profile are most relevant to slab dryness in terms of surface coatings (see next section) must precede determination of optimal HES design. If the near surface regions should be resolved well, then HES#2 or HES#3 will prove more useful. On the other hand should the uncertainty in measurement at shallow depths be unacceptable, four-probe resistance measurements may be necessary since these would decrease the variability

associated with electrode polarization. HES#1 is suited for four-probe resistivity measurement but at the expense of near surface resolution. If both are required further design of the horizontal electrode systems will be necessary.

The relationship between the time at which embedded electrode systems are calibrated and the accuracy or precision of measurement has been discussed in this report. In Chapter 8, it was suggested that the variability in the calibration constants (for transforming between the resistance measurements made using two or four of the embedded electrodes and the local resistivity) is due not only to the variation in aggregate distribution around otherwise equivalent electrodes, but, may also be a function of the age of the concrete when the electrode system is calibrated and of the period over which the concrete had been cured under conditions of high relative-humidity. The last two factors may really be aspects of one: the degree of hydration of the sample at the time of calibration. It is not clear at present how hydration affects the calibration constants however it may be very important to determine the optimal calibration time and the extent to which variations in both calibration time and curing conditions affect the calibration constants and hence the measured resistivity.

The question of to what extent variation in calibration constants owing to variation in age or maturity at calibration results in variation in measured resistivity is also worthy of investigation. If horizontal electrode systems were to be of commercial value, the more variation in curing conditions and age at calibration permitted, the better since there will be highly diverse conditions in the field.

11.3.3 Comparing existing methods of determination of slab dryness (as outlined in Chapter 1) and relative-humidity and resistivity profiles

Within the building industry at present, non-destructive methods of determination of slab dryness (see Chapter 1) are based on measurements made at or near the surface. The use of an embedded electrode system to determine slab dryness will entail either correlation of the resistivity or relative-humidity profiles with the moisture state as determined by existing methods, or a new assessment scheme which makes full use of the detailed profiles available using embedded electrode systems and relative-humidity-resistivity calibration curves. In either case the relative-humidity-resistivity calibration-cylinders described in this report will have immediate application.

11.3.4 Relative-humidity-resistivity calibration

If the use of embedded electrode systems as a method of determining slab dryness is pursued, then further research into the relative-humidity-resistivity relationship should be undertaken, and a body of relative-humidity-resistivity calibration data for concrete cured under a range of conditions, should be built up.

Ideally, calibration equations which are valid for a wide range of curing conditions should be identified. The more precise the calibration equation coefficients are required to be, the more specifically will they be related to certain curing conditions. Where the job warrants it calibration equations could be determined on site. However, their use will depend on knowing just what resistivity or relative-humidity profile characteristics are of relevance to the failure or otherwise of surface coatings on the concrete flooring slabs of interest.

12. Nomenclature

Greek symbol	*meaning*	*typical matlab variable name*	*reference*
α	temperature coefficient		*Ch. 3*
β	damping factor on Marquardt-Levenberg type least-squares inversion		*Ch 5, Appendix A*
γ	surface tension of pore solution		*Ch. 2*
ε	permittivity		*Ch. 3*
ϕ	angle of contact between pore solution and pore wall		*Ch. 2*
φ	porosity		*Ch. 2,3*
λ	variable of integration	*lam*	*Ch. 5*
θ	temperature		
ρ	resistivity	ro	*General*
ρ_a	apparent resistivity		*Ch. 5,6,7*
ρ_{ac}	apparent resistivity calculated from layer model parameters	roac	*Ch. 5,6,7*
ρ_{af}	apparent resistivity measured in field (experimental)	roaf	*Ch. 5,6,7*
ρ_{as}	Sclumberger apparent resistivity	roaf	*Ch. 5,6,7*
ψ, ψ_a	relative humidity (RH), ambient RH	rh	*General*

symbol	*meaning*	*typical matlab variable name*	*reference*
a	coefficient of calibration equation		*Ch. 3, 10*
A	area		
A (as matrix)	Jacobian matrix of partial differentials of the apparent resistivity with respect to the layer parameters of a resistivity profile	*a*	*Ch. 5, Appendix B*
A,B,M,N	common labels for current probes (A and B), and measurement probes (M and N), and subscripts for associated concrete-electrode interface resistance		*General*
AM, AN etc.	distance between electrodes *A* and *M* or *A* and *N* etc.		*Ch. 5*
a/c	aggregate- cement ratio {kg(agg.)/kg (cement)}		*Ch. 2*
b	measurement probe spacing = MN/2	*b*	*General*
b	coefficient of calibration equation	*b*	*Ch. 3, 10*
C_2S	dicalcium silicate		*Ch. 2*
C_3A	tricalcium aluminate		*Ch. 2*
C_3S	tricalcium silicate		*Ch. 2*
C_4AF	tricalcium aluminoferrite		*Ch. 2*
CSH, C-S-H	calcium-silicate hydrate		*Ch. 2*
d	depth to base of a layer in a resistivity profile	*d*	*General*

symbol	*meaning*	*typical matlab variable name*	*reference*
ΔV	potential difference	*delv*	*Ch. 3, 5, 6*
e_M	voltage at M electrode		*Ch. 6*
e_{CM}	common-mode voltage		*Ch. 6*
Δe	differential voltage		*Ch. 6*
e_s	error signal developed at input to instrumental amplifier		*Ch. 6*
F	Fourier transform of the resistivity transform		*Ch. 5*
f	frequency	*freq*	*Ch. 3, 5, 6*
FPC	falling profile constraint		*Ch. 5,7*
g	gain of instrumentation amplifier		*Ch. 6*
G	four-electrode-array geometric factor	*gfact*	*Ch. 5, Appendix B*
G	Fourier transform of apparent resistivity curve in the frequency domain		*Ch 5*
h	thickness of a layer in a one-dimensional resistivity profile	*h*	*General*
H	resistivity filter characteristic		*Ch. 5*
HES	horizontal electrode system		*General*
I, i	current	*curr*	*General*
J_o, J_1,	Bessel functions of the first kind, zeroth and first order respectively		*Ch. 5*
k	calibration constant for converting resistance measurements to resistivity		*Ch. 3, 8*
l	length		*Ch. 3, 8*
m, n, q	shape factors in modified Archie's law type equations		*Ch. 3*
OPC	ordinary portland cement		*Ch. 2.*
p, p_0	partial vapour pressure, saturated partial vapour pressure		*Ch. 2.*
PPES	parallel plate electrode system		*Ch.4, 8*
r	distance from point current source		*Ch.5*
r	radius of curvature of ideal pore		*Ch. 2*
R	gas constant		*Ch. 2*
R	resistance	*res*	*General*
R20	resistance measured between two adjacent electrodes in the HES#1		*Ch. 8*
R21	resistance measured between two electrodes in the HES#1, separated by one (electrically floating) electrode. Similarly for R22, R23		*Ch. 8*
R42	resistance measured using four adjacent electrodes in the HES#1		*Ch. 8*
R_A	concrete-electrode interface resistance at probe driven by cuurent drive A (etc)	*res*	*Ch. 5, 6*
RH	relative humidity		*General*
RH_a	ambient relative humidity		*Ch. 2, 9, 10*
roac	apparent resistivity calculated from a one-dimensional resistivity profilemodel	*roac*	*Ch 5*
roaf	field or measured resistivity	*roaf*	*Ch. 5*

symbol	*meaning*	*typical matlab variable name*	*reference*
RMS	measure of poorness of fit between two sets of data, typically between ρ_{af} and ρ_{ac} (see above)		*General*
s	pore saturation		*Ch. 3*
s	current probe spacing = AB/2	*s*	*general*
t	time,		*general*
t	thickness of moisture film adsorbed onto pore surfaces		*Ch. 2*
T	resistivity transform	*t*	*Ch. 5*
T	temperature		*Ch. 2, 3, 9*
V	Volume		*General*
V	voltage		*Ch. 3, 5, 6, 8*
VES	vertical electric sounding		*General*
w/c	water- cement ratio {kg (H_2o)/kg (cement)}		*General*
Δx	uncertainty in effective position of electrode		*Ch. 6*
x_c	distance of center of VES electrode array to the perpendicular non conducting boundary		*Ch. 5*
y_c	distance of center of VES electrode array to the parallel non conducting boundary		*Ch. 5*
w	moisture content {kg (H_2o)/kg (concrete)}		*General*
w_c	critical moisture content, non-evaporable moisture content moisture content at equilibrium {kg (H_2o)/kg (concrete)}		*Ch. 3*
w_o	moisture content when pores are fully saturated {kg (H_2o)/kg (concrete)}		*Ch. 3*
w^*	characteristic moisture content		*Ch. 3*
Z_{CM}	common-mode impedance of instrumentation amplifier		*Ch. 6*

13. REFERENCES

Anderson, W.L. (1975) Improved digital filters for evaluating Fourier and Hankel transform integrals. Report No. USGS-GD-75-012, US Geological Survey, Denver, Colorado.

Archie, G.E. (1942) The electrical resistivity log as an aid in determining some reservoir characteristics. Transactions of the American Institute of Mining and Metallurgical Engineers, vol 146: 54-62.

Arfken, G. (1985) Mathematical Methods For Physicists .Third Edition, Academic Press, London.

Basokur, A.T.(1990) Microcomputer program for the direct interpretation of resistivity sounding data. Computers and Geosciences vol 14(4): 587-601.

Berg, A., Niklasson, G. A., Hedberg, H. and Nilsson, L.O. (1992). Dielectric Properties as a Function of Water content. Journal of Applied Physics. Vol 71(12) 5897-5903.

Bhargava, J. and Lundberg, K. (1972) Determination of the moisture content of concrete by microwave-resonance method. Materiaux et Constructions, vol5(27): 165-168.

Bibby, H. M. and Fisk, G.F. (1988) Correction for finite distance between potential electrodes in Schlumberger resistivity soundings: Proceedings 10th New Zealand Geothermal Workshop, Auckland. University of Auckland Press, NewZealand, 133-138.

Brantervik, K. and Niklasson, G. A. (1991) Circuit models for cement based materials obtained from impedance spectroscopy. Cement and Concrete Research, vol 21: 496-508.

Camp, P. R. and Bilotta, S. (1989) Dielectric properties of cement paste as a function of time since mixing. Journal of Applied Physics vol 66: 6007-6013.

Chatterji, S. and Kawamura, M. (1992) Electrical double layer, ion transport and reactions in hardened cement paste. Cement and Concrete Research, vol 22: 774-782.

Considine, D. M. (Ed.) (1983) Von Nostrands Scientific Encyclopaedia, Von Nostrand, New York.

Czernin, W. (1980) Cement Chemistry and Physics For Engineers. Crosby Lockwood and Son LTD, London.

Das, U.C. and Ghosh, D.P. (1974) The determination of filter coefficients for the computation of standard curves for dipole resistivity sounding. Geophysical Prospecting, vol 22: 765-780.

Depperman, K. (1973) An Interpretation System for Geo-electrical sounding graphs, Geophysical Prospecting. vol 21: 424-463.

Double, D.D. (1983) New developments in understanding the chemistry of cement hydration. Philosophical Transactions of the Royal Society, London, A, vol 310: 53-66.

Ewins, A.J. (1985) A Resistivity Meter. UK PatentApplication 2156084A.

Ewins, A.J. (1990) Resistivity measurements in concrete. British Journal of Nondestructive Testing, vol32(3): 120-126.

Gardiol, F.E. (1984) Introduction to Microwaves. Artech House, Dedham, Mass., U.S.A.

Ghosh, D.P. (1971) The Application of Linear Filter Theory to the Direct Interpretation of Geoelectrical Resistivity Sounding measurements. Geophysical Prospecting, vol 19: 192-217.

Gregg, S. J. and Sing, K. S. S. (1967) Adsorption, surface area and porosity. Academic Press, London,

Gu, P., Xie, P., Beaudoin, J. J. and Brousseau, R. (1992) A.C. Impedance spectroscopy (I): a new equivalent circuit model for hydrated Portland cement paste. Cement and Concrete Research, vol 22: 833-840.

Guptasarma, D. (1982) Optimization of Short Digital Linear Filters for Increased Accuracy. Geophysical Prospecting, vol 30: 501-514.

Hamming, R. W. (1989) Digital Filters (3rd Edition), Prentice Hall, Englewood Cliffs, N.J.

Harriman, L. (1995b) Drying and Measuring Moisture in Concrete — Part II. Materials Performance, Februrary: 55-59.

Hashida, H., Tanaka, K. and Koike, M. (1990) Moisture distribution in concrete before and after application of the finish. Building Research and Practice, No.5: 303-308.

Hedenblad, G. (1993) Moisture Permeability of Mature Concrete, Cement Mortar and Cement Paste. Lund Institute of Technology, Lund.

Hedenblad, G. and Nilsson L.-O. (1985) Degree of Capillary Saturation: a tool for better evaluation of the moisture content in concrete. Report TVBM-7005, Division of Building Materials, Lund Institute of Technology, Sweden.

Hughes, B.P., Soleit, A.K.O. and Brierly, R.W. (1985) New technique for determining the electrical resistivity of concrete. Magazine of Concrete Research,Vol 37(133),

Johansen, H.K. (1975) An interactive computer/graphic-display-terminal system for interpretation of resistivity soundings. Geophysical Prospecting, vol 23: 449-458.

Keey, R.B. (1972) Drying Principles and Practice. Pergamon Press, Oxford.

Keey, R.B. (1992) Drying of Loose and Particulate Materials. Hemispere Publishing Corp., N.Y., U.S.A.

Koefoed, O. (1972) A note on the linear filter method of interpreting resistivity sounding data. Geophysical Prospecting, vol 20: 476-489.

Koefoed, O. (1976) Progress in the direct interpretation of resistivity soundings: an algorithm. Geophysical Prospecting, vol 24: 233-240.

Koefoed, O. (1979) Geosounding Principles. Elsevier, Amsterdam.

Koon, D. W. and Knickerbocker, C. J. (1992) What do you measure when you measure resistivity ? Review of Scientific Instruments, vol 63(1): 207-210.

Krazewski, A. W. (1991) Microwave aquametry - needs and perspectives. IEEE Transactions: Microwave Theory and Techniques, vol 39(5).

Lines, L. R. and Treitel, S. (1984) Tutorial: a review of least-squares inversion and its application to geophysical problems. Geophysical Prospecting, vol 32: 159-186.

Lopez, W. and Gonzalez, J. A. (1993) Influence of the degree of pore saturation on the resistivity of concrete and the corrosion rate of steel reinforcement. Cement and Concrete Research, vol 23: 368-376.

Marquardt, D.W. (1963) An algorithm for least-squares estimation of non-linear parameters. Journal of the Society for Industrial Applications of Mathematics, vol 11: 431-441.

Marsden, D. (1973) The automatic fitting of a resistivity sounding by a geometrical progression of depths. Geophysical Prospecting, vol 21: 266-280.

Marsland, T.P. and Evans, S. (1987) Dielectric measurements with an open-ended coaxial probe. IEE Proceedings, vol 134.(H40): 341-349.

McCarter, W.J. (1987) Gel Formation During Early Hydration. Cement and Concrete Research, vol 17: 55-64.

McCarter, W.J. (1991) Discussion on paper 9674: Reinforced concrete resistivity measurement techniques. . Proceedings: Institute of Civil Engineers, Part 2, vol 91: 895-896.

McCarter, W.J. and Barclay, S., (1993) A comparison of two methods for resistivity measurement on repair mortar for cathodic protection systems. Cement and Concrete Research, vol 23: 1178-1184.

McCarter, W.J. and Garvin, S. (1989) Dependence of electrical impedance of cement-based materials on their moisture condition. Journal of Physics D:Applied Physics vol 22: 1773-1776.

McCarter, W.J., Emerson, M. and Ezirim, H. (1995) Properties of concrete in the cover zone: developments in monitoring techniques. Magazine of Concrete Research, vol 47(720): 245-251.

McGlone, V.A. (1990) Drying rates of concrete floors. Unpublished BRANZ internal report, August 1990.

Merrick, N.P. (1977) A computer program for the inversion of Schlumberger sounding curves in the apparent resistivity domain. Hydrological report 1977/5,Water Resources Commission, N.S.W.

Millard, S.G. (1991a) Reinforced concrete resistivity measurement techniques. Proceedings: Institute of Civil Engineers, Part 2, vol 91: 71-88.

Millard, S. G. (1991b) Discussion on paper 9674: Reinforced concrete resistivity measurement techniques. . Proceedings: Institute of Civil Engineers, Part 2, vol 91: 896-898.

Millard, S. G., Harrison, J. A. and Edwards, A.J. (1989) Measurement of the electrical resistivity of reinforced concrete structures for the assessment of corrosion risk. British Journal of Non-Destructive Testing, vol 31 (11): 617-621.

Mindess, S. and Young, J.F. (1981) Concrete. Prentice-Hall, Englewood Cliffs, N.J.

Molina, L. (1990) Measurement of high humidity in cementitious material at an early age. CBI Report, Stockholm.

Neville, A.M. (1981) Properties of Concrete. 3rd. edition, Pitman, London.

Neville, A.M. and Brooks, J.J. (1987) Concrete Technology. Longman, Singapore.

Nilsson, L.-O. (1977) Moisture Problems at Concrete Floors. Report TVBM-3002, Division of Building Materials, Lund Institute of Technology, Sweden.

Niwas, S. and Israil, M. (1987) A simple method of interpretation of resistivity sounding data using exponential approximation of the kernel function. Geophysical Prospecting, vol 35: 548-567.

O'Neill, D.J. (1975) Improved Linear Filter Coefficients for Application in Apparent Resistivity Computations. Bulletin of the Australian Society of Exploration Geophysics, vol 6(4) December, 104-109.

O'Neill, D.J. and Merrick, N.P. (1984) A digital linear filter for resistivity sounding with a generalized electrode array. Geophysical Prospecting, vol 32: 105-123.

Otto, G.P. and Chew, W.C. (1991) Improved Calibration of a Large open-Ended Coaxial Probe for Dielectric Measurements. IEEE Transactions on Instrumentation and Measurement, vol 40(4), 742-746.

Parasnis, D.S. (1972) Principles of Applied Geophysics. Chapman and Hall, London.

Parasnis, D.S. (1982) Principles of Applied Geophysics. Chapman and Hall, London.

Parrott, L.J. (1990) A review of methods to determine the moisture conditions in concrete. British Cement Association - C Series December.

Parrott, L.J. (1991) Factors influencing the internal humidity in concrete. Magazine of Concrete Research, vol 43(154): 45-52.

Patella, D. (1975) A numerical computation procedure for the direct interpretation of geoelectrical soundings. Geophysical Prospecting, vol 23: 335-362.

Pekeris, C.L. (1940) Direct method in interpretation in resistivity prospecting. Geophysics vol 5(1): 31-46.

Radstake, F., Geirnaert, W., Kleinendorst, T.W. and Terhall, J. C. (1991) Applications of forward modeling resistivity profiles. Ground Water, vol 21(1): 13-17.

Roper, H. (1992) Surface Coatings and Treatments. In, Australian Concrete Technology. (258-268), Ryan, W.G. and Samarin, A. (Eds.) Longman Cheshire, Melbourne.

Ryan, W.G. and Samarin, A. (Eds.) (1992) Australian Concrete Technology. Longman Cheshire, Melbourne.

Sanadiki, B.A. and Mostafavi, M. (1991) Inversion of Inhomogeneous continuously varying dielectric profiles using open-ended waveguides. IEEE Transactions on Antennas and Propagation. vol39(2): 158-168.

Sandberg, S. K. (1990) Microcomputer software for individual or simultaneous inverse modelling of transient electromagnetic, resistivity and induced polarization soundings. New Jersey Geological Survey Open-File Report OFR 90-1, Trenton NJ.

Sasaki, M. and Nakayama, M. (1993) Behaviour of water entrapped in floor slab. Kajima Technical Research Institute report No. 98. Kajima Corporation, Tokyo.

Schulte, C., Mader, M. and Wittmann, F. H. (1978) Electrical conductivity, cement paste water content (Elektrische leitfahigkeit des zementsteins bei unterschiedlichem feuctigkeitsgehalt). Cement and Concrete Research, vol 8: 359-368.

Scuderi, C. A., Mason, T. O. and Jennings, H. M. (1991) Impedance spectra of hydrating cement pastes. Journal of Material Scieence, vol 26: 349-353.

Slichter, L.B. (1933) The interpretation of the resistivity prospecting method for horizantal structures. Physics, vol 4: 307-322.

Szaraniec, E. (1980) Direct resistivity interpretation byaccumulation of layers. Geophysical Prospecting, vol 28(2): 257-268.

Tashiro, C., Ishida, H. and Shimamura, S. (1987) Dependence of the electrical resistivity on evaporable water content in hardened cement paste. Journal of Materials Science Letters, vol 6: 1579-1381.

Valdez, L.B. (1954) Resistivity Measurements on Germanium for Transistors. Proceedings of the IRE: Institute of Radio Engineers. vol 42: 420-427, February

van Beek, L.K.H. (1967) Dielectric behaviour of Heterogeneous Systems. In Progress in Dielectrics, 69-114, Birks, J.B. (Ed.), Heywood Books, London.

Visscher, G. J. W. And Kornet, J. G. (1994) Long-term tests of capacitive humidity sensors. Measurement Science Technology vol. 5: 1294-1302

von Hippel, A.R. (1954) Dielectrics and Waves. MIT Press, Cambridge, Mass.

Warlow, W.J. et al., (1978) Osmosis as cause of blistering of in situ resin flooring on wet concrete, Magazine of concrete research, 30(104)

Waters, E. H. (1974) Determning the moisture content of concrete: the use of electrical resistance methods. Building Science, vol 9: 289-297.

Whittington, H.W. and Wilson, J.G. (1986) Low-frequency electrical characteristics of fresh concrete Proceedings IEE, vol133(A5): 265-271

Whittington, H.W., McCarter, J. and Forde, M.C. (1981) The conduction of electricity through concrete. Magazine of Concrete Research, vol 33(114):48-60.

Wiederhold, P. (1987) Humidity Measurements. In Handbook of Industrial Drying, 881-914, Mujumdar, A. (Ed.), Dekker, New York.

Wilkins, N.J.M. (1982) Resistivity of concrete. (Internal Paper), United Kingdom Atomic Energy Association, Harwell, Materials Development Division, January.

Wilson, J.G. and Whittington, H.W. (1990) Variations in the electrical properties of concrete with change in frequency. IEEE Proceedings, vol 137(A5): 246-254.

Wilson, J.G. Whittington, H.W. and Forde, M.C. (1983) Microprocessor based system for automatic measurement of concrete resistivity. Journal of Physics E: Scientific Instruments. vol 16: 700-705.

Woelfl, G.A. and Lauer, K. (1979) The electrical resistivity of concrete with emphasis on the use of electrical resistance for measuring moisture content. Cement, Concrete and Aggregates, vol1(2): 64-67.

Yaramanci, U. (1994) Relation of in situ resistivity to water content in salt rocks. Geophysical Prospecting, vol 41: 229-239.

Young, J. J. (1967) Humidity control in the laboratory using salt solution - a review. Journal of Applied Chemistry, vol 17: 241-245.

Zhdanov, M. S. and Keller, G. V. (1994) The geoelectrical methods in geophysical exploration. Methods in geochemistry and Geophusics, 31, Elsevier, Amsterdam

Zohdy, A.A.R. (1989) A new method for the automatic interpretation of Schlumberger and Wenner sounding curves. Geophysics, vol 54(2): 245-253.

Appendix A : the Marquardt-Levenberg method

Lines and Treitel (1984) note that "geophysical inverse problems are generally not well posed...In fact many of these problems are overdetermined, that is, the number of data points exceeds the number of model parameters;... the matrix $[\underline{\underline{A}}]$ may or may not be of full rank" (p. 162). The approach known as the Marquardt-Levenberg method can alleviate the problem of rank deficiency. This technique is also referred to as the method of "damped least squares" and as "ridge regression" (ibid p. 163).

The following discussion is adapted from their work.

Let $\underline{P}^o$ be an initial estimate of the layer parameters and $\underline{R}^o = \ln\left(\rho_{af}^o\right)$ be the initial model response. How can we improve this model? The question is one of finding the change to the model that brings its new response closest to the experimental data. If the model response $\underline{R}$ is a linear function of the parameters, a perturbation $\Delta\underline{P}$ of the model response about $\underline{P}^o$ can be represented by the first order Taylor expansion:

$$\underline{R}(\underline{P}+\Delta\underline{P}) = \underline{R}^o(\underline{P}) + \sum_{j=}^{2n-1}\left(\frac{\partial \underline{R}}{\partial P_j}\left(P_j - P_j^o\right)\right)$$

or

$$\underline{R} = \underline{R}^o + \underline{\underline{A}}\cdot\Delta\underline{P} \qquad \text{Equation A-1}$$

where $\underline{\underline{A}}$ is the $\underline{\underline{A}}$ is the Jacobian matrix of partial differentials of the model response with respect to the layer parameters. That is $\underline{\underline{A}}$ has elements

$$A_{ij} = \frac{\partial P_i}{\partial R_j}$$

and $\Delta\underline{P} = \underline{P} - \underline{P}^o$ is the parameter change vector with elements P_j representing the changes or perturbations in the parameters. That is $\Delta P_j = P_j - P_j^o$.

Let $\Delta\underline{R}$ represent the error vector expressing the difference between the model response R and the observed data R_f $\left\{= \ln\left(\rho_{af}\right)\right\}$, that is

$$\Delta\underline{R} = R_f - R, \qquad \text{Equation A-2}$$

so that we may write

$$\Delta\underline{R} = R_f - \left(\underline{R}^o + \underline{\underline{A}} \cdot \Delta\underline{P}\right)$$

or

$$\Delta\underline{R} = \underline{g} - \underline{\underline{A}} \cdot \Delta\underline{P}$$

where

$$\underline{g} = R_f - \underline{R}^o$$

is called the discrepancy vector which contains the differences between the initial model response and the observed data.

We want to choose the parameter change vector $\Delta\underline{P}$ so as to minimise the sum of squares of errors between the model response and the data.

In the "least squares" method, the cumulative squared error

$$S = \Delta\underline{R}^T \Delta\underline{R} = \left(\underline{g} - \underline{\underline{A}} \cdot \Delta\underline{P}\right)^T \left(\underline{g} - \underline{\underline{A}} \cdot \Delta\underline{P}\right)$$

is minimised with respect to the parameter change vector $\Delta\underline{P}$. Thus we require that

$$\frac{\partial S}{\partial(\Delta\underline{P})} = 0$$

or

$$\frac{\partial}{\partial \Delta\underline{P}}\left(\Delta\underline{P}^T \underline{\underline{A}}^T \underline{\underline{A}}\Delta\underline{P} - \underline{g}^T \underline{\underline{A}}\Delta\underline{P} - \Delta\underline{P}^T \underline{\underline{A}}^T \underline{g} + \underline{g}^T \underline{g}\right) = 0$$

Solution of this equation for the parameter change vector eventually yields

$$\Delta\underline{P} = \left(\underline{\underline{A}}^T \underline{\underline{A}}\right)^{-1} \underline{\underline{A}}^T \underline{g}$$

Lines and Treitel point out

> This so-called 'unconstrained' least-squares solution may have some undesirable properties...
>
> An obvious difficulty occurs when the inverse of $\underline{\underline{A}}^T \underline{\underline{A}}$ does not exist, that is when the matrix $\underline{\underline{A}}^T \underline{\underline{A}}$ is singular. Even if $\underline{\underline{A}}^T \underline{\underline{A}}$ exists, we may well be faced with a diverging solution , or we may have to contend with slow convergence. This can happen whenever the initial [trial model] is poor ...[and as]...soon as $\underline{\underline{A}}^T \underline{\underline{A}}$ becomes nearly singular, the elements of the solution vector tend to grow without bound (ibid p.163).

The Marquardt-Levenberg approach is to "impose the constraining condition that the sum of the squares, or energy of the elements of the parameter change vector [ΔP] be bounded by a finite quantity, say δ_o^2 ... The effect of this constraint is to ...smooth the parameter change vector...Thus we choose [ΔP] to minimise a cost function" (ibid p. 163)

$$S(\Delta P, \delta) = \Delta \underline{R}^T \Delta \underline{R} + \beta \left(\underline{\Delta P}^T \Delta P - \delta_o^2 \right)$$

with the solution

$$\underline{\Delta P} = \left(\underline{\underline{A}}^T \underline{\underline{A}} + \beta \underline{\underline{I}} \right)^{-1} \underline{\underline{A}}^T \underline{g}$$

This solution is "hybrid because it combines the so-called 'method of steepest descent' [which is optimal when the cumulative squared error S is large] with the method of least squares [which becomes effective when S is small]...

A particular choice of β... allows either the linear least-squares method or the steepest descent method to dominate the paramenter search. Setting $\beta = 0$ implies that the linear least squares method predominates, while allowing β to increase moves the technique towards the method of steepest descent. Initially β is set at a large positive value, so that the good initial convergence properties of the steepest descent method can come into play. Then, as this happens, β is reduced by multiplying it by a constant factor < 1 so that the linear least-squares method may take over in the region closer to a solution. If divergence occurs during an iteration, β is divided once more by this factoruntil the error drops and convergence resumes (at least one hopes it does) [sic]" (ibid pp. 164-166).

Appendix B : Correcting for the presence of non-conducting boundaries.

Valdez (1954) presented a series of correction functions for use when measuring resistivity of thin slices of semiconductor using using four surface probes in a Wenner array. Assuming the material is of uniform resistivity the functions enable determination of the resistivity when the array is near conducting or non-conducting boundaries (Figure B-1). The derivation of the correct expression for the resistivity when measured using a Schlumberger array in the presence of non-conducting boundaries is presented here.

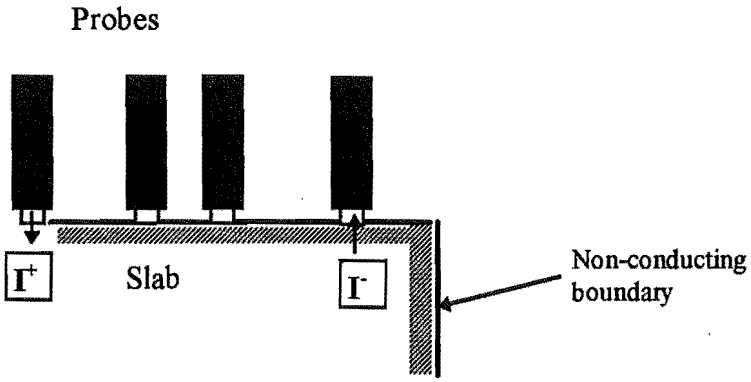

Figure B-1: A four probe array perpendicular to a non-conducting boundary

We may describe the position of the array on the slab as in Figure B-2. In this case, the line of the probes is perpendicular to the *end* boundary and parallel to the *side* boundary.

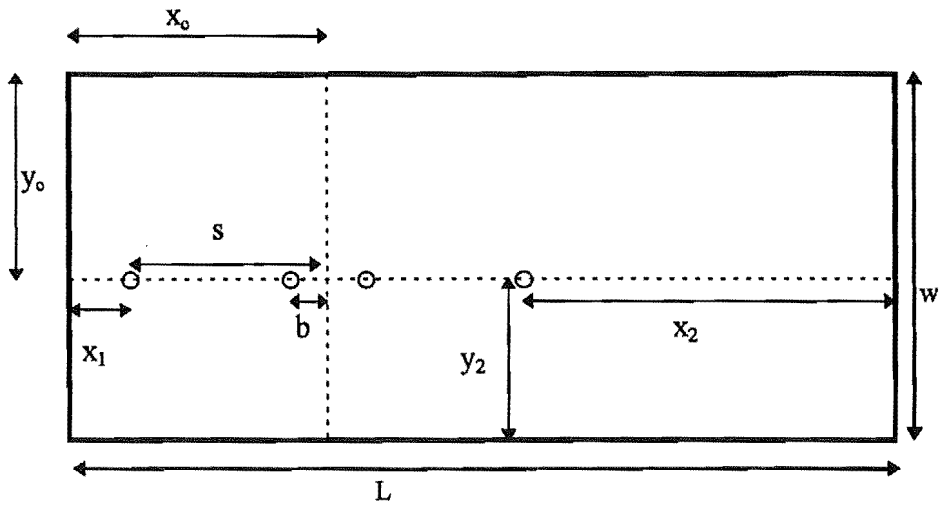

Figure B-2: Parameters describing the position of the Schlumberger array on the top surface of a concrete slab.

The values of x_1 and x_2 will be functions of the current probe spacing *s* and measurement probe spacing *b* as they change during the course of a sounding. x_1 and x_2 are parameters

describing the array's position perpendicular to a boundary. y_c and y_l describe the position relative to the parallel boundary.

Case 1. Probes perpendicular to a non-conducting boundary.

The end face of the slab presents a reflecting (nonconducting) boundary, so that images of the current sources may be used to obtain the floating potential of the voltage measurement probes (Figure B-3).

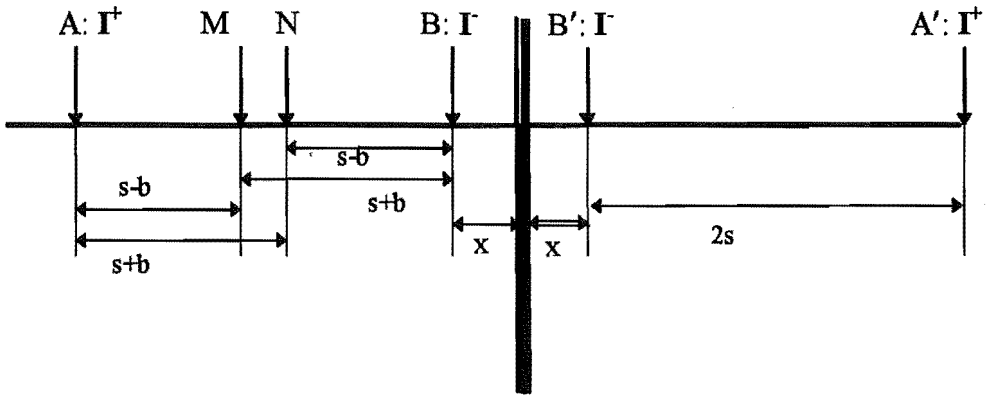

Figure B-3: Current sources (A and B) and their images (A' and B') reflected in a non-conducting plane (thick vertical line) and other relevant distances. Note the sign of each current source image.

The potentials at M and N are given by

$$V_M = \frac{\rho I}{2\pi}\cdot\left(\frac{1}{s-b}-\frac{1}{s+b}-\frac{1}{2x+s+b}+\frac{1}{2x+3s+b}\right)$$

$$V_N = \frac{\rho I}{2\pi}\cdot\left(\frac{1}{s+b}-\frac{1}{s-b}-\frac{1}{2x+s-b}+\frac{1}{2x+3s-b}\right)$$

so that the potential difference between M and N is given by

$$\begin{aligned}\Delta V &= V_M - V_N \\ &= \frac{\rho I}{2\pi}\cdot\left(\frac{2}{s-b}-\frac{2}{s+b}-\frac{1}{2x+s+b}+\frac{1}{2x+3s+b}+\frac{1}{2x+s-b}-\frac{1}{2x+3s-b}\right) \\ &= \frac{\rho I}{2\pi}\cdot\left(\frac{4b}{s^2-b^2}-\frac{1}{2x+s+b}+\frac{1}{2x+3s+b}+\frac{1}{2x+s-b}-\frac{1}{2x+3s-b}\right)\end{aligned}$$

Making resistivity the subject we have

$$\rho = 2\pi\frac{\Delta V}{I}\left(\frac{4b}{s^2-b^2}-\frac{1}{2x+s+b}+\frac{1}{2x+3s+b}+\frac{1}{2x+s-b}-\frac{1}{2x+3s-b}\right)^{-1}$$

$$= 2\pi\frac{\Delta V}{I}\cdot\frac{s^2-b^2}{4b}\left(1+\frac{s^2-b^2}{4b}\left[-\frac{1}{2x+s+b}+\frac{1}{2x+3s+b}+\frac{1}{2x+s-b}-\frac{1}{2x+3s-b}\right]\right)^{-1}$$

that is

$$\rho = \frac{\pi\cdot\left(s^2-b^2\right)}{2b}\left|\frac{\Delta V}{I}\right|\cdot\frac{1}{G_{end}}$$

where

$$G_{end}(x) = 1+\frac{1}{4}\left(\frac{s}{b}-\frac{b}{s}\right)\cdot\left\{\left(\frac{2x}{s}+1-\frac{b}{s}\right)^{-1}-\left(\frac{2x}{s}+1+\frac{b}{s}\right)^{-1}+\left(\frac{2x}{s}+3+\frac{b}{s}\right)^{-1}-\left(\frac{2x}{s}+3-\frac{b}{s}\right)^{-1}\right.$$

x_1 and x_2 may be substituted into these equations since similar arguments apply to each end, although x_1 and x_2 will be defined separately in terms of x_c thus

$$x_1 = x_c - s$$
$$x_2 = L - x_c - s$$

Case 2. Probes parallel to a non-conducting boundary.

A similar analysis may be carried out for the side (parallel) boundary (Figure B-4).

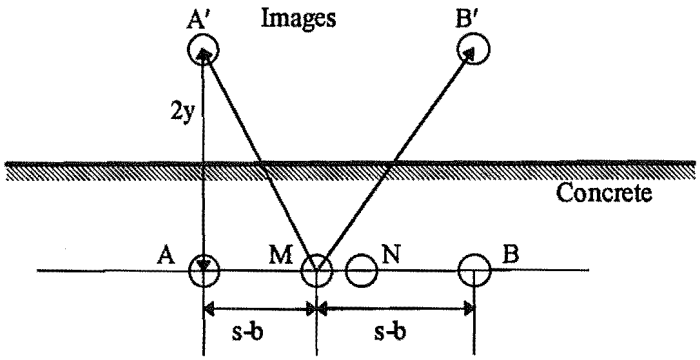

Figure B-4: Schlumberger array parallel to a non-conducting boundary

In this case we have

$$V_M = \frac{\rho I}{2\pi}\cdot\left(\frac{1}{s-b}-\frac{1}{s+b}+\frac{1}{\sqrt{(2y)^2+(s-b)^2}}-\frac{1}{\sqrt{(2y)^2+(s+b)^2}}\right)$$

$$V_N = \frac{\rho I}{2\pi}\cdot\left(\frac{1}{s+b}-\frac{1}{s-b}+\frac{1}{\sqrt{(2y)^2+(s+b)^2}}-\frac{1}{\sqrt{(2y)^2+(s-b)^2}}\right)$$

Once again

$$\Delta V = V_M - V_N$$

$$= \frac{\rho I}{2\pi}\cdot\left(\frac{4b}{s^2-b^2}+\frac{2}{\sqrt{(2y)^2+(s-b)^2}}-\frac{2}{\sqrt{(2y)^2+(s+b)^2}}\right)$$

$$= \frac{\rho I}{\pi}\cdot\frac{2b}{s^2-b^2}\left(1+\frac{s^2-b^2}{2b}\left[\left((2y)^2+(s-b)^2\right)^{-\frac{1}{2}}-\left((2y)^2+(s+b)^2\right)^{-\frac{1}{2}}\right]\right)$$

$$= \frac{\rho I}{\pi}\cdot\frac{2b}{s^2-b^2}\left\{1+\frac{1}{2}\left(\frac{s}{b}-\frac{b}{s}\right)\left[\left\{\left(2\frac{y}{s}\right)^2+\left(1-\frac{b}{s}\right)^2\right\}^{-1/2}-\left\{\left(2\frac{y}{s}\right)^2+\left(1+\frac{b}{s}\right)^2\right\}^{-1/2}\right]\right\}$$

and

$$\rho = \frac{\pi\cdot\left(s^2-b^2\right)}{2b}\left|\frac{\Delta V}{I}\right|\cdot\frac{1}{G_{side}(y)}$$

where

$$G_{side}(y) = \left\{1+\frac{1}{2}\left(\frac{s}{b}-\frac{b}{s}\right)\left[\left\{\left(2\frac{y}{s}\right)^2+\left(1-\frac{b}{s}\right)^2\right\}^{-1/2}-\left\{\left(2\frac{y}{s}\right)^2+\left(1+\frac{b}{s}\right)^2\right\}^{-1/2}\right]\right\}$$

Case 3: All boundaries significant

If the relative sizes of the slab and array are such that all four end and side boundaries are significant, the expression for ΔV wil contain terms corresponding to all the images. The result will be an expanded G term. Writing

$$G_{end} = 1 + \frac{1}{4}\left(\frac{s}{b} - \frac{b}{s}\right) \cdot f_{end}$$

and

$$G_{side} = 1 + \frac{1}{2}\left(\frac{s}{b} - \frac{b}{s}\right) \cdot f_{side}$$

where

$$f_{end}(x) = \left(\frac{2x}{s} + 1 - \frac{b}{s}\right)^{-1} - \left(\frac{2x}{s} + 1 + \frac{b}{s}\right)^{-1} + \left(\frac{2x}{s} + 3 + \frac{b}{s}\right)^{-1} - \left(\frac{2x}{s} + 3 - \frac{b}{s}\right)^{-1}$$

Equation B-1

and

$$f_{side}(y) = \left\{\left(2\frac{y}{s}\right)^2 + \left(1 - \frac{b}{s}\right)^2\right\}^{-1/2} - \left\{\left(2\frac{y}{s}\right)^2 + \left(1 + \frac{b}{s}\right)^2\right\}^{-1/2}$$

Equation B-2

the expanded *G is*

$$G_{all} = 1 + \left(\frac{s}{b} - \frac{b}{s}\right) \cdot \left[\frac{1}{4}\left(f_{end}(x_1) + f_{end}(x_2)\right) + \frac{1}{2}\left(f_{side}(y_1) + f_{side}(y_2)\right)\right]$$

Equation B-3

and the resistivity must be calculated as

$$\rho = \frac{\pi \cdot \left(s^2 - b^2\right)}{2b}\left|\frac{\Delta V}{I}\right| \cdot \frac{1}{G_{all}}$$

Equation B-4

Appendix C : A typical VES session

A VES sounding session involves placing the array board in position on the concrete, and measuring the apparent resistivity at each of the probe positions as defined in the multiplexer sequencing file (which will have a name of the form 'ves*.mux') to get a set of from one to four VES curves, depending on the file. Running through the multiplexer sequence once is called a 'run'.

If the first run does not seem to yield well formed VES curves (as displayed in the graph window), another run, or several more runs in the same position may allow improvement. Generally the older and drier the slab, the longer time is needed to achieve well formed curves. However, the user may get better results by accepting the first or second curve and then measuring apparent resistivity in a new position.

If VES curves are taken at several positions, without changing the sequencing file, the data may be combined and averaged. This is described in Chapter 6. All the VES runs taken constitute the VES sounding session.

1. Before the session starts, the 'Read VES' button is 'clicked'. This brings up the 'Open file' dialog box, with a listbox of 'ves*.mux' files which contain the data relating the multiplexer sequence and the associated current probe and measurement probe spacings. Many different array configurations were tried, with different numbers of data points and spacings used. In this session typical of the most recent soundings, a file called ves8x2d.mux is selected and read in. This will enable four VES curves to be taken concurrently, two at a measurement probe spacing of 10 mm and two at 20 mm. The actual spacings must be read in with the multiplexer sequence so that apparent resistivities can be calculated and saved.
2. The operator must ensure that the array board is loaded with probes and wired up correctly to match the selected file, otherwise incorrect data will be calculated.
3. The meter has default settings as given in Chapter 6 above. These may be changed. Reading in a 'ves*.mux' file will change others, such as the 'Autogain' and 'Auto Cycle Change' parameters which determine how long to wait for the voltage measuring amplifiers to de-saturate after a change in the gain setting or after a change in the voltage multiplexer setting..

The 'Run Mode' group of check and option boxes will show the following checked: 'Loop' (so that the meter will restart after each reading cycle), 'Cts Run' (so that the meter will restart once stopped for a timer controlled period), 'Auto Advance' (so that the multiplexer sequence will advance to the next setting once the present setting has been adequately read), 'VES' (to indicate that the meter is set for VES reading).

'Graph Now' may be checked if graphical display of the data is desired. The default graph a display of 'resistance' (ie. measured voltage divided by measured current) versus sample number for the reading cycle. Other options include current versus sample number or voltage versus sample number. 'Resistance', current and voltage can be displayed as instantaneous measurements or as a running average. Alternatively, apparent resistivity versus current probe spacing can be displayed, as a linear scatter graph, or as a loglinear graph. The latter is useful

when the concrete is older and measured resistivities can extend over several decades. Display of the VES curve as it is being formed is very useful in determining if there are any problems with poor electrode contact.

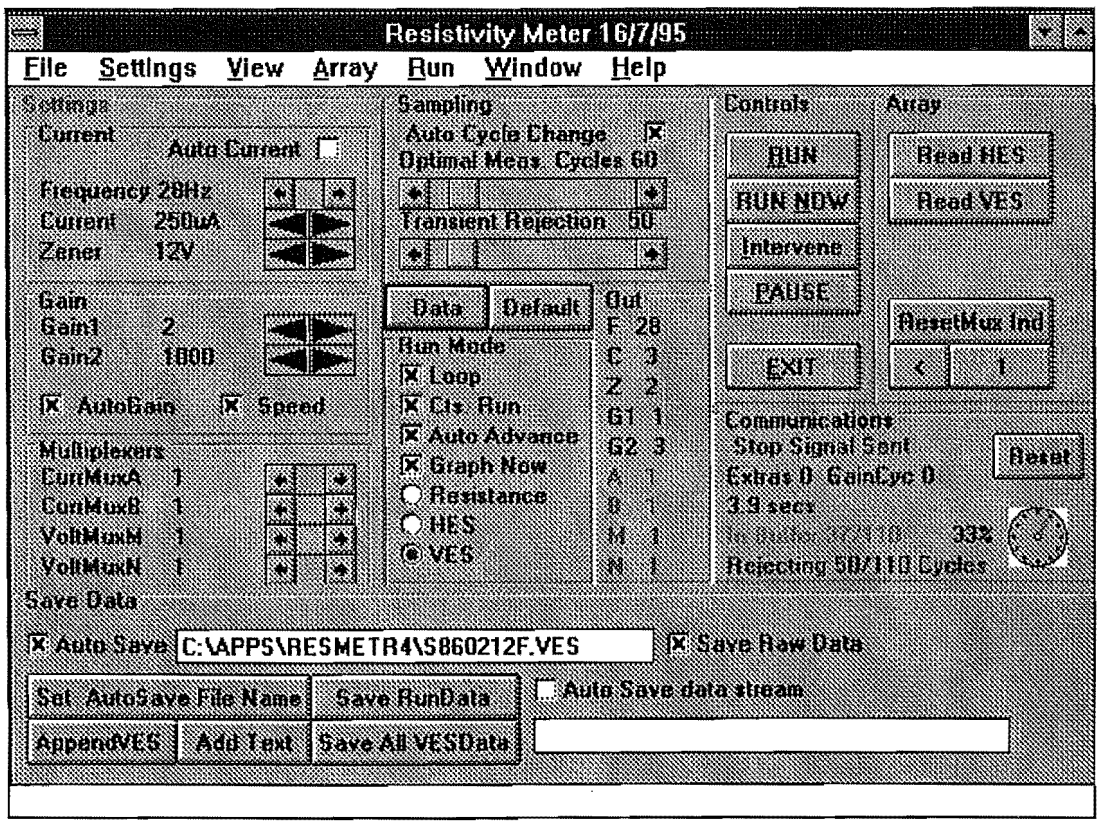

Figure C-1 Resistivity meter user interface, showing the "Save Data" window.

1. The array board is taken from where it sits with the electrodes in the conducting solution reservoir, is placed briefly on a sheet of plastic to deposit excess solution and then placed carefully in position on the concrete. Weights are placed on the holders at each end of the array board and a quick visual inspection is made to ensure all electrodes are resting on the surface.
2. A check of each of the multiplexer settings is carried out by switching off the auto advance, pushing 'RUN' checking the magnitude of the current signal when it comes up in the data window, and then 'clicking' the multiplexer advance button to advance to the next multiplexer setting. Unusually small current levels may indicate that one of the corresponding current electrodes is not contacting the concrete surface, or that it is too dry, or that the electrode is resting on aggregate. If one of the first two cases holds, then the current can be increased. If the last, then the data point is likely to be well away from the expected VES curve.
3. If all seems well, the 'Auto advance', 'Auto Gain', 'Auto Cycle Change' and the 'Run' buttons are clicked. The resistivity meter will then be operated automatically by the computer, taking a set of VES curves at predetermined intervals.
4. The data is displayed in a number of ways. In the 'Communications' window, the number of cycles which have arrived in the 'In Buffer' is displayed as a numeral and on a circular dial. Initially the samples coming in are from cycles that will be neglected to in an attempt to ensure the gain amplifiers have desaturated. Once the predetermined number of reject cycles has been reached, the colour of both the numerals and the dial, changes to bright red. In this window are also displayed, the last message passed to the meter (eg. 'Stop Signal Sent'), or error messages generated by the Visual Basic communications control, information showing what if any extra cycles are being read due to increased delay in desaturation (as happens at higher gain levels), the time that will be taken in reading the present number of cycles, and an indication of the number of cycles being rejected and the total number of cycles being read into the In Buffer. In this window also is a 'Reset' button which reboots the microprocessor should it get out of sequence or 'hang'.

   Once the required number of samples has been read in to the buffer and analysed, the results are presented in the two parts of the 'Data' window (see Figure C-2) In the first 'Data' window is displayed in the top two lines, the raw current and voltage samples

from the positive and negative d.c. portions of the respective square wave signals. These are given in analog-to-digital units (adu) and averaged over the range of accepted cycles. The 'negative' signal adu's are subtracted from the 'positive signal adu's, and multiplied by a calibration factor to get current and voltage which are also displayed. The meter will accept cycles so long as no 'saturated' cycles follow. That is, if of 200 cycles input, the last cycle showing saturation was number 147, cycles 148 to 200 will be accepted. If this number is too low, the number of cycles read into the buffer could be increased or the gain could be reduced. Also in this window are displayed the gain used to make the present reading, the 'resistance' and the standard deviation of the voltage which has much more error associated with it than the current. and a line showing the 'Run number' that where each run refers to transition over the whole set of multiiplexer sequence.

The second data window shows data pertinent to the VES aspect of the session. This window shows the multiplexer settings and the spacings, the resistance (again) and the geometrical array factor, and finally, the apparent resistivity and measured standard deviation. Also displayed is the present time, the time since the sounding session was begun, the time the VES run-through began and the time the next VES run is due to start.

Finally the data may be graphed either as an analysis of the current or voltage data for each reading (eg. Current vs cycle number), or by showing the apparent resistivity curve as it is being formed (Figure C-3).

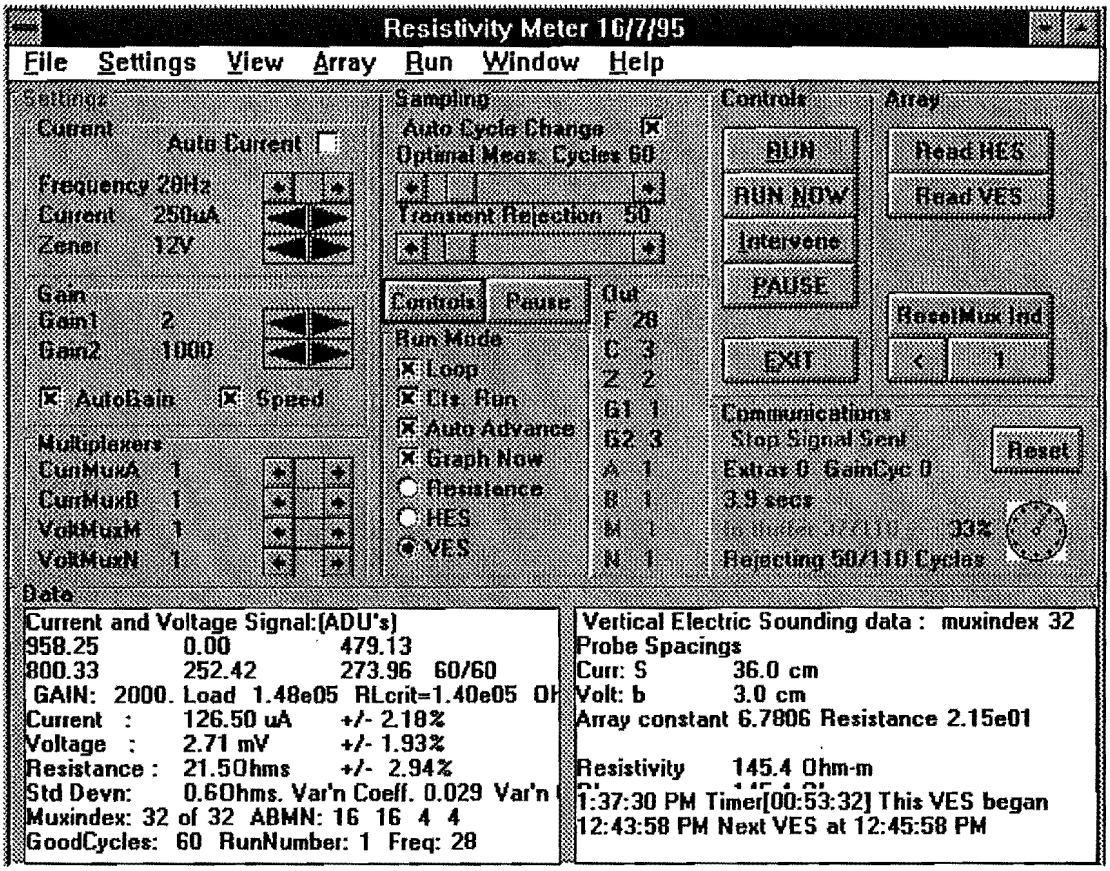

Figure C-2. User interface showing "Data" window.

1. When the complete multiplexer sequence has been run through, the data will be saved to a preset filename (see Figure C-1), or if the filename has not been already set, the user will first be prompted for a file-name. A typical filename includes the slab number, the date and a letter to label the positionand an extension indicating the type of data. Thus the data file for the second array board position taken from Slab #3 on the 23/2/96 will be named 's360223b.ves'. At present the data is stored in an ascii file suitable for direct interpretation by Matlab. the 'vesdat' matrix stores spacing and apparent resistivity data. Other matrices store current ('currdat'), voltage ('voltdat'), 'resistance' ('resdat'), variance ('varresdat'), and array data ('arraydat'). Each run through is represented in one column, although spread over several matrices. The date and time ('secs') information is also stored. During the course of the sounding the meter may be paused and lines of text may be added to the data to be stored. At the end of each run, the data for that run is added, in memory, to the earlier data. That is, matrices are expanded by one column. The expanded data is used to overwrite the existing file. In this way, if the meter is halted or the computer hangs during a run, previous data up to the beginning of the present run is secure.

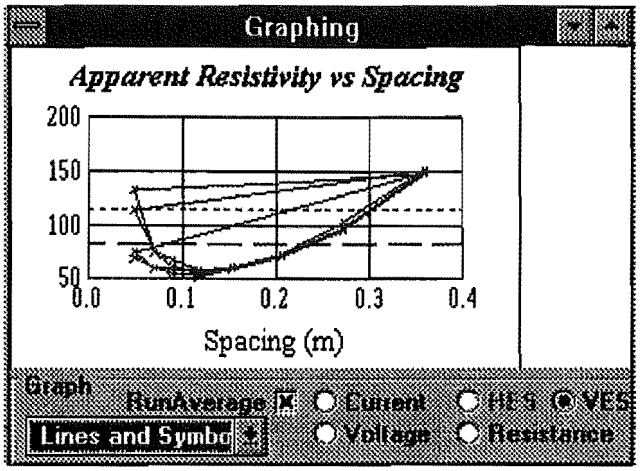

Figure C-3 The user interface graph window showing three complete VES curves and a fourth part the way through.

Data analysis

The file is transferred or copied to an appropriate Matlab directory, with a '.m' extension.The data may be pre-analysed by 'running' the data file (or files if there is more than one file from the VES session) within Matlab. The pre-analysis involves

1. selection of the one curve or one set of curves if there has been more than one 'run',
2. correction of the apparent resistivity to take account of the proximity of the slab edges,
3. averaging of data points for the same measurement probe spacing ('b') where there are several curves,

Appendix D Finite difference modelling of the measurement of resistivity.

This work follows on an early attempt to model a concrete slab in two dimensions using a resistance grid, in which layers of difference resistivity were modelled by one or more rows of resistances in a square grid pattern. Following a paper by Radstake et al (1991), the grid model was converted to the finite difference model outlined below.

The three dimensional concrete samples may be modelled in two dimensions by a thin slab of thickness *t*. The slab is then divided into a number of rectangular elements of varying height *h* and width *w*. Current is injected into two of the elements and the potential of each element is determined. (Figure D-1 and Figure D-2).

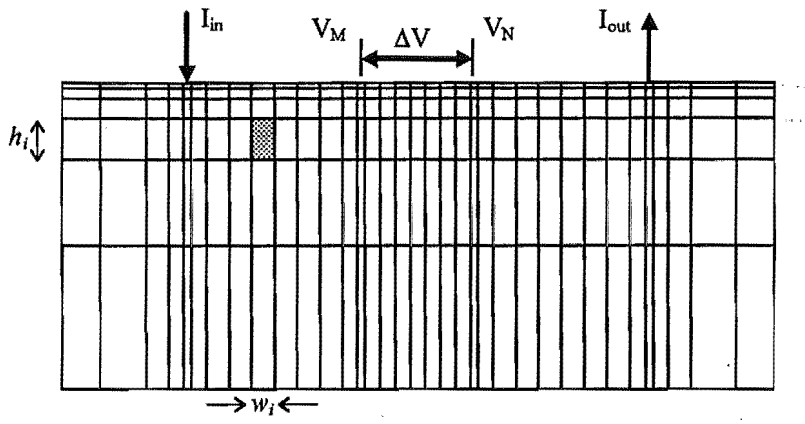

Figure D-1: Finite difference model suitable for surface mounted electrodes used in vertical electric sounding.

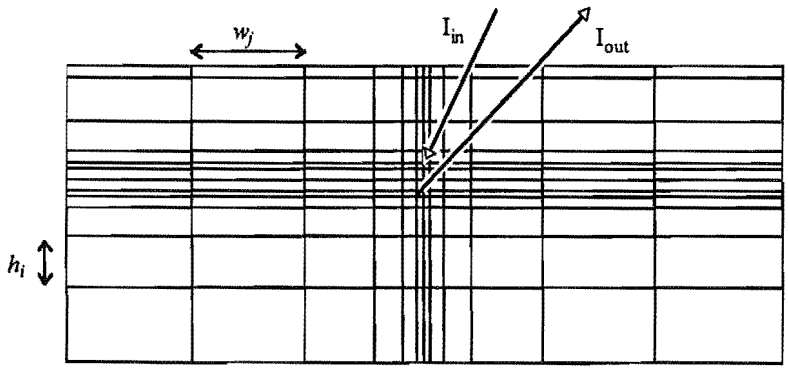

Figure D-2: Finite difference model suitable for two embedded electrodes. In this case the electrodes are displaced vertically from one another.

The width of each row and and the height of each column is set according to the position of the position of the electrodes. The dimensions are chosen to be smaller where the potential

is changing most rapidly, that is, nearer the electrodes. As the positions of the electrodes are changed, so are the cell dimensions.

Each element may be represented by a nodal point and has associated with it a potential V, and resistivity ρ (Figure D-3).

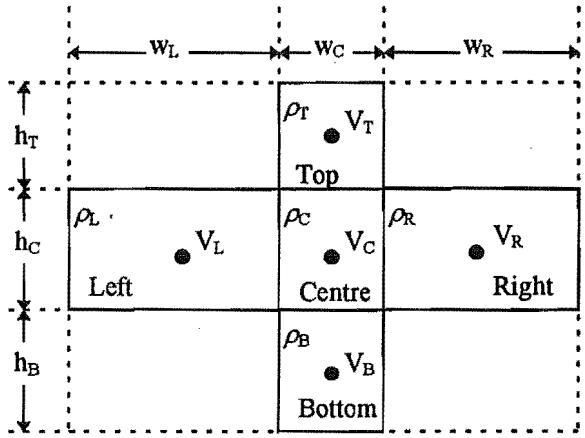

Figure D-3: Detailed portion of the rectangular grid showing notation relative to selected cell.

Each element is surrounded by up to four elements from which (or to which) current may flow. Letting the subscripts T, L, R and B respectively represent the cell above, to the left of, to the right of and below, the central cell (subscript C), we may write, for each element an equation for current flow

$$I_T + I_L + I_R + I_B = I_{in}$$

The flow of steady electrical current I within a rectangular volume element of resistivity ρ is governed by the relation

$$I = \frac{\Delta V A}{\rho l}$$

where ΔV is the difference in potential between opposite faces of area A a distance l apart.

Substituting the potential differences and resistance between the central cell and adjacent cells, into this equation gives

$$\frac{V_C - V_T}{R_T} + \frac{V_C - V_L}{R_L} + \frac{V_C - V_R}{R_R} + \frac{V_C - V_B}{R_B} = I_{in}$$

or

$$V_C\left[\frac{1}{R_T}+\frac{1}{R_L}+\frac{1}{R_R}+\frac{1}{R_B}\right]-\left[\frac{V_T}{R_T}+\frac{V_L}{R_L}+\frac{V_R}{R_R}+\frac{V_B}{R_B}\right]=I_{in}$$

where R_T is the resistance between the top and the central node, R_L is the resistance between the left and the central node and so on.

The resistance of an rectangular volume element of resistivity ρ measured between opposite faces of area A which are distance l apart, is given by

$$R=\frac{\rho}{A}l$$

R_T may be written in terms of the resistivities of the top and the centre element, that is

$$\begin{aligned}R_T &= \rho_T\frac{h_T}{2}\frac{1}{tw_C}+\rho_C\frac{h_c}{2}\frac{1}{tw_C}\\ &=\frac{\rho_T h_T+\rho_C h_C}{2tw_C}\end{aligned}$$

where tw_c is the area of the element at right angles to the current flow. Similar relations hold for the othe resistances. Thus, putting

$$a_C=\left[\frac{h_C}{\rho_L w_L+\rho_C w_C}+\frac{h_C}{\rho_R w_R+\rho_C w_C}+\frac{w_C}{\rho_T h_T+\rho_C h_C}+\frac{w_C}{\rho_B h_B+\rho_C h_C}\right]$$

$$a_L=\left[\frac{h_C}{\rho_L w_L+\rho_C w_C}\right]$$

$$a_R=\left[\frac{h_C}{\rho_R w_R+\rho_C w_C}\right]$$

$$a_T=\left[\frac{w_C}{\rho_T h_T+\rho_C h_C}\right]$$

$$a_B=\left[\frac{w_C}{\rho_B h_B+\rho_C h_C}\right]$$

for each cell in the model an equation may be constructed

$$a_C V_C-a_L V_L-a_R V_R-a_T V_T-a_B V_B-I_{in}=0.$$

Writing it in full we have

$$V_C\left[\frac{h_C}{\rho_L w_L+\rho_C w_C}+\frac{h_C}{\rho_R w_R+\rho_C w_C}+\frac{w_C}{\rho_T h_T+\rho_C h_C}+\frac{w_C}{\rho_B h_B+\rho_C h_C}\right]\cdots$$
$$-V_L\left[\frac{h_C}{\rho_L w_L+\rho_C w_C}\right]-V_R\left[\frac{h_C}{\rho_R w_R+\rho_C w_C}\right]\cdots$$
$$-V_T\left[\frac{w_C}{\rho_T h_T+\rho_C h_C}\right]-V_B\left[\frac{w_C}{\rho_B h_B+\rho_C h_C}\right]\cdots$$
$$-I_{in}=0$$

Cells at the boundaries may have one or more coefficients equal to zero. For example cells on the left hand side of the model will have $a_L = 0$, whilst both $a_L = 0$ and $a_T = 0$ for the top left hand cell.

Except for those elements or nodes representing the current electrodes, net current I_{in} into a node must equal zero.

At a current electrode, the voltage of the node is fixed but the current passing into the system is unknown. Generally, we define two current injection points A and B where the voltage is set at +1 V and -1 V respectively. Thus, for a system of m elements, there are a total of m equations with $m-2$ unknown voltages V_i $i=1,2,...m-2$, and 2 unknown currents I_{in} and I_{out}. The equations will take the form

$$a_C\cdot 1-a_L V_L-a_R V_R-a_T V_T-a_B V_B-I_{in}=0 \text{ at current electrode } A,$$
$$a_C\cdot(-1)-a_L V_L-a_R V_R-a_T V_T-a_B V_B-I_{in}=0$$

at current electrode B and

$$a_C V_C-a_L V_L-a_R V_R-a_T V_T-a_B V_B=0$$

at the other nodes.

The system of equations may be written and solved in matrix form:

$$\underline{\underline{A}}\cdot\underline{V}=\underline{b}$$

where $\underline{V}$ is a vector of unknowns (V_i and I_{in} and I_{out}) and $\underline{b}$ is a vector containing only two nonzero elements (+1 and -1, corresponding to the known voltages).

Three main grid patterns were used. To model vertical electric sounding (VES) on a thin slab, five horizontal zones were defined on each side of center of the array (see Figure D-4).

The array is symmetrical but may not be positioned symmetrically on the slab. The five zones are

1. *es,* the area between the end of the slab and the outside edge of a current electrode
2. *sd,* the area covered by the current electrode,
3. *sb,* the area between the current electrode and the voltage electrode,
4. *bd,* the area covered by the voltage electrode,
5. *bc,* the area between the voltage electrode and the center of the array.

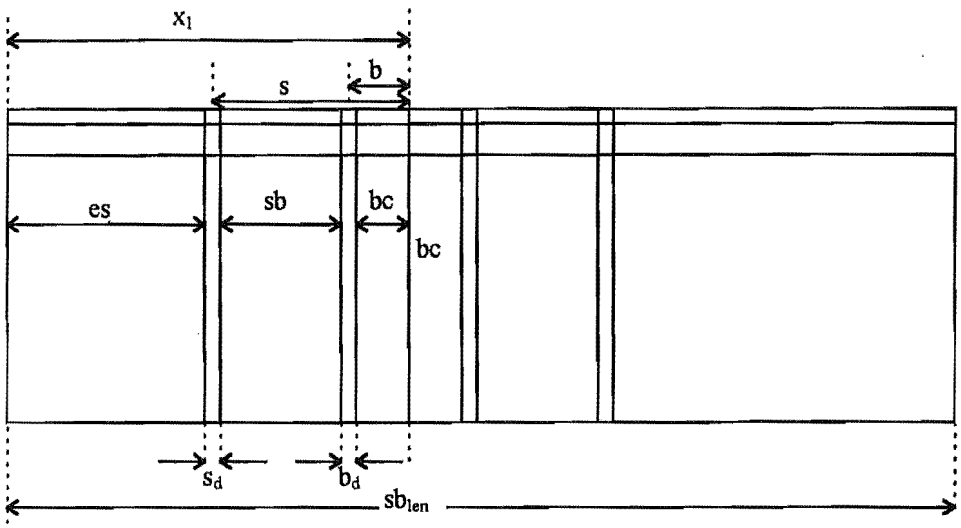

Figure D-4: Relevant horizontal parameters when modelling a two-dimensional slab for vertical electric sounding. Note that the symmetrical 'Schlumberger array' itself need not be positioned symmetrically on the slab.

The hoizontal spacing of the elements is arranged so that

- 8 columns are devoted to *es*
- 3 columns are devoted to *sd* and 3 columns to *bd*
- 11 columns are devoted to *sb*
- 5 columns are devoted to *bc*

Thus 30 columns are assigned to the zones on each side of the array centre, making 60 columns in all. The width of each column is a preset fraction of the total length assigned to the zone. Thus the elements of *es* get wider towards the edge of the slab, in the ratio 128:64:32:16:8:4:2:1 (from the edge to the current electrode). *Sd* and *bd* are divided into three equal parts. *Sb* is divided in the ratio 1:1:2:3:5:7:5:3:2:1:1, and the central zone *bc* is divided in the ratio 1:2:3:4:5.

There are 10 rows of cells making 600 elements in all. The depth from the surface of each each row of cells increases logarithmically.

With this scheme, the various parameters of the vertical electric sounding configuration can be changed easily, allowing the actual element dimensions to stretch or shrink correspondingly, without changing the number of elements devoted to each zone. The horizontal parameters which were under investigation were

- *s*, the current probe spacing (the distance between the current probe and the array center),
- *b*, the measurement probe spacing (defined similarly),
- *sd*, the width of the current probe,
- *bd*, the width of the measurement probe,
- *x*, the distance of the center of the array from one slab edge and
- sb_{len}, the length of the slab.

Also of interest was the effect of having a region of lowered resistivity in the vicinity of the current or measurement probes. This lowered resistivity would be expected of a 'wet' probe, that is of a wooden electrode soaked in a conducting solution. Since the resistivity of each cell is assigned individually, the effect of increasing the size of the region of lowered resistivity could be investigated quite easily.

Appendix E Directly measured resistivity profiles

Resistivity profiles measured using embedded electrode systems are described here. Descriptions of the electrode systems are found in Chapter 8.

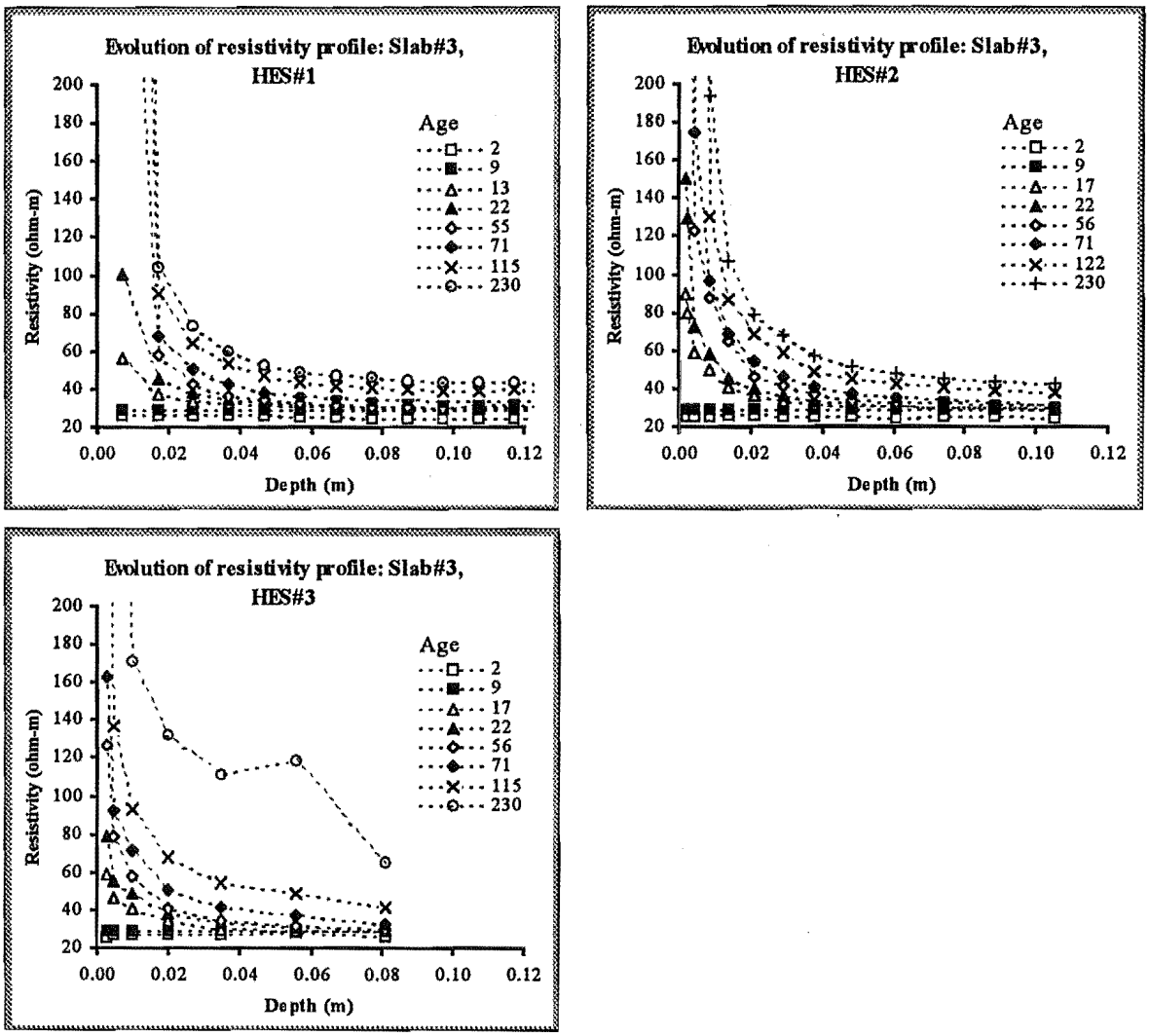

Figure E-1: Resistivity profiles from Slab #3

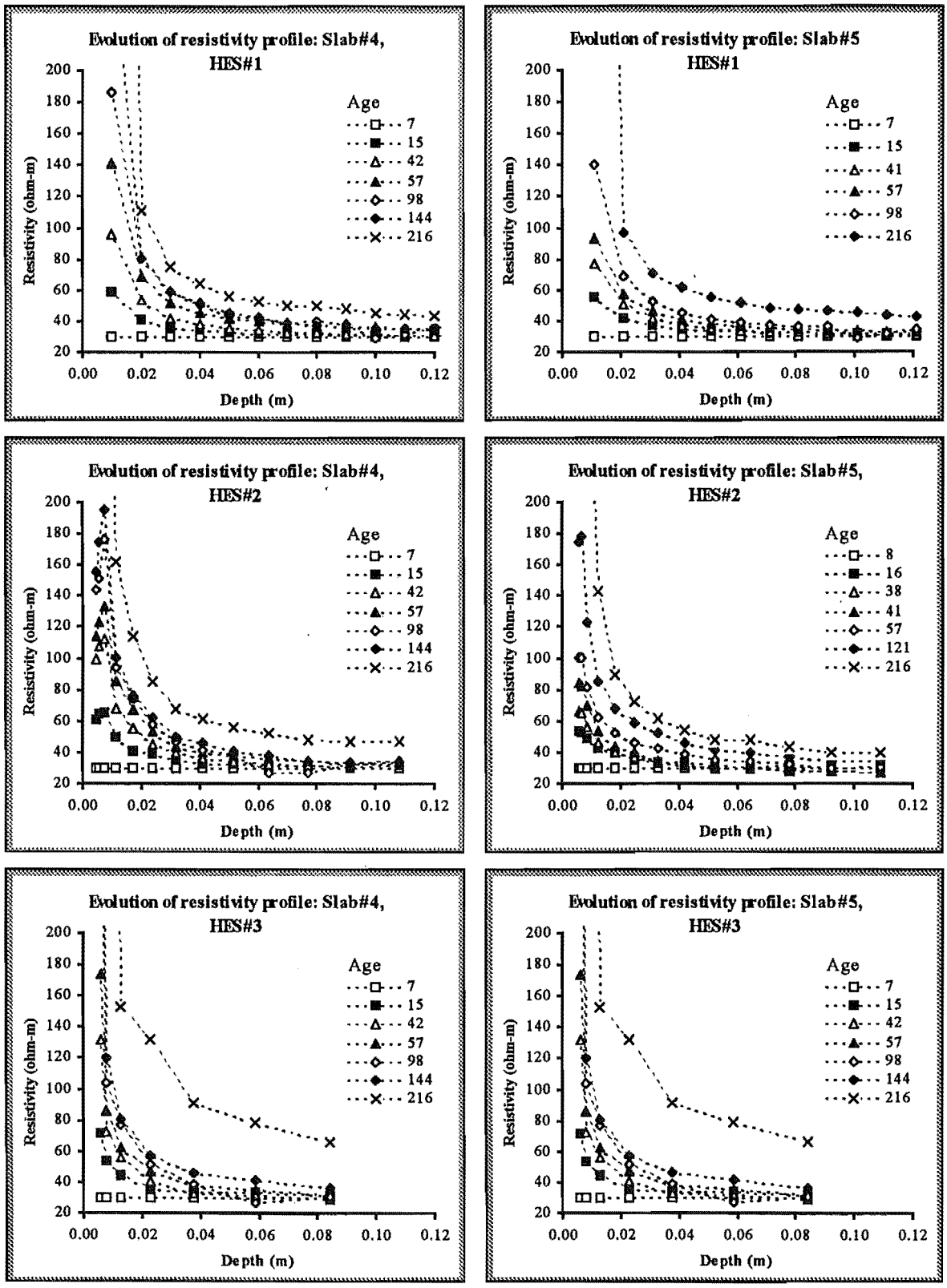

Figure E-2: Resistivity profiles from the equivalent Slabs #4 and #5

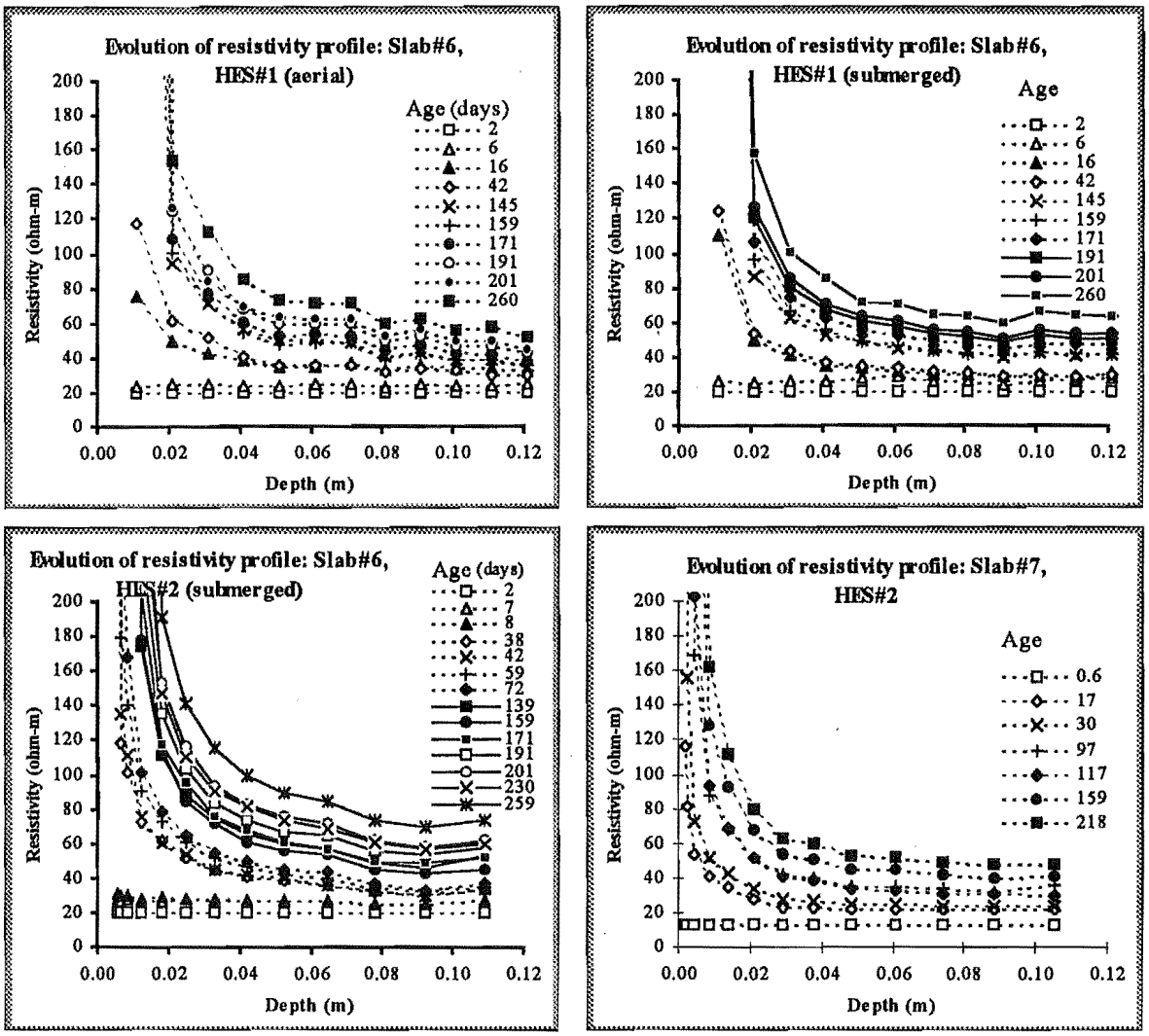

Figure E-3: Resistivity profiles from the nearly equivalent Slabs #6 and #7

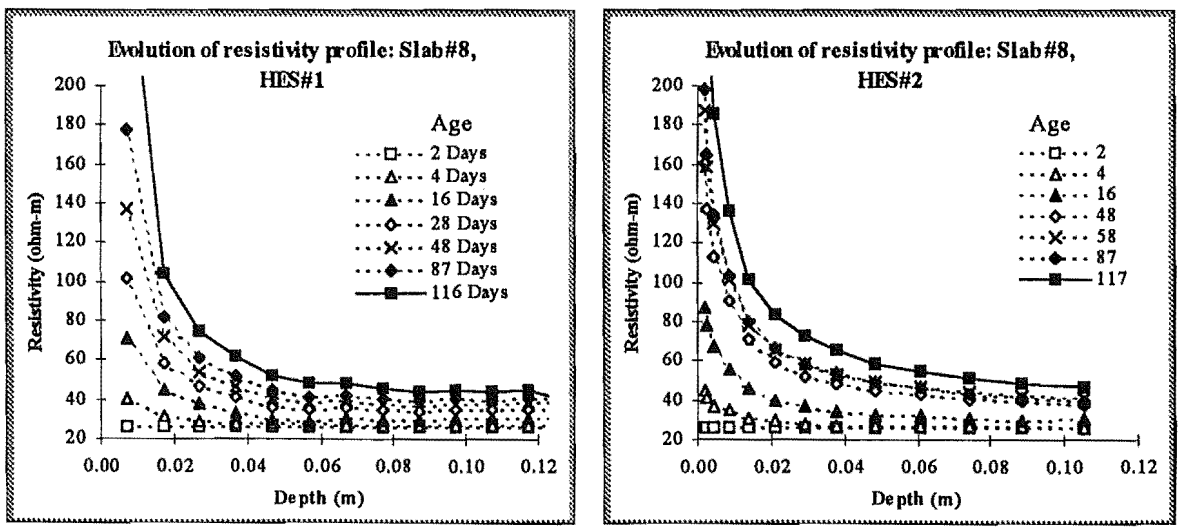

Figure E-4: Resistivity profiles from Slab #8

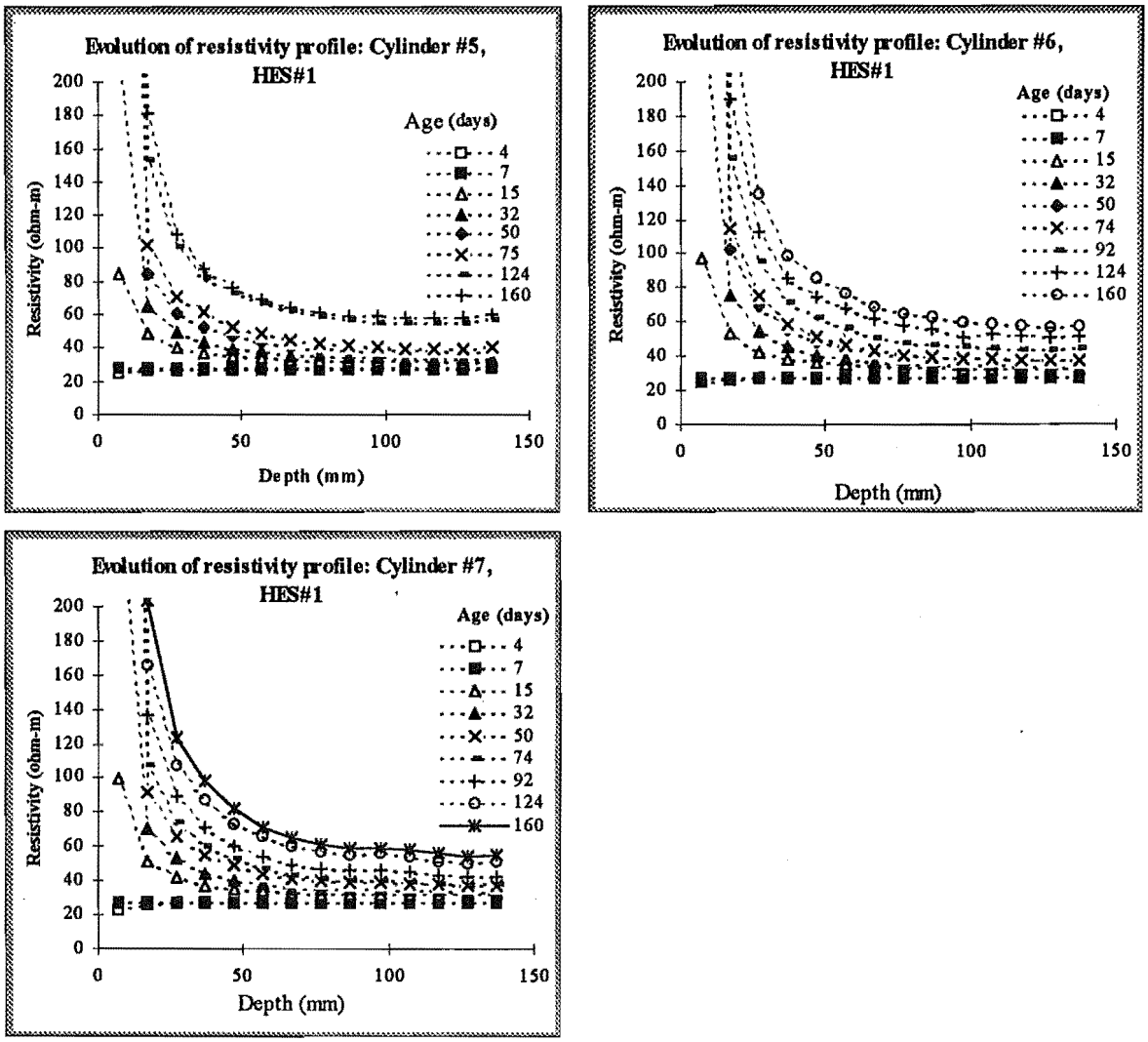

Figure E-5: Resistivity profiles fromCylinders #5, #6 and #7.

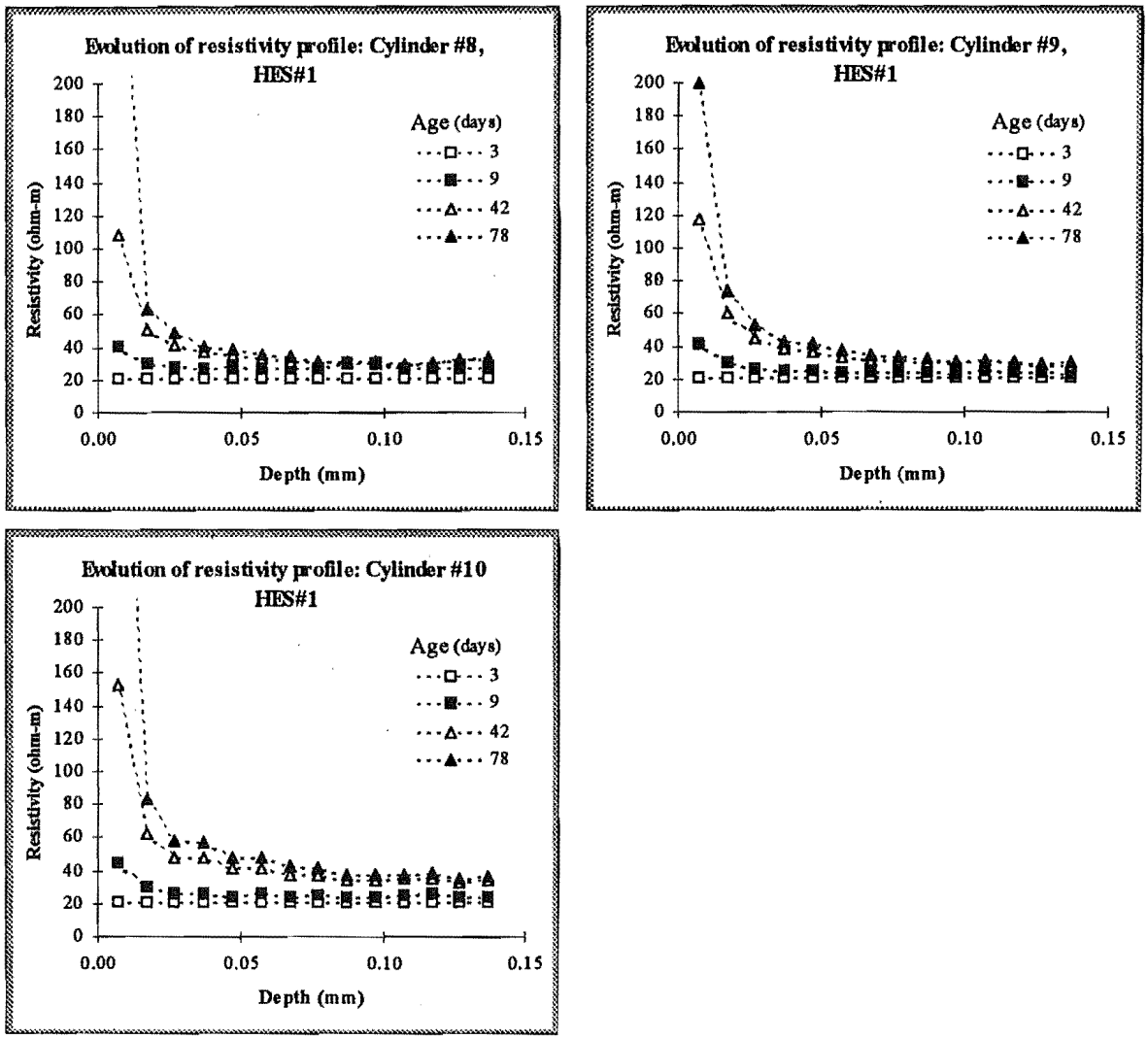

Figure E-6: Resistivity profiles fromCylinders #8, #9 and #10.

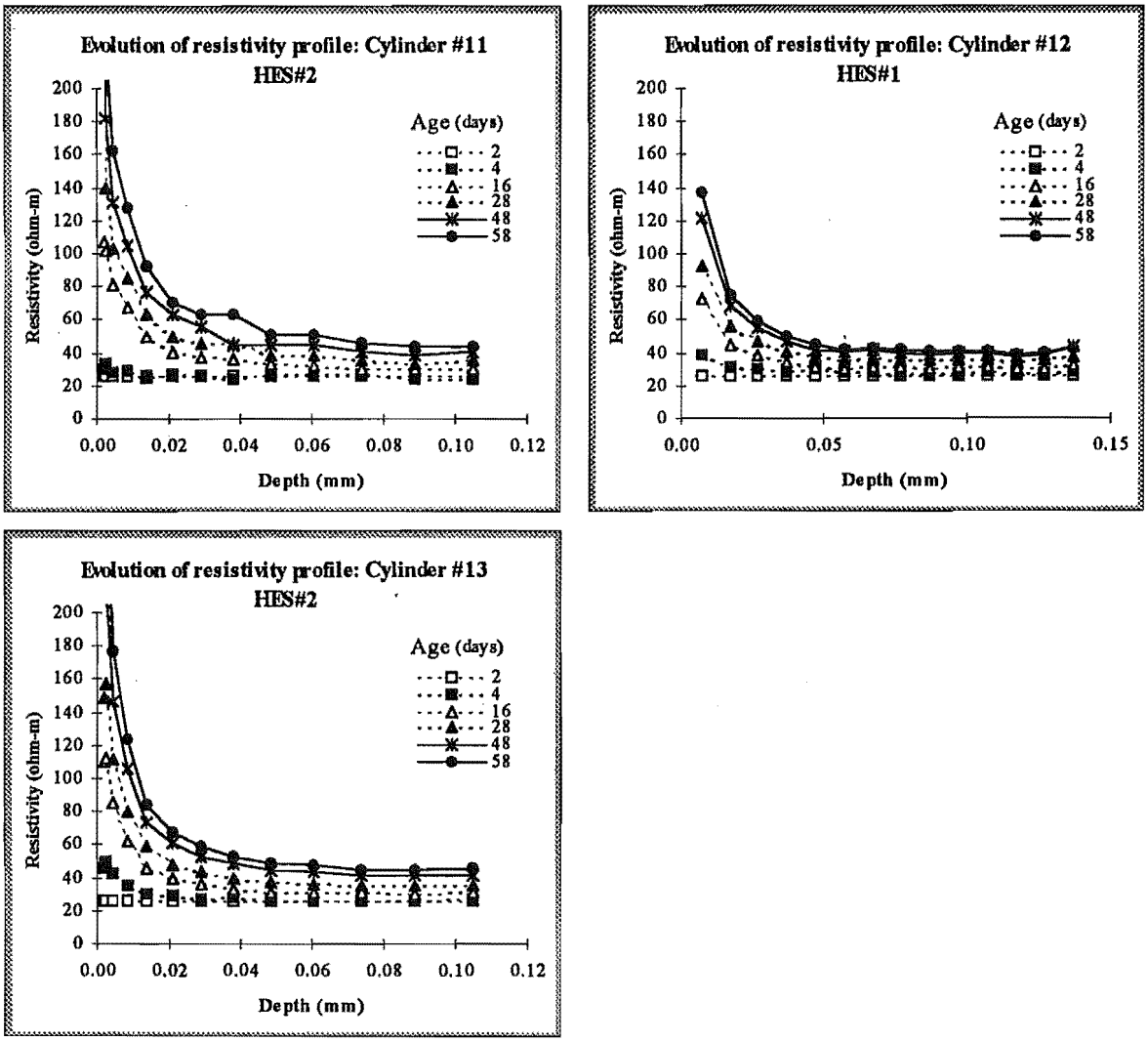

Figure E-7: Resistivity profiles fromCylinders #11, #12 and #13.

Appendix F : Relative Humidity Profiles

Relative-humidity profiles have been measured for seven cylinders and six slabs. The profiles are presented here in two forms. In the following figures, the left-hand graph shows the evolution of relative-humidity profiles over the measurement period. The right-hand graph shows the same data presented as the evolution of relative-humidity at particular measurement depths. Both presentations are useful in evaluating the measured profiles.

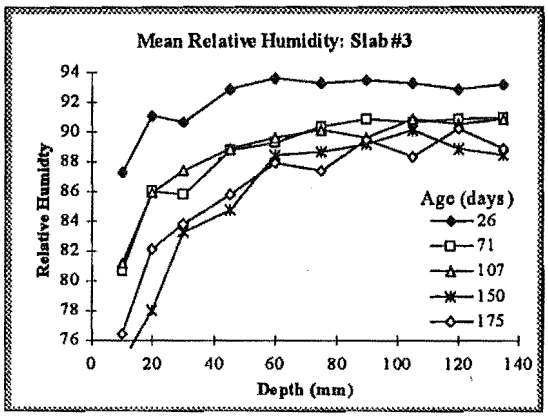

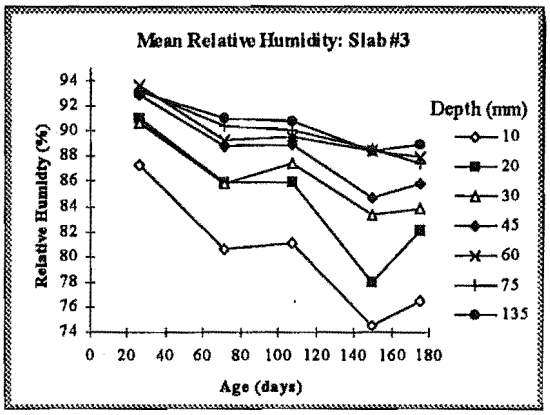

(b)

Figure F-1:Slab #3 (a)

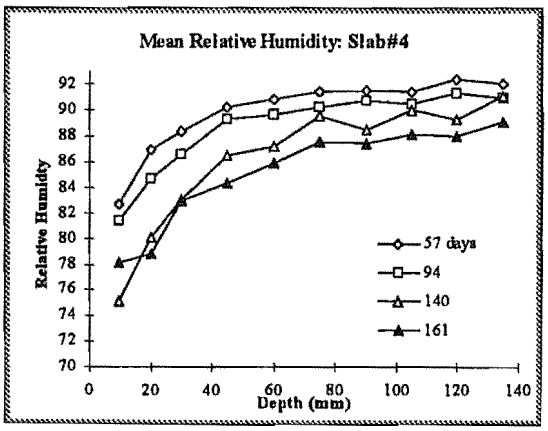

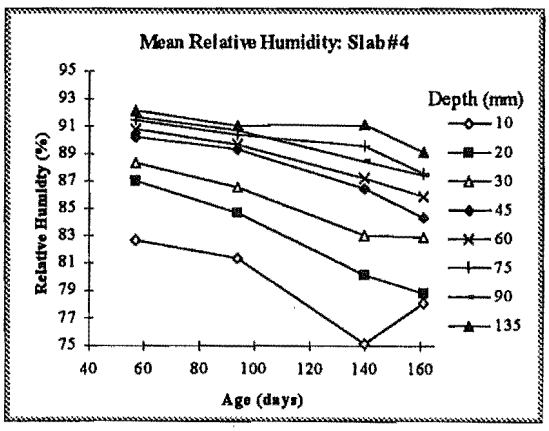

Figure F-2:Slab #4

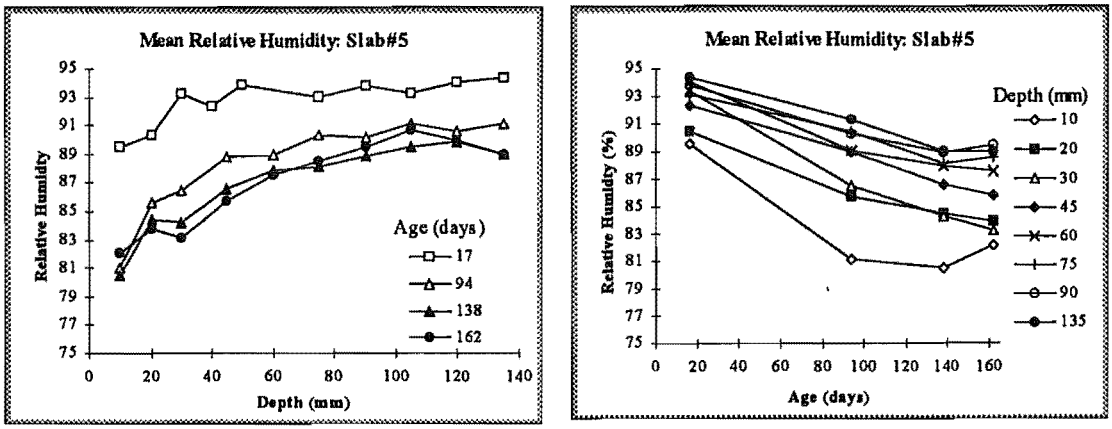

Figure F-3:Slab #5

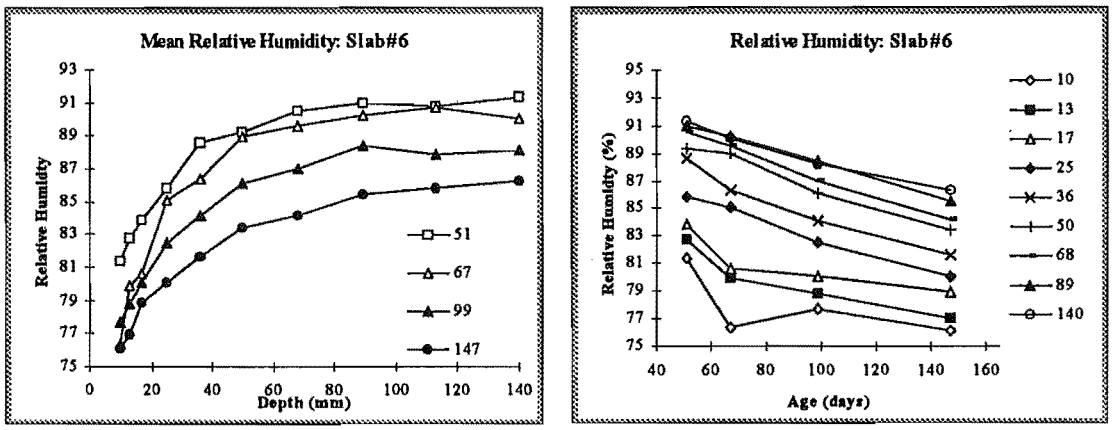

Figure F-4:Slab #6

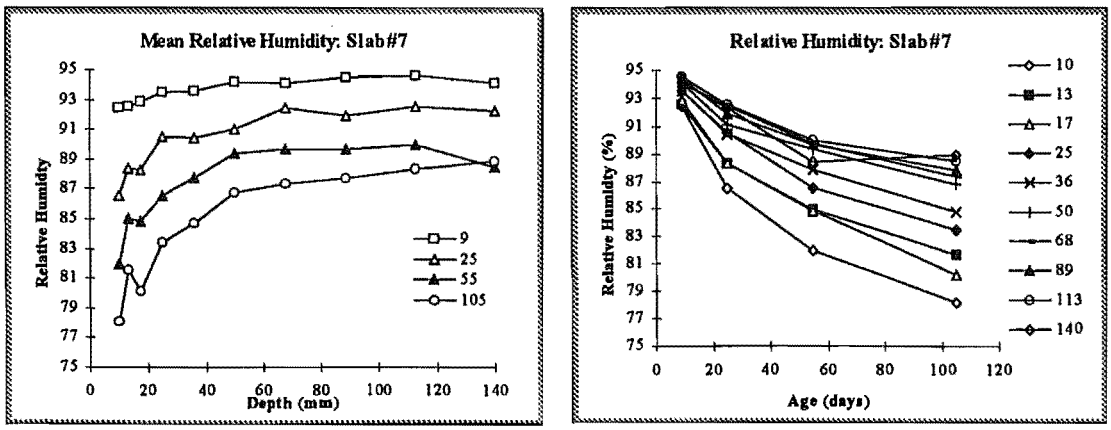

Figure F-5:Slab #7

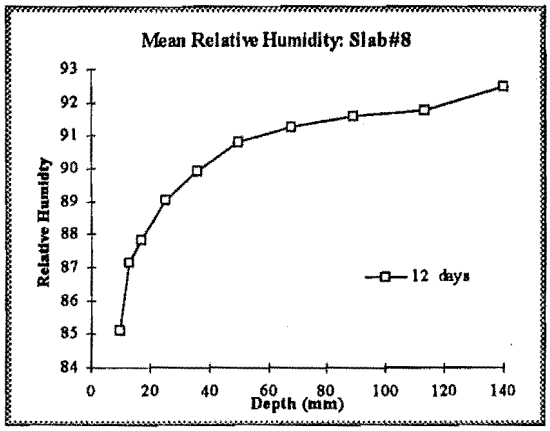

Figure F-6:Slab #8

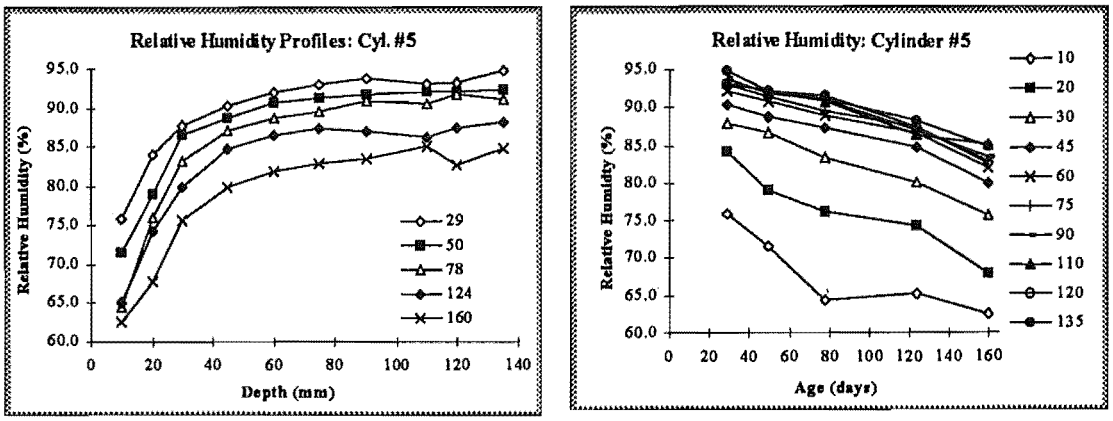

Figure F-7:Cylinder #5

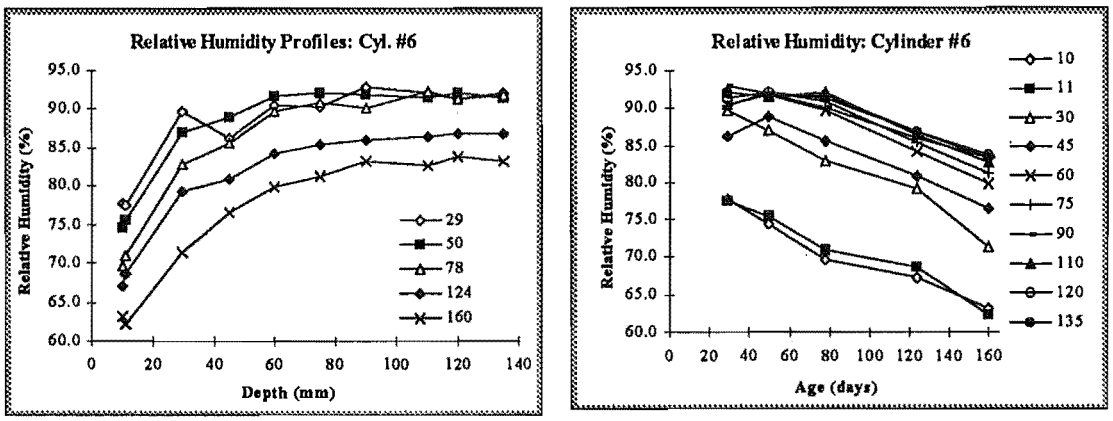

Figure F-8:Cylinder #6

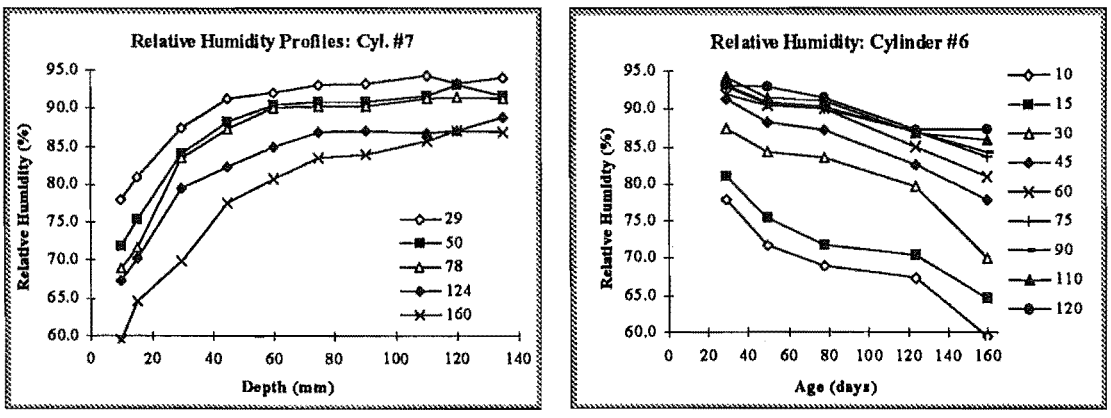

Figure F-9:Cylinder #7

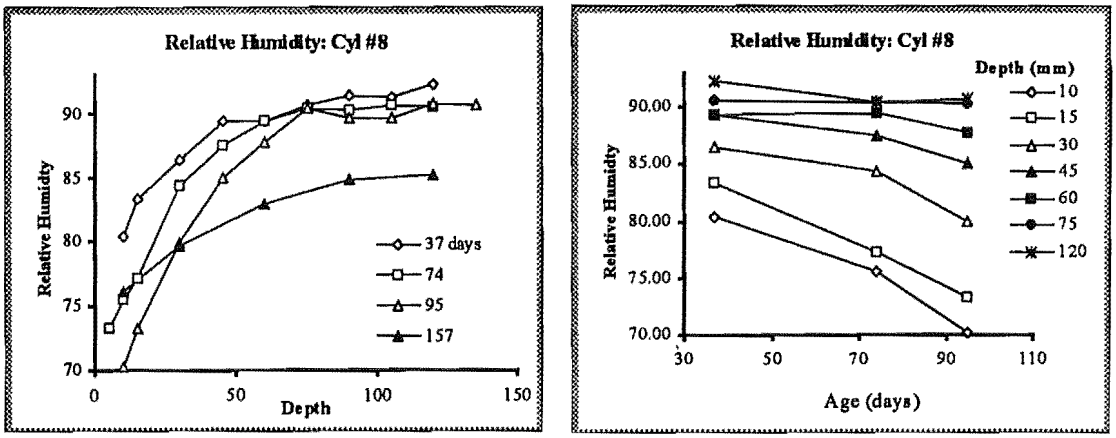

Figure F-10:Cylinder #8

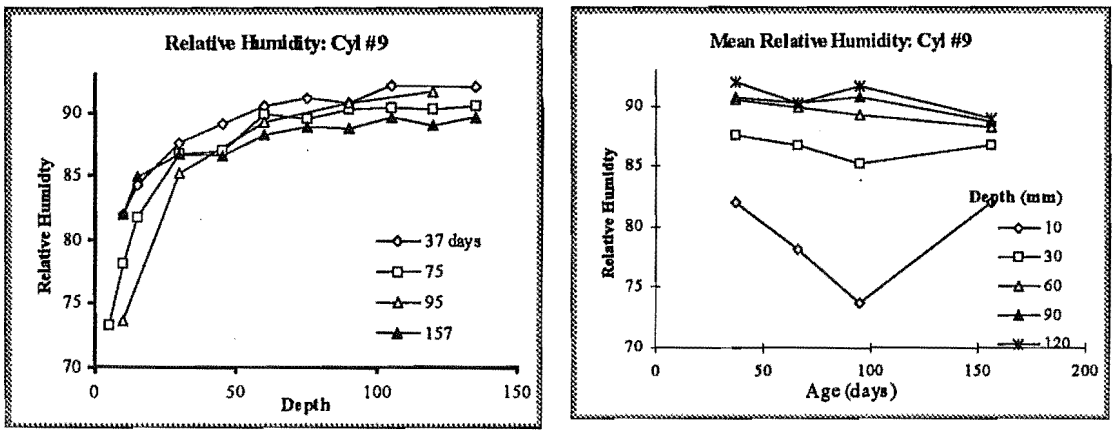

Figure F-11:Cylinder #9

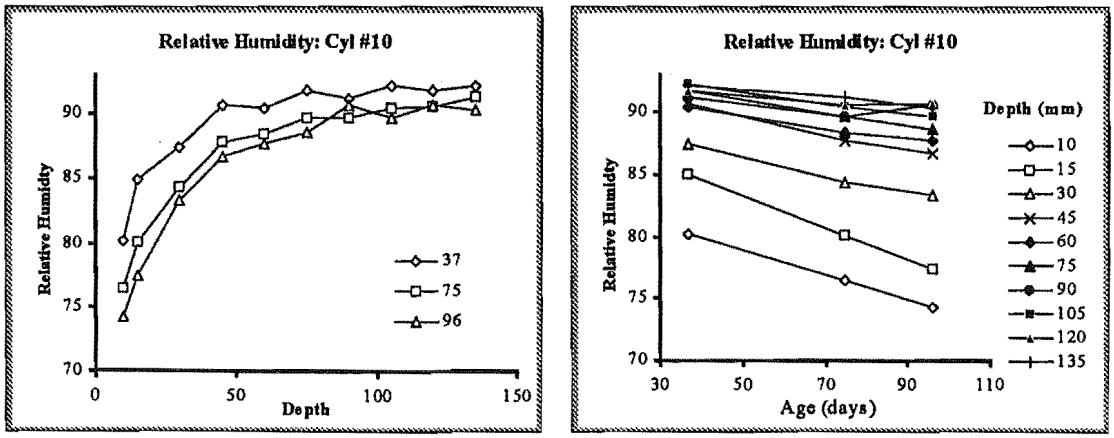

Figure F-12:Cylinder #10

Appendix G : Drift in calibration of relative-humidity probes

The relative-humidity probes were calibrated locally using three reference points: 64.4% RH (above a saturated solution of $NaNO_2$), 75% RH (above a saturated solution of NaCl) and 100% RH (above distilled water). The procedure involved recording each probe output voltage at each set point, using the three points to obtain a calibration curve for each probe. The calibration changes with time. A linear interpolation was carried out to determine the correct calibration curves at any intermediate time.

The following figures summarise the drift in calibration with time. In each set of three graphs, the first records the probe response (converted to an output RH by multiplying the output voltage by 100%) to an atmosphere of 64.4% RH, the second records the response to an atmosphere of 75% RH and the third, to 100% RH.

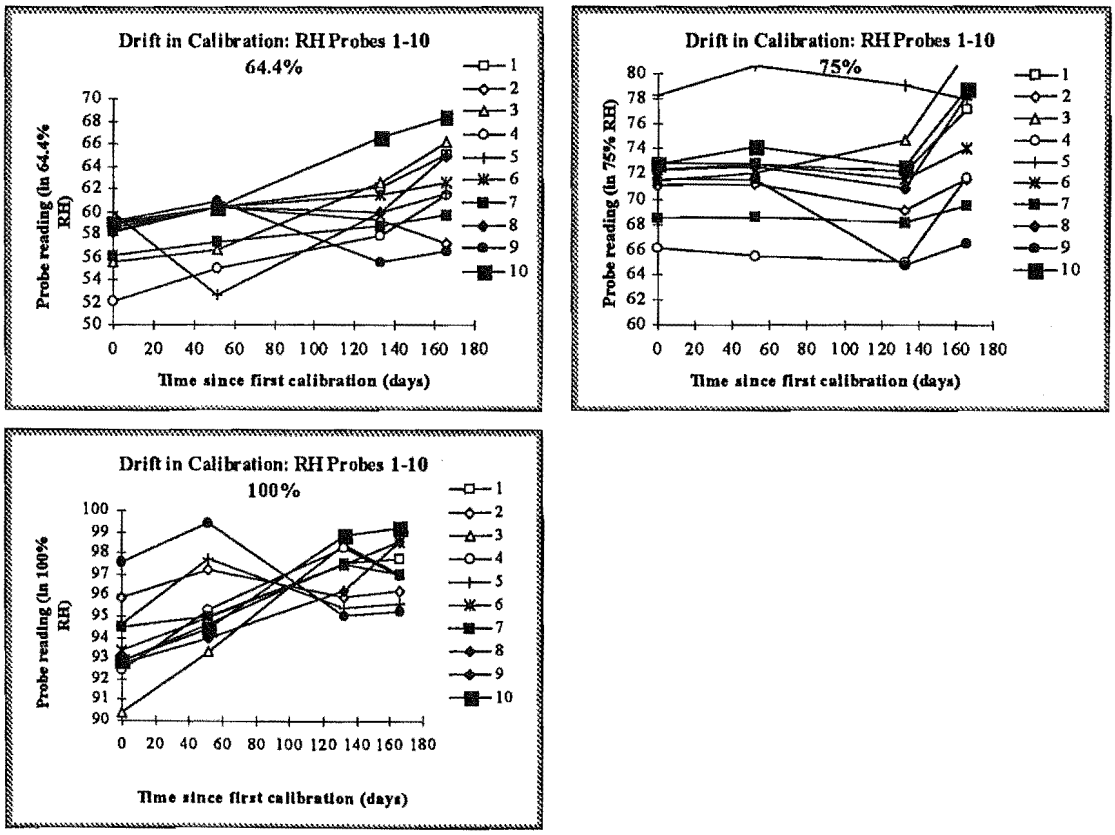

Figure G-1: Drift in calibration (uncorrected probe output multiplied by 100%), for probes 1-10.

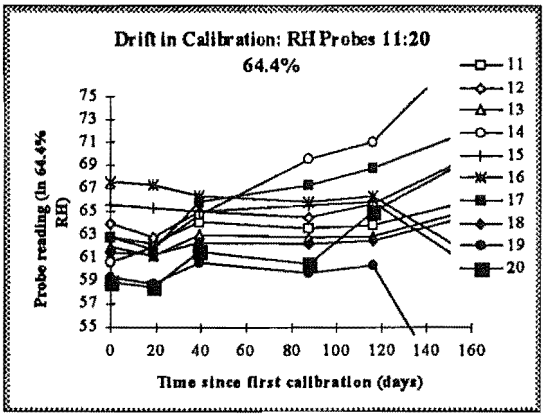

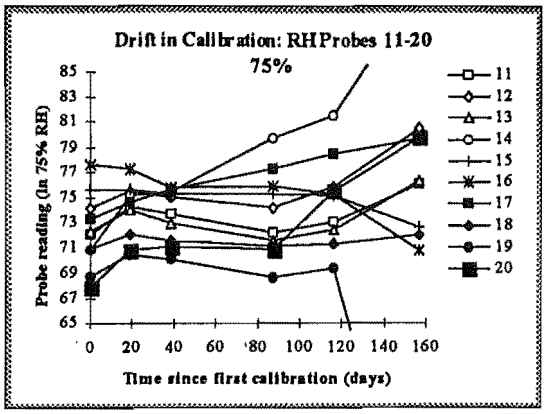

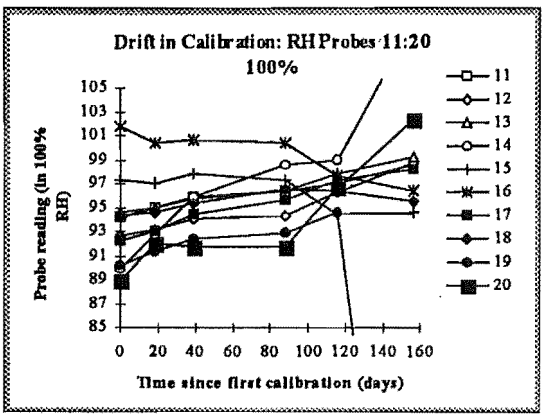

Over the set of probes the average drift is (+ 0.03) % RH /day

Figure G-2: Drift in calibration (uncorrected probe output multiplied by 100%), for probes 11-20.

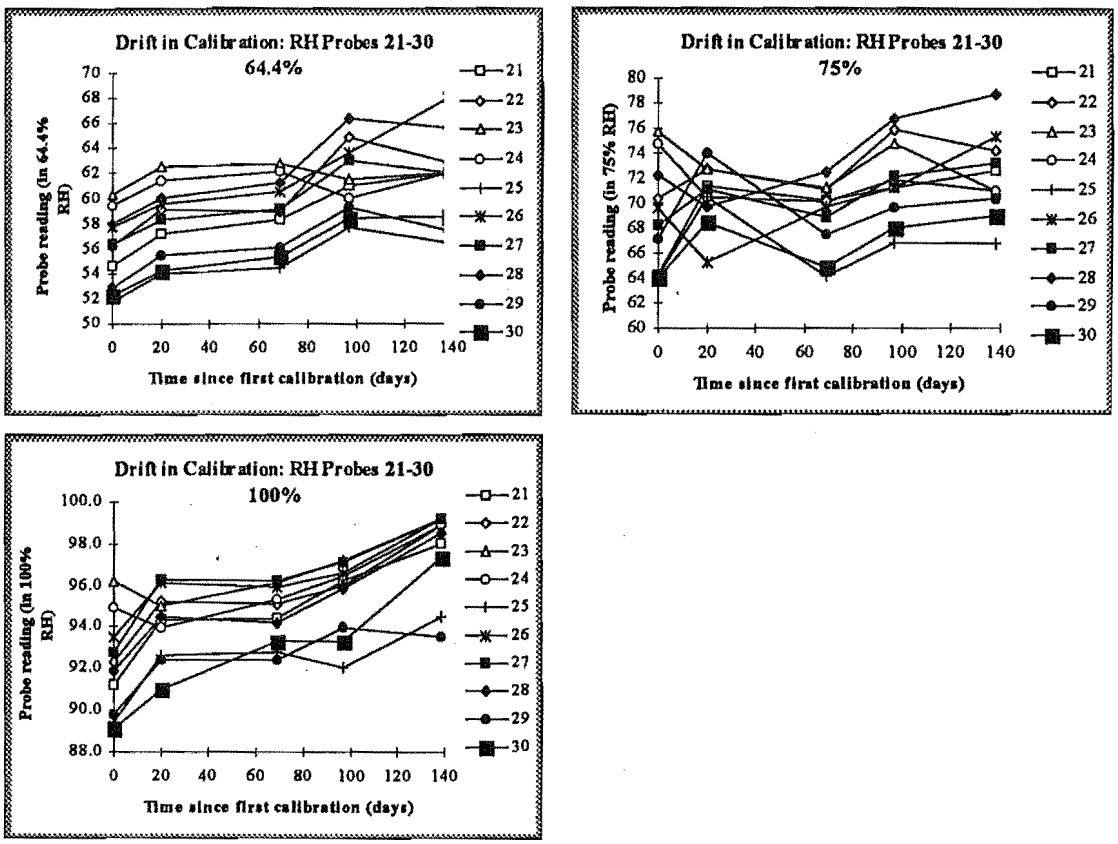

Figure G-3: Drift in calibration (uncorrected probe output multiplied by 100%), for probes 21-30.

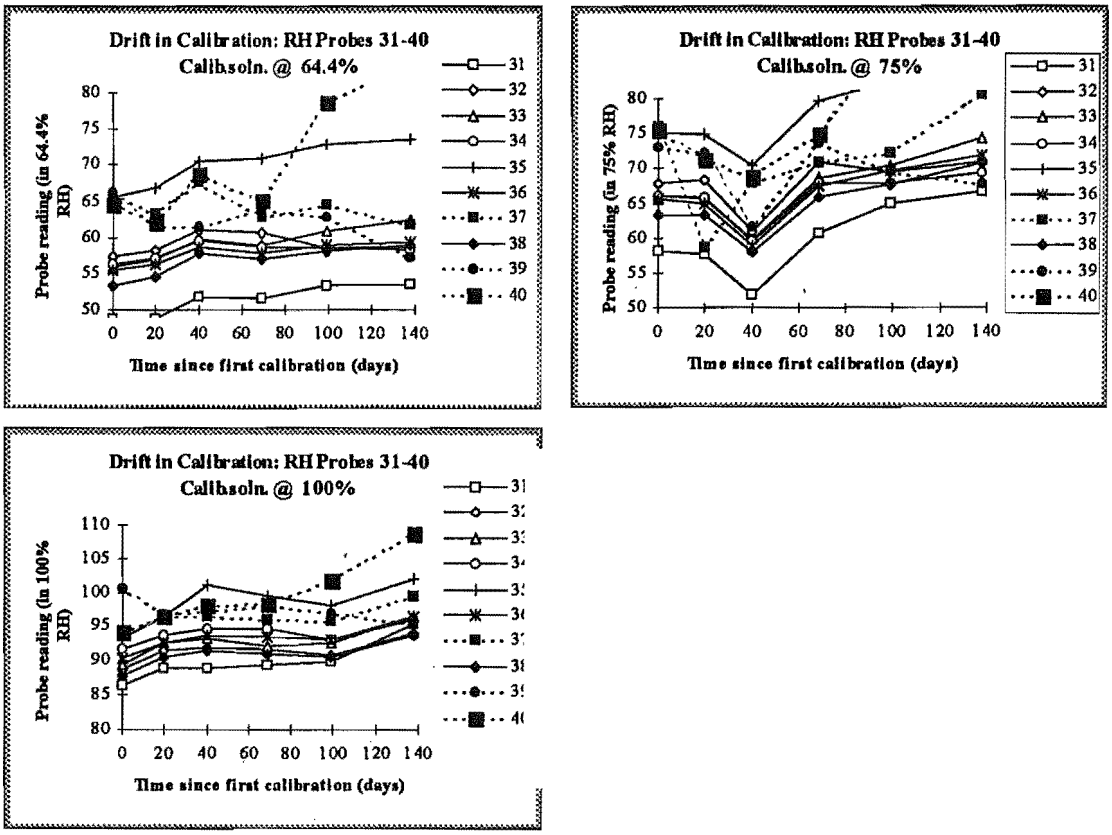

Figure G-4: Drift in calibration (uncorrected probe output multiplied by 100%), for probes 31-40.

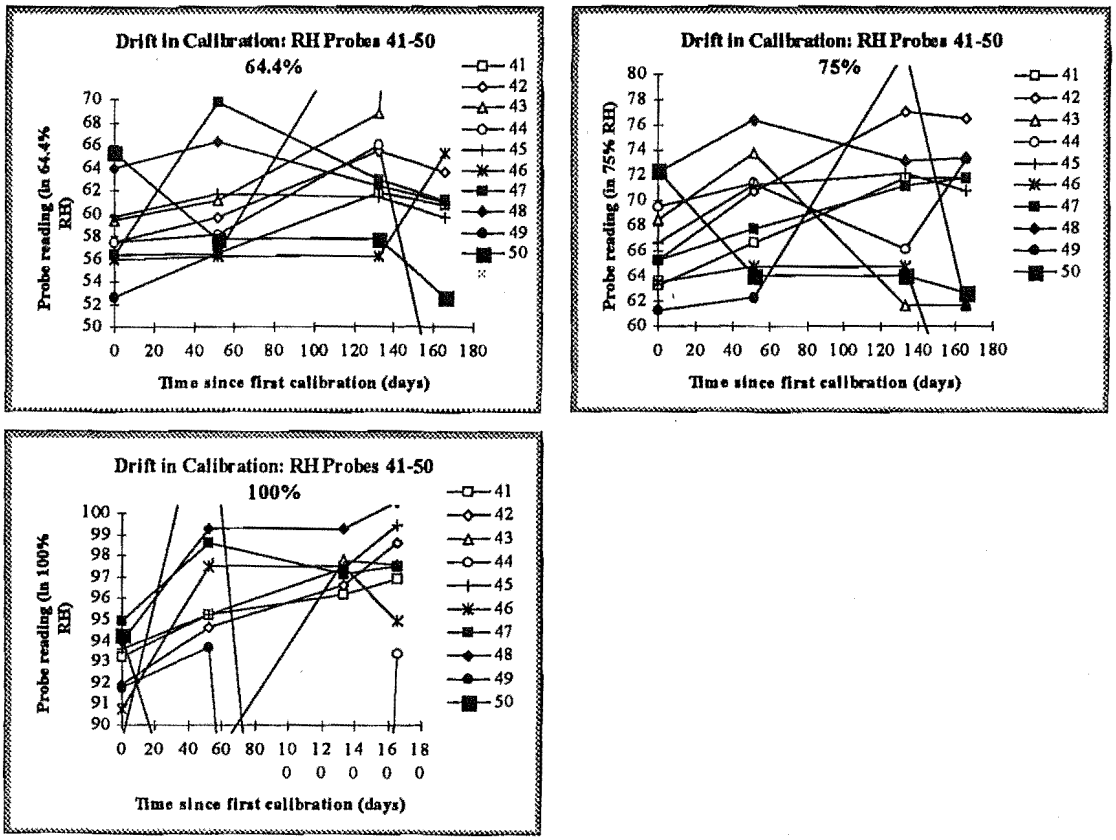

Figure G-5: Drift in calibration (uncorrected probe output multiplied by 100%), for probes 41-50.